



2013

Volume 32

Graduate School F.lli Pesenti

# Studies and Researches

*Annual Review of Structural Concrete*

Dipartimento di Ingegneria Strutturale  
*Structural Engineering Department*



EDIZIONI  
**VREADY**

**Editors:** Antonio Migliacci, Pietro G. Gambarova, Paola Ronca

**Title:** *Studies and Researches*  
*Annual Review of Structural Concrete*  
Volume 32

**All rights reserved**  
Antonio Migliacci, Pietro G. Gambarova, Paola Ronca

Pubblicato da:

E D I Z I O N I  
**IMREADY**

IMREADY Srl  
Strada Cardio, 4 - 47891 Galazzano (RSM)  
Tel. 0549 909090 – Fax 0549 909096  
info@imready.it

---

*Questa opera è protetta dalla Legge sul diritto d'autore.*

*(Legge n. 633/941: [http://www.giustizia.it/cassazione/leggi/1633\\_41.html](http://www.giustizia.it/cassazione/leggi/1633_41.html))*

*Tutti i diritti, in particolare quelli relativi alla traduzione, alla citazione, alla riproduzione in qualsiasi forma, all'uso delle illustrazioni, delle tabelle e del material software a corredo, alla trasmissione radiofonica o televisiva, alla registrazione analogica o digitale, alla pubblicazione e diffusione attraverso la rete Internet sono riservati, anche nel caso di utilizzo parziale. La riproduzione di questa opera, anche se parziale o in copia digitale, è ammessa solo ed esclusivamente nei limiti di legge ed è soggetta all'autorizzazione dell'Editore.*

*La violazione delle norme comporta le sanzioni previste dalla Legge.*

Politecnico di Milano

Concrete Structures  
"Fratelli Pesenti"

Costruzioni in Calcestruzzo  
"Fratelli Pesenti"

Studies and Researches  
*Annual Review of Structural Concrete*  
Volume 32

**Editorial Board**

Antonio Migliacci,  
Pietro G. Gambarova, Paola Ronca

**Scientific Committee**

Luigi Cedolin, Italy  
Horst Falkner, Germany  
Giorgio Macchi, Italy  
Piergiorgio Malerba, Italy  
Franco Massazza, Italy  
Franco Mola, Italy  
Luc Taerwe, Belgium  
Giandomenico Toniolo, Italy  
Joost Walraven, The Netherlands  
Folker Wittmann, Germany



# STUDIES AND RESEARCHES

## *Annual Review of Structural Concrete*

Volume 32 - 2013

<b>Guest Editorial</b> .....	7
<i>Luigi Cedolin</i>	
<b>Editors' Note</b> .....	11
<i>Pietro G. Gambarova, Antonio Migliacci and Paola Ronca</i>	
 <b>Technical Papers</b>	
Constitutive Behavior of a Fiber-Based Beam Element for Reinforced Concrete Modelling under Cyclic Loading.....	17
<i>T.R.S. Mullapudi and Ashraf Ayoub</i>	
Analysis of Reinforced-Concrete Structures Taking into Account Creep and Cracking.....	55
<i>Ali Faris</i>	
Time-Dependent Effects in Segmental Bridges: Predictive Models and Analysis via Simplified Methods.....	73
<i>Marcello Arici, Michele Granata and Piercarlo Margiotta</i>	
Assessment of the Effective Stiffness in R/C Frames Subjected to Seismic Loading.....	105
<i>Francesco Micelli and Angelo S. Carone</i>	
Evaluation of the Carrying Capacity of Reinforced Concrete Slabs Subjected To Concentrated Loads Close to the Supports.....	131
<i>Beatrice Belletti, Cecilia Damoni and Max Hendriks</i>	
Modelling of Large Lightly-Reinforced R/C Walls.....	159
<i>Marisa Pecce, Francesca Ceroni and Fabio Bibbò</i>	
Spalling and Tension Stiffening in Heat-Exposed Members Made of Self – Compacting Concrete.....	179
<i>Francesco Lo Monte</i>	
Damage Assessment of Concrete Subjected to High Temperature by Means of the Ultrasonic Pulse Velocity – UPV Method.....	201
<i>Izabela Hager, Hélène Carré and Katarzyna Krzemien</i>	

A Handy Model for Simulating the Hydration Phenomena in Concrete: General Formulation and Application to Recycled-Aggregate Concrete.....	217
<i>Eduardus A.B. Koenders and Enzo Martinelli</i>	

**Technical Notes**

Experimental Behaviour of Semi-Dry Column-Foundation Connections for Precast Buildings.....	249
<i>Bruno Dal Lago, Marco Lamperti and Gian Domenico Toniolo</i>	
Simplified Approach for Punching Shear in Fire Conditions.....	269
<i>Emmanuel Annerel, Limin Lu and Luc Taerwe</i>	
Actual Prestress Loss and Camber Evolution in Self-Compacting Prestressed Wing-Shaped Members.....	285
<i>Marco Breccolotti and Annibale Luigi Materazzi</i>	
Structural Behavior of Historical Stone Arches and Vaults: Experimental Tests and Numerical Interpretation.....	305
<i>Claudio Mazzotti, Marco Bovo and Marco Savoia</i>	

<b>Acknowledgements</b> .....	331
-------------------------------	-----

<b>Preparation of Manuscripts</b> .....	333
-----------------------------------------	-----

<b>News of the School “Fratelli Pesenti”</b> .....	337
----------------------------------------------------	-----

## Guest Editorial

The consequences of the current economic and financial crisis on civil engineering and its industry, and the saturation of the construction market for either office or industrial use have been analyzed in the foreword of the preceding Volume 31, where the lack of significant investments on new infrastructural projects was shown to derive from insufficient public funding and from the absence of political will for long-term economic strategies, beyond the horizon of the next electoral campaign. In the same editorial, the need for sustainable constructions was stressed (durability, affordability during the entire lifetime, low environmental impact and safety with regard to overloads such as earthquakes or meteorological hazards). A final observation concerned the rather limited effects that today's economic crisis seems to have on the activity of the academic and professional communities engaged in innovation and research, as tough times are providing additional stimuli to develop new materials and products, to better characterize their behavior and performance, and to revise and update the design codes.

The above three points are still valid after one year! The economic situation has not improved significantly, but the need for a public stimulus has become more evident. As a matter of fact, monetary economics studies indicate that the construction of new infrastructures and the renovation of existing infrastructures should be a primary concern, because any social and economic development is based on the easy access to goods, services and resources. The principles of sustainable development are more and more penetrating into everyday culture, through the actions of professional societies, educational institutions and the media. A multi-disciplinary approach, however, is needed in the design, that should take care of acoustical, functional and aesthetical aspects since its earliest phases, to avoid expensive modifications during the structural lifespan.

With reference to concrete infrastructures (bridges, containment structures, tunnels, dams, ports, airports and off-shore structures), in the current year at least fifteen international conferences and workshops have focused their attention on various aspects of sustainability, like structural performance (fracture propagation in punching and shear, size effect, seismic loading, creep and shrinkage effects, assessment of structural conditions, repair and updating), materials' performance (including fiber-reinforced cementitious composites and polymer-modified mortars), and materials' response (to understand the basic physical phenomena in order to develop reliable theoretical and numerical models).

All these issues would be worth of illustration and comments, but the modeling of materials' response is privileged in the following for both its generality and central role in the structural domain, as shown by the three topics presented below.

A first topic is the prediction of concrete long-term deformations. Recently-reported experimental results and well-documented excessive deflections exhibited by box-girder bridges have shown that creep deformations are underestimated by the creep-compliance curves recommended in the major design codes, where horizontal asymptotes are introduced. Comparative analyses among the creep and shrinkage strains predicted by the different codes have also highlighted another shortcoming, i.e. that the structure of the models does not allow to recalibrate their parameters on the basis of the short-term creep deformations measured in a lab environment. The practical relevance of this shortcoming

has been confirmed by a recent research project in progress at the Politecnico di Milano, on the delayed deformations of a concrete mix selected for the construction of a major P/C segmental bridge. With reference to a three-month period after concrete setting, the differences between the measured deformations and those predicted in accordance with standard code recommendations were sizeable indeed, as a demonstration of the inadequacy of these recommendations for the adjustment of tendon stressing during the construction process.

A second topic is the use of *discrete* models to characterize concrete behavior. This trend has been growing significantly in the last few years, as demonstrated by the sessions dedicated to this topic in many conferences and workshops. A first reason of this success is related to the difficulty met by *continuous* models in predicting concrete complex behavior under different stress states (tension, compression, multi-axial loading, crack propagation), while a second reason is related to the ability of *discrete* models to provide a direct description of concrete internal structure, which is responsible for the complexity of concrete behavior. *Discrete* models have also the capability of covering different length scales in the representation of concrete's internal structure, from the nano- and micro-levels of the cement paste to the meso-level of aggregate particles and fibers. A very effective model is the so-called Lattice Discrete Particle Model (LDPM), in which the coarse aggregates are modeled by means of rigid particles whose size respects the actual aggregate grading and which are connected by lattice elements obtained through a mathematical algorithm (Delaunay triangulation of the particle centers). By connecting the centers of the particles, these elements introduce into the model the constitutive relations established at the meso-level (i.e., softening in tension, shear tension and shear compression with low compression, hardening for compression, and shear with high compression). Progressively improved since its introduction, the LDPM is now able to describe concrete behavior under any stress state, from tension with crack propagation to compression in highly-confined conditions and rate effects.

A third topic is the need for any given type of concrete to be characterized under all the possible stress states to be met during the structural life, these stress states being represented by the available standard tests (uniaxial compression, uniaxial tension, confined compression, indirect tension by splitting, fracture in bending with notched specimens of different size, dynamic tests with the split Hopkinson's bar). This approach, well known to the developers of theoretical and numerical models (often obliged to switch from one experimental investigation to the other to validate their numerical models), has been recently adopted in an experimental campaign carried out in Milan to investigate the effect that aggregate size may have on the mechanical behavior of a typical concrete to be used in massive structures, like - for example - dams. This investigation is making it clear that complex tests designed to reproduce *ideal* experimental conditions (something often difficult or expensive) are less needed today than in the past, since the numerical models can simulate even very complex *actual* conditions.

Hence, rarely the apparent simplicity of a material like concrete has required – and will require - such high-level and challenging models and tests!

Luigi Cedolin (*Professor Emeritus, Politecnico di Milano, Milan, Italy*)



## Editoriale su invito

Le conseguenze dell'attuale crisi economica e finanziaria sull'ingegneria Civile e sulla sua industria, così come la saturazione del mercato delle costruzioni ad uso sia abitativo che industriale sono state analizzate nella premessa al Volume 31, ove è stato sottolineato come la mancanza di adeguati investimenti in campo infrastrutturale sia il risultato di insufficienti finanziamenti pubblici e di mancanza di volontà politica per strategie a lungo termine, oltre l'orizzonte delle tornate elettorali. Nella stessa premessa è stata sottolineata la necessità della sostenibilità delle costruzioni, in termini di durabilità, costi durante l'intera vita operativa, impatto ambientale, e sicurezza a fronte di carichi eccezionali dovuti – ad esempio - a sisma ed ambiente. Un'osservazione finale ha riguardato gli effetti tutto sommato limitati che l'attuale crisi sta avendo sull'attività di ricerca e sviluppo nel mondo accademico e professionale, probabilmente perchè i tempi difficili forniscono ulteriori stimoli allo sviluppo di materiali e prodotti innovativi, al miglioramento delle loro proprietà e prestazioni, ed alla revisione ed aggiornamento delle normative di progettazione.

I tre punti appena citati sono tuttora validi, ad un anno di distanza! La situazione economica non è sensibilmente migliorata, ma la necessità di uno stimolo pubblico è diventata sempre più evidente, in quanto molti studi indicano come la costruzione di nuove infrastrutture ed il rinnovamento di infrastrutture esistenti siano di fondamentale importanza per lo sviluppo sociale ed economico, basato – come è ben noto - su un facile accesso a beni, servizi e risorse. D'altro canto, i principi dello sviluppo sostenibile stanno sempre più diffondendosi nell'opinione pubblica, grazie all'azione combinata delle istituzioni professionali ed educative, e dei mezzi di informazione, e mostrano sempre più come sia necessario un atteggiamento multidisciplinare capace di tener conto di tantissimi aspetti (acustici, funzionali ed estetici) fin dalle fasi iniziali della progettazione, per evitare interventi e costi aggiuntivi durante la vita operativa della costruzione.

Con riferimento alle infrastrutture in calcestruzzo (ponti, gusci di contenimento, gallerie, dighe, porti, aeroporti e strutture marine), almeno una quindicina di conferenze e convegni internazionali hanno posto in prima linea nell'anno corrente i temi della sostenibilità, quali le prestazioni strutturali (propagazione della fessurazione nel punzonamento e taglio, effetto dimensionale, sollecitazioni sismiche, effetti di viscosità e ritiro, valutazione della sicurezza strutturale, riabilitazione e rafforzamento strutturale), le prestazioni dei materiali (ivi compresi i materiali cementizi fibrorinforzati e le malte polimeriche), e la risposta dei materiali (per comprendere i fenomeni fisici alla base del loro comportamento, al fine di sviluppare modelli teorici e numerici affidabili).

Tutti questi aspetti meritano considerazione, ma viene qui privilegiata la modellazione della risposta del materiale, per la sua centralità in campo strutturale, come mostrano i tre temi illustrati nel seguito.

Un primo tema riguarda la modellazione delle deformazioni a lungo termine del calcestruzzo. Recenti risultati sperimentali e ben documentate misure sulle eccessive deformazioni in ponti a cassone hanno mostrato come le deformazioni viscoso siano sistematicamente sottovalutate dai modelli presenti nelle normative progettuali più accreditate, che prevedono andamenti asintotici. L'analisi comparativa dei vari modelli relativi a viscosità e ritiro ha mostrato anche un'ulteriore limitazione dovuta al fatto che la

stessa struttura dei modelli non permette di ricalibrare i loro parametri sulla base delle deformazioni viscosi di breve durata misurate in prove di laboratorio. L'importanza pratica di questa limitazione è stata confermata da un recente progetto di ricerca in atto presso il Politecnico di Milano, in tema di deformazioni differite in un calcestruzzo per ponte precompresso costruito a conci. A tre mesi dalla maturazione del calcestruzzo, le differenze fra spostamenti misurati e spostamenti calcolati in base alle raccomandazioni da normativa si sono rivelate molto consistenti, a dimostrazione della inadeguatezza di tali raccomandazioni per la tesatura dei cavi.

Un secondo tema riguarda la descrizione del comportamento del calcestruzzo con modelli *discreti*, il cui uso è andato via via crescendo negli ultimi anni, come dimostrano le sessioni dedicate all'argomento in numerosi congressi e convegni. Una prima ragione di tale successo sta nella incapacità dei modelli *continui* nel descrivere adeguatamente il complesso comportamento del calcestruzzo al variare dello stato tensionale (trazione, compressione, regime pluriassiale, propagazione della fessurazione), mentre una seconda ragione ha a che fare con la capacità dei modelli *discreti* nel descrivere in modo diretto la struttura del calcestruzzo, che è la principale responsabile del complesso comportamento di tale materiale e che presenta vari livelli di scala, dal nano- e micro-livello della pasta di cemento al meso-livello delle particelle di aggregato e delle fibre. Tra i modelli *discreti* è di particolare efficacia il modello a particelle discrete collegate da un reticolo di aste (Lattice Discrete Particle Model - LDPM), in cui l'aggregato grosso è rappresentato da particelle rigide collegate da aste deformabili atte a tener conto del comportamento non lineare del calcestruzzo. (Il graticcio di aste è ottenuto con un algoritmo matematico basato sulla triangolazione di Delaunay). Fin dalla sua introduzione, il modello LDPM è stato progressivamente migliorato, al punto che è ora in grado di descrivere il comportamento del calcestruzzo in pressochè qualsiasi stato tensionale, dalla trazione con propagazione della fessurazione alla compressione in regime confinato ed alle alte velocità di deformazione.

Un terzo tema è rappresentato dalla necessità di caratterizzare ogni calcestruzzo per tutti i possibili stati tensionali prevedibili durante la vita strutturale, con uso di numerose prove in gran parte standardizzate (compressione e trazione monoassiale, compressione in regime confinato, trazione indiretta per spacco, frattura in flessione con provini intagliati di diverse dimensioni, prove dinamiche con uso della barra di Hopkinson). Tale modo di procedere – ben noto a coloro che si occupano di modellazione teorica o numerica (spesso obbligati a passare attraverso varie modalità sperimentali per validare i propri modelli) – è stato recentemente adottato a Milano per studiare i possibili effetti della dimensione dell'aggregato sul comportamento meccanico di un tipico calcestruzzo per strutture massicce, quali ad esempio le dighe. Questo studio sta mettendo in chiaro come sia oggi possibile rinunciare - almeno in parte - a condizioni *ideali* di sperimentazione (spesso di difficile e costosa realizzazione), dato che i modelli numerici possono simulare anche condizioni *reali* molto complesse.

Si può quindi concludere che raramente un materiale apparentemente così semplice come il calcestruzzo ha richiesto – e continuerà a richiedere - un così elevato livello di modellazione e di sperimentazione!

Luigi Cedolin (*Professore Emerito, Politecnico di Milano*)

## Editors' Note

The challenging framework described in the guest editorial is a worthy introduction for this Volume 32 of Studies and Researches, which intends to contribute in different directions, with nine Technical Papers and four Technical Notes.

Cyclic loading, creep, cracking and their structural effects are the unifying factor of the first four papers, where different types of analysis are applied to R/C and P/C beams, frames and segments (in segmental bridges) weakened by a variety of factors.

Mullapudi and Ayoub develop a fiber-based beam element for reinforced-concrete modeling under cyclic loading, while Ali simplifies the iterative procedure required to take care of creep-related stresses and creep-induced cracking in R/C frames.

Arici, Granata and Margiotta propose a procedure to evaluate time-dependent effects in segmental bridges, whose constraints are changed during the structural life, and Micelli and Carone apply five different approaches to evaluate the effective stiffness in R/C cracked members.

Bi-dimensional structures – either slabs or walls – are the subject of the fifth and sixth papers. R/C slab punching is treated by Belletti, Damoni and Hendriks, who apply nonlinear FE analysis to a comprehensive series of slabs subjected to near-support punching, while Pecce, Bibbò and Ceroni examine the nonlinear behavior of lightly-reinforced shear walls, to formulate a simplified model for the evaluation of their capacity in bending and shear, under seismic loading.

High temperature and fire come into play in the seventh and eighth papers, where cover spalling and tension stiffening in R/C beams are investigated and modeled by Lo Monte, while Ultrasonic Pulse Velocity is used by Hager, Carré and Krzemień to assess the heat-induced damage in the concrete after a fire.

Temperature – but at a much lower level – occurs in the ninth paper as well, where Koenders and Martinelli formulate a handy but consistent model to describe the heat-flow and transport phenomena occurring in hardening cement mixes, with an application to Recycled-Aggregate Concrete, a popular subject today in the vast domain of recycling.

As for the notes, the first three are about as many different topics, that range from the cyclic behavior of *dry* connections at the foot of pre-fabricated columns (an appealing subject in seismic areas, as shown by Dal Lago, Lamperti Tornaghi and Toniolo) to the punching shear in thin floors subjected to fire (a rather frequent event in parking garages, where restrained thermal dilation increases fire resistance, as indicated by Annerel and Taerwe), and to short-term prestress losses in wing-shaped large-span P/C girders, a rather critical problem in the prefabrication industry as illustrated by Breccolotti and Materazzi.

The fourth note is a very effective example of how to combine in-situ testing and numerical modeling to analyze the complex behavior of historical buildings. The ductility under horizontal forces is numerically investigated and experimentally checked by Bovo, Mazzotti and Savoia in the case of two huge interconnected storehouses located in Trieste (Italy), whose eighteenth-century structure consists of arches, vaults, barrel-shaped roofs, thick walls and short columns.

Reading the technical papers and notes of this volume allows to recognize that two are basically the issues, even if examined from different points of view: the seismic behavior of R/C and P/C structures, and the structural robustness.

For today's scholars, technicians, contractors and simple citizens aware of the social and economical challenges brought in by our complex way of living, the two above-mentioned issues are as many landmarks, that should shape both scientific activity and engineering applications, in order to improve the knowledge of seismic and unexpected actions, and to mitigate their consequences.

With reference to seismic actions and to their consequences – something of the upmost relevance in Italy, whose territory is entirely earthquake-prone – the activation of anticipated brittle-failure mechanisms should be avoided (like shear failure in short columns). This may be achieved by adopting a sound hierarchical organization of the structural members. Furthermore, “prevention” should be the password, as a far cheaper alternative to any intervention after often catastrophic events!

With reference to structural robustness, considering unexpected actions (like fire, blast, impact) since the earliest phases of the design is a must for many strategic or crowded structures. Similarly to seismic events, “prevention” in lieu of “intervention past the accident” should be the password, as many sad and often horrible terroristic attacks have demonstrated.

The previous issues have been debated for a long time in the specialized literature and are nowadays entering the design codes, as the recent Italian Technical Provisions for the Constructions (NTC 2008) are showing.

As usual, the news of the School “Fratelli Pesenti” ends this volume.

Milan, April 2013

Pietro G. Gambarova, Antonio Migliacci and Paola Ronca

## Premessa dei Curatori

L' editoriale su invito, ricco di sfide difficili ma avvincenti, è degna premessa a questo Volume 32 di Studies and Researches, che si prefigge di dare contributi in varie direzioni, con nove note tecnico-scientifiche (Technical Papers) e quattro note tecnico-progettuali (Technical Notes).

Il comportamento sotto carichi ciclici, la viscosità e la fessurazione sono i temi unificanti dei primi quattro lavori tecnico-scientifici, in cui l'analisi teorico-numerica viene applicata in forme diverse a travi, telai e conci in calcestruzzo armato o precompresso.

Mullapudi e Ayoub sviluppano un elemento di trave a fibra per la modellazione di travi in calcestruzzo armato soggette a carichi ciclici, mentre Ali propone una procedura iterativa semplificata per introdurre nell'analisi dei telai in c.a. le tensioni derivanti dal comportamento viscoso del calcestruzzo ed il conseguente regime fessurativo.

Le strutture bidimensionali – piastre o pareti – sono l'oggetto del quinto e sesto lavoro, ove Belletti, Damoni e Hendriks applicano l'analisi nonlineare ad elementi finiti alle piastre sottili soggette a carichi di punzonamento posti in prossimità dei vincoli, mentre Pecce, Bibbò e Ceroni propongono un modello semplificato per la valutazione della capacità resistente a taglio di pareti taglio-resistenti debolmente armate e soggette a carichi sismici.

L'alta temperatura e l'incendio accomunano il settimo e l'ottavo lavoro, ove Lo Monte tratta il problema assai critico per la sicurezza strutturale dello spacco superficiale del calcestruzzo (*spalling*) e dell'irrigidimento dell'armatura per effetto dell'aderenza (*tension stiffening*), mentre Hager, Carré e Krzemień valutano il danno da incendio nel calcestruzzo attraverso la misura della velocità degli ultrasuoni (Ultrasonic Pulse Velocity Method).

La temperatura – ma a livelli decisamente più bassi – interviene anche nel nono lavoro, ove viene modellata da Koenders e Martinelli l'idratazione del calcestruzzo con i suoi fenomeni igro-termici e di trasporto, e si fa un'applicazione al calcestruzzo con aggregato di riciclo, tema molto sentito oggi nell'ambito dello sviluppo sostenibile.

Dei quattro lavori tecnico-progettuali, i primi tre riguardano altrettanti e ben diversi temi, quali il comportamento ciclico dei giunti a secco fra colonne prefabbricate in c.a. e fondazione (di grande attualità in ambito sismico, come mostrano Dal Lago, Lamperti Tornaghi e Toniolo), il punzonamento delle solette in presenza di incendio (argomento di rilevante interesse trattato da Annerel e Taerwe con riferimento ai parcheggi multipiano ed alle loro deformazioni termiche impedito) e le perdite di precompressione a breve/medio termine nelle strutture alari di grande

luce, il cui calcolo Breccolotti e Materazzi mostrano essere alquanto complesso, pur introducendo ragionevoli ipotesi semplificatrici.

Il quarto lavoro rappresenta un efficace esempio di accoppiamento fra sperimentazione in sito e modellazione numerica, per studiare il comportamento – spesso molto complesso - delle costruzioni storiche. La duttilità in presenza di carichi orizzontali viene studiata per via numerica e controllata per via sperimentale da Bovo, Mazzotti e Savoia nel caso di due grandi magazzini interconnessi fra loro, siti a Trieste, la cui struttura settecentesca è costituita da arconi, voltine, volte a tunnel, pareti di grosso spessore e pilastri tozzi.

Dalla lettura dei lavori di questo volume, si capisce bene come i temi trattati siano riconducibili essenzialmente a due, seppure esaminati da diversi punti di vista: il comportamento sismico delle strutture ed la robustezza strutturale.

Questi due temi attualmente rappresentano per studiosi, tecnici, costruttori e semplici cittadini coscienti delle problematiche sociali ed economiche odierne due importantissimi riferimenti per l'indagine scientifica e per le applicazioni ingegneristiche, al fine di approfondire la conoscenza degli effetti di sisma ed azioni imprevedibili, e di mitigarne le conseguenze..

Con riferimento al sisma ed alle sue sollecitazioni, di particolare rilevanza in Italia – essendo “sismico” pressochè l'intero territorio nazionale - occorre evitare anticipate attivazioni di meccanismi fragili (dovuti ad esempio al taglio nelle colonne tozze), ricorrendo ad una organizzazione gerarchica intelligente degli elementi resistenti, nell'ottica del “prevenire” piuttosto che dell'intervenire a disastro avvenuto!

Con riferimento alla robustezza strutturale occorre – fin dalle prime fasi della progettazione strutturale – tener conto delle azioni imprevedibili (quali incendi, esplosioni, urti anomali). In particolare, la ripetizione di eventi dolorosi anche di origine terroristica, richiede di “attrezzarsi” in anticipo piuttosto che di intervenire sgomenti a disastro avvenuto!

Le suddette necessità, da tempo presenti nella letteratura tecnico-scientifica, stanno entrando anche nella normativa relativa alla progettazione strutturale, come dimostrano – ad esempio - le Norme Tecniche per le Costruzioni recentemente adottate in Italia (NTC 2008).

Come da tradizione, le notizie della Scuola “Fratelli Pesenti” terminano il volume.

Milano, Aprile 2013

Pietro G. Gambarova, Antonio Migliacci e Paola Ronca

## Technical Papers





## **CONSTITUTIVE BEHAVIOR OF A FIBER-BASED BEAM ELEMENT FOR REINFORCED CONCRETE MODELLING UNDER CYCLIC LOADING**

T. R. S. Mullanpudi<sup>1</sup> and Ashraf Ayoub<sup>2</sup>

### **ABSTRACT**

Reinforced concrete structures are prone to fail by an interaction of bending, shear and axial forces. This paper investigates the effect of combined loadings which can lead to a complex failure mechanism. A non-linear force-based Timoshenko beam element is formulated with the consideration of concrete orthotropic constitutive relation in which the directions of orthotropy are the principal directions of total strain. The structural tangent stiffness matrix is formulated which relates the increments of load to corresponding increments of displacement. Simplified cyclic uniaxial constitutive relationships are developed for cracked concrete in compression and tension. This model includes the softening effect of the concrete due to lateral tensile strain. Shear mechanism at each concrete fiber of a cross-section is modeled by assuming the strain field of the section as given by the superposition of the classical plane section hypothesis for the longitudinal strain field with a uniform distribution over the cross-section for the shear strain field. To establish the validity of the proposed model, correlation studies with experimental evidence have been conducted.

**KEYWORDS:** combined loading, Timoshenko Beam, R/C beams, uniaxial constitutive relations, tangent stiffness, force based model.

---

<sup>1</sup> Senior Staff Engineer, MMI Engineering Inc, Houston (Texas, USA).

<sup>2</sup> Associate Professor, Univ. of Houston, Houston (Texas, USA).

## 1. INTRODUCTION

The behavior of RC structures is affected by the combined effect of bending, shear, and axial loads. Accurate constitutive models of reinforced concrete (RC) elements for combined loadings is essential for reliably predicting structural behavior. In the past three decades constitutive models have markedly improved, thereby improving numerical performance of RC structures. The constitutive laws of concrete and steel bars are developed through large-scale panel testing and relating the smeared stresses to the smeared strains of the element. Belarbi and Hsu (1995) developed the Rotating-Angle Softened-Truss Model (RA-STM). In this model, the tension-stiffening effect of concrete is taken into account by assuming a shear stress along the crack direction. Pang and Hsu (1996) improved their work and developed the Fixed-Angle Softened-Truss Model (FA-STM), which can predict concrete contribution to shear resistance by assuming the cracks to be oriented at a fixed angle. Zhu et al. (2001) derived a rational shear modulus and developed a simple solution algorithm for the FA-STM. The work was further extended by developing the Hsu/Zhu Poisson's Ratio (Zhu and Hsu 2002), which led to the development of the Softened Membrane Model (SMM) to predict the complete behavior of the specimen including both pre- and post-peak responses. The SMM model is appealing for modeling shear behavior of concrete elements, as it is consistent with the fundamentals of materials mechanics, and is also accurately calibrated from panel testing.

Modeling shear behavior of reinforced concrete structures is typically performed with two-dimensional continuum elements, which can accurately describe the local behavior of the element. Continuum models, however, are computationally expensive, which limits their applicability to simulating the behavior of large structural systems. Beam-column elements, on the other hand, proved to be effective in describing the flexural behavior of concrete structures and are computationally efficient. By including shear deformations, these elements can simulate accurately reinforced concrete columns dominated by both shear and flexural behavior.

The fiber-based distributed beam elements have the ability to describe the inelastic behavior along the depth by discretizing the section into several fibers with appropriate constitutive behavior. Spacone et al. (1996) developed a force-based fiber model for the analysis of frame elements. Their model accounted for the axial-flexural interaction effect. Mullapudi and Ayoub (2010) developed a fiber-based beam element that accounts for shear-axial-flexure interaction effects.

The objective of this paper is to evaluate the behavior of concrete members using a fiber beam-column element formulation. The RC member is modeled with an assembly of interconnected beam elements that describe the nonlinear behavior of steel and concrete at the fiber level. The beam element is formulated with the help of flexibility or force-based method. The Fiber model for RC structures is developed by dividing each element into several sections along the member. The

sections at each end of the element are further divided into a number of areas, each pertaining to a fiber, representing either concrete or steel (Fig. 1). The strain in each fiber is calculated from the centroidal section strain and curvature with the help of the plane-section assumption. The stresses and modulus of fibers are calculated from the fiber strain values. The constitutive relation of the section is derived by integration of the response of the fibers; the response of elements is also derived by integration of the response of sections along the length of the element.

A Timoshenko beam theory is adopted in the model to account for shear deformation effects. To predict the complete pre- and post-peak responses of the shear stress-strain curves, the SMM model is adopted and the Hsu/Zhu ratios (Poisson's Ratio of cracked reinforced concrete) are used as well. This study is also focused on the development of the concrete uniaxial constitutive relations and on the prediction of RC bridge columns subjected to cyclic loads. During cyclic loading, RC structures undergo large deformations with the concrete exhibiting crack opening-and-closing. The problem is further complicated by considering softening, confinement, tension-stiffening and dilatancy, which accompany large shear strains. This study tackles the extension of the fiber-based beam element formulation to account for axial, bending, and shear interaction. The model is developed using the finite element program FEAPpv (Taylor 2005).

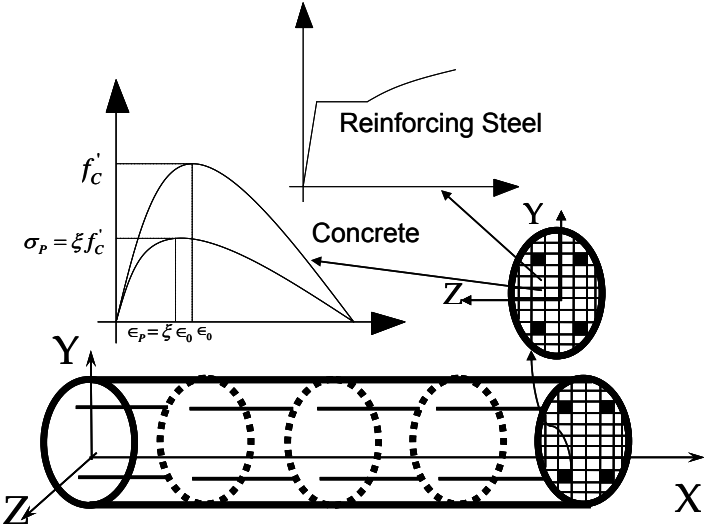


Figure 1 - Fiber model discretization.

**2. FORCE-BASED FORMULATION**

The force-based formulation proved to overcome most of the locking difficulties associated with the standard displacement approach, and requires a lower number

of model degrees of freedom for comparable accuracy when dealing with RC members.

The generalized nodal forces and nodal deformations of the element are shown in Fig. 2, where the rigid body modes are excluded. Thus the element force vector and element deformation vector respectively are

$$\{P\} = \begin{Bmatrix} N \\ M_1 \\ M_2 \end{Bmatrix} \quad \{d\} = \begin{Bmatrix} u \\ \beta_1 \\ \beta_2 \end{Bmatrix} \quad (1)$$

As in the displacement formulation, the section forces and corresponding section deformations are

$$S(x) = \begin{Bmatrix} N(x) \\ V(x) \\ M(x) \end{Bmatrix} \quad s(x) = \begin{Bmatrix} \varepsilon(x) \\ \gamma(x) \\ \chi(x) \end{Bmatrix}. \quad (2)$$

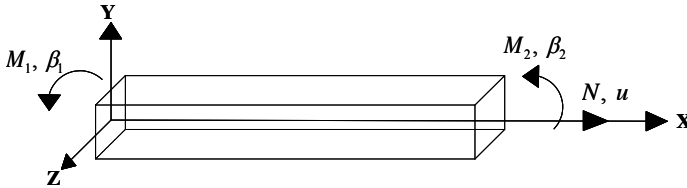


Figure 2 - Element nodal forces and nodal displacements.

By utilizing the force interpolation function  $b(x)$ , the section forces  $S(x)$  at a section  $x$  are related to the element end forces  $P$  by

$$S(x) = b(x)P, \quad (3)$$

and

$$\delta S^T(x) = \delta P^T b^T(x), \quad (4)$$

where

$$b(x) = \begin{bmatrix} 1 & 0 & 0 \\ 0 & \frac{-1}{L} & \frac{-1}{L} \\ 0 & \frac{x}{L} - 1 & \frac{x}{L} \end{bmatrix}. \quad (5)$$

Element-wise compatibility is enforced through the application of the virtual force principal, which results

$$\delta P^T \Delta d = \int_0^L \delta S^T(x) \Delta s^T(x) dx . \quad (6)$$

The section force vector  $S(x)$  and the section stiffness matrix  $K_{Section}(x)$  are determined by a known section deformation vector  $s(x)$ . The section deformation increments  $\Delta s(x)$  are determined by adding the residual section deformation  $r(x)$  from the previous iteration to the deformation caused by the section force increments  $\Delta S(x)$

$$\Delta s(x) = f(x) \Delta S(x) + r_d(x) , \quad (7)$$

where  $f(x) = K_{Section}^{-1}(x)$  is the section flexibility.

After substituting Eq. 4 and Eq. 7 in Eq. 6 and eliminating  $\delta P^T$  from the resulting equation, as it is arbitrary in this case, the element compatibility equation is written as

$$\Delta d = \bar{F} \Delta P + r_u , \quad (8)$$

where  $\bar{F}$  is the element flexibility matrix without rigid body modes; it is then evaluated using

$$\bar{F} = \int_0^L b^T(x) f(x) b(x) dx . \quad (9)$$

Here,  $r_u$  is the element residual deformation vector

$$r_u = \int_0^L b^T(x) r_d(x) dx , \quad (10)$$

whereas  $r_d$  is the residual of sectional deformation.

To implement the force-based model in a finite element program based on displacement degrees of freedom, Eq. 8 must be inverted

$$K_{element} \Delta d = \Delta R , \quad (11)$$

where the element stiffness matrix  $K = \bar{F}^{-1}$  for each element, and the resisting load increment  $\Delta R = \Delta P + \bar{F}^{-1} r_u$ ,  $\bar{F}^{-1}$  is evaluated from the previous iteration. The process of the state determination of force-based element requires internal element iteration in addition to the Newton-Raphson global iteration as described by Spacone et al. (1996), and Neuenhofer and Filippou (1997).

As stated earlier, the section behavior is evaluated through fiber discretization with appropriate material constitutive models. Longitudinal steel fibers are assumed to follow a bilinear stress-strain relation. The constitutive behavior of concrete fibers is described in the next section.

### 3. CONCRETE CONSTITUTIVE MODEL

According to the ACI 318 (2008) building code, the ultimate strength of an RC beam is the combination of shear strength provided by the concrete ( $v_c$ ) and shear strength provided by transverse reinforcement ( $v_s$ ). The term  $v_c$  cannot be estimated in the RA-STM theory, because the crack angle in this model is assumed to be rotating. The FA-STM and SMM theories are capable of accurately accounting for the effect of  $v_c$ ; this is due to the crack angle, which is based on the principal coordinates of the applied stresses of the RC element, with due consideration to the concrete shear stress term ( $\tau_c$ ). The RA-STM and FA-STM models can only predict the pre-peak behavior of RC members, while the SMM model is capable of predicting both the pre-peak and post-peak behavior by taking into account the Hsu/Zhu ratios (Modified Poisson's ratios of cracked RC members).

To formulate the SMM model, three coordinate systems are typically assumed, as shown in Fig. 3. The first coordinate system ( $x, y$ ) defines the local coordinate of the fiber element, the second coordinate system ( $1, 2$ ) represents the applied principal stresses, while the third coordinate system ( $r, d$ ) represents the concrete principal coordinate system in which the concrete shear stress  $\tau_{12}^c = 0$ . The angle  $\alpha_1$  is the angle between the  $x$ -axis and  $1$ -axis, and  $\alpha_r$  is the angle between the  $x$ -axis and  $r$ -axis.

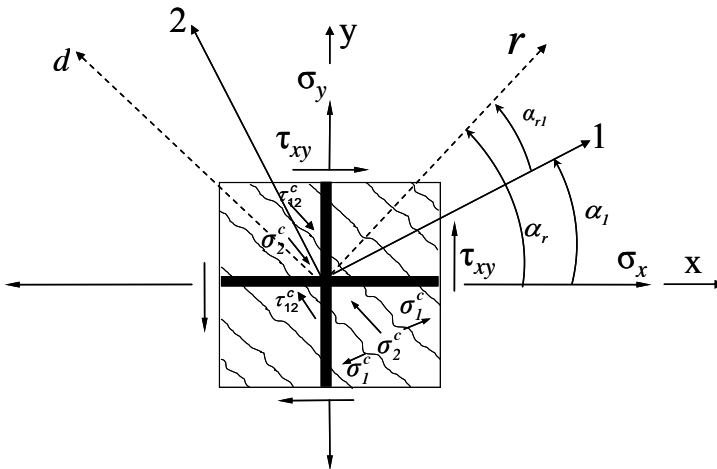


Figure 3 – Local coordinate ( $x, y$ ); principal stress directions ( $1, 2$ ); and concrete principal coordinate system ( $r, d$ ) of RC elements.

To rotate the stress and strain vectors from one system of axis to another, use the rotation matrix  $R(\theta)$

$$[R(\theta)] = \begin{bmatrix} \cos^2\theta & \sin^2\theta & 2\cos\theta\sin\theta \\ \sin^2\theta & \cos^2\theta & -2\cos\theta\sin\theta \\ -\cos\theta\sin\theta & \cos\theta\sin\theta & \cos^2\theta - \sin^2\theta \end{bmatrix}, \quad (12)$$

where the angle  $\theta$  is the angle between the two coordinate systems.

Three basic compatibility equations in the  $x$ - $y$  coordinate system are defined as

$$\{\varepsilon_x \quad \varepsilon_y \quad 0.5\gamma_{xy}\}^T = [R(-\alpha_l)]\{\varepsilon_1 \quad \varepsilon_2 \quad 0.5\gamma_{12}\}^T \quad (13)$$

Similar to the strain transformations, stress transformation equations in the  $x$ - $y$  coordinate system are

$$\{\sigma_x \quad \sigma_y \quad \tau_{xy}\}^T = [R(-\alpha_l)]\{\sigma_1^c \quad \sigma_2^c \quad \tau_{12}^c\}^T \quad (14)$$

The transformation equations are graphically represented by Mohr's stress and strain circles in Fig. 4.

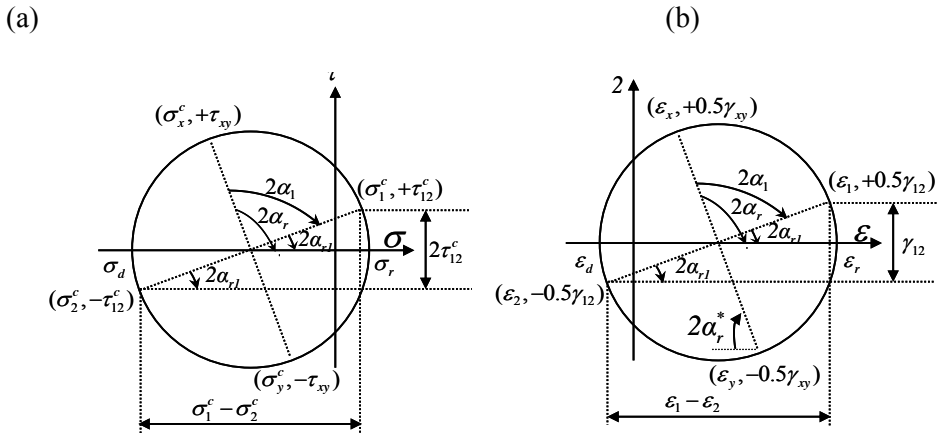


Figure 4 - Mohr Circle representation of stresses and strains.

In a fiber-based element formulation, the process of the state determination at the fiber level requires the calculation of the fiber stresses  $\{\sigma_x, \sigma_y, \tau_{xy}\}$  from the strain state  $\{\varepsilon_x, \varepsilon_y, \gamma_{xy}\}$ . Since the SMM is implemented in a Timoshenko-type beam element, the values of  $\varepsilon_x$  and  $\gamma_{xy}$  are typically known, while the lateral strain  $\varepsilon_y$  value must be evaluated from the equilibrium condition.

#### 4. EVALUATION OF LATERAL STRAIN

The equilibrium equations needed to evaluate the stresses in the  $x$ - $y$  coordinate system  $\{\sigma_x, \sigma_y, \tau_{xy}\}^T$  as a function of the principal stresses resisted by concrete  $\{\sigma_1^c, \sigma_2^c, \tau_{12}^c\}^T$  and the reinforcing bar stresses  $f_{sx}$  and  $f_{sy}$  along the  $x$  and  $y$  directions respectively are

$$\begin{Bmatrix} \sigma_x \\ \sigma_y \\ \tau_{xy} \end{Bmatrix} = \begin{bmatrix} \cos^2 \alpha_1 & \sin^2 \alpha_1 & -2\cos \alpha_1 \sin \alpha_1 \\ \sin^2 \alpha_1 & \cos^2 \alpha_1 & 2\cos \alpha_1 \sin \alpha_1 \\ \cos \alpha_1 \sin \alpha_1 & -\cos \alpha_1 \sin \alpha_1 & \cos^2 \alpha_1 - \sin^2 \alpha_1 \end{bmatrix} \begin{Bmatrix} \sigma_1^c \\ \sigma_2^c \\ \tau_{12}^c \end{Bmatrix} + \begin{Bmatrix} \rho_{sx} f_{sx} \\ \rho_{sy} f_{sy} \\ 0 \end{Bmatrix}, \quad (15)$$

where  $\rho_{sx}$  and  $\rho_{sy}$  are the smeared steel ratios in the direction of  $x$  and  $y$  respectively.

The second equilibrium equation in Eq. 15 is used to evaluate the lateral (stirrup) strain  $\varepsilon_y$  in fiber  $i$  (taking into consideration that the value of  $\sigma_y$  equals zero) and can be written as

$$\sigma_1^{c,i} \sin^2 \alpha_1 + \sigma_2^{c,i} \cos^2 \alpha_1 + \tau_{12}^{c,i} 2 \sin \alpha_1 \cos \alpha_1 + \rho_{sy}^i f_{sy}^i = 0, \quad (16)$$

which can also be written as

$$\sigma_{cy}^i A_{cy}^i + \sigma_{sy}^i A_{sy}^i = 0. \quad (17)$$

Here,  $\sigma_{cy}^i$  is the concrete stress in the transverse direction of fiber  $i$  and is equal to the sum of the first three terms in Eq. 16;  $\sigma_{sy}^i$  is the steel stress in the transverse direction of fiber  $i$ ;  $A_{cy}^i$  and  $A_{sy}^i$  are the respective areas of concrete and steel within the spacing  $S$  of the transverse reinforcement, as shown in Fig. 5;  $\rho_{sy}^i$  is the ratio of steel to concrete area in the transverse direction of fiber  $i$ ; and  $f_{sy}^i$  is the transverse steel bar stress which equals  $\sigma_{sy}^i$ .

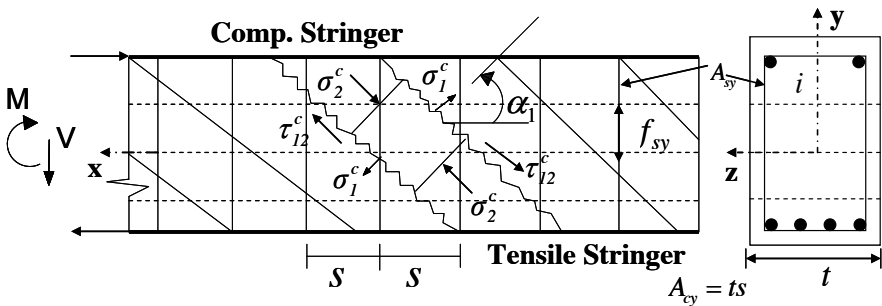


Figure 5 - Concrete strut and transverse reinforcement equilibrium.



Because of the nonlinear behavior of concrete and steel, an iterative procedure is needed to determine the lateral strain  $\varepsilon_y$  that satisfies Eq. 16, see Mullapudi and Ayoub (2010).

## 5. UNIAXIAL CONSTITUTIVE RELATIONSHIPS OF THE MATERIALS

Typical concrete stress-strain curves are derived from uniaxial tests; biaxial strains in the  $x$ - $y$  direction  $\{\varepsilon_x \ \varepsilon_y \ \gamma_{xy}\}^T$  must be converted to equivalent uniaxial strains in the  $I$ - $2$  direction  $\{\bar{\varepsilon}_1 \ \bar{\varepsilon}_2 \ \gamma_{12}\}^T$  to accurately calculate concrete stresses.

Typically, the direction of cracks is calculated based on a rotating angle,  $\alpha_r$ , derived from the strain state. At a rotating principal angle,  $\alpha_r$ , the concrete shear stress  $\tau_{12}^c = 0$  (Fig. 4) and the value of  $\alpha_r$  is

$$\tan 2\alpha_r = \frac{\gamma_{xy}}{\varepsilon_x - \varepsilon_y}. \quad (18)$$

The calculation of the rotating angle,  $\alpha_r$ , is dependent on the strain state. The calculation of the trial rotating angle,  $\alpha_r^*$ , from the Mohr circle (Fig. 4) is based on the strain values

$$\alpha_r^* = 0.5 \tan^{-1} \left( \left| \frac{\gamma_{xy}}{\varepsilon_x - \varepsilon_y} \right| \right). \quad (19)$$

If the value of the difference between the axial and transverse strains  $|\varepsilon_x - \varepsilon_y| = 0$ , then the value of the rotating angle  $\alpha_r$  depends upon the value of the shear strain  $\gamma_{xy}$  as follows.

Rotating angle  $\alpha_r = 45^\circ$  when the value of  $\gamma_{xy} > 0$ , and  $\alpha_r = 135^\circ$  when the value of the  $\gamma_{xy} < 0$ .

If the value of the shear strain  $\gamma_{xy} = 0$  then the rotating angle depends upon the value of the  $\varepsilon_x$  and  $\varepsilon_y$  as follows.

The rotating angle  $\alpha_r = 0^\circ$  when the value of  $\varepsilon_x > \varepsilon_y$  and,  $\alpha_r = 90^\circ$  when the value of  $\varepsilon_x < \varepsilon_y$ .

If both the shear strain and the difference of the axial and transverse strains are non-zero numbers, then the following laws will be applied.

- If the value of  $\varepsilon_x > \varepsilon_y$  and the shear strain  $\gamma_{xy} > 0$ , then the value of the rotating angle  $\alpha_r$  becomes the value of the  $\alpha_r^*$ .
- If the value of  $\varepsilon_x > \varepsilon_y$  and the shear strain  $\gamma_{xy} < 0$ , then the value of the rotating angle  $\alpha_r = 180^\circ - \alpha_r^*$ .
- If the value of  $\varepsilon_x < \varepsilon_y$  and the shear strain  $\gamma_{xy} > 0$ , then the value of the rotating angle  $\alpha_r = 90^\circ - \alpha_r^*$ .
- If the value of  $\varepsilon_x < \varepsilon_y$  and the shear strain  $\gamma_{xy} < 0$ , then the value of the rotating angle  $\alpha_r = 90^\circ + \alpha_r^*$ .

After evaluating the  $\varepsilon_y$  term that satisfies the equilibrium condition (Eq. 16), the calculated principal angle  $\alpha_1$  from the known stress state is evaluated as

$$\tan 2\alpha_1 = \frac{2\tau_{xy}}{\sigma_x - \sigma_y}. \quad (20)$$

The biaxial principal strains are then evaluated as

$$\{\varepsilon_1 \quad \varepsilon_2 \quad 0.5\gamma_{12}\}^T = [R(\alpha_1)]\{\varepsilon_x \quad \varepsilon_y \quad 0.5\gamma_{xy}\}^T. \quad (21)$$

Biaxial principal strains are needed to evaluate the equivalent uniaxial strains. The equivalent uniaxial strains are derived from the biaxial strains with the help of the modified Poisson's Ratio of cracked concrete, also called the Hsu/Zhu ratios ( $\mu_{12}, \mu_{21}$ ), see Zhu and Hsu (2002). The ratio  $\mu_{12}$  is that of resulting tensile strain increment, in the principal 1-direction, to the source compressive strain increment in the principal 2-directions, while  $\mu_{21}$  is the ratio of the resulting compressive strain increment in the principal 2-direction to the tensile source strain increment in the principal 1-direction. Based on test data the following equations are suggested by Zhu and Hsu (2002).

$$\mu_{12} = 0.2 + 850\varepsilon_{sf} \quad \varepsilon_{sf} \leq \varepsilon_y, \quad (22)$$

$$\mu_{12} = 1.9 \quad \varepsilon_{sf} > \varepsilon_y. \quad (23)$$

where  $\varepsilon_{sf}$  is defined as the strain in the reinforcement that yield first and  $\varepsilon_y$  is the yield strain of the reinforcing steel.

After concrete cracking, the Hsu/Zhu ratio  $\mu_{12}$  lies outside the typical range of zero to 0.5 for Poisson's Ratio of continuous materials. Before concrete cracking, the Hsu/Zhu ratio  $\mu_{21} = 0.2$  and, after concrete cracking, the Hsu/Zhu ratio  $\mu_{21} = 0$ , indicating that the tensile strain has no effect on compressive strain.

The equivalent uniaxial strains are derived from the biaxial principal strains with the Hsu/Zhu ratios ( $\mu_{12}, \mu_{21}$ ) as

$$\{\bar{\varepsilon}_1 \quad \bar{\varepsilon}_2 \quad 0.5\gamma_{12}\}^T = [\mu] \{\varepsilon_1 \quad \varepsilon_2 \quad 0.5\gamma_{12}\}^T, \quad (24)$$

where

$$[\mu] = \begin{bmatrix} \frac{1}{1-\mu_{12}\mu_{21}} & \frac{\mu_{12}}{1-\mu_{12}\mu_{21}} & 0 \\ \frac{\mu_{21}}{1-\mu_{12}\mu_{21}} & \frac{1}{1-\mu_{12}\mu_{21}} & 0 \\ 0 & 0 & 1 \end{bmatrix}. \quad (25)$$

The equivalent uniaxial principal strains in the longitudinal reinforcement and in the transverse reinforcement are given by Eqs. 26 and 27, respectively.

$$\bar{\varepsilon}_{sx} = \left( \frac{1}{1-\mu_{12}\mu_{21}} \varepsilon_1 + \frac{\mu_{12}}{1-\mu_{12}\mu_{21}} \varepsilon_2 \right) \cos^2(\alpha_1) + \left( \frac{\mu_{21}}{1-\mu_{12}\mu_{21}} \varepsilon_1 + \frac{1}{1-\mu_{12}\mu_{21}} \varepsilon_2 \right) \sin^2(\alpha_1) - \gamma_{12} \sin(\alpha_1) \cos(\alpha_1) \quad (26)$$

$$\bar{\varepsilon}_{sy} = \left( \frac{1}{1-\mu_{12}\mu_{21}} \varepsilon_1 + \frac{\mu_{12}}{1-\mu_{12}\mu_{21}} \varepsilon_2 \right) \sin^2(\alpha_1) + \left( \frac{\mu_{21}}{1-\mu_{12}\mu_{21}} \varepsilon_1 + \frac{1}{1-\mu_{12}\mu_{21}} \varepsilon_2 \right) \cos^2(\alpha_1) + \gamma_{12} \sin(\alpha_1) \cos(\alpha_1) \quad (27)$$

The equivalent uniaxial longitudinal steel stress  $f_{sx}$  and transverse steel stress  $f_{sy}$  are calculated from the steel strains  $\bar{\varepsilon}_{sx}$  and  $\bar{\varepsilon}_{sy}$  through a uniaxial stress-strain relationship.

The equivalent uniaxial strains  $\bar{\varepsilon}_1$  and  $\bar{\varepsilon}_2$  are used individually to calculate the concrete stresses  $\sigma_1^c$  and  $\sigma_2^c$  in the principal direction of the concrete element. Equivalent uniaxial steel strains  $\bar{\varepsilon}_{sx}$  and  $\bar{\varepsilon}_{sy}$  are used to calculate the steel stresses  $f_{sx}$  and  $f_{sy}$  from the uniaxial stress-strain relationship of the steel bar.

## 5.1 Concrete Model

The concrete model describes the cyclic uniaxial constitutive relationships of cracked concrete in compression and tension. The envelope curve of the concrete in compression follows the modified Kent and Park model (Park et al. 1982), which offers a balance between simplicity and accuracy. The model implemented in this study has the following characteristics:

- First, the effect of softening in both the stress and strain curves is considered.
- Second, the successive degradation of stiffness of both the unloading and reloading curves for increasing values of compressive strain is considered.
- Third, the effect of tension-stiffening is considered (Belarbi and Hsu 1994).

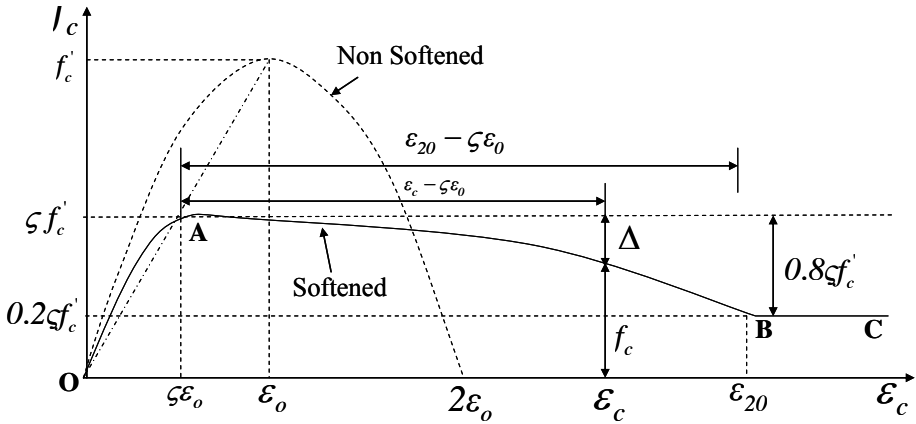


Figure 6 - Monotonic non softened and softened stress strain curve.

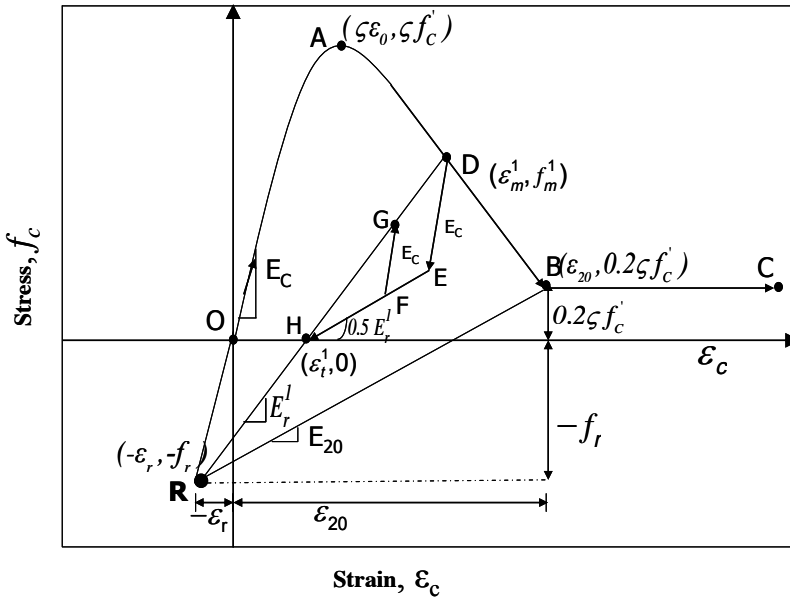


Figure 7 - Cyclic stress-strain curve of softened concrete.

Peak compressive stress  $f'_c$  and strain at peak stress  $\epsilon_0$  can be calculated with the help of the modified Kent and Park model (Park et al. 1982). The monotonic stress-strain envelope of concrete is represented by a parabolic curve (Fig. 6), see Eq. 28:

$$f_c = f_c' \left[ 2 \left( \frac{\varepsilon_c}{\varepsilon_0} \right) - \left( \frac{\varepsilon_c}{\varepsilon_0} \right)^2 \right]. \quad (28)$$

The compressive stress-strain curve of concrete in a structural element is softened because the perpendicular tensile stress will reduce the compressive stress and strain of concrete, with an appropriate softening coefficient  $\zeta$ . When the softened stress-strain curve is modeled, it is assumed that the slope of the line connecting the origin and peaks of the non-softened and softened curve is the same. The pre-peak ascending curve and the post-peak descending curve of the softened stress-strain curve are assumed to adhere to a parabolic shape. The descending section of the softened parabolic curve is gently sloped until the stress reaches 20 percent of maximum stress  $\zeta f_c'$  at a strain of  $\varepsilon_{20}$ . For the softened stress-strain curve and the tangent moduli, the following relationships are adopted:

$$\text{Region OA, } \varepsilon_c \leq \zeta \varepsilon_0, f_c = \zeta f_c' \left[ 2 \left( \frac{\varepsilon_c}{\zeta \varepsilon_0} \right) - \left( \frac{\varepsilon_c}{\zeta \varepsilon_0} \right)^2 \right] \quad (29)$$

$$\text{Region OA, } \varepsilon_c \leq \zeta \varepsilon_0, \text{ Tangent modulus } E_t = \frac{2\zeta f_c'}{\varepsilon_0} \left( 1 - \frac{\varepsilon_c}{\zeta \varepsilon_0} \right) \quad (30)$$

$$\text{Region AB, } \zeta \varepsilon_0 < \varepsilon_c \leq \varepsilon_{20}, f_c = \zeta f_c' \left[ 1 - 0.8 \left( \frac{\varepsilon_c - \zeta \varepsilon_0}{\varepsilon_{20} - \zeta \varepsilon_0} \right)^2 \right] \quad (31)$$

$$\text{Region AB, } \zeta \varepsilon_0 < \varepsilon_c \leq \varepsilon_{20}, \text{ Tangent modulus } E_t = -1.6\zeta f_c' \left( \frac{\varepsilon_c - \zeta \varepsilon_0}{(\varepsilon_{20} - \zeta \varepsilon_0)^2} \right) \quad (32)$$

$$\text{Region BC, } \varepsilon_c > \varepsilon_{20}, f_c = 0.2\zeta f_c'. \quad (33)$$

$$\text{Region BC, } \varepsilon_c > \varepsilon_{20}, \text{ Tangent modulus } E_t = 0. \quad (34)$$

The cyclic model (Fig. 7) considers the concrete damage and accounts for the opening and closing of cracks. The envelope for the cyclic stress-strain curves of concrete adheres to the monotonic stress-strain curve. The unloading and reloading path of the compressive side is simplified, as all the loading paths start from a common point  $R$ , which determines the degradation stiffness (i.e. the ratio between the slope of any given loading path and that of the monotonic envelope at the origin), which limit provided by the slope of the path RB.

Unloading modulus  $E_{20}$  at point  $B$  of the monotonic envelope curve is  $\frac{0.2\zeta f_c' - f_r}{\varepsilon_{20} - \varepsilon_r} \cdot E_{20}$  and must be determined experimentally. The strain and stress

at the intersection of point  $R$  and the origin are given by the following expressions

$$\varepsilon_r = \frac{0.2\zeta f_c' - E_{20}\varepsilon_{20}}{E_c - E_{20}} \quad (35)$$

$$f_r = E_c \varepsilon_r. \quad (36)$$

in which  $E_c$  is the initial tangent modulus at origin in compression; in the current model, it is assumed to equal  $\frac{2f_c'}{\varepsilon_0}$ . The unloading stress  $f_m^l$  and strain  $\varepsilon_m^l$  values at point  $D$  on the compressive monotonic envelope are used to calculate the reloading modulus and strain  $\varepsilon_t^l$  at zero stress point  $H$  from the following expressions

$$E_r^l = \frac{f_m - f_r}{\varepsilon_m - \varepsilon_r} \quad (37)$$

$$\varepsilon_t^l = \varepsilon_m^l - \frac{f_m^l}{E_r^l}. \quad (38)$$

From any unloading point  $D$ , stress will reach the zero stress axis at point  $H$  after completing two smaller cycles that are defined by these expressions

$$\text{Maximum stress (line HD)} \quad f_{max}^l = f_m^l + E_r^l (\varepsilon_c - \varepsilon_m^l), \quad \varepsilon_t^l \leq \varepsilon_c \leq \varepsilon_m^l \quad (39)$$

$$\text{Minimum Stress (line HE)} \quad f_{min}^l = 0.5E_r^l (\varepsilon_c - \varepsilon_t^l), \quad \varepsilon_t^l \leq \varepsilon_c \leq \varepsilon_m^l. \quad (40)$$

Loading and unloading cycles are carried out with the assumption that the model follows a straight line with modulus  $E_c$ . The trial stress  $f_c^T$  and tangent modulus  $E_t$  are assumed to be based on linear elastic behavior with initial tangent modulus  $E_c$ ; later this assumption is corrected to fall under the line  $HD$  and line  $HE$ .

$$f_c^T = f_c^P + E_c \Delta\varepsilon_c. \quad (41)$$

Here,  $f_c^P$  is the previous stress and  $\Delta\varepsilon_c$  is the strain increment.

Actual stress  $f_c$  and tangent modulus  $E_t$  are calculated based on the trial stress state

$$f_{min}^l \leq f_c^T \leq f_{max}^l \quad \text{then} \quad f_c = f_c^T \quad \text{and} \quad E_t = E_c \quad (42)$$

$$f_c^T < f_{min}^l \quad \text{then} \quad f_c = f_{min}^l \quad \text{and} \quad E_t = 0.5E_r^l \quad (43)$$

$$f_c^T > f_{max}^l \quad \text{then} \quad f_c = f_{max}^l \quad \text{and} \quad E_t = E_r^l. \quad (44)$$

If unloading from point  $D$  to point  $E$ , reloading will be on same path back to  $D$ . If unloading reaches point  $F$ , then reloading will result in the loop  $DEFGD$ . If unloading reaches point  $H$ , then reloading will result in the loop  $DEHD$ . The reloading line will always rejoin the compression monotonic envelope at the point of initial unloading,  $D$ . If unloading continues below point  $H$ , then reloading begins in tension. After the start of the reloading in compression, the model will re-enter the compression region at point  $H$ , and subsequent results in the tension region will not affect the behavior of the model once it returns to the compression region.

## 5.2 Steel Model

The smeared stress-strain relationships of mild steel bars embedded in concrete and subjected to uniaxial strains have been developed by Belarbi and Hsu (1994; 1995). The steel strain at cracked sections increases rapidly to reach the strain hardening region of the stress-strain curve compared to the adjacent regions because part of the stress is resisted by the concrete. Steel stresses are averaged along the steel bar traversing several cracks and the resulting smeared steel stress at first yield will be reduced compared to the local yield stress of a bare bar at the cracks. The smeared stress versus smeared strain curves of embedded steel bars (solid curves), as well as stress-strain relationship of bare bar (dotted curve) are summarized in Fig. 8.

The difference between the bare bar yield stress  $f_y$  and smeared steel bar yield stress  $f'_y$  depends on the parameter  $B$  defined by Belarbi and Hsu (1994; 1995). The parameter  $B$  is derived to be a function of three variables such as percentage of steel ( $\rho$ ), cracking strength or tensile strength of concrete ( $f_{cr}$ ) and the yield strength of the bare bar yield stress ( $f_y$ ). Parameter  $B$  depends on the crack width, crack spacing and interface bond slip behavior of steel bar and concrete. It can be seen that when the steel ratio  $\rho$  is decreased or when  $f_{cr}$  is increased then the smeared yield stress  $f'_y$  decreases and the smeared stress-strain curve moves downward.

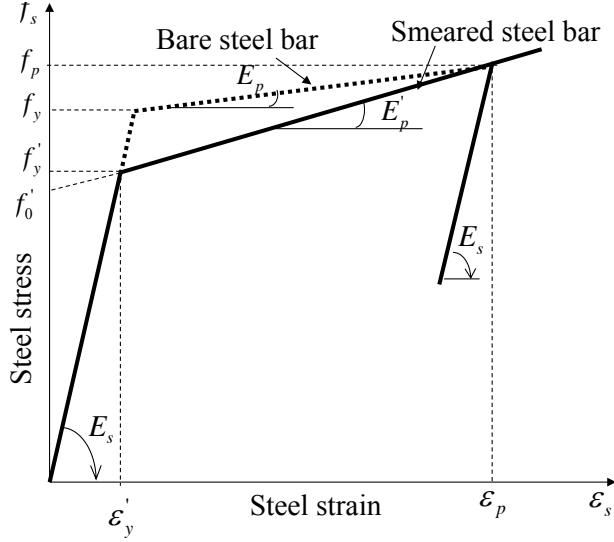


Figure 8 - Smeared mild steel stress-strain curve.

As shown in Fig. 8, the shape of the bare bar and the smeared stress-strain curve of mild steel resembles two straight lines. These two straight lines will have a slope of  $E_s$  before yielding and a slope of  $E'_p$  after yielding for smeared steel, and a slope of  $E_p$  after yielding for bare steel as illustrated in Fig. 8. The slope of the strain hardening region of the bare steel bar is assumed to be  $0.025 E_s$ . The stress level at which the two straight lines of smeared steel intersect is designated as the smeared yield stress  $f'_y$  and the corresponding strain is designated as the smeared yield strain  $\epsilon'_y$ .

The equations of the pre yield and post yield lines are given as

- $f_s = E_s \epsilon_s$  when  $f_s \leq f'_y$  (45)

- $f_s = f'_o + E'_p \epsilon_s$  when  $f_s > f'_y$ . (46)

The vertical intercept of the post yield straight line stress  $f'_o$  can be calculated as

$$f'_o = \frac{E_s - E'_p}{E_s} f'_y. \quad (47)$$

Belarbi and Hsu (1994; 1995) defined the parameter  $B$  as



$$B = \frac{1}{\rho} \left( \frac{f_{cr}}{f_y} \right)^{1.5}, \quad (48)$$

where  $f_{cr} = 0.31 \sqrt{f'_c (MPa)}$  and  $\rho \geq 0.15\%$ .

The smeared yield stress of a steel bar can be calculated as

$$f'_y = (0.93 - 2B) f_y \quad (49)$$

The smeared steel bar yield strain can be calculated as

$$\varepsilon'_y = \frac{f'_y}{E_s}. \quad (50)$$

The slope of the strain hardening region of the smeared steel bar is calculated as

$$E'_p = 0.02 + B. \quad (51)$$

The smeared steel stress before yielding can be calculated as

- $f_s = E_s \bar{\varepsilon}_s$  when  $\varepsilon_s \leq \varepsilon'_y$  (52)

- $f_s = (0.91 - 2B) f_y + (0.02 + 0.25B) E_s \bar{\varepsilon}_s$  when  $\varepsilon_s > \varepsilon'_y$ . (53)

When steel stress  $f_s$  reaches a peak stress  $f_p$  at a strain  $\varepsilon_p$  and starts to unload then the unloading branch of the stress-strain curve is assumed to be a straight line with a slope of  $E_s$ . The unloading stress can be expressed as

$$f_s = f_p - E_s (\varepsilon_p - \varepsilon_s) \text{ where } \varepsilon_s < \varepsilon_p. \quad (54)$$

The cyclic response of the smeared steel bar is formulated according to the Filippou et al. (1983) model which includes the isotropic strain hardening and Bauschinger effect.

## 6. TANGENT MATERIAL CONSTITUTIVE RELATIONS

The concrete model is simplified with a plane stress orthotropic material; it has mutually perpendicular planes of elastic symmetry. Directions one and two are the local principal material axes that are normal to the planes of symmetry. With the equivalent uniaxial strains, the stiffness values  $\bar{E}_1^c$  and  $\bar{E}_2^c$  are determined from a material uniaxial stress-strain diagram. The material constitutive equation is

$$\{\sigma_{12}^c\} = [D_{lo}]^c \{\varepsilon_{12}\}. \quad (55)$$

In this equation,  $\{\sigma_{12}^c\}$  is the local concrete stress vector,  $\{\varepsilon_{12}\}$  is the local principal strain vector, and  $[D_{lo}]^c$  is the local uniaxial concrete material tangent

stiffness matrix in the principal direction.

The tangent stiffness matrix of a reinforced concrete element is defined as

$$[D_{gl}]^{c+s} = \frac{d \begin{Bmatrix} \sigma_x \\ \sigma_y \\ \tau_{xy} \end{Bmatrix}}{d \begin{Bmatrix} \varepsilon_x \\ \varepsilon_y \\ \frac{1}{2} \gamma_{xy} \end{Bmatrix}}, \quad (56)$$

$$\begin{Bmatrix} \sigma_x \\ \sigma_y \\ \tau_{xy} \end{Bmatrix} = [T(-\alpha_1)] \begin{Bmatrix} \sigma_1^c \\ \sigma_2^c \\ \tau_{12}^c \end{Bmatrix} + \sum_i [T(-\alpha_{si})] \begin{Bmatrix} \rho_{si} f_{si} \\ 0 \\ 0 \end{Bmatrix}, \quad (57)$$

where  $\rho_{si}$  is the reinforcement ratio in the  $i^{\text{th}}$  direction; and  $[T(-\alpha_1)]$  and  $[T(-\alpha_{si})]$  are the transformation matrices from the local 1-2 coordinate and the  $x_{si}$ - $y_{si}$  reinforcement coordinate system to the x-y coordinate system, respectively (Fig. 9).

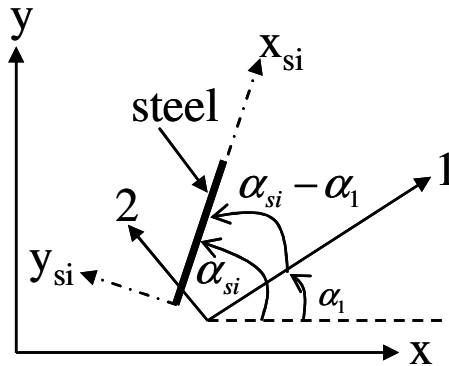


Figure 9 - Coordinate system for reinforced concrete element.

Substituting Eq. 57 into 56 gives

$$[D_{gl}]^{c+s} = \frac{\partial \left( [T(-\alpha_1)] \begin{Bmatrix} \sigma_1^c \\ \sigma_2^c \\ \tau_{12}^c \end{Bmatrix} + \sum_i [T(-\alpha_{si})] \begin{Bmatrix} \rho_{si} f_{si} \\ 0 \\ 0 \end{Bmatrix} \right)}{\partial \begin{Bmatrix} \varepsilon_x \\ \varepsilon_y \\ \frac{1}{2} \gamma_{xy} \end{Bmatrix}}. \quad (58)$$

Eq. 58 is split into a concrete stiffness  $[D_{gl}]^c$  and a reinforcement stiffness

$$[D_{gl}]^s \text{ as}$$

$$[D_{gl}]^c = \frac{\partial \left( [T(-\alpha_1)] \begin{Bmatrix} \sigma_1^c \\ \sigma_2^c \\ \tau_{12}^c \end{Bmatrix} \right)}{\partial \begin{Bmatrix} \varepsilon_x \\ \varepsilon_y \\ \frac{1}{2} \gamma_{xy} \end{Bmatrix}}, \quad (59)$$

and

$$[D_{gl}]^s = \frac{\partial \left( \sum_i [T(-\alpha_{si})] \begin{Bmatrix} \rho_{si} f_{si} \\ 0 \\ 0 \end{Bmatrix} \right)}{\partial \begin{Bmatrix} \varepsilon_x \\ \varepsilon_y \\ \frac{1}{2} \gamma_{xy} \end{Bmatrix}}. \quad (60)$$

Thus the total stiffness becomes

$$[D_{gl}]^{c+s} = [D_{gl}]^c + [D_{gl}]^s, \quad (61)$$

where  $[D_{gl}]^c$  is the tangent material constitutive matrix of concrete; and

$[D_{gl}]^s$  is the tangent material constitutive matrix of the steel bars.

The equivalent uniaxial strains can be derived from the global strains using

$$\begin{Bmatrix} \bar{\varepsilon}_1 \\ \bar{\varepsilon}_2 \\ \frac{1}{2}\gamma_{12} \end{Bmatrix} = [\mu] \cdot [T(\alpha_1)] \cdot \begin{Bmatrix} \varepsilon_x \\ \varepsilon_y \\ \frac{1}{2}\gamma_{xy} \end{Bmatrix}, \quad (62)$$

where  $[\mu]$  is the Hsu/Zhu ratio matrix as shown in Eq. 25.

After substituting Eq. 62 into Eq. 59

$$[D_{gl}]^c = [T(-\alpha_1)] \cdot \begin{Bmatrix} \frac{\partial \sigma_1^c}{\partial \bar{\varepsilon}_1} & \frac{\partial \sigma_1^c}{\partial \bar{\varepsilon}_2} & \frac{\partial \sigma_1^c}{\partial \left(\frac{1}{2}\gamma_{12}\right)} \\ \frac{\partial \sigma_2^c}{\partial \bar{\varepsilon}_1} & \frac{\partial \sigma_2^c}{\partial \bar{\varepsilon}_2} & \frac{\partial \sigma_2^c}{\partial \left(\frac{1}{2}\gamma_{12}\right)} \\ \frac{\partial \tau_{12}^c}{\partial \bar{\varepsilon}_1} & \frac{\partial \tau_{12}^c}{\partial \bar{\varepsilon}_2} & \frac{\partial \tau_{12}^c}{\partial \left(\frac{1}{2}\gamma_{12}\right)} \end{Bmatrix} \cdot [\mu] \cdot [T(\alpha_1)]. \quad (63)$$

From Eq. (63), the concrete local tangential stiffness can be written as

$$[D_{lo}]^c = \begin{Bmatrix} \frac{\partial \sigma_1^c}{\partial \bar{\varepsilon}_1} & \frac{\partial \sigma_1^c}{\partial \bar{\varepsilon}_2} & \frac{\partial \sigma_1^c}{\partial \left(\frac{1}{2}\gamma_{12}\right)} \\ \frac{\partial \sigma_2^c}{\partial \bar{\varepsilon}_1} & \frac{\partial \sigma_2^c}{\partial \bar{\varepsilon}_2} & \frac{\partial \sigma_2^c}{\partial \left(\frac{1}{2}\gamma_{12}\right)} \\ \frac{\partial \tau_{12}^c}{\partial \bar{\varepsilon}_1} & \frac{\partial \tau_{12}^c}{\partial \bar{\varepsilon}_2} & \frac{\partial \tau_{12}^c}{\partial \left(\frac{1}{2}\gamma_{12}\right)} \end{Bmatrix}. \quad (64)$$

After substituting Eq. 64 into Eq. 63

$$[D_{gl}]^c = [T(-\alpha_1)] \cdot [D_{lo}]^c \cdot [\mu] \cdot [T(\alpha_1)]. \quad (65)$$

The diagonal terms in Eq. 64 matrix can be found directly from the uniaxial stress and strains in the respective directions. The first diagonal term  $\frac{\partial \sigma_1^c}{\partial \bar{\varepsilon}_1} = \bar{E}_1^c$  is the tangential uniaxial modulus of concrete in the 1-direction, the second diagonal term  $\frac{\partial \sigma_2^c}{\partial \bar{\varepsilon}_2} = \bar{E}_2^c$  is the tangential uniaxial modulus of concrete in the 2-direction, and the third diagonal term  $\frac{\partial \tau_{12}^c}{\partial \left( \frac{1}{2} \gamma_{12} \right)} = \frac{\sigma_1^c - \sigma_2^c}{\varepsilon_1 - \varepsilon_2} = G_{12}^c$  is the shear modulus. The off-diagonal terms  $\frac{\partial \sigma_1^c}{\partial \bar{\varepsilon}_2}$  and  $\frac{\partial \sigma_2^c}{\partial \bar{\varepsilon}_1}$  are obtained using the uniaxial stresses and the uniaxial strains in the orthogonal direction. These off-diagonal terms are not zero because the stresses and strains of the concrete in compression are softened by the orthogonal tensile strains. Therefore,  $[D_{lo}]^c$  can be written as

$$[D_{lo}]^c = \begin{bmatrix} \bar{E}_1^c & \frac{\partial \sigma_1^c}{\partial \bar{\varepsilon}_2} & 0 \\ \frac{\partial \sigma_2^c}{\partial \bar{\varepsilon}_1} & \bar{E}_2^c & 0 \\ 0 & 0 & G_{12}^c \end{bmatrix}. \quad (66)$$

The off-diagonal terms can be determined with three cases as described below.

### 6.1 Equivalent uniaxial strains $\bar{\varepsilon}_1 > 0$ and $\bar{\varepsilon}_2 > 0$

When  $\bar{\varepsilon}_1 > 0$  and  $\bar{\varepsilon}_2 > 0$  then the uniaxial concrete stresses  $\sigma_1^c$  and  $\sigma_2^c$  are calculated only from uniaxial strains  $\bar{\varepsilon}_1$  and  $\bar{\varepsilon}_2$ , respectively,

$$\text{Therefore, } \frac{\partial \sigma_1^c}{\partial \bar{\varepsilon}_2} = 0 \text{ and } \frac{\partial \sigma_2^c}{\partial \bar{\varepsilon}_1} = 0. \quad (67)$$

### 6.2 Equivalent uniaxial strains $\bar{\varepsilon}_1 > 0$ and $\bar{\varepsilon}_2 < 0$

When the uniaxial strain is  $\bar{\varepsilon}_1 > 0$  then the uniaxial compressive stress  $\sigma_1^c$  is calculated directly from the  $\bar{\varepsilon}_1$ , and  $\sigma_1^c$  is not a function of the orthogonal concrete

strain  $\bar{\varepsilon}_2$ . Therefore,  $\frac{\partial \sigma_1^C}{\partial \bar{\varepsilon}_2} = 0$ .

To obtain  $\frac{\partial \sigma_2^C}{\partial \bar{\varepsilon}_1}$ , the constitutive law of the concrete strut in compression is needed.

In order to obtain  $\frac{\partial \sigma_2^C}{\partial \varepsilon_1}$ , the constitutive law of concrete in compression is needed.

$$\sigma_2^C = \zeta \cdot f_c' \cdot \left[ 2 \left( \frac{\bar{\varepsilon}_2}{\zeta \varepsilon_0} \right) - \left( \frac{\bar{\varepsilon}_2}{\zeta \varepsilon_0} \right)^2 \right], \quad \frac{\bar{\varepsilon}_2}{\zeta \varepsilon_0} \leq 1 \quad (68)$$

$$\sigma_2^C = \zeta \cdot f_c' \cdot \left[ 1 - \left( \frac{\bar{\varepsilon}_2 / (\zeta \varepsilon_0) - 1}{4/\zeta - 1} \right)^2 \right], \quad \frac{\bar{\varepsilon}_2}{\zeta \varepsilon_0} > 1, \quad (69)$$

where the softening coefficient  $\zeta$  (Hsu and Zhu, 2002)

$$\zeta = \left( \frac{5.8}{\sqrt{f_c' (MPa)}} \leq 0.9 \right) \left( \frac{1}{\sqrt{1 + 400 \bar{\varepsilon}_1}} \right) \left( 1 - \frac{|\alpha_{r1}^0|}{24^0} \right). \quad (70)$$

In Eq. 70,  $\alpha_{r1}$  is in degrees. If the value of the  $\alpha_{r1}$  is in radians then the value of  $24^\circ$  should be converted into radians. After making the required changes, Eq. 70 becomes

$$\zeta = \left( \frac{5.8}{\sqrt{f_c' (MPa)}} \leq 0.9 \right) \left( \frac{1}{\sqrt{1 + 400 \bar{\varepsilon}_1}} \right) \left( 1 - \frac{15 |\alpha_{r1}^c|}{2\pi} \right), \quad (71)$$

$$\alpha_{r1}^c = 0.5 \tan^{-1} \left( \frac{\gamma_{12}}{\varepsilon_1 - \varepsilon_2} \right) \quad \text{and} \quad (72)$$

$$\varepsilon_1 = \bar{\varepsilon}_1 - \mu_{12} \bar{\varepsilon}_2 \quad \text{and} \quad \varepsilon_2 = \bar{\varepsilon}_2 - \mu_{21} \bar{\varepsilon}_1, \quad (73)$$

where  $\varepsilon_1$  and  $\varepsilon_2$  are the biaxial strains in the 1-2 coordinate system and  $\bar{\varepsilon}_1$  and  $\bar{\varepsilon}_2$  are the equivalent uniaxial strains in the 1-2 coordinate system.

From Eq. 72 and 73

$$\alpha_{r1}^c = 0.5 \tan^{-1} \left( \frac{\gamma_{12}}{\bar{\varepsilon}_1 (1 + \mu_{21}) - \bar{\varepsilon}_2 (1 + \mu_{12})} \right), \quad (74)$$

where  $\mu_{12}$  and  $\mu_{21}$  are the Hsu/Zhu ratios (Zhu and Hsu, 2002).

$$\frac{\partial \sigma_2^C}{\partial \bar{\varepsilon}_1} \text{ can be written as } \frac{\partial \sigma_2^C}{\partial \bar{\varepsilon}_1} = \frac{\partial \sigma_2^C}{\partial \zeta} \cdot \frac{\partial \zeta}{\partial \bar{\varepsilon}_1}. \quad (75)$$

$\frac{\partial \zeta}{\partial \bar{\varepsilon}_1}$  can be derived after substituting Eq. 74 into Eq. 71

$$\frac{\partial \zeta}{\partial \bar{\varepsilon}_1} = \frac{\partial \left( \left( \frac{5.8}{\sqrt{f'_c(MPa)}} \right) \left( \frac{1}{\sqrt{1+400\bar{\varepsilon}_1}} \right) \left( 1 - \frac{15}{4\pi} \tan^{-1} \left( \frac{\gamma_{12}}{\bar{\varepsilon}_1(1+\mu_{21}) - \bar{\varepsilon}_2(1+\mu_{12})} \right) \right) \right)}{\partial \bar{\varepsilon}_1} \quad (76)$$

$$= \left( \frac{5.8}{\sqrt{f'_c(MPa)}} \right) \left[ \frac{-200}{(1+400\bar{\varepsilon}_1)^{1.5}} + \frac{200 \tan^{-1} \left( \frac{\gamma_{12}}{\bar{\varepsilon}_1(1+\mu_{21}) - \bar{\varepsilon}_2(1+\mu_{12})} \right)}{(1+400\bar{\varepsilon}_1)^{1.5}} + \frac{15}{4\pi} + \frac{\gamma_{12}(1+\mu_{21})}{(1+400\bar{\varepsilon}_1)^{0.5} \left( \frac{\gamma_{12}}{\bar{\varepsilon}_1(1+\mu_{21}) - \bar{\varepsilon}_2(1+\mu_{12})} \right)^2 \left( 1 + \frac{(\gamma_{12})^2}{(\bar{\varepsilon}_1(1+\mu_{21}) - \bar{\varepsilon}_2(1+\mu_{12}))^2} \right)} \right]. \quad (77)$$

where  $\frac{\partial \sigma_2^C}{\partial \zeta}$  can be derived as

when  $\frac{\bar{\varepsilon}_2}{\zeta \varepsilon_0} \leq 1$ ,

$$\frac{\partial \sigma_2^C}{\partial \zeta} = \frac{\partial \left( \zeta \cdot f'_c \cdot \left[ 2 \left( \frac{\bar{\varepsilon}_2}{\zeta \varepsilon_0} \right) - \left( \frac{\bar{\varepsilon}_2}{\zeta \varepsilon_0} \right)^2 \right] \right)}{\partial \zeta} = f'_c \cdot \frac{\partial \left( 2 \left( \frac{\bar{\varepsilon}_2}{\varepsilon_0} \right) - \frac{(\bar{\varepsilon}_2)^2}{\zeta \varepsilon_0^2} \right)}{\partial \zeta} \quad (78a)$$

$$= -f'_c \cdot \frac{(\bar{\varepsilon}_2)^2}{\varepsilon_0^2} \cdot \frac{\partial \left( \frac{1}{\zeta} \right)}{\partial \zeta} = -f'_c \cdot \frac{(\bar{\varepsilon}_2)^2}{\varepsilon_0^2} \cdot \left( -\frac{1}{\zeta^2} \right) = f'_c \cdot \frac{(\bar{\varepsilon}_2)^2}{(\zeta \varepsilon_0)^2}. \quad (78b)$$

when  $\frac{\bar{\varepsilon}_2}{\zeta \varepsilon_0} > 1$ ,

$$\frac{\partial \sigma_2^C}{\partial \zeta} = \frac{\partial \left( \zeta \cdot f'_c \cdot \left[ 1 - \left( \frac{\bar{\varepsilon}_2 / (\zeta \varepsilon_0) - 1}{4/\zeta - 1} \right)^2 \right] \right)}{\partial \zeta} \quad (79a)$$

$$= f'_c \cdot \left[ 1 - \frac{\partial}{\partial \zeta} \left( \zeta \cdot \left( \frac{\bar{\varepsilon}_2 / (\zeta \varepsilon_0) - 1}{4/\zeta - 1} \right)^2 \right) \right]. \quad (79b)$$

$$\text{Let } \frac{\partial}{\partial \zeta} \left( \zeta \cdot \left( \frac{\bar{\varepsilon}_2 / (\zeta \varepsilon_0) - 1}{4/\zeta - 1} \right)^2 \right) = A, \quad (80)$$

Eq. 79 can be written as

$$\frac{\partial \sigma_2^c}{\partial \zeta} = f_c' \cdot (1 - A), \quad (81)$$

$$\text{where } A = \left( \frac{\bar{\varepsilon}_2 / (\zeta \varepsilon_0) - 1}{4/\zeta - 1} \right)^2 + \zeta \cdot 2 \cdot \left( \frac{\bar{\varepsilon}_2 / (\zeta \varepsilon_0) - 1}{4/\zeta - 1} \right) \cdot \frac{\partial}{\partial \zeta} \left( \frac{\bar{\varepsilon}_2 / (\zeta \varepsilon_0) - 1}{4/\zeta - 1} \right). \quad (82)$$

$$\text{Let } B = \frac{\partial}{\partial \zeta} \left( \frac{\bar{\varepsilon}_2 / (\zeta \varepsilon_0) - 1}{4/\zeta - 1} \right), \quad (83)$$

Eq. 82 can be written as

$$A = \left( \frac{\bar{\varepsilon}_2 / (\zeta \varepsilon_0) - 1}{4/\zeta - 1} \right)^2 + \zeta \cdot 2 \cdot \left( \frac{\bar{\varepsilon}_2 / (\zeta \varepsilon_0) - 1}{4/\zeta - 1} \right) \cdot B, \quad (84)$$

$$\text{where } B = \frac{\partial}{\partial \zeta} \left( \frac{\bar{\varepsilon}_2 / (\zeta \varepsilon_0) - 1}{4/\zeta - 1} \right) = \frac{\bar{\varepsilon}_2 / \varepsilon_0 - 4}{(4 - \zeta)^2}. \quad (85)$$

Substituting Eq. (85) into (84) gives

$$A = \frac{\bar{\varepsilon}_2 / (\zeta \varepsilon_0) - 1}{(4/\zeta - 1)^3} \cdot \left( 1 - 12/\zeta + (4/\zeta + 1) \frac{\bar{\varepsilon}_2}{\zeta \varepsilon_0} \right), \quad \left( \frac{\bar{\varepsilon}_2}{\zeta \varepsilon_0} > 1 \right). \quad (86)$$

Substituting Eq. (86) into (81) gives

$$\frac{\partial \sigma_2^c}{\partial \zeta} = f_c' \cdot \left( 1 - \frac{\bar{\varepsilon}_2 / (\zeta \varepsilon_0) - 1}{(4/\zeta - 1)^3} \cdot \left( 1 - 12/\zeta + (4/\zeta + 1) \frac{\bar{\varepsilon}_2}{\zeta \varepsilon_0} \right) \right). \quad (87)$$

Substituting Eqs. 78 and 77 into 75 gives

$$\text{When } \frac{\bar{\varepsilon}_2}{\zeta \varepsilon_0} \leq 1, \quad \frac{\partial \sigma_2^c}{\partial \bar{\varepsilon}_1} = f_c' \cdot \left( \frac{\bar{\varepsilon}_2}{\zeta \varepsilon_0} \right)^2 \cdot \frac{\partial \zeta}{\partial \bar{\varepsilon}_1}. \quad (88)$$

Substituting Eqs. 87 and 77 into 75 gives

$$\text{When } \frac{\bar{\varepsilon}_2}{\zeta \varepsilon_0} > 1, \quad \frac{\partial \sigma_2^c}{\partial \bar{\varepsilon}_1} = f_c' \cdot \left( 1 - \frac{\bar{\varepsilon}_2 / (\zeta \varepsilon_0) - 1}{(4/\zeta - 1)^3} \cdot \left( 1 - 12/\zeta + (4/\zeta + 1) \frac{\bar{\varepsilon}_2}{\zeta \varepsilon_0} \right) \right) \cdot \frac{\partial \zeta}{\partial \bar{\varepsilon}_1}. \quad (89)$$

When the equivalent uniaxial strains  $\bar{\varepsilon}_1 < 0$  and  $\bar{\varepsilon}_2 > 0$ , then the same procedure should be followed.



### 6.3 Equivalent uniaxial strains $\bar{\varepsilon}_1 < 0$ and $\bar{\varepsilon}_2 < 0$

When  $\bar{\varepsilon}_1 < 0$  and  $\bar{\varepsilon}_2 < 0$  then concrete will not soften, instead it increases its compressive strength in one direction depending on the confining stress in the orthogonal direction. Because of this reason the value of  $\zeta$  should be greater than or equal to 1. The current research uses Vecchio's (1992) simplified version of Kupfer et al. (1969) biaxial compression strength equation. These equations are strength-based; strain-based equations are not available in the literature and need to be investigated in future.

$$\frac{\partial \zeta}{\partial \bar{\varepsilon}_1} = 0 \text{ and } \frac{\partial \zeta}{\partial \bar{\varepsilon}_2} = 0 \quad (90)$$

$$\frac{\partial \sigma_1^c}{\partial \bar{\varepsilon}_2} = \frac{\partial \sigma_1^c}{\partial \zeta} \cdot \frac{\partial \zeta}{\partial \bar{\varepsilon}_2} = 0 \quad (91)$$

$$\frac{\partial \sigma_2^c}{\partial \bar{\varepsilon}_1} = \frac{\partial \sigma_2^c}{\partial \zeta} \cdot \frac{\partial \zeta}{\partial \bar{\varepsilon}_1} = 0. \quad (92)$$

The global tangential constitutive matrix of steel  $[D_{gl}]^s$  can be derived From Fig. 9 as

$$\begin{Bmatrix} \varepsilon_x \\ \varepsilon_y \\ \frac{1}{2} \gamma_{xy} \end{Bmatrix} = [T(\alpha_1)]^{-1} \cdot [\mu]^{-1} \cdot [T(\alpha_{si} - \alpha_1)]^{-1} \begin{Bmatrix} \bar{\varepsilon}_{si} \\ \bar{\varepsilon}_{si}^* \\ \frac{1}{2} \gamma_{si} \end{Bmatrix}. \quad (93)$$

Substituting Eq.93 into 60 gives

$$[D_{gl}]^s = \frac{\partial \left( \sum_i [T(-\alpha_{si})] \begin{Bmatrix} \rho_{si} f_{si} \\ 0 \\ 0 \end{Bmatrix} \right)}{\partial \left( [T(\alpha_1)]^{-1} \cdot [\mu]^{-1} \cdot [T(\alpha_{si} - \alpha_1)]^{-1} \begin{Bmatrix} \bar{\varepsilon}_{si} \\ \bar{\varepsilon}_{si}^* \\ \frac{1}{2} \gamma_{si} \end{Bmatrix} \right)}, \quad (94a)$$

$$\begin{aligned}
& \sum_i [T(-\alpha_{si})] \cdot \rho_{si} \cdot \begin{bmatrix} \frac{\partial f_{si}}{\bar{\varepsilon}_{si}} & \frac{\partial f_{si}}{\bar{\varepsilon}_{si}^*} & \frac{\partial f_{si}}{\partial \left(\frac{1}{2}\gamma_{si}\right)} \\ 0 & 0 & 0 \\ 0 & 0 & 0 \end{bmatrix} \\
= & \frac{\quad}{[T(\alpha_1)]^{-1} \cdot [\mu]^{-1} \cdot [T(\alpha_{si} - \alpha_1)]^{-1}}, \tag{94b}
\end{aligned}$$

$$\begin{aligned}
= & \sum_i [T(-\alpha_{si})] \cdot \rho_{si} \cdot \begin{bmatrix} \frac{\partial f_{si}}{\bar{\varepsilon}_{si}} & \frac{\partial f_{si}}{\bar{\varepsilon}_{si}^*} & \frac{\partial f_{si}}{\partial \left(\frac{1}{2}\gamma_{si}\right)} \\ 0 & 0 & 0 \\ 0 & 0 & 0 \end{bmatrix} [T(\alpha_{si} - \alpha_1)] \cdot [\mu] \cdot [T(\alpha_1)], \tag{94c}
\end{aligned}$$

$$\text{Let } [D_{lo}]^s = \rho_{si} \cdot \begin{bmatrix} \frac{\partial f_{si}}{\partial \bar{\varepsilon}_{si}} & \frac{\partial f_{si}}{\bar{\varepsilon}_{si}^*} & \frac{\partial f_{si}}{\partial \left(\frac{1}{2}\gamma_{si}\right)} \\ 0 & 0 & 0 \\ 0 & 0 & 0 \end{bmatrix}, \tag{95}$$

where  $\frac{\partial f_{si}}{\partial \bar{\varepsilon}_{si}} = \bar{E}_{si}$ , which is the equivalent uniaxial tangential modulus in the longitudinal direction of the reinforcement. The dowel action of the reinforcement is neglected, thus  $\frac{\partial f_{si}}{\partial \bar{\varepsilon}_{si}^*} = 0$ , and also the shear deformation in the reinforcing bar is neglected, thus  $\frac{\partial f_{si}}{\partial \left(\frac{1}{2} \gamma_{si}\right)} = 0$ .

With these simplifications Eq.95 can be written as

$$[D_{lo}]^s = \begin{bmatrix} \rho_{si} \cdot \bar{E}_{si} & 0 & 0 \\ 0 & 0 & 0 \\ 0 & 0 & 0 \end{bmatrix}. \quad (96)$$

Eq. 94 can be written as

$$[D_{gl}]^s = \sum_i [T(-\alpha_{si})] \cdot [D_{lo}]^s \cdot [T(\alpha_{si} - \alpha_1)] \cdot [\mu] \cdot [T(\alpha_1)]. \quad (97)$$

After substituting Eqs. 97 and 64 into Eq. 61 the global tangent material constitutive matrix  $[D_{gl}]^{c+s}$  can be evaluated as

$$k_{fiber} = [D_{gl}]^{c+s} = [T(-\alpha_1)] \cdot [D_{lo}]^c \cdot [\mu] \cdot [T(\alpha_1)] + \sum_i [T(-\alpha_{si})] \cdot [D_{lo}]^s \cdot [T(\alpha_{si} - \alpha_1)] \cdot [\mu] \cdot [T(\alpha_1)]. \quad (98)$$

The total stiffness of the section is derived from the sum of concrete and steel stiffness

$$[K_{Section}] = \sum_1^n K_{fiber}, \quad (99)$$

The total force of the section is the sum of concrete and steel forces in their respective directions

$$\{F_{Section}\} = \sum_1^n F_{fiber}. \quad (100)$$

where  $n$  is the number of concrete and steel fibers in a section.

The element stiffness and forces are calculated with numerical integration respectively

$$[K_{Element}] = J \int_{-1}^{+1} B(x)^T k(x)_{Section} B(x) \partial \xi = J \sum_{ii=1}^{nIP} W_{ii} B(x_{ii})^T k(x_{ii})_{Section} B(x_{ii}), \quad (101)$$

$$\{F_{Element}\} = J \int_{-1}^{+1} B(x)^T F(x)_{Section} \partial \xi = J \sum_{ii=1}^{nIP} W_{ii} * B(x_{ii})^T F(x_{ii})_{Section}, \quad (102)$$

where  $W$  is the Gaussian weight,  $nIP$  is the number of integration points, and  $J$  is the Jacobian.

## 7. NUMERICAL CORRELATIONS WITH EXPERIMENTS

### 7.1 Comparison of Concrete Model with the experimental 1-D Cyclic Stress-Strain Curves

The uniaxial material models developed in this paper are compared with the experimental results by Mansour (2001).

Mansour (2001) tested three panels of the CVE3 – series. The steel grids in these panels are set parallel to the applied principal stresses in horizontal and vertical directions.

The three panels of this series CVE3-1, CVE3-2 and CVE3-3 are subjected to 1-D cyclic loading in the horizontal direction, while maintaining a constant lateral tensile strain ( $\epsilon_t$ ) of 0.0044, 0.012 and 0.030.

Each panel has the following dimensions: length 1397 mm, height 1397 mm, and thickness 178 mm. The panels are reinforced in each direction with No. 6 bars at 267 mm spacing. The concrete compressive strengths of CVE3-1, CVE3-2, and CVE3-3 are 48 MPa, 41 MPa, and 43 MPa. The yield stress of longitudinal and transverse steel of panels CVE3-1, CVE3-2, and CVE3-3 is 425.4 MPa.

The numerical result of the three panels CVE3-1, CVE3-2, and CVE3-3 with the current model are presented in Fig. 10, Fig. 12, and Fig. 14. The experimental results of CVE3-1, CVE3-2, and CVE3-3 panels, along with the cyclic model results developed by Mansour (2001), are presented in Fig. 11, Fig. 13, and Fig. 15. (In these figures, the horizontal axes represent the smeared concrete strain in the longitudinal direction, and the vertical axes represent the smeared concrete stress in the longitudinal direction.)

Comparison of the current model results for the three panels in the CVE3 series showed an increase in lateral tensile strain; the ultimate value of the horizontal compression stress decreases because of the softening behavior of the concrete. Figs. 10 - 15 show that the current model predicts fairly well the experimental behavior at both the compression and tension regions.

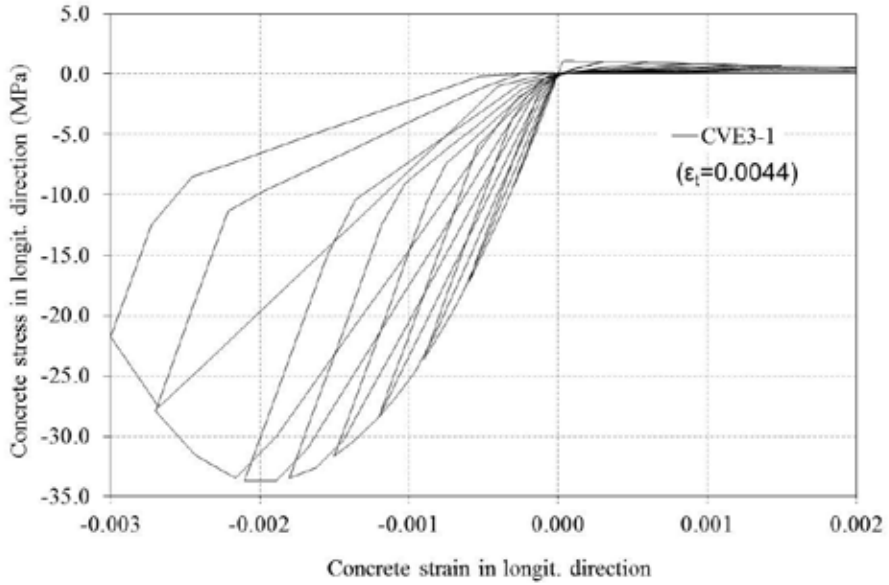


Figure 10 - Predicted concrete stress-strain curve of CVE3-1.

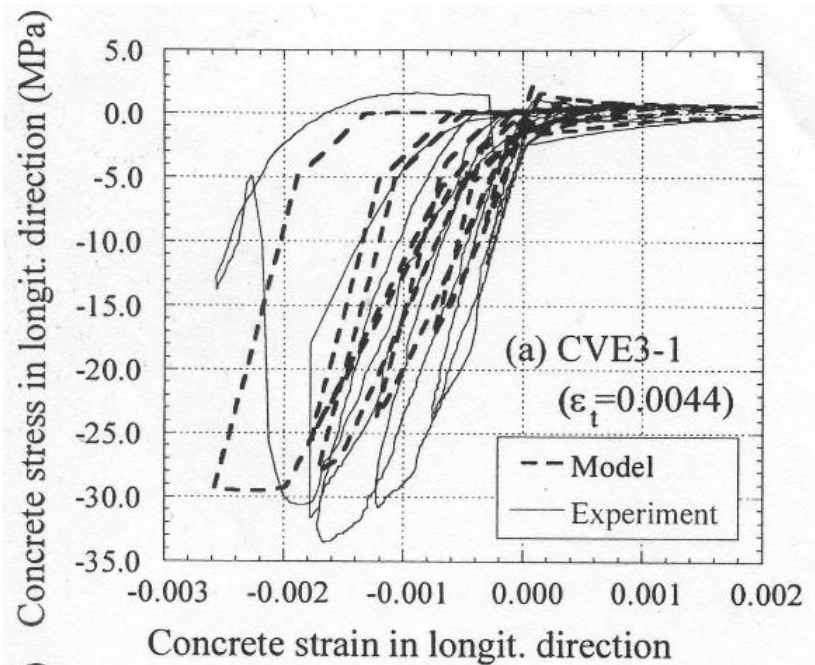


Figure 11 - Experimental and model predicted concrete stress-strain curve of CVE3-1 (Mansour, 2001).

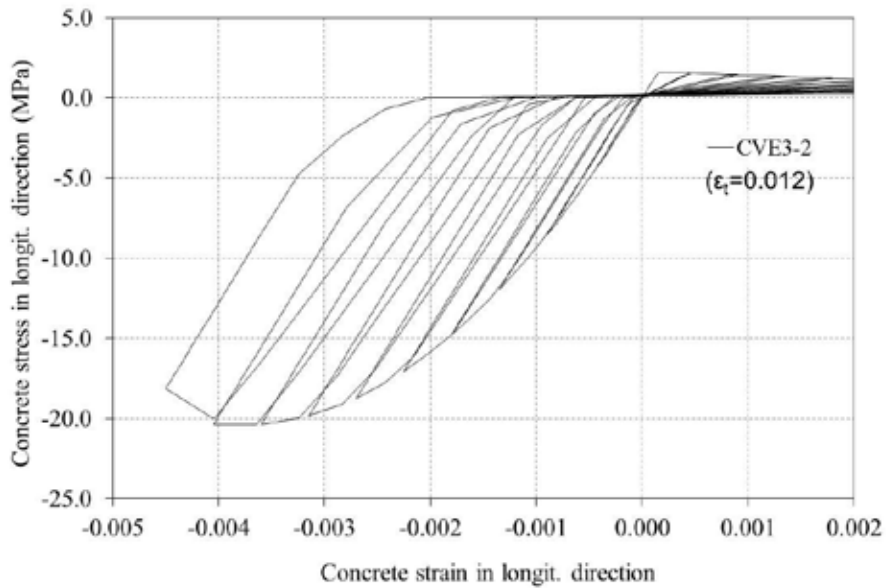


Figure 12 - Predicted concrete stress-strain curve of CVE3-2.

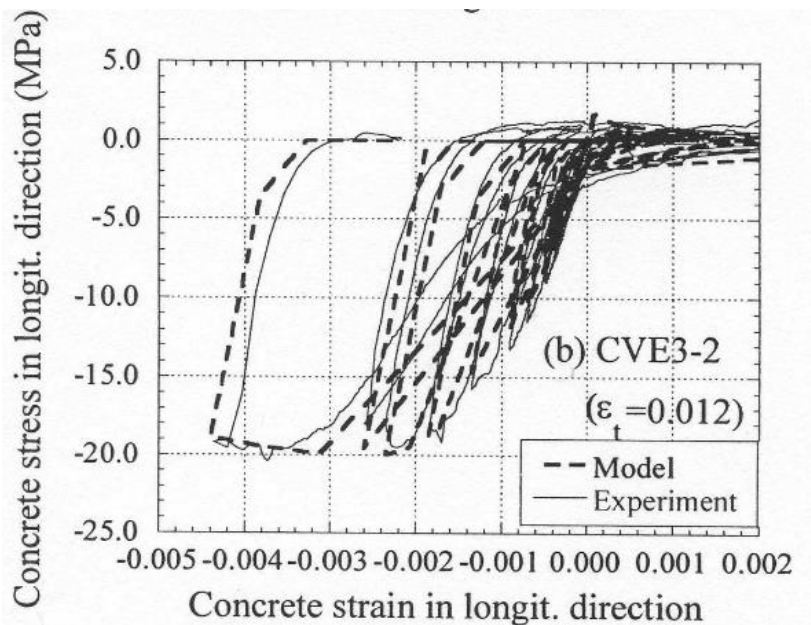


Figure 13 - Experimental and model predicted concrete stress-strain curve of CVE3-2 (Mansour, 2001).

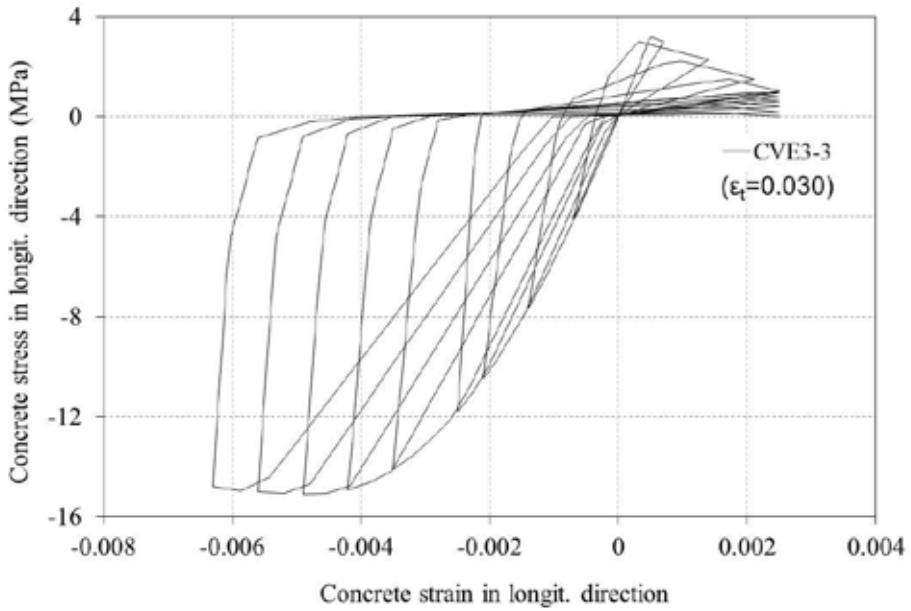


Figure 14 - Predicted concrete stress-strain curve of CVE3-3.

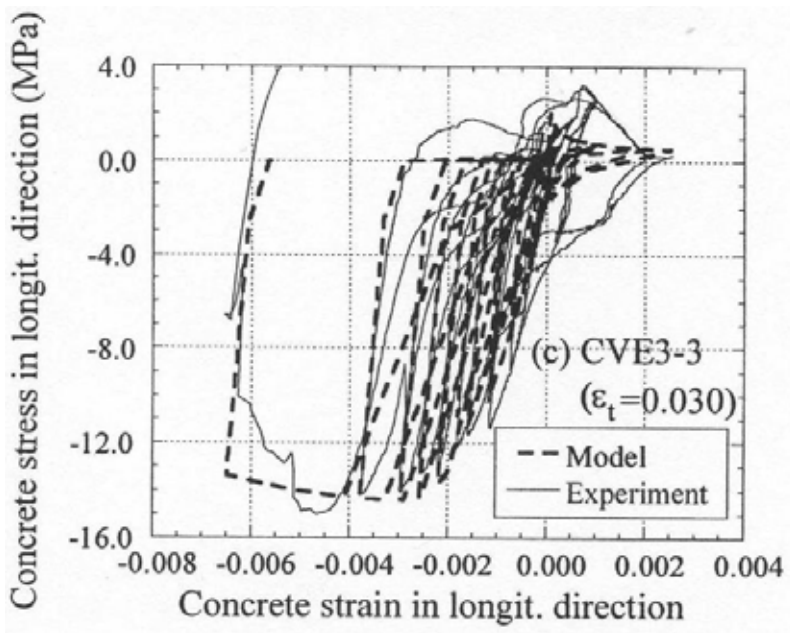


Figure 15 - Experimental and model predicted concrete stress-strain curve of CVE3-3 (Mansour, 2001).

## 7.2 Simulation of Columns

Three hollow, rectangular prototype bridge piers PI1, PI2, and PS1 were tested under reverse cyclical loading at the National Center for Research on Earthquake Engineering in Taiwan (Yeh and Mo, 1999). These prototypes are analyzed using the fiber beam element. The specimens are tested as cantilevers; the relevant material properties of concrete and reinforcement are given in Table 1. Fig. 16 shows the details of cross section dimensions and reinforcement details of the specimens. The columns are tested under displacement control with cyclically-reversed horizontal load.

Table1 - Properties of bridge piers (Yeh and Mo, 1999)

Specimen Name	$f_c'$ (MPa)	Length (mm)	Longitudinal reinforcement			Transverse reinforcement		
			<i>Dia.</i> (mm)	$f_y$ (MPa)	$f_{su}$ (MPa)	<i>Dia.</i> (mm)	$f_y$ (MPa)	<i>Spacing</i> (mm)
PS1	34.0	6500	22	460.0	647.0	13	343.0	80
PI1		4500				10	510.0	120
PI2	32.0	3500		418.2	626.5	10	420.0	200

Note:  $f_c'$  = Concrete compressive strength;  $f_y$  = Steel yielding strength;  $f_{su}$  = Steel ultimate strength; *Dia.* = Diameter of steel bar.

The specimens are modeled with only one force based element and five Gauss Lobatto integration points. The cross section is divided into 28 fiber sections. The boundary condition at the bottom is assumed to be fixed while the lateral load is applied to the top of the column.



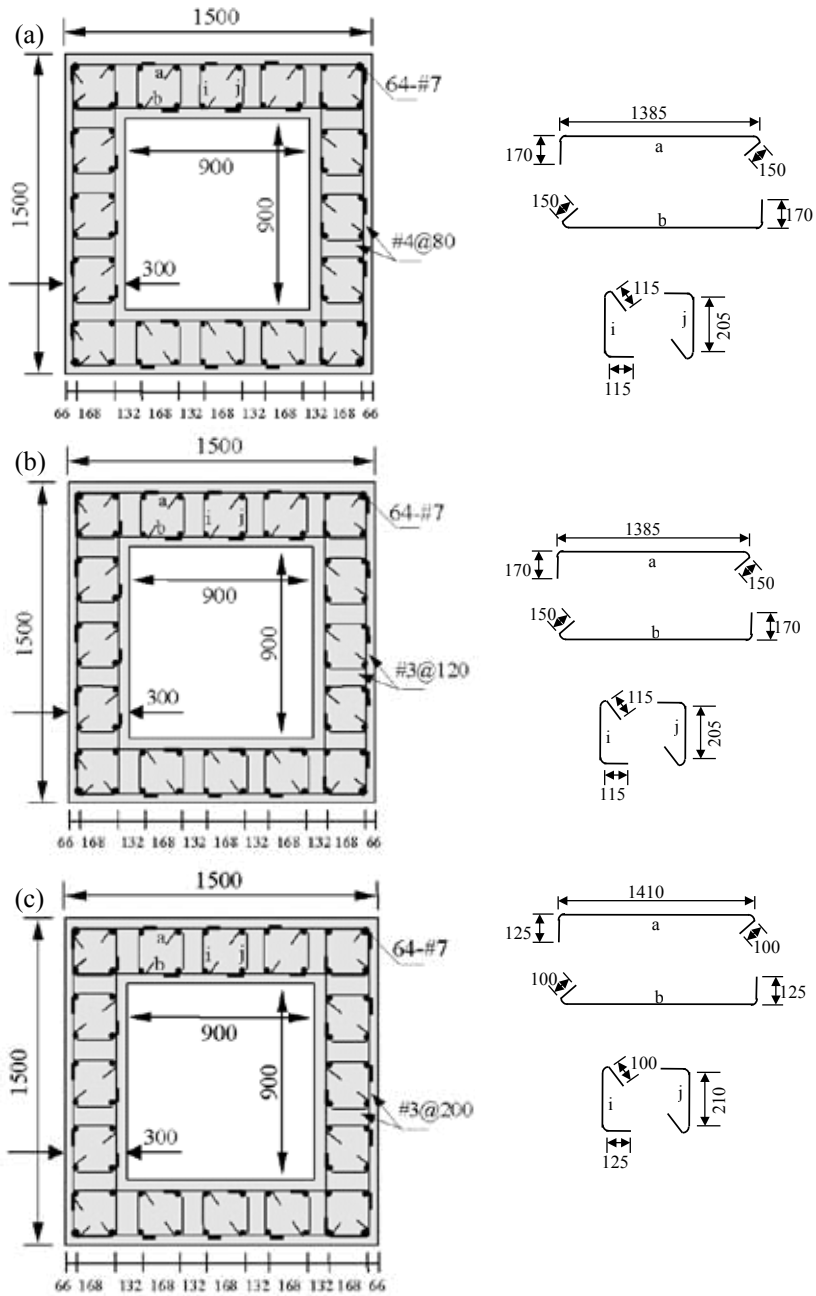


Figure 16 - Dimensions (in mm) of cross sections and reinforcement details of specimens (a) PS1 (b) P11 and (c) P12 (Yeh and Mo, 1999).

The longitudinal and transverse steel ratios are calculated based on the dimensions and spacing of the reinforcements. Concrete enveloped by the stirrups is modeled as confined concrete, while the remaining concrete (mostly in the cover) is considered as unconfined. The horizontal forces are increased based on the cyclic displacement control scheme.

The analytical shear force versus displacement relationships of the specimens are predicted with the 2-D fiber beam element as shown in Figs. 17-19; the results are then compared to the experimental results.

The moment lever arms for specimens PS1, PI1, and PI2 are 6.5 m, 4.5 m, and 3.5 m respectively. The reinforcement of the columns is designed such that column PS1 is dominated by a flexural failure, column PI1 is dominated by a flexure-shear failure, and column PI2 is dominated by shear failure. The experimental results (Yeh and Mo 1999; Yeh, Mo and Yang 2001) showed that specimens PS1 and PI1 failed in a flexure mode with the formation of plastic hinges at the bottom of the column and specimen PI2 failed under shear failure mode without rupturing the longitudinal reinforcement. The failure modes and ductility levels are reflected in the shape of the load displacement relationships. The rebar yielded significantly prior to the crushing of the concrete in specimens PS1 and PI1 (Fig. 17 and Fig. 18), which resulted in a long yield plateau and higher energy dissipation. Specimen PI2 (Fig. 19) showed a much shorter yield plateau and pinching with less energy dissipation than specimens PS1 and PI1. Specimen PS1 developed a displacement ductility of 10.8, specimen PI1 developed a displacement ductility of 7.8, and specimen PI2 developed a displacement ductility of only 3.7.

The numerical load-displacement relationships with the fiber beam element accurately captured the different behaviors of each of the three specimens. The fiber beam element predicted the initial stiffness, yield point, ultimate strength, and ductility of specimens PS1 and PI1 very well. The predicted cyclic load-displacement curve of symmetric specimen PI1 (Fig. 18) showed less ultimate strength in the negative cycles compared to experimental results. The fiber beam element also predicted the behavior of specimen PI2 (Fig. 19) to a degree in the positive direction, including the ultimate strength and strength degradation in the descending branch. The predicted ultimate strength of specimen PI2 in the negative direction is slightly higher than the test result, while the ultimate strength is slightly less with the plane stress element analysis. The predicted hysteresis loops of specimen PI2 with fiber beam element showed much less energy dissipation and predicted the experimental results.

## **8. CONCLUSIONS**

This paper presents a new finite element for cyclic analysis of reinforced concrete structures. A fiber-based beam element is developed to analyze reinforced concrete structures with the incorporation of mechanisms of shear deformation and strength.

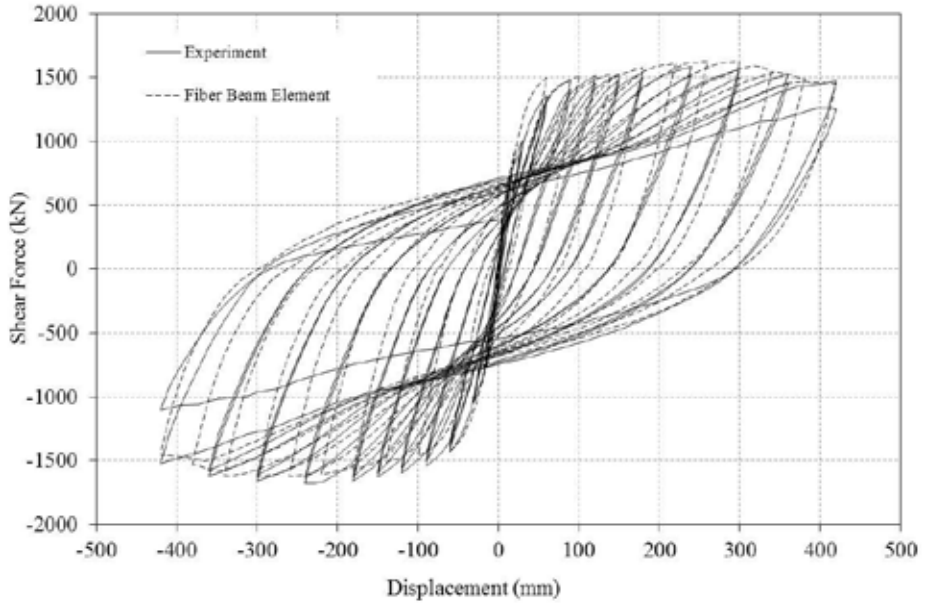


Figure 17 - Comparison of load-displacement behavior of specimen PS1 with fiber beam element, and experiment (Yeh and Mo, 1999).

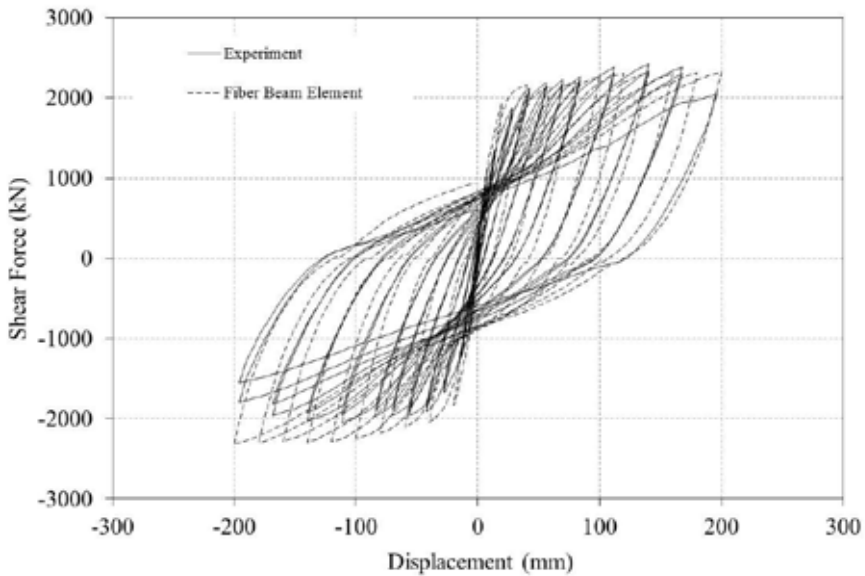


Figure 18 - Comparison of load-displacement behavior of specimen P11 with fiber beam element, and experiment (Yeh and Mo, 1999).

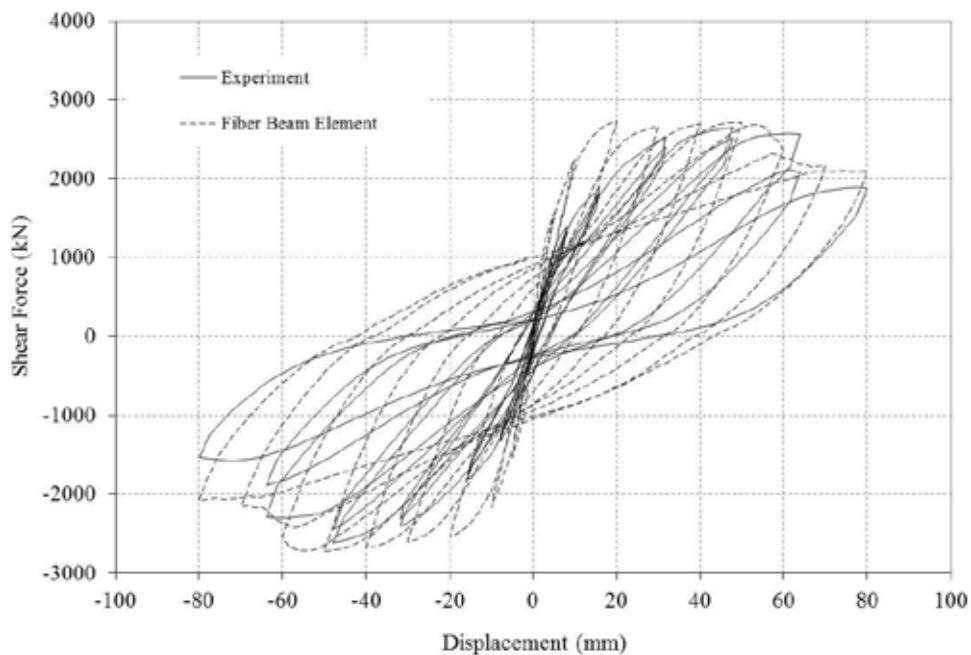


Figure 19 - Comparison of load-displacement behavior of specimen PI2 with fiber beam element, and experiment (Yeh and Mo, 1999).

Simplified cyclic uniaxial constitutive relations are developed and validated against the 1-D cyclic tests on panels by Mansour (2001). The tangent stiffness is formulated with the inclusion of the softening and dilatation effects. The reverse cyclic analyses of different columns with rectangular cross-sections are analyzed with the 2-D fiber beam element. The cyclic tests on columns by Yeh and Mo (1999) are analyzed by means of the 2-D fiber beam element. The shear walls with different aspect ratio exhibit different behaviors. The numerical results concerning the columns agree with the experimental results throughout the entire loading history. The FE analysis using the generalized Softened Membrane Model predicted the experimental results throughout the loading history, including the initial stiffness, yield point, ultimate strength, and failure mode.

## ACKNOWLEDGEMENTS

The research project was financially supported by the National Science Foundation under Grant number CMMI-0530737 and partially supported by the ASCE O.H. Ammann Research Fellowship. This support is gratefully acknowledged.

## REFERENCES

- ACI 318 (2008). "Building Code Requirements for Structural Concrete and Commentary". *American Concrete Institute*, Farmington Hills (Michigan, USA).
- Belarbi A. and Hsu T.T.C. (1994). "Constitutive Laws of Concrete in Tension and Reinforcing Bars Stiffened by Concrete". *Structural Journal - American Concrete Institute*, Vol 91, pp. 465-474.
- Belarbi A. and Hsu T.T.C. (1995). "Constitutive Laws of Softened Concrete in Biaxial Tension-Compression". *Structural Journal - American Concrete Institute*, Vol 92, No 5, pp. 562-573.
- Filippou F.C., Popov E.P. and Bertero V.V. (1983). "Effects of Bond Deterioration on Hysteretic Behavior of Reinforced Concrete Joints". *Report SESM 77-1, Division of Structural Engineering and Structural Mechanics*, University of California, Berkeley (California, USA).
- Hsu T. T. C. and Zhu R. R. H. (2002). "Softened Membrane Model for Reinforced Concrete Elements in Shear". *Structural Journal - American Concrete Institute*, Vol. 99, No. 4, pp. 460-469.
- Kupfer H. B., Hildorf H. K. and Rusch H. (1969). "Behavior of Concrete under Biaxial Stresses". *Structural Journal - American Concrete Institute*, Vol 66, No 8, pp. 656-666.
- Mansour, M. (2001). "Behavior of Reinforced Concrete Membrane Elements under Cyclic Shear Experiments to Theory," *PhD dissertation*, Department of Civil and Environmental Engineering, University of Houston.
- Mullapudi T.R.S. and Ayoub A.S. (2010). "Modeling of the Seismic Behavior of Shear-Critical Reinforced Concrete Columns". *Journal of Engineering Structures*, Vol.32, No.11, pp. 3601-15.
- Neuenhofer A. and Filippou F.C. (1997). "Evaluation of Nonlinear Frame Finite-Element Models". *Journal of Structural Engineering - ASCE*, V. 123, No. 7, pp. 958-966.
- Pang X. B. and Hsu T. T. C. (1996). "Fixed-Angle Softened-Truss Model for Reinforced Concrete". *Structural Journal - American Concrete Institute*, Vol. 93, No. 2, pp. 197-207.
- Park R, Priestley M.J.N and Gill W.D. (1982). "Ductility of Square Confined Concrete Columns". *Journal of Structural Division - ASCE* , Vol 108, No 4, pp. 929-950.

- Spacone E., Filippou F. C. and Taucer F. F. (1996). "Fiber Beam-Column Model for Nonlinear Analysis of R/C Frames, Part I Formulation". *Earthquake Engineering and Structural Dynamics*, V. 25, pp. 711-725.
- Taylor R. L. (2005). *FEAP User Manual v2.0*. Department of Civil and Environmental Engineering, University of California, Berkeley (California, USA), <http://www.ce.berkeley.edu/~rlt/feap/>.
- Vecchio F.J. (1992). "Finite Element Modeling of Concrete Expansion and Confinement". *Journal of Structural Engineering – ASCE*, Vol 118, No 9, pp. 2390-2405.
- Yeh Y.K. and Mo Y. L. (1999). "Full Scale Tests on Ductility, Shear Strength and Retrofit of Reinforced Concrete Hollow Columns (I)". *Report, No. NCREE-99-024*, National Center for Research on Earthquake Engineering, Taipei, Taiwan (Republic of China), in Chinese.
- Zhu R. H., Hsu T.T.C. and Lee, J.Y. (2001). "Rational Shear Modulus for Smearred Crack Analysis of Reinforced Concrete". *Structural Journal - American Concrete Institute*, Vol 98, No 4, pp. 443-450.
- Zhu R. H. and Hsu, T.T.C. (2002). "Poisson Effect of Reinforced Concrete Membrane Elements". *Structural Journal - American Concrete Institute*, Vol 99, No 5, pp. 631-640.

## **ANALYSIS OF REINFORCED-CONCRETE STRUCTURES TAKING INTO ACCOUNT CREEP AND CRACKING**

Faris Ali<sup>1</sup>

### **ABSTRACT**

This paper presents a simplified method of determining the flexural stiffness of reinforced-concrete members under sustained loads. The derived equations were used in the stiffness method to develop a procedure which enables the analysis of statically-indeterminate reinforced-concrete structures under sustained loads at any time in the loading history. The full solution of such structures requires two iteration types in the analytical procedures. The first iterative process calculates the creep stresses and evaluates the creep-induced cracking. The second iterative process calculates the bending moments and the forces in the whole structure. The proposed method eliminates the first iteration type and uses the second type only, in which the stiffness matrix of the structure is modified and updated until a reasonable accuracy is achieved. The paper includes an application by presenting an analysis of a reinforced-concrete frame under two cases of loading and foundation settlement over 10 years.

**KEYWORDS:** cracking, creep, reinforced concrete (R/C), flexural stiffness (in R/C), R/C frames, iterative processes.

---

<sup>1</sup> Professor, School of The Built Environment, University of Ulster, Jordanstown, BT37 0QB, UK.

## **1. INTRODUCTION**

It is well known that the deflection of a loaded R/C member increases with time and that this generally unfavourable effect is due to creep in the concrete. There are, however, beneficial effects of creep action. If a simply-supported R/C beam is subjected to sustained deformations that are constant over a period of time, a stress relaxation takes place. This relaxation of stress is due to creep effects, and can be significant depending upon factors such as the concrete properties, the reinforcement details, the loading level, and the length of the time period. An example for this phenomenon is a foundation settlement of a pier in a reinforced concrete bridge. Within time, the creep of concrete reduces the stresses in the reinforced concrete beam connected to the pier.

Moreover, in statically-indeterminate R/C structures creep may cause a redistribution of internal forces between the structural members, that takes place over a period of time. This means that in some parts of the structure the creep action may produce high moments that have not otherwise been considered in the analysis, whilst in other parts of the structure high localised moments may actually be reduced by the creep effects. Therefore, an iterative process is required to analyse the statically-indeterminate reinforced-concrete structure. This is due to the fact that the stiffness of the structure is function of the internal forces (moments and shear forces) and the internal forces are functions of the flexural stiffness of the structure.

The primary factor for this is the change that occurs with time in the flexural stiffness of the reinforced-concrete members. This can significantly be influenced by the developing presence of cracks and creep, which reduce the flexural stiffness of the members. In turn, this reduced stiffness affects the distribution of moments around the structure, which causes further variation in the crack pattern and therefore in the moment distribution amongst the structural members.

Hence, the analysis of statically-indeterminate R/C structures under sustained loads and deformations is significantly dependent on the flexural stiffness, that in turn depends on the mechanical properties including creep and crack development in the structure. Taking into account creep and cracks effects, therefore, has a crucial role in determining the actual flexural stiffness of concrete members and consequently in the calculation process of the whole structure.

## **2. THE FLEXURAL STIFFNESS OF A R/C ELEMENT**

The appearance of cracks and the creep of concrete affect the flexural stiffness of a R/C beam and reduces its value with time. The amount of change in the flexural stiffness due to creep depends on several factors, the most important of which are the amount of reinforcement, the loading level, the length of the loading period and the properties of the concrete. The effect of creep on the development of concrete



deformations has been investigated by many authors (Sapountzakis and Katsikadelis, 2002; Bazant, 1988; Bazant and Li, 2008; Bazant et al., 2009).

Methods of determining the long-term deformations of R/C structures due to creep may be divided into two main groups. The first group consists of techniques based on multiplying the immediate deformations that occur at the time of loading by multipliers. Although easy to use, these methods have a degree of inaccuracy in their results. Procedures of the second group are based on determining the stresses and the position of the neutral axis of the section at any particular moment of the structure age using time steps. Although the latter methods are more accurate, they are more complicated analytically. The method used in the EC2 (2004) is related to the first group. Using the approach adopted by Ali et al. (1996), the flexural stiffness of a reinforced concrete beam  $K(t)$  may be presented as:

$$K(t) = \left[ F_{\text{imd}} + F_{\text{crp}}(t) \right]^{-1} \quad (1)$$

where  $F_{\text{imd}}$  and  $F_{\text{crp}}(t)$  are flexibility functions that take into account the immediate flexural stiffness at the time of loading and the change in the flexural stiffness with time due to creep. Eq. 1 enables the immediate and the long-term values of the flexural stiffness of a singly- or doubly-reinforced beam - with either rectangular or Tee section - to be determined. The equation applies to beams loaded in flexure either with or without an axial compressive force. The immediate change in the flexural stiffness, which is associated with loading at the initial time  $t_0$ , can be found from the expression:

$$F_{\text{imd}} = K_0 \cdot F_S \cdot F_{\text{ld}} \cdot F_N \cdot F_{\text{Tee}} \cdot F_t \quad (2)$$

Each function  $F$  on the right hand side of Eq. 2 takes into consideration the effect of one of the factors of influence on the flexibility.  $F_S$  considers the influence of the reinforcement ratio in the section;  $F_{\text{ld}}$  the influence of loading level;  $F_N$  the influence of axial compressive forces (if any) in the section;  $F_{\text{Tee}}$  the shape of beam section (whether rectangular or Tee); and  $F_t$  the influence of time factor and creep coefficient. The values of these functions and the value of  $K_0$  can be calculated as follows:

$$F_S = f_1 \cdot (\rho n)^2 + f_2 \cdot (\rho n) + f_3 \quad (3-a)$$

$$F_{\text{ld}} = 1 - (f_4 \cdot \zeta^m) \quad (3-b)$$

$$F_N = 1 - (f_5 \cdot \nu) \quad (3-c)$$

$$F_{\text{Tee}} = 1 - 0.5f_6 \cdot h_T(8 + b_T) \quad (3-d)$$

$$F_t = 1 \quad ; \quad K_0 = \frac{1}{E_S \cdot A_S \cdot d^2} \quad (3-e,f)$$

where:  $E_s$  = Young's modulus of steel;  $n = E_s/E_c$ ;  $E_c$  = Young's modulus of concrete;  $\zeta =$  loading level ( $\zeta = M_{cr}/M$ );  $M_{cr}$  = cracking moment;  $\rho = A_s/A_c$ ;  $A_s, A_c$  = area of tension steel and concrete respectively;  $\nu =$  coefficient of axial compressive force [ $\nu = N \cdot Z_a/M(t)$ ];  $M(t)$  = the bending moment at any moment of time;  $d$  = effective depth of the section;  $N$  = axial compressive force;  $Z_a$  = lever arm of the section;  $h_T = h_f/h$ ;  $b_T = b_f/b$ ;  $m = 2$ ; and  $h_f$  and  $b_f$  are Tee beam dimensions;  $h$  = height of the section;  $b$  = width of the section.

The coefficients  $f_i$  ( $i = 1 \rightarrow 6$ ) in Eqs. 3a-b can be determined according to the following expressions:

- if  $i = 1, 2, 3$  then :

$$f_i = c_{i1} \cdot (\rho'')^2 + c_{i2} \cdot \rho'' + c_{i3} \quad (4)$$

- if  $i = 4, 5, 6$  then :

$$f_i = c_{i1} \cdot (\rho n) + c_{i2} \quad (5)$$

where  $\rho'' = A'_s/A_s$ ;  $A'_s$  = area of compression steel. The values of the coefficient  $c_{ij}$  associated with immediate flexibility, are given in Table 1.

The value of  $F_{crp}(t)$  - which takes into account the creep effects - can be calculated using the right-hand side of Eq. 2 and the related Eqs. 3-5, using coefficients  $c_{ij}$  associated with long-term flexibility as shown in Table 1. In this case  $m = 1$  in Eq. 3b, and  $F_t$  in Eq. 3f becomes

$$F_t = C_u \cdot \left[ 1 - 0.33e^{-\gamma_1(t-t_0)} - 0.67e^{-\gamma_2(t-t_0)} \right] \quad (6)$$

In Eq. 6,  $C_u$  is the ultimate coefficient of creep and

$$\gamma_1 = (0.023\rho n - 6.4 \cdot 10^{-4}) \cdot \rho'' - (5.044\rho n - 2.57) \cdot 10^{-3}$$

$$\gamma_2 = (0.0612\rho n + 9.76 \cdot 10^{-4}) \cdot \rho'' + 0.0154.$$

It is obvious from Eq. 6 that if the loading period is long, and since  $t \gg t_0$ , then  $F_t \approx C_u$ . In such a case, there is no need to use Eq. 6 and to calculate  $\gamma_1, \gamma_2$  (derivation  $\gamma_1$  and  $\gamma_2$  is given in Ali. et. al., 1996). As indicated above, each of the functions  $F_s, F_{ld}, F_N, F_{Tee}$  and  $F_t$  in Eq. 2 deals with one of the factors that affect the flexibility. It is therefore only necessary to calculate the value of a function if a particular case requires it.

When a factor is absent the value of the associated function becomes unity. For example, to calculate the immediate flexural stiffness of a singly-reinforced rectangular beam subjected to a very high bending moment ( $\zeta \leq 0.1$ ) and no applied

axial forces ( $N = 0$ ), then  $F_t = 1$ ,  $F_{Tee} = 1$ ,  $F_N = 1$ , and  $F_{ld} \approx 1$ . Expression (2) therefore simplifies significantly to become  $F_{imd} = K_o \cdot F_s$  and Eq. 4 also reduces to  $f_i = c_{i3}$ . Eqs. 1-6 enable the determination of the flexural stiffness of a R/C beam subjected to flexure, with or without axial forces under sustained loads. The equations take into account the development of cracks and allow the calculation of stiffness at any moment of the loading history with less effort as the long-term deformation can be calculated without time steps (Bazant and Li, 2008; Bazant et al., 2008).

A comparison between flexural stiffness values calculated by Eqs. 1-6 and experimental values showed 8.6% and 9.1% difference in the short- and long-term loading, respectively (Ali et al., 1996). This compares favourably with the results of other calculation procedures (Ali et al., 1998).

### 3. ANALYSIS OF STATICALLY-INDETERMINATE R/C FRAMES USING THE STIFFNESS METHOD

The stiffness method was chosen for the analysis of indeterminate structures subjected to long-term loading as it is more appropriate for computer programming. Moreover, the flexural stiffness of the structure members is contained in one matrix which facilitates the calculation process. In comparison with the conventional (elastic) analysis of indeterminate structures, two main parameters will be involved, creep and cracks appearance. As is commonly known, in a kinematically indeterminate structure the unknown displacements at any moment of time  $t$  can be found using the standard equation of the stiffness method:

$$\Delta^*(t) \cdot K^*(t) + P^*(t) = 0 \quad (7)$$

where  $\Delta^*(t)$  = matrix of deflection in the fictitious restraint,  $K^*(t)$  = stiffness matrix of the structure;  $P^*(t)$  = matrix of external loads. The elements of the matrices in Eq. 7 are functions of time as the effect of concrete creep is considered in this investigation.

#### 3.1. Stiffness Matrix $K^*(t)$ of Beam Element

The stiffness matrices of two types of beams will be presented in this section. The first type is a beam with fixed ends. The second is a beam with fixed-pinned ends as shown in Figure 1.

The procedure of determining two elements in the stiffness matrix of the first type will be given in detail.

**Table 1.** Determination of the coefficients  $c_{ij}$  (F = Function).

I	F	Immediate flexural stiffness $K_{imd}$			Long time flexural stiffness $K_{crp}(t)$		
		$c_{i1}$	$c_{i2}$	$c_{i3}$	$c_{i1}$	$c_{i2}$	$c_{i3}$
	$f_1$	6.42	-9.27	-5.00	9.80	-9.10	-2.34
2	$f_2$	0	-2.34	6.98	3.13	-7.69	4.96
3	$f_3$	0	0.05	1.23	-0.09	0.15	0.10
4	$f_4$	-1.41	0.50	0	$-2.46\rho'' + 0.3$	$-0.02\rho'' - 0.17$	0
5	$f_5$	-1.48	0.76	0	$0.44\rho'' - 0.41$	$0.05\rho'' + 0.17$	0
6	$f_6$	$-2.2h_T + 0.9$	$-1.44h_T + 0.32$	0	$7.17h_T - 1.75$	$-3.7h_T + 1$	0



Figure 1 - Types of beams considered in this study.

### 3.1.1. Beam with Fixed Ends

Figure 2 shows the reinforced beam a-b considered for determining the stiffness matrix. The main dilemma in determining the stiffness matrix for a R/C beam is the presence of cracks which may appear at low loading levels and which develop as the flexure increases. The development of the cracks means that the flexural stiffness of the section is a function of the bending moments affecting that beam, so that for most loading cases the flexural stiffness changes along the beam length.

The other important factor to be considered is the concrete creep represented by the time factor  $t$ . For the analysis of such a beam (where these two mentioned factors are involved) it is preferable to use the flexibility method to determine the elements of the stiffness matrix and the fixed-end moments. According to this method, the statically-indeterminate R/C beam shown in Figure 2-a can be transformed into the simply supported beam shown in Figure 2-b, where the unknown end moments  $M_a(t)$ ,  $M_b(t)$  can be determined using the standard equations of the flexibility method:

$$\begin{aligned}
M_a(t)\delta_{aa}(t) + M_b(t)\delta_{ab}(t) + \Delta_a^*(t) &= 0 \\
M_a(t)\delta_{ba}(t) + M_b(t)\delta_{bb}(t) + \Delta_b^*(t) &= 0
\end{aligned}
\tag{8}$$

To determine the coefficients  $\delta_{ij}(t)$ , ( $i, j = a, b$ ) of Eq. 8 the unit load method for deflection (virtual work) may be used:

$$\delta_{ij}(t) = \int_0^L \frac{\bar{M}_i(x)\bar{M}_j(x)}{K(t,x)} dx
\tag{9}$$

where  $K(t,x)$  = flexural stiffness; and  $\bar{M}_i(x)$ ;  $\bar{M}_j(x)$  are the bending moments induced by unit moments imposed at ends a and b in the direction of the sought displacement, as shown in Figure 2c-d. For example, if the case of a unit rotation  $\theta = 1$  of end a is considered, then the simultaneous Eqs. 8 become:

$$\begin{bmatrix} \delta_{aa}(t) & \delta_{ab}(t) \\ \delta_{ba}(t) & \delta_{bb}(t) \end{bmatrix} \times \begin{bmatrix} M_a(t) \\ M_b(t) \end{bmatrix} = \begin{bmatrix} 1 \\ 0 \end{bmatrix}
\tag{10}$$

Consequently

$$M_a(t) = \frac{\delta_{bb}(t)}{D}; \quad M_b(t) = \frac{\delta_{ab}(t)}{D}
\tag{11}$$

where  $D$  is the determinant of the matrix (10):

$$D = \delta_{aa}(t) \cdot \delta_{bb}(t) - (\delta_{ab}(t))^2
\tag{12}$$

Using the same procedure, other elements of the matrix can be derived. The full stiffness matrix of a reinforced concrete beam with fixed ends is shown in Fig.3.

The moments shown in Eq. 11 represent elements 3,3 and 3,6 in this matrix. By examining the stiffness matrix shown in Figure 3 it can be noticed that its elements have to be determined using Eq. 9, where  $K(t,x)$  represents the flexural stiffness of the single beam a-b. Because of the presence of cracks,  $K(t,x)$  in Eq. 9 is dependent on the bending moments affecting the beam. Therefore, its value is a function of the beam length  $x$ . Hence, in order to calculate  $\delta_{ij}(t)$ , the R/C beam a-b shown in Figure 2 must be divided into segments  $U$ , in each of which the value of the stiffness is considered to be constant. Thus, the value of  $\delta_{ij}(t)$  will equal to the sum of the displacements of these segments:

$$\delta_{ij}(t) = \sum_{m=1}^U K_m(t) \bar{\delta}_{ij}(t) \quad (13)$$

where  $\bar{\delta}_{ij}(t)$  is the value of  $\delta_{ij}(t)$  for the relevant segment  $m$ . The flexural stiffness values in Eq. 13 are calculated using Eqs. 1-6.

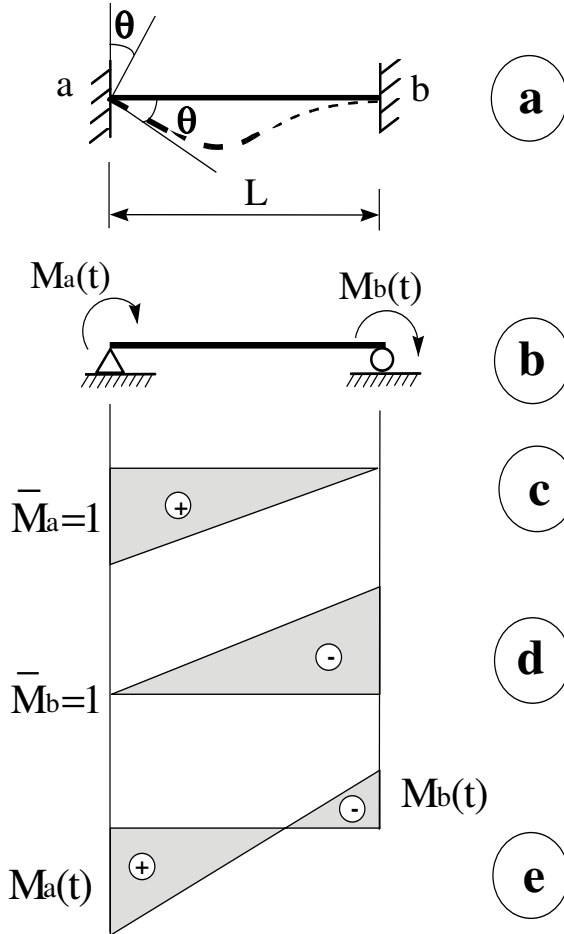


Figure 2 - Case of unit rotation of a beam with fixed ends.

$$\begin{array}{c}
 \left[ \begin{array}{c} P_{x_1} \\ P_{y_1} \\ M_1 \\ \hline P_{x_2} \\ P_{y_2} \\ M_2 \end{array} \right] = \left[ \begin{array}{ccc|ccc}
 \frac{AE}{L} & 0 & 0 & -\frac{AE}{L} & 0 & 0 \\
 0 & \Psi & \frac{\delta_{bb}(t) + \delta_{ab}(t)}{L \cdot D} & 0 & -\Psi & \frac{\delta_{bb}(t) + \delta_{ab}(t)}{L \cdot D} \\
 0 & \frac{\delta_{bb}(t) + \delta_{ab}(t)}{L \cdot D} & \frac{\delta_{bb}(t)}{D} & 0 & \frac{-(\delta_{bb}(t) + \delta_{ab}(t))}{L \cdot D} & \frac{\delta_{ab}(t)}{D} \\
 \hline
 -\frac{AE}{L} & 0 & 0 & \frac{AE}{L} & 0 & 0 \\
 0 & -\Psi & \frac{-(\delta_{bb}(t) + \delta_{ab}(t))}{L \cdot D} & 0 & \Psi & \frac{-(\delta_{bb}(t) + \delta_{ab}(t))}{L \cdot D} \\
 0 & \frac{\delta_{bb}(t) + \delta_{ab}(t)}{L \cdot D} & \frac{\delta_{ab}(t)}{D} & 0 & \frac{-(\delta_{bb}(t) + \delta_{ab}(t))}{L \cdot D} & \frac{\delta_{bb}(t)}{D}
 \end{array} \right] \left[ \begin{array}{c} dx_1 \\ dy_1 \\ \theta_1 \\ \hline dx_2 \\ dy_2 \\ \theta_2 \end{array} \right]
 \end{array}$$

$$\Psi = \frac{\delta_{bb}(t) + \delta_{ba}(t) + 2\delta_{ab}(t)}{L^2 \cdot D}$$

Figure 3 - Stiffness matrix of a beam with fixed ends.

### 3.1.2 Fixed-End Moments Due to External Loads

To determine the fixed-end moments induced by external loads, a similar procedure can be followed. Solving Eqs. 8 gives the end moments  $M_{aI}(t)$ ,  $M_{bI}(t)$ , induced by loads:

$$\begin{aligned}
 M_{aI}(t) &= \frac{\Delta_a^*(t)\delta_{bb}(t) + \Delta_b^*(t)\delta_{ba}(t)}{D} \\
 M_{bI}(t) &= \frac{\Delta_a^*(t)\delta_{ba}(t) + \Delta_b^*(t)\delta_{bb}(t)}{D}
 \end{aligned} \tag{14}$$

Figure 3 shows the considered R/C beam a-b under different types of loading on the end supports as shown in Figure 4. Therefore,  $\Delta_a^*(t); \Delta_b^*(t)$  of Eqs. 14 can be written as:

$$\begin{aligned}
 \Delta_a^*(t) &= \Delta_{aF}(t) + \Delta_{aT}(t) + \Delta_{aS}(t) \\
 \Delta_b^*(t) &= \Delta_{bF}(t) + \Delta_{bT}(t) + \Delta_{bS}(t)
 \end{aligned} \tag{15}$$

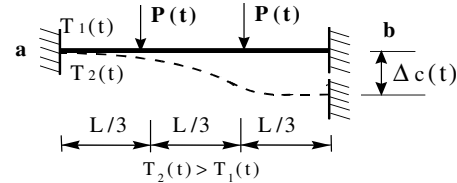
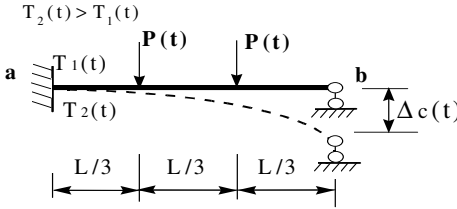
where:  $\Delta_{iF}(t); \Delta_{iT}(t); \Delta_{iS}(t)$ ; ( $i=a,b$ ) are displacements of ends a, b caused by point loads  $P(t)$ , temperature  $T(t)$  change and support settlement respectively (see Figure

4). Values of  $\Delta_{aF}(t)$ ,  $\Delta_{bF}(t)$  can be determined by basics of structural mechanics. The two other terms in Eqs. 15 can be found using the relationships:

$$\Delta_{iS}(t) = \frac{\Delta_c(t)}{L}, \Delta_{iT}(t) = \frac{0.5\alpha_T \cdot (T_2(t) - T_1(t)) \cdot L}{h} \quad (16)$$

where:  $\Delta_c(t)$  = vertical settlement of the support (see Figure 4);  $\alpha_T$  = coefficient of thermal expansion; and  $h$  = section depth;  $T_1$ ,  $T_2$  are top and bottom surface temperatures. The fixed-end moments of a beam are shown in Table 2.

**Table 2.** Fixed end moments due to external loads.

Case	Fixed End Moments
	$M_a(t) = \frac{\Delta_a(t)\delta_{bb}(t) + \Delta_b(t)\delta_{ab}(t)}{D}$ $M_b(t) = \frac{\Delta_a(t)\delta_{ba}(t) + \Delta_b(t)\delta_{aa}(t)}{D}$
	$M_a(t) = \frac{\Delta_a(t)}{D}$ $M_b(t) = 0$

### 3.2.1 Beam with One End Fixed and the Other Pinned

The stiffness matrix for this beam can be determined by following the same procedure taking into account the support type. The full stiffness matrix is shown in Fig. 5. The fixed-end moments created by external loads are shown in Table 2.

## 3.3 Calculation Procedure

Despite the fact that Eq. 1 eliminates the internal iterative process that is usually necessary to determine creep effects, there is still a necessity of one iteration in which the stiffness matrix is adjusted depending on bending moments values. Therefore, the analysis of a statically-indeterminate R/C structure under sustained loads includes the following steps:



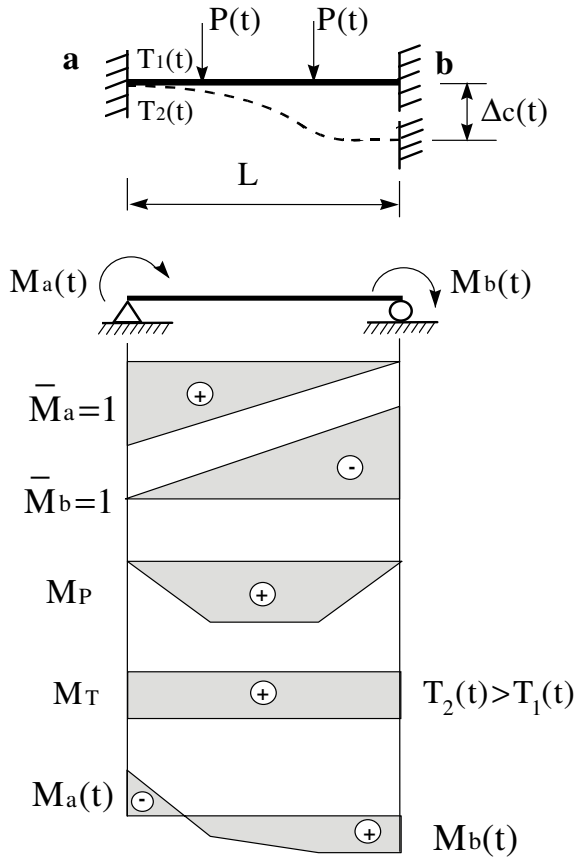


Figure 4 - External load case for a beam with fixed ends.

1. Elastic analysis of the structure: this is the standard analysis by stiffness method assuming that no cracks are present; this assumption means that the elastic values of the flexural stiffness should be used.
2. Analysis of the structure at a specific age (usually a concrete age = 28 days is used), taking into account the cracks effect; this step requires an iterative process, where in the first iteration the values of bending moments calculated in step one can be used:
  - Determining the stiffness matrix  $K^*(t)$  and the loads matrix  $P^*(t)$  of Eq. 7 using Figures 3,5 and Table 2; in determining the elements of matrix  $K^*(t)$ , Eqs. 13 and 9 have to be used where the flexural stiffness  $K(t,x)$  is calculated using Eqs. 1-6, taking into consideration coefficients associated with short-term loading in Table 1.

$$\begin{bmatrix} P_{x_1} \\ P_{y_1} \\ M_1 \\ \hline P_{x_2} \\ P_{y_2} \\ M_2 \end{bmatrix} = \begin{bmatrix} \frac{AE}{L} & 0 & 0 & -\frac{AE}{L} & 0 & 0 \\ 0 & \frac{1}{L^2\delta_{aa}(t)} & \frac{1}{L\delta_{aa}(t)} & 0 & \frac{-1}{L^2\delta_{aa}(t)} & 0 \\ 0 & \frac{1}{L\delta_{aa}(t)} & \frac{1}{\delta_{aa}(t)} & 0 & \frac{-1}{L\delta_{aa}(t)} & 0 \\ \hline -\frac{AE}{L} & 0 & 0 & \frac{AE}{L} & 0 & 0 \\ 0 & \frac{-1}{L^2\delta_{aa}(t)} & \frac{-1}{L\delta_{aa}(t)} & 0 & \frac{1}{L^2\delta_{aa}(t)} & 0 \\ 0 & 0 & 0 & 0 & 0 & \frac{1}{L^2\delta_{aa}(t)} \end{bmatrix} \begin{bmatrix} dx_1 \\ dy_1 \\ \theta_1 \\ \hline dx_2 \\ dy_2 \\ \theta_2 \end{bmatrix}$$

Figure 5 - Stiffness matrix for a beam with fixed-pinned ends.

- Solving the system (7) and find the matrix  $\Delta^*(t)$ .
  - Determining the bending moments and forces by conventional approach and comparing them with the values used in the previous iteration; if the difference is higher than the required accuracy, then repeat the procedure using the values of internal forces calculated in the last iteration.
- 3) Analysis for long time period ( $t > 28$  days) taking into account creep effects; a similar procedure as in step 2 should be used where the final values of bending moments and forces calculated at age = 28 days have to be used in the first iteration; function  $K(t,x)$  is calculated using Eqs. 1-6 taking into account coefficients associated with long-term loading presented in Table 1.

#### 4. APPLICATION - ANALYSIS OF A TWO-STORY, TWO-SPAN R/C FRAME

##### 4.1 Case One - Loads and Foundation Settlement

To study the effect of creep and cracking on distribution of bending moments and forces, the two-story two-span R/C frame shown in Figure 6 was considered for analysis. Sections of lateral beam 2-5 and column 0-1 are shown in Figure 6. All other beams and columns have the same cross sections. The lateral beams are

loaded with two point loads  $P = 90 \text{ kN}$  (representing the secondary beams in a structure) and the columns are loaded with point loads  $P_1 = 5000 \text{ kN}$ . It is assumed that the middle support 7 suffers from a sudden settlement  $\Delta_c = 30 \text{ mm}$  at age = 28 days. This settlement remains constant during the life of the structure. The other external effect is a rise in the external temperature of the upper story from  $10^\circ\text{C}$  to  $50^\circ\text{C}$ .

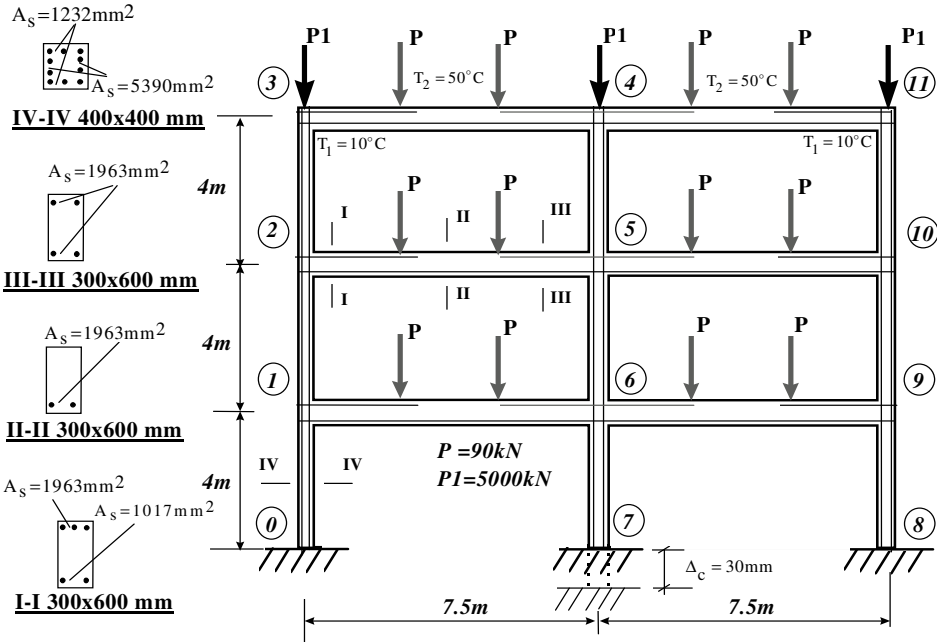


Figure 6 - The R/C frame considered in the analysis.

Also required are:  $E_c = 32.5 \times 10^3 \text{ MPa}$ ;  $f_{cu} = 30 \text{ MPa}$ ;  $E_s = 20 \times 10^4 \text{ MPa}$ . The creep coefficient of concrete changes according to the equation

$$C(t) = C_u \left[ 1 - e^{-0.008(t-28)} \right]$$

reaching the maximum values  $C_u = 1.9$  and  $3.9$  at temperatures =  $10^\circ\text{C}$  and  $50^\circ\text{C}$ , respectively. The analysis was performed to calculate the bending moments for ages  $t = 28, 120$  days and  $t = 10$  years. The procedure outlined in sections 2 and 3 was implemented using a computer to determine the bending moments.

The analysis revealed a considerable relaxation in the stresses and consequently in the bending moments of the frame columns and beams over the 10 years period of time (Figure 7). Figure 8 illustrates the bending moments diagrams of the frame at ages 28 and 120 days, as well at 10 years.

From Figure 8 it is obvious that the degree of relaxation varied between the structural parts. For example, in the middle joints 4 the bending moments were reduced by almost 48% over the ten years period of time, while a 20% relaxation took place in the lower column at joint 8. This mainly can be attributed to the settlement of the middle support 7 (constant with time). A much lesser effect had the temperature raise of the upper beams on the moment redistribution.

The relaxation took place gradually along the period of time. Figure 7 shows the rate of relaxation in the bending moments of beam 3-4 and column 0-1. It is obvious that the rate of relaxation is very high at early ages of the concrete, but reduces significantly after 2 years.

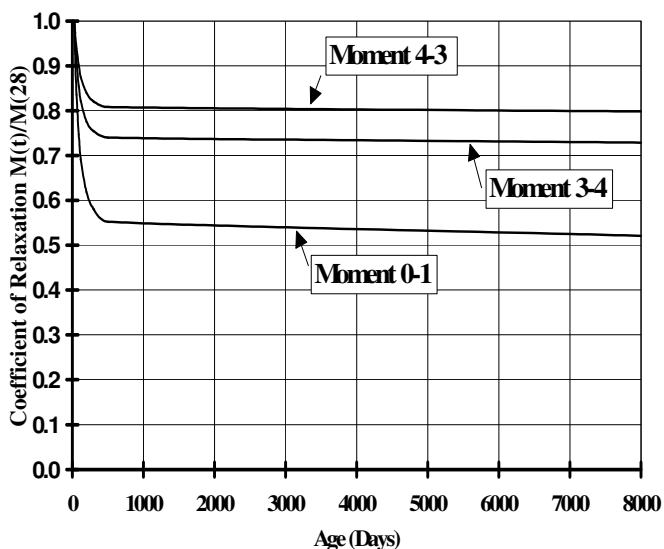


Figure 7 - Relaxation of bending moments during 10 years period.

## 4.2 Case Two - Loads Only

It has been shown in the previous example that the constant settlement of joint 7 had a significant effect on the redistribution and relaxation of bending moments. Therefore the same frame was analysed but under the effect of the point loads only, in order to identify the redistribution of moments when only loads are imposed. For all the other calculation data, the values were used the same as in the first case.

The analysis of the frame was performed for age = 28 days and 10 years only. Figure 9 shows the bending moments diagrams of the frame at these time stages.

The Figure shows that insignificant moment redistribution took place during the ten-years period. The other conclusion is that the moments increased in some joints and decreased in other joints, while there was a reduction only in the previous case

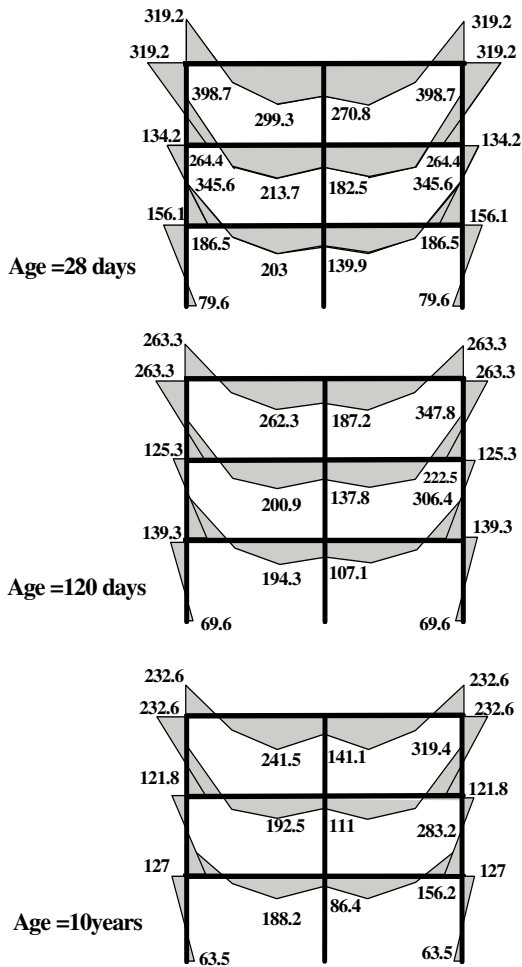


Figure 8 - Bending moment diagrams (kN.m) for different ages.

For example, the bending moments in joint 3 were reduced by some 8% while the moments were increased in joint 5 by almost 2%.

The study of this case shows that the creep has no significant effect when conventional loads are applied to a rheologically-uniform structure with perfect constraints, even if the effect of cracking is included. On the contrary, creep has considerable effect when a time-constant settlement occurs and smaller effect when thermal loads are applied.

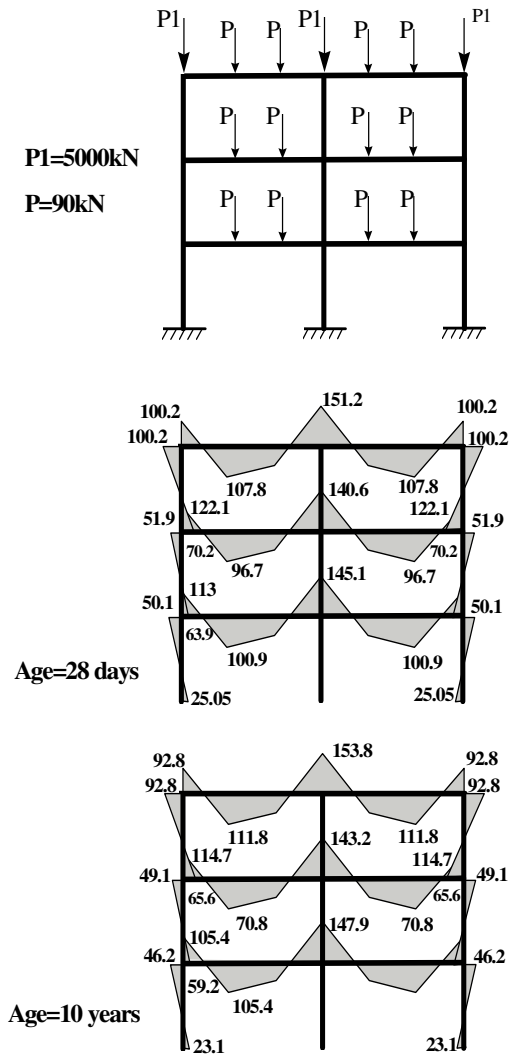


Figure 9 - Bending moments diagram (kN.m) for the load only case.

## 5. CONCLUSIONS

1. A procedure for the analysis of statically-indeterminate reinforced-concrete structures subjected to sustained loads is presented within the framework of the stiffness method.

2. The method takes into account the creep effects and the development of cracks, and allows the determination of the bending moments and forces with relatively little effort, as the creep iterative process is eliminated.
3. The analysis of a reinforced-concrete frame shows that creep has a positive effect (stress relaxation) in cases of foundation settlements that are constant with time.
4. The analysis indicates also that the moment redistribution and stress relaxation induced by creep is minimal in cases of conventional force loading acting on a structure subjected to cracking, provided that the structure is rheologically uniform and perfectly constrained.
5. The rate of stress relaxation under imposed settlements is initially very high but reduces significantly (almost to zero) as concrete ages.

## REFERENCES

- Sapountzakis E.J. and Katsikadelis J.T. (2002). "Creep and Shrinkage Effect on Reinforced Concrete Slab-and-Beam Structures". *Journal of Engineering Mechanics*, V.128, No.6, pp. 625-634.
- Bažant Z. P. (1988). *Mathematical Modelling of Creep and Shrinkage of Concrete*. John Wiley, New York, N. Y. (USA).
- Bažant Z.P. and Li G.H. (2008). "Comprehensive Database on Concrete Creep and Shrinkage". *ACI Materials Journal*, V.105, No.6, pp. 635-637.
- Bažant, Z.P., Li, G.-H. and Yu, Q. (2008). "Prediction of Creep and Shrinkage and their Effects in Concrete Structures: Critical Appraisal." *Proc. 8<sup>th</sup> Int. Conf. on Creep, Shrinkage and Durability Mechanics of Concrete and Concrete Structures – CONCREEP-8*, Sept.2-Oct.2, Ise-Shima (Japan), T. Tanabe et al. eds., CRC Press/Balkema, Taylor & Francis Group, Boca Raton–London, pp. 1275-1289.
- Eurocode 2 (2004). *Design of Concrete Structures in Fire (2004). Part 1- 1. Design of Concrete Structures: General Rules and Rules for Buildings*. EN 1992-1-1, European Committee for Standardization, Brussels, Belgium.
- Ali F. A., Baranoveski V. E. and Morrell P. J. B. (1996). "Long-Term Stiffness and Deflection of R/C Beams". *International Journal of Structures*, V.16, No.2.





## **TIME-DEPENDENT EFFECTS IN SEGMENTAL BRIDGES: PREDICTIVE MODELS AND ANALYSIS VIA SIMPLIFIED METHODS**

Marcello Arici<sup>1</sup>, Michele Fabio Granata<sup>2</sup> and Piercarlo Margiotta<sup>3</sup>

### **ABSTRACT**

The effects of delayed deformations on prestressed concrete segmental bridges are investigated in this paper. An analytical approach based on the principles of aging linear viscoelasticity and the Age-Adjusted Elastic Modulus (AAEM) method are proposed. The paper aims to provide an efficient and simplified tool for the evaluation of the structural response in the early stages of the design. Moreover a comparison among the results obtained with different predictive shrinkage and creep models applied to actual bridges is presented. The study concerns the case of segmental bridges built by a sequence of stages in which geometry, restraints and loads vary until the final configuration is achieved. The differences among the predictive models are underlined and the analysis is extended to very long time periods, as requested by the long service life of these structures. Numerical applications show that the influence of the stress redistribution on the bending moments, due to the change in the static schemes, is reduced by the load-balancing effect of the dead load and of the prestressing, and that bending-moment diagrams during the service life are little affected by the use of different predictive models. Opposite results are found for deflections, which differ significantly depending on the adopted model, the more the longer the time considered. The case of segmental bridges with an internal hinge at mid-span in the final scheme is investigated as well. This scheme exhibits increasing deflections due to creep, especially for very long time periods, such aspect being fundamental for the evaluation of bridge safety during the service life.

**KEYWORDS:** segmental bridges, concrete, creep, shrinkage, aging linear viscoelasticity, variable static schemes, delayed deformations.

---

<sup>1</sup> Professor, <sup>2</sup> Assistant Professor, <sup>3</sup> PhD Associate Researcher  
DICAM – Dipartimento di Ingegneria Civile, Ambientale, Aerospaziale e dei Materiali,  
Università di Palermo, Palermo, Italy

# 1. INTRODUCTION

The state of stress and deformation of a prestressed concrete bridge is influenced by the in-time behavior of the materials: creep and shrinkage of concrete, and relaxation of the prestressing steel. Among the time-dependent properties of concrete that are of interest to the structural engineer are the shrinkage due to cement hydration (self-desiccation), and loss of moisture to the environment and the creep under sustained loads. The mechanical properties of concrete are significantly affected by the temperature and availability of water during curing, the environmental humidity and temperature after curing, and the composition of the concrete, including the mechanical properties of the aggregates (ACI, 2008). These phenomena modify the internal forces and deflections of concrete girder bridges, especially during the construction stages, when the structure achieves its final configuration through different phases. The effects of delayed deformations imply increasing costs, because the structure has to be checked for stresses and deformations at the time of load application (time  $t_0$ ) and afterwards, during the service life (time  $t_\infty$ ).

The principal effects of creep in prestressed concrete bridges are:

- 1) increasing deformations due to sustained loads;
- 2) reduction of the stresses induced by the imposed strains acting on redundant structures;
- 3) redistribution of the stresses due to the changes in the static scheme when restraints are added after the application of sustained loads;
- 4) migration of the stresses in non-homogeneous cross-sections or among structural members exhibiting different viscoelastic properties;
- 5) prestressing losses.

In non-homogeneous structures, cast with different concretes or with composite cross-sections, the stress migration from softer materials to stiffer materials (with reference to the viscous-elastic behavior) can induce critical states regarding concrete cracking or over-stressing in the steel members. Structures with a high degree of heterogeneity are more sensitive to time-dependent phenomena than homogeneous structures. Moreover, heterogeneity can play a sizeable role in the structures composed of steel and concrete members, as in cable-stayed bridges with concrete or composite decks (Arici *et al.*, 2011; Granata *et al.*, 2012b) or in arch bridges built with the suspended cantilever methodology (Granata *et al.*, 2012a) and with lattice cantilevers (Granata *et al.*, 2013b). In this paper, the rheological homogeneity is referred to structures with homogeneous linear creep properties, which do not exhibit major variations in the concrete and whose reinforcement can be neglected, due to the small steel ratio.

In the case of bridge decks, the effects of time-dependent phenomena are strictly related to the construction methodology, because the final geometry is often achieved by a sequence of stages in which restraints and loads change

several times. The most common techniques to build concrete girder bridges are:

- decks composed of prefabricated beams;
- decks built by movable launching gantries;
- decks built by balanced cantilevers (especially for segmental bridges);
- incremental launching (Granata *et al.*, 2013a).

In all these construction techniques, the sequence of static-scheme variations is critical for establishing the actual state of the strains and stresses at the end of the construction and afterwards, during the service life. An interesting example is offered by segmental bridges, whose final static scheme is that of a continuous girder on piers. Cast-in-place or precast segments are assembled from the piers to midspan thanks to the introduction of prestressing cables close to the extrados, in order to obtain long cantilevers. Subsequently, when the two cantilevers protruding from contiguous piers meet at mid-span, the mutual link is constructed by casting the key segment and by adding continuity prestressing cables, which are placed close to the intrados in the mid-span sections and are raised close to the piers. This sequence implies the addition of internal restraints in the key section, so that the initial statically-determined scheme consisting in two balanced cantilevers becomes statically redundant. As a consequence, the static and kinematic regime evolves as time goes by, and the increase of the deflection may put serviceability at risk.

Examples of high values for the deflections during the service life were registered in the Rio Sinigo bridge, built in Italy in 1982 with lightweight concrete, in the Yuan-Shan bridge in Taiwan (Chiu *et al.*, 1996) and in other bridges built with this technique. Moreover, the excessive deflections and subsequent collapse of the Koror-Babeldaob bridge in Palau were attributed to the effects of the heterogeneity of bridge structures with long spans (Bažant *et al.*, 2008). Other authors underlined concomitant causes justifying the collapse (Burgoyne & Scantlebury, 2006). Bažant *et al.* (2012a,b) presented an extensive study on the causes of excessive deflections in this kind of bridges and their connection to the time-dependent phenomena.

In many cases the culprit of the failures was the final static scheme with the continuous girder exhibiting an internal hinge in the mid-span section. As a matter of fact, this scheme is not suitable because its sensitivity to creep and creep-induced deflections. Many drawbacks can be recognized in this structural typology with reference to the case of full continuity: a reduced bearing capacity, complexities in the conception and execution of the hinge, greater number of expansion joints and progressively increasing deflections of cantilever tips due to delayed deformations (Mathivat, 1979).

Today the scheme of continuous girders that are fully constrained in the midspan section is becoming more popular, because it facilitates the introduction of bottom prestressing cables, that induce upward displacements, opposite to those ensuing from the permanent loads.

Medium-span bridges are usually less sensitive to creep in terms of structural capacity at the ultimate limit state, but effects on the deflections at the serviceability limit state cannot be ruled out. By contrast, large structures are generally more sensitive to time-dependent phenomena with reference to the ultimate limit state, due to the nonlinearities and cracking caused by non-uniform shrinkage and creep.

Two different but interrelated problems have to be considered in the analysis of any structure affected by delayed deformations (Chiorino, 2011): the first problem is the determination of the structural response, which is a structural-analysis problem, while the second problem is the prediction of creep and shrinkage strains, which is a problem related to materials properties. Regarding the first point, today it is possible to refer to an international format that is available in the literature and in international codes, in order to evaluate the response of a structure subjected to creep and shrinkage. This format is mainly based on the theory of aging linear viscoelasticity. Regarding the second point, different prediction models are available, but the international scientific community still does not agree on a unified approach, even though the more recent prediction models are based on the RILEM international database. As a consequence, while the methodologies used to solve the problem of the structural response are today well-established and internationally accepted, significant uncertainties still hover over the shrinkage and creep predictive models suggested by the European and American Codes (EC2, 2005; ACI, 2008), because of the extensively dispersed results yielded by the different models (Chiorino, 2005; Bažant, 2008).

Within this context, the targets of this paper are the following:

- to establish simplified and closed-form relations for the practical evaluation of the structural response of prestressed concrete girders, by considering the effects of creep and shrinkage on the state of stress and deformation, with special attention to the preliminary design phases, to both invariant and variable static schemes, the latter occurring when changes in the static scheme are introduced during the construction.
- to compare the numerical results, by applying the proposed equations to actual bridges, by evaluating the materials parameters through the predictive models provided by the European and North American codes; this aspect has great relevance, because of the sizeable differences exhibited by the results ensuing from structural analysis based on different predictive models.

In the last fifty years, many authors have studied the effects of time-dependent phenomena on bridge structures and a large literature is available on this topic.

The general method for the evaluation of the structural response is based on the solution of a system of integral or integral-differential equations, which are obtained by substituting the elastic constitutive laws with the integral hereditary laws in the viscoelastic formulation of the problem. Because the solution of the

system of equations for creep can only be found by using step-by-step procedures, simplified and approximated methodologies of analysis have been proposed by a number of researchers. Among them, the most popular and handy is that introduced by Bažant (1972), which is based on an approach initially proposed by Trost (1967), through the definition of the so-called aging coefficient (Age Adjusted Elastic Modulus - AAEM Method). A rational and systematic approach based on the aging linear viscoelastic theory (for homogeneous structures) was proposed by Chiorino (2005), with the focus on the variation in the static scheme due to the addition of delayed restraints. This approach has recently been introduced into the new draft of the ACI 209 Committee document on the effects of time-dependent phenomena on structural behavior (ACI, 2012). Sassone *et al.* (2007) proposed a numerical approach to the viscoelastic analysis based on the equilibrium method, while Casalegno *et al.* (2011) formulated a general computational procedure to evaluate time-dependent effects on concrete structures. Recently Yu *et al.* (2012) presented a numerical approach aimed at performing a realistic creep analysis of large structures, based on the rate-type methodology, which considers nonlinear aspects due to moisture variations, cracking, etc. This approach is handy because the computational load of the general method implies the storage of the entire stress history and the evaluation of the history integral, something that is computationally heavy, while the rate-type laws are immediately compatible with the finite element method.

Chiorino, Mola *et al.* (1986) introduced the reduced relaxation functions for the analysis of redundant structures with elastic restraints, which is very useful for the evaluation of delayed deformations on cable-supported structures (Mola & Giussani, 2003). Dezi *et al.* (1993) studied the effect of static-scheme variations on continuous girders with heterogeneous spans, while Arici & Granata (2007) proposed the application of the principles of linear viscoelasticity to the case of static scheme subjected to changes because of the addition and removal of restraints during the construction stages of bridges.

Dilger (1982) introduced the study of heterogeneous steel-concrete cross-sections through the so-called “creep transformed section”, adopted by the ACI 209 Document. Tadros *et al.* (1975) examined the prestressing loss due to creep, shrinkage and steel relaxation, by finding formulas now used in the ACI, PCI and Eurocode documents (ACI, 2012; PCI, 2003; CEN, 2005).

In this study the analysis of P/C girder bridges is presented, with reference to the bridges built directly in their final configuration (invariant static scheme) and to the bridges built by a sequence of stages in which geometry, restraints and loads are subjected to changes until the final configuration is achieved (sequential construction with various static schemes). The in-time histories of the stresses and deformations in P/C girder bridges are found through a simplified analytical approach, based on the AAEM method, with special attention to segmental bridges, as an example of the variable static scheme. The rheological behavior related to prestressing (which is conceptually very different from that ensuing

from sustained loads) will be mentioned as well.

The final aim of the study is to compare the numerical results of the analyses performed on case-study bridges, in which the different shrinkage and creep predictive models provided by the Eurocode and by the North American recommendations are adopted. The case of a segmental bridge built by cantilevering is examined through both the analytical approach and FE analyses based on the integral-type numerical procedure. The sequence of the operations required by the sequential construction and the heterogeneity due to the different cast ages are introduced. Comparisons are made with the results found on the same bridge exhibiting an internal hinge at mid-span and no bottom prestressing cables.

## 2. AGING LINEAR VISCOELASTIC THEORY : PREDICTIVE MODELS OF CREEP AND SHRINKAGE

The sustained actions on a prestressed girder during the construction stages are generally the self-weight, the superimposed dead loads and the prestressing forces. While dead loads can be considered as sustained loads, prestressing is a sustained mutual imposed deformation applied between the prestressing steel and the concrete members.

The level of concrete stresses during the service life of P/C bridges is below 40-50% of concrete strength; hence, the principle of superposition can be applied for sustained sequentially-applied actions, according to the hypothesis of Mc Henry (Chiorino, 2005). If the thickness of concrete cross section members (slabs, webs, ...) is of the same order of magnitude, then the hypothesis of homogeneity can be assumed, by considering the structure as a one-dimensional viscoelastic system along its geometrical axis.

Delayed strains can be modeled by means of the *creep function*  $J(t, t_0)$ , which represents the total strain at time  $t$  due to a unitary stress applied at  $t_0$ . The creep strain rate is given by the *creep coefficient*  $\varphi(t, t_0)$ , through the following relation:

$$\varepsilon_{\sigma}(t) = \sigma_c(t_0) J(t, t_0) = \varepsilon_{\sigma}(t_0) [1 + \varphi(t, t_0)] = \sigma_c(t_0) \frac{1 + \varphi(t, t_0)}{E_c(t_0)} = \sigma_c(t_0) \left[ \frac{1}{E_c(t_0)} + \frac{\varphi_{28}(t, t_0)}{E_{c28}} \right] \quad (1)$$

in which  $\varepsilon_{\sigma}(t)$  is the total strain at time  $t$  after the application of the sustained load;  $\sigma_c(t_0)$  is the concrete stress induced by the load;  $\varepsilon_{\sigma}(t_0) = \sigma_c(t_0)/E_c(t_0)$  is the elastic strain due to the stress  $\sigma_c(t_0)$ ;  $E_c(t_0)$  is the elastic modulus at the time of load application and  $\varphi_{28}(t, t_0) = \varphi(t, t_0)E_{c28}/E_c(t_0)$  is the creep coefficient referring to 28 days of concrete curing, which is used by some predictive models.

If the stress history varies with time, by dividing it into intervals  $d\sigma_c$  due to sequential application of the loads, the principle of superposition at any given time  $t$  can be written as follows:

$$\varepsilon_c(t) = \sigma_c(t_0)J(t, t_0) + \int_{t_0}^t J(t, \tau) d\sigma_c(\tau) \quad (2)$$

where the value of the stress-independent strain (thermal or cracking strain) is here disregarded.

Reciprocally, in a redundant structure with rigid restraints, if sustained imposed deformations are applied, the induced stress state changes according to the following expression:

$$\sigma_c(t) = \varepsilon_\sigma(t_0)R(t, t_0) + \int_{t_0}^t R(t, \tau) d\varepsilon_\sigma(\tau) \quad (3)$$

where  $R(t, t_0)$  is the *relaxation function*, representing the total stress at time  $t$ , due to a unitary imposed deformation applied at time  $t_0$ . The relaxation function can be found starting from the creep function, by solving the following Volterra integral equation:

$$1 = R(t_0, t_0)J(t, t_0) + \int_{t_0}^t J(t, \tau) dR(\tau, t_0) \quad (4)$$

which requires an accurate solution, that can be numerically obtained by a step-by-step integration in time. The creep function  $J(t, t_0)$  - provided by the creep models - depends on different parameters, like environmental relative humidity  $RH$  (%), concrete strength  $f_{ck}$ , and perimeter of the cross section exposed to the environment ( $\Rightarrow$  Volume/Surface ratio  $V/S$ ). Design aids for the evaluation of the creep and relaxation functions with different predictive models are now available (see – for instance – the web page [www.polito.it/creepanalysis](http://www.polito.it/creepanalysis) of the Politecnico di Torino, Turin, Italy). A simplified method for estimating the long-term relaxation function has been recently pointed out by Bazant *et al.* (2013).

The Eurocode shrinkage and creep predictive models were derived from those proposed by CEB-FIP in the Nineties (CEB Model Code 90) and are now proposed also in the new Model Code 2010 (*fib*, 2012), with some refinements. In its new version (ACI, 2008), the ACI 209 Document proposes four models to be used by designers: the old ACI 209-R92 model, a model directly derived by CEB Model Code 90, the model proposed by Bažant & Baweja (2000) named “B3 model”, and the model proposed by Gardner and Lockman (2001), named “GL2000 model”.

In Figure 1 the diagrams of the creep coefficient provided by these different creep models are shown, for fixed values of the parameters  $f_{ck}$ ,  $RH$  and  $V/S$ . An immediate difference can be noted by comparing these diagrams: while EC2 and ACI 209-92 models give a creep coefficient which remains almost constant after 10000 days with a horizontal asymptotic behavior, the creep coefficient given by B3 and GL2000 models grow very much, reaching higher values, without a clear horizontal asymptotic behavior. It implies that delayed deformations given by the

Eurocode are lower than those given by North American models; as a consequence, B3 and GL2000 models predict significantly larger creep deformations in the long run. This is a general tendency for all the combinations of load time  $t_0$ , humidity  $RH\%$ , concrete strength  $f_{ck}$  and Volume/Surface ratio.

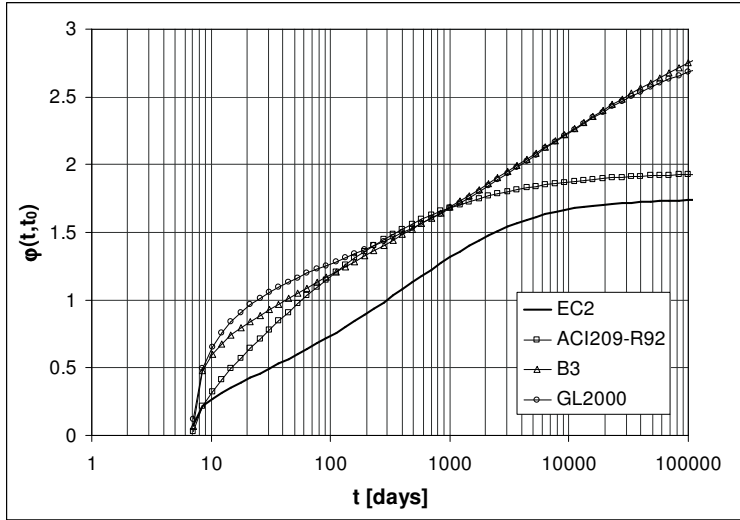


Figure 1 – Plots of the creep coefficients obtained by using different creep models:  $t_0 = 7$  days,  $f_{ck} = 35$  MPa,  $RH = 80\%$ ,  $V/S = 300$  mm.

As for shrinkage, Figure 2 makes it possible to compare the total shrinkage strain for the same parameters and the same above-mentioned models. In this case Eurocode 2 gives higher values with respect to the old ACI model and the tendency is asymptotic, while B3 and GL2000 give the highest values of the total shrinkage strain with a significant increment in the long run.

By adopting the AAEM approach, an algebraic solution of the previous integral equations can be found for strain histories representing a linear transformation of the creep coefficient curves (Jirasek & Bažant, 2002). In this way the constitutive equations of the viscous-elastic problem are replaced by a constitutive law that is similar to the elastic law, and contains an aging time-dependent elastic modulus, taking into account the accumulation of creep strains. Eq. 2 can be re-written by expressing the creep function through the creep coefficient and the corresponding elastic modulus:

$$\varepsilon_c(t, t_0) = \sigma_c(t_0) \frac{1 + \varphi(t, t_0)}{E_c(t_0)} + \int_{t_0}^t \frac{1 + \varphi(t, \tau)}{E_c(\tau)} \frac{\partial \sigma_c(\tau)}{\partial \tau} d\tau \quad (5)$$

By introducing the aging coefficient  $\chi(t, t_0)$ , Eq. 5 can be expressed by an equivalent algebraic relation:



$$\varepsilon_c(t, t_0) = \sigma_c(t_0) \frac{1 + \varphi(t, t_0)}{E_c(t_0)} + \frac{\sigma_c(t) - \sigma_c(t_0)}{E_c(t_0)} [1 + \chi(t, t_0) \varphi(t, t_0)] \quad (6)$$

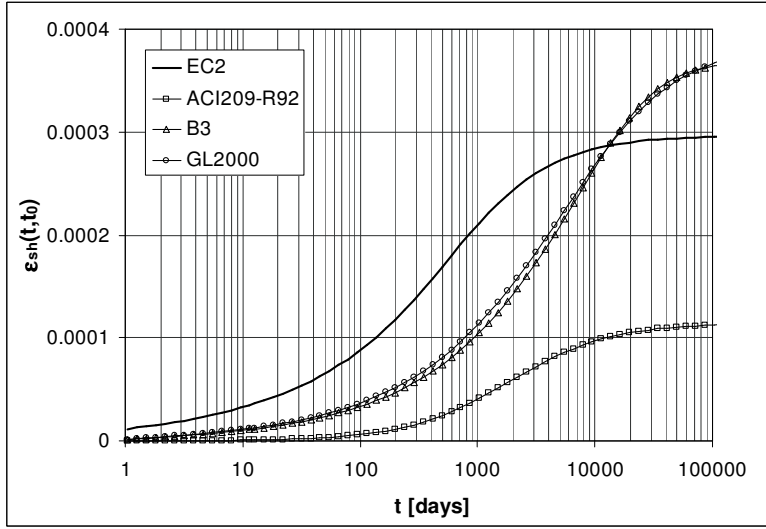


Figure 2 - Plots of the total shrinkage strain provided by different models,  $f_{ck} = 35$  MPa,  $RH = 80\%$ ,  $V/S = 300$  mm.

From Eq. 6 the *Effective Modulus*, (*EM*) and the *Age Adjusted Effective Modulus* (*AAEM*) can be defined: the first one (*EM*) is related to sustained actions that keep the stress values constant in time, while the second one (*AAEM*) is related to the case of variable stresses between two values  $\sigma_c(t_0)$  and  $\sigma_c(t)$ . Eq. 6 can be written as follows:

$$\varepsilon_c(t, t_0) = \frac{\sigma_c(t_0)}{E_{c,eff}(t, t_0)} + \frac{\sigma_c(t) - \sigma_c(t_0)}{E_{c,adj}(t, t_0)} \quad (7)$$

in which the *EM* and *AAEM* moduli are:

$$E_{c,eff}(t, t_0) = \frac{E_c(t_0)}{1 + \varphi(t, t_0)}, \quad E_{c,adj}(t, t_0) = \frac{E_c(t_0)}{1 + \chi(t, t_0) \varphi(t, t_0)} \quad (8a,b)$$

and the aging coefficient is defined by:

$$\chi(t, t_0) = \frac{1}{1 - R(t, t_0)/E_c(t_0)} - \frac{1}{E_c(t_0)J(t, t_0) - 1} = \frac{E_c(t_0)}{E_c(t_0) - R(t, t_0)} - \frac{1}{\varphi(t, t_0)} \quad (9)$$

Through the AAEM method an analytical expression of the relaxation function can be found:

$$R(t, t_0) = \left( 1 - \frac{\varphi(t, t_0)}{1 + \chi(t, t_0)\varphi(t, t_0)} \right) E_c(t_0) \quad (10)$$

In the literature different simplified expressions have been formulated for the function  $\chi(t, t_0)$ , see for instance Jirasek & Bažant (2002), and Chiorino *et al.* (1984); however  $\chi(t, t_0)$  varies between the values of 0.6 e 1.0, and for practical applications the mean value 0.8 was suggested.

The principles of linear viscoelasticity are strictly valid only for homogenous structures with rigid restraints.

When creep effects have to be considered in redundant structures with  $n$  elastic restraints, the theory can be considered still valid by introducing a modified creep function for the  $i$ -th elastic restraint:

$$J_i^*(t, t_0) = \frac{1 - \omega_i}{E_c(t_0)} + \omega_i J(t, t_0) \quad (11)$$

In Eq. 11  $\omega_i$  is the  $i$ -th eigenvalue of a matrix given by the ratio of the deformability matrices of the concrete part alone (at time  $t_0$ ) and of the entire structure (with elastic restraints or composed of concrete and steel, see Chiorino *et al.*, 1986).

When an imposed deformation is applied on a structure in which a single elastic restraint is present, the evolution of the correspondent reaction  $X(t)$  is given by the equation

$$X(t) = X_\eta(t_0) \frac{R^*(t, t_0)}{E_c(t_0)} \quad (12)$$

in which  $X_\eta(t_0)$  is the initial reaction of the elastic restraint in the structure subject to the imposed deformation  $\eta$  and  $R^*(t, t_0)$  is the so-called “reduced relaxation function”.

Eq. 12 shows that for a structure with elastic restraints, the stresses follow a modified relaxation function, which depends on the modified creep function through the integral equation:

$$1 = R_i^*(t_0, t_0) J_i^*(t, t_0) + \int_{t_0}^t J_i^*(t, \tau) dR_i^*(\tau, t_0) \quad (13)$$

analogous to the Eq. 4, but written for the case of elastic restraints.

### 3. STATE OF STRESS AND STRAIN IN STRUCTURES WITH INVARIABLE STATIC SCHEMES

Let us consider a structure with  $k$  redundancies (for  $k = 0$  the structure is statically determined). If a sustained action is applied at the time  $t_0$ , being either the dead load  $q$  or the prestressing  $p$ , the state of stress and deformation varies with time, due to creep.

While dead load is a sustained load applied to the structure, prestressing can be treated as an imposed mutual deformation in a structure with internal elastic restraints (given by prestressing tendons). The consequences are different because for a sustained load applied to a homogeneous structure with rigid restraints, the deformations change with time but the stresses remain unchanged and equal to the elastic stresses. On the contrary, the prestressing force diminishes with time and the relaxation of the stresses, due to the imposed deformation, coincides with the prestressing losses.

If the structure with rigid restraints is subjected to the sustained load  $q$  applied at time  $t_0$ , any given internal force  $S^q(t)$  is equal to the elastic one  $S_0^{el,q}$ :

$$S^q(t) = S_0^{el,q} \quad (14)$$

Creep deflections develop instead with time and any given component of the deformation  $D^q(t)$  is:

$$D^q(t) = D_0^{el,q} E_c(t_0) J(t, t_0) \quad (15)$$

where  $D_0^{el,q}$  is the deformation evaluated according to the elastic scheme, with the load  $q$  applied.

When prestressing is applied at time  $t_0$ , it can be considered as an imposed deformation on the structure in which strain compatibility is established between the tendon and the concrete. If a unique equivalent tendon is considered, passing in each section through the centroid of all post-tensioned tendons, this equivalent tendon acts like an elastic internal restraint with an initial elastic deformation imposed by the jack and totally independent from the concrete section. Afterwards, when compatibility is established between the concrete and the tendon by injecting the ducts with grout, the reaction of the elastic restraint  $X_\eta(t_0)$  to the imposed deformation  $\eta$  coincides with the internal force in the tendon. It varies with time due to creep, so that the reaction  $X(t)$  at any given time  $t > t_0$ , follows the law established by Eq. 12. The initial reaction  $X_\eta(t_0)$  is the initial prestressing force  $P_0$  in the tendon (after the jacking is concluded) and Eq. 12 becomes:

$$P(t) = P_0 \frac{R^*(t, t_0)}{E_c(t_0)} \quad (16)$$

which expresses the decrease of the prestressing force with time, due to creep. The reduced relaxation function  $R^*(t, t_0)$  depends on the eigenvalue  $\omega$  of the elastic restraint associated to the tendon through Eqs. 11 and 13 in each section:

$$\omega = \frac{n_0 \rho_p k_p}{1 + n_0 \rho_p k_p} \quad (17)$$

where  $n_0 = E_p/E_c(t_0)$  is the ratio between elastic moduli of the prestressing steel and concrete;  $\rho_p = A_p/A_c$  is the ratio between the areas of the prestressing tendons and the concrete cross-section;  $k_p = 1 + e^2/r_c^2$  is the contribution of the tendon eccentricity  $e$  with respect to the centroid of the cross-section, and  $r_c$  is the radius of inertia of the concrete cross section.

Eq. 16 shows that the initial value of the prestressing force  $P_0$  decreases in time following the function  $[1 - R^*(t, t_0)/E_c(t_0)]$ , which represents the prestressing loss with time. The development of the stress state in the prestressed structure is then proportional to that function and the history of any given internal force with time can be expressed by the relation:

$$S^p(t) = S_0^{el,p} - S_0^{el,p} \left[ 1 - \frac{R^*(t, t_0)}{E_c(t_0)} \right] \quad (18)$$

where  $S_0^{el,p}$  is the initial state of stress in the elastic scheme with the prestressing load acting on it.

By applying Eq. 13, the analogous relation that gives the development of deformations is:

$$D^p(t) = D_0^{el,p} + \frac{D_0^{el,p}}{n_0 \rho_p k_p} \left[ 1 - \frac{R^*(t, t_0)}{E_c(t_0)} \right] \quad (19)$$

Eqs. 18 and 19 can be re-written using the AAEM method:

$$1 - \frac{R^*(t, t_0)}{E_c(t_0)} = \frac{n_0 \rho_p k_p \varphi(t, t_0)}{1 + n_0 \rho_p k_p [1 + \chi(t, t_0) \varphi(t, t_0)]} \quad (20)$$

where  $R^*(t, t_0)$  is obtained by Eqs. 11 and 13, as it has been done for Eq. 10.

The state of stress is given by:

$$S^p(t) = S_0^{el,p} \left[ 1 - \frac{n_0 \rho_p k_p \varphi(t, t_0)}{1 + n_0 \rho_p k_p [1 + \chi(t, t_0) \varphi(t, t_0)]} \right] \quad (21)$$

and the state of deformation is given by:

$$D^p(t) = D_0^{el,p} \left[ 1 + \frac{\varphi(t, t_0)}{1 + n_0 \rho_p k_p [1 + \chi(t, t_0) \varphi(t, t_0)]} \right] \quad (22)$$

The previous expressions take into account only the influence that creep has on the prestressing loss, but other parameters should be introduced:

- the actual value of the stress in the fibre of concrete section next to prestressing tendons, by considering the dead load associated with the prestressing force (in most cases the self-weight);
- the value of the bending moment due to prestressing in redundant structures, which does not coincide with that ( $P_0 \cdot e$ ) as in statically-determined structures;
- concrete shrinkage and steel relaxation, that are associated with the development of creep-delayed deformations and that modify the strain value in the concrete fibre next to the prestressing reinforcement.

For these reasons, the value of the losses expressed by the previous relations has to be modified. From expression (16) the loss due to creep alone is:

$$\Delta P(t) = P_0 \frac{n_0 \rho_p k_p \varphi(t, t_0)}{1 + n_0 \rho_p k_p [1 + \chi(t, t_0) \varphi(t, t_0)]} \quad (23)$$

while the more complete expression can be written in the following way (ACI, 2012; Tadros *et al.*, 1975; CEN, 2005):

$$\Delta f_p(t) = \frac{n_0 f_{c0} \varphi(t, t_0) + \varepsilon_{sh}(t) E_p + f'_{re}(t)}{1 + n_0 \rho_p k_p [1 + \chi(t, t_0) \varphi(t, t_0)]} \quad (24)$$

where  $f_{c0} = P_0/A_c(1+e^2/r_c^2) = P_0/A_p \rho_p k_p$ , is the compressive stress in the concrete fibre next to the prestressing steel tendon;  $\varepsilon_{sh}(t)$  is the shrinkage strain at the time  $t$  with respect to the time of prestressing application;  $f'_{re}(t)$  is the steel stress variation due to the reduced relaxation ( $f'_{re} = 0.8 f_{re}$ ). In fact, the delayed strain in the concrete fibre next to the steel reinforcement is the sum of three components, due respectively to creep, shrinkage and steel relaxation. Moreover, the compressive stress  $f_{c0}$  in the concrete depends on the bending moments due to the dead loads applied simultaneously with the prestressing force. By evaluating all contributions, Eq. 24 becomes:

$$\Delta f_p(t) = \frac{n_0 \frac{P_0}{A_c} \left[ 1 + \left( \frac{M_d}{P_0 \cdot e} + \frac{M_p}{P_0 \cdot e} \right) (k_p - 1) \right] \varphi(t, t_0) + \varepsilon_{sh}(t) E_p + f'_{re}(t)}{1 + n_0 \rho_p k_p [1 + \chi(t, t_0) \varphi(t, t_0)]} \quad (25)$$

where  $M_d$  is the bending moment due to the self-weight and to all the dead loads acting together with the prestressing, while  $M_p$  is the bending moment due to prestressing in a redundant structure.

The total loss due to creep, shrinkage and steel relaxation is given by the relation:

$$\Delta P(t) = P_0 \frac{n_0 \rho_p k_p \left[ 1 + \left( \frac{M_d}{P_0 \cdot e} + \frac{M_p}{P_0 \cdot e} \right) (k_p - 1) + \frac{\varepsilon_{sh}(t) E_c A_c}{\varphi(t, t_0) P_0} + \frac{f'_{re}(t) A_c}{\varphi(t, t_0) n_0 P_0} \right] \frac{1}{k_p} \varphi(t, t_0)}{1 + n_0 \rho_p k_p [1 + \chi(t, t_0) \varphi(t, t_0)]} \quad (26)$$

Eq. (23) can be re-written as:

$$\Delta P(t) = \alpha_p P_0 \frac{n_0 \rho_p k_p \varphi(t, t_0)}{1 + n_0 \rho_p k_p [1 + \chi(t, t_0) \varphi(t, t_0)]} \quad (27)$$

where

$$\alpha_p = \left[ 1 + \left( \frac{M_d}{P_0 \cdot e} + \frac{M_p}{P_0 \cdot e} \right) (k_p - 1) + \frac{\varepsilon_{sh}(\infty) E_c A_c}{\varphi(\infty, t_0) P_0} + \frac{f'_{re}(\infty) A_c}{\varphi(\infty, t_0) n_0 P_0} \right] \frac{1}{k_p} \quad (28)$$

is a time-independent coefficient. Eq. 28 is valid under the hypothesis for which shrinkage and steel relaxation develop with time in the same way of creep delayed deformations. The  $\alpha_p > 1$  coefficient modifies the prestressing loss value due to creep as such, including the contributions of concrete shrinkage and steel relaxation.

From Eq. 27, for any given internal force, the following relation can be written:

$$S^p(t) = S_0^{el,p} \left[ 1 - \alpha_p \frac{n_0 \rho_p k_p \varphi(t, t_0)}{1 + n_0 \rho_p k_p [1 + \chi(t, t_0) \varphi(t, t_0)]} \right] \quad (29)$$

which substitutes Eq. 21, valid only for the creep-induced loss. Any given component of the deformation can be formulated as follows:

$$D^p(t) = D_0^{el,p} [1 + \varphi(t, t_0)] + D_0^{el,p} \alpha_p \varphi(t, t_0) \left[ \frac{1}{1 + n_0 \rho_p k_p [1 + \chi(t, t_0) \varphi(t, t_0)]} - 1 \right] \quad (30)$$

where the first term is related to the prestressing force considered as a sustained load, while the second term brings in the influence that the prestressing loss has on the time-history of deformations.

The sum of the deflections given by Eq. 15 for dead loads and those given by Eq. 30 for prestressing, make it possible to follow the whole time-history of the structural deflections, something that is instrumental in predicting the value of the pre-camber in prestressed members and in checking prestressed members at the serviceability limit state, with reference to cracking and deformation.

#### 4. STATE OF STRESS AND STRAIN IN STRUCTURES WITH VARIED STATIC SCHEMES

In the previous section the case of structures directly built in accordance with the final static scheme has been considered. For the case in which the construction sequence implies a single or a multiple variation of the static scheme because of the addition of delayed restraints in a homogeneous structure with rigid restraints, the *principle of acquisition of the modified static system* has to be considered: “in a structure subjected to sustained loads at time  $t_0$ , whose initial static system is modified into a final structural system by the introduction of additional restraints at time  $t_1 > t_0$ , the system of the stresses (stresses, internal forces and external reactions) evolves for  $t > t_1$  and approaches the system of the stresses corresponding to the application of the loads to the structure in its final structural system” (ACI, 2012).

In fact, when a sustained load is applied to a structural system, creep-delayed deformations increase the elastic deformations; if a delayed restraint is added in a section of the structure, the structural system changes and creep deformations cannot further develop in that section. A reaction increases in the added restraint for  $t > t_1$ , because the delayed deformations are blocked. Hence, the stress system exhibits in-time modifications.

The redistribution of the stresses in the modified system and the consequent partial recovery of the final elastic system can be expressed by introducing a “redistribution function”  $\xi(t, t_0, t_1)$ , which can be found by evaluating the delayed strain prevented by the added restraint:

$$D^q(t) - D^q(t_1) = -D_0^{el,q} [\varphi(t, t_0) - \varphi(t_1, t_0)] \quad (31)$$

Because of the redistribution function, the stress history becomes a linear combination of the stresses found in the elastic systems:

$$S^q(t) = S_0^{el,q} + (S_1^{el,q} - S_0^{el,q}) \xi(t, t_0, t_1) \quad (32)$$

In Eq. 32,  $S_1^{el,q}$  is the stress according to the modified elastic scheme, after the addition of the delayed restraint, under the sustained load  $q$ . Through the AAEM method an approximation of the redistribution function can be found:

$$\xi(t, t_0, t_1) \equiv [\varphi(t, t_0) - \varphi(t_1, t_0)] E_c(t_1) / [(1 + \chi(t, t_1) \varphi(t, t_1)) E_c(t_0)]$$

Figure 3 shows a comparison of the redistribution functions obtained with the different creep models adopted by Eurocode and in North America. A similar behaviour can be observed, but there are significant differences among predicted values at any given time  $t$ , especially between 100 and 10000 days. In particular, B3 model yields the largest final value of  $\xi(t, t_0, t_1)$ .

The deformation history under the sustained loads with the modified system, for any time instant  $t > t_1$ , is as follows:

$$D^q(t) = D_0^{el,q} [1 + \varphi(t_1, t_0)] + D_1^{el,q} [\varphi(t, t_0) - \varphi(t_1, t_0)] \quad (33)$$

where  $D_0^{el,q}$  and  $D_1^{el,q}$  are the elastic deformations, due to the sustained load  $q$ , in the static systems without and with the delayed restraint (initial and final elastic systems), respectively.

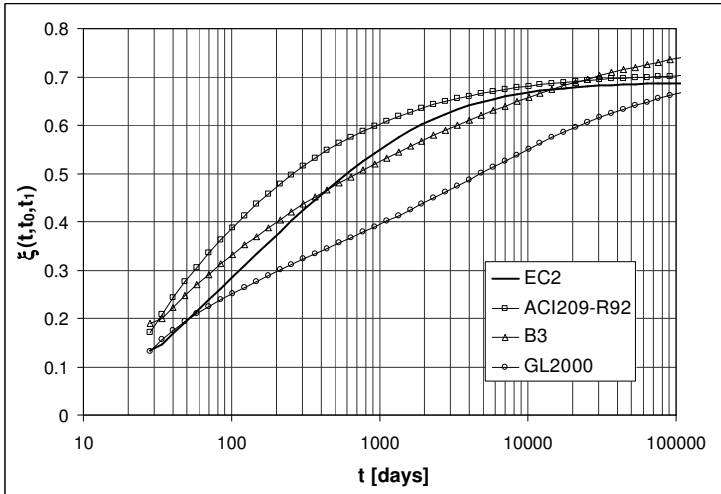


Figure 3 - Comparison of the redistribution functions  $\xi(t, t_0, t_1)$  according to the AAEM method, for different creep models;  $t_0=7$  days,  $t_1=28$  days,  $f_{ck}=35$  MPa,  $RH=80\%$ ,  $V/S=300$  mm.

The first term of Eq. 33 shows that, with the change of the static scheme, the increase of the deformations stops at time  $t_1$  with the value of the creep coefficient  $\varphi(t_1, t_0)$ . The second term instead shows that the delayed deformation re-starts, following another law which depends on the prevented creep deformations in the restrained sections and – consequently – on the elastic strains of the modified system  $D_1^{el,q}$ . The effect that the modified static scheme has on prestressing is a redistribution of the stresses, as in the case of sustained loads, with the fundamental difference ensuing from the concomitant prestressing losses. In order



to evaluate the stress and deformation histories in P/C structures characterized by a variable static scheme, the increment of the creep deformation that is prevented by the added restraint has to be formulated, analogously to Eq. 31, that is valid for sustained loads. The prevented deformation due to the added restraint is:

$$D^p(t) - D^p(t_1) = -D_0^{el,p} \alpha_p [\varphi(t, t_0) - \varphi(t_1, t_0)] - \frac{D_0^{el,p} \alpha_p}{n_0 \rho_p k_p} \left[ \frac{R^*(t, t_0)}{E_c(t_0)} - \frac{R^*(t_1, t_0)}{E_c(t_0)} \right] \quad (34)$$

In Eq. 34 the first term is responsible for the stress redistribution of the prestressing force considered as a sustained load, while the second term gives rise to another function  $\vartheta^*(t, t_0, t_1)$  which takes care of the effect that the prestressing loss has on the stress redistribution after the change of the static scheme:

$$\vartheta^*(t, t_0, t_1) = -\frac{1}{n_0 \rho_p k_p} \frac{\frac{R^*(t, t_0)}{E_c(t_0)} - \frac{R^*(t_1, t_0)}{E_c(t_0)}}{1 + \chi(t, t_1) \varphi(t, t_1)} \frac{E_c(t_1)}{E_c(t_0)} \quad (35)$$

By recalling Eq. 20, through the AAEM method, Eq. 35 can be simply expressed by means of a combination of creep coefficient values:

$$\vartheta^*(t, t_0, t_1) = \frac{E_c(t_1)/E_c(t_0)}{1 + \chi(t, t_1) \varphi(t, t_1)} \left[ \frac{\varphi(t, t_0)}{1 + n_0 \rho_p k_p [1 + \chi(t, t_0) \varphi(t, t_0)]} - \frac{\varphi(t_1, t_0)}{1 + n_0 \rho_p k_p [1 + \chi(t_1, t_0) \varphi(t_1, t_0)]} \right] \quad (36)$$

which is very handy in practical applications. For the prestressing force applied to a structure with a variable static scheme, the stress history can finally be expressed by means of the following relation:

$$S^p(t) = S_0^{el,p} \left[ 1 - \frac{\alpha_p n_0 \rho_p k_p \varphi(t, t_0)}{1 + n_0 \rho_p k_p [1 + \chi(t, t_0) \varphi(t, t_0)]} \right] + (S_1^{el,p} - S_0^{el,p}) \left[ (1 - \alpha_p) \left( \frac{\varphi(t, t_0) - \varphi(t_1, t_0)}{1 + \chi(t, t_1) \varphi(t, t_1)} \right) \frac{E_c(t_1)}{E_c(t_0)} \right] + (S_1^{el,p} - S_0^{el,p}) \frac{\alpha_p E_c(t_1)/E_c(t_0)}{1 + \chi(t, t_1) \varphi(t, t_1)} \left[ \frac{\varphi(t, t_0)}{1 + n_0 \rho_p k_p [1 + \chi(t, t_0) \varphi(t, t_0)]} - \frac{\varphi(t_1, t_0)}{1 + n_0 \rho_p k_p [1 + \chi(t_1, t_0) \varphi(t_1, t_0)]} \right] \quad (37)$$

In Eq. 37, the first term represents the stress history before the addition of the delayed restraint and the static scheme modification, by considering the creep-induced prestressing loss, shrinkage and steel relaxation. The second term represents the contribution of the static-scheme variation to the stress history of the prestressing force, considered as a sustained load. The third term refers to the contribution of the prestressing loss to the stress redistribution. Compared to Eq.

32, that is valid for sustained loads, Eq. 37 is about the different effect that the static scheme variation has on the prestressing force respect to sustained loads; in this case, the stress variation depends on two different but simultaneous and interrelated causes: the prestressing loss and the stress redistribution in the modified static scheme.

In the same way, the deformation history can be written as follows:

$$\begin{aligned}
 D^p(t) = & D_0^{el,p} [1 + \varphi(t, t_0)] + D_0^{el,p} \alpha_p \varphi(t, t_0) \left[ \frac{1}{1 + n_0 \rho_p k_p [1 + \chi(t, t_0) \varphi(t, t_0)]} - 1 \right] + \\
 & + (D_1^{el,p} - D_0^{el,p}) [(1 - \alpha_p) (\varphi(t, t_0) - \varphi(t_1, t_0))] + \\
 & + (D_1^{el,p} - D_0^{el,p}) \left[ \alpha_p \left( \frac{\varphi(t, t_0)}{1 + n_0 \rho_p k_p [1 + \chi(t, t_0) \varphi(t, t_0)]} - \frac{\varphi(t_1, t_0)}{1 + n_0 \rho_p k_p [1 + \chi(t_1, t_0) \varphi(t_1, t_0)]} \right) \right]
 \end{aligned} \tag{38}$$

The prestressing loss is influenced by the value of the bending moment  $M_d$  introduced in Eq. 27, with the consequent variation of the coefficient  $\alpha_p$ . This value can change in the different stages of bridge construction and service life, due to sustained loads applied after tensioning the tendons, as occurs for the superimposed permanent loads, like pavement, guard rails, lighting system, etc. Furthermore, introducing second-phase prestressing causes  $\alpha_p$  to change, as occurs – for instance – in segmental bridges built by cantilevering, where second-phase prestressing is introduced in the bottom part of the box structure at the mid-span, in order to resist the positive bending moments due to variable loads. The additional prestressing modifies the effect of previously-applied cantilever prestressing and the stress state in the whole structure. Losses are then evaluated by means of Eq. 28, but different values of the coefficient  $\alpha_p$  have to be considered for the sequential prestressing application.

The additional bottom prestressing is applied to a static scheme that has been already changed, after the construction has been completed, and no effects of stress redistribution has to be considered for it. Of course, in segmental bridges with an internal hinge at mid-span, bottom prestressing cannot be introduced and permanent-load deflections by far prevail.

The previous equations show the difference between the effects that time-dependent phenomena have on sustained loads and prestressing. For structures whose static scheme can vary, redistribution of stresses is different for prestressing and sustained loads, due to prestressing losses. Designers tend to consider self-weight and prestressing merely as two loads with opposite effects so that their balance may minimize – automatically – creep effects. If no changes in the static scheme occur and the prestressing losses are adequately considered, the previous opinion is correct, but this is not true for those structures exhibiting variable schemes, because the redistribution of the stresses induced by sustained loads and

prestressing is different. As a matter of fact, in such a situation the values of the bending moments due to self-weight go back to the elastic value related to the modified system more than prestressing, and the same occurs to deformations. In most cases, the consequence is that the downward deflections due to dead loads are predominant with respect to the upward displacements due to prestressing. Moreover, an insufficient level of prestressing, a rough evaluation of prestressing losses and the use of inappropriate creep models may markedly increase the deflections with respect to those expected in the design stage, with negative consequences on the deflections during the service life and insufficient pre-camber in the construction phases.

## 5. NUMERICAL APPLICATIONS

Applications on segmental bridges built by cantilevering are presented in the following. Two cases are examined. In the first the entire bridge is considered as a homogeneous structure, with only one change in the static scheme. A comparison of the results obtained by means of the analytical approach proposed in the previous sections with those obtained by using a FE procedure is presented. In the second case the analysis of the same bridge is performed assuming a sequential construction, by implementing the time-dependent phenomena directly into the FE code and by considering the heterogeneity due to the different casting times of the segments (without applying the analytical approach). Sustained loads, as well as top and bottom prestressing cables are considered. The analysis is aimed at validating – through a finite-element procedure - the behavior of a segmental bridge built by cantilevering, with specific reference to the effects of time-dependent phenomena found in the analytical approach based on aging linear viscoelasticity. Afterwards another comparison is proposed about the same bridge with a different final static scheme (an internal hinge is introduced at mid-span). It is demonstrated that this little difference may have a marked influence on the final delayed deflections, with unacceptable values for the vertical displacements.

Bridge geometry and tendons layout are shown in Figure 4. The deck has a box cross-section with variable depth and bottom-slab thickness (Ghinassi *et al.*, 1994). A finite element model was implemented with 113 joints and 112 frame elements; the boundaries are simple supports over the piers and on the abutments. Creep and shrinkage were introduced according to the previously-mentioned four models (EC2 and ACI). The internal forces and the deflections are compared. The parameters used in this case are  $f_{ck} = 45$  MPa,  $RH = 80\%$  and  $V/S = 300$  mm.

### 5.1 Rheological homogeneous bridge with full continuity

The first analysis was performed by considering all segments built at the same time  $t_0 = 14$  days, by cantilevering, and the time of closure at the midspan of all

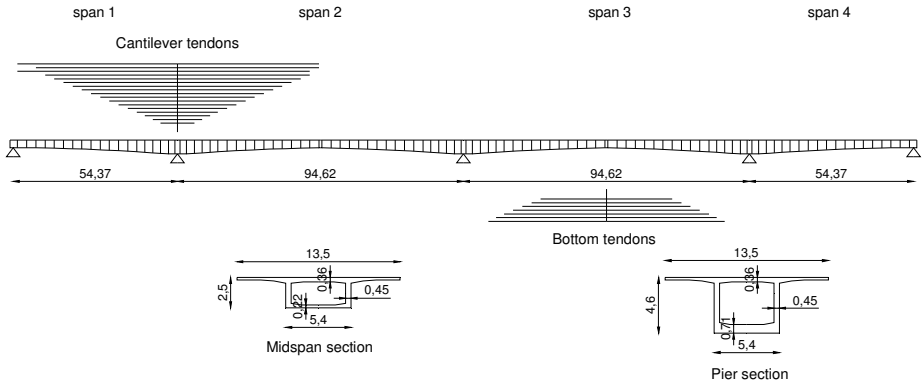


Figure 4 - Geometry of the bridge [dimensions in m], from Ghinassi et al. (1994).

spans at  $t_1 = 45$  days. In this case the bridge is considered a rheological homogeneous structure with concrete segments loaded at the same age.

The approach adopted in FE software to compute the delayed deformations consists in an integral-type procedure, which stores the delayed deformations at each step of the stress and strain history, by dividing the entire time of the analysis into a convenient number of steps (in the present case the entire time is divided into about 50 intervals with a geometric progression). The analytical approach was followed, by applying Eqs. 32 and 33 for the dead load and Eqs. 37 and 38 for cantilever prestressing.

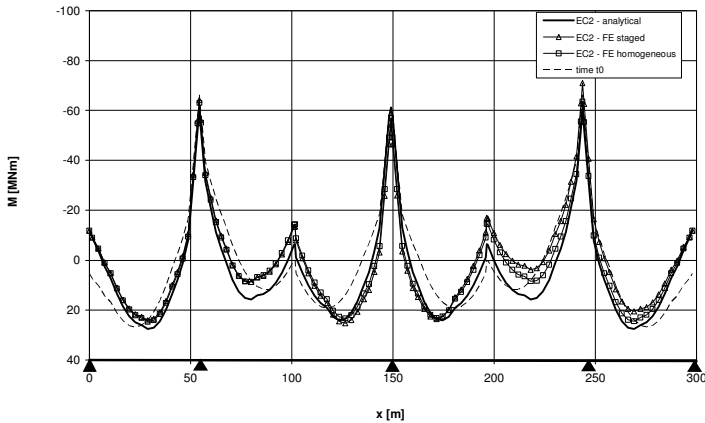


Figure 5 - Bending moments found by using EC2 creep and shrinkage models for the structure considered as homogeneous with a variable scheme. The final time of the analysis is  $t = 10000$  days. Comparison with initial values at the time  $t_0$ .

Figure 5 shows the diagrams of the bending moment due to the combination of dead load, cantilever prestressing and bottom prestressing at the final time of analysis ( $t = 10000$  days), using the EC2 model. A comparison is made with the values at the initial time of load  $t_0$ , in order to show the effects that stress redistribution has on the change of the static scheme. Diagrams of the bending moment obtained with the analytical approach, the FE software (based on EC2 model, rheological homogeneous structure) and FE staged analysis (sequential construction) are plotted together for the sake of comparison. The load-balancing effect related to prestressing does not significantly affect the bending moment.

Table 1. Values of creep coefficients and redistribution functions for different predictive models.

	Eurocode 2	ACI 209-R92	B3	GL2000
$\varphi(10^5, t_0)$	1.344	1.777	2.837	2.614
$\varphi(10^5, t_1)$	1.090	1.548	2.561	2.283
$\varphi(t_1, t_0)$	0.416	0.789	0.722	0.939
$\xi(10^5, t_1, t_0)$	0.522	0.485	0.763	0.650
$\alpha_p$	1.075	1.087	1.025	1.060
$\varphi^*(10^5, t_1, t_0)$	0.384	0.332	0.458	0.390
$\varepsilon_{sh}(10^5, t_{0sh})$	2.9E-04	1.1E-04	3.4E-04	3.2E-04

The values of the parameters adopted in the creep and shrinkage models are reported in Table 1, where significant differences appear among the models, especially for the creep coefficient, the shrinkage strain and the redistribution function.

In Figure 6 a similar comparison is performed for displacements, between the analytical approach and FE analysis with either homogeneous or heterogeneous structure; in this case the comparison is between the increase of deflections due to creep from the end of the construction process to the final time of the analysis. The increase of deflections is referred to dead load, cantilever and bottom prestressing, estimated by the EC2 creep model. Time-dependent deflections have very similar maximum values in the three cases; the diagrams are symmetrical because the entire bridge has been considered as an average rheological homogeneous structure.

In Figure 7 a comparison is performed among the diagrams of the final bending moment provided by the analytical approach with the different creep and shrinkage models. It can be seen that the stress redistribution increases in the long run ( $t = 100000$  days), when the predictive models B3 and GL2000 are used. Hence the predictions provided by these models are the most unfavourable, as sizeable stress variations occur many years after the end of the construction, especially over supports.

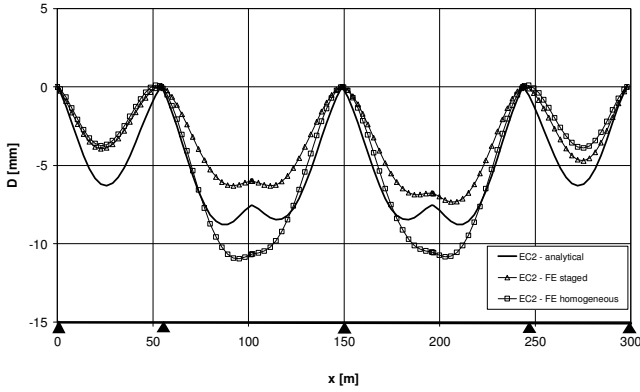
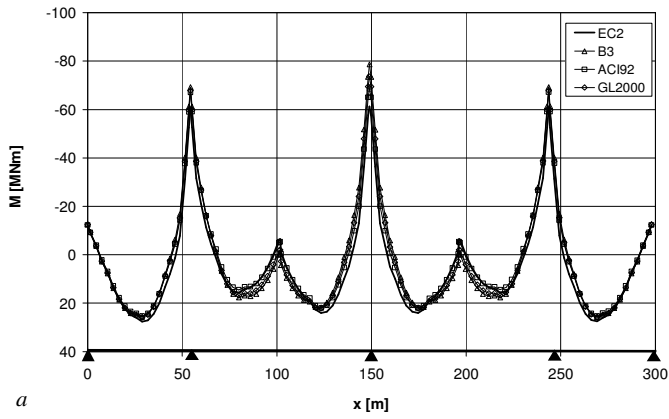
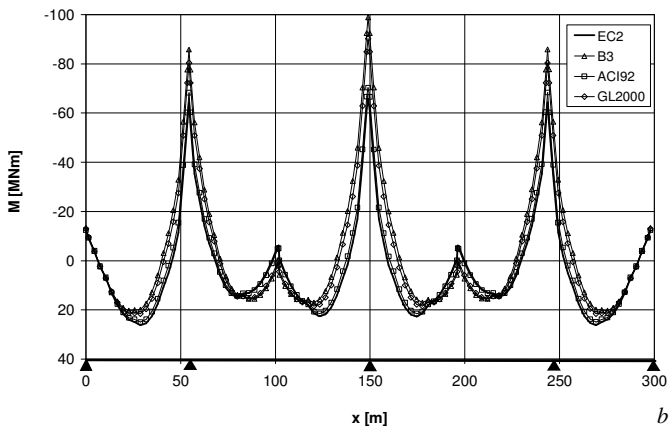


Figure 6 - Deflections from the end of the construction to  $t = 10000$  days (homogeneous structure, variable static scheme, EC2 for creep and shrinkage).



a



b

Figure 7 - Bending moments (homogeneous structure): analytical approach, different predictive models: (a)  $t = 10000$  days; and (b)  $t = 100000$  days.

Predicting the displacements over very long periods is required by serviceability checks on bridges, because nowadays longer service lives are requested and delayed deflections (for instance, for  $t = 100000$  days) can be very significant. (In some cases, delayed deflections could be twice as much as those evaluated at 10000 days).

For very long periods, Models B3 and GL2000 yield significantly higher values of the moment at the central support. In Fig. 8 the increasing deflections from the end of construction to the final time of the analysis exhibit very different values depending on the adopted model for creep. (The maximum values yielded by Model B3 are three times larger than those yielded by the Eurocode).

The predictions over very long periods ( $t = 100000$  days) are reported in this example because they are instrumental in quantifying the differences among the models, especially for long service lives.

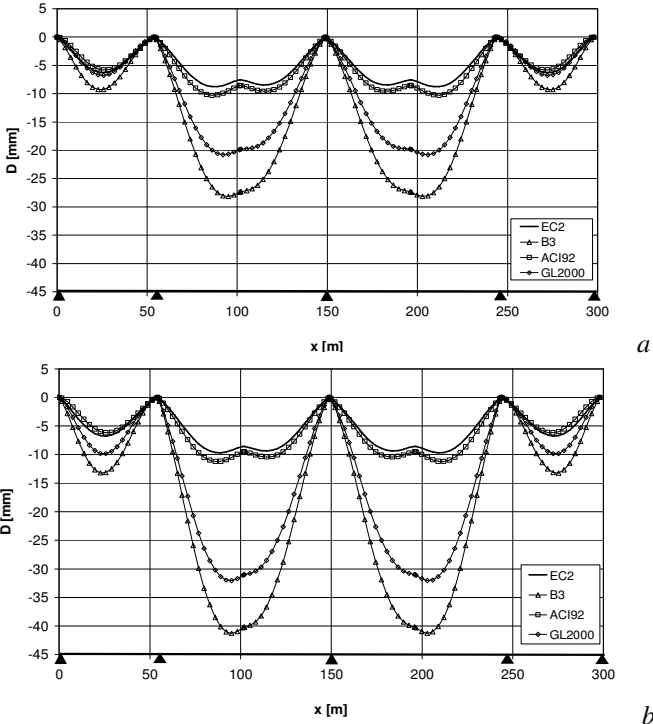


Figure 8 - Deflections from the end of construction to  $t = 10000$  days (a) and  $100000$  days (b); analytical approach, homogeneous structure.

### 5.2 Sequential construction of the bridge with full continuity

A second analysis was performed by adhering to the actual sequence of the construction stages, that are assumed to be four: each cantilever stage is composed of segments of half central span and it is considered homogeneous with respect to

creep, but the entire structure is heterogeneous (different casting times for each cantilever stage). No analyses with the analytical approach are performed in this case. The following chronology is assumed: mean loading time of each cantilever stage: 14 days; key segment at mid-span (closure of the span): 7 days, with another 7 days of curing; total duration until the end of the construction: 91 days; final time of analysis 100000 days. The applied loads are: self-weight, top prestressing (in each segment) and bottom prestressing (for continuity).

In Figure 9, the diagrams of the bending moment along the deck at the final time of analysis allow to quantify the effect of structural heterogeneity and different times of construction. Note that the influence of the various creep models is more evident in the second part of the bridge (that was built later).

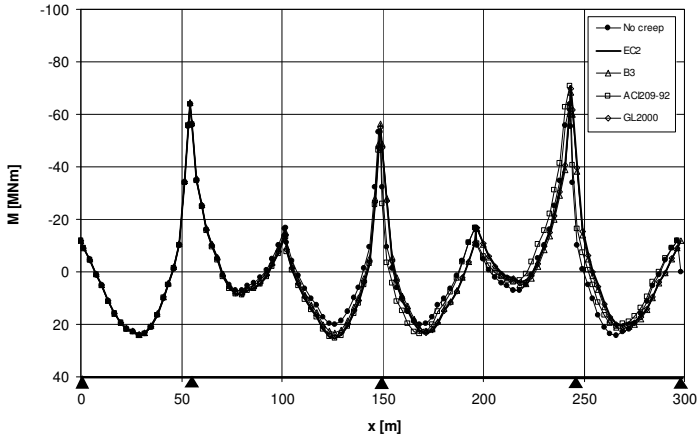


Figure 9 – Plots of the bending moment for  $t = 100000$  days (numerical approach, sequential construction).

Regarding the general behavior of the bridge, the stress redistribution is different from model to model, as already observed, but not that much under both the self-weight and prestressing, for either positive or negative bending moments, the former along the span and the latter on the piers. Compared to Fig.7, the analytical approach is shown to yield higher negative moments (for the rheological homogeneous structure) than FE analysis, but the differences are rather limited.

Figure 10 shows the diagrams of the delayed deflections, registered after the construction end until the final time of analysis (combination of self-weight + upper and bottom prestressing). The heterogeneity due to the different casting ages causes the asymmetry of the deflection diagrams. As for the differences caused by the adoption of the different code models, they are sizeable in terms of bending-moment diagrams. B3 and GL2000 yield the largest deflections, while ACI 209-92 and Eurocode yield the lowest values. This behavior is confirmed by the higher values of the creep coefficient provided by the recent North American models. By comparing these diagrams with those of Figure 8, the analytical approach appears



to be more conservative than FE analysis, as it yields higher values for the maximum deflection. Hence, Eurocode predictions may not be on the safe side in predicting the deflections, with possible negative effects on the calculation of the pre-camber required by the segments during their construction and on the respect of the limitations of the service limit states.

Because of sequential construction implies different times of loading and different deformed shapes of cantilevers, even though the structure is geometrically symmetrical, in the evaluation at time  $t_0$ , the geometric corrections imposed to the cantilever tips during the erection process have been taken into account. In fact, in absence of geometric corrections at cantilever tips, vertical and horizontal jumps occur, so they have to be avoided by operating on working site with corrective displacements of cantilevers and pre-cambers, as indicated by Mathivat (1979).

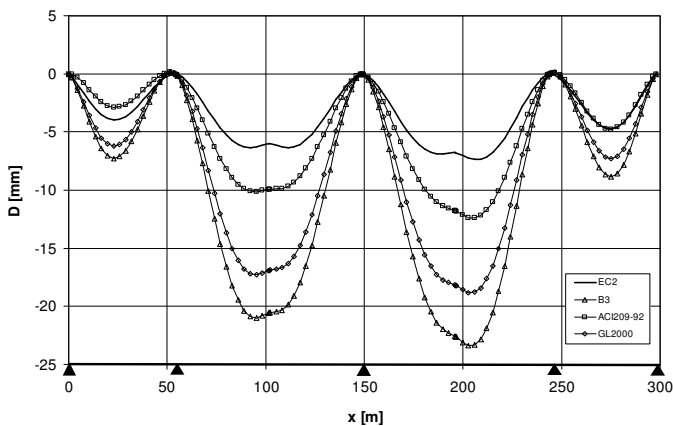


Figure 10 – Plots of the increasing deflections from the end of construction to  $t = 100000$  days (the numerical approach).

### 5.3 Rheological homogeneous bridge with partial continuity

For the same bridge, the analysis was repeated by considering a final static scheme with partial continuity due to internal hinges inserted at mid-span of the two main spans. The aim was to compare the effects that time-dependent phenomena have on two different final static schemes, the focus being on the final deflections. As previously said, many bridges with internal hinges exhibit time-related serviceability problems.

The results obtained by the analytical procedure are compared with those found by means of FE analysis assuming a sequential construction, as previously seen in the case of the bridge with full continuity. In Figure 11 the bending moment diagrams obtained by the scheme with partial continuity, using the different predictive models, at the final time of the analysis are presented.

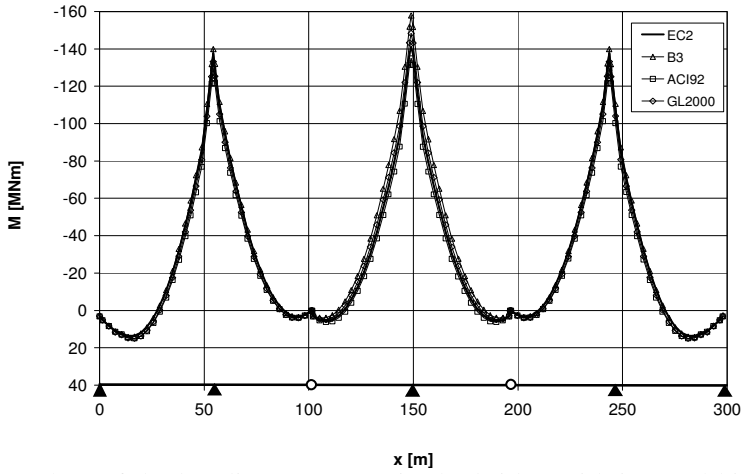


Figure 11 – Plots of the bending moments in the bridge with internal hinges, for  $t = 100000$  days (analytical approach; homogeneous structure; variable scheme).

There are no significant differences with respect to the results given by the analytical model, as the in-time redistribution of the stresses is very limited (the bending-moment redistribution is much greater when the full constraint in the mid-span section is introduced as the delayed restraint). As a consequence, positive bending moments in the span do not increase significantly and negative moments remain very high.

Figure 12 shows the increasing deflections obtained through the analytical method, from the end of the construction process to the final time of the analysis. It can be seen that deflections increase very much indeed, especially when North-American models are used.

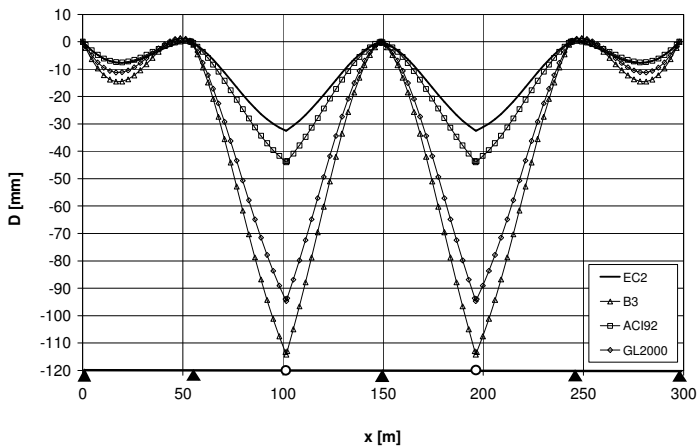


Figure 12 – Plots of the increasing deflections for  $t = 100000$  days (analytical approach; internal hinges; homogeneous structure; variable scheme).

The shape of the deflection diagrams clearly show the effect of the internal hinge (downward spike at mid-span), that causes the delayed deformations to rapidly increase in mid-span sections, in so leading to high final deflections. Compared with the diagrams of Figure 8, this scheme clearly brings in three-time larger deflections compared to the case of the bridge with full continuity. This behavior confirms that the final scheme with the internal hinge is not advisable for these bridges, especially for serviceability limits.

### 5.3 Sequential construction of the bridge with partial continuity

The analysis was repeated again for the case of sequential construction. Figure 13 is about the bending moment-diagrams obtained by the FE analysis on the bridge with internal hinges, including the different times of loading. The comparison with Figure 11 shows that the analytical method gives higher values for the final bending moments compared to the sequential construction, with a greater influence of the delayed deflections on stress redistribution, particularly in the case of B3 and GL2000 models. Such differences depend on the way the stress redistribution due to sustained load, prestressing force and prestressing loss are treated in the two approaches. For instance, according to FE analysis the stress redistribution is completely negligible.

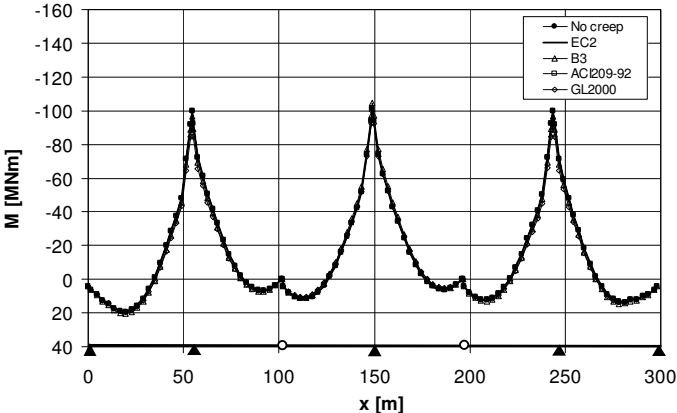


Figure 13 – Plots of the bending moment found via FEs for  $t = 100000$  days (self-weight + prestressing, internal hinges).

Figure 14 shows the diagrams of the increasing deflection in the bridge with internal hinges (sequential construction). The values are smaller than those predicted by the analytical approach (Fig. 12). The behavior of this kind of bridges is confirmed by the final values of the deflections that are three-time larger than those of the equivalent bridge with clamped mid-span sections.

The asymmetry ensuing from the construction stages is evident (spans 3 and 4 were cast later than spans 1 and 2, see Fig.4), because of the greater deflections

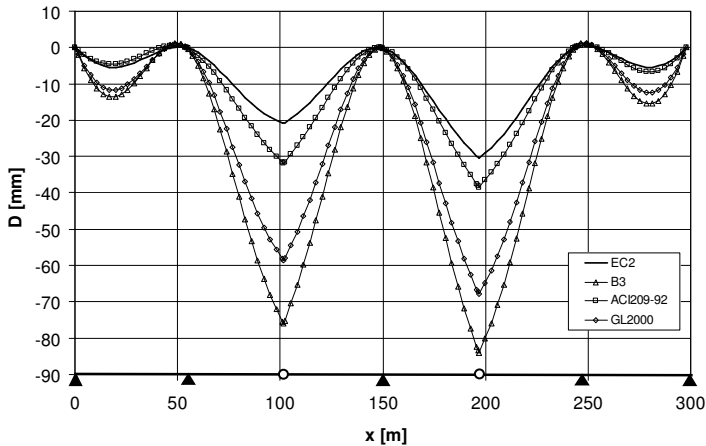


Figure 14 – Plots of the increasing deflections from the end of construction to  $t = 100000$  days (internal hinges).

in the younger spans. The analytical approach is more conservative than FE analysis, for both the bending moment and the deflection.

One should note that all the previous calculations and comments refer to a medium-span bridge, without including such nonlinear effects as concrete cracking, humidity variations, etc. For large-span bridges and for structures that are more sensitive to creep, a numerical solution based on the rate-type laws should be used, as proposed by Yu *et al.* (2012). The influence that the superimposition of the permanent and variable loads has on the deflections should be taken care of, in order to properly evaluate the total values of the vertical displacements during the service life.

## 6. CONCLUDING REMARKS

A study on the influence of time-dependent phenomena in the construction stages and service life of prestressed concrete girder bridges has been presented. The case of a segmental bridge built by cantilevering has been especially investigated.

Handy analytical expressions to describe the stress and deformation histories due to creep in P/C segmental bridges are provided, for homogeneous structures, to assess the structural response from the early design stages. Numerical applications are presented on bridges with variable static schemes, by comparing the numerical results yielded by different creep and shrinkage predictive models (European and American Codes).

The comparison shows the significant differences between the predictions supplied by these models, especially for delayed deflections. A validation of the general behaviour of non-homogeneous prestressed girders for different casting times is presented by using FE analysis performed on an actual case of a

segmental bridge, using the different creep and shrinkage models provided by the codes.

The results show that the influence that stress redistribution has on bending moments, due to the change in the static scheme, is reduced by the load-balancing effect of the dead load and of prestressing. As a consequence, the bending moment diagrams during the service life do not change significantly by using the different creep and shrinkage models provided by the codes. Opposite results are found for deflections, which differ significantly depending on the model adopted in the analysis.

The analytical approach, which gives the solution in terms of stress and deformation histories with time, is based on closed-form equations and only the solution of simple elastic schemes is required. This approach is suitable for the first design phase, as any analysis of the sequential construction is avoided, this latter analysis being postponed – by using a FE software - to the subsequent final design phases.

Moreover, the results show that the recent North American models (B3 and GL2000) supply the highest values for the creep coefficient and consequently lead to the largest stress-state variations, should the static scheme be modified during the construction phases, and to the largest values for the deflections. Further, these models bring to significant increases of the delayed strains even for very long times. (Hence, the deflections of prestressed bridges continue to increase even in the case of long service lives). On the contrary, Eurocode 2 yields the smallest delayed deflections and stress variations in all the cases examined in this paper.

The differences among the various models in predicting the delayed deflections may play a sizeable role in the determination of the construction camber and in the fulfilment of the requirements at the Serviceability Limit State, in terms of cracking and deformation.

Finally, comparing the behaviour of bridges with full continuity or partial continuity due to hinges at mid-span sections, confirms that the scheme with partial continuity is much more sensitive to creep, especially in terms of delayed strains, that may – in some cases – bring in unacceptable final values for the deflections.

## REFERENCES

- ACI 209.2R08 (2008). *Guide for Modelling and Calculating Shrinkage and Creep in Hardened Concrete*, Report by ACI Committee 209, pp. 1-45.
- ACI 209.3RXX (2012). *Time-Dependent Effects in Concrete Structures*, preliminary draft of a report by ACI Committee 209.
- Arici M. and Granata M.F. (2007). “Removal of Temporary Supports and Creep Effects in the Sequential Construction of Bridges”, *ACI SP246-3 “Structural Implication of Shrinkage and Creep of Concrete”*, Chiorino & Gardner eds., pp. 37-51

- Arici M., Granata M.F. and Recupero A. (2011). “The Influence of Time-Dependent Phenomena in Segmental Construction of Concrete Cable-Stayed Bridges”, *Bridge Structures*, Vol.7, No.4, pp. 125-137.
- Bažant Z.P., Guang-Ha Li and Qiang Yu. (2008). “Explanation of Excessive Long-Time Deflections of Collapsed Record-Span Box Girder Bridge in Palau”, *Preliminary Report No.08-09/A222e, Proc. 8<sup>th</sup> Int. Conf. on Creep and Shrinkage of Concrete CONCREEP-8*, Ise Shima (Japan), pp. 1-36.
- Bažant Z.P., Guang-Ha Li and Qiang Yu. (2008). “Prediction of Creep and Shrinkage and their Effects in Concrete Structures: Critical Appraisal”, *Creep, Shrinkage and Durability Mechanics of Concrete and Concrete Structures*, Tanabe ed., Taylor & Francis, London, pp. 1275-1289
- Bažant Z.P. (1972). “Prediction of Concrete Creep Effects Using Age-Adjusted Effective Modulus Method”, *J. of the American Concrete Inst.*, 69, 212-217.
- Bažant Z.P. and Baweja S. (2000). “Creep and Shrinkage Prediction Model for Analysis and Design of Concrete Structures: Model B3”, *Proc. of Adam Neville Symposium: Creep and Shrinkage - Structural Design Effects*, ACI SP-194, Al-Manaseer A. ed., Farmington Hills, Michigan, pp. 1-83.
- Bažant Z.P., Qiang Yu and Guang-Ha Li (2012a). “Excessive Long-Time Deflections of Prestressed Box Girders. Part I: Record-Span Bridge in Palau and Other Paradigms”, *J. of Struc. Eng. ASCE*, Vol.138, No.6, pp. 676-686.
- Bažant Z.P. and Qiang Yu, Guang-Ha Li (2012b). “Excessive Long-Time Deflections of Prestressed Box Girders. Part II: Numerical Analysis and Lessons Learned”, *ASCE - J. of Structural Eng.*, Vol.138, No.6, pp. 687-696.
- Bažant Z.P. Hubler M. H., Jirasek M. (2013). “Improved estimation of long-term relaxation function from compliance function of aging concrete”, *ASCE J. of Eng. Mech.*, Vol.139, No.2, pp. 146-152.
- Burgoyne C.J. and Scantlebury R.C. (2006). “Why Did Palau Bridge Collapse?”, *The Structural Engineer*, Vol.84, No.11, pp. 30-37
- Casalegno C., Sassone M. and Chiorino, M. A. (2011)., “Time-Dependent Effects in Concrete Structures: a General Computational Approach”, *Proc. of Structural Engineers World Congress - SEWC 2011*, Erba (Italy), pp. 1-8.
- CEB (1993). *CEB-FIP Model code 1990*, Bulletin d'Information No.213/214 - Thomas Telford, London.
- CEN (2005) EN 1992-1-1 (2005). *Eurocode 2 – Design of Concrete Structures – Part 1.1: General Rules and Rules for Buildings*, CEN.
- Chiorino M.A., Napoli P., Mola F. and Koprna M. (1984). *CEB Design Manual on Structural Effects of Time-Dependent Behaviour of Concrete*, CEB Bulletin d'Information 142/142bis, Georgi Publishing Co.(Saint-Saphorin, CH).

- Chiorino M.A., Creazza G., Mola F. and Napoli P. (1986). “Analysis of Aging Viscoelastic Structures with n-Redundant Elastic Restraints”, *Proc. Fourth RILEM Int. Symposium on Creep and Shrinkage of Concrete*, Bažant Z.P. ed., Northwestern University, Evanston (Illinois, USA), pp. 623-644.
- Chiorino M.A. (2005). “A Rational Approach to the Analysis of Creep Structural Effects”, *ACI SP-227 “Shrinkage and Creep of Concrete”*, Gardner & Weiss eds., pp. 107-141.
- Chiorino M.A. (2011). “Analysis of Structural Effects of Time-Dependent Behaviour of Concrete: an Internationally Harmonized Format”, *Proc. Structural Engineers World Congress SEWC 2011*, Erba (Italy), pp.1-8.
- Chiu H.S., Chern J.C. and Chang K.C. (1996). “Long-Term Deflection Control in Cantilever Prestressed Concrete Bridges”, Parts I and II, *ASCE – Journal of Engineering Mechanics*, Vol.122, pp. 489-501.
- Duan L., Chen K. and Tan A. (2000). “Prestressed Concrete Bridges”, in *Chen Wai-Fah & Duan L. Bridge Engineering Handbook*, Chapter 10, CRC Press, Washington (USA).
- Dezi L., Menditto G. and Tarantino A. M. (1993). “Viscoelastic Heterogeneous Structures with Variable Structural System”, *ASCE - Journal of Engineering Mechanics*, Vol.119, pp. 238-250.
- Dilger W.H. (1982). “Creep Analysis of P/C Structures Using Creep-Transformed Section Properties”, *PCI Journal*, Vol.27, No.1, pp. 98–117.
- Fib (2012). *Bulletin d'Information 65 - Model Code 2010 - Final draft*, Volume 1, fib, Lausanne, 350 pp.
- Gardner N.J. and Lockman M.J. (2001). “Design Provisions for Drying Shrinkage of Normal-Strength Concrete”, *ACI Materials Journal*, Vol.2, pp. 159-161.
- Ghinassi G., Fazio J. and Dreas G. (1994). *Creep Effects and Construction Methods in Continuous Segmental P/C Bridges (in Italian: “Viscosità e metodi costruttivi nei ponti in c.a.p. a travata continua, realizzati per fasi”)*, Alinea pub., Florence (Italy), 181 pp.
- Granata M.F., Margiotta P., Recupero A. and Arici M. (2012a). “Partial Elastic Scheme Method in Cantilever Construction of Concrete Arch Bridges”, *ASCE Journal of Bridge Engineering* DOI 10.1061/(ASCE)BE.1943-5592.0000396.
- Granata M.F., Margiotta P., Recupero A. and Arici M. (2012b). “Construction Stages of Cable-Stayed Bridges with Composite Deck”, *Bridge Structures*, Vol.8, No.4, pp.93-106.
- Granata M.F., Margiotta P. and Arici M. (2013a). “A Parametric Study of Curved Incrementally-Launched Bridges”, *Engineering Structures*, Vol.49, pp. 373-384.

- Granata M.F., Margiotta P., Recupero A. and Arici M. (2013b). “Concrete Arch Bridges built by Lattice Cantilevers”, *Structural Engineering and Mechanics*, Vol.45, No.5, pp.703-722.
- Jirasek M. and Bažant Z.P. (2002). *Inelastic Analysis of Structures*, Chichester: J. Wiley and Sons, 735 pp.
- Mathivat J. (1979). *Incremental Construction of Prestressed-Concrete Bridges* (in French : *Construction par encorbellement des ponts en beton précontraint*), Editions Eyrolles, pp. 98-106, and 119-129.
- Mola F. and Giussani F. (2003). “Long-Term Behaviour of Cable-Stayed Bridges”, *Studies and Researches*, Fratelli Pesenti, Politecnico di Milano, Vol.24, pp. 153-187
- Müller H.S. (1993). “Considerations on the Development of a Database on Creep and Shrinkage Tests”, *Proc.5<sup>th</sup> Int. RILEM Symposium on Creep and Shrinkage of Concrete*, Barcelona (Spain), Bažant and Carol eds., E & FN Spon, London, pp. 859-872.
- PCI (2003). *Bridge Design Manual*, Chapter 8, Portland Cement Institute (Chicago, Illinois, USA), 8.0-8.14
- Sassone M., Bigaran D. and Casalegno C. (2007). “Numerical Approach to Viscoelastic Analysis of Concrete Structures Using Equilibrium and FEM”, *ACI-SP-246 “Structural Implication of Shrinkage and Creep of Concrete”*, Chiorino & Gardner eds., pp. 21-36.
- Tadros M.K., Ghali A. and Dilger W.H. (1975). “Time-Dependent Prestress Loss and Deflection in Prestress Concrete Members”, *PCI Journal*, Vol.20, No.3, pp. 86–98
- Trost H. (1967). “Effects of the Principle of Superimposition on Creep and Relaxation Problems in Concrete and Prestressed Concrete” (in German: “Auswirkungen des Superpositionsprinzips auf Kriech und Relaxationsprobleme bei Beton und Spannbeton”), *Beton und Stahlbetonbau*, Vol.62, No.10 and 11, pp. 230-238 and 261-269.
- Yu Q., Bažant Z.P. and Wendner R. (2012). “Improved Algorithm for Efficient and Realistic Creep Analysis of Large Creep-Sensitive Concrete Structures”, *ACI Structural Journal*, Vol.109, No.5, pp. 665-675.



## ASSESSMENT OF THE EFFECTIVE STIFFNESS IN R/C FRAMES SUBJECTED TO SEISMIC LOADS

Francesco Micelli<sup>1</sup> and Angelo S. Carone<sup>2</sup>

### ABSTRACT

The current design codes and technical recommendations often provide rough indications for the assessment of the effective stiffness in R/C frames subjected to seismic loads, which is a key factor when a linear analysis is performed. The Italian design code (NTC-08), the Eurocode 8 and ACI 318 do not take into account all the structural parameters affecting the effective stiffness, something that may not be on the safe side when second-order effects P- $\Delta$  occur, or when incorrect distributions of the internal forces are obtained.

In this paper the factors influencing the effective stiffness of R/C beams, columns and walls under seismic forces are analyzed. Five different approaches are adopted in order to evaluate the effective stiffness of R/C members, in accordance with the scientific literature and the international design codes. A parametric analysis is performed on an actual R/C building and its results are presented and discussed, as a contribute to the improvement of design practice.

The main variables considered in the analysis are: the reinforcement ratio, the ratio of the axial load, the compressive strength of the concrete, and the type of the shallow beams (*wide beams* with  $b > d$  and *ordinary beams* with  $b < d$ ). The second-order effects are quantified and the resulting displacements related to the Damage Limit State (DLS) under seismic loads are discussed. The analytical results show that, although the effective stiffness increases with the steel ratio, the limit of 50% of the initial stiffness turns out to be an upper bound for small values of the axial-load ratio, rather than a lower bound as indicated by both the Italian Design Code and EC-8. As a result, in some cases the current Italian and European provisions tend to underestimate second-order P- $\Delta$  effects, when the DLS is investigated under seismic loading.

**Keywords:** stiffness (in R/C), R/C frames, columns, beams, seismic design.

---

<sup>1</sup> Assistant Professor, <sup>2</sup> BS Engineer, University of Salento - Dept. of Innovation Engineering, 73100 Lecce, Italy.

## 1. STATE-OF-THE-ART OVERVIEW AND RESEARCH SIGNIFICANCE

Linear analysis is very popular with practitioners in the seismic design of R/C frames, and the values of the assumed effective stiffness strongly influence the results of the analysis, which – however - cannot into account progressive cracking.

Although scientific studies suggest a more accurate evaluation of the effective stiffness of R/C elements under seismic loading,, the Italian design code NTC-08 (CS LL PP, 2008), the Eurocode 8 (2005) and ACI 318 (2002) provide indications that may appear too simplified. In NTC-08 it is reported that the effective stiffness may be reduced by 50% with respect to the initial stiffness, depending on the entity of the normal force; EC-8 suggests to assume a cracked stiffness equal to 0.50 times the gross stiffness, unless a more accurate analysis (nonlinear) is performed. In the authors' opinion, this approach is unsatisfactory for the following reasons: it is not clear how the stiffness values should be assigned according to the different limit states (Seismic Ultimate Limit State – SULS - and Seismic Damage Limit State (SDLS); the cracked stiffness of the beams is introduced in the same way as that of the columns; and critical structural parameters influencing the stiffness are disregarded.

Other international design codes provide useful indications about the effective stiffness to be introduced into the design of R/C frames in seismic conditions. The New Zealand code NZS 3101 (2006), provides the following values for the effective stiffness at the ultimate limit state:  $0.40I_g$  for rectangular beams;  $0.35I_g$  for T or L beams; and  $0.40I_g / [1+8(h/l_c)^2]$  for coupling beams.

The stiffness of the columns is taken as a function of the normal stress acting on them:  $0.80I_g$  when  $N^*/ f'_c A_g > 0.5$ ;  $0.60I_g$  when  $N^*/ f'_c A_g = 0.2$ ;  $0.40I_g$  when  $N^*/ f'_c A_g = -0.05$ . For RC walls the effective stiffness is:  $0.45I_g$  when  $N^*/ f'_c A_g = 0.2$ ;  $0.50 I_g$  when  $N^*/ f'_c A_g = 0$ ;  $0.25I_g$  when  $N^*/ f'_c A_g = -0.1$ , where:  $I_g$  is the moment of inertia of the gross uncracked section,  $h$ ,  $l_c$  are the height of the cross section and the span of the beam respectively;  $A_g$  is the area of the gross section, disregarding the area of the reinforcing steel;  $f'_c$  is the compressive strength of concrete;  $N^*$  is the normal force acting at the ultimate limit state, that is taken positive in compression mode.

American ACI 318 (2002) contains design recommendations for both serviceability and failure. The effective stiffness under the service loads is taken as:  $0.50I_g$  for beams;  $I_g$  for columns and for uncracked walls;  $0.5I_g$  for cracked walls. For the ultimate limit state the effective stiffness is taken as:  $0.35I_g$  for beams;  $0.70I_g$  for columns and for uncracked walls;  $0.35I_g$  for cracked walls.

The distinction between the stiffness to be introduced in cracked or uncracked walls is addressed in ACI 318; comments on the stiffness of cracked or uncracked walls along their length are available in Wallace and Orackal (2002) and in Petrini et al. (2004).

Another scientific work that show the importance of considering a reduced stiffness in cracked walls is found in Chen and Scawthorn (2003).

Component	Flexural Stiffness	Shear Stiffness	Axial Stiffness
R/C Beams	$0.5 E_c \cdot I_g$	$0.4 E_c \cdot A_w$	-
P/C Beams	$E_c \cdot I_g$	$0.4 E_c \cdot A_w$	-
Columns subjected to compression due to design gravity loads $\geq 0.5 A_g \cdot f'_c$	$0.7 E_c \cdot I_g$	$0.4 E_c \cdot A_w$	$E_c \cdot A_g$
Columns subjected to compression due to design gravity loads $\leq 0.3 A_g \cdot f'_c$ or in tension	$0.5 E_c \cdot I_g$	$0.4 E_c \cdot A_w$	$E_c \cdot A_g$
Uncracked walls	$0.8 E_c \cdot I_g$	$0.4 E_c \cdot A_w$	$E_c \cdot A_g$
Cracked walls	$0.5 E_c \cdot I_g$	$0.4 E_c \cdot A_w$	$E_c \cdot A_g$
R/C slabs	-	$0.4 E_c \cdot A_w$	-
P/C slabs	-	$0.4 E_c \cdot A_w$	-

Table 1 – Effective stiffness in R/C sections according to FEMA 356 (2000)

In FEMA 356 (2000), Chapter 6 "Concrete" is dedicated to design recommendations. (The values of the reduced stiffness are reported in Table 1, FEMA 356, 2000).

The Canadian Standard Association (2005) design code indicates the following values for the reduced stiffness:  $0.40I_g$  for beams;  $0.20I_g/[1+3(h/l_c)^2]$  for coupling beams;  $\alpha_c I_g$  for columns;  $\alpha_w I_g$  for walls, where the coefficients  $\alpha_c$ ,  $\alpha_w$  are related to the ratio between the applied normal stress and compression strength  $f'_c$ .

Unfortunately a limited number of scientific works is available in spite of the relevance of the topic. The first paper dealing with the problem of computing the stiffness in cracked regions was written by Branson (1965), which is still a reference (ACI-318). Sugano (1970) proposed a reduced stiffness for beams and columns, based on some experimental results and on the ratio between the secant stiffness at yielding and the stiffness of the gross uncracked section:

$$\alpha_y = K_r/K_i = (0.043 + 1.64n\rho_t + 0.043 a/D + 0.33\eta)(d/D)^2 \quad [1]$$

The value  $n = E_s/E_c$  is the ratio between the elastic modulus of the steel and of the concrete;  $d$  is the effective depth of the cross section. However, the following conditions should be respected: steel ratio  $\rho_t$  between 0.4% and 2.8%;  $a/D$  = shear span-to-depth of the cross section ratio between 2 and 5; normalized axial force  $\eta = N/(f_c A)$  between 0 and 0.55.

Grossman (1981) proposed to compute the stiffness of cracked beams subjected to bending on the basis of the ratio between the first-cracking moment  $M_{cr}$  and the applied moment  $M_a$ , and introduced also a parametric coefficient  $K_e$  for high moment values, depending on the mechanical properties of concrete and steel:

$$I_g = (M_{cr}/M_a)^4 I_g \text{ if } M_a/M_{cr} \leq 1.6 \quad [2a]$$

$$I_g = 0.1K_e (M_{cr}/M_a)^4 I_g \text{ if } 1.6 < M_a/M_{cr} \leq 10 \quad [2b]$$

Mirza (1990) introduced the following expression for the effective stiffness of

R/C columns:

$$\alpha_y = K_r/K_i = (0.043 + 1.64n\rho_t + 0.043 a/D + 0.33\eta)(d/D)^2 \quad [3]$$

where:  $l$  is the free height of the column;  $h$  is the depth of the cross section;  $e$  is the load eccentricity;  $E_c$ ,  $E_s$  are the moduli of the concrete and of the steel, respectively;  $I_g$ ,  $I_{se}$  are the inertia moments of the gross section and of the reinforcement computed with respect to the central axis of the gross section.

Paulay, Priestley (1992) indicated the following values for the effective stiffness of both columns and beams, based on a range of possible values for the moment of inertia of the gross section (Table 2).

R/C member	Range	Recommended Stiffness
Rectangular section (beams)	0.30-0.50 $I_g$	0.40 $I_g$
T,L sections (beams)	0.25-0.45 $I_g$	0.35 $I_g$
Columns with $P > 0.5 \cdot f_c \cdot A_g$	0.70-0.90 $I_g$	0.80 $I_g$
Columns with $P = 0.2 \cdot f_c \cdot A_g$	0.05-0.70 $I_g$	0.60 $I_g$
Columns with $P = -0.05 \cdot f_c \cdot A_g$	0.30-0.50 $I_g$	0.40 $I_g$

Table 2 – Values of the effective stiffness recommended by Paulay and Priestley (1992).

In Table 2  $I_g$ ,  $A_g$  are the inertia moment and area of the gross concrete section (disregarding the reinforcement). For coupling beams, the recommended stiffness is  $0.20I_g/[1+3(h/l_n)^2]$ , where  $h$ ,  $l_n$  are the depth of the cross section and the span, respectively. These recommendations were taken as a reference by ACI guidelines.

In Wang (2001) a revisited Branson's approach for beams in bending was proposed; in the same year Mehanny (2001) introduced a value for the effective stiffness based also on the area of the reinforcement. Crowley (2003) confirmed the validity of the earlier experimental approach proposed by Sugano (1970).

Recent studies by Khuntia and Ghosh (2004) were focused on the evaluation of the effective stiffness of R/C frames subjected to lateral loads, by introducing also the steel ratio. The effective stiffness  $EI_{eff}$  of a R/C column under seismic or wind loads was proposed as well, in the following form:

$$EI_{eff} = E_c I_g (0.80 + 0.25\rho_g) \times \left( 0.30 + 0.5 \frac{P_u}{P_0} \right) \leq E_c I_c \text{ and } \geq E_c I_{beam} \quad [4]$$

A simplified expression was also proposed for R/C beams made with normal-strength concrete:

$$EI_e = E_c I_g (0.10 + 25\rho) \left(1.2 - 0.2 \frac{b}{d}\right) \leq 0.6 E_c I_g \quad [5a]$$

In the case of high-performance/high-strength concrete Eq.5a should be modified as follows:

$$EI_e = E_c I_g (0.10 + 25\rho) \left(1.2 - 0.2 \frac{b}{d}\right) \times (1.15 - 4 \times 10^{-5} f'_c) \leq 0.6 E_c I_g \quad [5b]$$

where:  $(1.2 - 0.2 b/d) \leq 1.0$ ;  $\rho$  is the steel ratio;  $b$ ,  $d$  are the width and effective height of the cross section;  $f'_c$  is the concrete strength;  $I_g$ ,  $A_g$  are computed for the gross section disregarding the reinforcement;  $E_c$  is the elastic modulus of the concrete;  $P_u/P_0$  is the axial-load ratio where the ultimate axial load is computed as  $P_U = 0.85 f'_c (A_g - A_{st}) + f_y A_{st}$ .

On the basis of their test results, Elwood and Eberhard (2009) proposed the following values to reduce the stiffness for R/C columns with rectangular cross sections in R/C frames under seismic loading:

$$EI_{eff}/EI_g = 0.2 \quad \text{if } P/A_g f'_c \leq 0.2 \quad [6a]$$

$$EI_{eff}/EI_g = 5P/3A_g f'_c - 4/30 \quad \text{if } 0.2 < P/A_g f'_c \leq 0.5 \quad [6b]$$

$$EI_{eff}/EI_g = 0.7 \quad \text{if } P/A_g f'_c > 0.5 \quad [6c]$$

A general equation was proposed for rectangular and circular columns, disregarding the reinforcement ratio in the cross section:

$$\frac{EI_{effcalc}}{EI_g} = \frac{0.45 + 2.5P/A_g f'_c}{\left[1 + 110 \left(\frac{d_b}{D}\right) \left(\frac{D}{a}\right)\right]} \leq 1.0 \text{ and } \geq 0.2 \quad [7]$$

where  $I_g$ ,  $A_g$ ,  $f'_c$ ,  $E$ , are the same quantities as those used in Eq.5;  $P$  is the applied axial load;  $d_b$  is the diameter of the steel bars;  $D$  is the diameter of the circular cross section or the depth of the rectangular section; and  $a$  is the shear span. A tentative value for  $d_b/D$  may be 1/25 for bridge piers and 1/18 for the columns in an ordinary building.

A recent research by Kumar and Singh (2010) has provided design values for the effective stiffness of cracked R/C frames, in the two cases of normal-strength or high-strength concrete:

$$\frac{E_{eff}}{E_c I_g} = \left( \begin{array}{c} 0.35 \text{ for } \frac{P}{A_g f'_c} \leq 0.2 \\ 0.175 + 0.875 \frac{P}{A_g f'_c} \text{ for } 0.2 \leq \frac{P}{A_g f'_c} \leq 0.6 \\ 0.7 \text{ for } \frac{P}{A_g f'_c} \geq 0.6 \end{array} \right) \quad [8a]$$

$$\frac{E_{eff}}{E_c I_g} = \left( \begin{array}{c} 0.35 \text{ for } \frac{P}{A_g f'_c} \leq 0.1 \\ 0.24 + 1.1 \frac{P}{A_g f'_c} \text{ for } 0.1 \leq \frac{P}{A_g f'_c} \leq 0.6 \\ 0.9 \text{ for } \frac{P}{A_g f'_c} \geq 0.6 \end{array} \right) \quad [8b]$$

where the symbols are the same used in previous equations.

According to the studies available in the scientific literature and to international design codes, five different approaches are used in the following parametric analysis. The values of the effective stiffness of R/C elements are computed according to the following codes or models: the Italian Code and EC-8 (based on the same approach); NZS-3101 code; and the models by Khuntia and Ghosh (2004), Elwood and Eberhard (2009), and Kumar and Singh (2010).

## 2. STRUCTURAL ANALYSIS

Structural analysis was performed by considering a regular R/C frame building in a seismic area having a rectangular plan section (size 31 x 22.5 m) and two vertical symmetry planes. (A very limited asymmetry occurs with respect to the vertical mean plane aligned with the long side, due to the presence of the stairwell and of the lift). The long side is aligned with the horizontal axis (x axis) of the global reference system and the short side is aligned with the vertical axis (y axis), Fig.1.

The concrete slabs consist of unidirectional T beams with the direction y indicated in Figure 1; the six-storey building (Figure 2) has an inter-storey height of 3.80 m on the ground floor and 3.0 m at the remaining levels. The stairway and lift well has R/C walls (Figure 1).

The design of the building and the earthquake-resistant scheme are in the class of frame structures with low ductility (CDB), in accordance with the Italian Code (2008) and EC8 (2005). In the seismic analysis the floors were considered as in-plane rigid diaphragms. The walls and the columns are 3 and 44, respectively, with axis-to-axis spacing equal to 4-5 m in the x direction, and to 4.5 m in the y direction (Figure 1). The section of the columns is 500x500 mm for the first three floors, 400x400 mm for the fourth floor and 300x300 mm for the last two floors (Figure 2). According to these schemes different parameters were chosen to compare the different approaches for the evaluation of the effective stiffness under seismic loads.

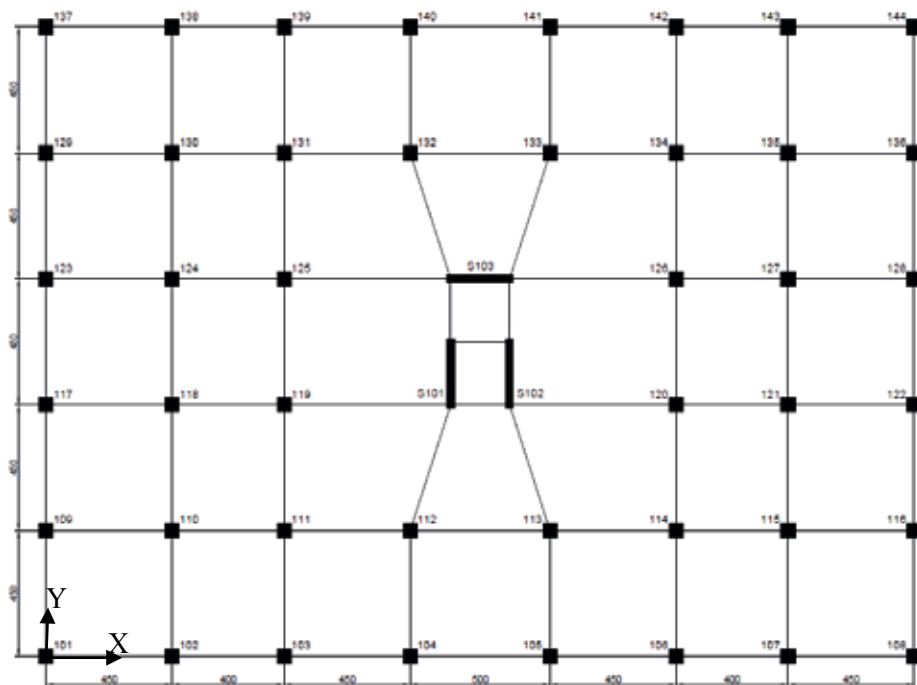


Figure 1 – Plan section of the R/C frame.

The acceleration spectra were used in conformity with the Italian Code (2008) and EC8 (2005), the elastic spectrum at the ultimate limit state (SLV) in the site of the building (residential), for damping equal to 5% and regular topography is shown in Fig 3. The design spectrum was obtained from the elastic spectrum by dividing by the dissipation factor  $q$  (computed according to the Italian Code, 2008, and EC8, 2005):  $q = q_0 K_R = 3.0 \alpha_w / \alpha_1 K_R = 3.0 \times 1.3 \times 1.0 = 3.9$ . The design spectra for the ultimate and damage limit states are shown in Figure 3. According to the above-mentioned design assumptions, a parametric study was performed in order to test the response of the modal analysis according to the five different approaches used for the evaluation of the effective stiffness.

The variables chosen in the parametric study are: type of the shallow R/C beams (ordinary or wide); compressive strength of the concrete; reinforcement ratio; axial- load ratio.

Deep beams with section size 300x400 mm were used as an alternative to shallow beams having a section size of 700x250 mm. Two concrete grades were used : C20/25 and C45/55 (compressive strength on cylinders  $f'_c = 20$  MPa and 45 MPa, respectively). Two steel ratios were considered for the longitudinal reinforcement in the columns (1% and 2%). The reinforcement ratio in the columns appears only in the Khuntia and Ghosh model in the evaluation of the reduced stiffness.

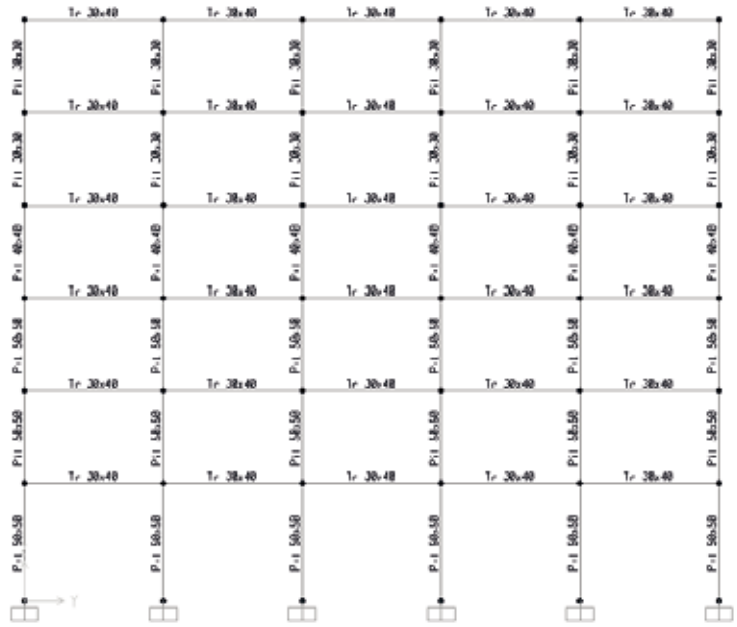
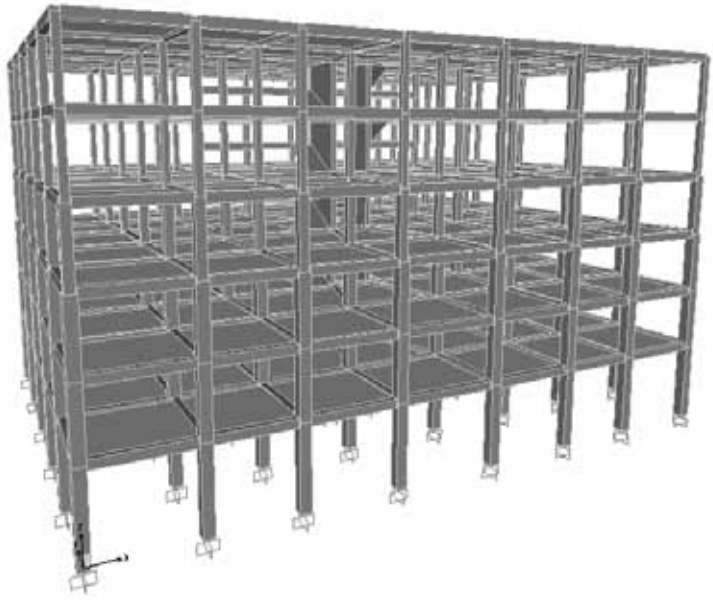
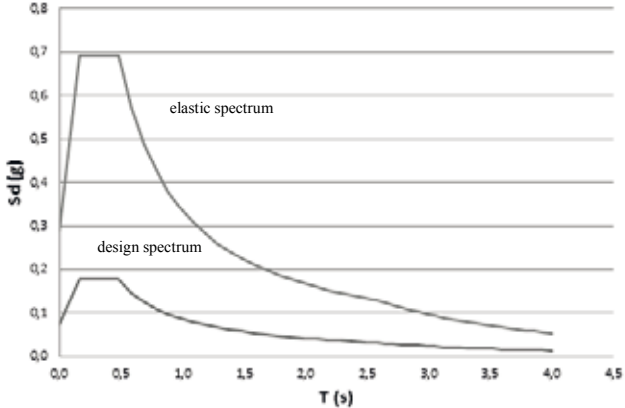


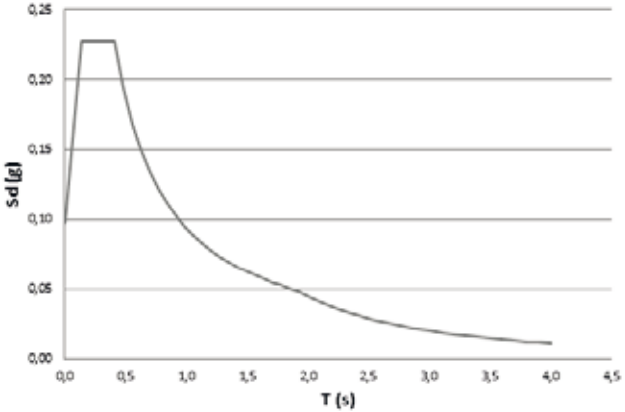
Figure 2 – Geometry and size of the R/C frame investigated in this study.



For the evaluation of the reduced stiffness, the distinction between SULT and SDLS should be introduced, in order to maximize the displacements in the evaluation of second-order effects (parameter  $\theta$  in EC-8) at the ultimate limit state. However, in the present case there were no significant differences between the values of the reduced stiffness at the SULT and SDLS. This is due to the fact that the axial load ratio  $P/A_g f'_c$  is almost the same for the two limit states.



(a)



(b)

Figure 3 – Acceleration spectra for the Ultimate Limit State (a); and for the Damage Limit State (b).

**2.1 Effect of concrete compressive strength**

In the parametric study two values of  $f'_c$  (20 and 45 MPa) have been considered. For the columns, the axial-load ratio  $P/A_g f'_c$  ranges from 0.05 to 0.25 (deep beams or shallow beams); the results obtained with the various stiffness models show that in this range the influence of concrete is quite small and the effective

stiffness ratio  $EI_{eff}/E_c I_g$  decreases slightly at increasing values of  $f_c'$ , as illustrated in Figure 4.

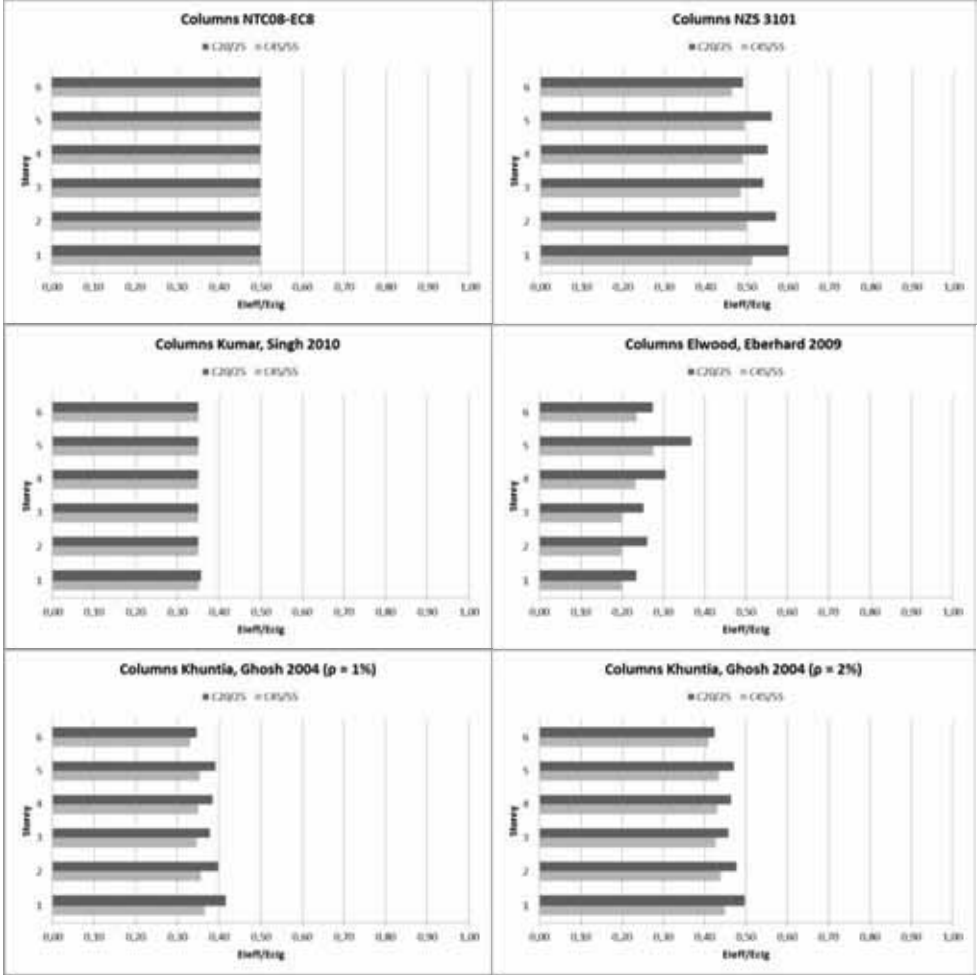


Figure 4 – Effective stiffness-ratio in the columns for different values of concrete strength  $f_c'$ .

This result agrees with Kumar and Singh’s findings (2010), namely that the concrete compressive strength has a nonlinear complex dependence on the effective stiffness. In the range of the axial-load ratio 0.4-0.7, the effective stiffness ratio increases significantly with  $f_c'$ . This fact was also observed by Khuntia and Ghosh (2004), and by Elwood and Eberhard (2009). For smaller values of the axial-ratio, however, the effect of  $f_c'$  is much smaller and of opposite sign (that is, the effective stiffness-ratio decreases at increasing values of  $f_c'$ ). For

low values of the axial-load ratio, the crisis of the section is governed by the yielding of the steel; therefore, the effective stiffness is hardly sensitive to the concrete strength. Furthermore, at very high values of the axial-load ratio, a similar trend can be observed; this range of the axial-load ratio has little practical significance. The Italian Design Code brings in a limitation for the axial load in the columns; when the axial-load ratio does not exceed 0.65 the influence of concrete compressive strength is low and the effective stiffness ratio decreases slightly or remains almost constant with any increase of  $f'_c$ .

In the present case, the model less sensitive to the compressive strength was found to be that of Kumar and Singh which is the only model that provides different relations for normal-strength and high-strength concretes in columns.

With reference to beams, all the stiffness models considered in this study are devoid of any dependence on concrete compressive strength, except Khuntia and Ghosh's model (2004). In this case, the greater the compressive strength  $f'_c$ , the smaller the effective stiffness-ratio, as shown in Figure 5.

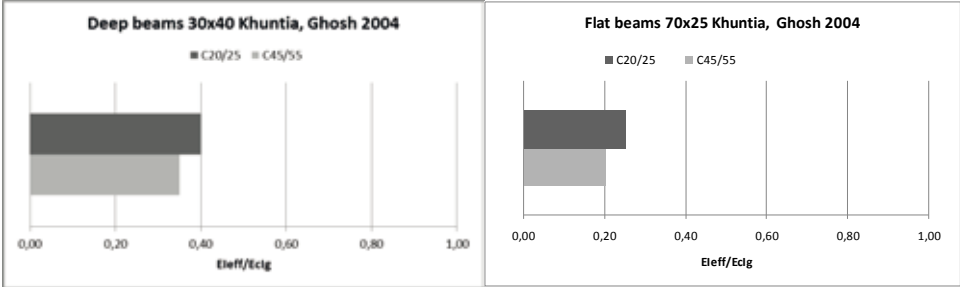


Figure 5 – Effective stiffness-ratio in a beam for different values of concrete strength  $f'_c$  (deep/flat beam = ordinary/wide beam).

## 2.2 Effect of the beam type

To study the effect that the beam type has on the effective stiffness, shallow beams, either ordinary (section  $b \times h = 300 \times 400$  mm) or wide (section  $b \times h = 700 \times 250$  mm) were considered as slab-bearing members; all other coupling beams were had a rectangular section (400x250 mm).

For both low-grade and high-strength concretes, the results obtained with the various stiffness models show that the effective-stiffness ratio for the columns is little affected by the beam type, as illustrated in Figure 6, because in neither case (deep beams or shallow beams) the axial load  $P$  (and the corresponding internal force) changes. The only model showing a slight effect of the beam type on the stiffness of the columns (even if limited to the lower floors), is that of Elwood and Eberhard (2009), since in this model the  $D/a$  ratio between the depth of column section in the loading direction and the shear span is considered. Thus in the case of shallow beams, especially in the lower floors, there is a reduction of the shear

span of the columns with respect to the case with deep beams, leading to increasing values for the ratio  $D/a$  and – consequently to decreasing values for the effective stiffness. As for the beams, all stiffness models provide identical values for the ordinary beams and for the wide beams, except Khuntia and Ghosh’s model (2004). This model contains a relationship for the calculation of the effective stiffness that includes the  $b/d$  ratio (between the width of the section and its effective depth). In this case, any increase of the  $b/d$  ratio is accompanied by a reduction of the effective-stiffness ratio, which means that the stiffness of shallow beams is reduced more than that of deep beams (by almost 50%, Figure 7).

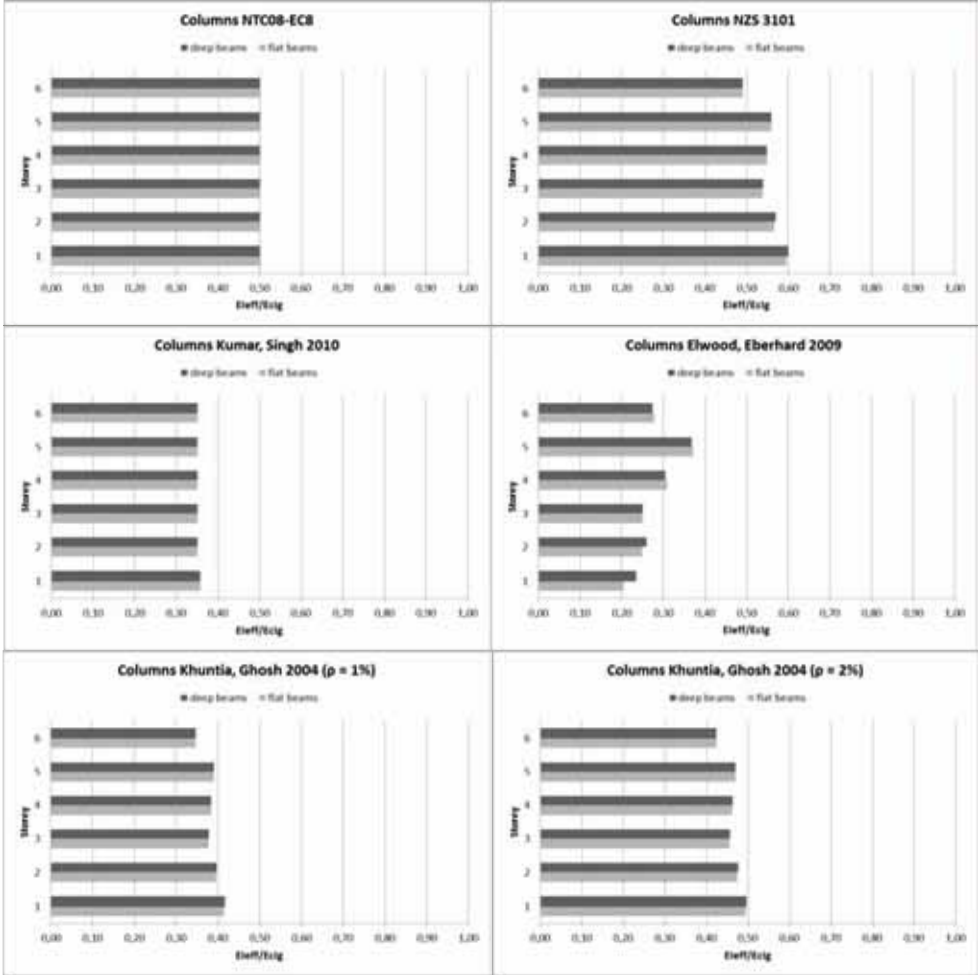


Figure 6 – Effective-stiffness ratio in the columns for different beam types.

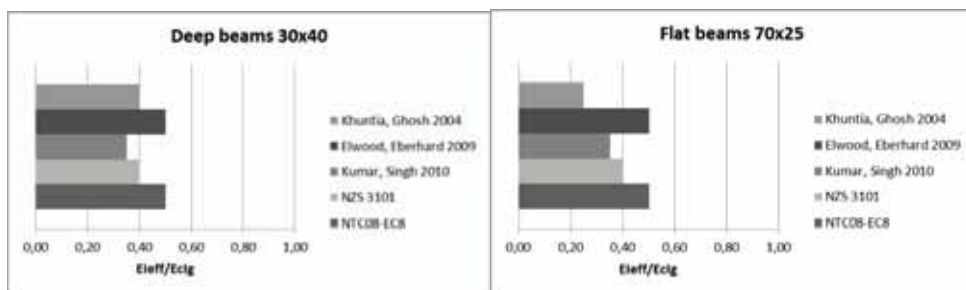


Figure 7 – Effective-stiffness ratio in the beams for different beam types (deep/flat beam = ordinary/wide beam).

### 2.3 Effect of the steel ratio

The Italian Code requires the area of the longitudinal reinforcement to be comprised between the lower limit  $0.01A_g$  and the upper limit  $0.04A_g$ . The common design practice, however, limits the steel ratio to 2-3% to avoid any reinforcement congestion. Therefore, two reinforcement ratios ( $\rho = 1\%$  and  $2\%$ ) are considered in the following.

The effect of the steel ratio in the columns was evaluated taking advantage of the stiffness model proposed by Khuntia and Ghosh (2004), because this is the only model (among those considered in this study) that includes this parameter in the calculation of the effective-stiffness ratio. In either ordinary or wide beams, made of either low-grade or high-grade concrete, any increase of the steel ratio leads to a significant increase of the effective stiffness of the columns (see Figure 8 for deep beams, but the same occurs in the case of shallow beams).

It can be seen that the effect of the steel ratio is not uniform for all possible values of the axial-load ratio. For  $P/A_g f'_c < 0.4$ , as required by the Italian Code,

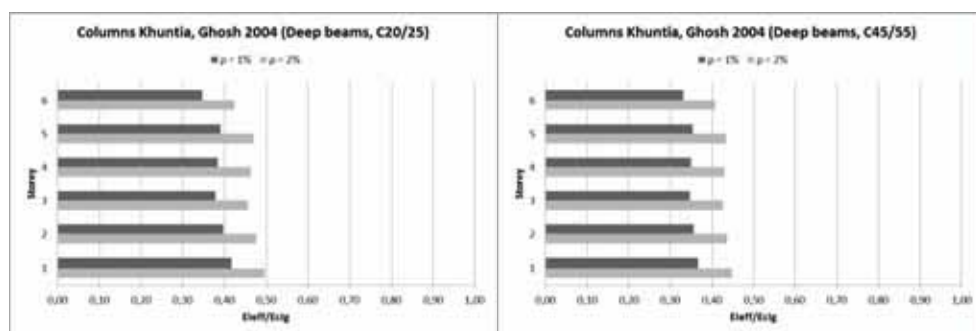


Fig. 8 –Effective stiffness ratio in columns for different reinforcement ratios (1% and 2%); deep beam = ordinary beam.

the crisis of the section is governed by the yielding of the reinforcement; therefore, the influence of the steel ratio is greater than for the values of the axial-load ratio comprised between 0.4 and 0.7. At very high axial-load ratios ( $\geq 0.7$ ), the steel ratio plays a greater role, but the corresponding values of the axial force are of no practical significance.

### 3. DISCUSSION AND COMPARISON OF THE ANALYTICAL RESULTS

The analytical results obtained for the columns with the different stiffness models are shown in Figures 9 and 10, respectively for low-grade (C20/25) and high-grade concrete (C45/55). The comparison shows that in the case of low-grade concrete, the effective stiffness prescribed for the columns by the New Zealand Standard is higher - on average - by 10% in the higher floors ( $0.55E_cI_g$ ) and by 20% at the first level ( $0.60E_cI_g$ ), if compared to the lower limit of  $0.50E_cI_g$  provided by the Italian Code and EC-8, except for the last level, where a similar stiffness ratio was obtained.

For high-grade concrete the NZS 3101 guidelines is aligned with the Italian Code and EC-8 in terms of effective stiffness, with a slightly lower value for the last level because of its lower axial load. Similarly, in the case of low-grade concrete, Khuntia and Ghosh's model provides the same stiffness values as EC-8 in the first floor, for  $\rho = 2\%$ , but lower values elsewhere, this being more evident when a 1% steel ratio is adopted. In this case an effective stiffness lower by 10 ÷ 15% was found if compared with EC-8 and the Italian Code NTC-08. The effective-stiffness values were about  $0.40E_cI_g$  and  $0.35E_cI_g$  for C20/25 and C45/55, respectively. A residual stiffness value of  $0.35E_cI_g$  was obtained for the columns by using the equations recommended by Kumar and Singh (both concretes).

With reference to columns, Elwood and Eberhard's model turned out to be the most conservative. For low-grade concrete the effective stiffness of  $0.25E_cI_g$  (computed for the first three levels) tends to increase at the higher floors (up to approximately  $0.35E_cI_g$ ) and to decrease again at the top floor. This variation along the height of the building is due to the fact that – as already mentioned - the relation proposed by Elwood and Eberhard introduces the effect that the shear span of the columns has on the stiffness, beside the effect of the axial-load ratio  $P/A_gf'_c$ .

With a slight numerical difference, the same considerations apply to the building made of high-grade concrete. New Zealand recommendations and the scientific literature, however, agree in attributing lower stiffness values to the columns placed along the sides and in the corners, something that is not taken into account in the Italian and European codes, which give constant values to the reduced stiffness.

A comparison among the different models, concerning the effective stiffness ratio ( $EI_{eff}/E_cI_g$ ) in the columns, is presented in Figure 11, as a function of the axial-load ratio ( $P/A_gf'_c$ ), for both the low-grade and the high-grade concrete.

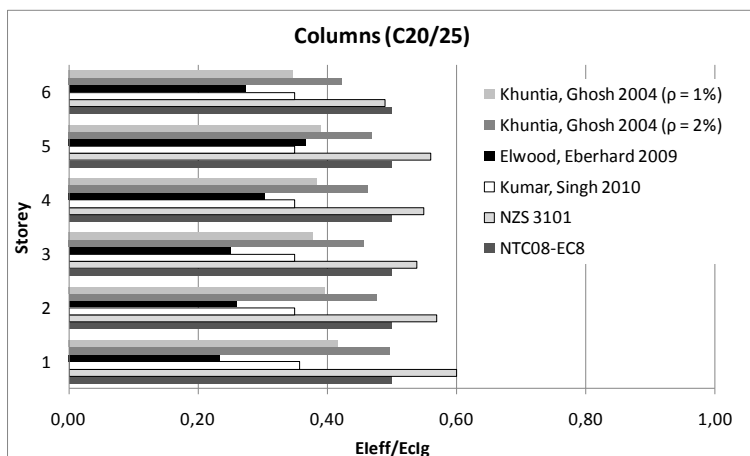


Figure 9 – Comparison between different models in terms of reduced stiffness in R/C columns ( $f_c = 25$  MPa).

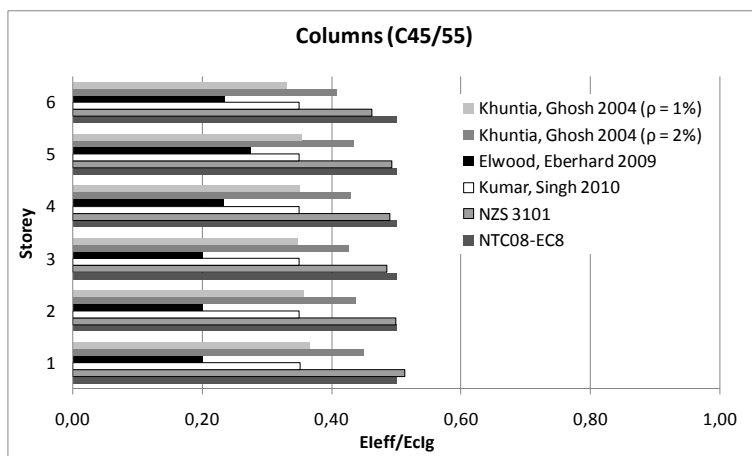


Fig. 10 – Comparison between different models in terms of reduced stiffness in R/C columns ( $f_c = 45$  MPa).

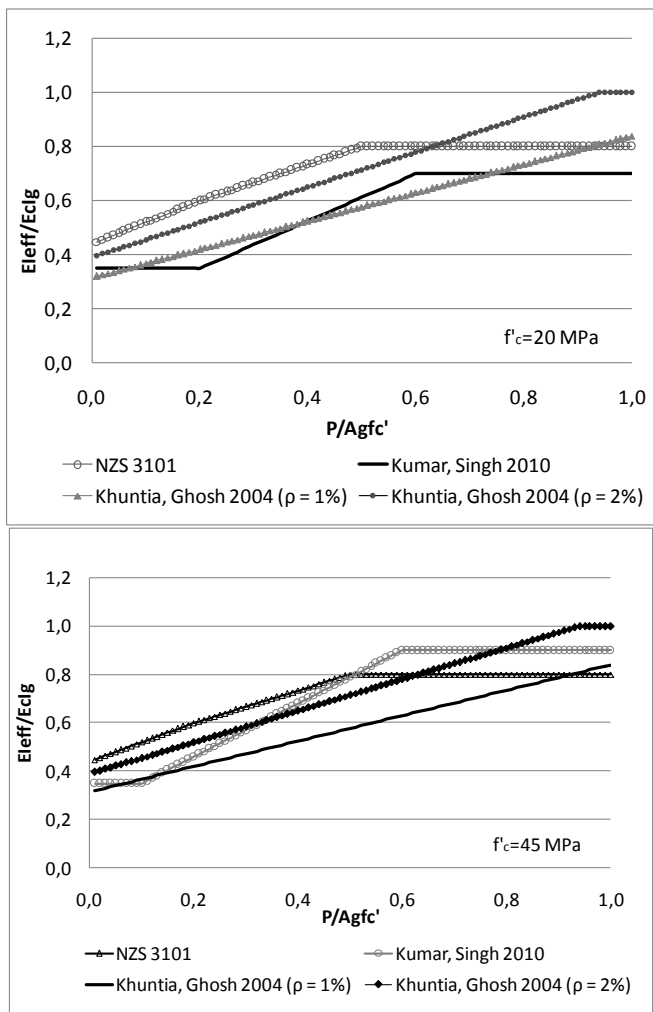


Figure 11 – Effective stiffness ratio of the columns compared to the normalized axial load (= axial-load ratio).

It should be observed from the figures that - for low axial loads, such as those imposed by the Italian Code ( $P/A_g f'_c \leq 0.31$  for high-ductility design and  $P/A_g f'_c \leq 0.37$  for low-ductility design) - the models under investigation bring in lower stiffness values for the cracked sections than the lower limit required by both the Italian and EC-8 design codes.

With reference to beams (Figure 12), all the models provide stiffness values, that are lower than those suggested by both the Italian Code and EC-8. NZS 3101 assumes for the beams a constant value ( $= 0.40E_c I_g$ ), while according to Kumar



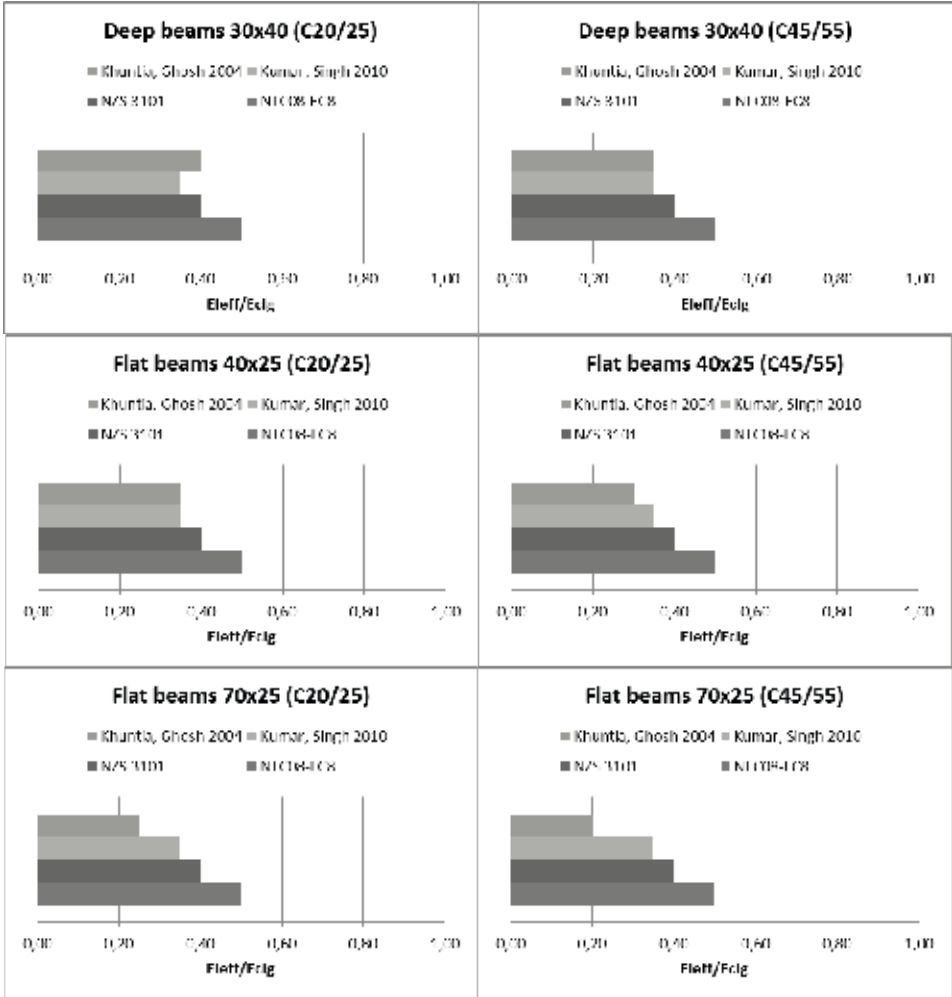


Figure 12 – Effective stiffness ratio of the beams according to different models and codes (deep/flat beam = ordinary/wide beam).

and Singh’s model the value of the effective stiffness is  $0.35 E_c I_g$  for both ordinary and wide beams, and for both concrete grades.

Khuntia and Ghosh’s model, instead, brings a reduction in the effective stiffness ratio with an increase of the  $b/d$  ratio. Thus wide beams exhibit a greater stiffness reduction compared to ordinary beams. Moreover, as in the case of the columns, increasing  $f'_c$  brings in a reduction of the effective-stiffness ratio. In particular, for the wide beams and the high-grade concrete there is a minimum ( $0.20E_c I_g$ ), while for the ordinary beams and the low-grade concrete there is a maximum ( $0.40E_c I_g$ ).

The results of the analysis were instrumental in quantifying second order P-Δ effects (if any) because of the reduced stiffness. The Italian design Code (2008)

and EC8 (2005) neglect geometric nonlinearities when - at each floor - the following ratio does not exceed 10%:

$$\theta = \frac{P \cdot d_r}{V \cdot h} \leq 0.10 \quad [9]$$

where  $P$  is the total vertical load applied above the level of the structure under consideration in the seismic design;  $d_r$  is the average lateral drift between two subsequent floors;  $V$  is the total horizontal shear force at the floor in question;  $h$  is the vertical spacing between the floor under investigation and the floor underneath.

The displacements  $d_E$  under seismic action at the ultimate limit state (ULS) are obtained by multiplying the values  $d_{Ee}$  (obtained from linear, dynamic or static analysis) by the factor  $\mu_d$ , according to the following expression:

$$d_r = d_E = \pm \mu_d \cdot d_{Ee} \quad [10]$$

where  $d_r$  = displacement under the design seismic action at the ULS;  $d_{Ee}$  = displacement determined by linear analysis; and  $\mu_d$  = parameter depending on the natural frequency of the structure and seismic spectrum, easy to be computed according to the Italian Code (2008) and to EC8 (2005). When  $\theta$  ranges from 0.1 to 0.2, the effects of geometric nonlinearities may be taken into account by increasing the effect of the horizontal seismic action by a factor equal to  $1/(1 - \theta)$ , while for  $\theta$  between 0.2 and 0.3 it is necessary to perform a nonlinear analysis; however,  $\theta$  cannot exceed 0.3.

The factor  $\theta$  is analyzed in this paper, according to the structural parameters used, and models with beams and columns with reduced stiffness were taken for the computation of  $d_r$ . the purpose being to determine whether and to what extent the current Italian code and EC-8 may underestimate geometric nonlinearities, if compared to other design recommendations. The results are presented in Figure 13 with reference to the more severe case of low-grade concrete, for seismic forces acting along the x and y axes.

In the case of high-grade concrete (Figure 14), the above-mentioned results were confirmed. The analysis gives rather useful information, since NZS 3101, Khuntia-Ghosh's model and Elwood-Eberhard's model bring in values of  $\theta$  greater than 0.1 in both x and y directions. Only Elwood-Eberhard's model leads to some second-order effects in the first floor (direction y). The model that brings in the highest P- $\Delta$  effect is that of Kumar and Singh; the effective stiffness leads to values of  $\theta$  that are close to 0.10-0.13 in the first and second floor in x direction, and values of  $\theta$  that are close to 0.19 in the second and third floor in y direction, for shallow beams.

It is interesting to observe that Khuntia-Ghosh's model brought in values of  $\theta$  in the x direction very similar to those obtained with Kumar-Singh's model, while in the y direction  $\theta$  is lower, as predicted also by Elwood and Eberhard's model. This is due to a reduction of the effective stiffness of the beams that is introduced through the  $b/d$  ratio. The results seem interesting since the stiffness reduction of

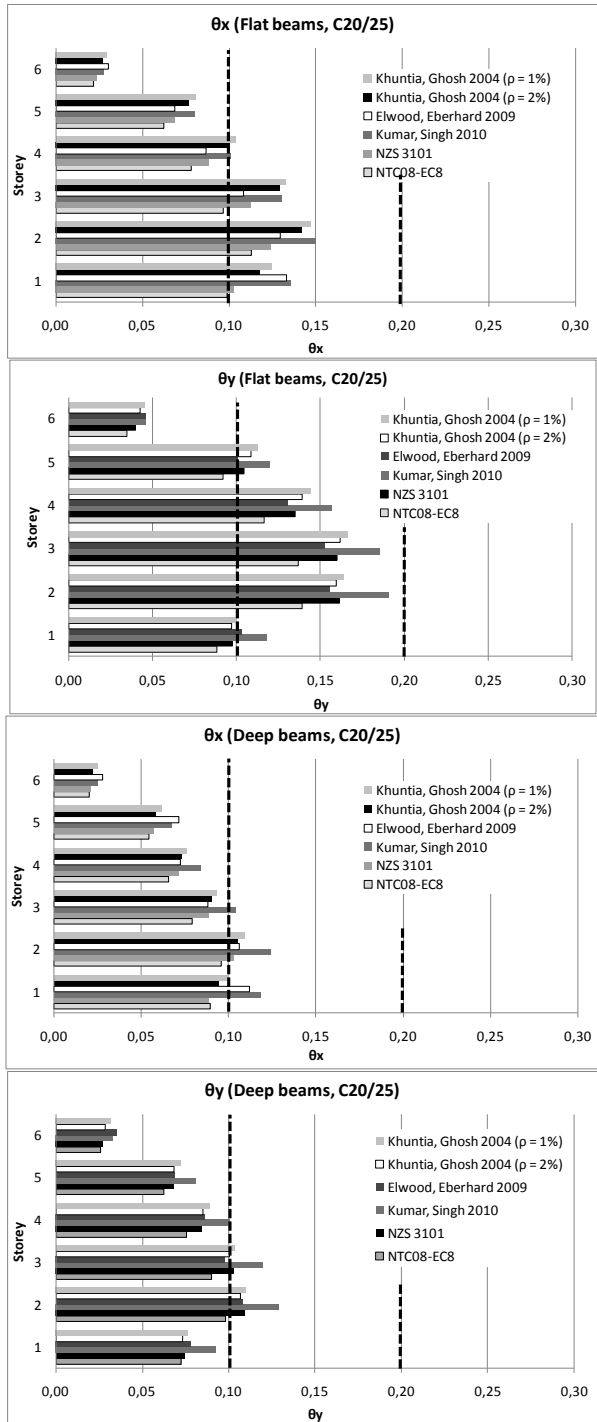


Figure 13 – P-Δ effect ( $f_c = 20$  MPa); deep/flat beam = ordinary/wide beam.

the wide beams in the x direction ( $b = 700$  mm) is higher than that of the wide coupling beams ( $b = 400$  mm) in y direction.

The results of the analysis for the Seismic Damage Limit State were compared with the limitation introduced by the Italian Design Code:

$$D_r < 0.005 h \quad [11]$$

that means a 0.5% limit ratio between the lateral drift and the inter-storey height.

In this case, the model was assumed with reduced stiffness for both columns and beams. One should remember also that the values of the internal forces at the DSL are quite different from those at the ULS. This is why the internal forces are computed according to different load combinations based on a different ground acceleration spectrum. In such a case, the Italian Design Code (2008) and EC8 (2005) amplify the drift according to the values of  $\theta$ . This analysis was aimed to check whether the results obtained by using the Italian Code or EC-8 may underestimate the drift compared to the values computed with different reduced-stiffness models. The results (Figure 15, low-grade concrete) show sizeable differences among the different approaches. According to New Zealand Design Code, the building with ordinary beams exhibits lateral-drift values 4% higher than those computed according to EC-8 and the Italian Code. Furthermore, such difference increases by applying the equations provided by Khuntia-Ghosh's model (+7% and +5% for  $\rho = 1\%$  and  $\rho = 2\%$ , respectively).

Comparing the results obtained with EC-8 with those obtained with Elwood and Eberhard's model, the latter exhibit a reduced stiffness greater by 15% at the first level, that decreases by 8-9% at the top level. The largest difference occurs when comparing the displacements computed with EC-8 and those computed according to Kumar-Singh's reduced-stiffness model. The difference in this case is about 15% along the total height of the structure. It is worth noting that in all cases the limitation provided by Eq.11 is always verified (the largest values - 0.004 - were found at the second floor using Kumar-Singh's model).

In the case of wide beams, the differences between EC-8 and the other approaches are more evident. NZS 3101 provides drift values 7% higher, while Elwood and Eberhard's model brings in an increment of 20% at the first level, decreasing until 10% at the top level. The reduced stiffness recommended by Kumar and Singh leads to lateral-drift values that are 17-19% higher than those obtained with both the Italian Code and EC-8, for all the floors of the building. In the last case, it happens that Eq. 11 is verified when the stiffness provided by the Italian Code is used, while the ratio exceeds the value 0.005 at the levels 2-3-4 and 5 when the other models are used.

For both low-grade and high-grade concrete, the results are not reported in this paper, but it was found that in all cases Eq.11 is verified and the highest values of the drift in direction Y was is  $0.0035h$ . Applying different approaches shows how NZS 3101, Elwood-Eberhard's model and Khuntia-Ghosh's model reduce the effective stiffness when the value of  $f_c'$  increases, leading to large lateral drifts in

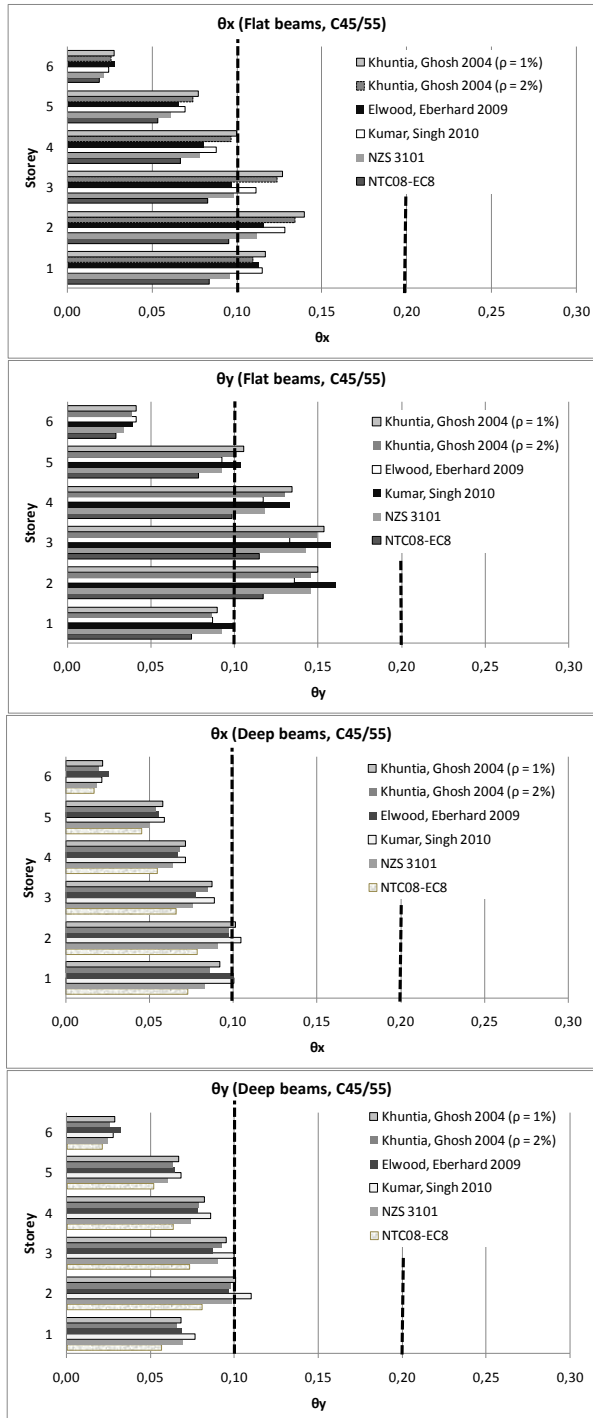


Figure 14 – P-Δ effect ( $f_c = 45$  MPa); deep/flat beam = ordinary/wide beam.

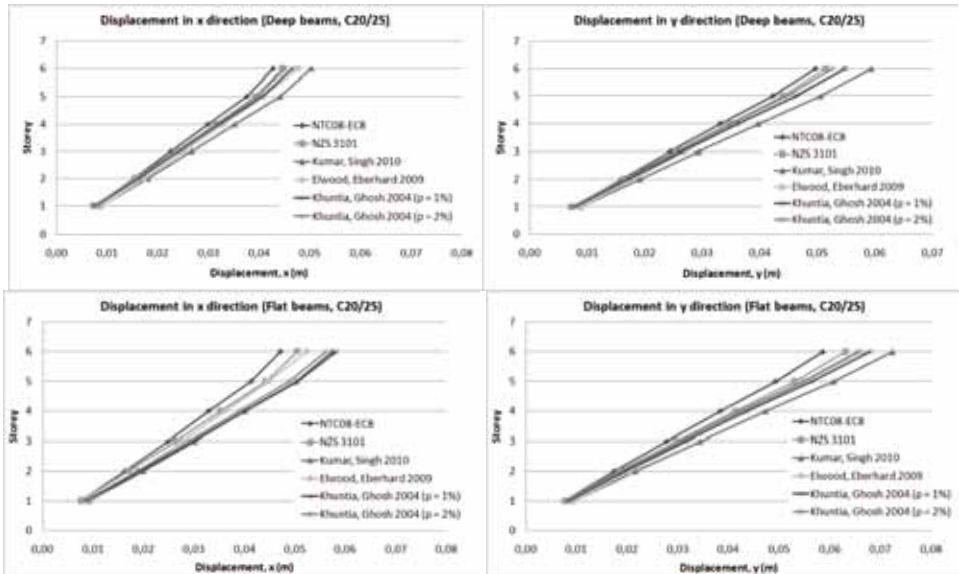


Figure 15 – Lateral drift at the Damage Limit State in directions x and y ( $f_c = 20$  MPa)

both x and y directions, closer to those computed by means of Kumar and Singh's model.

Summing up, the stiffness reductions proposed by both the Italian Code and EC-8 underestimate the lateral drift at the Damage Limit State, compared to the predictions given by other non-European codes and models..

#### 4. CONCLUSIONS AND RECOMMENDATIONS

Modal analysis is the most popular method in the seismic design of regular R/C frames, even if linear analysis is unable to take care of those nonlinear phenomena that bring in a continuous variation of the structural stiffness because of concrete cracking and section reduction. Thus reduced-stiffness values are recommended to introduce these phenomena. Comparing different approaches to evaluate the reduced stiffness is at the same time necessary and not easy, as shown in this study for R/C columns and beams belonging to a building subjected to seismic loading.

The Italian Code and EC8, both based on the simple recommendation that the cracked stiffness be reduced by 50% with respect to the gross section do not seem to be on the safe side in some cases, as the effects of a number of relevant variables are neglected (steel ratio, stiffness of the beams, concrete properties). Thus a parametric analysis was performed in this study with the focus on R/C frame buildings designed according to EC-8. The structural analysis was

performed by comparing the European recommendations with those provided by the New Zealand Design Code, which include further structural parameters in the computation of the effective stiffness.

Three different theoretical models available in the scientific literature, based on experimental evidence and on different theoretical assumptions to take care of the effective stiffness, were used as well, to compare their predictions on the behavior of R/C frame buildings. The parameters investigated in this study were concrete compressive strength, beam type (wide beams as an alternative to ordinary beams to support the floors), the steel ratio and the axial-load ratio (that is variable along the height of the frame). Two concrete grades were considered, to represent old existing buildings (low-grade concrete, C20/25) and more recent earthquake-resistant buildings (high-grade concrete, C45/55).

It was found that, when the axial load respects the limitations imposed by the Italian code, there is no effect of concrete strength in the computation of the reduced stiffness, while the steel ratio plays a sizeable role, independently from the axial-load ratio. Hence, an accurate evaluation of the effective stiffness should also include the steel ratio.

In the design at the Ultimate Limit State, using wide beams or ordinary beams does not influence the effective stiffness of the columns, since the axial load remains almost the same.

It should be noted also that the New Zealand code and the analytical models considered in this study unanimously require the columns placed along the sides or at the corners of the building to have a reduced stiffness, while this is not required in EC-8 and in the Italian Code. In more details, the reduction of the effective stiffness computed by using the above-mentioned models (all based on well-documented test results) may be remarkable indeed (more than -50% of the stiffness of the gross section), even within the range of the axial loads permitted by the Italian Code.

In particular, in the heavily-loaded columns of the lower floors the reduced stiffness is limited to  $0.50 E_c I_g$  by EC-8 and the Italian Code, while in the upper floors - especially in tapered columns - having  $P/A_g f'_c > 0.2$  is hardly possible; hence, values for the reduced stiffness as low as  $0.35-0.40 E_c I_g$  are often found. With regard to this point, values in the range  $0.45-0.50 E_c I_g$  are admissible according to the New Zealand Design Code, which is rather close to EC8 and the Italian Design Code. Summing up, the current requirements of EC8 and of other European codes should be updated in order to consider the value  $0.50 E_c I_g$  as an upper limit for low axial loads, rather than a lower limit.

As for the reduced stiffness of cracked beams, the European approach is less cautious if compared with the other four methods of analysis adopted in this study. Only Khuntia-Ghosh's model takes care of the aspect ratio  $b/d$  of the cross section, by making reference to *wide beams* ( $b > d$ ) and *ordinary beams* ( $b < d$ ).

Another topic investigated in this study is the P- $\Delta$  effect, which requires second-order analysis. It was found that geometrical nonlinearities may occur

depending on the way the reduced stiffness is computed. As a matter of fact, using the analytical models found in the scientific literature leads to an amplification of the seismic action, something that is not contemplated in the European and Italian Design Codes. In this type of analysis, sizeable differences ensue from the beam type, since ordinary beams strongly contribute to the reduction of second-order effects, for both concrete grades.

The same conclusions hold at the Damage Limit State (Serviceability Limit State under seismic loading), since the values of the lateral drift changed significantly, depending on the model adopted in the analysis. For instance, when shallow beams are used, the differences between the Italian Code and the other models or codes are more evident. NZS 3101 leads to higher drift values (+7%); Elwood and Eberhard's model leads to even higher values (+20% at the first level and 10% at the top level).

The same occurs with the reduced stiffness recommended by Kumar and Singh (+17-19%) for all the floors of the building. Hence, should a more accurate evaluation of the effective stiffness be performed, the maximum lateral drift admitted by the Italian code would not be respected.

Now, two final remarks. Firstly, in the analysis at the ultimate limit state both configurations with cracked and un-cracked columns should be considered. At the ULS, uncracked sections should be introduced to evaluate the natural frequencies and to maximize the earthquake-induced forces. The subsequent analysis should be based on cracked sections to maximize the inter-storey drift and check possible non-linear P- $\Delta$  effects. For the damage limit state a cracked model should be used for the computation of the lateral deformations

Secondly, the present study strongly suggests code-makers to introduce a more accurate evaluation of the effective stiffness of R/C frames under seismic loads in both EC8 and the Italian Design Code. This should be done by considering a larger number of structural parameters.

## REFERENCES

- ACI Committee 318 (2002). "Building Code Requirements for Reinforced Concrete (ACI 318-02) and Commentary (318R-02)", *ACI - American Concrete Institute*, Farmington Hills, Michigan (USA), 443 pp.
- Branson D. E. (1965). "Instantaneous and Time Dependent Deflections of Simple and Continuous Reinforced-Concrete Beams", *HPR Publications, No.7, Part 1*, Alabama Highway Department (Alabama, USA), U.S. Bureau of Public Roads, 93 pp.
- Canada Standards Association (2005). "Design of Concrete Structures", *CSA A23.3-04*, Mississauga ( Ontario, Canada), 470 pp.
- Chen Wai-Fah and Scawthorn C. (2003). "Earthquake Engineering Handbook", *CRC Press* (Boca Raton, Florida, USA), 1512 pp.



- Crowley H. (2003). "Periods of Vibration for Displacement-Based Assessment of R/C Buildings", MS Dissertation, *Rose School, University of Pavia, Pavia (Italy)*, 101 pp.
- EC8 UNI EN 1998-1-2005 (2005). "Design of Structures for Earthquake Resistance - Part 1: General Rules, Seismic Actions and Rules for Buildings", *Comité Européen de Normalisation, Brussels*, 232 pp.
- Elwood K. J. and Eberhard M. O. (2009). "Effective Stiffness of Reinforced-Concrete Columns", *ACI Structural Journal*, V. 106, No. 4, July-August, pp. 476-484.
- Italian Design Code (2008). "Technical Provisions for Constructions - Norme Tecniche per le Costruzioni", Italian Ministry of Public Works.
- NZS 3101: Part 2, (2006). "Concrete Structures Standard, Part 2 – Commentary on the Design of Concrete Structures", *Standards New Zealand, Wellington, N.Z.*, 646 pp.
- FEMA 356, (2000). "Prestandard and Commentary for the Seismic Rehabilitation of Buildings", *FEMA Publications No. 356, prepared by the American Society of Civil Engineers for the Federal Emergency Management Agency, Washington, DC.*, 518 pp.
- Grossman J. S. (1981). "Simplified Computations for Effective Moment of Inertia and Minimum Thickness to Avoid Deflection Computations", *ACI Journal*, V.78, No. 6, Nov.-Dec., pp.423-439
- Khuntia M. and Ghosh S. K. (2004). "Flexural Stiffness of Reinforced-Concrete Columns and Beams: Analytical Approach", *ACI Structural Journal*, V.101, No. 3, May-June, pp. 351-363.
- Kumar R. and Singh Y. (2010). "Stiffness of Reinforced-Concrete Frame Members for Seismic Analysis", *ACI Structural Journal*, V. 107, No. 5, Sept.-Oct., pp. 607-615.
- Mehanny S. S. F., Kuramoto, H. and Deierlein G. G. (2001). "Stiffness Modeling of R/C Beam-Columns for Frame Analysis", *ACI Structural Journal*, V.98, No. 2, Mar.-Apr., pp. 215-225.
- Mirza S. A. (1990). "Flexural Stiffness of Rectangular Reinforced-Concrete Columns", *ACI Structural Journal*, V.87, No. 4, July-August, pp. 425-435.
- Paulay T. and Priestley M.J.N. (1992). "Seismic Design of Reinforced-Concrete and Masonry Buildings", *J. Wiley & Sons, New York*, 768 pp.
- Petrini L., Pinho R. and Calvi G. M. (2004). "Guidelines for Seismic design" (in Italian), *IUSS Press*, 184 pp.
- Sugano S. (1970). "Experimental Study on Restoring-Force Characteristics of Reinforced-Concrete Members", Thesis submitted to the University of Tokyo, 768 pp..
- Wallace J. W. Orakcal K. (2002). "ACI 318-99 Provisions for Seismic Design of Structural Walls", *ACI Structural Journal*, Vol. 99, No. 4, July-August, pp. 499-508.
- Wang Q. (2001). "Nonlinear Stiffness Design Optimization of Tall Reinforced-Concrete Buildings under Service Loads", *MS Thesis, Hong Kong Univ. of Science and Technology, Hong Kong*, 149 pp.



## EVALUATION OF THE CARRYING CAPACITY OF REINFORCED- CONCRETE SLABS SUBJECTED TO CONCENTRATED LOADS CLOSE TO THE SUPPORTS

Beatrice Belletti<sup>1</sup>, Cecilia Damoni<sup>2</sup> and Max Hendriks<sup>3,4</sup>

### ABSTRACT

The behaviour of reinforced-concrete (R/C) slabs subjected to concentrated loads close to their supports is investigated in this paper. An experimental program was carried out at Delft University of Technology on eighteen large-scale R/C slabs. After testing, three of the slabs were chosen as case studies. Nonlinear finite-element (NLFE) analyses were performed, and analytical models - either proposed by the standard codes or available in the literature – were used as well.

The aim of the research is to compare the prediction of the carrying capacity of the slabs obtained through simplified analytical and numerical procedures, usable by analysts in the current design process. The research fits into a research program driven by the Dutch Ministry of Infrastructure and the Environment for the re-evaluation of the carrying capacity of existing bridges and viaducts, and of their components (beams and slabs), through the use of nonlinear FE analysis.

The project provided the final publication of guidelines for nonlinear finite-element analyses to be followed by users in order to reduce modelling efforts and save time.

The research well matches with the philosophy of the Model Code 2010 that offers different analytical and numerical calculation methods for the evaluation of the design shear resistance of R/C members according to different safety levels of approximation.

**KEYWORDS:** reinforced-concrete slabs, shear resistance, nonlinear finite element analysis, guidelines (for R/C slabs subject to punching), safety levels.

---

<sup>1</sup> Assistant Professor, <sup>2</sup> PhD Student, DICATA – Dept. of Civil and Environmental Engineering and Architecture, University of Parma, Parma, Italy.

<sup>3</sup> Assistant Professor, Dept. of Structural Mechanics, Delft University of Technology, Delft, The Netherlands.

<sup>4</sup> Professor, Dept. of Structural Engineering, Norwegian University of Science and Technology, Trondheim, Norway.

# 1 INTRODUCTION

Reinforced concrete slabs have been widely used since 20<sup>th</sup> century for many applications (bridge decks, flat soffits etc.). The behaviour up to failure of R/C slabs has been object of several experimental programs well documented in literature (e.g. Regan, 1982; Kinnunen and Nylander, 1960; Furuuchi et al., 1998; Graff, 1933; Baskaran and Morley, 2004; Foster et al., 2004).

The experimental test programs often provided the basis for the development of mechanical models to estimate the resistance of reinforced concrete slabs. Well known formulations have been proposed for the evaluation of the shear resistance through the strip method (e.g. Hillerborg, 1996), the punching strength (e.g. Regan and Rezai-Jorabi, 1988; Muttoni, 2003; Muttoni, 2008) and the investigation of the behaviour of R/C slabs through the yield-line method (e.g. Johansen, 1962; Chen, 1982; Park and Gamble, 2000; Gambarova et al., 2008).

Several works available in literature concern the investigation of the behaviour up to failure of R/C slabs through NLFE analyses and the comparison with experimental test data and analytical formulations (e.g. Vidosa et al., 1988; Hu and Schnobrich, 1991; Huang et al., 1999).

An experimental test program including large-scale R/C slabs subjected to concentrated loads applied close to their supports was carried out at Delft University of Technology (Lantsoght 2012, Lantsoght et al. 2013). A total of eighteen slabs (size: 2500 x 5000 x 300 mm) were tested. Three of the slabs (Slabs S1T1, S1T2 and S4T1) were chosen as case studies. The failure mode and the carrying capacity of the slabs was evaluated with analytical formulations according to either current building code provisions or available in the literature, and numerically with NLFE analyses. The results obtained analytically and numerically were then compared with the experimental results.

The research fits into a project driven by the Dutch Ministry of Infrastructure and the Environment for the re-assessment of the carrying capacity of existing bridges and viaducts, and their composing beams and slabs. The urgency of the project comes from the increase of traffic and the reallocation of emergency lanes to traffic lanes in the last years. For a certain number of Dutch bridges the safety verifications are not satisfied if the usual analytical procedures (proposed by the current norms) are adopted in the calculations. For this reason, the Dutch Ministry of Infrastructure and the Environment proposed to make structural assessment of existing structures through the use of NLFE analyses, with the final release of a document containing guidelines for nonlinear finite element analyses of reinforced and prestressed concrete elements (Guidelines RTD, 2012). NLFE analyses, which are increasingly becoming a usual tool in the daily design process, can in fact take into account hidden structural capacities and offer refined modelling based on realistic material properties. Nevertheless the power of NLFE analyses should not be overestimated. The results of NLFE analyses strongly depend on the modelling choices and therefore a large scatter in the results obtained for the same structure

by different analysts usually occurs. For this reason, the availability of guidelines on how to perform NLFE analyses is a big help for the analyst, as indicated by some previous researches focused on reinforced- and prestressed-concrete beams (Rots et al., 2010; Belletti et al., 2011).

As previously stated, the carrying capacity of the slabs has been evaluated with analytical and numerical methods. The NLFE analyses presented in this paper have been carried with the software DIANA (Manie, 2009); however the guidelines are valid for any commercial software in which relatively simple crack models are implemented. Analytical formulations have been applied to determine the carrying capacity of the slabs: the one-way shear resistance has been calculated according to Model Code 2010 (2010), the punching resistance with Regan's formulation (Regan and Rezai-Jorabi, 1988), Eurocode 2 (EN 1992) and with the *Critical Shear Crack Theory (CSCT)* developed by Muttoni (2003, 2008); and – last but not least - the bending resistance with the yield line method.

Furthermore, the design shear resistance of the slabs has been evaluated following the provisions of the Model Code 2010, where different analytical and numerical calculation methods are proposed to evaluate the design shear resistance of R/C members, according to different safety levels of approximations. In the Model Code 2010, the calculation methods fall into four categories with as many levels of approximation: by increasing the level of approximation, the complexity and the accuracy of the results increase. Level I, II and III refer to analytical calculation methods, while level IV refers to numerical calculation methods, deriving from the results of NLFE analyses.

Finally, this research (a) offers an overview on the behaviour of R/C slabs; (b) gives practical indications for the evaluation of their carrying capacity; and (c) contains one of the first systematic applications of the Model Code 2010 for the evaluation of the design resistance of R/C slabs through safety-level methods.

## 2 EXPERIMENTAL PROGRAM

All specimens were loaded by means of a concentrated load (Lantsoght, 2012). In Figure 1 the test set-up of S1T1 is schematically reported. Crack width was measured by using crack-width comparators and the displacements were measured by using lasers placed over the supports and around the load. As indicated in Fig.1, each slab was constrained by a simple support, denoted as Support 1, a continuous support, denoted as Support 2 and three prestressed dywidag bars (Support 3). Between the supports and the concrete slab, layers of felt and plywood were inserted. In Figure 2 the experimental stress-strain relationships of the felt/plywood and felt stacks placed along the support-slab interfaces and the reinforcing steel are plotted.

The forces over the simple support were measured by load cells placed underneath the elastomeric bearings, while the forces over the continuous support

were measured at selected points. In Figure 3 the reinforcement layout, the support details and the loading scheme are presented for the three slabs investigated in this study. In Table 1 the main mechanical properties measured during the test are reported.

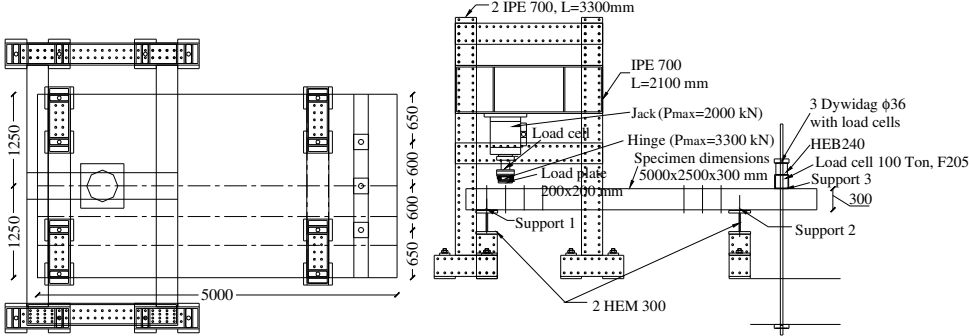


Figure 1- Test set-up of Slab S1T1.

Table 1- Mechanical properties of the materials.

Concrete		$E_c$	$f_c$	$f_t$	steel		$E_s$	$f_y$	$F_{pe}^*$
		(Mpa)	(Mpa)	(Mpa)			(Mpa)	(Mpa)	(KN)
Concrete	S1T1	30910	29.7	2.8	steel	$\phi 10$	210000	537	-
	S1T2	30910	29.7	2.8		$\phi 20$	210000	541	-
	S4T1	34930	42.9	3.8		$3\phi 36$	210000	1000	3·15

$F_{pe}^*$  = prestressing force in the dywidag bar

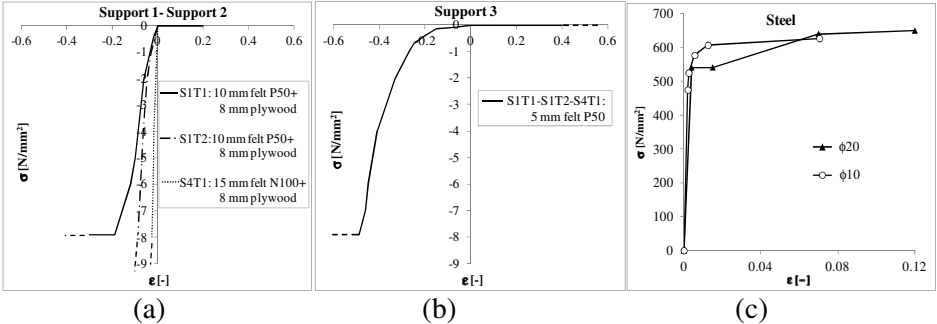
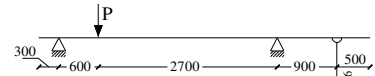
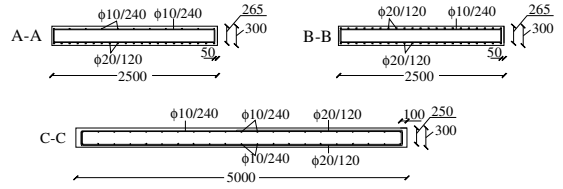
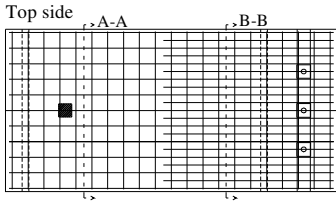
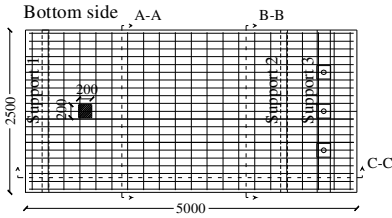
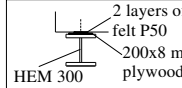


Figure 2- Experimental stress-strain relationship of (a) felt/plywood; (b) felt; and (c) reinforcing steel.

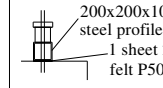
### S1T1



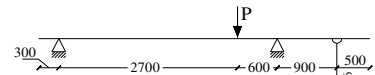
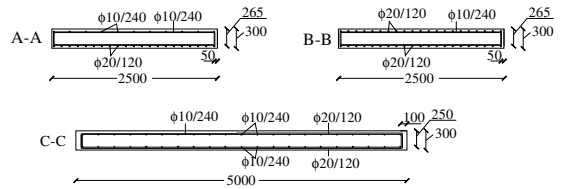
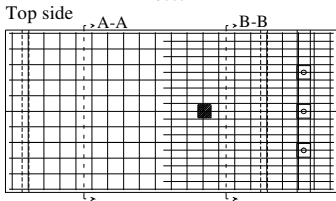
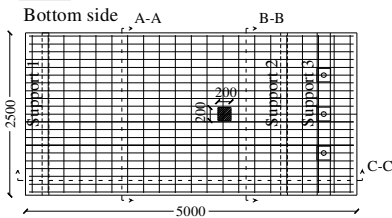
#### Support 1 - 2



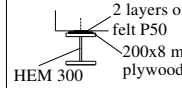
#### Support 3



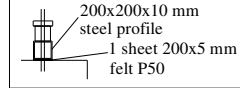
### S1T2



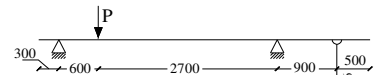
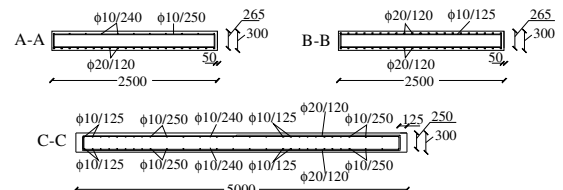
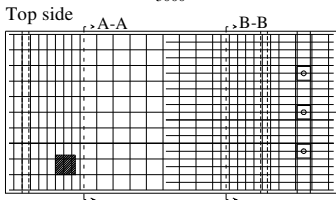
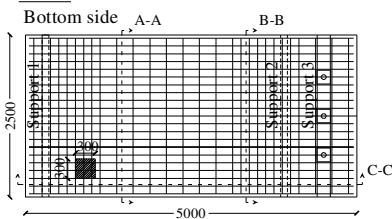
#### Support 1 - 2



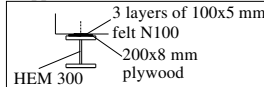
#### Support 3



### S4T1



#### Support 1 - 2



#### Support 3

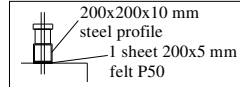


Figure 3 - Geometry, reinforcement and support details of slabs S1T1, S1T2 and S4T1.

## 2.1 Experimental failure mode and ultimate load

### 2.1.1 S1T1

At 700 kN a flexural crack appeared at the front face, Figure 4b. Failure occurred at 954 kN. The width of the crack at the front face at failure was about 1.8 mm. On the bottom face, a flexural crack pattern could be observed. The main cracks appeared around the load and ran towards and away from the support. The load plate at failure penetrated into the top face of the concrete. The failure was a sort of one-way shear failure. However the crack developed at the front face could also be due to a support subsidence. In Figure 4 the crack patterns of S1T1 at the intrados and on a lateral face at failure are reported.

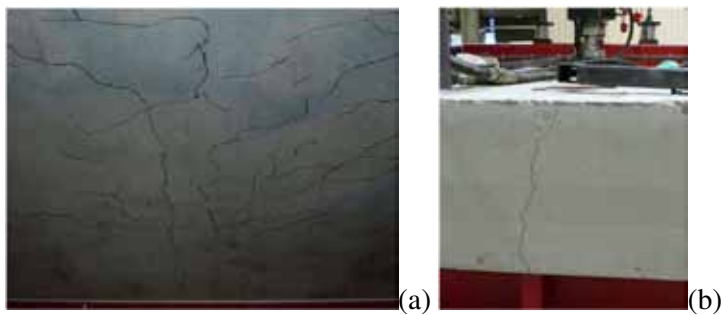


Figure 4 - Crack patterns of Slab S1T1 (a) intrados; and (b) on a lateral face.

### 2.1.2 S1T2

The first cracks appeared at the intrados around the position of the load at 200 kN. At 600 kN flexural cracks could be clearly observed along the intrados and the first crack on a lateral face became visible. At 800 kN the intrados showed a fully-developed flexural crack pattern.

When the load reached 900 kN the concrete touched the plywood of the support.

Failure occurred at 1023 kN. The largest observed crack, located at mid-width and extended over more than half of the span, was along the intrados with a width of 2.5 mm.

At failure the loading plate penetrated into the extrados of the slab. Even for Slab S1T2, as for Slab S1T1, the failure was in the form of a one-way shear failure. In Figure 5 the crack pattern of Slab S1T2 along the intrados and on a lateral face are reported at failure.



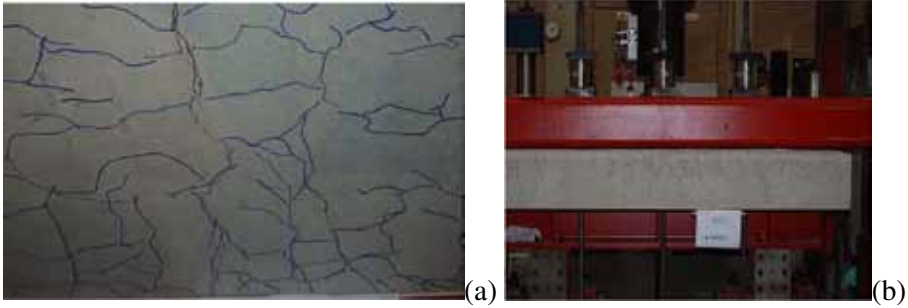


Figure 5- Crack patterns of Slab S1T2: (a) intrados; and (b) on a lateral face.

### 2.1.3 S4T1

At 400 kN a crack of 0.15 mm was observed along the lateral face, and flexural cracks were observed along both the lateral face and the intrados. At 800 kN the crack along the lateral face was 0.4 mm wide and the first shear crack became visible. At 990 kN a second shear crack appeared. Failure occurred at 1160 kN. The maximum crack width at the extrados was 0.45 mm. The width of the shear crack along the lateral west face was 4 mm. The failure mode of Slab S4T1 was clearly activated by shear. In Figure 6 the crack patterns of Slab S4T1 along the intrados and on the front lateral face at failure are reported.

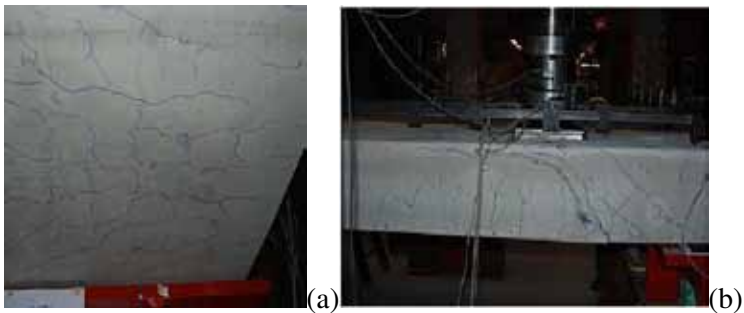


Figure 6- Crack patterns of Slab S4T1: (a) intrados; and (b) on a lateral face.

## **3 FINITE-ELEMENT MODEL**

The slabs were modelled following the main indications of the guidelines. Slab S1T1 was modelled by using both shell and solid elements. The comparison between shell and brick elements allowed to investigate the effects of two different approaches on the results, in terms of failure modes and ultimate loads. Since the slabs failed in shear, according to both experimental test and NLFE

analyses, the shell elements, as expected, were unable to describe the shear failure (see Section 5). For this reason, Slabs S1T2 and S4T1 were modelled only by means of brick elements.

### 3.1 Model with brick elements

Full 3D modelling has been used. To model concrete members and steel plates 20-node brick elements with a full Gaussian integration scheme (3x3x3) were adopted; the average element's dimension was 110 x 100 x 100 mm.

It is well known that the accuracy would have been much better, had more elements been used to describe slab's thickness. However, as analyses with more refined meshes require more computer memory and calculation time, efforts are in progress to model the slab as a *multi-layer continuum*.

For the reinforcement, embedded truss elements were adopted and perfect bond was assumed.

The dywidag bars were modelled with truss elements too. Between the steel plates and the slab 16-node interface elements were inserted, these elements having the mechanical properties of felt and plywood.

Appropriate boundary conditions were applied to the nodes of the steel plates and of the dywidag bars. Rigid movement of the slab in the  $x$  and  $y$  direction were prevented. The analyses comprised two phases. In the first phase the prestressing force in the dywidag bars ( $F_{pe}$ ) and the own weight were applied, while in the second phase a displacement along the  $z$  axis was applied to the central node of the loading plate.

The analyses were carried out by using a regular Newton-Raphson iteration method based on force and energy convergence criteria, with a tolerance of  $10^{-2}$  and  $10^{-3}$ , respectively.

In Figure 7 the mesh and boundary conditions adopted in the finite-element discretization are shown for Slab S1T1.

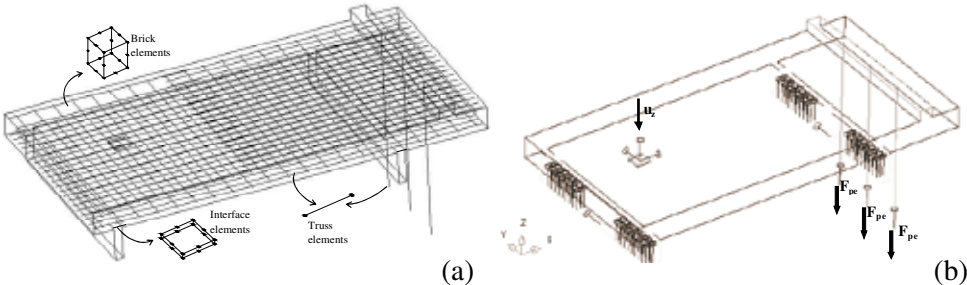


Figure 7- Slab S1T1: (a) mesh adopted; and (b) boundary conditions.

### 3.2 Model with shell elements

Eight-node shell elements were used to discretize the slab with a fully integration scheme (3x3x9); the average element's dimension was 300 x 325 mm. As in 3 dimensions, for the reinforcement embedded truss elements were used and perfect bond was assumed. The dywidag bars were modelled with truss elements. Between the steel beams and the slab 6-node interface elements were inserted. The mesh and the boundary conditions adopted in the finite-element discretization are shown in Figure 8. The same phases and convergence criteria as in the brick elements model were adopted.

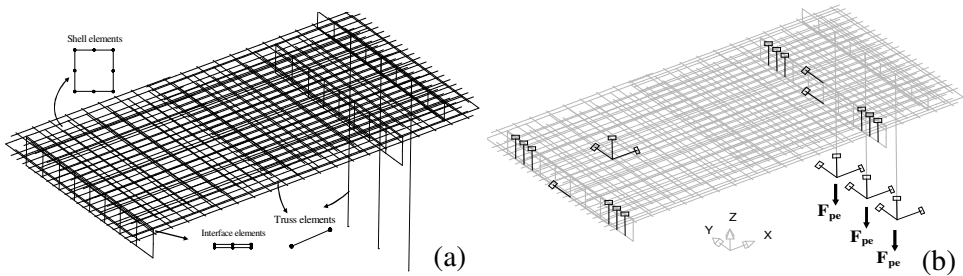


Figure 8- Slab S1T1: (a) mesh adopted; and (b) boundary conditions.

### 3.3 Constitutive models and crack model

To favor applicability, the guidelines provide relatively simple crack models, available in several commercial software packages. Basic crack models, such as those based on total strains with rotating or fixed cracks are adopted in the following (Feenstra et al., 1998).

Similar crack models have been proposed by several authors (Cervenka, 1985; Vecchio and Collins, 1986; Foster et al., 1996; Belletti et al., 2001; Hsu and Mo, 2010).

For concrete a parabolic law in compression based on compressive fracture energy  $G_c$ , and an exponential law in tension based on tensile fracture energy  $G_f$ , were adopted, Figure 9. For the reinforcement and the interface elements, the relationships derived from the experimental tests presented in Figure 2 were adopted in the analyses.

As for crack modelling, see Manie (2009) and Belletti et al. (2011) for details.

The main parameters and phenomena characterizing crack behaviour – like aggregate interlock, diminished compressive strength due to lateral cracking, Poisson effect, fracture energy, etc...were introduced with different values to carry out a parametric study (see Section 5 for details).

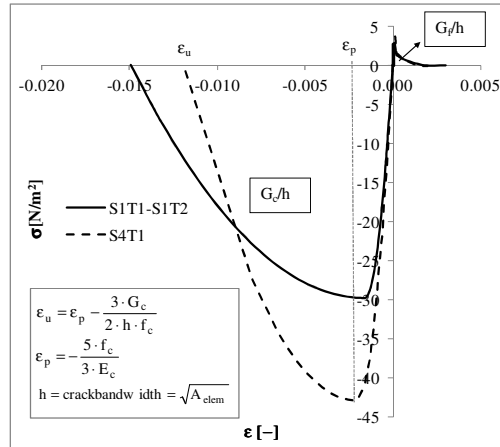


Figure 9- Constitutive model of concrete adopted in the NLFE analyses.

#### 4 EVALUATION OF THE CARRYING CAPACITY OF THE SLABS WITH ANALYTICAL AND NUMERICAL PROCEDURES

For Slab S1T1, the one-way shear resistance and the punching resistance were evaluated by applying Model Code 2010 provisions, and Eurocode 2 provisions/Regan and Rezai-Jorabi's formulation (1988)/Critical Shear-Crack Theory (Muttoni, 2003, 2008), while the bending resistance was worked out via the yield line method.

The results obtained from the analytical calculations were compared with those yielded by NLFE analyses (shell and brick elements), by using the actual properties of the materials.

For Slabs S1T2 and S4T1, the one-way shear resistance was evaluated by applying Model Code 2010 provisions and the punching resistance by applying Eurocode 2 provisions, and Regan and Rezai-Jorabi's formulation (1988). The results yielded by the analytical calculations were compared with those yielded by NLFE analyses (model with brick elements).

Furthermore, since one of the objectives of this paper is to provide general approaches to evaluate the design resistance of reinforced concrete slabs, the design shear resistance of all three slabs was worked out following the calculation methods suggested by Model Code 2010, that are based on four different levels of approximation.

Level I, II and III refer to the evaluation of the design shear resistance by means of analytical calculations, while Level IV provides calculation methods, denoted as *safety format methods*, for the evaluation of the design shear resistance based on the results of NLFE analyses.

Within analytical calculations, R/C slabs are treated as beams without shear reinforcement, for which only Level I and II are provided and the definition of an effective width for the slabs is required.

Within Level IV, in order to evaluate the design shear resistance from the results of NLFE analyses, three different safety format methods are proposed: the Partial Factor Method (PF), the Global Resistance Factor Method (GRF) and the Estimation of Coefficient-of-Variation-of-Resistance Method (ECOV). The peak load values obtained from NLFE analyses are reduced through the different safety format methods in order to calculate the design shear resistance of the slabs.

In Sections 4.1 and 4.2, (a) the calculation of the shear resistance for the three slabs and further details of the Levels of Approximations, and (b) the calculation of the punching resistance of the slabs are reported, respectively; in particular, Subsection 4.2.3 refers to the *Critical Shear Crack Theory* (Muttoni, 2003, 2008), which has been applied only to Slab S1T1. Finally, Section 4.3 is about the calculation of the bending resistance of Slab S1T1.

### 4.1 Shear resistance

The one-way shear capacity of the slabs was evaluated according to Model Code 2010 formulations. In this paper the effective width reported in Figure 10 was assumed in the calculations, as suggested by the experimental observations.

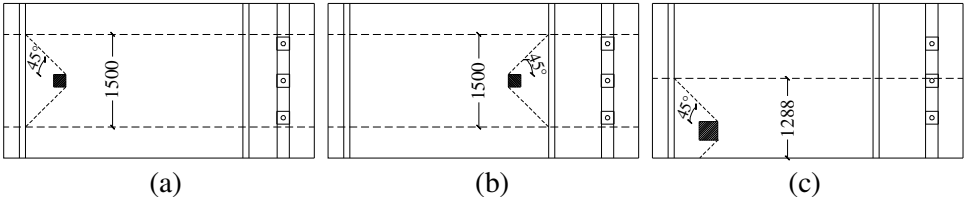


Figure 10- Effective width assumed in Slabs S1T1 (a); S1T2 (b); and S4T1 (c).

As mentioned in Section 4, only level I and II apply to the analytical calculations of the shear resistance of slabs without shear reinforcement. Level I and II were used to calculate both the *shear resistance* and the *design shear resistance*, using the actual mechanical properties and the design mechanical properties of the materials, respectively.

Level IV was adopted to determine the *shear resistance* of the slabs, using the actual mechanical properties of the materials as input data in NLFE analyses, and the *design shear resistance* applying the safety format methods, that properly reduce the results obtained from NLFE analyses.

In Section 4.1.1 the main indications for the evaluation of the design shear resistance with the different levels of approximation are reported.

### 4.1.1 Design shear resistance

#### 4.1.1.1. Levels I and II approximation

As a general rule, level I approximation may be used in the design of a new structure, and level II not only in the design of a new structure, but also in the preliminary assessment of an existing structure. The design shear resistance  $V_{Rd,c}$  of a slab without shear reinforcement is calculated as:

$$V_{Rd,c} = k_v \frac{\sqrt{f_{ck}}}{\gamma_c} z b_{eff} \quad (1)$$

where:

$$\begin{cases} k_{v, \text{Level I}} = \frac{180}{1000 + 1.25z} \\ k_{v, \text{Level II}} = \frac{0.4}{1 + 1500\varepsilon_x} \cdot \frac{1300}{1000 + k_{dg}z} \end{cases} \quad (2)$$

$$\varepsilon_x = \frac{1}{2E_s A_s} \left( \frac{M_{Ed}}{z_1} + V_{Ed} \right) \quad (3)$$

$$k_{dg} = \frac{32}{16 + d_g} \geq 0.75 \quad (4)$$

$\varepsilon_x$  = strain at mid-depth evaluated through an iterative procedure;

$z$  = shear depth taken equal to  $0.9d$ ;

$b_{eff}$  = effective slab width (see Figure 10).

For further details refer to Section 7.3 of the Model Code 2010.

#### 4.1.1.2. Level IV approximation: safety format methods

Level IV approximation may be applied to NLFE analyses to evaluate the carrying capacity. In order to obtain the design shear resistance from NLFE analyses, the Model Code 2010 proposes three different methods based on as many safety formats: the Partial Factor method (PF), the Global-Resistance Factor method (GRF) and the method based on the Estimation of the Coefficient of Variation of resistance (ECOV).

In the PF method, the design mechanical properties of the materials, evaluated according to the Model Code 2010 from the characteristic mechanical properties, are used as input data, so that the shear resistance obtained from the analysis,  $R_d$ , is the design shear resistance:

$$R_d = R(f_d, \dots) \quad (5)$$

where the subscript  $d$  denotes *design mechanical properties*.

In the GRF method, the mean mechanical properties of the materials, evaluated from the characteristic mechanical properties according to the Model Code 2010, are used as input data. The global resistance of the structure,  $R_d$ , is considered as a random variable, so that the effects of the uncertainties are integrated into a global design resistance expressed by a global safety coefficient equal to 1.27:

$$R_d = \frac{R(f_m, \dots)}{\gamma_R \gamma_{Rd}} = \frac{R(f_m, \dots)}{1.2 \cdot 1.06} = \frac{R(f_m, \dots)}{1.27} \quad (6)$$

where the subscript  $m$  denotes *mean mechanical properties*.

In the ECOV method, two analyses should be carried out, the first with the mean values and the second with the characteristic values of the mechanical properties of the materials. A lognormal distribution of the resistance is assumed; the coefficient of variation of the resistance is derived from the two calculated resistances:

$$R_m = R(f_m, \dots), R_k = R(f_k, \dots) \quad (7)$$

$$R_d = \frac{R_m}{\gamma_R \gamma_{Rd}} \quad (8)$$

$$\begin{aligned} \gamma_R &= \exp(\alpha_R \beta V_R) \\ &= \exp\left(0.8 \cdot 3.8 \cdot \left[\frac{1}{1.65} \ln(R_m/R_k)\right]\right) \end{aligned} \quad (9)$$

where the subscript  $k$  denotes *characteristic mechanical properties*.

For further details refer to Section 7.11 of the Model Code 2010.

## 4.2 Punching resistance

The calculations reported in Sections 4.2.1, 4.2.2 and 4.2.3 refer to the actual (i.e., measured) mechanical properties and to a safety material coefficient equal to 1.

### 4.2.1 Eurocode2 formulation

In Eq. 10 the punching resistance calculated according to Eurocode 2 prescriptions is as follows:

$$V_{Rdc} = v_{Rdc} \cdot u \cdot d_{eff} \quad (10)$$

where:

$$v_{Rdc} = C_{Rd,c} k (100 \cdot \rho \cdot f_{ck})^{1/3}; \quad C_{Rd,c} = 0.18; \quad k = 1 + \sqrt{\frac{200}{d_{eff}}}; \quad \rho = \sqrt{\rho_l \cdot \rho_t};$$

$$u = 2 \cdot a + 2 \cdot b + 4\pi d_{eff}$$

where  $a$  and  $b$  denote the loading plate size (see Figure 3). The resulting perimeter  $u$  is indicated in Figure 11.

#### 4.2.2 Regan's formulation

The punching resistance calculated according to Regan's formulation is:

$$P_R = P_{R1} + P_{R2} \quad (11)$$

where  $P_{R2}$  refers to the perimeter side parallel and next to the support ( $u_2$ ), and  $P_{R1}$  to the remaining part of the perimeter ( $u_1$ ), Figure 11.

$$P_{R1} = \xi_{sl} \cdot v_{cl} \cdot u_2 \cdot d_1 + 2 \cdot \xi_{st} \cdot v_{ct} \cdot u_1 \cdot d_t \quad (12)$$

$$P_{R2} = \frac{2d_1}{a_v} \cdot \xi_{sl} \cdot v_{cl} \cdot u_2 \cdot d_1 \quad (13)$$

where:

$$\xi_{sl} = \sqrt[4]{\frac{500}{d_1}} ; \xi_{st} = \sqrt[4]{\frac{500}{d_t}} ; v_{cl} = 0.27 \cdot \sqrt[3]{100\rho_l f_{ck}} ; v_{ct} = 0.27 \cdot \sqrt[3]{100\rho_t f_{ck}} ;$$

$a_v$  = the distance from the support to the point of application of the load

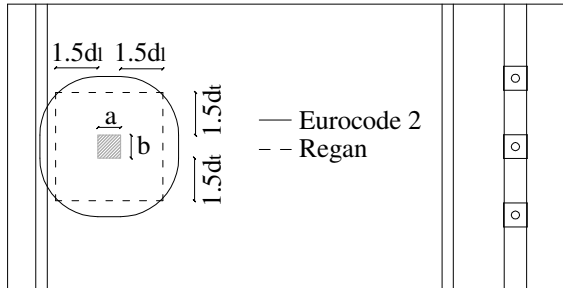


Figure 11- Control perimeter according to Eurocode 2 and Regan's formulations for Slab S1T1.

#### 4.2.3 Critical Shear Crack Theory (CSCT) applied to S1T1

The punching resistance was calculated by applying the Critical Shear Crack Theory - CSCT (Muttoni, 2003, 2008). According to this approach the rotation  $\theta$  of the slab is chosen as the control parameter, since it has been found that the opening of the critical shear crack reduces the strength of the inclined concrete compression strut that carries the shear and eventually leads to the punching shear failure, Figure 12. The shear that can be transferred across the critical shear crack depends on the roughness of the crack (Bažant and Gambarova, 1980; Walraven, 1981).



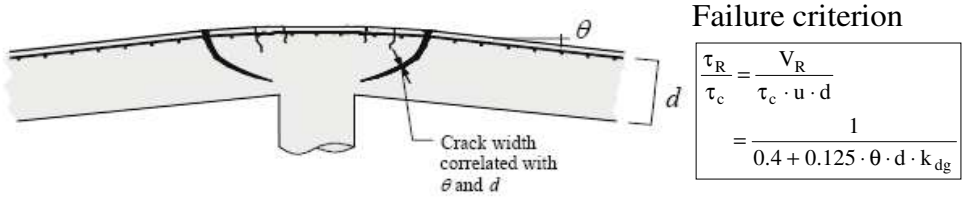


Figure 12- Relationship between the rotation  $\theta$  and the width of the critical crack (Muttoni, 2008) and failure criterion.

The CSCT was applied to Slab S1T1 using a shell model. Details of the shell model can be found in Section 3.2. The main difference with the model explained in Section 3.2 are listed below.

The steel profiles used as supports were not modeled and fixed boundary conditions were applied, Figure 13. The effect of post-tensioning applied to Dywidag bars was introduced by enforcing fixed boundary conditions in correspondence of support 2 (see Figure 3; in such a way, all possible displacements and rotations along the  $y$  axis are prevented).

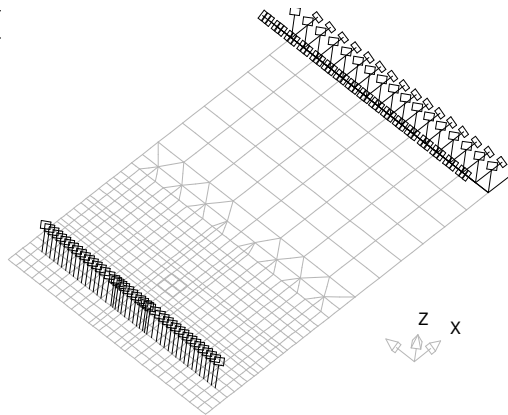


Figure 13 – Critical Shear Crack Theory: boundary conditions of the shell model.

In correspondence of the support 1, fixed boundary conditions preventing the translation along the  $z$  axis were enforced. In the nodes subjected to positive reaction forces, the boundary conditions were omitted to allow the free slab uplift. Both the dead load and the post-tensioning effects were neglected in this analysis.

The main calculation steps followed in the application of CSCT to Slab S1T1 are the following:

- a linear elastic (LE) finite-element analysis to determine the maximum shear force  $v_{\max,el}$  and the control perimeter  $u$ ;
- a NLFE analysis to determine the rotation  $\theta$ ;
- determination of failure load from the intersection point between the curve obtained from NLFE analysis and the failure criterion.

In Figure 14 the distribution of the principal shear stress ( $v_{,el}$ ), obtained from the LE analysis, is plotted.

The principal shear stresses were calculated along the perimeter  $p$ , measured at a distance  $d/2$  from the edge of the loaded surface. The maximum principal shear stress is equal to  $0.00295 \text{ N/mm}^2$ . The effective depth  $d$  and the maximum shear force  $v_{\max,el}$  are:

$$d = \sqrt{d_x \cdot d_y} = 257 \text{ mm} \quad \text{and} \quad v_{\max,el} = 0.00295 \cdot 257 = 0.758 \text{ N/mm}$$

The LE analysis was carried out by applying a pressure to the loading steel-plate equivalent to a resultant force of 1 kN, so the control perimeter  $u$  is equal to:

$$u = \frac{Q}{v_{\max,el}} = \frac{1000}{0.758} = 1.32 \text{ m}$$

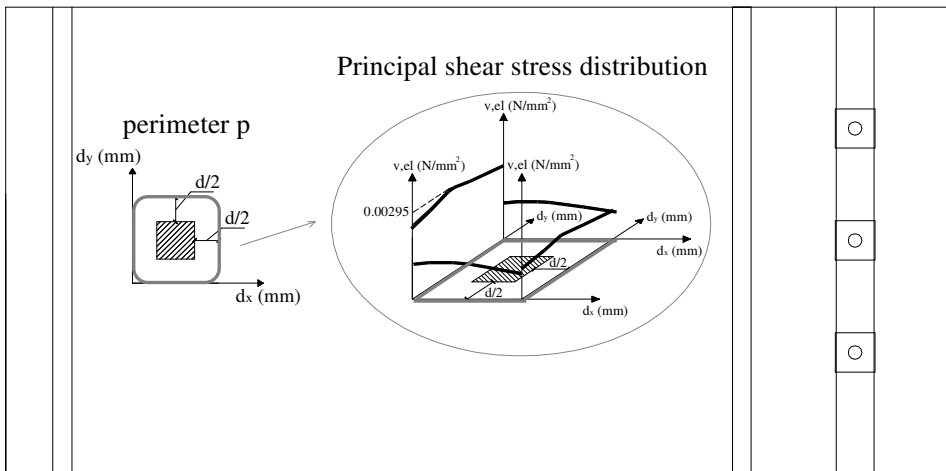


Figure 14- Principal shear stress distribution along the perimeter  $p$ .

A NLFE analysis was carried out to determine the  $(\tau/\tau_c-\theta)$  relationship. In case of slabs subjected to concentrated loads, the rotation  $\theta$  is considered as the difference between the rotations of the slab at two points. The first point (Point 1 in Figure 15) is located at the centroid of the applied load, the second point (Point 2 in Figure 15) is chosen so that the maximum relative rotation is obtained. The

rotation is calculated along the longitudinal symmetry axis of the slab for a load  $P$  of 500, 750 and 1000 kN.

Figure 15 shows that the point where the relative rotation is maximum is not the same for each load step. It has been arbitrarily chosen to evaluate the point with maximum relative rotation at a load equal to  $P = 750$  kN.

In Figure 16 the failure load determined from the intersection between the results of NLFE analysis and the failure criterion is indicated.

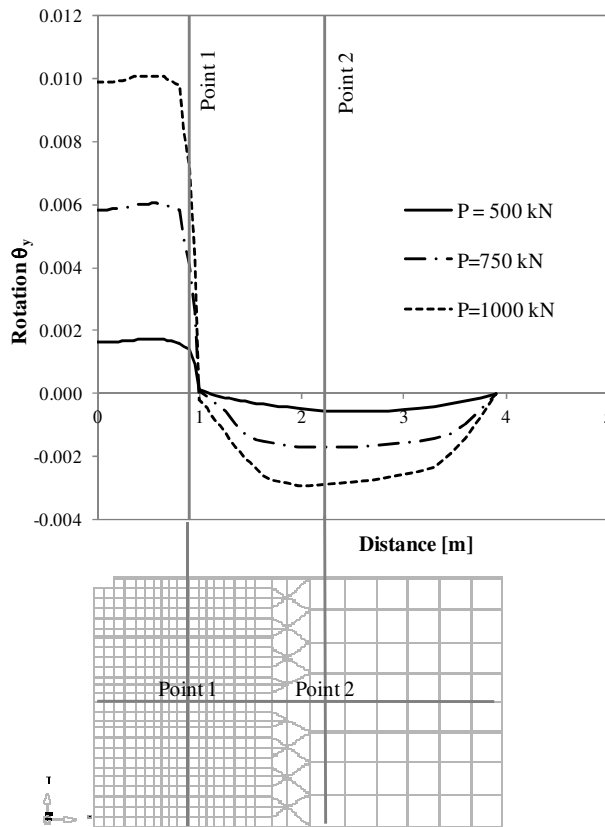


Figure 15- Determination of the rotation  $\theta$  .

### 4.3 Bending resistance of S1T1

The bending resistance of Slab S1T1 was evaluated by applying the yield line method on possible collapse mechanisms identified on the basis of the supports and loading point positions. The calculations reported in the following refer to the actual mechanical properties of the materials and to a safety coefficient equal to 1.

The yield line method is an efficient tool that can give useful information on the structural behaviour of reinforced-concrete slabs. As well known, the yield line

method makes it possible to obtain upper bound solutions through the application of the Virtual Work theorem, written for a set of possible yield-line patterns.

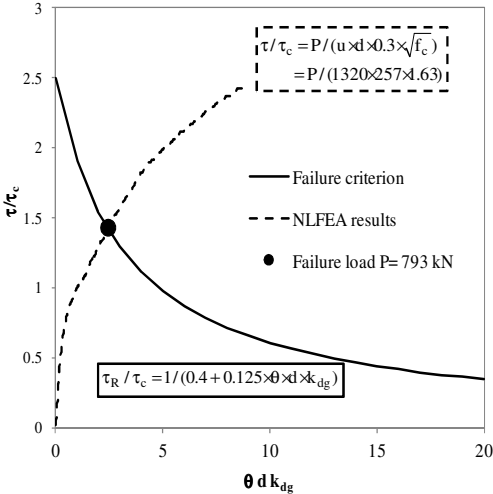


Figure 16- Failure load.

The results depend on the adopted collapse mechanism and - according to the kinematic theorem of limit analysis – among the kinematically-admissible mechanisms the *critical* (i.e., *most probable*) collapse mechanism is the one that provides the lowest ultimate load.

It is therefore mandatory to analyze several possible collapse mechanisms in order to determine the critical one.

In Figure 17 three collapse mechanisms for the determination of the bending resistance of Slab S1T1 slab are presented. For the boundary conditions of the slab refer to Figure 3.

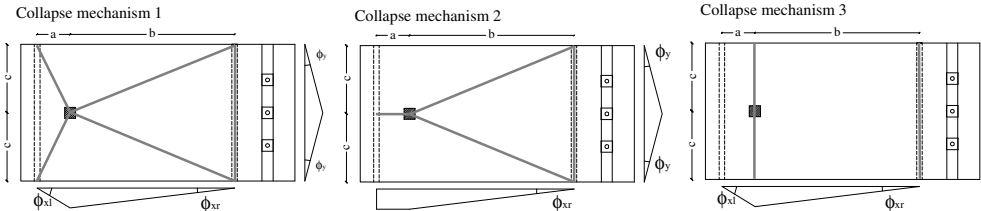


Figure 17 – Slab S1T1: collapse mechanisms considered for the determination of the bending resistance through the yield line method.

The rotations plotted in Figure 17 are equal to:

$$\phi_{xl} = \frac{\delta}{a}; \phi_{xr} = \frac{\delta}{b}; \phi_y = \frac{\delta}{c}$$

The longitudinal and transversal bending resisting moment (respectively  $m_x$  and  $m_y$ ) have been determined in a simplified way as:

$$m_x^+ = m_x^- = A_{sl} \times f_y \times 0.9 \times d_1 = 337.79 \text{ kNm / m}$$

$$m_y = A_{st} \times f_{yt} \times 0.9 \times d_t = 39.54 \text{ kNm / m}$$

For the geometric and mechanical details refer to Figure 3 and Table 1.

In Eqs. 14-16 the Virtual Work equation is written for the three collapse mechanisms analyzed in order to determine the bending resistance  $P_c$ :

Collapse mechanism 1:

$$\begin{aligned} L_{Vi} &= m_x^+ \times 2c \times \phi_{xl} + m_x^+ \times 2c \times \phi_{xr} + m_x^- \times 2c \times \phi_{xr} + 2m_y \times a \times \phi_y + 2m_y \times b \times \phi_y \\ &= L_{ve} = P_{c1} \delta \end{aligned} \quad (14)$$

Collapse mechanism 2:

$$\begin{aligned} L_{Vi} &= m_x^+ \times 2c \times \phi_{xr} + m_x^- \times 2c \times \phi_{xr} + 2m_y \times a \times \phi_y + 2m_y \times b \times \phi_y \\ &= L_{ve} = P_{c2} \delta \end{aligned} \quad (15)$$

Collapse mechanism 3:

$$\begin{aligned} L_{Vi} &= m_x^+ \times 2c \times \phi_{xl} + m_x^+ \times 2c \times \phi_{xr} + m_x^- \times 2c \times \phi_{xr} \\ &= L_{ve} = P_{c3} \delta \end{aligned} \quad (16)$$

By substituting the variables in eqs.(14)-(16) it results:

$$P_{c1} = 2198.22 \text{ kN}; P_{c2} = 790.74 \text{ kN}; P_{c3} = 1970.47 \text{ kN} \quad (17)$$

The critical collapse mechanism is the mechanism 2, whose yield-pattern is in good agreement with the crack pattern observed in the test (see Figure 4).

## 5 RESULTS AND DISCUSSION

In Table 2 the ultimate load of the slabs, obtained from the analytical calculations, NLFE analyses and experimental tests are summarized. Table 2 shows that the lowest resistance obtained from analytical calculations is - for all slabs - the one-way shear resistance according to the Model Code 2010.

In Figure 18 the load-deflection curves of Slab S1T1 obtained from NLFE analyses with shell and brick elements are compared with the experimental load-deflection curve and with the analytical resistance values. In Figure 18,

reinforcement yielding and concrete crushing are indicated on the load-deflection curves.

In Figure 19 the crack pattern of Slab S1T1 is shown, according to the shell discretization and to the brick discretization (load close to 880 KN).

Regarding NLFE analyses, Figure 18 shows that - as expected - shell elements are unable to properly describe the shear failure of the slab and substantially overestimates the capacity of the slab.

On the contrary, the carrying capacity of the slab was well predicted by brick elements, with a difference of about 5% between the values of the ultimate loads evaluated numerically and experimentally. A sizeable difference, however, was detected in the maximum deflection, probably because of the substantial role played in the analysis by both the interface properties and boundary conditions. (As it is well known, in testing too the boundary conditions of R/C slabs can markedly influence the results).

Table 2- Ultimate load of the Slabs S1T1, S1T2 and S4T1 obtained with the actual mechanical properties of the materials.

Exp	Analytical calculations							NLFE analyses	
	One-way shear*		Punching			Bending	Shell model	Brick model	
	Level I	Level II	Regan	EC2	C SCT	Yield line			
	[kN]	[kN]	[kN]	[kN]	[kN]	[kN]	[kN]	[kN]	
S1T1	954.0	307.3	536.5	708.2	698.1	793	790.7	1811.8	906.1
S1T2	1023.0	242.4	734.1	708.2	698.1	-	-	-	1020.1
S4T1	1160.0	344.6	559.4	769	952.6	-	-	-	883.1

\* The ultimate loads were evaluated from the shear resistances according to the static scheme shown in Figure 3.

As mentioned in Sections 1 and 3.3, the results obtained from NLFE analyses strongly depend on the modelling choices. Appropriate checks should be therefore performed in order to make the results reliable. For this reason a parametric study was carried out on the model with brick elements by varying the most significant parameters of the crack model.

The main parameters of the crack models used in the parametric study are briefly described in the following and the parameter combinations are summarized in Table 3:

- $\nu$  denotes the Poisson's ratio, whose role was investigated by adopting a constant value ( $= 0.15$ ) and by adopting a linearly-decreasing function, from the initial value ( $= 0.15$ ) in the elastic phase to zero in the cracked phase.

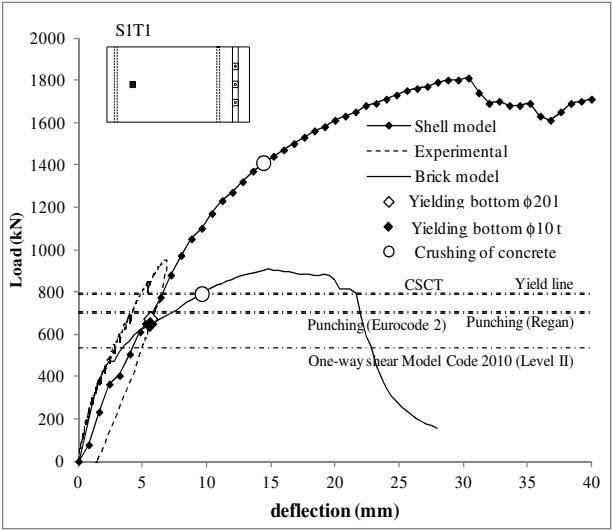


Figure 18- Load-deflection curves of Slab SIT1.

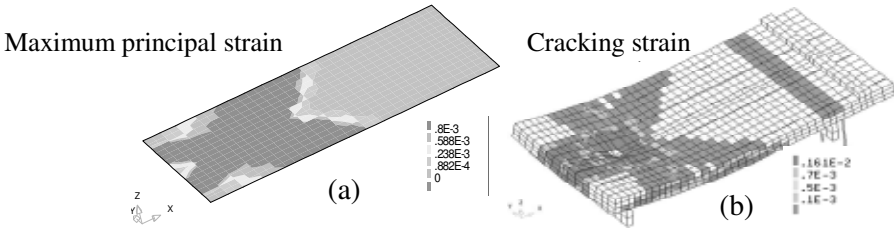


Figure 19- Slab SIT1: crack pattern at 880 kN: (a) shell and (b) brick elements.

- $f_{c,red}/f_c$  denotes the limit to the reduction of the compressive strength due to lateral cracking; in DIANA the reduction trend of the compressive strength due to lateral cracking follows the Model B of Vecchio and Collins (1986), thus the compressive strength is reduced due to lateral cracking, while the peak strain remains the same, Figure 20; the maximum reduction of the compressive strength was set equal to 40% ( $f_{c,red}/f_c = 0.6$ ) or neglected ( $f_{c,red}/f_c = 1$ ).
- $G_f$  denotes the fracture energy in tension; in the analyses the value of  $G_f$  is calculated according to the new fib Model Code 2010 ( $G_f = 73 f_c^{0.18}$ ).
- $G_c$  denotes the fracture energy in compression; the value of  $250 \cdot G_f$ , suggested by Nakamura and Higai. (2001), and a lower value equal to  $120 \cdot G_f$  were adopted in the analyses.

- $\beta$  denotes the shear-retention factor value; in the Analyses A-D and E,F the rotating-crack model and the fixed-crack model were used, respectively; in the latter case, the crack model implemented in DIANA was adopted (shear-retention factor linearly variable from 1.0 in the elastic phase to 0.0 according to the decreasing Young's modulus).

Table 3- Parametric study.

	$\nu$	$f_{c,red}/f_c$	$G_f$	$G_c$	crack model	$\beta$
Analysis A	0.15	1	MC2010	$250G_{fMC2010}$	rotating	/
Analysis B	variable	1	MC2010	$250G_{fMC2010}$	rotating	/
Analysis C	variable	0.6	MC2010	$250G_{fMC2010}$	rotating	/
Analysis D	variable	0.6	MC2010	$120G_{fMC2010}$	Rotating	/
Analysis E	variable	0.6	MC2010	$250G_{fMC2010}$	Fixed	variable
Analysis F	variable	0.6	MC2010	$120G_{fMC2010}$	Fixed	variable

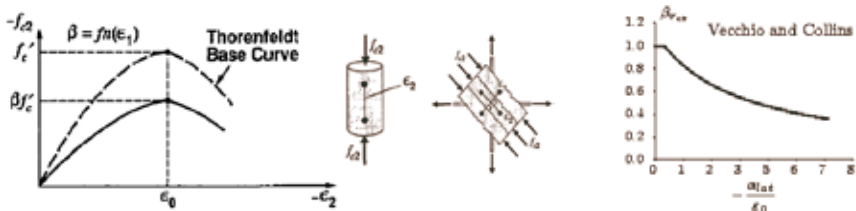


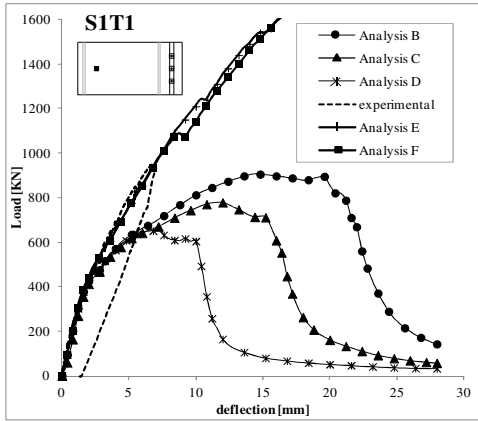
Figure 20- Reduction of the compressive strength due to lateral cracking according to Model B by Vecchio and Collins (1986).

In Figure 21 the load-deflection curves yielded by the parametric study are plotted for all slabs, as well as the cracking strain, at the ultimate load. Analysis B leads to the best fitting of the test results for all slabs. (As a matter of fact, in Figure 18 the load-deflection curve obtained with the brick model refers to Analysis B). Hence, the parameters used in Analysis B can be considered reasonable and rather realistic. (Note the large scatter in the numerical results ensuing from the different values given to the parameters of the crack model, Figure 21; the variation in the peak load reaches 46%).

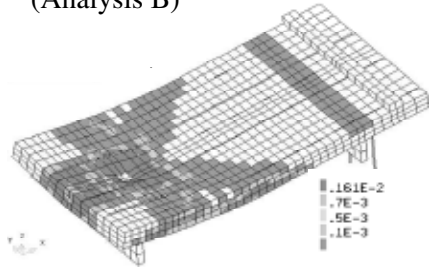
As regards the fixed crack model, should the aggregate-interlock effect be incorrectly introduced (especially in shear-critical specimens), the results would be rather unrealistic. Refined models of aggregate interlock can be found in the literature (Bažant and Gambarova, 1980; Walraven, 1981).

As mentioned in Section 4.1, the provisions of the Model Code 2010 for the determination of the design shear resistance were systematically applied to all slabs. Hence the parametric study carried out (Table 3 and Figure 21) was used to choose a reference analysis for the application of the safety format methods. The reference analysis chosen is - in all cases - Analysis B.

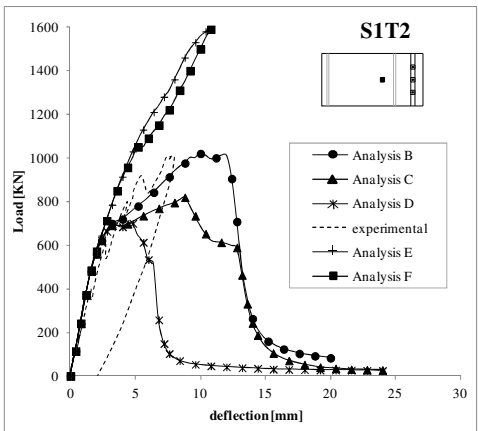




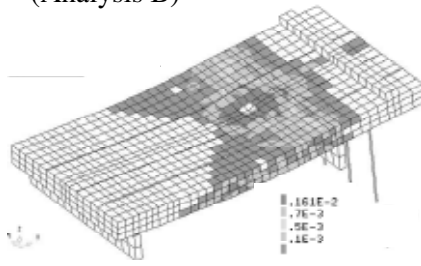
Crack pattern at failure (Analysis B)



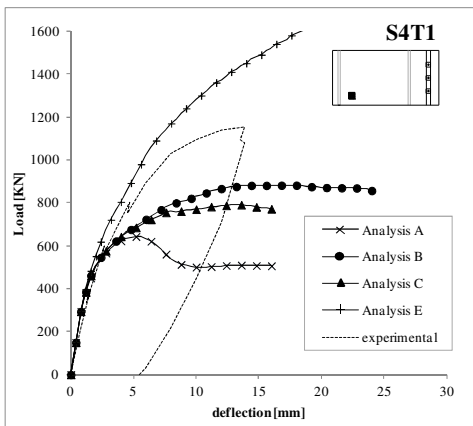
(a)



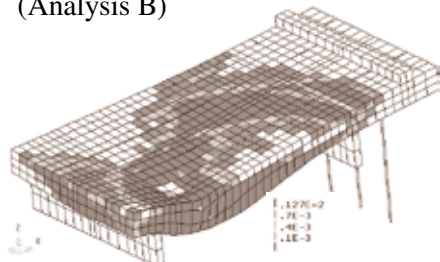
Crack pattern at failure (Analysis B)



(b)



Crack pattern at failure (Analysis B)



(c)

Figure 21- Load-deflection curves and crack pattern at failure obtained in the parametric study for Slabs S1T1 (a), S1T2 (b), and S4T1 (c).

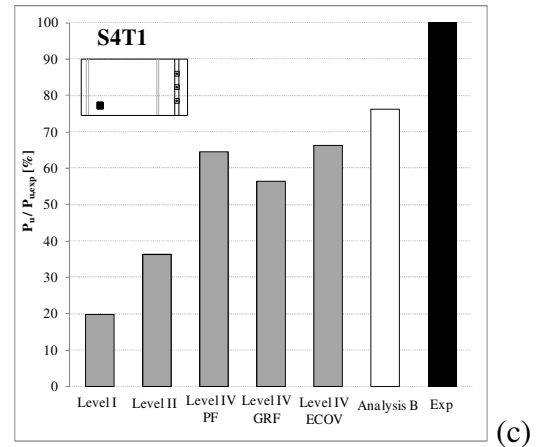
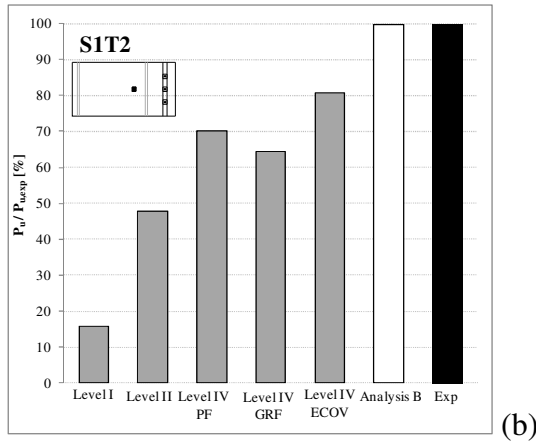
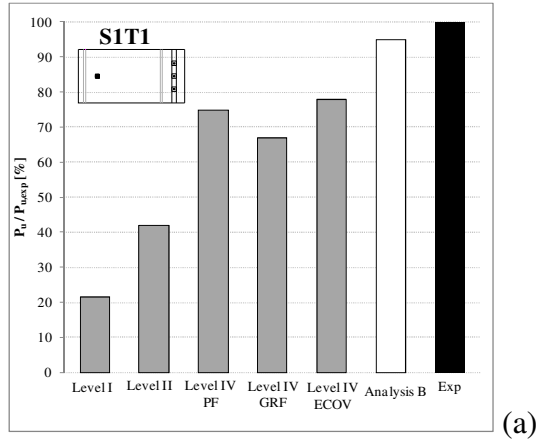


Figure 22 – Slabs S1T1 (a), S1T2 (b), and S4T1 (c): normalized values of the ultimate design load obtained analytically (Level I-II) and numerically (Level IV); the normalizing factor is the experimental value  $P_{u,exp}$ .

Figure 22 shows that the trend of the results obtained with safety format methods well fits the new Model Code 2010 philosophy: by increasing the level of approximation the design load value increases. Level II provides a higher design load value than level I, and level IV provides higher design load values than level I and II. Among the three safety format methods, ECOV method gave in all cases the highest design ultimate loads. A significant increase of the design load, ranging from +69% to +87%, can be observed from level II to level IV. This makes it clear that - once finite-element modeling has been validated - NLFE analysis can take care of the *hidden* resources of the structure, in terms of *extra capacity*.

The design ultimate load,  $P_u$ , obtained with the different levels of approximation are plotted in Figure 22 as a percentage of the experimental ultimate load,  $P_{u,exp}$  (grey bars). The ratio  $P_u/P_{u,exp}$  of the reference analysis (Analysis B), carried out without applying any safety coefficient, is indicated as a white bar and the experimental ultimate load value (which represents 100% in the comparison) is shown in black.

## 6 CONCLUSIONS

In the paper the behaviour of reinforced concrete slabs was investigated. Three slabs subjected to concentrated loads close to their supports were analyzed. The carrying capacity of each slab was determined with NLFE analyses and with analytical procedures, according to current code provisions and calculation methods available in literature. The results obtained were compared with the experimental results provided by Delft University of Technology. The Model Code 2010 was systematically applied for the evaluation of the design shear resistance in the three case studies.

The main conclusions of the research are:

- For all slabs, the lowest resistance values calculated with analytical procedures were the one-way shear resistance, evaluated according to the Model Code 2010; hence, the most critical failure detected analytically is in accordance with the experimental observations; however, Slabs S1T1 and S1T2 also showed a fully-developed flexural cracking pattern at failure during experiments.
- For Slab S1T1, the critical collapse mechanism calculated with the yield-line method was in agreement with the crack pattern observed experimentally at failure.
- The results yielded by NLFE analysis strongly depend on the modeling choices, e.g. shell model or brick model; as expected, shell elements gave unrealistic results and led to substantial overestimations of the punching resistance of Slab S1T1.

- On the contrary, the same shell elements, which are simpler and less computationally onerous than brick elements, gave consistent results in the evaluation of the punching resistance of Slab S1T1, if the Critical Shear Crack Theory is used.
- Within NLFE analyses, even with a more refined and realistic brick model, the results can strongly depend on the modeling choices made by the analyst, especially with regards to relatively simple crack models; as a matter of fact, in the cases analyzed in this paper, some aspects of the adopted crack model (like the formulation of the shear retention factor, the value of the fracture energy in compression and the reduction of the compressive strength due to lateral cracking) markedly affected the structural response of the slabs investigated in this study.
- For these reasons, the availability of guidelines (like those published by the Dutch Ministry of Infrastructure and Environment) on how to properly perform NLFE analyses is definitely a great help for the analysts.
- In the paper, the main indications provided by the Dutch guidelines for nonlinear finite-element analyses were followed. The analyst, however, should be able to critically validate the input data and the output results based on his/her familiarity with both physical phenomena and numerical modeling.
- Model Code 2010's provisions were adopted in the evaluation of the design shear resistance of R/C slabs. The numerical results adhere well to Model Code 2010's philosophy: the higher the approximation level, the greater the punching resistance of the slab. Level IV provides substantially higher values for the punching resistance than the analytical calculations (Level I and Level II).
- For such reasons, once finite-element modeling has been properly validated, the structural assessment carried out by means of multiple approximation levels can be of great benefit in any intervention on existing structures (e.g. maintenance, repair, demolition etc.).

## ACKNOWLEDGMENTS

The authors acknowledge the financial support provided by the Dutch Ministry of Infrastructure and the Environment, which was instrumental in guaranteeing the success of this research project.

## REFERENCES

- Baskaran K. and Morley C.T. (2004). "A New Approach to Testing Reinforced Concrete Flat Slabs". *Magazine of Concrete Research*, Vol.56, No.6, pp. 367-374.
- Bažant Z.P. and Gambarova P.G. (1980). "Rough Cracks in Reinforced Concrete". *Journal of the Structural Division*. ASCE, Vol.106, No.4, pp. 819-842.

- Belletti B., Cerioni R. and Iori I. (2001). "A Physical Approach for Reinforced Concrete (PARC) Membrane Elements". *J. Structural Engineering.*, Vol. 127, No.12, pp. 1412-1426.
- Belletti, B., Damoni, C. and Hendriks, M.A.N. (2011). "Development of Guidelines for Nonlinear Finite Element Analyses of Existing Reinforced and Prestressed Beams". *European J. of Environmental and Civil Engineering*, Vol.15, No.9, pp. 1361-1384.
- Cervenka V. (1985). "Constitutive Model for Cracked Reinforced Concrete". *ACI Structural Journal*, Vol.82, No.6, pp. 877-882.
- Chen W.F. (1982). *Plasticity in Reinforced Concrete*. McGraw Hill.
- EN 1992-1-1:2004. *Design of concrete structures-Part 1-1: General rules and rules for buildings*.
- Feenstra P.H., Rots J.G., Arnesen A., Teigen J.G. and Høiseith K.V. (1998). "A 3D Constitutive Model for Concrete Based on a Co-rotational Concept". *Computational Modeling of Concrete Structures*, ed. by De Borst, Bicanic, Mang & Meschke, Rotterdam (The Netherland), pp. 13-22.
- Foster S.J., Budiono B. and Gilbert R.I. (1996). "Rotating Crack Finite Element Model for Reinforced Concrete Structures". *Computers & Structures*, Vol.58, No.1, pp. 43-50.
- Foster S.J., Bailey C.G., Burgess I.W. and Plank R.J. (2004). "Experimental Behaviour of Concrete Floor Slabs at Large Displacements". *Engineering Structures*, Vol. 26, pp. 1231-1247
- Furuuchi H., Takahashi Y., Ueda T. and Kakuta Y. (1998). "Effective Width for Shear Failure of RC Deep Slabs," *Trans. of Japan Concrete Institute*, Vol. 20, pp. 209-216.
- Gambarova P.G., Coronelli D. and Bamonte P. (2008). *Guidelines for R/C Slab Design (in Italian)*. Patron Editore, Bologna (Italy), 118 pp.
- Graf O. (1933). "Tests on the Strength of R/C Slabs Subjected to a Concentrated Load Applied Close to a Support" (in German: "Versuche über die Widerstandsfähigkeit von Eisenbetonplatten unter konzentrierter Last nahe einem Auflager"). *Deutscher Ausschuss für Eisenbeton*, Vol.73, Berlin (Germany), pp. 10-16.
- Hillerborg A. (1996). *Strip Method Design Handbook*. Ed by E&FN Spon, London (UK), 295 pp.
- Hsu T.T.C. and Mo Y.L. (2010). *Unified Theory of Concrete Structures*. Ed. by John Wiley & Sons, Chichester (UK), 489 pp.
- Hu H.T. and Schnobrich W.C. (1991). "Nonlinear Finite Element Analysis of Reinforced Concrete Plates and Shells under Monotonic Loading". *Computers & Structures*, Vol.38, No.5-6, pp. 637-651.
- Huang Z., Burgess I.W. and Plank R.J. (1999). "Nonlinear Analysis of Reinforced Concrete Slabs Subjected to Fire", *ACI Structural Journal*, Vol.96, No.1, pp. 127-135.
- Johansen KW. (1962). *Yield-Line Theory*. Cement and Concrete Association, London (UK), 181 pp.
- Kinnunen S. and Nylander, H. (1960). "Punching of Concrete Slabs without Shear Reinforcement". *Transactions of the Royal Institute of Technology*, No. 158, Stockholm (Sweden), 112 pp.

- Lantsoght E. (2012). *Shear Tests of Reinforced Concrete Slabs - Experimental Data of Undamaged Slabs*. Technical Report 06-01-2012, Stevin laboratory, Delft University of Technology, Delft (The Netherlands), 504 pp.
- Lantsoght E., van der Veen C. and Walraven J.C. (2013). "Shear in One-Way Slabs under Concentrated Load Close to Support", *ACI Structural Journal*, V. 110, No. 2, pp. 275-284.
- Manie, J. 2009. *DIANA User's Manual*. TNO DIANA BV.
- Model Code MC2010-ceb-fip bulletin d'information 65&66 - Final Draft. (2012). International Federation for Structural Concrete (fib), Lausanne, Switzerland.
- Muttoni A. (2003). "Shear Strength and Punching of Concrete Slabs Devoid of Transverse Reinforcement" (in German: "Schubfestigkeit und Durchstanzen von Platten ohne Querkarftbewehrung"), *Beton- und Stahlbetonbau*, Vol. 98, No 2, pp. 74-84.
- Muttoni A. (2008) "Punching Shear Strength of Reinforced Concrete Slabs without Transverse Reinforcement," *ACI Structural Journal*, V. 105, No. 4, pp. 440-450.
- Nakamura H. and Higai T. (2001). "Compressive Fracture Energy and Fracture Zone Length of Concrete". *Modeling of Inelastic Behavior of RC Structures under Seismic Loads*, ed. by P. B. Shing and T.Tanabe, ASCE, pp. 471-487.
- Park R. and Gamble W.L. (2000). *Reinforced Concrete Slabs*. Ed by John Wiley & Sons, 716 pp.
- Regan P.E. (1982). *Shear Resistance of Concrete Slabs at Concentrated Loads close to Supports*. Engineering Structures Research Group, Polytechnic of Central London, London, United Kingdom.
- Regan P.E. and Rezai-Jorabi H. (1988). "Shear Resistance of One-Way Slabs under Concentrated Loads". *ACI Structural Journal*, Vol.85, No.2, pp. 150-157.
- Rots J., Belletti B., Damoni C. and Hendriks M.A.N. (2010). "Development of Dutch Guidelines for Nonlinear Finite Element Analyses of Shear Critical Bridge and Viaduct Beams", *fib Bulletin 57: Shear and Punching Shear in RC and FRC Elements*, pp. 139-154.
- RTD (2012). *Guidelines for Non-linear Finite Element Analyses of Concrete Structures*. Rijkswaterstaat Technisch Document (RTD), Rijkswaterstaat Centre for Infrastructure, RTD:1016:2012, 65 pp.
- Vecchio F.J. and Collins M.P. (1986). "The Modified Compression-Field Theory for Reinforced Concrete Elements Subjected to Shear", *ACI Structural Journal*, Vol.83, No.2, pp. 219-231.
- Vidosa F.G., Kotsovos M.D. and Pavlovic M.N. (1988). "Symmetrical Punching of Reinforced Concrete Slabs: An Analytical Investigation Based on Nonlinear Finite Element Modeling", *ACI Structural Journal*, Vol.85, No.3, pp. 241-250.
- Walraven J.C. (1981). "Fundamental Analysis of Aggregate Interlock". *Journal of Structural Engineering*, Vol.107, No.11, pp 2245-2270.

## MODELLING OF LARGE LIGHTLY-REINFORCED CONCRETE WALLS

Marisa Pecce<sup>1</sup>, Fabio A. Bibbò<sup>2</sup>, Francesca Ceroni<sup>3</sup>

### ABSTRACT

The performance of reinforced-concrete (R/C) shear walls subjected to seismic action depends on the structural type, as shear walls can be *ductile* or *lightly-reinforced*, the latter being frequently characterized by large size.

In this paper, the two classes are examined with reference to their differences, mainly consisting in the details of the reinforcement, that is more elaborate in ductile walls to improve their ductility.

Large lightly-reinforced walls were commonly designed and built in the past, but new motivations are arising today for their use in a variety of buildings, for instance whenever strict requirements concerning the thermal insulation of the façades are to be met. Furthermore, new types of integrated formworks including insulating materials (such as polystyrene) are used for casting concrete, and to obtain at the same time structural and functional efficiency.

R/C walls characterized by uniformly-distributed reinforcement with low steel ratios and without any specific detailing of the bars to improve their ductility are the subject of this research project, which considers also some test results available in the literature. The focus is on shear-walls nonlinear and cyclic behaviour, that plays a leading role in the seismic performance of any structural system. A nonlinear model based on the Finite Element method is developed, by using two codes (SAP2000 and DIANA TNO 9.4), in order to make comparisons with the experimental results.

Finally, a simplified approach is proposed to evaluate the flexural capacity of uniformly-reinforced walls. The procedure allows to calculate the M-N domains of the wall cross-section at the Ultimate Limit State, by replacing the longitudinal bars distributed along the front and back faces with equivalent steel layers, with no need to introduce the geometry and position of each single bar in the system of equations.

**KEYWORDS:** shear walls, R/C ductility, reinforcement details, cyclic loads, nonlinear analysis.

---

<sup>1</sup> Professor, <sup>2</sup> Ph.D Student, <sup>3</sup> Assistant Professor, DING – Department of Engineering, University of Sannio, Benevento, Italy.

## 1. INTRODUCTION

The use of R/C walls in seismic areas generally implies the design of strong and stiff buildings, even if the global ductility strongly depends on the ductility of each single wall. However, in a framed building, the global ductility can be improved by adopting statically-redundant structural systems characterized by many dissipative zones and – consequently – by a high potential for stress redistribution.

With reference to seismic performance, R/C walls can be subdivided into two types: ductile walls and (large) lightly-reinforced walls. In particular, the first type of wall consists in cantilever members characterized by specific constructive details for the reinforcement to improve their ductility. The longitudinal reinforcement and the stirrups at the end sections of the wall guarantee a ductile flexural behaviour, especially if the concrete is highly confined. In such cantilever-type members, plastic hinges with a high dissipative capacity tend to form in the critical zones at the foot of the wall. Furthermore, the longitudinal reinforcement prevents sliding-shear failures, that imply brittle mechanisms with low dissipative capacity, especially under cyclic loads.

Moreover, the transverse reinforcement provides shear resistance and should be designed to respect the shear-flexure hierarchy. (An appropriate over-strength in shear must guarantee that the flexural failure be attained first).

The seismic performance of large lightly-reinforced walls is mainly based on the strength brought in by their “large extension” in the building; in this case, the construction details are limited, and the failure mechanism is not ductile. However, in general, rocking at the base occurs, and shear effects are mobilized.

Currently, this type of wall is extensively used in those buildings, that are designed according to innovative technologies, with integrated formworks partly made of insulating materials to improve the overall thermal resistance of the building (CEN EN 15217, 2007; Decree No.192, 2005 and Decree No.311, 2006) and to facilitate the construction. This solution allows a faster erection of the structure, but requires the walls to be extended to the entire perimeter of the building to ensure thermal insulation. However, the typical rather elaborate reinforcement details found in ductile walls cannot be extended to the walls cast inside these innovative formworks, since the only possible reinforcement is a uniformly-distributed reinforcement, in both longitudinal and transverse directions.

In terms of seismic performance, large lightly-reinforced walls are not considered ductile, and the European Code for seismic constructions (EC8, 2003) gives the same definition as the Italian Code (NTC, 2008). Both codes assume a behavioural factor for uncoupled walls in agreement with the provisions for class B ductility, comprised between 1.5 and 3.0 depending on the wall slenderness.

Furthermore, EC8 clarifies that the energy dissipation of large lightly-reinforced walls occurs through rigid-body displacements (i.e., rocking) without the formation of plastic hinges; however, some reinforcement details are



suggested. On the contrary, in the Italian Code (NTC, 2008), no details are provided for lightly-reinforced walls and the same behavioural factor of ductile walls can be assumed.

Summing up, in the case of large lightly-reinforced walls there is still no consensus on the performance to be requested and on design provisions, even more since the experimental results are not exhaustive; moreover, it is not easy to design the longitudinal reinforcement under the requirement of uniform distribution in two directions, as typically happens in bi-dimensional structures.

In this paper, a simplified approach is presented to check or to design the uniform longitudinal reinforcement of a wall, with reference to bending.

The consistency of the proposed approach is continuously enforced. A nonlinear bi-dimensional model is used to describe an experimental test documented in the technical literature, in order to investigate the behaviour of large lightly-reinforced walls under seismic actions.

## **2. EXPERIMENTAL RESULTS DOCUMENTED IN THE LITERATURE**

### **2.1 Performance of lightly-reinforced walls**

Numerous experimental tests on transversely-loaded R/C walls are well documented in the technical literature (Vallenas et al., 1979). Currently, further studies are in progress with particular reference to specimens provided with additional longitudinal reinforcement, as well as with transverse reinforcement at the end sections, to enhance concrete confinement and to have fresh information on the efficacy of the reinforcement details in improving structural ductility.

All these studies have allowed to investigate the behaviour of “ductile” R/C walls and to formulate appropriate design provisions in those case in which the failure in bending is reached under seismic actions. However, some tests on R/C walls with low steel ratios and uniformly-distributed reinforcement (i.e., no elaborate reinforcement details at the end sections) are documented. Hence, some relevant information on the seismic performances of large lightly-reinforced walls is available.

The tests carried out by Orakcal et al. (2009) are well known in this research area, as they were specifically aimed at investigating the behaviour of horizontal (spandrels) and vertical (piers) parts of lightly-reinforced walls placed along the perimeter of a building, such structural solutions being rather common for instance in a number of hospitals built in California in the sixties of the last century. Of the 14 specimens tested in the experimental campaign, 6 represented *piers* and 8 *spandrels*.

The experimental measures made it possible to separate the shear deformation from the flexural deformation. The latter hardly contributed to the overall structural behaviour, as most of the deformation was due to the sliding along the

shear-induced diagonal cracks. The failure was caused by concrete crushing in the central part of the inclined strut.

The Orakcal et al. investigated as well the influence that various parameters have on the shear strength of R/C walls, taking advantage of the experimental tests carried out by other researchers (Hidalgo et al., 2002; Barda et al., 1977; Cardenas et al., 1980): such parameters as steel ratio in the longitudinal direction, number of bar layers (one or two), 90°-hooks at the extremities of the transverse reinforcement, transverse-steel ratio at the end sections and level of the axial load.

The examination of the literature showed that the hooks of the transverse reinforcement at the end sections have no positive effect on the shear strength, while the axial load brings in a reduction in the lateral drift capacity of the walls.

Some experimental results were compared with code predictions on shear strength (FEMA450; ACI318); the formulae provided by the codes turned out to be not always on the safe side for R/C walls loaded in bending in their mean plane, without axial load and with light reinforcement close to the end sections.

In Wallace et al. (2008) new formulae to evaluate the residual strength for vertical loads in shear-damaged R/C walls were introduced on the basis of the experimental results presented by Orakcal et al. (2009); these formulae consider the resistant contributions offered by the sliding mechanisms developed along the interfaces of the inclined shear cracks.

In Kuang and Ho (2008) the behaviour of 8 squat R/C panels (shape ratio  $L/H = 1.0-1.5$ ) with and without special reinforcement details (consisting in stirrups and longitudinal reinforcement, concentrated at the end sections) was investigated. Concrete strength in compression was comprised between 30.4 and 37.7 MPa, and steel strength at yielding was 520 MPa. The shear tests on axially loaded walls showed that the failure occurred with the crushing of the concrete at the end of the wall sections. Furthermore, the results showed distributed stirrups confining the concrete along 15% of the entire depth (at both extremities) increased the ductility by 70% and the energy dissipation by 300%. In contrast, the concentration of the longitudinal reinforcement at the ends of the panels did not improve the ductility. However, the panels with uniform reinforcement and without specific details at the end sections could achieve a ductility of 2.5-3.

The results of the experimental campaign on six R/C walls tested on a shaking table are reported in Carrillo and Alcocer (2012). The variable parameters were the steel type (ordinary and welded wire mesh for both the longitudinal and transverse reinforcement), the steel ratio (100% and 50% of the amount suggested by ACI-318), the concrete mass per unit volume (normal- and light-weight aggregate concrete), and the geometry (with/without openings). The following main observations were made:

- concrete mass per unit volume has hardly any effect;
- steel type has sizeable effects on the ductility, because the welded wire mesh reduces structural ductility, due to the brittle failure of the transverse reinforcement, while ordinary steel leads to shear-flexural failures.

Other authors have analysed the effect that the welded wire mesh has on the nonlinear behaviour of R/C walls because this type of reinforcement can be easily placed in large lightly-reinforced walls.

In particular, Riva and Franchi (2001) carried out an extended experimental campaign on 18 R/C cantilever walls subjected to in-plane cyclic loads and reinforced by means of hot-rolled welded mesh (HR), traditional cold-drawn welded mesh (CD) and ordinary bars. The tests showed that the specimens reinforced with hot-rolled welded meshes exhibited a ductility comparable to that of the specimens reinforced with ordinary reinforcement, while traditional cold-drawn welded meshes proved to be unsuitable for seismic applications. In this case, the use of stirrups close to the end sections can be beneficial to the post-elastic nonlinear behaviour.

## 2.2 Test results considered for the comparison with the numerical predictions

The flexural strength of some specimens tested by Riva and Franchi (2001) was calculated by means of a simple method, and one of the specimens tested by Orakcal et al. (2009) was modelled via nonlinear finite elements.

The characteristics of the specimens tested by Riva and Franchi, used in the numerical analysis are listed in Tables 1 and 2.

The main characteristics of the walls tested by Orakcal et al. (2009) are briefly recalled in the following. The size of the specimens was  $\frac{3}{4}$  that of the walls often used in actual buildings (thickness 152 mm, depth 1370 mm; height

Table 1 - Properties of the specimens tested by Riva and Franchi (2001).

Specimen [dimensions in mm]	Ordinary steel reinforcement	Steel grid Ø12/100	Axial load [kN]
HR12C-1 [1200x150x2500]	No	cold drawn Ø12	600
CD12C-1 [1200x150x2500]	No	hot rolled Ø12	600
HR12C-2 [1200x150x2500]	No	cold drawn Ø12	600
CD12C-2 [1200x150x2500]	No	hot rolled Ø12	600
HR12S [1300x150x2500]	No	cold drawn Ø12	No
HR12U [1300x150x2500]	No	hot rolled Ø12	No
CD12S [1300x150x2500]	No	cold drawn Ø12	No
CD12U [1300x150x2500]	No	hot rolled Ø12	No

Table 2 -Mechanical properties of the materials used by Riva and Franchi (2001).

Specimen	$f_c$ [MPa]	Steel mesh		
		$f_y$ [MPa]	$f_t$ [MPa]	$\epsilon_u$ [%]
HR12C-1	40	552	619	4.0
CD12C-1	40	442	568	8.3
HR12C-2	40	552	619	4.0
CD12C-2	40	442	568	8.3
HR12S	28	522	603	10.0
HR12U	28	522	603	10.0
CD12S	28	632	687	4.6
CD12U	28	632	687	4.6

1220 mm); the materials used in the specimens were commonly-used materials ( $f_c = 30$  MPa and  $f_y = 240$  MPa). Single layers were used for the reinforcement.

The specimens – representing vertical walls - were 6, subdivided into 3 different types (2 identical specimens in each subcase). The 3 types differed in the value of the axial force (= 0, 5% and 10% of the axial capacity  $A_g f_c$ , where  $A_g$  is the gross section). The reinforcement - same in all specimens - consisted of longitudinal bars (1 $\varnothing$ 13/330 mm), that were doubled at the end sections, where transverse bars were added as well (1 $\varnothing$ 13/305 mm, Figure 1).

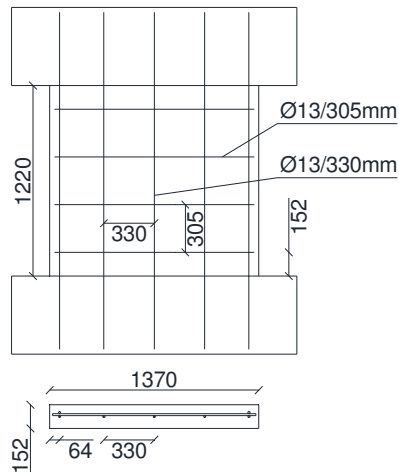


Figure 1 - Steel reinforcement of wall WP-T5-N10-S2 (Orakcal et al., 2009) [mm].

Therefore, the steel ratio of the longitudinal reinforcement was 0.23%, although the local ratio – close to the end sections - was slightly higher. The transverse reinforcement had no hooks.

The tests were displacement controlled; a constant axial load was applied by means of two actuators, that prevented the rotation of the top head of the specimen; the horizontal cyclic loads imposed drift levels equal to 0.2, 0.3, 0.4, 0.6, 0.8, 1.2, 1.6, 2.0 and 2.4%.

### 3. NUMERICAL FITTING OF THE EXPERIMENTAL RESULTS

#### 3.1 Evaluation of the flexural strength of R/C walls

The calculation of the flexural strength of the section under axial loading is particularly demanding in the case of R/C walls, because of the large number of the horizontal bars that have to be included with their lever arm with respect to centroid of the vertical sections. Hence, a simplified approach was adopted for lightly-reinforced walls, which are typically reinforced by means of uniformly-distributed bars along the depth of the cross-section. This approach allows to evaluate the resistant moment at yielding and ultimate moment, both under bending with/without any axial load.

The geometry of the R/C wall with rectangular (vertical) section is shown in Figure 2a:  $B$  = thickness;  $L$  = depth;  $c$  = concrete cover, and  $A_{s,tot}$  = total reinforcement area (distributed close to the front and back faces), i.e. sum of the areas of the bars,  $A_{s,i}$ .

The reinforcement can be lumped into a single *equivalent* rectangular area (Figure 2b), with length  $L'$  and thickness  $\alpha$ , which are calculated as follows:

$$L' = L - 2c \quad \alpha = \frac{\sum_i A_{s,i}}{L - 2 \cdot c} = \frac{A_{s,tot}}{L'} \quad (1)$$

This scheme introduces an error in the evaluation of the contribution of the bars to the flexural strength due to their actual position, and, clearly, the approximation is high and tends to the refined one as the spacing of the bars is reduced.

Any constitutive relationship can be assumed for the materials, but a linear behaviour is considered at the yielding conditions and a rigid-plastic one at the ultimate conditions in the following application.

At the ultimate limit state, the stress block indicated in Figure 3 is adopted to write the equations of equilibrium of the section, as it is done in steel-concrete composite columns (Eurocode 4, 2004). In particular, the steel reinforcement contributes with two stress blocks (Figure 3): an anti-symmetric stress block typical of simple bending in steel sections (the axial resultant is zero, and the flexural capacity or strength is that of the rectangular steel section) and a stress

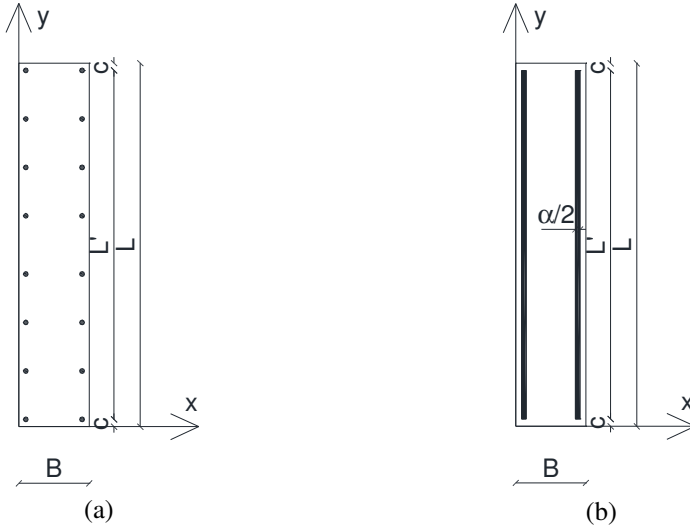


Figure 2 – Actual section (a); and equivalent section with uniformly-distributed reinforcement (b).

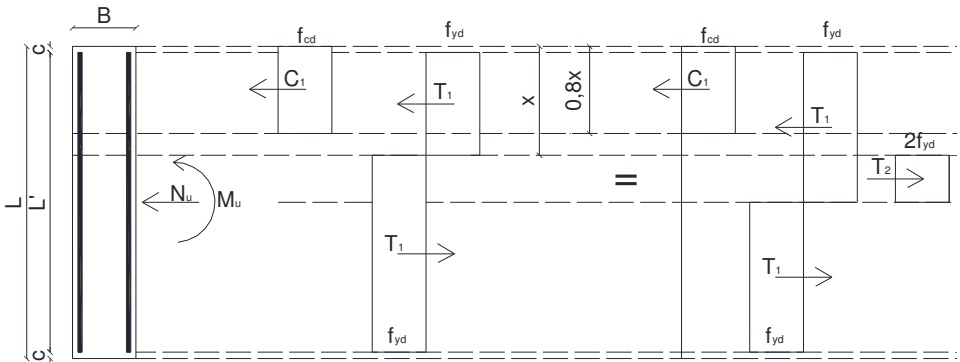


Figure 3 - Stress distribution in the equivalent section.

block with the axial resultant  $T_2$  that is necessary to restore the actual position of the neutral axis.

Considering the diagrams of Figure 3, the equilibrium along the longitudinal axis can be written in the following way:

$$C_1 + T_1 - T_1 - T_2 = N_u \rightarrow C_1 - T_2 = N_u \quad (2a)$$

where

$$- C_1 = 0.80 \cdot x \cdot B \cdot f_{cd}$$

$$- T_1 = \alpha \cdot \frac{L'}{2} \cdot f_{yd}$$

$$-T_2 = 2 \cdot \alpha \cdot \left( \frac{L}{2} - x \right) \cdot f_{yd}$$

-  $f_{cd}$  = design strength of concrete strength in compression;  
-  $f_{yd}$  = design strength of steel at yielding.

Therefore,

$$0.8 \cdot x \cdot B \cdot f_{cd} - 2 \cdot \alpha \cdot \left( \frac{L}{2} - x \right) \cdot f_{yd} = N_u \quad (2b)$$

and the neutral axis can be evaluated as

$$x = \frac{N_{Ed} + \alpha \cdot L \cdot f_{yd}}{0.80 \cdot B \cdot f_{cd} + 2 \cdot \alpha \cdot f_{yd}} \quad (3)$$

After the evaluation of the neutral axis, the ultimate moment, which is the plastic moment ensuing from the stress blocks, can be calculated by writing the condition of equilibrium around the rotation axis of the section, with respect to the centroid of the section, where the axial force  $N_u$  is applied (Figure 3):

$$M_u = C_1 \cdot \left( \frac{L}{2} - 0.4x \right) + T_1 \cdot \frac{L'}{2} - T_2 \cdot \frac{1}{2} \left( \frac{L}{2} - x \right) \quad (4)$$

The reliability of this simplified approach clearly appears in Figure 4, where the  $M_u$ - $N_u$  domain obtained in this way is compared with the same domain obtained by a more refined procedure that considers the actual position of the bars and the constitutive relationship for the concrete in compression, in the well-known form of a parabola plus a rectangle (NTC, 2008). The section considered in the comparison is 150 mm wide and 1500 mm deep; the rebars are 1Ø10/200 mm for each side; the design strength of the concrete is  $f_{cd} = 14$  MPa and that of the steel is  $f_{yd} = 391$  MPa.

Another comparison between the simplified and refined procedures was made with reference to the flexural strength of the walls with single bar layers tested by Orakcal et al. (2009), see Fig.1, and by Riva and Franchi (2001). The dimensions and the reinforcement of the sections and the material characteristics have already been introduced in Section 2.2.

In Table 3, the ultimate moment evaluated with the simplified and refined approaches,  $M_{u,sim}$  and  $M_{u,ref}$ , are listed together with their ratio. The maximum error of the simplified procedure with respect to the refined procedure is 5%. Finally, in the last column of Table 3, the experimental maximum moment,  $M_{exp}$ , is given. Both theoretical values are lower than the experimental values because the beneficial effects of steel hardening and of the axial load due to the self-weight are neglected in the calculations.

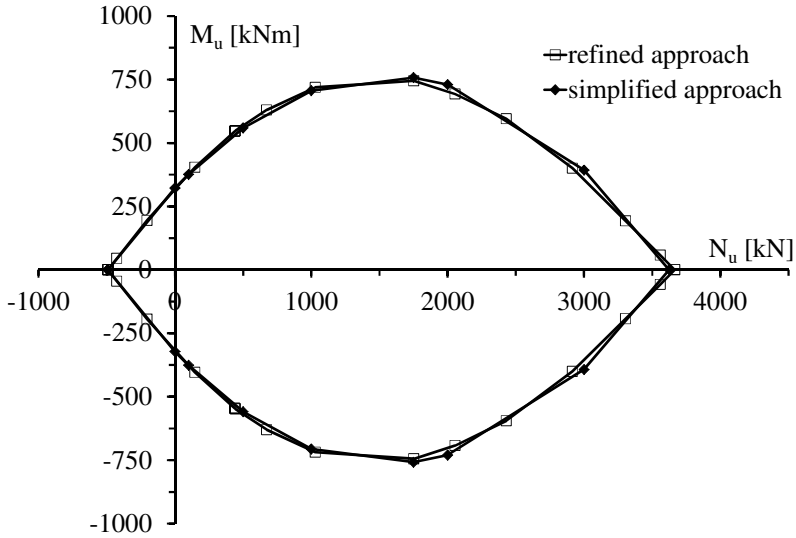


Figure 4 -  $M_u-N_u$  domains of a R/C deep-wall section according to the simplified approach (rhombuses) and the refined approach (squares).

To use the same simplified procedure in the design of the section (thickness and reinforcement area), the distance  $c$  was assumed to be equal 0, which means the length of the equivalent steel section  $L'$  coincides with section depth  $L$ . Considering Figures 3, the equilibrium concerning the rotation of the section with respect to the centroid of the compressive stresses in the concrete can be written as follows:

$$\alpha \cdot f_{yd} \cdot x \cdot (0.5x - 0.4x) - \alpha \cdot f_{yd} \cdot (L - x) \cdot \left( \frac{L - x}{2} + 0.6x \right) = M_u + N_u \cdot \left( \frac{L}{2} - 0.4x \right) \quad (5)$$

Table 3 - Comparison between theoretical and experimental ultimate moment for specimens tested by Orakcal et al. (2009), and by Riva and Franchi (2001).

Specimen	$M_{u,sim}$ [kN m]	$M_{u,ref}$ [kN m]	$M_{u,sim}/M_{u,ref}$	$M_{exp}$ [kN m]
WP-T5-N10-S2	609	623	1.02	999
HR12C	564	549	0.97	745
CD12C	682	648	0.95	888
HR12S	750	757	1.01	945
HR12U	750	757	1.01	945
CD12S	881	883	1.00	1063
CD12U	881	883	1.00	1063



For design purposes, the neutral axis is normalised with respect to the depth of the section ( $x/L$ ), in order to determine the value of  $\alpha$  by means of Eq.5. Then, the reinforcement area  $A_{s,tot}$  is calculated as  $\alpha L$ . The thickness  $B$  of the wall can be calculated by introducing  $\alpha$  in the equilibrium equation (Eq. 2bis).

In the same way, the yielding moment of the section  $M_y$  can be evaluated by assuming the equivalent area of the reinforcement; in this case, all materials are assumed to be elastic, and the yielding moment corresponds the attainment of the yielding strength at the most stressed point of the reinforcement in tension. The well-known distribution of the stresses is presented in Figure 5.

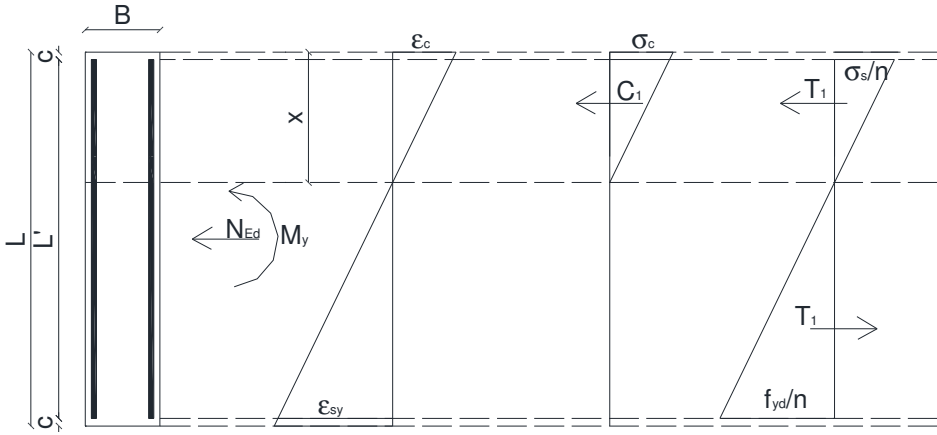


Figure 5 – Stress distributions in a section at yielding moment  $M_y$ .

To calculate the moment at yielding, when an axial load,  $N_{Ed}$ , is also applied, the following expression can be used:

$$M_y = N_{Ed} \cdot \left( \frac{I_n}{S_n} - x + \frac{H}{2} \right) \quad (6)$$

The depth of the neutral axis  $x$  is given by the expression:

$$f_{yd} = \frac{n \cdot N_{Ed}}{S_n} \cdot (L - x - c) \quad (7)$$

where  $n$  is the homogenisation factor equal to  $E_s/E_c$ .

The values of the inertia and static moments,  $I_n$  and  $S_n$ , under the hypothesis of continuous reinforcement, can be evaluated by means of the following expressions:

$$I_n = \frac{B \cdot x^3}{3} + \frac{n \cdot \alpha \cdot (x - c)^3}{3} + \frac{n \cdot \alpha \cdot (L - x)^3}{3} \quad (8)$$

$$S_n = \frac{B \cdot x^2}{2} + \frac{n \cdot \alpha \cdot (x - c)^2}{2} - \frac{n \cdot \alpha \cdot (L' - x)^2}{2} \quad (9)$$

Considering the same section as in the case of the  $M_u-N_u$  domains (Figure 4) and assuming  $n = 15$ , the moment at yielding gives  $M_y = 330$  kNm (simplified method) and  $M_y = 302$  kNm when (refined method, with the bars in their actual position).

### 3.2 Nonlinear modelling of the wall

The nonlinear model of a R/C wall was implemented by using two codes SAP2000 (SAP2000. Version 14, see Pecce et al., 2012) and DIANA (DIANA TNO, Release 9.4). The general approach is approximately the same, though DIANA can better describe the cracking behaviour of bidimensional members in shear.

In both programs, a bidimensional model is implemented by assuming that the wall is composed of layers of concrete and steel; the materials are defined by their constitutive relationships uncoupled along each principal direction. In particular:

- the bidimensional element used for modelling the concrete are shell elements (with both in-plane and out-of-plane stiffnesses), while membrane elements were used for the reinforcement (stiffness only in its own plane);
- multi-axial nonlinear constitutive laws are adopted for the concrete and a mono-axial nonlinear constitutive law for the reinforcement;
- Mander's law (Mander et al., 1984) is adopted for the concrete in compression, according to the following formulation:

$$\sigma_c = \frac{f_c' \cdot x \cdot r}{r - 1 + x^r} \quad \text{if } \varepsilon \leq 2\varepsilon_c' \quad (10)$$

where

- $f_c'$  = concrete strength in compression;
- $\varepsilon_c'$  = concrete strain at  $f_c'$  (= 0.002 without confinement);
- $x = \varepsilon / \varepsilon_c'$ ;
- $r = \frac{E}{E_c - (f_c' / \varepsilon_c')}$
- $E_c$  = Young's modulus of concrete.

The constitutive relationship of the concrete in tension takes into account cracking by means of smearing the cracks and introduces tension stiffening after cracking through the softening branch suggested by Vecchio et al. (1986). Therefore, the first branch of the  $\sigma$ - $\varepsilon$  relation in tension is linear up the strength  $f_{cr}$ , and is followed by a nonlinear softening branch, as described by the

following expressions:

$$\begin{aligned} \sigma &= E_c \cdot \varepsilon && \text{before cracking} \\ f_{cl} &= \frac{f_{cr}}{1 + \sqrt{200 \cdot \varepsilon_1}} && \text{after cracking} \end{aligned} \quad (11)$$

The tensile strength  $f_{cr}$  is evaluated by means of the formulation of Vecchio et al. (1986):

$$f_{cr} = 0.33 \sqrt{f'_c} \quad (12)$$

The constitutive relations in compression and in tension for concrete are plotted in Figure 6.

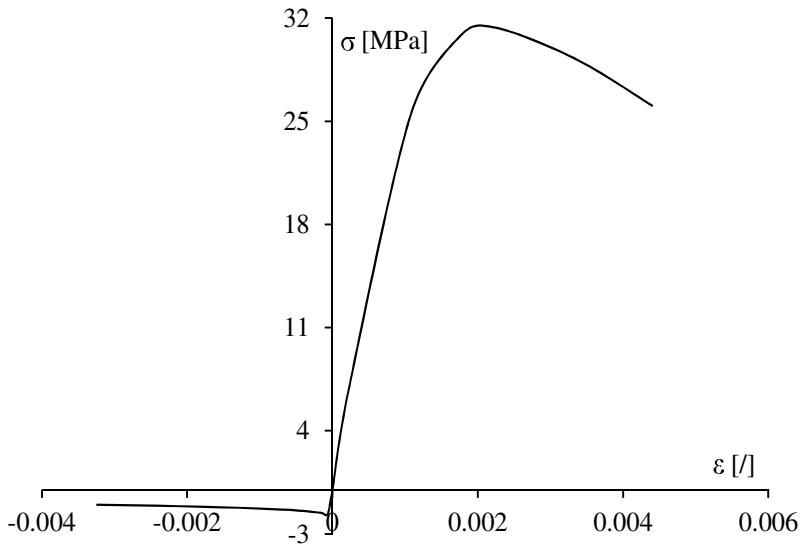


Figure 6 - Constitutive laws in tension and compression for concrete.

Further information is given in the following on crack modelling. SAP2000 adopts a *smearred-crack* approach in which a  $\tau$ - $\gamma$  curve is generated by the by considering smooth cracks. DIANA allows the use of *smearred rotating cracks* and *smearred fixed cracks*. The two approaches can be synthetically defined as follows:

- (1) *smearred rotating cracks*: the concrete has an elastic behaviour up to cracking, i.e. up to the attainment of the tensile strength in the most stressed fibres; thereafter, the alignment of the cracks is at right angles to the local direction of the principal tensile stress and vary with this direction;
- (2) *smearred fixed cracks*: the concrete has an elastic behaviour up to cracking; thereafter, the alignment of the cracks is at right angles to the local direction of the principal stress at the onset of cracking and remains constant throughout the loading process; since

shear stresses and strains arise at crack interface, the shear stiffness along the interface has to be introduced as a fraction  $\beta (\leq 1)$  of the shear modulus  $G$ .

The value of the parameter  $\beta$  (*shear-retention factor*) was determined by using the experimental results of the diagonal tests on R/C panels described in the following Section.

### 3.3 Calibration of the parameter $\beta$

The authors carried out a diagonal test on a R/C panel to calibrate the shear-retention factor to be introduced into the DIANA code after cracking.

The specimen dimensions were 900 x 900 x 150 mm. Ordinary-steel bars were used as a reinforcement (1 $\varnothing$ 10/200 mm in two directions). Concrete mean strength in compression was 36 MPa; steel mean strength at yielding and at failure in tension were 467 and 551 MPa, respectively.

The load was applied by means of a displacement-controlled hydraulic universal machine (capacity 3000 kN; displacement rate 0.015 mm/min) fitted up with a load cell. Two inductive displacement transducers - LVDTs were placed along the diagonals of the specimen, on the front and back faces (gage length = 400 mm).

The response of the panel was monitored both before and after the peak load. The sketch of the test set-up is shown in Figure 7a, and a picture of a specimen after the test is shown in Figure 7b.

The load-displacement curves  $F-\delta$ , measured by the four LVDTs are reported in Figure 8a, two for each side, one for compression (vertical direction V) and one for tension (horizontal direction H).

The relation between the shear stress and the shear deformation  $\tau-\gamma$  is plotted in Figure 8b. The shear stress is calculated as

$$\tau = \frac{0.707 \cdot F}{A_n} \quad (13)$$

where:

- $\tau$  = shear stress;
- $F$  = applied load;
- $A_n$  = net area of the specimen calculated as follows:

$$A_n = \left( \frac{w+h}{2} \right) \cdot t \quad (14)$$

where  $w$ ,  $h$  and  $t$  are the width, height and thickness of the specimen, respectively.

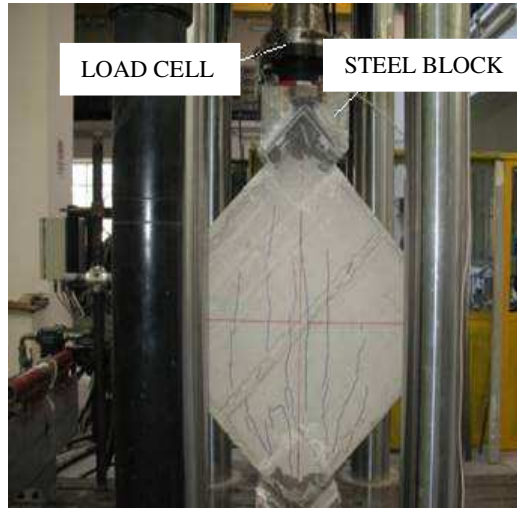
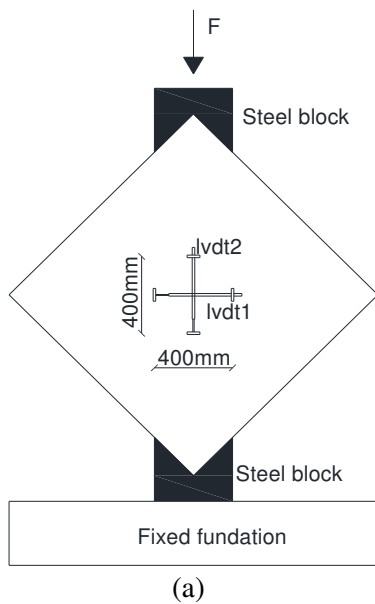


Figure 7 – Diagonal-tension test. (a) Set-up ; (b) the panel after the test.

The shear strain is calculated as:

$$\gamma = \frac{\Delta V + \Delta H}{g} \quad (15)$$

where:

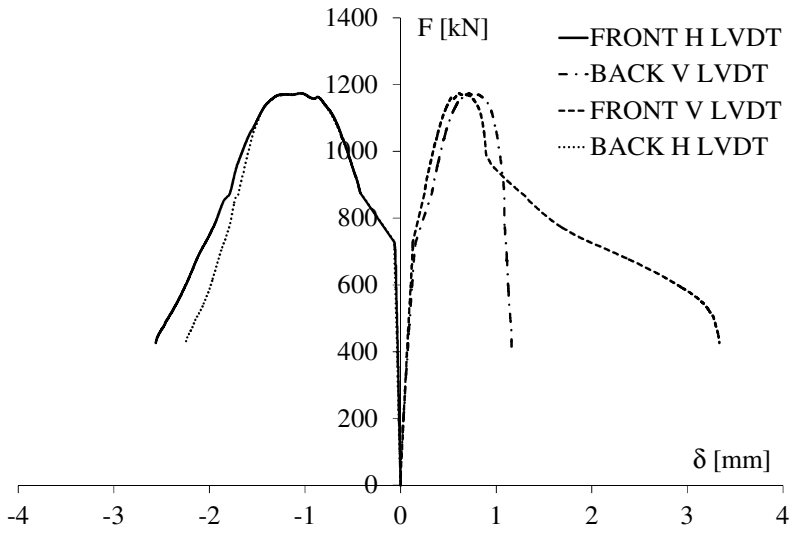
- $\gamma$  = shear strain;
- $\Delta V$  and  $\Delta H$  = vertical shortening and horizontal elongation, respectively;
- $g$  = gauge length for the measurement of  $\Delta V$  and  $\Delta H$ , respectively.

Figure 8b shows that the behaviour is linear up a stress value of 3.8 MPa and then becomes nonlinear up to approximately 6.1 MPa.

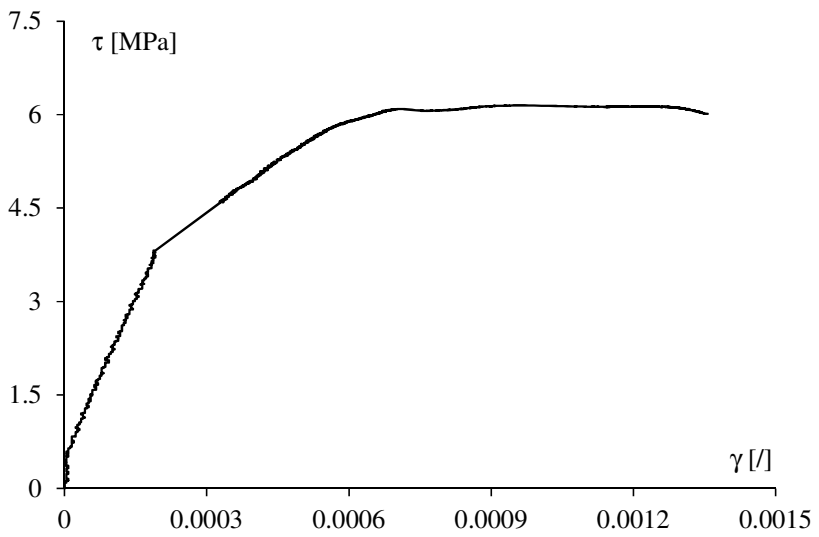
The model of the panel has been implemented in DIANA, assuming both *smeared rotating cracks* and *smeared fixed cracks*, in the latter case with various values of  $\beta$  (0.005, 0.01, 0.1).

The constraint conditions were simulated by modelling in 2D the steel shoes used in the test.

Figure 9 shows a good fitting of the experimental results, but confirms the role of  $\beta$ , which allows a better agreement after shear cracking; in particular  $\beta = 0.01$  and 0.005 yield the best fitting.



(a)



(b)

Figure 8 – Experimental results of the diagonal test on a R/C wall: (a)  $F$ - $\delta$  curves; and (b)  $\tau$ - $\gamma$  curves.

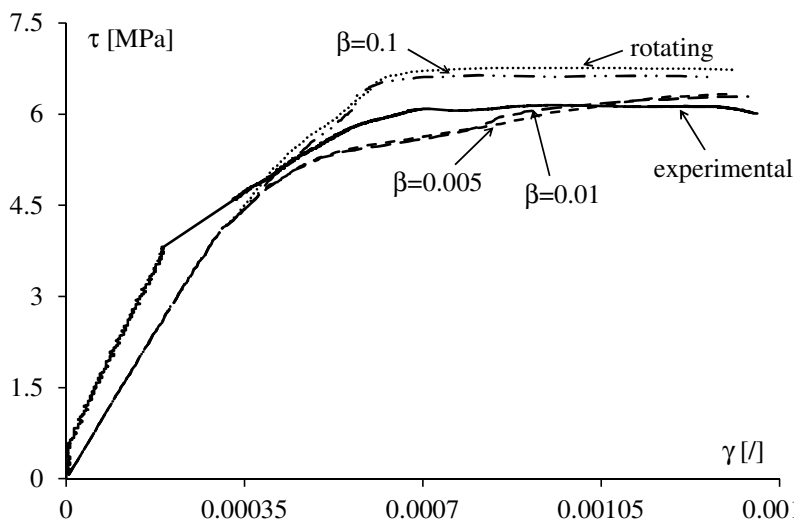


Figure 9 - Theoretical and experimental comparison of the diagonal test.

### 3.4 Fitting of the test results

The FE models implemented in SAP2000 and DIANA were also applied to the wall WP-T5-N10-S2 tested by Orackal et al. (2009) and described in Section 2.2. The thicknesses of the three layers (one of concrete and two of steel reinforcement, in the two directions) and the properties of the materials are as follows:

1. the concrete layer has a thickness equal to the total thickness of the section (152 mm);
2. the thickness of the layer simulating the longitudinal reinforcement is 0.35 mm and is calculated by dividing the reinforcement area by the panel depth (990 mm); close to the end sections, the thickness is 2.47 mm (same procedure as before; length of 229 mm);
3. the thickness of the layer simulating the transverse reinforcement is 0.44 mm.
4. concrete compressive strength:  $f_c = 31.4$  MPa;
5. steel strength at yielding:  $f_y = 424$  MPa; the constitutive law of the steel is elastic-perfectly plastic, with the ultimate strain  $\varepsilon_u = 12\%$ .

The fitting of the experimental results is shown in Figure 10 in terms of the force-displacement relationship. Cracking was modelled as *distributed with a fixed direction (smeared fixed cracks)* and as *distributed with a variable direction (smeared rotating cracks)*. The *shear factor*  $\beta$  was introduced with various values (0.005, 0.01, 0.1) in the first model.

As shown in Fig.10, DIANA predicts a stiffer behaviour compared to the experimental results concerning the loading phase, while in the same phase SAP2000 allows a much better fitting.

In the post-elastic field, the best agreement with the experimental results is achieved by the approach based on *smearred fixed cracks* ( $\beta = 0.005$ ).

In contrast, the approach based on *smearred rotating cracks* yields similar results to those obtained with *smearred fixed cracks* for  $\beta = 0.1$  in the loading branch but then there is a divergence, and only by giving  $\beta$  lower values (0.01 and 0.005) the fitting improves.

Finally, SAP2000 appears to be less efficient in predicting steel yielding because the load at yielding obtained numerically overestimates the actual load; however, the post-elastic branch of the curve agrees fairly well with the test, softening included.

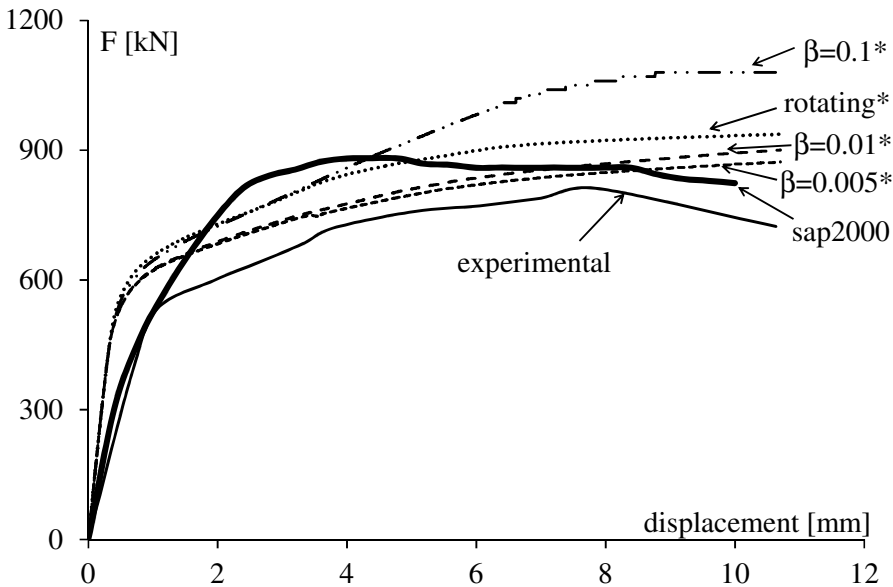


Figure 10 – Specimen WP-T5-N10-S2 (Orakcal et al., 2009): fitting of the experimental results by means of \*DIANA models.

#### 4. CONCLUDING REMARKS

Large lightly-reinforced walls are still not commonly used in many seismic countries because the design provisions in their national codes and even the international codes lack the necessary details. However, the available experimental tests demonstrate that large lightly-reinforced walls exhibit a good performance in terms of ductility in the case of single panels with low steel ratios and uniformly-distributed reinforcement. Hence, it is necessary to calibrate suitable models able to describe the nonlinear behaviour of the buildings containing this type of walls and to check the global ductility of their structure.



The nonlinear FE models mentioned in this study exhibit a good agreement with the experimental results, depending on the choice of the model assumed to describe concrete cracking. In particular, the approach based on *smearred fixed cracking* appears to be more effective than the approach based on *smearred rotating cracking*, if the parameter governing the shear deformability after cracking, is well calibrated. Once more, the relevance of shear behaviour in this type of walls is confirmed, since these structural members are not reinforced to mobilize the flexural behaviour, as occurs in ductile walls that - on the contrary - are reinforced with appropriately-detailed reinforcement. Within this context, the model implemented in SAP2000 appears to be efficient in terms of global behaviour, even if it is unable to predict the load at bars yielding in the case examined.

The simplified procedure developed to evaluate the  $M_u-N_u$  domains at the ultimate limit state or to design the flexural reinforcement of the wall is rather effective and handy, and can be used also in the elastic range (before bar yielding).

Summing up, the results yielded by the procedures proposed for estimating the flexural capacity of the section and by the FE models for describing the nonlinear behaviour of the lightly-reinforced shear walls are a reliable basis for future improvements in the analysis and design of the seismic performance of the buildings containing large lightly-reinforced walls.

## REFERENCES

- CEN – EN 15217 (2007). *Energy Performance of Buildings. Methods for Expressing Energy Performance and for Energy Certification of Buildings*, European Committee for Standardization.
- Decree August 19 – 2005 (2005). *Application of the Instruction 2002/91/CE on Energy Efficiency of Buildings*” (in Italian: “Attuazione della direttiva 2002/91/CE relativa al rendimento energetico nell'edilizia”), No. 192, Official Gazette of the Italian Republic No.222.
- Decree December 29 – 2006 (2006). *Corrections and Integrations to the Decree August 19 – 2005 No.192 on the Application of the Instruction 2002/91/CE on Energy Efficiency of Buildings* (in Italian: *Disposizioni correttive ed integrative al decreto legislativo 19 agosto 2005, n. 192, recante attuazione della direttiva 2002/91/CE, relativa al rendimento energetico nell'edilizia*), No.311, Official Gazette of the Italian Republic No.26.
- Eurocode 8, prEN 1998-1:2003 (2003). *Design of Structures for Earthquake Resistance – Part 1: General Rules – Seismic Action and Rules for Buildings*, CEN—European Committee for Standardization.
- Decree January 14 – 2008 (2008). *NTC – Technical Provisions for the Constructions* (in Italian: “Norme Tecniche per le Costruzioni”), Italian Ministry of Public Works, Official Gazette of the Italian Republic No.29.

- Vallenas J.M., Bertero V.V. and Popov E.P. (1979). "Hysteretic Behavior of Reinforced Concrete Structural Walls", *Earthquake Engineering Research Center*, University of California, Los Angeles. Report No. UCB/EERC – 79/20, August 1979.
- Orakcal K., Massone L. and Wallace J. (2009). "Shear Strength of Lightly-Reinforced Wall Piers and Spandrels", *ACI - Structural Journal*, Vol.106, No.4, pp. 455-465.
- Hidalgo P.A., Ledezma A. and Jordan R.M. (2002). "Seismic Behavior of Squat Reinforced Concrete Shear Walls", *Earthquake Spectra*, Vol.18, pp. 287-308.
- Barda F., Hanson J.M. and Corley W.J. (1977). "Shear Strength of Low-Rise Walls with Boundary Elements", *Reinforced Concrete Structures in Seismic Zones*, SP-53, American Concrete Institute, Farmington Hills, Michigan (USA), pp. 149-202.
- Cardenas A.E., Russell H.G. and Corley W.J. (1980). "Strength of Low-Rise Structural Walls", *Reinforced Concrete Structures Subject to Wind and Earthquake Forces*, SP-63, American Concrete Institute, Farmington Hills, Michigan (USA), pp. 221-242.
- FEMA 450 (2003). *National Earthquake Hazards Reduction Program - Recommended Provisions for Seismic Regulations for New Buildings and Other Structures*, ed.2003.
- ACI Committee 318 (2005). *Building Code Requirements for Structural Concrete (ACI 318-05) and Commentary (318R-05)*, American Concrete Institute, Farmington Hills, Michigan (USA).
- Wallace J.W., Elwood K.J. and Massone L.M. (2008). "Investigation of the Axial Load Capacity for Lightly-Reinforced Wall Piers", *ASCE - Journal of Structural Engineering*, Vol. 134, No.9, pp. 1548-1557.
- Kuang J.S. and Ho Y.B. (2008). "Seismic Behavior and Ductility of Squat Reinforced Concrete Shear Walls with Non seismic Detailing", *ACI Structural Journal*, Vol.105, No.2. pp. 225-231.
- Carrillo J. And Alcocer S.M. (2012). "Seismic Performance of Concrete Walls for Housing Subjected to Shaking Table Excitations", *Engineering Structures*, No 41, pp. 98–107.
- Riva P. and Franchi A. (2001). "Behavior of Reinforced Concrete Walls with Welded Wire Mesh Subjected to Cyclic Loading", *ACI Structural Journal*, Vol. 98, No. 3, pp. 324-334.
- Eurocode 4 - ENV 1994-1-1:2004E (2004). *Design of Composite Steel and Concrete Structures – Part 1-1. General Rules and Rules for Buildings*, CEN—European Committee for Standardization.
- SAP 2000. *Version 14*, CSI – Computers and Structures Inc.
- TNO DIANA BV. DIANA. *Release 9.4*.
- Mander J.B., Priestley M.J.N. and Park R. (1984). *Seismic Design of Bridge Piers*, Research Report No. 84-2, University of Canterbury, Christchurch (New Zealand).
- Vecchio F.J. and Collins M.P. (1986). "The Modified Compression-Field Theory for Reinforced Concrete Elements Subjected to Shear", *ACI Journal*, Vol.83, No.2, pp. 219-231.
- Pecce R., Bibbò F.A. and Ceroni F. (2012). "Seismic Behavior of R/C Buildings with Large Lightly-Reinforced Walls", *Proc. 15<sup>th</sup> WCEE*, Lisbon (Portugal), September 24-28.

## **SPALLING AND TENSION STIFFENING IN HEAT-EXPOSED MEMBERS MADE OF SELF-COMPACTING CONCRETE**

Francesco Lo Monte<sup>1</sup>

### **ABSTRACT**

Heat-induced damage, surface scaling and cover cracking always occur – with different severity - in R/C members subjected to a fire. Hence, bar-concrete bond in general and cover integrity in particular are at risk in fire, with consequences that can span from the loss of anchoring ability and tension stiffening to cover spalling, followed by the exposure of the reinforcement to the flames.

In this research project, concrete spalling and tension stiffening are addressed, the attention being focused on corner spalling in reinforced and unreinforced prismatic specimens in the former case, and on reinforced tension members in the latter case. An experimental procedure to assess concrete sensitivity to spalling is proposed as well. Though very different in their nature, concrete spalling and tension stiffening are investigated within the same project, because (a) the same prismatic specimens are firstly subjected to a rather severe temperature-time ramp to provoke spalling and later to sustained high temperature to induce a generalized damage in the concrete; and (b) the bars placed in the corners are the most exposed to the risk of spalling and to the loss of bond, to the detriment of tension stiffening.

Twenty one prisms made of SCC (target strength  $f_c = 50, 80$  and  $90$  MPa) were put inside an electric furnace at  $750^\circ\text{C}$  to investigate spalling (9 unreinforced and 11 reinforced with a single bar totally embedded in the concrete). Later, the reinforced prisms were cleared of the concrete at their extremities, to allow the application of opposite tensile forces and to investigate tension stiffening.

On the whole, the spalling tendency was rather weak, with 10% (20%) of the specimens affected by severe (light) spalling, while residual tension stiffening appeared to be still effective in only 50% of the reinforced specimens, where bond stiffness exhibited a roughly linear relationship with the residual compressive strength of the concrete.

**KEYWORDS:** high temperature; concrete spalling; tension stiffening; bond stiffness; self-compacting concrete.

---

<sup>1</sup>Structural Engineer, PhD Candidate, Dept. of Civil and Environmental Engineering, Politecnico di Milano, Milan 20133, Italy.

## 1. INTRODUCTION

Anchoring ability and tension stiffening are the two faces of bond in reinforced-concrete structures, but - while the former mostly involves equilibrium (as the bond stresses balance the load-induced tensile force in the reinforcement) - the latter mostly involves the compatibility between concrete and reinforcement strains. Both anchoring ability and tension stiffening are severely affected by fire, and - more generally - by high temperature, but while the former has been extensively investigated in the past (and even recently), no information is available on the temperature sensitivity of tension stiffening.

In terms of anchoring ability, not only heat-induced damage in the concrete has detrimental effects, but also surface damage, that is unavoidable at high temperature and in fire (Xi et al., 1994). The damage may exhibit different features, from hairlike cracking to discrete cracking, from scaling to more or less severe spalling, with aggregate splitting and/or enucleation (Khoury, 2000).

In some cases spalling (that is the most severe form of damage; Dehn and Koenders, 2009; Koenders and Dehn, 2011; Smith and Atkinson, 2009; Kodur and Dwaikat, 2009; Pimienta et al., 2010) is rather local and progressive, in other cases it is extended and explosive. Also the reinforcement plays a sizable role on concrete damage, since spalling is generally limited to the cover or (alternatively) cracks parallel to the bars appear and widen after cooling down to room temperature. In unreinforced members, discrete cracks may form at right angles to the corners, mostly because of concrete desiccation. The different forms of damage, however, are rather elusive, since - depending on a number of parameters - one form or another may prevail in nominally-identical specimens, for no specific reasons. Hence, not only spalling as such has become a very hot topic, but standardized tests to assess the spalling sensitivity of the many cementitious composites available today are badly needed. The tests should be as simple and reproducible as possible, with the least possible number of parameters, beside those related to the thermal field. The setting should be rather demanding (for instance, a corner exposed to the fire) and the fire scenario should be rather severe (for instance, close to the hydrocarbon fire), in order to activate pore pressure (Xi et al. 1994; Kalifa et al. 2001; Jansson and Boström, 2008) and aggregate splitting. At the same time, thermal self-stresses and load-induced stresses should be ruled out or kept to a minimum, since they depend on the structural context, while the driving force of spalling - pore pressure (Fig.1a) - has to do with the very nature of the material.

With reference to tension stiffening, it is worth recalling that the flexural cracks cause the unloading of the concrete at the cracked interface and the activation of the reinforcement in tension, the latter being accompanied by bond stresses, that bring in a partial unloading of the bars between the cracks and some tension in the surrounding concrete. Hence, any embedded bar - being *relieved* by the concrete - exhibits a *stiffer* behavior compared to a similar naked bar. This is tension

stiffening, that plays a considerable role in crack control and in enhancing structural stiffness. Since tension stiffening is related to bond, tension stiffening and fire should be examined within the context of bond and high temperature.

Bond versus high temperature was extensively studied in the eighties of the past century (RILEM, 1985), with reference to the effects of: mix design, aggregate type, curing conditions, shape/size/surface conditions of the reinforcement, shape of the specimens and test procedures.

Beside the great difference between smooth and deformed bars, the roughness of the reinforcement, the aggregate type, the testing procedure (at high temperature/in residual conditions), the curing conditions and the shape of the specimen were recognized as being the major factors controlling bond at high temperature. Bar roughness, calcareous aggregates, air curing (of the concrete) and high temperature (compared to residual conditions) bring in a better bond behavior in the heat-exposed reinforcement. Other topics, like the effect of metallic and polymeric fibers, and the role of expanded clay for large/medium aggregate, have been reconsidered lately (Lublóy and Balázs, 2012).

To give an idea about bond decay at high temperature, the normalized bond strength is plotted in Fig.1b as a function of the temperature, for smooth and ribbed bars, as well as for deformed prestressing reinforcement. It should be observed that bond decay seems to be halfway between concrete decay in compression and in tension (for recent data on concrete behavior at high temperature, see Felicetti and Gambarova, 2008).

Since the late eighties of the past century, limited attention has been given to bond and high temperature or fire, and less than half a score of valuable papers can be found in major magazines (El-Hawary and Hamoush, 1996; Chiang and Tsai, 2003; Haddad et al., 2008; Haddad and Shannis, 2004; Bingöl and Gül, 2009; Huang, 2010). Hence, new information is needed, on both the anchoring ability at high temperature and tension stiffening.

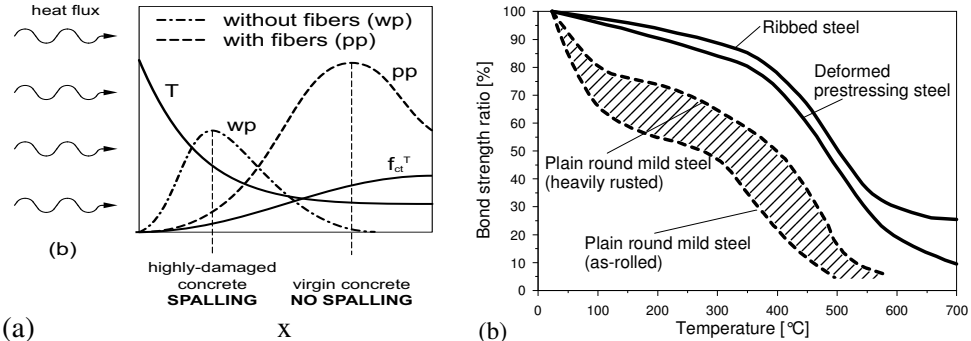


Figure 1 - (a) Qualitative plots of temperature (T), pore pressure (wp, pp) and tensile strength ( $f_{ct}^T$ ) in a concrete wall exposed to fire; and (b) normalized bond strength versus temperature in hot conditions (Sager, 1980, see RILEM, 1985);  $x$  = distance from the heated surface.

Within this context, the rather unpretentious project presented in this paper aims to yield some preliminary results (a) on the definition of an experimental procedure to assess the spalling sensitivity of a given concrete, and (b) the evolution of tension stiffening in R/C tension members exposed to roughly 650°C. The prismatic specimens were made of three different self-compacting concretes (target strength  $f_c = 50, 80$  and 90 MPa), whose behavior at high temperature was investigated within a rather comprehensive research project in 2006 – 2010 (Bamonte and Gambarova, 2012), with reference to: stress-strain law in compression, fracture and thermal properties, in *hot* and *residual* conditions.

## 2. OBJECTIVES

The objective of the first phase of this project was to investigate corner spalling in self-compacting concrete and to work out a proposal for the design of an experimental set-up aimed to investigate concrete sensitivity to spalling in fire (Bamonte et al. 2011). Investigating tension stiffening was the objective of the second phase (Bamonte et al., 2012).

The prismatic specimens – and the test set-up - were designed to represent the rather severe situation of a corner subjected to the heat flux coming from two directions at right angles, as in R/C columns and beams Figs.2a,b). From the point of view of the heat flux, the internal sides of the cross-sections depicted in Fig.2 are in either adiabatic conditions (both sides in Fig.2a and vertical side in Fig.2b, because of the symmetries), or close enough to adiabaticity (horizontal side in Fig.2b). After being exposed to a thermal shock to produce spalling (with the introduction of the reinforced/unreinforced specimens into a furnace pre-heated to 750°C), the specimens were left at 750°C for two hours in order to cause a rather uniform damage in the concrete. Then, after cooling down to room temperature the unspalled reinforced specimens were reworked at their extremities, to allow the reinforcing bar to be loaded in tension at both ends, in order to investigate tension stiffening in residual conditions.

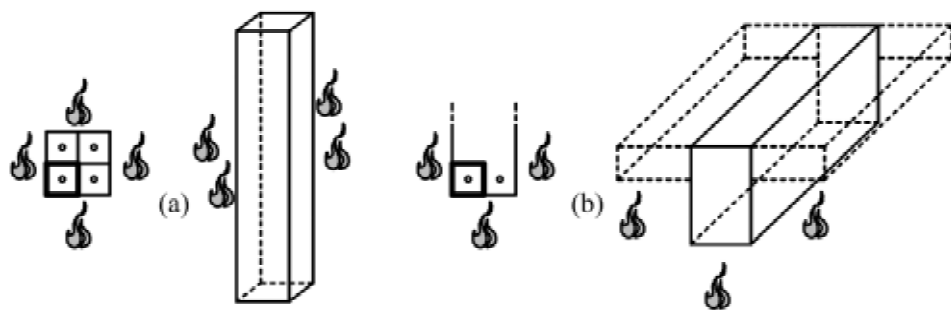


Figure 2 - Typical sections of a R/C column (a); and of a R/C beam (b); the part enveloped by the thick black line is recreated in the specimens.

### 3. SPECIMENS, MATERIALS AND FIRE CURVE

Twenty prismatic specimens ( $a \times b \times L = 80 \times 80 \times 450\text{-}500$  mm, Fig.3) made of three different self-compacting mixes (Table 1) were cast. Eleven specimens were reinforced with a single hot-rolled 16 mm-bar (close to #5, made of carbon steel with  $f_y = 400$  MPa,  $f_{yk} = 373$  MPa, Type FeB38k according to the Italian Norms,  $E_s = 205$  GPa).

Sixteen specimens were “standard” specimens, as will be explained later, while 2 unreinforced and 2 reinforced specimens were *preliminary* specimens, slightly different from the standard specimens, in terms of insulation, instrumentation or heating procedure (for more details, see Bamonte et al., 2011).

Since the focus was (a) on corner spalling because of pore pressure and (b) on tension stiffening as such, the specimens were unstressed during the heating process inside the electric furnace (= no loads applied inside the furnace) and also the thermal self-stresses were reduced to a minimum, thanks to the rather small size and boundary conditions of the specimens.

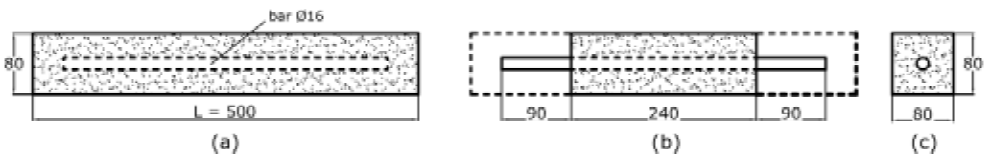


Figure 3 - Geometry of the reinforced specimens: lateral views of the specimens used to investigate spalling (a) and tension-stiffening (b); and cross-section (c);  $L = 500$  mm. Same geometry for the unreinforced specimens used only to investigate spalling ( $L = 450$  mm).

Table 1 – Mix design of the three self-compacting concretes used in this project.

Concrete No. and type	No.1 NSC	No.2 HPC	No.3 HSC
Cement type	II/A-LL 42.5	I 52.5	I 52.5
Cement content (c) [ $\text{kg}/\text{m}^3$ ]	350	480	520
Calcareous filler [ $\text{kg}/\text{m}^3$ ]	130	100	100
Acrylic superplasticizer/cement	1.2%	2.0%	2.0%
Water [ $\text{kg}/\text{m}^3$ ] (w/c)	175 (0.50)	168 (0.35)	172 (0.33)
Aggregate: natural round river gravel $d_a$ [mm]/mass [ $\text{kg}/\text{m}^3$ ]	16/1700	16/1600	16/1600
Mass per unit volume [ $\text{kg}/\text{m}^3$ ]	2359	2358	2402
Compressive strength: target/actual [MPa]	50/51	80/82	90/90

Note that the denominations NSC (Normal-Strength Concrete), HPC (High-Performance Concrete) and HSC (High-Strength Concrete) are used only to facilitate the identification of the three materials.

Cylinders, cubes and prisms were cast in 2007 and appropriately cured for 28 days; then, in 2007-09 the various specimens were tested in compression and indirect tension (by bending and splitting), generally in both hot and residual conditions, to work out the stress-strain laws in compression, and to evaluate the compressive and tensile strengths, as well as the fracture energy. The conclusion of the previous study on SCCs' mechanical properties at high temperature was that there are no systematic and sizable differences with respect to ordinary concrete (Bamonte and Gambarova, 2012). In Fig.4 the decay of the Young modulus and the thermal diffusivity are plotted as functions of the temperature.

Twenty prisms, some cubes and cylinders were put aside and kept in ordinary environmental conditions ( $T = 15-25^{\circ}\text{C}$ ; R.H. = 50-70%), for further investigations on spalling and tension stiffening (2011 and 2012). At the beginning of this project, the moisture content was close to 1.0% in NSC specimens, and close to 2.5-3% in both HPC and HSC specimens. Later, some specimens were put in a 50 cm-deep water tank for one week and a few for two weeks. The final moisture content was 4% in NSC, 4.5% in HPC and 3.3% in HSC. (There was hardly any difference between the moisture content after one week and after two weeks in water). All wet specimens were left in air for 24 hours, before being insulated, fastened to a steel saddle and introduced into the furnace, as indicated in the next chapter. The initial moisture content was evaluated by drying several small plates (80x80x20 mm, NSC, HPC and HSC) for 24-48 hours at  $105^{\circ}\text{C}$ . The increased moisture content was evaluated by weighing the cylindrical specimens before and after being placed in the water tank.

Each specimen (and its saddle-like support, as explained later) was introduced inside an electric furnace kept at the nominal temperature of  $750^{\circ}\text{C}$  (min.  $740^{\circ}\text{C}$ , max.  $780^{\circ}\text{C}$ ), in order to let the surface temperature increase (in the first 20 minutes) in a way intermediate between those ensuing from the hydrocarbon and the standard fire curves (Fig.5). It was a sort of thermal shock intended to create the most favourable conditions for spalling. After the first 20 minutes and in the next 100 minutes, the thermal field progressively became homogeneous, with the mean temperature close to  $640^{\circ}\text{C}$ .

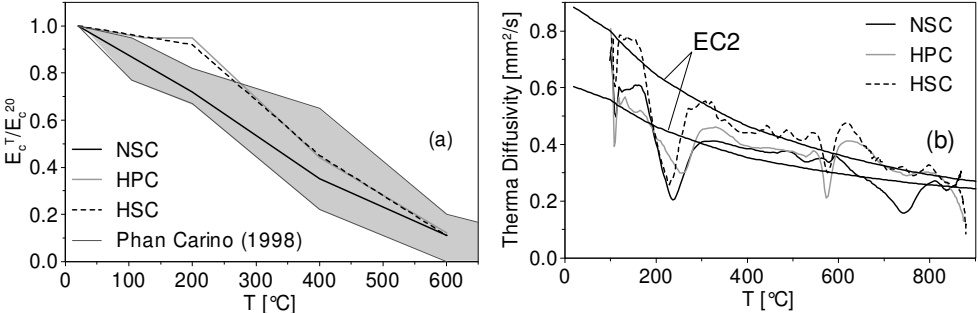


Figure 4 – (a) Decay of the residual Young modulus; and (b) thermal diffusivity, as functions of the temperature (Bamonte and Gambarova, 2012).



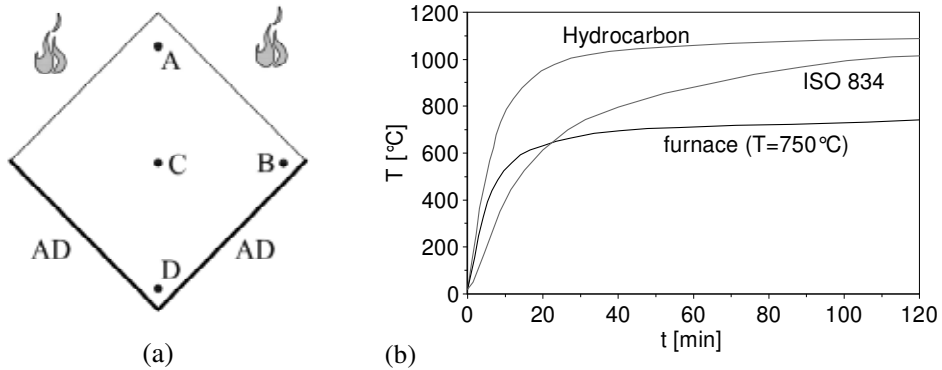


Figure 5 – (a) Cross section of the specimen and reference points; and (b) temperature evolution close to the corner (Point A, 10 mm from both edges) after the introduction of the specimens inside the furnace at 750°C (thick curve). AD = quasi-adiabatic surfaces.

The specimens were identified by means of an alpha-numeric code consisting of three letters (NSC, HPC, HSC) for the mix; one letter (P, R) for plain/reinforced concrete; one letter (D, W) for dry/moist concrete (1-2.5% or 3.5-4.5% by moisture mass); and one number ( $\leq 4$ ) identifying each nominally-equal specimen. Hence, for example, HPC/P/D/2 means 2nd dry unreinforced specimen made of high-performance concrete.

## 4. TEST SET-UP AND THERMAL FIELD

### 4.1 Spalling

Each prism was exposed to high temperature (Figs.5,6,7) on the two faces defining a corner, while the other two faces and the end sections were kept in quasi-adiabatic conditions (by means of proper insulation, Figs.6,7). In this way, the thermal field of the prism coincides with that of a quarter of a square column (side 160 mm), while the kinematic field is in principle different, because the planarity of the adiabatic faces is not guaranteed (something that is guaranteed by symmetry in a column exposed on four faces). The thermal field is also close to that of a corner in a 160 mm-wide beam exposed on three faces.

To avoid any moisture transfer across the adiabatic surfaces (as in a column exposed on four faces or in a beam across the vertical mean plane), their permeability was greatly reduced by impregnating the unexposed surfaces with a temperature-resistant silicate-based coating (thickness = 1 mm). After gluing thin metallic sheets (*barriers*) to the impregnated surfaces (thickness = 1 mm), each



Figure 6 - Typical specimen placed on the saddle-like support and ready to be introduced into the furnace: transverse and lateral views.

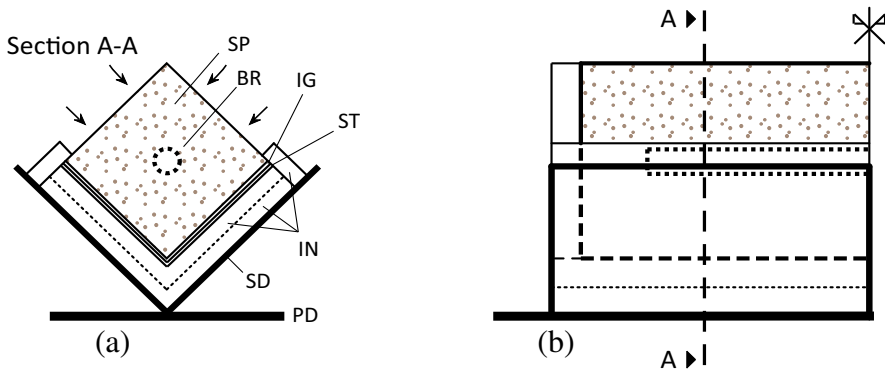


Figure 7 - Front (a) and lateral view (b) of the specimens tested in this project; SP = specimen; BR = bar; IN = insulating plate; IG = impregnating coating + glue; ST = steel barrier; SD = V-shaped supporting saddle; and PD = pedestal.

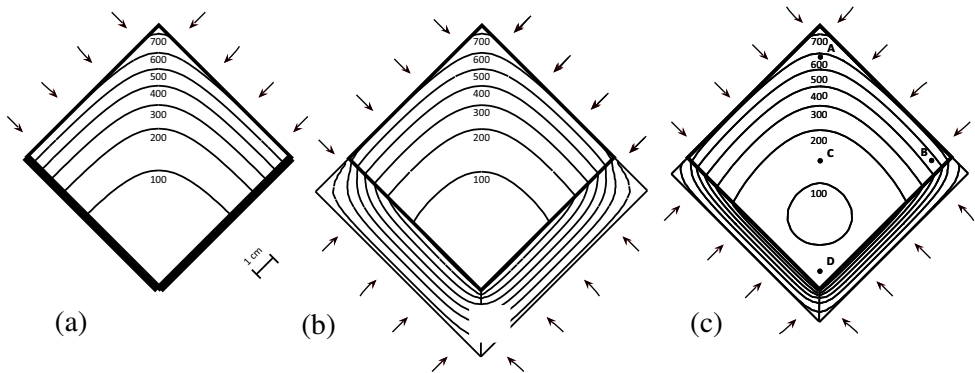


Figure 8 - Thermal analysis 15 minutes past the introduction of the specimen inside the furnace at 750°C: (a) adiabatic unexposed faces; (b) insulated unexposed faces, as in standard specimens; and (c) partially-insulated unexposed faces, as in Specimen HPC/P/D/2, which was instrumented with four thermocouples placed in A,B,C,D. The thermal properties of the concrete were those indicated in EC2 – Fire Design (2004).

specimen was placed on a metallic V-shaped saddle, by interposing one or two insulating plates containing ceramic fibres (thickness of each plate 10 mm); similar but smaller plates were used to insulate the end sections. Later, the system saddle+insulated specimen was introduced into the furnace.

The total weight of the system was close to 16 daN. (After opening the door of the furnace, the operator could easily and safely introduce the saddle and the specimen, and push it with a special rod in the proper position, inside a sort of steel cage fixed to the floor of the furnace, to prevent the electric coils from being damaged by the flying debris resulting from concrete spalling.

As previously mentioned, the specimen was left inside the furnace for 2 hours at 750°C; then the electric power was switched off and the furnace started cooling naturally, until at 300°C the specimen was extracted. Then the furnace was brought back to 750°C to allow the introduction of another specimen. In this way, the thermal ups and downs of the furnace were minimized. After the extraction from the furnace, the specimens were wrapped in an insulating blanket, until they cooled down to ambient temperature.

The effectiveness of one insulating plate (between the specimen and the saddle) was checked: (a) experimentally by inserting 4 thermocouples (Fig.5a, points A, B, C and D) in Specimen HPC/P/D/2 (HPC/unreinforced/dry/No.2), and (b) numerically by means of the FE software ABAQUS (Fig.8c).

The experimental values of the temperature were in satisfactory agreement with the predictions of thermal analysis. (For instance, 15 minutes past the introduction of the specimen into the furnace, the actual temperatures in A and D were 540°C and 140°C, respectively, i.e. 9% lower and 13% higher than those predicted numerically).

In all other specimens (*standard specimens*) two insulating plates were used (Fig.8b) and the isothermal lines turned out to be very close to those evaluated by assuming perfect adiabatic faces against the saddle (Fig.8a).

Last but not least, it is worth noting that the heat-exposed faces of each prism were (a) the bottom face and (b) one of the vertical faces during concrete casting, the two of them being against the formwork. In this way, the effect of segregation (if any) at the heated corner was minimized, as this corner was one of the two bottom corners during casting. (In other terms, the two impregnated faces included the top face during concrete casting, where the effect of segregation brings in more porosity and finer aggregates).

## 4.2 Tension Stiffening

As will be explained later, the majority of the eleven reinforced specimens exhibited some scaling and indentation during the thermal shock, and only a few underwent medium-severity spalling. One specimen, however, was so badly damaged after the thermal cycle (Specimen NSC/R/D/1, severe longitudinal cracking on one face), that could be used only to check the loading set-up and the

instruments to be used in the tension-stiffening tests. Among the other 10 specimens, 3 were made of NSC, 4 of HPC and 3 of HSC.

After clearing the extremities of the specimens (Fig.9), each concrete prism was 240 mm long and the bar protruded by 90 mm at each extremity. Such a free length was sufficient to clamp the bar between the top and bottom hydraulic jaws of the electro-mechanical press Schenck (capacity 1000 kN). All tests were displacement-controlled.

Note that the length of each concrete prism ( $L = 240 \text{ mm} = 15\varnothing$ ) is comprised between the values of crack spacing  $S_{cr,max}$  in R/C beams (BM) and tension members (TM), see EC2 – Part 1-1 (2004):

$$S_{cr,max} = k_3 \cdot c + k_1 \cdot k_2 \cdot k_4 \cdot (\varnothing / \rho_{p,eff}) = 195 \text{ mm (BM)} - 282 \text{ mm (TM)}$$

where  $k_1 = 0.8$  (ribbed bars);  $k_2 = 0.5$  or  $1.0$  in pure bending or tension);  $k_2 = 3.4$ ;  $k_4 = 0.425$ ;  $c = \text{net cover} = 32 \text{ mm}$ ;  $\varnothing = 16 \text{ mm}$ ;  $\rho_{p,eff} = 3.1\%$ .

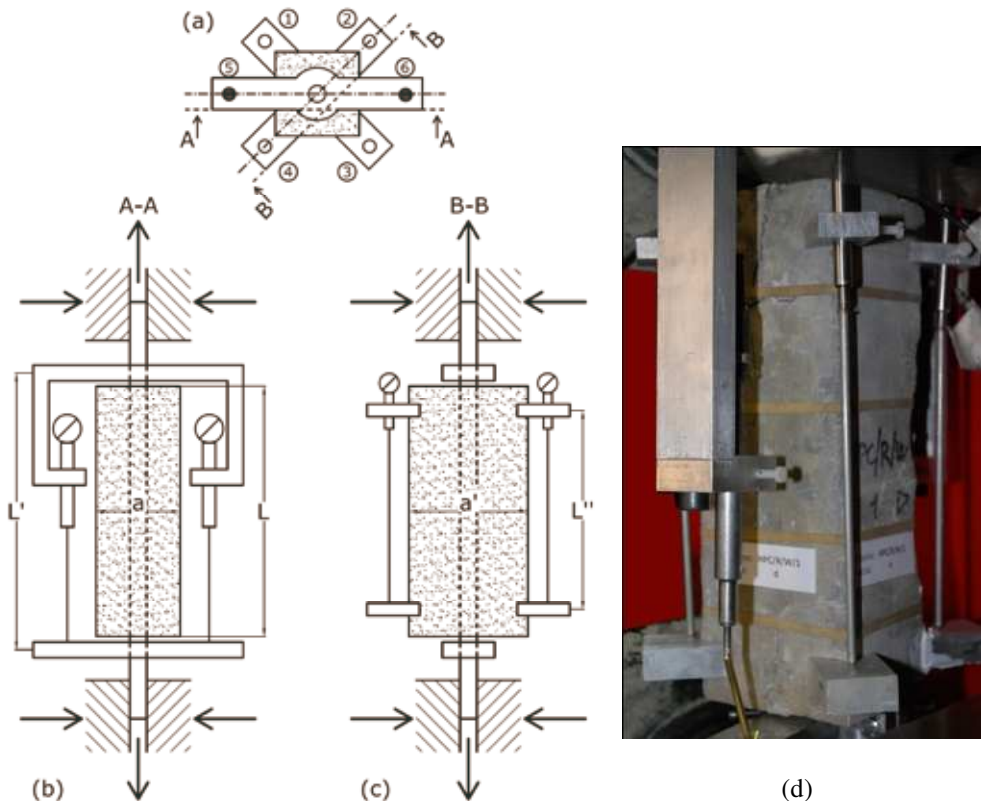


Figure 9 – Instrumented specimen ready for a tension-stiffening test: (a) cross section; (b) lateral view with the two LVDTs applied to the bar; (c) lateral view with two of four LVDTs applied to the corners: and (d) Specimen HPC/R/W/1;  $L = 240 \text{ mm}$ ;  $L' = 270 \text{ mm}$ ;  $L'' = 180 \text{ mm}$ ;  $a = 80 \text{ mm}$ ;  $a' = 113 \text{ mm}$ .

Note that  $L = 15\varnothing$  may seem too small to investigate tension stiffening, but this is not the case, as the very good bond properties of both SCC and deformed reinforcement guarantee a sizable tension-stiffening effect even on rather short embedments.

Four LVDTs were placed along the corners (Figs.9c,d), with base length  $L'' = 180$  mm, to measure the mean elongation of the concrete, cracking included (if any). Two aluminium cross bars were fixed to the reinforcing bar close to the extremities of the concrete prism, in order to allow the placement of two LVDTs (base length  $L' = 270$  mm) to measure the mean elongation of the bar. Later, each *naked* bar was tested in tension, to have the stress-strain curve in residual conditions (past heating to  $640^{\circ}\text{C}$ ), and to evaluate the strength at yielding and the elastic modulus. Unfortunately, no *reference* specimens were available to carry out the tests in virgin conditions (no heating to  $640^{\circ}\text{C}$ ).

Among the 10 tests, that were successfully carried out, only 5 exhibited some tension stiffening, probably because the heat-induced damage at  $640^{\circ}\text{C}$  was so severe that in some cases there was hardly any bond left.

## 5. RESULTS

### 5.1 Spalling

A close examination of the twenty reinforced/unreinforced dry/moist specimens allows to subdivide the damage after the thermal cycle in five broad categories, as shown in Table 2 and Fig.10: no visible damage (15% of the specimens); partial/extended longitudinal cracking (20-25%); corner cracking (25%); light scaling and/or indentation of the corners (25-30%); and spalling (10%). In detail:

- Unreinforced dry specimens (moisture content from 1% in NSC to 2.5-3% in HPC/HSC): very light scaling in NSC; some corner cracks in HPC and HSC, from hairlike to large (at least 0.5 mm wide, Fig.10d); probably the higher moisture content – and the following desiccation - was responsible for the corner cracks in both HPC and HSC specimens.
- Reinforced dry specimens (same moisture content as in the previous case): single continuous longitudinal crack on one face of the exposed corner in NSC, with some scaling and indentation along the corner; practically no visible damage along the corner and on both faces in HPC and HSC specimens (Fig.10e).
- Unreinforced moist specimens (moisture content from 3.3% in HSC to 4% and 4.5% in NSC and HPC, respectively): severe spalling with aggregate splitting and enucleation in NSC (Fig.10a); light spalling, scaling, indentation and corner cracking in both HPC and HSC (Fig.10c); on the whole, the heat-induced damage was rather light.

- Reinforced moist specimens (same moisture content as in the previous case): in general, light discontinuous longitudinal cracking on one or both faces (Fig.10f); in one case (HPC) severe spalling with aggregate splitting and enucleation (Fig.10b).

Even if the data base is very limited, what appears is that exposing either unreinforced or reinforced dry corners to a severe fire tends to produce corner cracking in unreinforced HPC/HSC specimens and longitudinal cracking in reinforced NSC specimens, while the unreinforced NSC specimens and reinforced HPC/HSC specimens tested in this project were hardly damaged.

In moist corners, spalling is an actual or impending occurrence, accompanied by some indentation and corner cracking, in both unreinforced (NSC) and reinforced (HPC) specimens; as in reinforced dry specimens, longitudinal cracking occurs in wet specimens as well, but in a rather limited form.

Table 2. Summary of the tests.

Mix	Plain/ Reinf.	Dry Wet	Specimen No.	Behavior
NSC	P	D	1	very light scaling
		W	1	severe spalling extended over 70% of total length
	R	D	1	light indentation, thin/large longitudinal continuous crack on one face
		W	1 <sup>**</sup> ,2,3	partial longitudinal cracks/thin discontinuous longitudinal cracks/no visible damage
HPC	P	D	1,2 <sup>^</sup>	few hairlike or thin cracks cutting the corner
		W	1,2	localized scaling/light spalling (25% of total length) with scaling and corner cracking
	R	D	1,2 <sup>^^</sup>	no visible damage
		W	1,2	severe spalling (70% of bar length)/thin discontinuous longitudinal cracks
HSC	P	D	1 <sup>*</sup>	several hairlike or large cracks cutting the corner
		W	1,2	several hairlike or thin cracks cutting the corner/few hairlike or thin cracks cutting the corner
	R	D	1	no visible damage
		W	1,2	light indentation, light discontinuous longitudinal cracks

(<sup>^</sup>) Instrumentation with 4 thermocouples (Fig.5a), one single 10 mm-thick insulating plate, no impregnating coating and no steel barrier.

(<sup>^^</sup>) As in (<sup>^</sup>), but without the thermocouples.

(<sup>\*</sup>) One single 10 mm-thick insulating plate, 0.5 mm-thick steel barrier, impregnation by means of an uncertified heat resistant product.

(<sup>\*\*</sup>) Standard insulation (two 10 mm-thick insulating plates), 1 mm-thick steel barrier, impregnation by means of a certified heat-resistant product, introduction inside the furnace at ambient temperature and progressive heating up to 750°C (heating rate = 12.5°C/min).

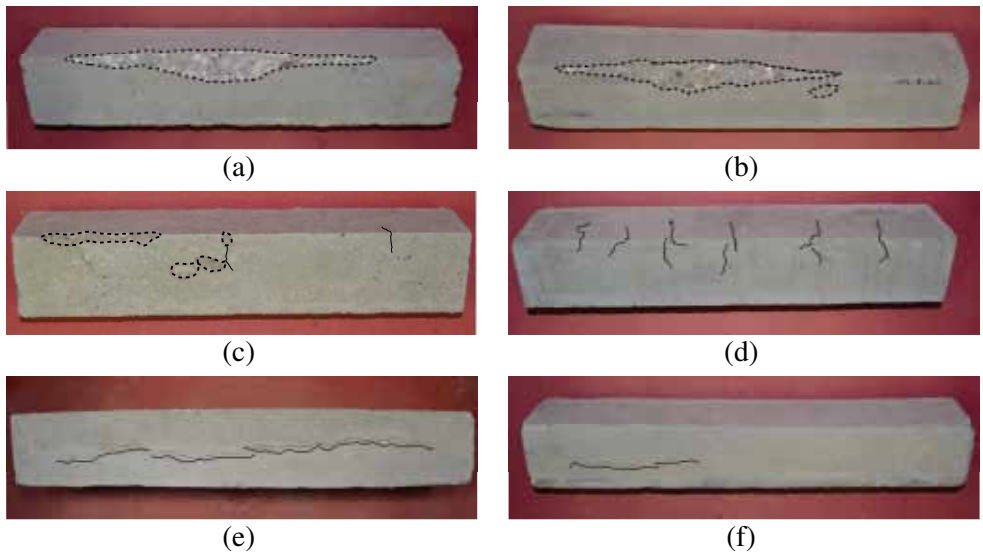


Figure 10 - Typical damage in unreinforced (a,c,d) and reinforced specimens (b,e,f): (a) severe spalling in Specimen NSC/P/W/1; (b) severe spalling in Specimen HPC/R/W/1; (c) light spalling with some indentation and scaling in Specimen HPC/P/W/2; (d) severe corner cracking in Specimen HSC/P/D/1; (e) fully-developed longitudinal cracking in Specimen NSC/R/D/1; and (f) partially-developed longitudinal cracking in Specimen NSC/R/W/1.

**5.2 Tension Stiffening**

Experimental results

Five of the ten tests, that were successfully carried out on reinforced specimens, exhibited some tension stiffening, probably because the heat-induced damage at 640°C was so severe that in 50% of the cases there was hardly any bond left. After each test, the concrete was removed and the bar was tested in tension to work out its stress-strain law including the heat-induced damage at 640°C. Hence, comparisons were made between *embedded bars* (with tension stiffening) and *naked bars* (no tension stiffening).

In Figures 11a-e the stress-strain curves of four specimens are reported (thick curves), together with the curves representing the behavior of each naked bar (thin curves) and the dashed lines, whose slope is the mean value of the elastic modulus of the naked bars ( $E_s^{640} = 186 \text{ GPa}$ ). With reference to Specimens NSC/R/W/1, HPC/R/D/1 (*reference specimen* in the following), HPC/R/D/2, HPC/R/W/2 and HSC/R/W/1, at 95% of the maximum load ( $N_{max} = 70\text{-}75 \text{ kN} =$  depending on the actual strength at yielding of the bars) the mean share of the load

borne by the concrete is comprised between 10% and 17%. (However, according to the theoretical model – Section 5 – the previous figures go up to 15% and 25% in the mid-span section).

After each test, the concrete around the bar was removed and the naked bar was loaded in tension to work out its stress-strain law. The elastic modulus of the heat-damaged steel was roughly 10% lower than that of the undamaged steel ( $E_s^{640} = 186$  GPa - mean value measured on 11 bars, compared to  $E_s^{20} = 205$  GPa).

As for the elastic modulus of the concretes after a thermal cycle at 640°C, six 80x80x240 mm prisms were tested in compression (two per each concrete mix), and the modulus  $E_c^{640}$  turned out to be close to 6.0 GPa (*stabilized modulus* comprised between 5.5 and 6.6 GPa, according to the Italian Standard UNI 6556, 1978). Hence, in residual conditions the ratio of the elastic moduli  $E_s^{640}/E_c^{640}$  was roughly 30. Note that the six prisms were cut out from the least-damaged unreinforced specimens (80x80x450mm) belonging to the series of 10 unreinforced specimens investigated to get information on spalling in the first phase of this project.

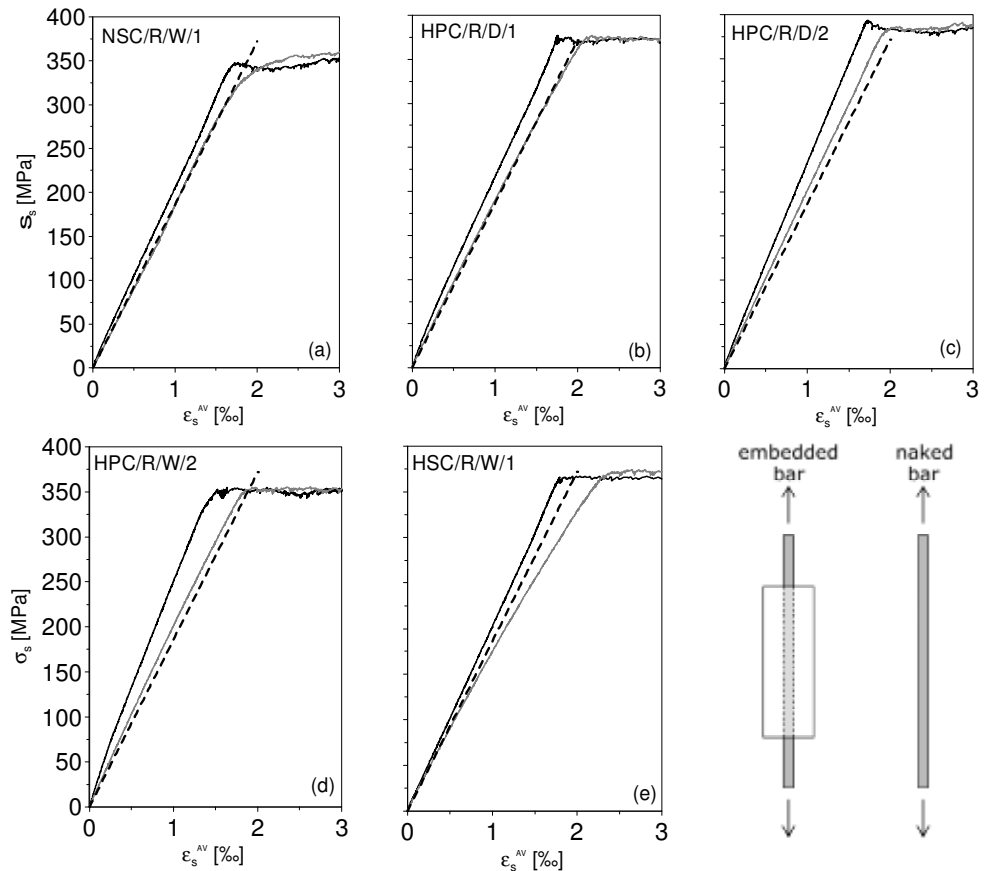


Figure 11 - Stress-strain curves of 5 specimens, exhibiting a sizable tension stiffening (thick and thin curves represent embedded and naked bars, respectively).



### Uni-dimensional slip-dependent model

In order to justify the rather limited *residual* tension stiffening found in the tests, the well-known uni-dimensional axisymmetric model based on bar slip is used in the following. The main assumptions are:

- both the bar and the concrete are subjected to a uni-axial state of stresses:  $\sigma_s(x)$  and  $\sigma_c(x)$ ;
- both materials behave linearly and elastically ( $E_s$  and  $E_c$ );
- all relevant quantities depend only on the longitudinal coordinate  $x$  (in the tension-stiffening problem, there is a symmetry with respect to the transverse mean plane and the origin of  $x$  is on this plane;  $L$  is the total length of the concrete+bar system);
- the bond stress-slip law is assumed to be linear  $\tau_B(x) = k \cdot s(x)$ , where  $k$  is the *bond stiffness* (or *bond shear modulus*).

The equation of bond and the boundary conditions are:

$$\frac{d^2s(x)}{dx^2} - k \frac{\pi\emptyset}{E_s A_s} (1 + n\rho) \cdot s(x) = 0 \quad \text{with } s(0) = 0 \text{ and } \sigma_s(L/2) = \sigma_{s0} \quad (1)$$

where:  $s$  = bar-concrete slip;  $\rho = A_s/A_c = 3.1\%$ ;  $\emptyset$  = bar diameter = 16 mm;  $k$  = bond stiffness;  $n = E_s/E_c$ ; and  $\sigma_{s0}$  = applied stress, see Fig.12a for the symbols and the conventions.

The solution in terms of bar slip  $s$  and stresses  $\tau_B$ ,  $\sigma_s$ ,  $\sigma_c$  is:

$$s(x) = \frac{\sigma_{s0}}{\lambda E_s} \frac{\text{Senh}(\lambda x)}{\text{Cosh}(\lambda L/2)} \quad (2)$$

$$\tau_b(x) = k \frac{\sigma_{s0}}{\lambda E_s} \frac{\text{Senh}(\lambda x)}{\text{Cosh}(\lambda L/2)} \quad (3)$$

$$\sigma_s(x) = \frac{\sigma_{s0}}{(1 + n\rho)} \left[ n\rho + \frac{\text{Cosh}(\lambda x)}{\text{Cosh}(\lambda L/2)} \right] \quad (4)$$

$$\sigma_c(x) = \frac{\rho\sigma_{s0}}{(1 + n\rho)} \left[ 1 - \frac{\text{Cosh}(\lambda x)}{\text{Cosh}(\lambda L/2)} \right] \quad (5)$$

where  $\lambda = \sqrt{k \frac{\pi\emptyset}{E_s A_s} (1 + n\rho)}$

Note that in residual conditions the parameters  $E_s$ ,  $E_c$ ,  $n$  and  $k$  are a function of the maximum temperature reached during the thermal cycle.

Modeling tension stiffening as an axisymmetric problem requires the prismatic specimens to be turned into equivalent cylinders, which can be done by replacing the square section (80 x 80 mm) with a circular section of the same area ( $\emptyset_c = 90$  mm).

Specimen HPC/R/D/1

In all the five specimens exhibiting tension stiffening, the bond stiffness was evaluated after heating to 640°C, by means of a sort of back analysis. In the following the Specimen HPC/R/D/1 is treated in some details.

By giving  $k$ ,  $E_s$  and  $E_c$  the following values at 640°C:  $k^{640} = 22$  MPa/mm;  $E_s^{640} = 186.3$  GPa;  $E_c^{640} = 6.2$  GPa, the diagrams of the internal forces  $N_s^{640}(x)$  and  $N_c^{640}(x)$  were obtained (Fig. 12b,  $N = 0.95 \cdot N_{max} = 71$  kN). The mean value  $N_s^*$  of  $N_s^{640}(x) = 63.3$  kN (dash-dotted line) practically coincides with the mean experimental value  $N_s^{AV} = 62.3$  kN (dashed line) obtained by multiplying the experimental mean strain  $\epsilon_s^{AV}$  by  $E_s^{640}$  and  $A_s$ .

The same occurs for the mean value  $N_c^*$  of  $N_c^{640}(x) = 7.5$  kN, that is hardly different from the mean experimental value  $N_c^{AV} = 7.5$  kN (dashed line) obtained by multiplying the mean strain  $\epsilon_c^{AV}$  by  $E_c^{640}$  and  $A_c$ . Note that in any given section the stress in the concrete depends on the distance  $r$  from the axis of the bar (Fig.12c). Such a dependency was taken care of by assuming for  $\epsilon_c$  an inverse proportionality with  $r$  (i.e.,  $\epsilon_c \approx 1/r$ ), starting from the values measured along the longitudinal edges of the specimens.

The agreement between the results yielded by the model (in terms of mean values of the axial forces in the bar,  $N_s^{AV}$ , and in the concrete,  $N_c^{AV}$ ), and those yielded by testing confirms that the value adopted for  $k^{640}$  ( $= 22$  MPa/mm) is reliable.

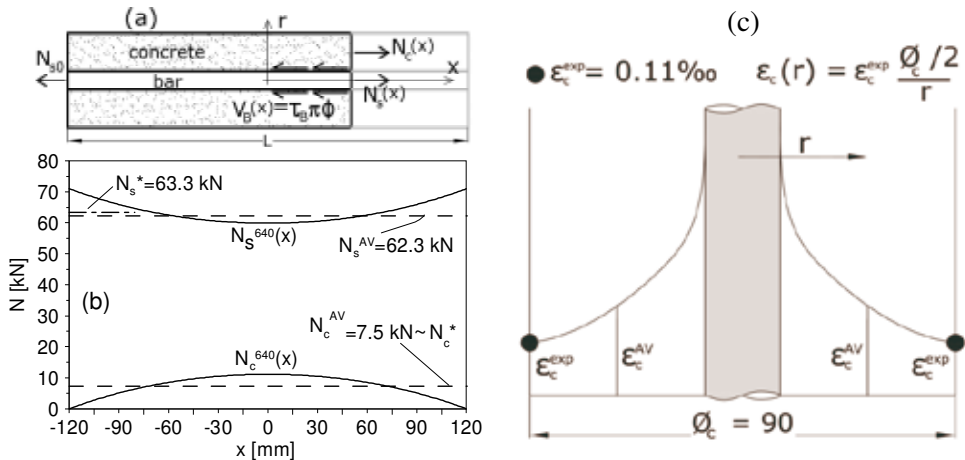


Figure 12 - Specimen HPC/R/D/1: (a) sign conventions; (b) diagrams of the axial forces in the bar  $N_s^{640}(x)$  and in the concrete  $N_c^{640}(x)$ , and mean experimental values  $N_s^{AV}$  and  $N_c^{AV}$  (dashed lines) at 95% of the load at steel yielding  $N_{max}$ ; and (c) mean diagram of the normal longitudinal strain in the concrete (the mean stress  $\sigma_c^{AV} = E_c \epsilon_c^{AV}$  in tension confirms the experimentally-measured unloading of the reinforcing bar).

Furthermore, the low value of  $k^{640}$  (compared to the values inferred from the tests in ordinary conditions) was expected, as similar or lower values are reported in the literature. For instance, El-Hawary and Hamoush (1996) measured very low values of the bond stiffness, up to one order of magnitude at 500°C with respect to 20°C. It is worth noting that the secant slope of the  $\tau_B - s$  curve given in CEB-FIP MC 90 (1990) is comprised between 50 MPa/mm for  $s \leq 0.4$  mm, and 200 MPa/mm for  $s \leq 0.1$  mm, in ordinary environmental conditions.

In Figure 13a, the axial forces in the bar and in the concrete after heating to 640°C ( $N_s^{640}$  and  $N_c^{640}$ , thick curves), and in virgin conditions (no thermal damage,  $N_s^{20}$  and  $N_c^{20}$ , thin curves) are plotted as a function of the longitudinal coordinate  $x$ , in accordance with the uniaxial slip-based model. Note the sizable decay of tension stiffening from 20°C to 640°C, following the mechanical decay of bond (see Fig. 13b). As a matter of fact, in ordinary environmental conditions tension stiffening is very effective and in the mid-span section roughly 40% of the load is resisted by the concrete, while after the exposure to 640°C concrete carries not more than 15% of the load.

In Figure 13b, the bond force per unit length  $V_B = \pi \varnothing \tau_B$  [N/mm] is plotted as a function of the longitudinal coordinate  $x$ , after a thermal cycle at 640°C (thick curve) and in virgin conditions (no thermal damage, thin curve). The much lower bond force at 640°C results from the temperature-triggered mechanical decay of bond.

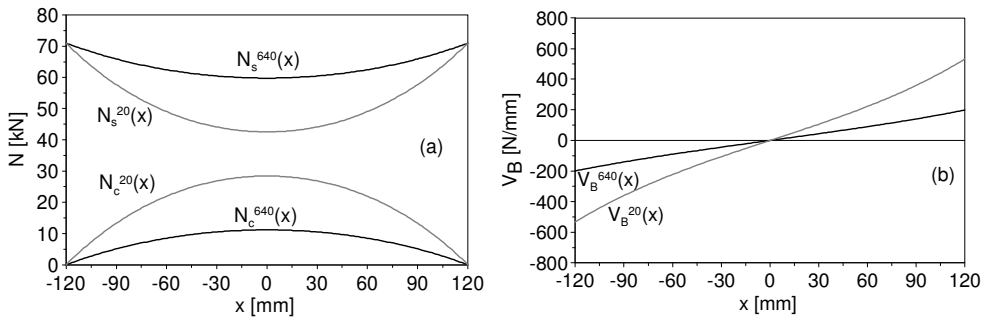


Figure 13 - Specimen HPC/R/D/1: (a) diagrams of the axial forces  $N_s(x)$  and  $N_c(x)$  after heating to 640°C and in virgin conditions (no thermal damage); and (b) diagrams of the bond force per unit length  $V_B(x)$  [N/mm], assuming  $k^{20} = 110$  MPa/mm and  $k^{640} = 22$  MPa/mm.

### Bond stiffness as a function of the temperature

The same procedure was applied to the remaining 4 specimens in order to evaluate their bond stiffness, as a function of the actual compressive strength. (As previously mentioned, the compressive strength at 640°C was evaluated by testing six specimens - two per each mix - obtained by cutting the least-damaged

unreinforced prisms past the thermal shock and the rest at 750°C; a x b = 80 x 80 mm; h = 160 mm).

In particular:

- NSC (Specimen NSC/R/W/1) :  $k_{NSC}^{640} = 19$  MPa/mm for  $f_c^{640} = 16$  MPa
- HPC (Specimens HPC/R/D/1,2 and W/2) :  $k_{HPC}^{640} = 32$  MPa/mm for  $f_c^{640} = 24$  MPa
- HSC (Specimen HSC/R/W/1) :  $k_{HSC}^{640} = 37$  MPa/mm for  $f_c^{640} = 26$  MPa

The previous results suggest a simple linearity for the relationship between the bond stiffness  $k$  and the compressive strength of the concrete  $f_c$ , be it heat damaged or not (Fig.14):

$$k = \alpha f_c \quad \text{or} \quad k^T/k^{20} = f_c^T/f_c^{20} \quad (6a, 6b)$$

The coefficient  $\alpha$  is equal to 1.31 if HSC and HPC are considered as one single class (being rather similar concretes, especially after heating) and equal to 1.35 if HPC and HSC are considered as different materials (Fig.14a,b). According to Eq.6a, the bond stiffness in virgin conditions for the three concretes examined in this project has the following values, for  $\alpha = 1.31$  (1.35):

$$k_{NSC}^{20} = 66 \text{ (69) MPa/mm}$$

$$k_{HPC}^{20} = 105 \text{ (110) MPa/mm}$$

$$k_{HSC}^{20} = 118 \text{ (122) MPa/mm}$$

which are in good agreement with the range 50-200 MPa/mm suggested by MC 90 (1990), for  $s \leq 0.4$  mm and  $s \leq 0.1$  mm, respectively.

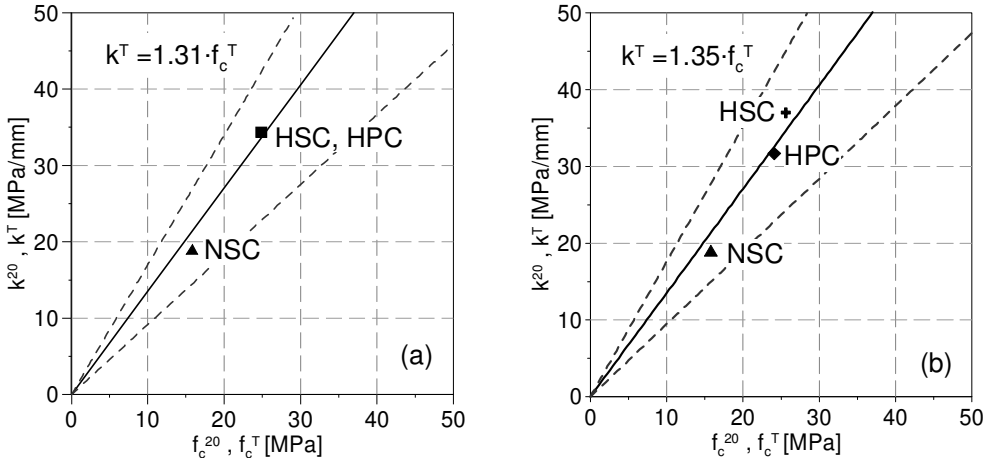


Figure 14 – Proposed linear relationship between the bond stiffness and concrete compressive strength, with/without thermal damage, considering: (a) HSC and HPC as one single class; and (b) as two different classes. The dashed lines indicate the dispersion of the results.

As indicated by the three values of  $k$  concerning the HPC specimens ( $k_{\text{HPC}}^{640} = 22, 32$  and  $42$  MPa/mm, average value  $32$  MPa/mm), the dispersion of the results is rather high for the same concrete and thermal conditions. Hence Eqs.6a,b are merely indicative of a trend, and for any given concrete strength (and temperature) a dispersion of  $\pm 30\%$  has to be expected (see the dashed lines in Fig.14).

## 6. CONCLUSIONS

Concrete spalling at high temperature is a rather elusive phenomenon, as demonstrated by the tests performed in the first phase of this study, where a number of reinforced and unreinforced prismatic specimens made of three different self-compacting concretes were subjected to a severe thermal shock to induce corner spalling. A specific procedure was proposed as well, to make the tests on spalling as systematic as possible. Only a limited number of specimens exhibited severe spalling (10%) or light spalling (10%), something unexpected, whose reasons are still under scrutiny. One possible explanation may be that the relatively small size of the specimens prevented in most cases the formation of a *moisture clog*, even if the permeability of the adiabatic surfaces (not exposed to the heat) was greatly reduced by impregnating them with silicon layers, gluing steel barriers and adding insulating layers.

A second reason – and more important in author’s mind - may be the lack of load-induced stresses and/or thermal self-stresses, the latter being small – or absent - because of the lack of geometric continuity along the adiabatic surfaces. Finally, the realistic, but rather limited moisture content did not help, as well as the lack of certain additives like microsilica.

As for the proposed set-up, both the preparation of the specimens and their introduction inside the furnace required simple and safe operations, compatible with the use of off-the-shelf furnaces.

In the second phase of this study, the reduction of tension-stiffening effectiveness after a prolonged rest at high temperature was investigated. The preliminary results presented in this paper shed some light on three aspects, that should be looked at more thoroughly:

- bond stiffness decreases sharply with the temperature, as it appears to be linearly related to the decay of the compressive strength; hence, after being exposed to temperatures in excess of  $600^{\circ}\text{C}$ , at least a 3-times decrease of bond stiffness should be expected, and even more, like in the *reference case* developed in this study;
- for the geometry of the specimens tested in this project and for the three self-compacting mixes, assuming for the materials (steel and concrete) and for bond perfect elasticity, up to 40% of the applied load is transferred to concrete via bond in virgin conditions, while only 15-25% is transferred after the exposure to  $640^{\circ}\text{C}$ ;

- in virgin conditions, the uniaxial slip-based model adopted in this study yields rather high values for the maximum bond stress (close to  $1/6 f_c^{20}$ , not incompatible with self-compacting concrete, whose very good bond properties are well documented), while both the model and the experimental results yield much lower maximum stresses after the exposure to  $640^\circ\text{C}$  (but still close to  $1/5 f_c^{640}$ ); hence, even if these rather high values are mitigated by bond nonlinearity in actual embedded bars, the ratio of the maximum bond-stress value to the compressive strength tends to remain rather constant (close to  $1/5$ - $1/6 f_c$ ), as if the heat-damaged concrete were simply a different lower-grade material, embracing a bar mostly unaffected by the heat.

Summing up, from the point of view of spalling, even during a severe fire, corner spalling (that is among the most severe types of spalling) may or may not occur, depending on the load-induced stresses and on the thermal self-stresses, that seem to play a critical role. Furthermore, the elusiveness of cover spalling makes tension stiffening during a fire an open problem. After a fire, however, in the absence of cover spalling tension stiffening is not negligible, even if it is markedly impaired. Hence, in planning any repair activity after a fire care should be taken of the residual tension stiffening and of its contribution to the actual structural stiffness.

## ACKNOWLEDGEMENTS

The experimental campaign was jointly financed by CTG-Italcementi (Bergamo, Italy), which cast all the specimens, and by the Italian Ministry of Higher Education within the National Project “Optimization of Construction Methods and Materials in Tunnel Linings” (2007-2009).

The author would like to thank Dr. Patrick Bamonte, and MS Candidates Alessandro Maggioni and Silvia Biancini, whose cooperation was instrumental in successfully performing the tests on spalling (2011) and tension stiffening (2012).

The author is also indebted to Prof. Pietro Gambarova and Prof. Roberto Felicetti (Supervisors of author’s PhD thesis) for their continuous support and understanding.

## REFERENCES

- Bamonte P., Biancini S. and Lo Monte F. (2012). Preliminary Results on Tension Stiffening in Heat-Exposed R/C Tension Members. *Proc. 4th Int. Conf. “Bond in Concrete – BIC’2012”*, ed. by John W. Cairns, Giovanni Metelli and Giovanni A. Plizzari, Brescia (Italy), June 18-20, V.2, 559-565.
- Bamonte P. and Gambarova P.G. (2012). A Study on the Mechanical Properties of Self-Compacting Concrete at High Temperature and After Cooling. *Materials and Structures*, DOI 10.1617/s11527-012-9839-9, 13 pp.

- Bamonte P., Gambarova P.G., Maggioni A. and Lo Monte F. (2011). A Proposal for an Experimental Set-Up to Investigate Fire-Induced Corner Damage in R/C Members. *Proc. 2nd Int. RILEM Workshop on "Concrete Spalling due to Fire Exposure"*, ed. by Eduard Koenders and Frank Dehn, Delft (The Netherlands), October 5-7, 369-376.
- Bingöl A.F. and Gül R. (2009). Residual Bond Strength between Steel Bars and Concrete after Elevated Temperatures. *Fire Safety Journal*, V.44, 854-859.
- CEB-FIP *Model Code 1990*. Comité Euro-International du Béton-Fédération International de la Précontrainte, Lausanne, Switzerland.
- Chiang C.H. and Tsai C.L. (2003). Time-Temperature Analysis of Bond Strength of a Rebar after Fire Exposure. *Cement and Concrete Research*, V.33, 1651-1654.
- Dehn F. and Koenders E.A.B. (editors, 2009). Concrete Spalling due to Fire Exposure. *Proc. 1<sup>st</sup> Int. Workshop*, pub. by Leipzig University, Leipzig – Germany, 548 pp.
- El-Hawary M.M. and Hamoush S.A. (1996). Bond Shear Modulus of Reinforced Concrete at High Temperatures. *Engineering Fracture Mechanics*, V.55, No.6, 991-999.
- EN 1992-1-1:2004, Eurocode 2 (2004). *Design of concrete structures - Part 1-1: General rules and rules for buildings*, European Committee for Standardization (CEN), Brussels.
- EN 1992-1-2:2004, Eurocode 2 (2004). *Design of concrete structures - Part 1-2: General rules - Structural fire design*, European Committee for Standardization (CEN), Brussels.
- Felicetti R. and Gambarova P.G. (2008). Expertise and Assessment of Materials and Structures. *FIB Bulletin No.46 "Fire Design of Concrete Structures – Structural Behaviour and Assessment"*, ed. by Luc Taerwe and Niels Peter Høj, 63-114.
- Haddad R.H., Al-Saleh R.J. and Al-Akhras N.M. (2008). Effect of Elevated Temperature on Bond between Steel Reinforcement and Fiber-Reinforced Concrete. *Fire Safety Journal*, V.43, 334-343.
- Haddad R.H. and Shannis L.G. (2004). Post-Fire Behavior of Bond between High-Strength Concrete and Reinforcing Steel. *Construction and Building Materials*, V.18, 425-435.
- Huang Z. (2010). Modelling the Bond between Concrete and Reinforcing Steel in a Fire. *Engineering Structures*, V.32, 3660-3669.
- Jansson R. and Boström L. (2008). The Influence of Pressure in the Pore System on Fire Spalling of Concrete", *Proc. 5th Int. Conf. "Structures in Fire" – SIF'08*, ed. by K.H. Tan, V.K.R. Kodur and T.H. Tan, pub. by Nanyang Tech. University, City of Singapore – Singapore, 418-429.

- Kalifa P., Chéné G. and Gallé C. (2001). High-Temperature Behaviour of HPC with Polypropylene Fibres: from Spalling to Microstructure. *Cement and Concrete Research*, V.31, 1487-1499.
- Khoury A.G. (2000). Effect of Fire on Concrete and Concrete Structures. *Progress in Structural Engineering Materials*, V.2, 429-447.
- Kodur V.K.R. and Dwaikat M.B. 2009. Fire-Induced Spalling in Concrete – State-of-the-Art and Research Needs, *Proc. 1<sup>st</sup> Int. Workshop on Concrete Spalling due to Fire Exposure*, ed. by Frank Dehn and E.A.B. Koenders, pub. by Leipzig Univ., Leipzig – Germany, 248-268.
- Koenders E.A.B. and Dehn F. (editors, 2011). *Proc. 2nd Int. RILEM Workshop on “Concrete Spalling due to Fire Exposure”*. October 5-7, Delft (the Netherlands), RILEM Publications S.A.R.L., 433 pp.
- Lublóy, E. and Balázs, G.L. (2012). Influence of High Temperatures on Bond. *Proc. 4th Int. Conf. “Bond in Concrete – BIC’2012”*, ed. by John W. Cairns, Giovanni Metelli and Giovanni A. Plizzari, Brescia (Italy), June 18-20, V.2, 567-572.
- Phan L.T. and Carino N.J. (1998). Review of Mechanical Properties of HSC at Elevated Temperature. *ASCE - Journal of Materials in Civil Engineering*, Vol.10, No.1, 58-64.
- Pimienta P., Pardon D. and Mindeguia J.C. (2010). Fire Behaviour of HPC – An Experimental Investigation on Spalling Risk, *Proc. 6th Int. Conf. “Structures in Fire” – SIF’10*, ed. by V.K.R. Kodur and J.M. Franssen, DEStech Publ. Inc., East Lansing – Mi - USA, 880-889.
- RILEM (1985). *Properties of Materials at High Temperatures: Concrete*, ed. by U. Schneider, Dept. of Civil Eng., University of Kassel (Germany), 131 pp.
- Smith K. and Atkinson T.W. (2009). Factors to Consider in Using PP Fibres for Explosive Spalling resistance. *Proc. 1<sup>st</sup> Int. Workshop on Concrete Spalling due to Fire Exposure*, ed. by F. Dehn and E.A.B. Koenders, pub. by Leipzig University, Leipzig – Germany, 364-373.
- UNI 6556 (1978). *Tests of concretes. Determination of static modulus of elasticity in compression*, Italian Standard.
- Xi Y., Bažant Z.P., Molina L. and Jennings H.M. (1994). Moisture Diffusion in Cementitious Materials. *Advances in Cement-Based Materials*, V.1, 258-266.



## DAMAGE ASSESSMENT OF CONCRETE SUBJECTED TO HIGH TEMPERATURE BY MEANS OF THE ULTRASONIC PULSE VELOCITY – UPV METHOD

Izabela Hager <sup>1</sup>, H el ene Carr e <sup>2</sup>, Katarzyna Krzemie n <sup>1</sup>

### Abstract

The results of a study on the effect that high temperature has on concrete mechanical performance are presented, with reference to the compressive strength and ultrasonic pulse velocity, in ordinary (OC) and high-performance concrete (HPC). The relationship between concrete residual compressive strength ( $f_{cT}$ ) and ultrasonic pulse velocity ( $V_T$ ) is investigated, and a regression curve  $f_{cT}(V_T)$  with a logarithmic formulation is proposed. The basic curve provided by EN 12504-4 appears to be unsuitable to describe the correlation between  $f_{cT}$  and  $V_T$  in heat-damaged concrete, since the basic curve is limited to ultrasonic pulse velocities ranging from 4000 to 4800 m/s.

In this study most of the values of the ultrasonic pulse velocity turned out to be below 4000 m/s, even for concrete specimen not exceeding 200  C. (Of course, increasingly smaller values were found at higher temperatures, up to  $T_{max} = 800^\circ\text{C}$  in this project). The damage extent in heat-affected concrete members was investigated with transducers provided with *exponential* and *cylindrical* probes, using point-by-point measurements on cores.

**KEYWORDS:** concrete, damage assessment, exponential transducers, fire damage, high temperature, ultrasonic pulse velocity.

---

<sup>1</sup> Cracow University of Technology, Institute of Building Materials and Structures, Cracow, Poland <ihager@pk.edu.pl>

<sup>2</sup> University de Pau and des Pays de l'Adour, SIAME, Anglet, France <helene.carre@univ-pau.fr>

## 1 INTRODUCTION

As it is well known, concrete structures require a damage assessment after a severe fire. The aim of post-fire investigation is to determine the extent of the damage and the thickness of the heat-damaged concrete. As the duration of actual fires is limited and concrete structures usually do not collapse in fire, most of fire-affected structures can be efficiently repaired [1]. However, the assessment of the actual safety level after a severe fire is a must to make the right decision on the strategy to be adopted in structural repairing, rehabilitation or strengthening, as an alternative to demolition. Most of the in-situ techniques available for the assessment of concrete conditions after being exposed to a fire are well-known and extensively used [1, 2, 3], but they require laboratory tests to ascertain concrete integrity. Hence, sampling the material is a pre-condition to testing.

The tests carried out on concrete cores are aimed to determine the residual mechanical properties of the damaged concrete (direct approach) or to estimate the maximum temperature that has affected the concrete during the fire (indirect approach). Such tests include various methods based on resonance frequency, ultrasonic waves, Differential Thermo-Gravimetric Analysis – TGA, Differential Thermal Analysis – DTA, Thermo-Dilatometric Analysis – TMA, X - ray diffraction, scanning microscopy, thermo-luminescence, chemical or petrographic analysis, and colourimetry [4].

## 2 ULTRASONIC PULSE VELOCITY - UPV METHOD

### 2.1 Measurement principles and applicability to heat-damaged concrete

The UPV measurements is one of the various non-destructive test methods used to evaluate concrete integrity and – more generally – the level of the damage in the material. In particular, the velocity of sound in concrete is a high-quality thermal-damage indicator, due to its sensitivity to any change of the Young modulus. As a matter of fact, the evolution of the elastic modulus because of heating is progressive, with a quasi-linear decrease coming from portlandite decomposition and CSH gel dehydration, but also from the thermal incompatibility between the aggregates (which expand) and the cement paste (which at first undergoes shrinkage and later expands). Moreover it is well known that the velocity of sound in concrete depends strongly from its moisture content. During the heating process, the moisture is progressively expelled from the material. The order in which the water is removed from heated concrete depends on the energy that binds the water and the solid fraction. Thus, free water evaporates first, followed by capillary water, physically-bound water and chemically-bound water. The process of removing the chemically-bound water (that is a part of the cement hydrates) is the last to occur. On the whole, water expulsion due to dehydration and heating strongly affects sound velocity.

When concrete is exposed to a fire, the increase of the temperature in the deeper layers of the material is rather slow and progressive. Because of its slowness (due to the rather low thermal diffusivity of concrete), this process produces significant temperature gradients between the outer layers and the inner layers of any given concrete structure (i.e. between the surface and the core). UPV technique may also be applied to determine the reduced quality of concrete by means of indirect or direct techniques on cores ([3, 4] and [4], respectively).

## 2.2 Ultrasonic measurement equipment and probes

In this research project, a PUNDIT plus - Portable Ultrasonic Non-destructive Digital Indicating Tester was used. Transducers with either exponential or cylindrical probes were used to investigate concrete conditions. (In the following the transducers are simply called *exponential transducers* or *cylindrical transducers*). Both types of transducers were characterized by the nominal frequency of 54 kHz.

The exponential transducers have exponentially-curved tips which concentrate the ultrasonic energy in a small zone (*point*). The concentrator-tip end diameter is 6 mm; hence, it may be treated as the point source of spherical longitudinal waves. These probes require no acoustic-coupling or polishing agent. Moreover, these probes can be easily applied to curved surfaces (like in cores) or to the rough surfaces of spalled concrete. The signals provided by these probes, however, are relatively weak compared to those of conventional transducers. For this type of probes a preamplifier is absolutely necessary in order to amplify the ultrasonic signal. A 20 dB preamplifier was used with the exponential probes.



Figure 1 - PUNDIT plus ultrasonic test equipment.

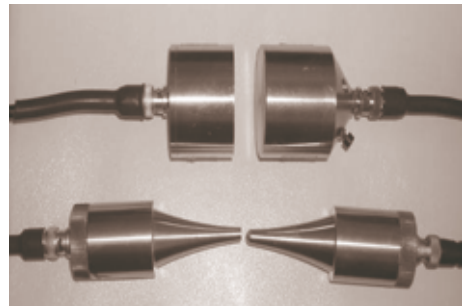


Figure 2 - The cylindrical and exponential probes, frequency of 54 kHz.

The UPV measurements can be performed very easily, but initial *calibration tests* are required to interpret the results. Trying to determine concrete strength ( $f_c$ ) just on the basis of the ultrasonic pulse velocity ( $V_T$ ) leads to unreliable results unless preliminarily the velocity data are correlated with the results of destructive

tests on the heat-affected material. For such reasons, EN 206-1 rules out the possibility of determining concrete strength only on the basis of non-destructive testing. Hence UPV tests should always accompany the destructive tests on cores. The appropriate calibration procedures (direct correlation with cores, and calibration with cores for a limited strength range using an established relationship) are described in EN 13791 standard [5]. Following this standard recommendations, the scaling approximation is based on the basic curve derived from the formula:

$$f_c = 62.5 V_T^2 - 497.5 V_T + 990 \quad (1)$$

This formula holds for any concrete where the ultrasonic pulse velocity ranges from 4000 to 4800 m/s.

In case of no calibration, concrete quality can only be estimated by measuring the ultrasonic pulse velocity in accordance with the assumptions listed in Table 1. Some studies [3, 6, 7, 8] have demonstrated the validity of the ultrasonic method in assessing the uniformity of heated concrete. According to [7], the ultrasonic method can be successfully applied in both comparative and qualitative testing, such as those performed to assess fire damage, but not in quantitative testing aimed to determine concrete strength.

### 3 OBJECTIVES AND SCOPE

In this project, the tests were performed on concrete samples heated to a temperature between 200 and 800°C. The range was limited to 800°C because some preliminary tests had shown that the damage caused by temperature up to 1000 °C was so pervasive and severe that mechanical tests were impossible.

The objective of this study was to identify the relationship between the results of non-destructive testing and the strength evolution due to heating. The results made it possible to determine the correlation between the residual compressive strength  $f_{cT}$  and the ultrasonic pulse velocity  $V_T$ .

As already mentioned, in this research project, two types of transducers were used, with either cylindrical or exponential probes, in order to make comparisons between the two types. Moreover, the results of the point-by-point analysis of the concrete cores were performed on specimens drilled from concrete members characterized by high thermal gradients in the section. In so doing, the depth of the damaged-concrete layer was determined.

#### 3.1 Materials

The tests were performed on ordinary (OC;  $f_c = 50$  MPa) and high-performance (HPC;  $f_c = 98$  MPa) concretes. Both concretes were produced with the same constituents mixed in different proportions to achieve different properties. The mix designs of the two concretes are summarised in Table 2. Note that the amount

of the aggregate is the same in both mixes, and that the mass of the cement paste and that of the mortar are roughly the same. Of course, since the water-cement ratio is very different, the content of superplasticizer was different in the two mixes to guarantee appropriate workability.

Table 1. Classification of concrete quality according to UPV [8].

Ultrasonic pulse velocity $V_T$ [m/s]	Concrete quality
> 4500	Very good
3500 – 4500	Good
3000 – 3500	Dubious
2000 – 3000	Poor
< 2000	Very poor

Table 2. Mix designs of the ordinary (OC) and high-performance (HPC) concretes.

Concrete Component	Unit	OC	HPC
Cement CEM II/A-V42.5R	kg/m <sup>3</sup>	322	478
Water	kg/m <sup>3</sup>	193	129
w/c ratio	-	0.60	0.27
River-bed aggregates			
- sand 0 - 2 mm	kg/m <sup>3</sup>		623
- gravel 2 - 8 mm	kg/m <sup>3</sup>		660
- gravel 8 - 16 mm	kg/m <sup>3</sup>		550

### 3.2 Samples and heating method

All tests were performed on concrete cubes (side = 150 mm). Concrete age at the beginning of the tests was of 120 days. The samples were heated in a programmable Nabertherm laboratory furnace at the heating rate of 0.5°C/min. Once, the reference value was reached (T = 200, 400, 500, 600, 800 °C), the temperature was kept constant for five hours to achieve a uniform distribution inside the sample. Later, the samples were cooled down in the oven (*natural cooling*) and stored for two months in ordinary conditions (T = 18°C and R.H. > 50%) prior to testing, to represent real-life conditions, since concrete diagnostics is not normally performed immediately after a fire.

As the surface of the heated samples showed no clear evidence of damage, cylindrical transducers were placed in the centre of two opposite faces of each cube. To avoid excessive energy losses at the interface between the measuring head and the concrete surface, a coupling medium was used. Subsequently, the exponential transducers were used for the measurements in the case of direct ultrasonic transmission; also in this case the probes were located in the centre of two opposite faces. After the completion of the non-destructive tests, two cubes per reference temperature were tested in compression in the case of heat-damaged specimens, while three cubes were tested in virgin conditions (no heating).

In order to check whether the damage assessment in the heated specimens subjected to severe thermal gradients is feasible, the point-by-point analysis based on exponential transducers was performed. A HP concrete slab (size = 305 x 305 x 150 mm) was fixed to the open furnace in lieu of the door (Figure 3). In this way, a temperature gradient was achieved across the slab thickness, as in the real-life conditions during a fire.

The furnace was programmed to develop the maximum thermal power in order to obtain a steep temperature distribution of the temperature inside the slab, starting from the surface directly exposed to the electrically-heated chamber. The heating gradient obtained within the slab was of  $4.3^{\circ}\text{C}/\text{mm}$ . Type K thermocouples were embedded during slab casting in its centre at depths of 10, 30, 50, 70, 90 and 110 mm. A LUMEL KD7 data acquisition station was used and all signals were recorded at 60s intervals. The sample was heated until the surface temperature reached  $900^{\circ}\text{C}$ . Figure 3 shows the temperature evolution within the HPC slab. The in-time and space temperature measurement allowed the full monitoring of the thermal field. After heating, the cores were extracted by drilling the slab and later were tested by the direct transmission.

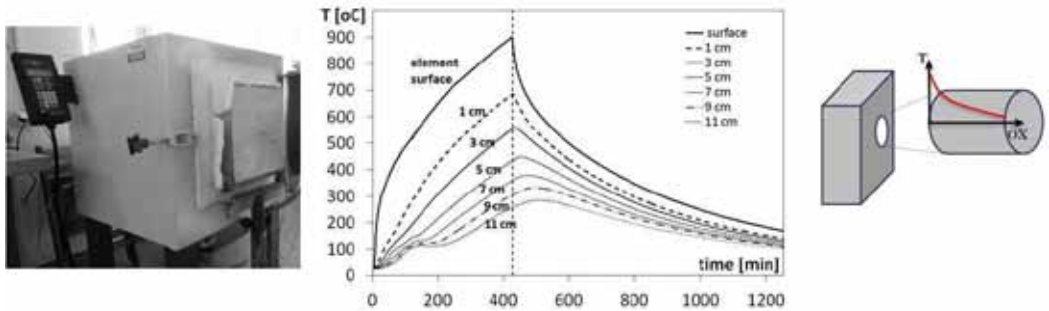


Figure 3 - HPC slab mounted at the mouth of the furnace: (a) temperature-time curves at different depth values; and (b) slab coring.

## 4 RESULTS ANALYSIS AND DISCUSSION

### 4.1 Results of uniformly-heated cubic samples

For both ordinary and high-performance concretes a gradual compressive strength decrease was observed with the temperature (Figure 4 [9]).

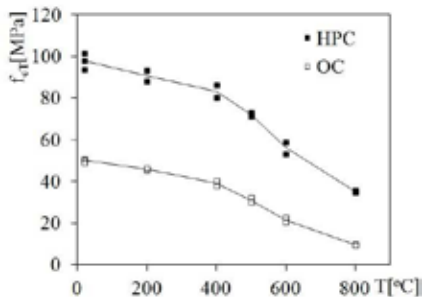


Figure 4. Impact of temperature on residual compressive strength (OC and HPC).

This is primarily a consequence of the progressive dehydration of the CSH gel, the breakdown of portlandite and the destruction of the contact zone between the shrinking cement paste and the expanding aggregate. Figure 4 illustrates the change in residual compressive strength values as a function of temperature as determined using a destructive method [9].

For all specimens the transit time of the ultrasonic waves was measured to determine the sound velocity. The results of ultrasonic pulse velocity measurements were obtained by using both the cylindrical and the exponential probes (Figure 2). In spite of the use of a preamplifier in the case of exponential probes, the velocities measured with these probes were significantly lower than those determined with the use of cylindrical probes, something that was attributed to an erroneous assumption concerning the distance travelled by the sound in the case of the exponential transducers (Figure 5). In all the tests with exponential transducers (performed on uniformly-damaged cubes, side  $a = 150$  mm), the velocity was measured over the distance AB (Figure 5) and the time of travelling measured with PUNDIT device was of  $t_{AB}$ . Hence the distance and the travelling time included also the stainless-steel tips. A close examination of the travelling times in the concrete and in the steel tips allowed to evaluate the difference between the travelling time from A to B and that across the concrete ( $\delta = 17.38$   $\mu$ s). This correction was subsequently implemented in all the measurements performed by means of exponential transducers.

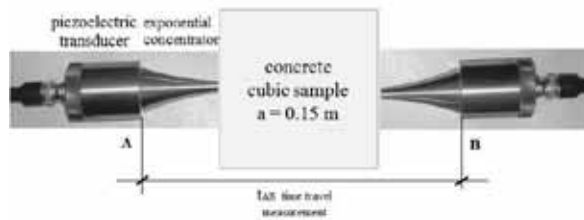


Figure 5 – Measurement of the travelling time using exponential transducers.

When the correction factor  $\delta$  was taken into account, a good agreement was found between the measurements performed with cylindrical and exponential transducers, see Figures 6 for both ordinary and high-performance concretes, instrumented with either cylindrical or exponential probes.

For undamaged (no heating) concrete the ultrasonic pulse velocity was of 4180 m/s in the OC and 4870 m/s in the HPC. Similarly as in the case of the compressive strength, heating caused a gradual reduction of the pulse velocity. In samples heated to the maximum temperature of 800°C, the velocities measured with the cylindrical transducers were 1050 m/s and 1670 mm/s, respectively. In order to justify the travel-time delay, an oscilloscope (Picoscope 4224) was used to visualise the ultrasonic wave form.

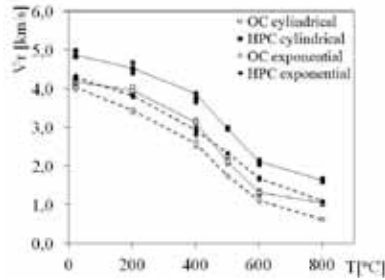


Figure 6 - Effect of the temperature on the ultrasonic pulse velocity (OC and HPC).

The PUNDIT ultrasonic device was fitted up with cylindrical and exponential transducers. The cylindrical probes were zeroed and the travelling time of the wave form was recorded using the oscilloscope when the two probes were in contact. Afterwards, the exponential probes were mounted and the device was zeroed again. The signals recorded after zeroing are presented in Figure 7. In spite of zeroing, the delay in the travelling time was systematically observed in the case of exponential probes. (The delay was close to 22  $\mu$ s).

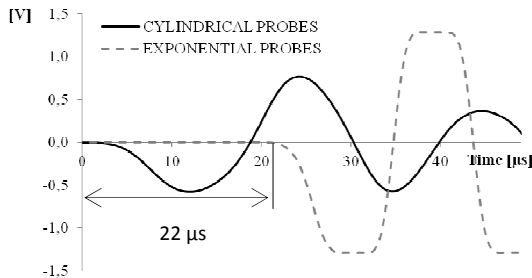


Figure 7 - Typical signals obtained with an experimental setup fitted up with an oscilloscope; the signals were recorded with the two probes in contact.

## 4.2 Decay factors

In Figure 8, the *reduction coefficients* for the compressive strength ( $D_{fc}$ ) and the ultrasonic pulse velocity ( $D_V$ ) are plotted for both heated OC and HPC concrete, as a means to quantify the heat-induced decay. These coefficients are formulated as indicated by Eqs. 2 and 3:

$$D_{fc} = 1 - f_{cT}/f_{c20^{\circ}\text{C}} \quad D_V = 1 - V_T/V_{20^{\circ}\text{C}} \quad (2,3)$$

These graphs show that the ultrasonic method is an effective tool for assessing qualitatively the damage caused by high temperature. When compared to the actual damage ( $D_{fc}$ ) measured using a destructive method, the damage coefficient  $D_V$  identified with the ultrasonic method is slightly higher, with the exception of



800°C. From the engineering perspective the overestimated  $D_V$  values mean that the ultrasonic method allows for the safe assessment of the concrete deterioration.

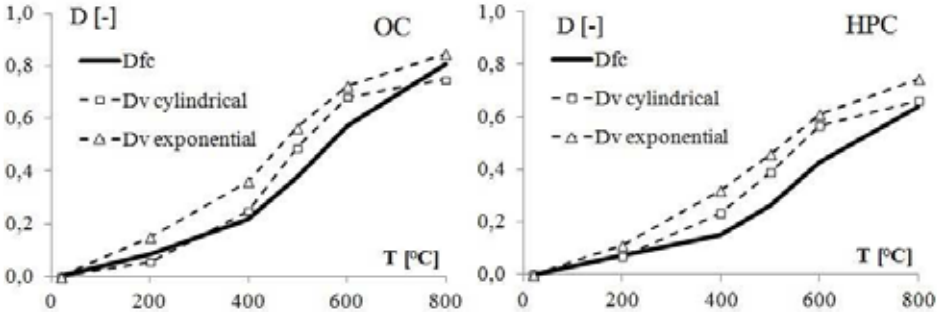


Figure 8 – Plots of the reduction coefficients of the compressive strength ( $D_{fc}$ ) and of the ultrasonic pulse velocity ( $D_V$ ) as a function of temperature: (a) ordinary concrete (OC); and (b) high performance concrete (HPC).

### 4.3 Regression curve

In both concretes the evolution of the ultrasonic pulse velocity as a function of the temperature is almost the same, with either cylindrical or exponential probes. This similarity can be found also in Figures 9, where the  $f_{cT}(V_T)$  relationships for OC and HPC are plotted.

A satisfactory agreement between the measurements made with cylindrical and exponential transducers may be observed, provided that the correction of the travel time  $\delta$  is applied. The best fitting line was determined by regression analysis on the data pairs that were obtained in the experimental programme. The tests results were fitted by using logarithmic functions.

The equations of the regression curves and the coefficients,  $R^2$ , describing the quality of the fitting are also plotted in Figures 9.

The regression curves for the exponential transducers were then corrected by adjusting the transit time by the factor  $\delta$  of 17.34  $\mu s$ . As a result, corrected logarithmic curves were obtained:

$$f_{cV} = 44.86 \ln(V_T) + 25.15 \tag{4}$$

$$f_{cV} = 22.09 \ln(V_T) + 15.81 \tag{5}$$

The comparison of the test curves obtained in this study and the basic curve prescribed in EN 13791 [5] shows a total discrepancy (Figure 9). Indeed, only the non-heated samples (both concretes) and the high-performance concrete samples heated to 200 °C are close to the velocity range of 4000 – 4000 m/s required by the standard.

The basic curve envisaged by the standard can therefore only be used for high-quality concrete. However, after being heated to 400 °C, concrete samples still exhibit a sizeable residual strength, close to 39 MPa in OC and 83 MPa in HPC.

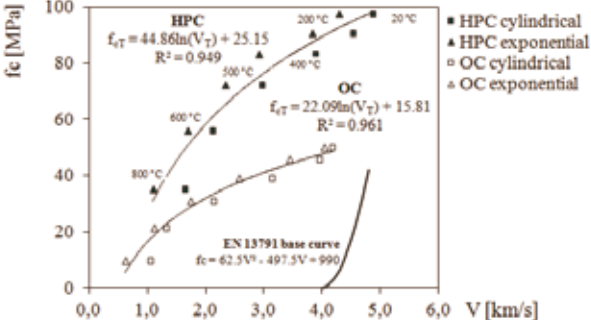


Figure 9 - Regression curves concerning the relationship between the compressive strength and the ultrasonic pulse velocity, for OC and HPC, at increasing temperature.

Because of the limitations concerning the velocity range, the base curve has little practical meaning.

According to the classification shown in Table 1, all concrete samples heated to more than 600°C and tested with the ultrasonic method showed a poor or very poor quality. Furthermore, ordinary-concrete samples (OC) turned from good to dubious quality at temperatures as low as 400°C, in accordance with the classification proposed in [8].

This is nothing new, as it is well known that concrete mechanical decay starts between 400 and 500°C, with certain concretes more affected by high temperature (for instance those containing highly siliceous aggregates [11]) and other concretes little affected up to 600°C (for instance those containing basalt aggregates [12]).

### 5 POINT-BY-POINT ANALYSES OF CONCRETE CORES

Three cores (diameter Ø 80 mm and length 150 mm) were drilled from the HPC slab heated according to the procedure presented in Chapter 3.2. For each of the cores the point-by-point measurements were taken following two axes at an interval of 10 mm. When making the measurement, the probe tip was rubbed against the surface of the concrete until the minimum transit time was obtained. The results of the direct transmission time are presented in Figure 10 as a function of the distance from the heated surface.

The lower-quality outer layer turned out to have a 80 mm depth, which corresponds to the maximum temperature of 500 °C. The temperature of 500°C is slightly greater than that of portlandite decomposition  $[Ca(OH)_2 \rightarrow CaO + H_2O\uparrow]$ .

The CaO created in this reaction – or resulting from *calcination* above 700°C (dissociation of calcium carbonate into calcium oxide and carbon dioxide) - weakens structural members after cooling – and often makes them useless - mainly because of the ensuing combination of CaO with the water contained in the atmosphere, that produces an expansion in the concrete, accompanied by further damage. From the design view point, the 500°C isotherm subdivides the section into two parts, that enveloped by the isotherm itself, where the concrete is little or no damaged, and that outside the isotherm where the concrete is more or less severely damaged.

The so-called *500°C isotherm method* (proposed also in EC2 “Fire Design”) allows the designer to neglect the concrete outside this isotherm and to consider the concrete inside the isotherm as undamaged. It is worth noting that lower isotherms have been proposed for high-performance concrete and higher isotherms for special checks (as in the case of buckling [13]). As for the reinforcement, the bars inside the isotherm should be considered as unaffected by the heat, while those outside the isotherm have the mechanical properties corresponding to their own temperature.

The local values of the velocity were measured point-by-point along the height of the core, cut from the thermally damaged slab and were also determined on the basis of the travelling time. Subsequently, after the UPV tests, the end sections of the cores were ground and polished to make them plane and parallel, before testing in compression.

The mean compressive strength of the HPC cores (Figure 11) was of 34.6 MPa (mean of 35.6, 32.2 and 36.1MPa).

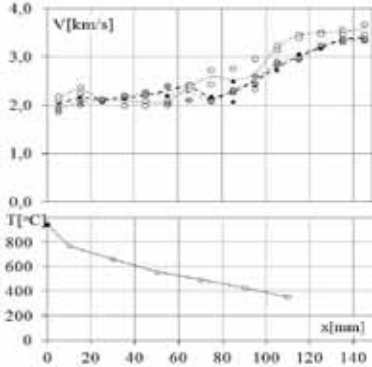


Figure 10 - Point-by-point analysis of concrete on cores drilled from a thermally-damaged HPC slab.

Figure 11 – Cores extracted from HPC before and after being tested in compression.

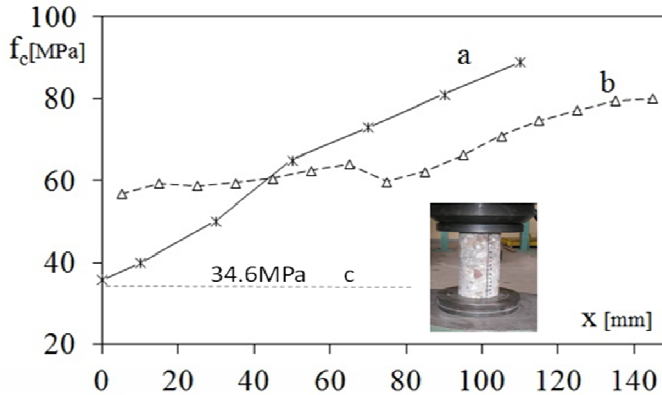


Figure 12 – Plots of the *local compressive strength* at the depth of 1 mm determined on the basis (a) of the maximum temperature measured in the section starting from the heated surface; (b) of UPV point-by-point analysis using exponential transducers; and (c)  $f_c$  value obtained by testing in direct compression the HPC cores (34.6 MPa).

From the ultrasonic pulse velocity measurements made on HPC with exponential transducers, the lower-quality layer close to the heated surface exhibited an ultrasonic speed of 2000 m/s (Figure 10). For this layer the calculated *local values of the compressive strength* from the calibration curve (Figure 12, curve *b*) was close to 60 MPa.

The value of the *local compressive strength* was also evaluated inside the slab starting from the maximum temperature measured in any given section, using the  $f_{cT}(T)$  relationship (Figure 4).

At the depth of 1 mm, the temperature of 770°C was recorded which corresponds to a compressive-strength value of 40 MPa. The *local compressive strength* determined at 1 mm depth is plotted in Figure 12, curve *a*.

Both techniques used to evaluate indirectly the residual compressive strength (on the basis of the maximum temperature and via UPV) overestimated the strength  $f_c$  (40 and 60 MPa, respectively) compared to the compressive strength determined by testing the cores sawn from the thermally-damaged slabs (34.6 MPa, Figure 12, value indicated with *c*).

## 6 CONCLUSIONS

In view of the test methods presented in this paper and of their results, the following conclusions seem justified:

- the temperature reached by the concrete has a clear and straightforward influence on the ultrasonic pulse velocity up to 800°C, as a consequence of concrete mechanical decay in compression;

- the values of the ultrasonic pulse velocity differ markedly between ordinary and high-performance concrete; however, the general evolution of the ultrasonic velocity with the temperature is similar in both cases;
- measuring the ultrasonic pulse velocity by means of exponential transducers provided with a preamplifier systematically brings in lower values for the ultrasonic velocity than in the case of cylindrical transducers; a correction of the travelling time must be applied when exponential transducers are used;
- the basic curve proposed in EN 13791:2007 is not appropriate in describing the relationship between the compressive strength and the ultrasonic velocity in heated concrete, even more since the range of the ultrasonic velocity implied by the basic curve is rather limited; other empirical equations should be used;
- logarithmic regression curves for heated concrete are proposed for a range of the ultrasonic velocity comprised between 1000 and 4800 m/s; a satisfactory agreement between the measurements made with cylindrical and exponential transducers has been observed, provided that the travelling time of the ultrasonic waves is appropriately corrected;
- comparing the decay factors of the compressive strength and of the ultrasonic pulse velocity demonstrates that using ultrasonic measurements may be an effective method to assess the quality of heat-affected concrete; from an engineering perspective, the rather overestimated decay brought in by the ultrasonic method (with either cylindrical or exponential transducers) leads to a safe qualitative assessment of concrete damage;
- the point-by-point ultrasonic measurements performed in this research project on cores drilled from thermally-damaged concrete slabs show that the concrete layer mostly affected by heat is subjected to a temperature close to 500°C, this being a demonstration that exponential transducers applied to cores allow the determination of the 500°C isotherm, that is the *reference isotherm* in R/C design in fire;
- the quantitative assessment of the compressive strength in thermally-damaged concrete using exponential transducers applied to cores extracted from thermally-damaged slabs tends to provide higher values for the compressive strength than those determined by testing the cores in direct compression.

Last but not least, the relationships formulated in this study are valid for a typical concrete containing natural river-bed aggregates; further tests are needed to determine the relationship between the compressive strength and the ultrasonic pulse velocity for other types of aggregates.

## ACKNOWLEDGEMENTS

This study was supported by the Polish National Research Centre (Grant N N506 045 040).

## REFERENCES

- [1] The Concrete Society (2008). *Assessment, Design and Repair of Fire-Damaged Concrete Structures*, Technical Report No. 68, London (UK), 80 pp.
- [2] Fib Task Group 4.3 (2008). *Fire Design of Concrete Structures – Structural Behavior and Assessment*, State-of-Art Report prepared by Task Group 4.3 “Fire Design of Concrete Structures, 209 pp.
- [3] Felicetti R. and Colombo M. (2007). “New Non-Destructive Techniques for the Assessment of Fire-Damaged Concrete Structures”, *Fire Safety Journal*, Vol. 42, Issues 6-7, Sept.-Oct., pp. 461-472.
- [4] LCPC – Laboratoire Central des Ponts et Chaussées (2005). *Présentation des techniques de diagnostic de l'état d'un béton soumis à un incendie*, Décembre 2005, No.62, Paris (France), 114 pp.
- [5] EN 13791:2007 (2007). *Assessment of in-situ compressive strength in structures and precast concrete components*, 28 pp.
- [6] Abraham O. and Dérobert X. (2003). “Non-Destructive Testing of Fired Tunnel Walls: the Mont-Blanc Tunnel Case Study”, *NDT & E International*, Volume 36, No. 6, pp. 411-418
- [7] Stawiski B. (2006). “Attempt to Estimate Fire Damage to Concrete Building Structures”, *Archives of Civil and Mechanical Engineering*, Vol.VI, No. 4, pp. 23-29.
- [8] Whitehurst E.A. (1966). *Evaluation of Concrete Properties from Sonic Tests*, ACI Monograph No. 2, ACT, Detroit (Michigan, USA), 94 pp.
- [9] Hager I. (2011). “Compressive Strength and Ultrasonic Pulse Velocity in Ordinary and High-Performance Concretes Subjected to High Temperature” (in Polish), *Zeszyty Naukowe Politechniki Rzeszowskiej. Budownictwo i Inżynieria Środowiska (Scientific Papers of Rzeszow University of Technology. Civil and Environmental Engineering)*, Vol. 276, pp. 307-312.
- [10] EN 12504-4:2004 (2004). *Testing concrete. Determination of ultrasonic pulse velocity*, 16 pp.
- [11] Felicetti R. and Gambarova P.G. (1998). “Effects of High Temperature on the Residual Compressive Strength of High-Strength Siliceous Concretes”, *ACI-Materials Journal*, Vol.95, No.4, pp. 395-406.
- [12] Bamonte P., Cangiano S., Felicetti R., Gambarova P.G. et al. (2007). “Thermo-Mechanical Characterization of Concrete Mixes Suitable for the Rehabilitation of Fire-Damaged Tunnel Linings”, *Studies and Researches Vol.26 and 27, Politecnico di Milano, pub. by Starrylink (Brescia)*, pp. 233-286 and 235-280.
- [13] Buchanan A.H. (2001). *Structural Design for Fire Safety*, John Wiley & Sons, LTD, 421 pp.

## SYMBOLS

- $D_{fc}$ ,  $D_v$  = reduction coefficients of the compressive strength and of the ultrasonic pulse velocity;
- $f_c$ ,  $f_{cT}$  = concrete compressive strength on cylinders, in virgin conditions and after heating to the temperature T;
- $f_{cv}$  = concrete compressive strength obtained by measuring the ultrasonic pulse velocity;
- T = temperature;
- $V_T$  = ultrasonic pulse velocity;
- $\delta$  = difference between the travelling time of the ultrasonic waves from probe-to-probe and across the concrete sample.





## **A HANDY MODEL FOR SIMULATING THE HYDRATION PHENOMENA IN CONCRETE : FORMULATION AND APPLICATION TO RECYCLED-AGGREGATE CONCRETE**

Eduardus A. B. Koenders<sup>1,2</sup> and Enzo Martinelli<sup>3</sup>

### **ABSTRACT**

Concrete mechanical properties are strictly controlled by the physical and chemical phenomena induced by the hydration reactions developing during the setting and hardening phases. Hence, modelling such phenomena is instrumental in predicting the time evolution of the relevant mechanical properties and their possible correlations with both the mix constituents and the actual curing conditions. Particularly, heat transfer due to the exothermal hydration reaction of cement is the key physical phenomenon occurring during concrete hardening.

This paper presents a consistent theoretical formulation to model the heat-flow occurring in hardening concrete mixes. The model is based on the Fourier equation of heat transfer: an adiabatic hydration curve is assumed to describe the heat source deriving by the hydration reaction and the well-known Arrhenius approach is adopted to describe the relationship between reaction kinetics in ideal adiabatic conditions and in the actual temperature field developed inside the concrete sample. A Finite-Difference numerical solution is presented as a further relevant contribution. The model is formulated under the simplified assumption of 1D heat flow and the proposed numerical solution is particularly suitable to be implemented into a common spreadsheet, this being - in the authors' opinion – a very attractive feature. Temperature measurements obtained for the samples of two different mixes, cured under both adiabatic and semi-adiabatic conditions, are considered for validating the proposed model.

Finally, the application of the proposed model to simulate the hydration processes occurring in Recycled Aggregates Concrete (RAC) allows to clarify the role that some key parameters play on the mechanical properties of RAC. It is an attempt to introduce a more fundamental approach in the analysis of RAC's mechanical properties, that are often investigated under a merely empirical perspective.

**Keywords:** hydration (of cement), heat flow, recycled aggregates, numerical modelling (of cement hydration).

---

<sup>1</sup> Visiting Professor, COPPE, Universidade Federal do Rio de Janeiro, Rio de Janeiro, Brazil.

<sup>2</sup> Associate Professor, Microlab, Delft University of Technology, Delft, The Netherlands.

<sup>3</sup> Assistant Professor, DICiv, Università degli Studi di Salerno, Fisciano (Salerno), Italy.

# 1 INTRODUCTION

The use of recycled aggregates and alternative binders is one of the key strategic choices to reduce the environmental impact of construction activities and enhance the sustainability of the related industrial processes. However, the key concrete properties can be significantly affected by replacing ordinary constituents with other ones, and a change in the performance of structural systems can be potentially expected (Naik, 2005).

Monitoring in more detail the hardening processes developing in concrete mixes made with either recycled aggregates or alternative binders is a possible fundamental approach to evaluate the altered performance of such sustainable concretes (van Breugel, 1991). Particularly, the key aspects of the actual hydration mechanisms (Bullard et al., 2011) can be observed by measuring the so-called *degree of hydration* of concrete (Koenders, 1997) and by investigating its possible correlations with the development of the relevant material properties, such as compressive strength and elastic modulus (Lokhorst, 1999; De Schutter, 1996, 2004; Laube 1991; Pane and Hansen, 2005).

As a matter of fact, the degree of hydration can be easily measured only in the case of adiabatic conditions, as in that case it is directly related to the temperature development (Koenders, 1997; De Schutter, 1996). On the contrary, in more general conditions, advanced techniques are generally required to directly evaluate the degree of hydration during concrete setting and hardening (Feng et al., 2004).

In principle, modern techniques, such as those based on Finite Elements (FEs) featuring heat transfer and hardening simulation capabilities, can be employed to model the hydration process and the time evolution of the temperature during the hardening phase (Jeong and Zollinger, 2006). However, investigating the hydration processes actually developing in the concrete subjected to a (partial) replacement of the cement and/or aggregates would be a more fundamental approach to understand the relationships among the mechanical properties, the actual mix composition and the curing conditions. This would lead to an extension of some analytical formulations concerning the temperature development and the hydration process already available for ordinary concrete mixes, with the objective of predicting the time evolution of the relevant material properties (de Schutter and Taerwe, 1996; Schindler and Folliard, 2005). This approach gives a deeper insight into the dependency of materials properties on the basic parameters that control the progress of the hydration process and implicitly accounts for the internal moisture changes introduced by the uncontrolled addition of extra water by the saturated and porous recycled aggregates. In this way, the direct correlation between the degree of hydration and the outcome of the formulae for the development of material's properties can be systematically envisioned (Lokhorst, 1999).

This paper presents the complete theoretical formulation and the numerical implementation of a model aimed at simulating the cement hydration process and

its consequences on the relevant mechanical properties of concrete (Laube, 1991; Lokhorst, 1999). Particularly, based on the widely-accepted Arrhenius model of chemical kinetics (van Breugel, 1991; Koenders, 1997, De Schutter 1995) and the well-established theory of heat flow (Narasimhan, 1999), the proposed model is a general and handy tool for estimating the degree of hydration from simple temperature measurements carried out in non-adiabatic conditions during the setting and hardening phases. In principle, the model can be applied to both ordinary concretes and concrete with partial replacements of Portland cement or the addition of recycled aggregates.

The application of the proposed model to calibrate sound correlations between the relevant material's properties, taking into account the effect of concrete mixtures and the possible replacement of Portland cement by pozzolans and/or the aggregates by recycled ones, is one of the key novelties of the present paper, as the behaviour of this type of concrete is generally investigated through direct experimental testing and empirical considerations.

In this framework, Section 2 outlines the theoretical formulation of the physical/chemical problem under consideration. For the sake of simplicity, and to comply with the aim of this paper, such a model is formulated in a 1D space domain and its validity is clearly limited to the current state of scientific knowledge.

A consistent numerical solution based on the Finite Difference (FD) technique is developed in Section 3 with the declared aim of pointing out all the mathematical details needed by Readers who are possibly interested in writing their own numerical code: in this regard, the numerical solution is particularly fit for a spreadsheet-based solution.

The proposed model is validated in Section 4 by considering the experimental results obtained on two concrete mixes, for which temperature measurements are available in both adiabatic and non-adiabatic conditions.

Finally, Section 5 shows a relevant application of the proposed model aimed at unveiling the possible correlation between the compressive strength and the hydration-related parameters, such as the degree of hydration, for the so-called Recycled Aggregate Concrete (RAC).

## **2 THEORETICAL FORMULATION**

This section describes the main physical phenomena occurring during the concrete setting and hardening phases; it outlines both the key theoretical assumptions and the mathematical formulations currently available to describe such phenomena. They are mainly related to the heat production due to the exothermal nature of the cement hydration. Moreover, the heat-flow generated in a hardening concrete sample subjected to non-adiabatic boundary conditions should be modelled to properly describe the effect of the time evolution of the temperature inside the concrete sample.

## 2.1 Adiabatic heat development of concrete

The chemical reactions which occur during the concrete setting and hardening phases are mainly driven by the hydration process of the cement grains within the concrete mix. The exothermal hydration reaction of the cement produces a significant amount of heat inside the hardening concrete.

The actual status of the cement hydration reaction can be described by the so-called *degree of hydration*  $\alpha_h(t)$  which is defined as the ratio between the amount of hydrated cement at any given time  $t$  and the original amount of cement in the mix. Since the amount of hydrated cement at any time  $t$  is proportional to the total amount of heat  $Q(t)$  produced up to that same time,  $\alpha_h(t)$  can be defined as follows:

$$\alpha_h(t) = \frac{Q(t)}{Q_{max}} \quad (1)$$

where  $Q_{max}$  is the heat potentially produced by the hydration of all the cement grains actually present in the concrete mix under consideration.

The heat produced by the hydration reaction is significantly influenced by the temperature which depends on sample size and boundary conditions, as well as by the produced heat itself, that acts as a controlling parameter. Particularly, a simple analytical relationship can be written between the degree of hydration  $\alpha_h$  - or the heat  $Q_a(t)$  produced in the same conditions - and the corresponding temperature variation  $\Delta T_a$  in the ideal case of adiabatic conditions (Koenders, 2005):

$$\Delta T_a(t) = \frac{C}{\rho_c c_c} \cdot Q_a(t) = \frac{C \cdot Q_{max}}{\rho_c c_c} \cdot \alpha_h(t) \quad (2)$$

where

$C$  = cement content per unit volume [ $\text{g}/\text{m}^3$ ];

$c_c$  = specific heat of concrete [ $\text{J}/\text{gK}$ ];

$\rho_c$  = specific mass of concrete [ $\text{g}/\text{m}^3$ ].

Thus, the current temperature achieved within the hardening concrete can be expressed by introducing in Eq. 1 the definition of  $\alpha_h$  (Eq. 2):

$$T_a(t) = T_R + \Delta T_a(t) = T_R + \frac{C \cdot Q_{max}}{\rho_c c_c} \cdot \alpha_h(t) \quad (3)$$

where  $T_R$  is the room temperature.

Since the hydration process results in a partial reaction of cement grains which produces the reaction heat denoted as  $Q_{max}^* \leq Q_{max}$ , the following relationship can be introduced between  $Q_{max}^*$  and  $Q_{max}$  by considering the definition of  $\alpha_h$  reported in Eq.1:

$$Q_{max}^* = Q_{max} \cdot \left[ \lim_{t \rightarrow \infty} \alpha_h(t) \right] = Q_{max} \cdot \alpha_{h,max} \quad (4)$$

where  $\alpha_{h,max}$  is the degree of hydration theoretically achieved at the end of the hydration process (namely, in the limit case of  $t \rightarrow \infty$ ). Thus, the degree of hydration in adiabatic conditions (consistently denoted as  $\alpha_{a,h}$ ) can also be expressed in terms of temperature increase:

$$\alpha_{a,h}(t) = \frac{Q_a(t)}{Q_{max}} = \frac{\Delta T_a(t)}{\Delta T_{a,max}} \cdot \alpha_{h,max} \quad (5)$$

where  $\Delta T_{a,max}$  is the asymptotic value achieved by the temperature in adiabatic conditions.

Finally, based on the results of tests performed on concrete samples cured in adiabatic conditions, the following analytical expression was proposed to approximate the observed time evolution of the heat  $Q_a(t)$  (van Breugel, 1991):

$$Q_a(t) = Q_{max}^* \cdot e^{-\left(\frac{\tau}{t}\right)^\beta} \quad (6)$$

where  $Q_{max}^*$  is the total heat produced by the hydration reaction in adiabatic conditions, and  $\tau$  and  $\beta$  control the shape of the function  $Q_a(t)$ .

## 2.2 Heat flow and degree of hydration during setting and hardening

Since concrete is generally cured in non-adiabatic conditions, a heat-flow develops throughout the concrete mass during the setting and hardening phases, resulting in a transient temperature field.

As a matter of principle, the non-stationary heat conduction problem characterising the thermal behaviour of concrete during the setting and hardening phases can be described by means of the well-known Fourier equation (Narashimhan, 1999). In the case considered in this study (1D geometry, Figure 1), such a Partial Differential Equation (PDE) has the following analytical expression:

$$\rho_c c_c \frac{\partial T}{\partial t} = \lambda_c \cdot \frac{\partial^2 T}{\partial x^2} + q_c(x,t) \quad (7)$$

where

$\lambda_c$  = heat conduction coefficient [W/mK];

T = temperature field in concrete [K];

$t$  = time [s];  
 $q_c$  = rate of heat source [ $J/m^3s$ ].  
 and

$$q_c(x,t) = C \cdot \frac{dQ_c}{dt} \tag{8}$$

where  $Q_c$  describes the heat produced by the hydration reaction per unit mass of cement in general (non-adiabatic) conditions.

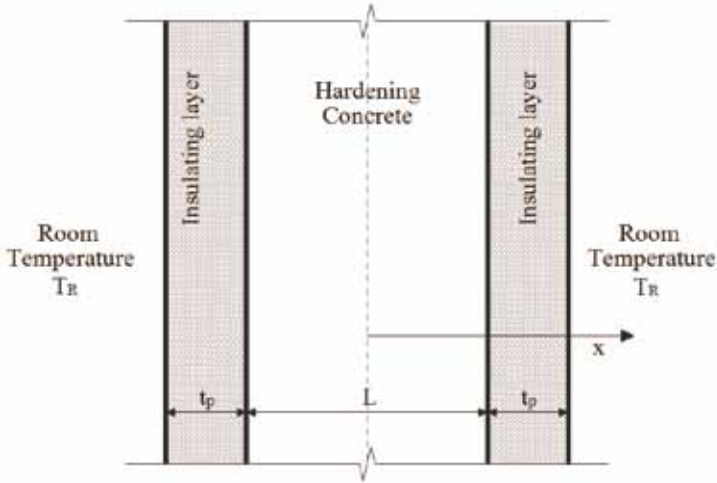


Figure 1 – Geometrical description of the 1D problem.

As already mentioned in subsection 2.1, the heat source  $q_c$  is significantly affected by the actual values of the temperature developed inside the concrete sample. Then, since the temperature itself depends on the produced heat, a clear feedback effect can be recognised between  $q_c$  and  $T$ . Therefore, the effect of the absolute temperature  $T$  on the rate  $V(T)$  of the chemical reaction can be generally expressed through the well-known Arrhenius equation, which can be analytically described by the following relationship (van Breugel, 1991):

$$V(T) = A_V e^{-\frac{E_A}{R \cdot T}} \tag{9}$$

where  $A_V$  is a reference rate value,  $E_A$  is the apparent activation energy (usually expressed in  $J/mol$ ) and  $R$  is the universal gas constant ( $R \approx 8.3145 J/molK$ ). In principle, the values of  $A_V$  and  $E_A$  can be determined by measuring the rate  $V$  under two different temperature values. However, the following applications will be based on assuming  $E_A = 33000 J/mol$  for hardening concrete, according to the experimental results currently available in the scientific literature (van Breugel, 2004; Kada-Benameur et al, 2000; D'Aloia and Chanvillard, 2002).

The Arrhenius equation (Eq. 9) is useful to express the relationship between the actual heat production rate  $q_c(T)$  and the corresponding one  $q_a(T_a)$ , which should have been measured under ideally adiabatic conditions at the same stage of the hydration reaction (Figure 1). Thus, if the semi-adiabatic process has achieved the degree of hydration  $\alpha_h(t)$  at the time  $t$ , an equivalent time  $t_{eq}$  can be defined to identify the corresponding status of the hydration reaction in adiabatic conditions:

$$Q_a(t_{eq}) = \alpha_h(t) \cdot Q_{max} \quad (1)$$

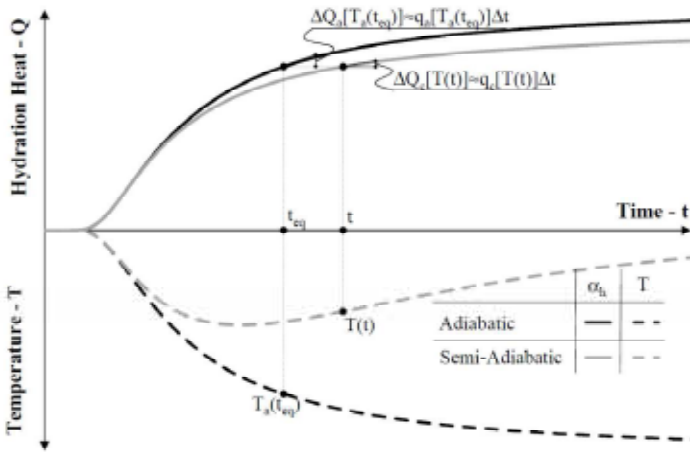


Figure 1 – Hydration heat produced and temperature developed in adiabatic and non-adiabatic conditions.

The actual analytical expression of  $t_{eq}$  depends on the analytical form chosen for describing the function  $Q_a(t_{eq})$ . For instance, the following expression corresponds to the function reported in Eq. 6, respectively:

$$e^{-\left(\frac{\tau}{t_{eq}}\right)^\beta} = \frac{\alpha_h(t)}{\alpha_{h,max}} \quad t_{eq} = \frac{\tau}{\left\{-\ln\left[\frac{\alpha_h(t)}{\alpha_{h,max}}\right]\right\}^{\frac{1}{\beta}}} \quad (2)$$

Although, in principle, the amount of heat  $Q_c(T)$  produced by any given hydration process is equal to that correspondingly generated in the ideal adiabatic process up to the time  $t_{eq}$ , the two temperatures  $T$  and  $T_a$  developed in the two systems at time  $t$  and  $t_{eq}$  are not the same, as a result of the heat transfer phenomena taking place in non-adiabatic conditions. Having underlined this point, a clear relationship can be stated through Eq. 9, between the rate of heat production in the two above-mentioned conditions:

$$\frac{q_c [T(t)]}{q_a [T_a(t_{eq})]} = \frac{e^{-\frac{E_A}{R \cdot T(t)}}}{e^{-\frac{E_A}{R \cdot T_a(t_{eq})}}} = e^{-\frac{E_A}{R} \cdot \frac{T_a(t_{eq}) - T(t)}{T_a(t_{eq}) \cdot T(t)}} \quad (12)$$

As clearly demonstrated by De Schutter and Taerwe (1996), the Arrhenius approach is more accurate for concretes whose binder is mainly made of Portland Cement (e.g., CEM I and CEM II according to the EN 197-1, 2011), as a unique dominant reaction phase, i.e.  $C_3S$ , can be recognised in such materials.

Under this limitation, the following analytical expression can be determined for the Partial Differential Equation (PDE) describing the heat flow in hardening concrete by introducing in Eq. 7 the expression of  $q_c [T(t)]$  derived by Eq. 12:

$$\rho_c c_c \frac{\partial T}{\partial t} = \lambda_c \cdot \frac{\partial^2 T}{\partial x^2} + q_a [T_a(t_{eq})] \cdot e^{-\frac{E_A}{R} \cdot \frac{T_a(t_{eq}) - T(t)}{T_a(t_{eq}) \cdot T(t)}} \quad (13)$$

where the flow source in adiabatic conditions can be determined as follows:

$$q_a [T_a(t_{eq})] = C \cdot \left. \frac{dQ_a}{dt} \right|_{t=t_{eq}} \quad (14)$$

It is worth highlighting that Eqs. 13 and 14 involve the degree of hydration through the definition of  $t_{eq}$  provided by Eq. 11 and, then, they clearly assume an integral-differential structure. They can be solved numerically, as explained in Section 3, once proper initial and boundary conditions are defined.

The initial conditions are rather simple, as room temperature  $T_R$  has to be imposed to the entire space domain at  $t=0$ :

$$T(x, t=0) = T_R \quad (15)$$

The boundary conditions at the two external sides can be directly imposed if the time evolution of temperatures  $T_{left}(t)$  and  $T_{right}(t)$  measured there during the hydration process are available:

$$T(x = -L/2, t) = T_{left}(t) \quad T(x = L/2, t) = T_{right}(t) \quad (16)$$

where  $L$  is the characteristic length of the 1D system under consideration. More often, an insulating layer bounds the two external surfaces of the concrete specimen (Figure 1). If  $t_p$  is the thickness of such a layer, and  $\lambda_p$  is its heat



conduction coefficient, the boundary conditions can be derived by expressing the continuity of the heat flows  $q_{left}(t)$  and  $q_{right}(t)$  throughout the insulation-concrete interfaces:

$$q_{left}(t) = \lambda_p \cdot \frac{T_{left}(t) - T_R}{t_p} = \lambda_c \cdot \left. \frac{\partial T}{\partial x} \right|_{x=\frac{L}{2}} \quad (17)$$

$$q_{right}(t) = \lambda_p \cdot \frac{T_{right}(t) - T_R}{t_p} = -\lambda_c \cdot \left. \frac{\partial T}{\partial x} \right|_{x=\frac{L}{2}} \quad (18)$$

Thus, Eqs. 13 and 14, the initial conditions described by Eq. 13, and the boundary conditions provided by Eqs. 17 and 18, completely simulate the 1D heat-flow occurring within the hardening concrete element described in Figure 1. It is worth highlighting that the expressions of Eqs. 17 and 18 for the boundary conditions are implicitly based on neglecting possible convection effects at the external side of the insulating layer, as can be approximately assumed in the laboratory conditions under consideration.

### 3 A SPREADSHEET-TYPE NUMERICAL SOLUTION

The equations outlined in Section 2 can be solved numerically through a Finite Difference (FD) approach which is described in subsection 3.1. Furthermore, such a solution for the heat-flow problem and the further calculations needed to determine the degree of hydration and the corresponding mechanical properties of concrete is described in details like in a “numerical recipe” (subsection 3.2).

#### 3.1 Finite difference solution

The integral-differential Eqs. 13 and 14 which describe the heat-diffusion process throughout the hardening concrete can be turned into a convenient FD expression in each node of a time-space mesh. Particularly, the space domain is subdivided in  $n_s$  spaces and, then,  $(n_s+1)$  nodes whose distance is:

$$\Delta x = \frac{L}{n_s} . \quad (19)$$

Moreover, a time increment  $\Delta t$  is assumed to develop a time-explicit solution scheme. Figure 3 shows the FD discretization of the space-time domain of relevance for the problem under consideration. Then, the FD expression of Eq. 13 is obtained by introducing the central-difference scheme for the space derivative and the forward - or backward - scheme for the time derivative. Particularly, the

following FD expressions are adopted herein to approximate the second space derivative and the first time derivative of the temperature field  $T(x,t)$  in the  $(n,k)$ -node of the space-time domain:

$$\left[ \frac{\partial^2 T}{\partial x^2} \right]_{n,k} \approx \frac{T_{n+1,k} - 2 \cdot T_{n,k} + T_{n-1,k}}{\Delta x^2} \quad (20)$$

$$\left[ \frac{\partial T}{\partial t} \right]_{n,k} \approx \frac{T_{n,k+1} - T_{n,k}}{\Delta t} \quad (21)$$

where a forward scheme is actually assumed for the latter, leading to an explicit numerically integration scheme.

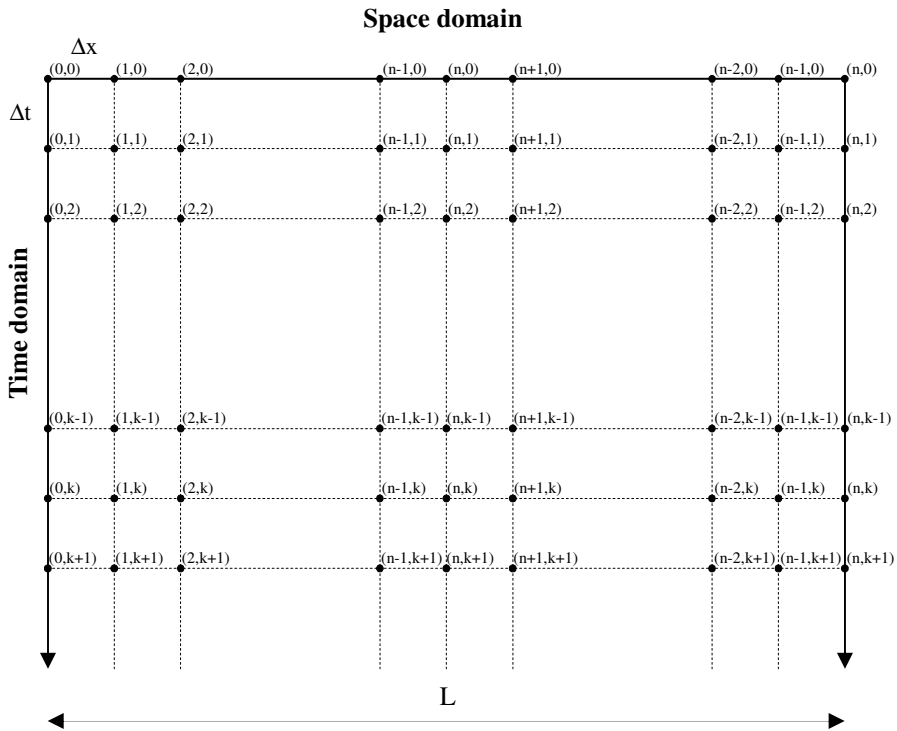


Figure 3 – Finite-difference scheme integration in time and space.

Thus, the following FD algebraic equation can be determined by introducing Eqs. 20 and 21 in Eq. 13 to express the value  $T_{n,k+1}$  of the temperature field in the  $(n,k+1)$ -node:

$$T_{n,k+1} = T_{n,k} + a_c \cdot \frac{\Delta t}{\Delta x^2} \cdot (T_{n+1,k} - 2 \cdot T_{n,k} + T_{n-1,k}) + \frac{\Delta Q_a [T_a(t_{eq,n,k})]}{\rho_c c_c} \cdot e^{-\frac{E_A}{R} \left( \frac{T_{a,eq,n,k} - T_{n,k}}{T_{a,eq,n,k} \cdot T_{n,k}} \right)} \quad (22)$$

where  $n$  ranges from  $1$  to  $(n_s-1)$  and

$$a_c = \frac{\lambda_c}{\rho_c c_c} \quad (23)$$

and then  $T_{a,eq,n,k}$  is the temperature which would have been developed in adiabatic conditions at the time  $t_{eq,n,k}$  defined in Eq. 11, through the analytical expression described by Eq. 10. In fact, it can be determined through Eq. 3, which can be finally expressed as follows, taking into account the Eqs. 4 and 5:

$$T_{a,eq,n,k} = T_a(t_{eq,n,k}) = T_R + \frac{C}{\rho_c c_c} \cdot Q_a(t_{eq,n,k}) \quad (24)$$

Particularly, the definition of  $t_{eq,n,k}$  is based in the degree of hydration  $\alpha_{h,n,k}$  developed up to the end of the  $k$ -th step of the forward time integration. It can be evaluated as follows:

$$q_{c,n,k+1} = q_c(T_{n,k+1}) = q_a(T_{a,eq,n,k+1}) \cdot e^{-\frac{E_A}{R} \frac{T_{a,eq,n,k+1} - T_{n,k+1}}{T_{a,eq,n,k+1} \cdot T_{n,k+1}}} \quad (25)$$

$$Q_{c,n,k+1} = \sum_{i=1}^{k+1} \frac{q_{c,n,i} + q_{c,n,i-1}}{2} \cdot \Delta t \quad (26)$$

$$Q_{c,k+1} = \frac{1}{L} \sum_{n=1}^{n_s} \frac{Q_{c,n,k+1} + Q_{c,n-1,k+1}}{2} \cdot \Delta x \quad (27)$$

$$\alpha_{h,n,k+1} = \frac{Q_{c,n,k+1}}{Q_{max}} \quad \alpha_{h,k+1} = \frac{Q_{c,k+1}}{Q_{max}} \quad (28)$$

The initial conditions can be easily imposed as follows according to Eq. 13:

$$T_{n,0} = T_R \quad \text{for } n = 0, \dots, n_s \quad (29)$$

Moreover, the boundary conditions in space can be turned into a convenient FD form by transforming the analytical expressions reported in Eqs. 17 and 18:

$$\begin{aligned}
\lambda_p \cdot \frac{T_R - T_{0,k+1}}{t_p} &= \frac{\lambda_p \cdot T_R + \frac{\lambda_c}{\Delta x} \cdot T_{1,k+1}}{t_p} \\
= \lambda_c \cdot \frac{T_{1,k+1} - T_{0,k+1}}{\Delta x} &\Rightarrow T_{0,k+1} = \frac{\lambda_p \cdot T_R + \frac{\lambda_c}{\Delta x} \cdot T_{1,k+1}}{\frac{\lambda_p}{t_p} + \frac{\lambda_c}{\Delta x}}
\end{aligned} \tag{30}$$

$$\begin{aligned}
\lambda_p \cdot \frac{T_{n_s,k+1} - T_R}{t_p} &= \frac{\lambda_p \cdot T_R + \frac{\lambda_c}{\Delta x} \cdot T_{n_s-1,k+1}}{t_p} \\
-\lambda_c \cdot \frac{T_{n_s,k+1} - T_{n_s-1,k+1}}{\Delta x} &\Rightarrow T_{n_s,k+1} = \frac{\lambda_p \cdot T_R + \frac{\lambda_c}{\Delta x} \cdot T_{n_s-1,k+1}}{\frac{\lambda_p}{t_p} + \frac{\lambda_c}{\Delta x}}
\end{aligned} \tag{31}$$

Eq. 22 demonstrates that the outlined numerical procedure is explicit in space and time, as the value  $T_{n,k}$  depends on the values of the temperature field at both time  $t_{k+1}$  and  $t_k$ . However, for each instant  $t_k$  the value of the temperature field in  $(n_s+1)$  nodes should be determined. In fact,  $(n_s-1)$  field equations (Eq. 22) along with the two boundary conditions (Eqs. 30 and 31) balance the number of unknowns. In order to achieve a stable solution for the explicit numerical integration scheme considered in this approach, a convergence criterion has to be introduced. For standard steady state 1D schematisations for time integration, the following criterion holds for the maximum timestep  $\Delta t$  (van Kan et al., 2008; Laube, 1991):

$$\Delta t \leq \frac{\Delta x^2}{2a_c} . \tag{32}$$

### 3.2 Further details about the numerical implementation

The proposed numerical solution of the heat-flow problem (subsection 3.1) can be easily implemented in either a high-level programming language or a spreadsheet tool. In this second case each node of the space-time domain represented in Figure 3 can correspond to a cell of the spreadsheet and Eqs. 22, 30 and 31 can be solved iteratively for each time step. The numerical scheme described by Eq. 22 can be copied in all cells corresponding to the internal nodes of the FD mesh represented in Figure 3. The boundary conditions in space are imposed by considering at each time step Eqs. 30 and 31 on the left and right lateral borders, respectively. The starting conditions of the PDE represent the actual temperature of the concrete mix. This is the temperature after mixing and represents the initial condition of the elements  $T(x,t=0)=T_R$ .

As long as hydration proceeds ( $Q_d(t)>0$ ), heat will be generated according to the heat curve described by Eq. 6 and the temperature will be transferred to the boundaries according to the heat flow (Eq. 22). The continuous increase of heat

leads to a corresponding increase in temperature. From the calculated temperature field the distribution of the degree of hydration can be calculated at the end of the current time step through Eqs. 25-28. The degree of hydration depends on the development of the temperature in the different cells and indicate the amount of the hydration products formed in the concrete during the hydration process.

Finally, a flow-chart of the proposed numerical “recipe” is shown in Figure 4 which describes the sequence of the operations possibly needed to implement the proposed numerical simulation. The time integration ends when the amount of heat rate production in the last iteration falls below a given user-defined tolerance represented by the parameter  $\epsilon_Q$  reported in the last diamond-shaped block.

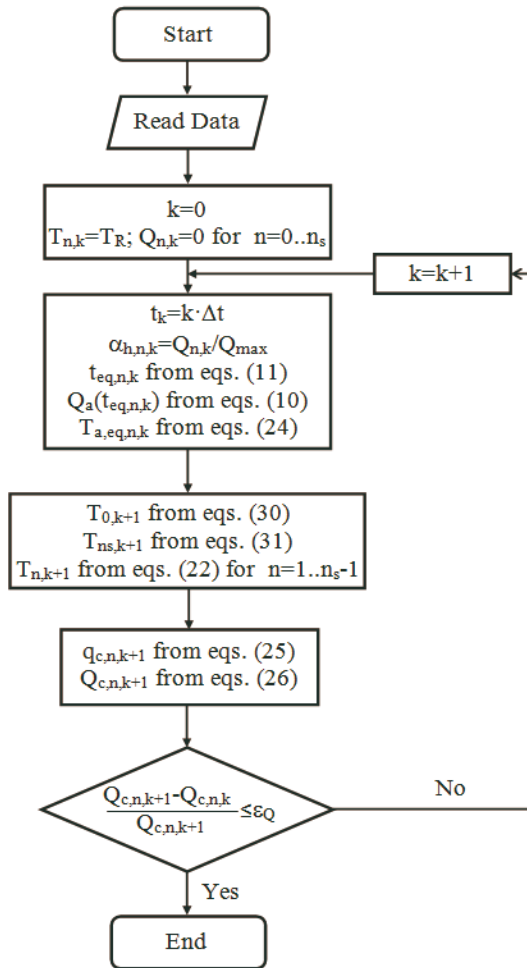


Figure 4 – Flow-chart of the proposed numerical procedure.

## 4 VALIDATION

The model presented in Sections 2 and 3 needs to be validated to assess its capability to describe the hydration process in both adiabatic and non-adiabatic conditions.

To this end, the necessary experimental data characterising the hydration process of four concrete mixtures (water-cement ratio  $w/c = 0.4$ ) were obtained from temperature measurements conducted at Delft University of Technology (Delft, The Netherlands) and reported by Koenders (2005). However, since the proposed model relies upon the Arrhenius function for controlling the rate of the hydration heat mentioned in subsection 2.2, and is - therefore - particularly accurate for applications with Portland Cement-based concretes (Voglis et al., 2005; Wang et al., 2010), only the samples indicated as “Mixture 3” and “Mixture 4” are considered in the present study. In fact, Mixture 3 and Mixture 4 contain  $450 \text{ kg/m}^3$  of CEM I 32.5 (+ 5% of silica-fume) and  $450 \text{ kg/m}^3$  of CEM II/A (no silica fume), respectively.

From the experimental data, a set of temperature measurements carried out on different concrete samples cured at both adiabatic and non-adiabatic conditions was available (Koenders, 2005).

### 4.1 Outline of the experimental test setups

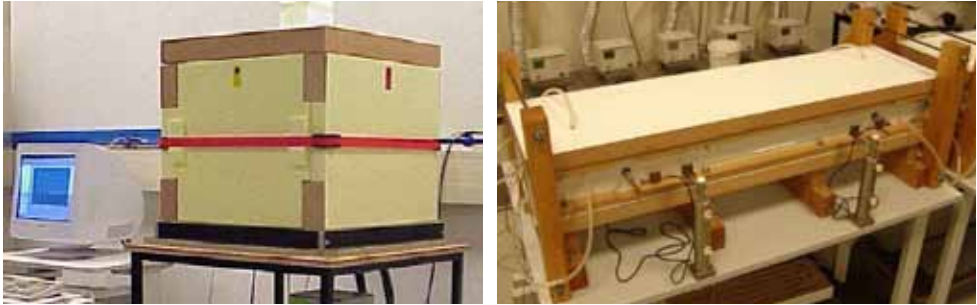
Figure 5 shows the experimental equipment employed at Delft University of Technology in the tests outlined in this Section. The adiabatic hydration curve was measured from a freshly-cast concrete cube for which the thermal boundary conditions were controlled in such a way that no heat transfer occurred and all the heat generated inside the concrete cube contributed to the rise of the temperature (and, then, boosted to the hydration reaction).

The test set-up to determine the adiabatic hydration curve consisted of an insulated mould whose thermal boundary conditions were controlled by means of a computer and a cryostat unit (Figure 5a).

To measure the semi-adiabatic temperature evolution, the dummy setup of the Thermal Stress Testing Machine (TSTM) was used, see Figure 5b. The temperature evolution was measured in the centre of the sample and at mid-height; the thickness and width of the sample were 100 mm and 150 mm, respectively (Figure 5b).

The compressive strength was measured by testing a number of cubic specimens (size  $150 \times 150 \times 150 \text{ mm}^3$ , according to EN 12390-3, 2009) at 1, 3, 7 and 28 days (3 cubes for each age). After casting, the cubes were vibrated and covered with a plastic sheet.

The semi-adiabatic temperature evolution was measured by means of the test setup shown in Figure 5b.



(a) Adiabatic conditions

(b) Semi-adiabatic conditions

Figure 5 – Experimental equipment (Koenders, 2005).

#### 4.2 Temperature experiments and numerical predictions

To validate the flow and hydration model formulated in Sections 2 and 3, the temperature evolution was simulated with reference to both adiabatic and semi-adiabatic conditions.

Figure 6 describes the time evolution of the temperature measured in the samples of Mixtures 3 and 4 in the above-described conditions.

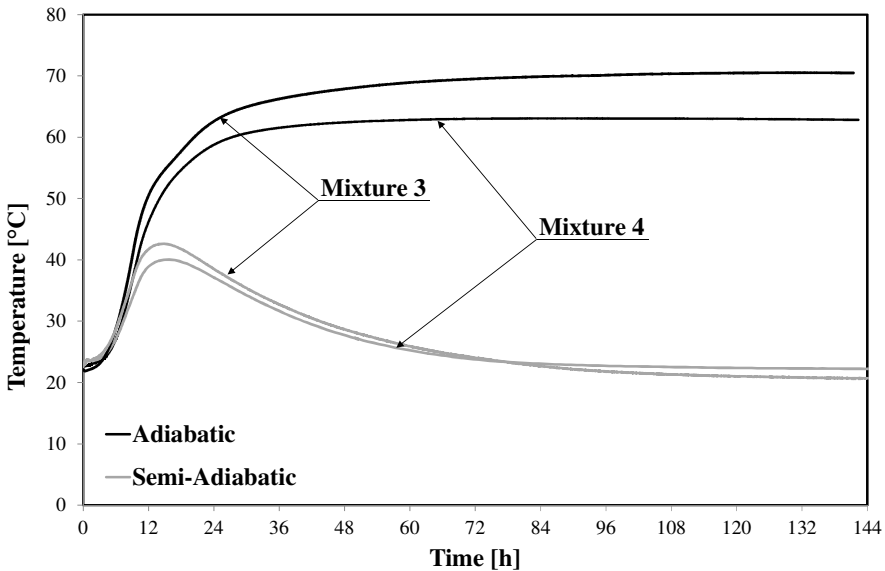


Figure 6 – Experimental results: time evolution of the temperature (Koenders, 2005).

The adiabatic temperature curves show the upper boundaries of the temperature evolution, whereas the temperature measurements in semi-adiabatic conditions

show a maximum after which the temperature turns back to the actual room value. Both the adiabatic and semi-adiabatic temperature are simulated with the proposed flow model using the input values given in Table 1. Note that the simulation was carried out by fine-tuning the values of  $\tau$  and  $\beta$  according to an Inverse Identification Procedure (Faella et al., 2009).

Table 1 – Overview of the input data used to simulate Mixture 3 and 4 (Koenders, 2005).

<b>Input data for the flow model</b>	<b>Symbol</b>	<b>Mixture 3</b>	<b>Mixture 4</b>
Maximum degree of hydration [-]	$\alpha_{h,max}$	0.78	0.77
Maximum potential heat [kJ/kg]	$Q_{max}$	350	300
Cement content [kg/m <sup>3</sup> ]	$C$	450	450
Density times specific heat [kJ/m <sup>3</sup> K]	$\rho_c c_c$	2500	2500
Heat conduction coefficient [W/mK]	$\lambda_c$	2.5	2.5
Heat diffusion coefficient [m <sup>2</sup> /sK]	$a_c$	1E-6	1E-6
Time increment [s]	$\Delta t$	20	20
Space increment [m]	$\Delta x$	0.0075	0.0075
Insulation thickness [m]	$t_p$	0.04	0.04
Heat conduction coefficient [W/mK]	$\lambda_p$	0.125	0.125
Apparent activation energy [J/mol]	$E_A$	33000	33000
Universal gas constant [J/molK]	$R$	8.31	8.31
Coefficient for adiabatic function in Eq. 6 [h]	$\tau$	8.5	9
Coefficient for adiabatic function in Eq. 6 [-]	$\beta$	1.6	2.1

The results are plotted in Figure 7 and 8. The model describes very well the evolution of the thermal field resulting from the experimental campaign.

In the simulations, the adiabatic temperature evolution acts as the heat source (Eq. 6), whereas the semi-adiabatic temperature evolution represents the response of the model. The potential of the model to simulate in a single run the temperature evolution in both adiabatic and semi-adiabatic conditions is clearly demonstrated.



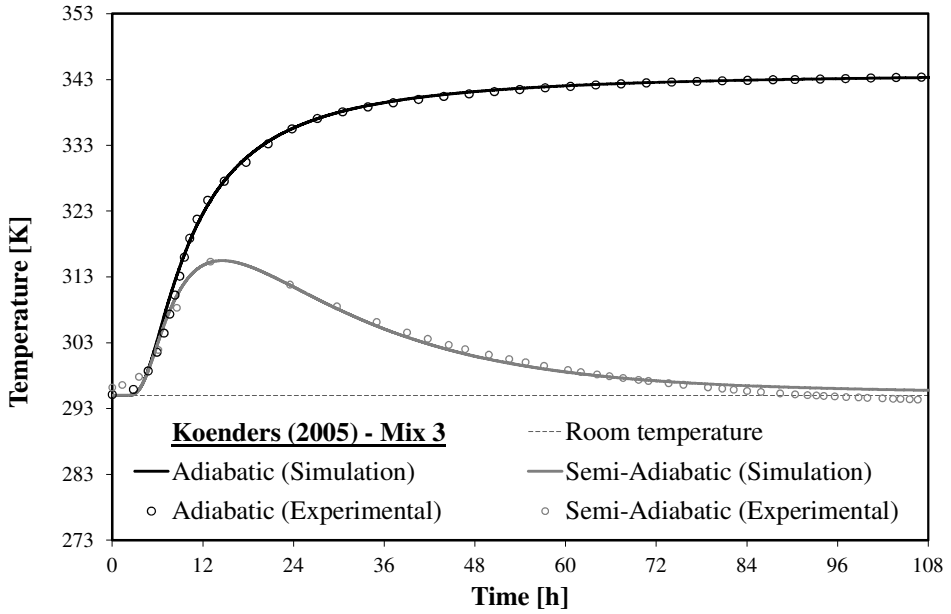


Figure 7 – Mixture 3: time evolution of the temperature (adiabatic heat production according to Eq. 7).

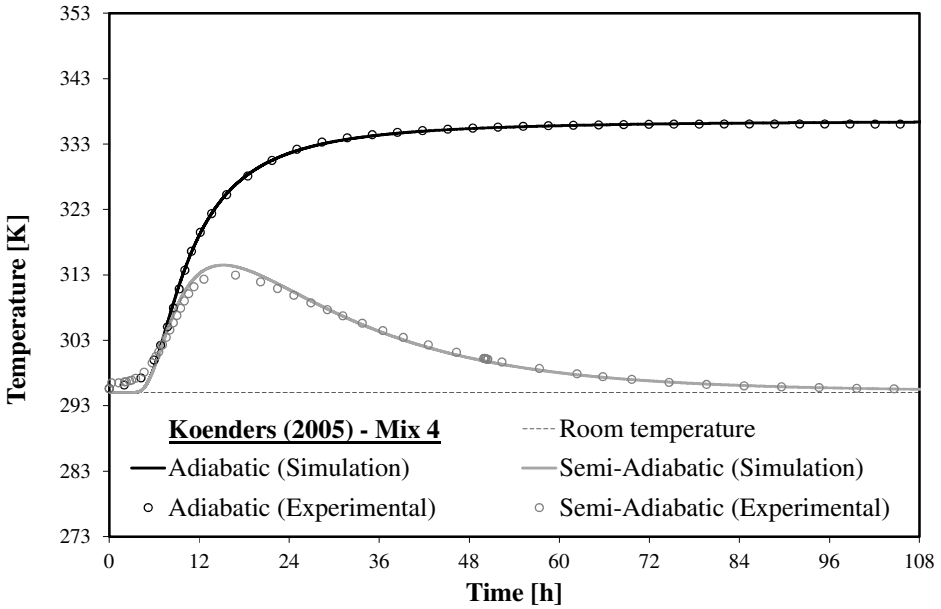


Figure 8 – Mixture 4: time evolution of the temperature (adiabatic heat production according to Eq. 7).

## 5 APPLICATION TO RECYCLED-AGGREGATE CONCRETE

As already mentioned at the beginning of this paper, the formulation of the present model was mainly intended as an operational tool to investigate the hydration processes developing in concrete mixes with recycled aggregates and alternative binders. Based on the fundamental correlation between hydration processes and mechanical properties, such an investigation is intended to achieve a more fundamental understanding of the possible influence that the aforementioned constituents have on the final mechanical properties of concrete.

Hence, a first application of the proposed hydration model deals with the behaviour of some samples of Recycled Aggregate Concrete (RAC) whose mixes are described in subsection 5.1. The time evolution of both the compressive strength measured on cubes at different curing times and the temperature fields developed inside each cube during the hardening phase are reported in subsection 5.2. The experimental results reported therein are later employed in subsection 5.3 to identify the hydration reactions through a back analysis of such results carried out by means of the model proposed in this paper. Finally, subsection 5.4 is devoted to unveil the correlation between the (simulated) degree of hydration in the concrete samples tested in compression and the corresponding strength observed in such tests.

### 5.1 Description of the RAC mixes under consideration

As already explained in Section 2, monitoring the time evolution of temperature in the samples of curing concrete is an indirect way for scrutinising their hydration processes. This procedure was carried out on the samples of four concrete mixes made by using recycled concrete aggregate with a 30% replacement ratio of the natural aggregate (basically, a significant part of the coarse aggregate). Table 2 reports the specific features of the four mixes under consideration which are characterised by two values of the (nominal) w/c ratio and two different moisture conditions (either saturated or dry, denoted as "SAT" and "DRY", respectively) for the aggregates.

Table 2 – Key parameters of the Recycled Aggregate Concrete (RCA) mixes.

MIX	CEM I [kg/m <sup>3</sup> ]	Free water [l/m <sup>3</sup> ]
0.45SAT	410	185
0.60SAT	310	185
0.45DRY	410	185
0.60DRY	310	185

As a matter of fact, it is widely known in the scientific literature that recycled aggregates are characterised by a higher water absorption capability. Hence, their moisture conditions may have a significant influence in modifying the water content actually available to cement hydration, and may affect the final physical and mechanical properties of concrete. Thus, the four mixes outlined in Table 2 were considered to investigate the influence of these two parameters (namely, water-cement ratio and moisture conditions of the recycled aggregates) on the behaviour of RAC samples.

### 5.2 Time evolution of temperature and compressive strength in RAC samples

Since the compressive strength is the key mechanical property of concrete, some cubic samples were tested at different curing ages to monitor the time evolution of concrete strength  $R_c$ .

Figure 9 shows the results in terms of average compressive strength  $R_{cm}$  and confirms that - as expected - the w/c ratio plays an important role. However, Figure 9 clearly shows the role played by moisture conditions of the recycled aggregates employed in the concrete mixes. In this regard, dry aggregates led to higher values of  $R_{cm}$  through the whole investigated time span and for both the w/c ratios considered in this study. Moreover, the mechanical properties developed in the sample of 0.60DRY mixes are slightly higher (but rather close) to the corresponding ones measured for 0.45SAT, as well as the time evolution of temperatures developed during the curing phase.

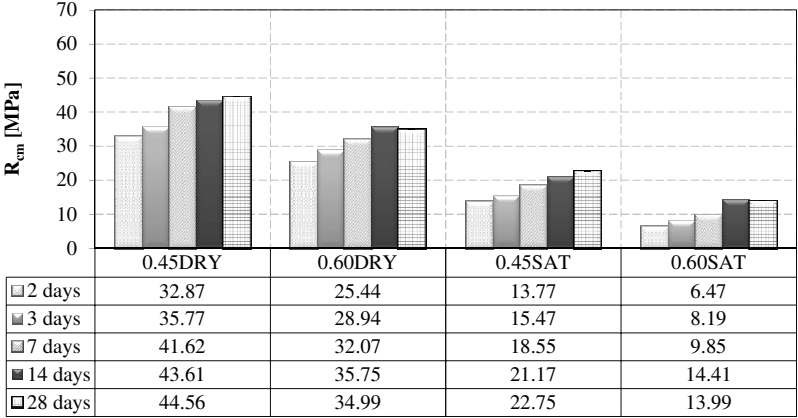


Figure 9 – Time evolution of the average compressive strength.

Temperature was also monitored in four 150 mm cubic samples of the same mixes, which were cured in semi-adiabatic conditions inside an insulated box (with a sizeable temperature development in the concrete specimens, in spite of their small size). Figure 10 shows the aforementioned insulated box. Note that the four lateral faces of the cubic samples are in contact with thick insulating layers, while the layers at the top and at the bottom were rather thin. Hence, hydration

heat was mainly dissipated throughout such faces in a basically one-directional flow. Moreover, Figure 10 depicts the simple temperature measurement equipment.



Figure 10 – Insulated box for semi-adiabatic curing conditions used for temperature measurements of the RAC mixtures.

Figure 11 describes the time evolution of the temperature measured inside the two concrete samples with  $w/c=0.45$ . It is shown that higher temperatures were reached by the sample with dry aggregates, as a consequence of the faster hydration reaction taking place in the mix with the lower amount of water. On the contrary, the sample with saturated recycled aggregates exhibited a long-lasting reaction, fed by the higher amount of available water, and testified by the slower reduction of temperature in the post-peak branch.

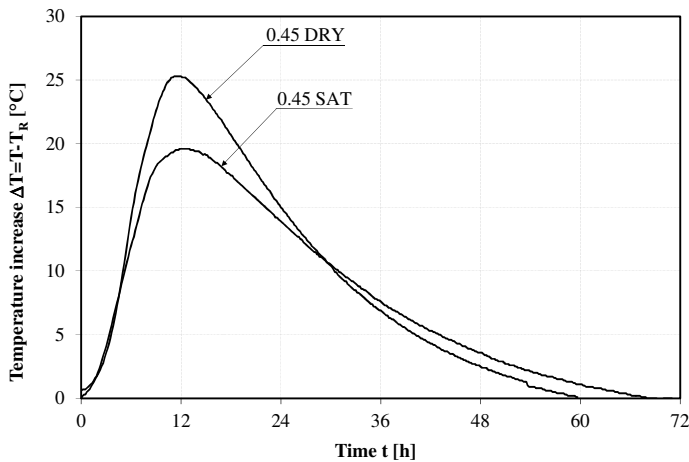


Figure 11 – Time evolution of the temperature in the curing phase ( $w/c = 0.45$ ).

Similar considerations can be drawn out by the diagram reported on the right of Figure 12 ( $w/c = 0.60$ ). Higher peak values were achieved in the concrete sample

with dry aggregates, and such peak values were very close to the one developed for the 0.45SAT mix.

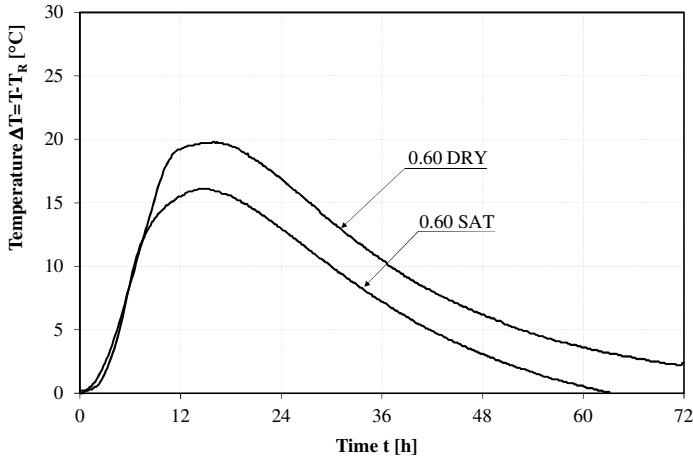


Figure 12 – Time evolution of the temperature inside the curing concrete sample (w/c=0.60).

Figure 9, 11 and 12 show that the strength in compression and the temperature evolution of the four concrete mixes under consideration are clearly correlated. A deeper investigation towards a quantitative relationship between hydration-related measurements and the strength in compression is proposed in the following.

### 5.3 Indirect identification of the hydration reaction processes

As a matter of principle, the model formulated in Section 2 and, particularly, the solution of the partial integral-differential Eq. 13 with the initial and boundary conditions (Eqs. 15 and 16-18), respectively, leads to the definition of a temperature field which can be symbolically denoted as follows:

$$T_{th} = T_{th}(x,t;\mathbf{q}_r,\mathbf{q}_f) \tag{33}$$

where the vectors  $\mathbf{q}_r$  and  $\mathbf{q}_f$  include the two sets of parameters listed below:

$$\mathbf{q}_f = [\tau,\beta,\lambda_p] \tag{34}$$

$$\mathbf{q}_r = [T_R, Q_{max}, \alpha_{h,max}] \tag{35}$$

In the proposed identification procedure, the values of the components of the  $\mathbf{q}_r$  vector are assumed “a priori”. Particularly,

- $T_R$  = room temperature which has been measured for all the four mixes;
- $Q_{max}$  = 450 kJ/kg, as generally assumed for CEM I (Lokhorst, 1999);

- $\alpha_{h,\max}$  = function of the w/c ratio according to the following analytical relationship (Mills, 1966; Hansen, 1986):

$$\alpha_{h,\max} = \frac{1.031 \cdot w/c}{0.194 + w/c} \quad (36)$$

Since the time evolution of the temperature  $T$  developed inside the concrete (namely, at  $x = 0$  in the equivalent 1D domain, Figure 1) during the curing process was monitored for all the four samples under consideration, the following objective error parameter can be defined for the outcome of the numerical simulation  $T_{th}(x=0, t_k; \mathbf{q}_r, \mathbf{q}_f)$ :

$$\Delta(\mathbf{q}_r, \mathbf{q}_f) = \sum_{k=1}^n \left[ T_{exp}^{(k)} - T_{th}(x=0, t_k; \mathbf{q}_r, \mathbf{q}_f) \right]^2 \quad (37)$$

where  $T_{exp}^{(k)}$  is the temperature value measure at the time  $t_k$  in the reference position ( $x = 0$ ). Thus, an inverse identification procedure for the model presented in Section 2 can be written as the following unrestrained optimisation problem:

$$\bar{\mathbf{q}}_f = \underset{\mathbf{q}_f}{\operatorname{argmin}} [\Delta(\mathbf{q}_r, \mathbf{q}_f)] \quad (38)$$

which leads to the values of the parameters collected in the vector  $\mathbf{q}_f = [\tau, \beta, \lambda_p]$  resulting in the best approximation of the numerical simulation with respect to the observed phenomenon.

Table 3 reports the numerical values of the parameters identified by solving the optimisation problem described by Eq. 38 for the four mixes under consideration. Note that the calibration process led to different values of  $\tau$  and  $\beta$  for each mix, as these parameters are directly related to mix composition and curing conditions, and control the hydration heat produced according to Eq. 7. On the contrary, a single value for  $\lambda_p$  was worked out, as this parameter is directly related to the insulation system, that is the same in all tests.

To have an idea of the actual quality of the simulation after the calibration and the introduction of the numerical values summarised in Table 3 for the key parameters of the model, the comparison between the temperature evolution measured inside the sample of the curing concrete (the grey points) and the corresponding numerical simulation (the gray continuous line) is presented in Fig. 13: the theoretical-experimental agreement is very good in terms of maximum values and time evolution of the temperature due to the heat transfer phenomena occurring throughout the semi-adiabatic equipment. Furthermore, Figure 13 depicts the temperature evolution that would have occurred for the same concrete sample under adiabatic curing conditions.

Table 3 – Parameters calibrated through the indirect identification of the hydration model.

System parameters	MIX	w/c	$\alpha_{h,max}$	$Q_{max}$ [kJ/kg]	$\tau$ [h]	$\beta$
$\rho_c c_c = 2500$ kJ/m <sup>3</sup> K $\lambda_c = 2.5$ W/mK $t_p = 0.04$ m $\lambda_p = 0.072$ W/mK	<b>0.45DRY</b>	0.45	0.70	450	5.0	1.50
	<b>0.45SAT</b>	0.45	0.74	450	6.8	1.10
	<b>0.60DRY</b>	0.60	0.76	450	9.5	1.60
	<b>0.60SAT</b>	0.60	0.80	450	8.0	1.60

Similar results were obtained for the other three concrete samples which were subjected to the same indirect identification procedure leading to the numerical parameters outlined in Table 3. Thus, the corresponding diagrams are omitted for the sake of brevity.

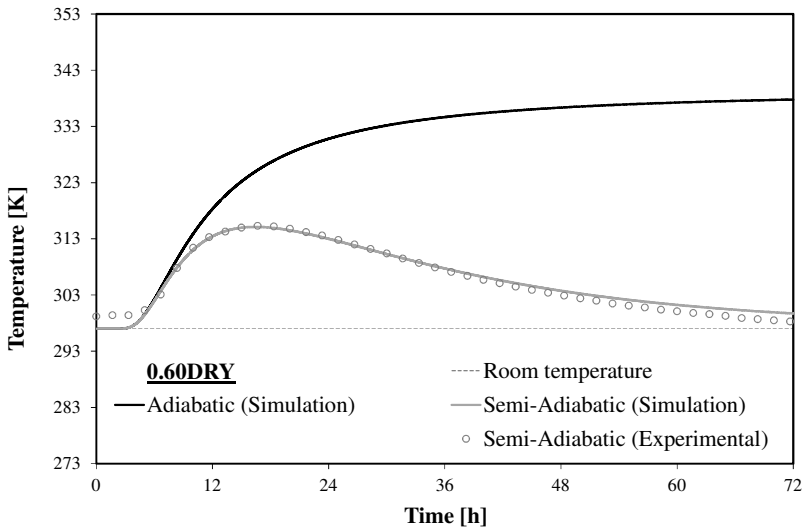


Figure 13 – Experimental-theoretical comparison in terms of temperature evolution during the hydration process (0.60DRY).

Finally, it is worth highlighting that the solution in terms of time evolution of the temperature field can be employed to determine the corresponding evolution of the degree of hydration by applying Eqs. 22-28.

## 5.4 Degree of hydration and compressive strength

Once the hydration processes of the four concrete mixes under consideration are identified, the model presented in Sections 2 and 3 can be applied to simulate the hydration reaction which takes place in the cubic concrete specimens to be tested in compression. As in usual applications, the specimens were cured in water under isothermal conditions at a constant room temperature  $T_R$ . Later, the hydration process was simulated by solving the integral-differential Eq. 15 with the following boundary conditions to replace those described by Eqs. 15, 17 and 18:

$$T(x, t = 0) = T_R \quad (39)$$

$$T(x = -L / 2, t) = T_R \quad (40)$$

$$T(x = L / 2, t) = T_R$$

Eq. 13 with the initial and boundary conditions described by Eqs. 39 and 40 were actually solved for all the four mixes by considering  $T_R=22^\circ\text{C}$ . The corresponding time evolution of the degree of hydration  $\alpha_h(t)$  in isothermal conditions was obtained via Eq. 1. Figure 14 describes the time evolution of the degree of hydration under adiabatic, semi-adiabatic and iso-thermal conditions.

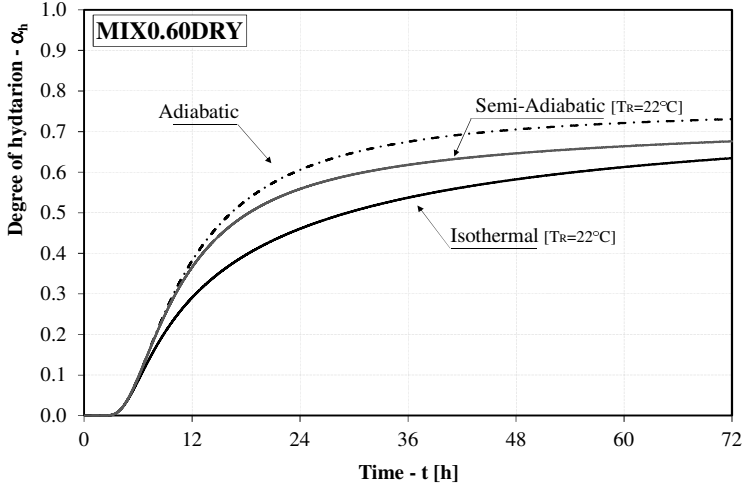


Figure 14 – Time evolution of the degree of hydration – 0.60DRY.

The curve obtained for the adiabatic reaction is clearly proportional to the corresponding temperature curve represented in Figure 13, as a result of the absence of heat dissipation which led to Eq. 4. Moreover, the time evolution of  $\alpha_h(t)$  in semi-adiabatic conditions is initially close to the ideal adiabatic process,



but later there is a divergence, as a result of the heat-rate reduction due to the dissipative phenomena occurring in the former conditions. Finally, the  $\alpha_h(t)$  curve for the isothermal reaction is always beneath the two aforementioned curves, as a result of the lower heat production-rate due to the lower temperature actually developing in this conditions. Similar considerations can be made for the other concrete mixes whose corresponding graphs are omitted here for the sake of brevity.

The simulation of the time evolution of the degree of hydration for the four batches of specimens tested in compression suggests the opportunity to relate the values of  $\alpha_h(t)$  to the corresponding  $R_{cm}(t)$  for each of the concrete mixes under consideration. Figure 15 shows that a clear linear correlation emerges between the two aforementioned quantities.

Although such a linear correlation between  $\alpha_h(t)$  and  $R_{cm}(t)$  was already observed and documented in the scientific literature for ordinary concrete (Lokhorst, 1999), the results of this study demonstrate that a similar correlation holds in the case of recycled-aggregate concrete. Note that this correlation takes into account the influence that both the water-cement ratio and the initial moisture content have on the mechanical properties of RAC. As a matter of fact, recycled aggregates absorb more water than ordinary aggregates at the time of mixing, and such occurrence can significantly affect the actual water content and water-cement ratio, which – in turn – control concrete workability and mechanical properties.

The procedure presented in Section 2 indirectly takes care of the initial moisture content of recycled aggregates, by means of the parameters contained in Eq. 6, and describes the resulting hydration process.

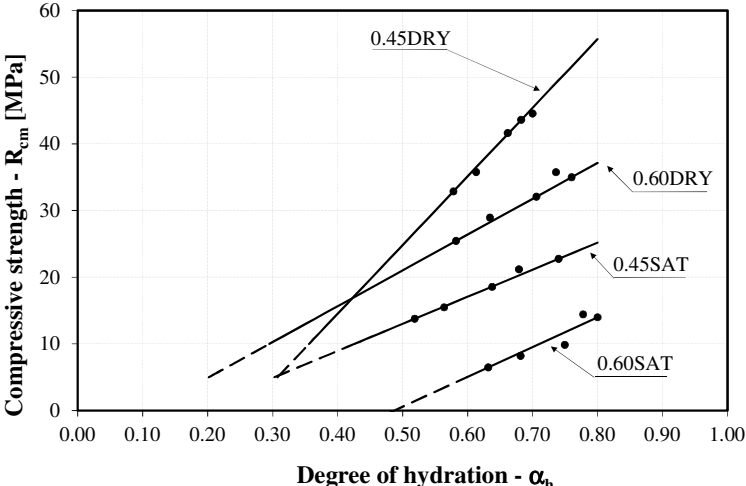


Figure 15 –  $\alpha_h$ - $R_{cm}$  correlations for RAC samples with saturated (SAT) and dry (DRY) aggregate particles.

The linear correlation clearly shown in Figure 15 makes it possible to formulate and calibrate a set of simple relationships (like the one reported below) to describe the effect that both the water-cement ratio and the moisture content have on the hydration reaction of concrete mixes with recycled aggregate:

$$R_{cm} = R_{cm,max} \frac{\alpha - \alpha_0}{1 - \alpha_0} \quad (41)$$

Finally, the numerical values of the couples  $(R_{cm,max}, \alpha_0)$  determined through a least-square regression for the four mixes under consideration are reported in Table 4 and the quality of the fitting is very satisfactory (Figure 15).

Table 4 – Parameters describing the linear correlation  $\alpha_h$ - $R_{cm}$ .

MIX	$R_{cm,max}$ [MPa]	$\alpha_0$
0.45DRY	76.3	0.26
0.45SAT	33.3	0.18
0.60DRY	47.9	0.11
0.60SAT	22.9	0.49

## 6 CONCLUDING REMARKS

This paper proposes a theoretical model to describe both the hydration and heat production processes in hardening concrete. A step-by-step “numerical recipe” is presented with the aim of making reasonably feasible the numerical implementation of the complex theoretical formulations needed to accurately analyse the above mentioned phenomena. Hence, the model can be easily used to analyse the change of the mechanical properties by simulating the time evolution of the *degree of hydration*.

The proposed model is validated by means of temperature measurements carried out on two different hardening concretes in both adiabatic and semi-adiabatic conditions. The main aim of this validation is to demonstrate the potential of the model, by comparing both the adiabatic hydration curve (heat source) and the semi-adiabatic temperature response (output), for given boundary and initial conditions, during one single run. A very satisfactory agreement was found between the measured and the theoretical values of the temperature.

The proposed model was developed within the framework of the “EnCoRe” Project and should be considered as a first step towards the design of a tool for the analysis of concretes containing innovative aggregates and binders, as demonstrated by the application to recycled-aggregate concrete.

The model will be further developed with the emphasis (a) on the mechanical performance of natural and recycled aggregates, partly in combination with replaced binders such as fly ash, and (b) on the correlation between the evolution of the degree of hydration and the development of concrete properties.

## ACKNOWLEDGEMENTS

This study is part of the activities carried out by the Authors within the “EnCoRe” Project (FP7-PEOPLE-2011-IRSES n. 295283; [www.encore-fp7.unisa.it](http://www.encore-fp7.unisa.it), years 2012-2014) funded by the European Communities within the Seventh Framework Programme.

The results presented in this paper were obtained during the two-month stages of the two co-authors at the University of Salerno (Italy) and at the Federal University of Rio de Janeiro (Brazil) in the periods May-June and July-September 2012, respectively.

## REFERENCES

- van Breugel K. (1991). “Simulation of Hydration and Formation of Structure in Hardening Cement-Based Materials”, *Ph.D. Thesis, Delft University of Technology*, Delft (The Netherlands), 171 pages.
- van Breugel, K. (2004). “Concrete Structures under Temperature and Shrinkage Deformations”, *Lecture notes CT5120, Delft University of Technology*, Delft (The Netherlands).
- Bullard J.W., Jennings H.M., Livingston R.A., Nonat A., Scherer G.W., Schweitzer J.S., Scrivener K.L. and Thomas J.J. (2011). “Mechanisms of Cement Hydration”, *Cement and Concrete Research*, 41(12), pp. 1208–1223.
- D'Aloia L. and Chanvillard G. (2002). “Determining the *Apparent* Activation Energy of Concrete:  $E_A$  — Numerical Simulations of the Heat of Hydration of Cement”, *Cement and Concrete Research*, 32(8), pp. 1277–1289.
- EN 197-1 (2011). Cement - Composition, Specification and Conformity Criteria - Part 1: Common Cements.
- EN-12390-3 (2009). Testing Hardened Concrete. Part 3: Compressive Strength of Test Specimens.
- Faella C., Martinelli E. and Nigro E. (2009). “Direct versus Indirect Method for Identifying FRP-to-Concrete Interface Relationships”, *ASCE Journal for Composites for Construction*, 13(3), pp. 226-233.
- Feng X., Garboczi E.J., Bentz D.P., Stutzman P.E. and Mason T.O. (2004). “Estimation of the Degree of Hydration of Blended Cement Pastes by a Scanning Electron Microscope Point-Counting Procedure”, *Cement and Concrete Research*, 34(10), pp. 1787-1793.

- Freiesleben-Hansen P. and Pedersen E. J. (1977). "Maturity Computer for Controlled Curing and Hardening of Concrete", *Nordic Concrete Research*, 1, pp. 21-25.
- Gutsch A. and Rostásy F.S. (1994). "Young Concrete under High Tensile Stresses – Creep, Relaxation and Cracking", *Proc. of RILEM Symposium on Thermal Cracking in Concrete at Early Ages*, Munich (Germany), pp. 111-118.
- Gutsch A.W. (2003), Properties of early age concrete – experiments and modelling, *Proceedings Int. RILEM Conference on Early Age Cracking in Cementitious Systems*, pp 11 – 18.
- Hansen T.C. (1986). "Physical Structure of Hardened Cement Paste. A classical Approach", *Materials and Structures*, 19(114), pp. 423-436.
- Kada-Benameur H., Wirquin E. and Duthoit B. (2000). "Determination of Apparent Activation Energy of Concrete by Isothermal Calorimetry", *Cement and Concrete Research*, 30(2), pp. 301–305.
- van Kan J., Segal A. and Vermolen F. (2008). "Numerical Methods in Scientific Computing", *Department of Applied Mathematics*, Delft University of Technology, Delft (The Netherland).
- Koenders E.A.B. (1997). "Simulation of Volume Changes in Hardening Cement-Based Materials", *Ph.D. Thesis, Delft University of Technology*, Delft (The Netherland), 171 pages.
- Koenders E.A.B. (2005). "Mix Design for Venice Barriers", *Report Nr. 15.5-05-08*, Confidential Communication.
- Krauss M., Hariri, M. and Rostásy, F. (2003), Determination of initial degree of hydration by ultra-sonic pulse technique, *Proceedings Int. RILEM Conference on Early Age Cracking in Cementitious Systems*, pp 199 – 208.
- Han N. (2005). "Maturity Method in Advanced Testing of Cement-Based Materials during Setting and Hardening", *Final Report of RILEM TC 185-ATC*, Editors Reinhardt H.W. and Grosse C.U., RILEM Publications SARL, pp. 277 – 296.
- Jeong J. and Zollinger D. (2006). "Finite-Element Modeling and Calibration of Temperature Prediction of Hydrating Portland Cement Concrete Pavements", *Journal Materials in Civil Engineering*, 18(3), pp. 317–324.
- Laube M. (1991). "On the Modelling of Construction Materials to Compute the Thermal Stresses in Massive Concrete Structures at Early Ages Werkstoffmodell zur Berechnung von Temperature-spannungen in massigen Betonbauteilen im jungem Alter", *PhD-Thesis*, TU Braunschweig (Germany).
- Lokhorst S.J. (1999). "Deformation Behavior of Concrete Influenced by Hydration Related Changes of the Microstructure", *Internal Report Nr. 5-99-05*, *Delft University of Technology*, Delft (The Netherland).
- Mills R.H. (1966). "Factors Influencing Cessation of Hydration in Water-Cured Cement Pastes", *Special Report No.90, Proceedings of the Symposium on the Structure of Portland Cement Paste and Concrete*, Highway Research Board, Washington, D.C., pp.406-424.

- Naik T.R. (2005). “Sustainability of Cement and Concrete Industries”, Report No. 562, Center for By-Products Utilization, *The University of Wisconsin – Milwaukee* (United States).
- Narasimhan T. N. (1999). “Fourier’s Heat Conduction Equation: History, Influence and Connections”, *Reviews of Geophysics*, 37(1), pp. 151–172.
- Pane I. and Hansen W. (2005), Investigation of blended cement hydration by isothermal calorimetry and thermal analysis, *Cement and Concrete Research* 35 (2005) 1155–1164.
- Schindler A.K. and Folliard K.J. (2005). “Heat of Hydration Models for Cementitious Materials”, *ACI Material Journal*, 102(1), pp. 24-33.
- De Schutter G. and Taerwe, L. (1995), General hydration model for portland cement and blast furnace slag cement, *Cement and Concrete Research*, Volume 25, Issue 3, April 1995, Pages 593–604.
- De Schutter G. and Taerwe, L. (1996). “Degree of Hydration-Based Description of Mechanical Properties of Early-Age Concrete”, *Materials and Structures*, 29(6), pp. 335-344.
- De Schutter G. (2004). “Applicability of Degree of Hydration Concept and Maturity Method for Thermo-Visco-Elastic Behaviour of Early-Age Concrete”, *Cement and Concrete Composites*, 26(5), pp. 437-443.
- Voglis N., Kakali G., Chaniotakis E. and Tsivilis S. (2005). “Portland-Limestone Cements: their Properties and Hydration Compared to those of other Composite Cements”, *Cement and Concrete Composites*, 27(2), pp. 191-196.
- Wang X.-Y., Lee H.-S., Park K.-B., Kim J.-J. and Golden J. S. (2010). “A Multi-Phase Kinetic Model to Simulate Hydration of Slag–Cement Blends”, *Cement and Concrete Composites*, 32(6), pp. 468-477.



## Technical Notes





## **EXPERIMENTAL BEHAVIOUR OF SEMI-DRY COLUMN-FOUNDATION CONNECTIONS FOR PRECAST BUILDINGS**

Bruno Dal Lago<sup>1</sup>, Marco Lamperti Tornaghi<sup>2</sup>, Giandomenico Toniolo<sup>3</sup>

### **ABSTRACT**

Column-to-foundation connections are experimentally investigated in this research project, as there is an increasing interest for using innovative connections in precast concrete structures. The focus is on their behaviour under horizontal cyclic loads, that is of primary importance in case of seismic actions.

This project was developed within the framework of a comprehensive European research programme called SAFECAST. The tests were carried out to compare different connection systems: bars inserted in the foundation and innovative semi-dry mechanical connections.

In all specimens and for all connection types, the column and the foundation had the same geometry (column cross-section 40 x 40 cm; column height 2.50 m), and also the loading procedure - with increasing load intensity – was the same.

The columns were tested under a constant axial compressive force (380 kN). The aim of the tests was to measure the ultimate capacity of each connection under cyclic horizontal loads, as well as to assess the ductility, the energy dissipation capability and the extension of the plastic hinge forming at the foot of the column.

A numerical investigation was carried out as well, to give designers simple calculation tools based on the fitting of first-hand test results.

**KEYWORDS:** precast concrete, seismic behaviour, column-foundation connections, dry joints, mechanical devices (for coupling pre-fabricated members)

---

<sup>1</sup> PhD candidate, <sup>2</sup> MS Engineer, <sup>3</sup> Professor  
DICA - Department of Civil and Environmental Engineering, Politecnico di Milano,  
Milan, Italy

## 1. INTRODUCTION

The development of the European prefabrication industry has been characterized in the last five decades by the objective of optimizing the constructive process, one of the main steps being the introduction of dry and semi-dry assembled structures (mostly frames). The typical industrial and commercial structural scheme for this technology consists in cantilever columns and hinged beam-to-column connections. Under horizontal loading, the strength demand is concentrated at the base of the columns, which turns out to be the only critical region of the whole frame, provided that all other connections are calculated according to capacity design. Other types of dry or semi-dry assembled precast frame- or wall-structures have entered the market in the last decades (Nakaki *et al.*, 1999; Dal Lago and Dal Lago, 2012). The base of the columns, however, remains still critical.

Pocket foundation is the traditional wet column-to-foundation connection, where the column is inserted into a special pocket arising from the base footing. The upright is ensured by provisional props and the joint is then filled with concrete, providing a fully-fixed support. Nowadays, the market demand for new technologies allowing reduced dimensions, faster erection procedures and no need for in-situ concreting is favouring the development of mechanical connections of different types, whose main features are the dry or semi-dry assemblage and the upright regulation (so that the holding time of the crane can be strongly reduced).

Within the European SAFECAST Project (aimed to study the seismic performance of precast structures provided with these new connections, see Toniolo, 2012), the research team of the Politecnico di Milano has recently carried out an extended experimental investigation on column-to-foundation connections. This paper summarizes the experimental results and provides comments on the design of the connections. Numerical simulations were performed as well, and the agreement with the experimental results turned out to be more than satisfactory, as a demonstration of the soundness of the adopted design methodology.

Five types of column-to-foundation connections were tested on full-scale sub-assemblies subjected to cyclic and monotonic loading (only one type), for a total of 10 tests. Figure 1 shows the five types of the connections, ranging from the technology with protruding bars to a few mechanical solutions recently introduced into the market with bolted sockets and couplers. Figure 2 shows the details of the three commercial solutions utilized. Two proposals for improving the current bolted-socket technology are presented as well. Another innovative solution consisting in unbonded mechanical connectors has been recently developed by Riva *et al* (2011). The results of the tests on bolted-socket technology are available in Fagà *et al* (2011).

In this research project, all columns have a square cross section (side = 400 mm) and a central hole ( $\varnothing = 100$  mm, running along the whole height of the column = 2.5 m). All foundations are properly reinforced (size = 1.1 x 0.7 x 0.5 m). The concrete and steel grades are C55/45 and B450C, respectively.

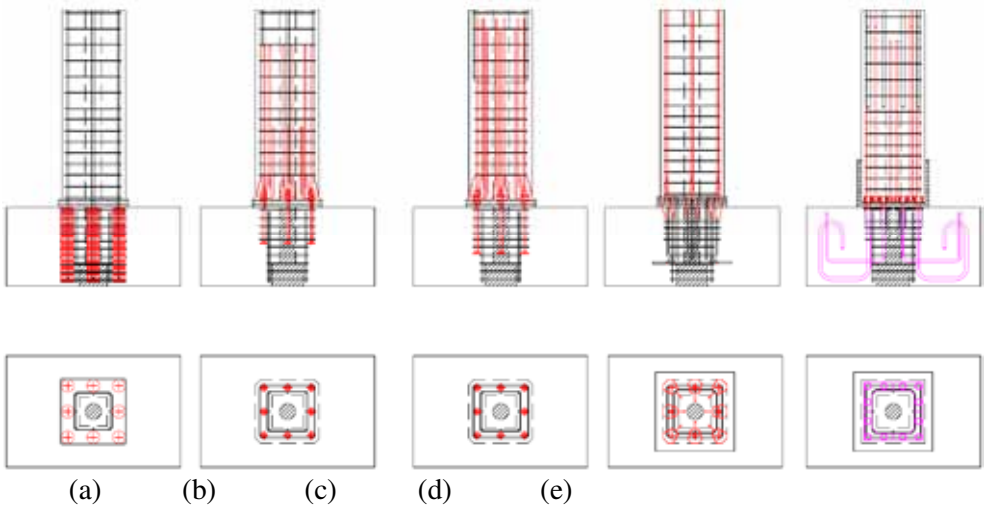


Figure 1 – Column-to-foundation connections tested in this project: (a) *post-inserted protruding bars*; (b) *column shoes bolted sockets*; (c) *weakened column shoes bolted sockets*; (d) *foundation shoes bolted sockets*; and (e) *couplers*.

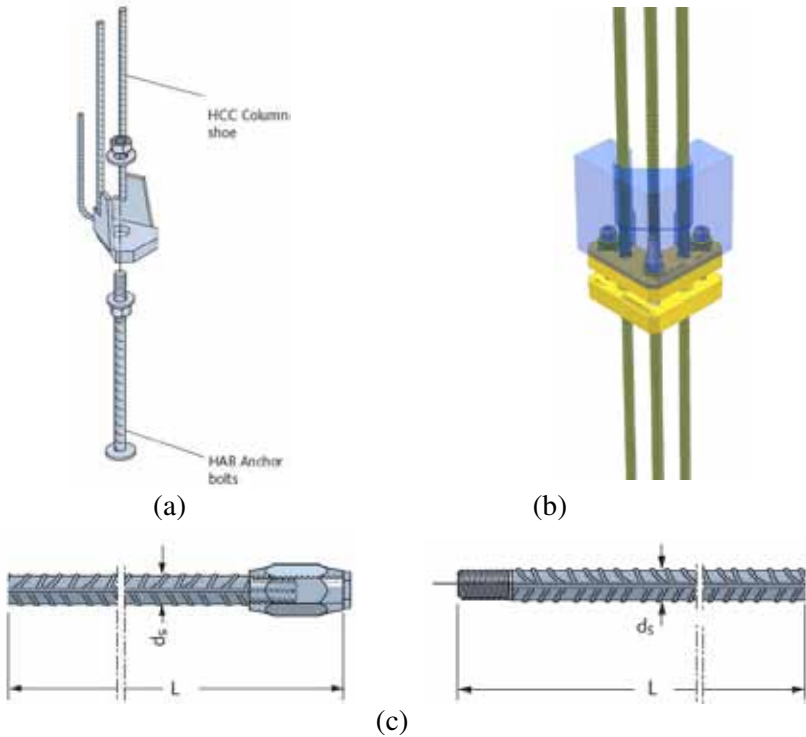


Figure 2 – Mechanical connections: (a) Halfen HCC column-shoe bolted socket; (b) Ruredil *Kaptor* coupler; and (c) Halfen HBS coupler for post-inserted bars.

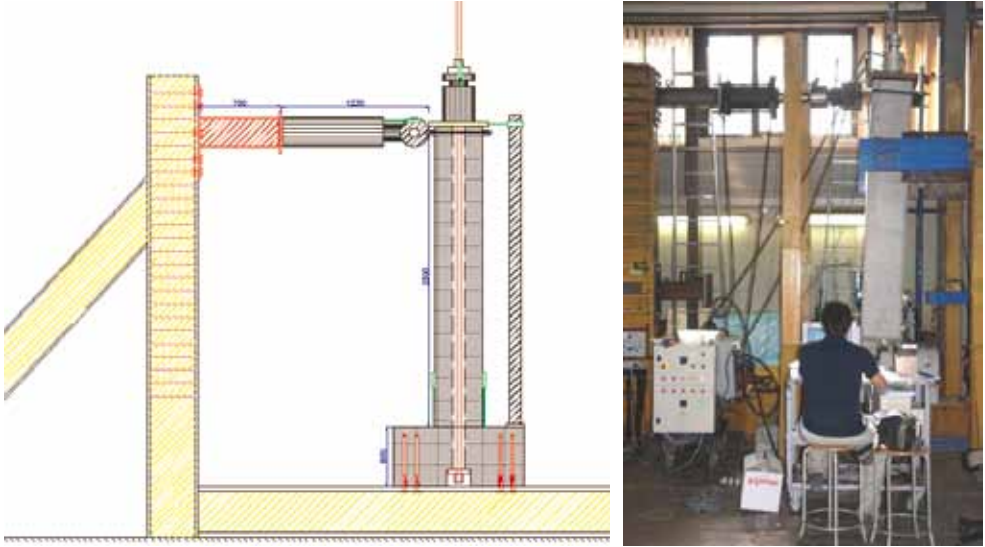


Figure 3 – Test setup.

Each column is subjected to a constant axial load (380 kN, see the setup in Fig.3) applied by tightening a Dywidag bar running in the central hole, connected to a vertical jack placed on top of the column. Since the axial load  $P$  follows the displacement with a rigid rotation, the shearing force  $V$  at the base is not just the horizontal force  $F$  exerted at the top by the hydraulic jack, but should include the shearing component of the axial load (380 kN) due to 2<sup>nd</sup>-order effects (Figure 4):

$$V = F - P \Delta / h; \quad M = F h$$

where the bending moment  $M$  at the base of the column is not affected by 2<sup>nd</sup>-order effects, because the force is always directed towards the centroid of the base section and has no lever arm.

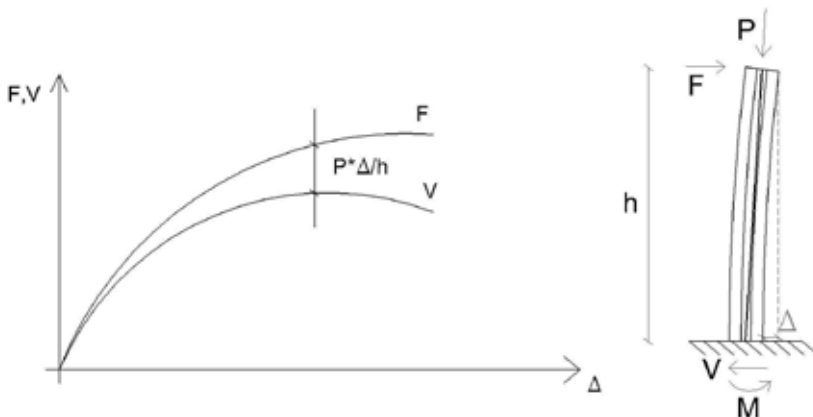


Figure 4 – Second order effect.

## 2. BOLTED SOCKETS

### 2.1. Column shoes

These bolted sockets consist of metallic shoes made of steel plates welded together, connected by welding to over-designed rebars for the splicing with the longitudinal rebars of the column. A hole in the centroid of the horizontal base plate allows a threaded bar acting as an anchor (called *bar-anchor* in the following) provided with a bottom nut on which the column is placed to regulate the upright and an upper nut to tighten it. The connection joint is filled with no-shrinkage high-resistance mortar. The specimens were reinforced with the minimum reinforcement allowed by Eurocode 8 (steel ratio = 1%; 8 Ø16 mm bars placed at the corners of the section and at mid-side). Two cyclic and one monotonic tests were performed. The hysteretic cycles coming from the first cyclic test are shown in Figure 5 in terms of moment-drift diagram. The cyclic behaviour is stable and exhibit some ductility until failure, with a clear and well developed plastic phase.

The failure is activated by the progressive rupture of the threaded bar-anchors embedded in the foundation block, the first of which failed at 4.5 % of drift. A marked pinching effect of the cycles was recorded, especially at large values of the drift, due to boundary non-linearity at the nut-shoe interface: once the threaded bar is stretched enough to compensate the deformation given by the manual tightening of the nuts, the column starts rocking without any sizeable bending stiffness, following the increasing gap at the base. Most of the damage is concentrated at the joint between the column and the foundation, with the spalling of the unconfined mortar. The two corner bar-anchors - broken and buckled – and the crack pattern developed in the foundation block are shown in Figure 6b.

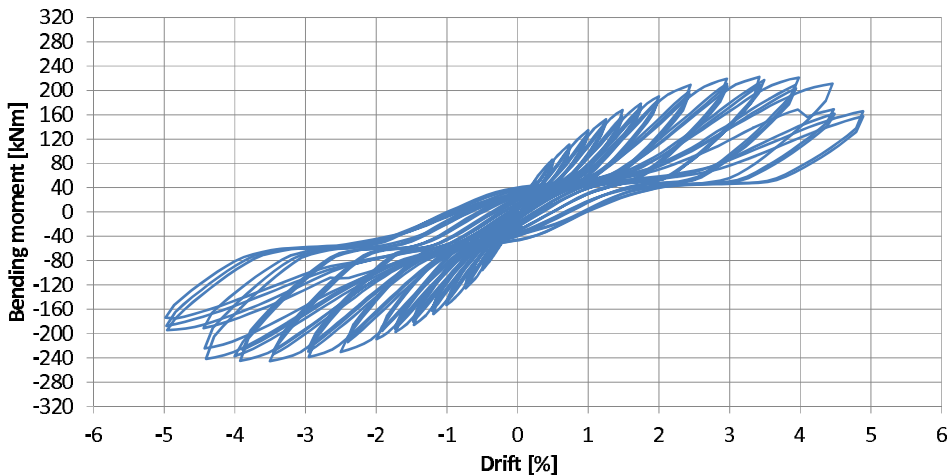


Figure 5a – Column shoes bolted sockets: hysteretic cycles.

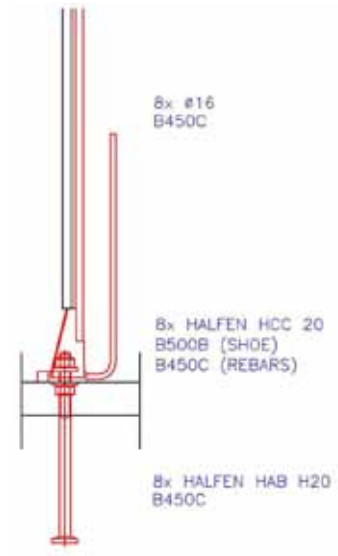


Figure 5b – Column shoes bolted sockets: lateral face of the column (parallel to the horizontal load) after testing and details of the anchoring device.

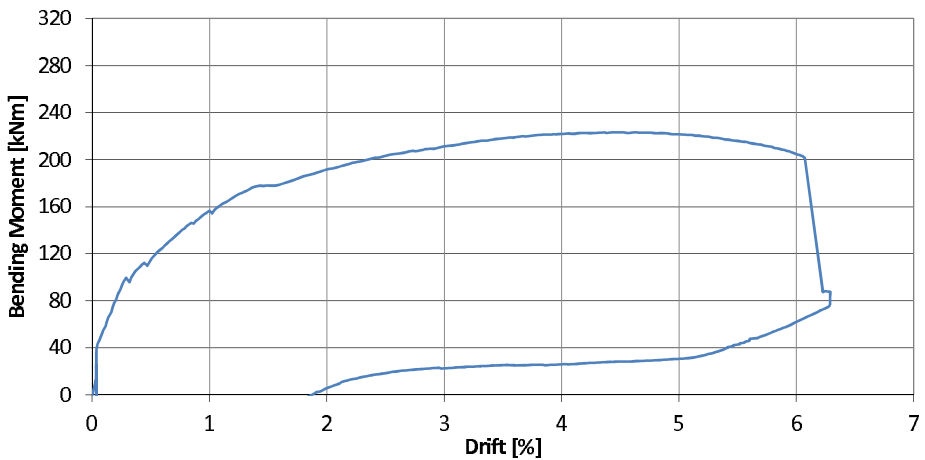


Figure 6a – Column shoes bolted sockets: hysteretic cycle.

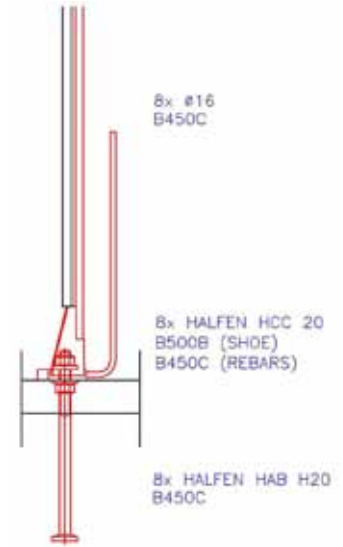


Figure 6b – Column shoes bolted sockets: (left) lateral face and transverse face in tension after testing; and (right) details of anchoring device.

## 2.2. Foundation shoes

In the configuration with foundation shoes, the sockets are overturned and inserted as supports inside the foundation, with the last 5 cm protruding from it.

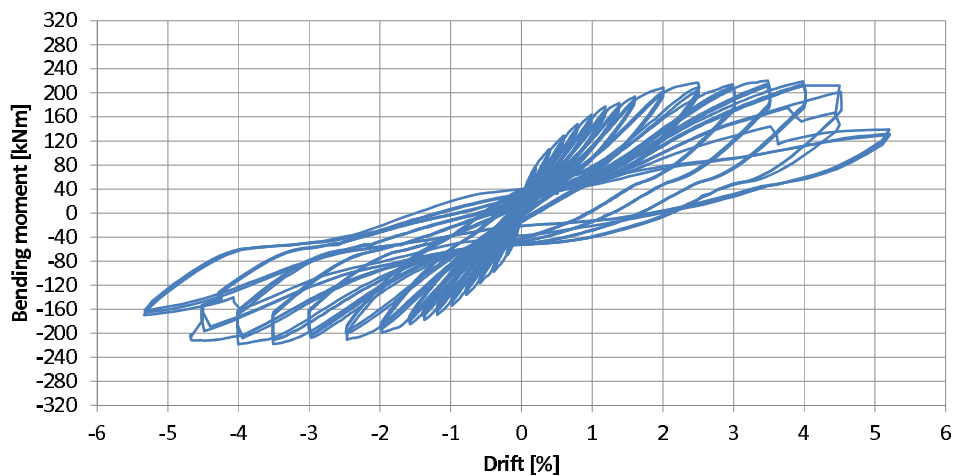
The longitudinal reinforcement of the column was provided with end cropped bushes.

The single connection is assembled with the insertion of a short over-designed M20 threaded bar provided with two nuts, for the mechanical regulation of the upright.

This configuration is aimed at moving the plastic hinge away from the short threaded length protruding from the foundation of the bar-anchor to the column base through yielding of its longitudinal reinforcement, in order to improve the structural response under cyclic loading.

The column has the minimum reinforcement (1% steel ratio;  $\varnothing 16$ mm bars placed at the corners and at mid-side of the section). The hysteretic curves are plotted in Fig.7a.

The cyclic behaviour is stable and ductile until failure, with a clear and well developed plastic phase. Failure occurred within the base joint and started at 4.5 % drift. In Figure 7b a broken bush is visible.



(a)



(b)

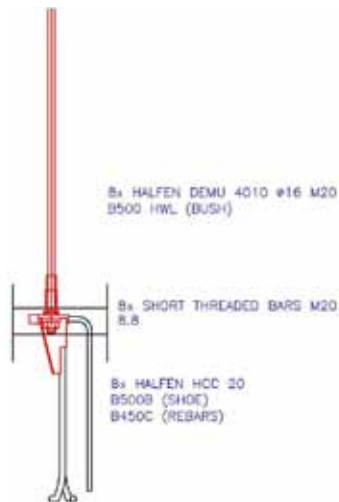


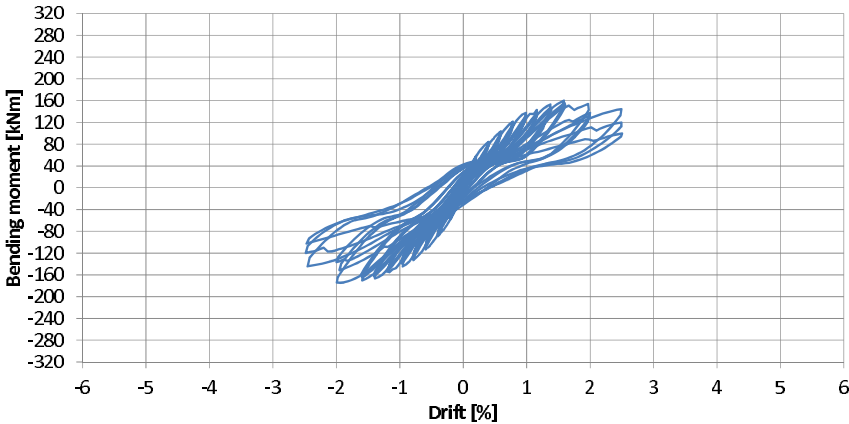
Figure 7 - Foundation shoes bolted sockets: (a) hysteretic cycles; and (b) transverse face with a broken bush and details of the anchoring device.

### 2.3. Weakened shoes

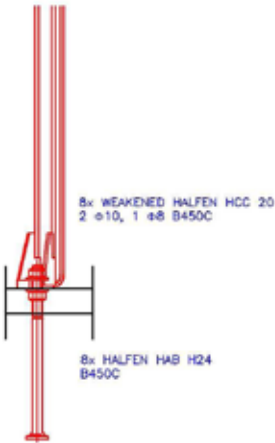
The configuration with weakened bolted sockets has the column shoes provided with under-designed welded rebars ( $\varnothing 10$  mm). The current longitudinal bars of the column were moved upward, leaving 60 cm with the under-designed bars. Over-designed bar-anchors were inserted inside the foundation and the assembly of the connection follows the same scheme as in the standard case. As in the previous case, this configuration was aimed at moving the plastic hinge away from the short threaded length of the bar-anchor at the base of the column, to



improve energy dissipation under cyclic loading. As in the previous case, the column has the minimum reinforcement (1% steel ratio; 8Ø16mm bars placed at the corners and at mid-side of the section). The hysteretic curves are plotted in Figure 8a, in terms of moment-drift cycles. The cyclic behaviour is unstable and brittle, since failure occurs before bar yielding, with the unexpected rupture of the bars welded to the shoes, maybe due to poor welding. At 2% drift a significant concrete spalling occurred above the shoes, causing the detachment of rather large blocks of concrete. At the end of the test most of the shoes on both the column sides perpendicular to the loading had the welded bars broken (Figure 8b). The combination of welding in critical zones, angular shoes and unconfined concrete contributed to the early failure of this connection. The foundation did not exhibit any crack, not even at column-mortar interface.



(a)



(b)

Figure 8 - Weakened shoes bolted sockets: (a) hysteretic cycles; and (b) broken shoe bar weld and details of the anchoring device.

### 3. COUPLERS

Couplers are in general over-dimensioned devices that guarantee the continuity of the longitudinal bars of the column with those embedded inside the foundation.

The patented device used in the specimens tested in this project consists in two thick steel plates, one inserted inside the column and the other inside the foundation, the reinforcement of the column being mechanically connected to the latter plate by an upset end enlargement.

The connection is assembled with high-strength bolts tightened between the plates, the angular of which is provided with a lower nut for the regulation of the upright. The short gap is then filled with no-shrinkage high-strength mortar, that can also fill the concrete holes required by bolt insertion and used to include additional stirrups. The steel ratio of the columns is rather high (2.3%; 8Ø24mm bars). The hysteretic moment-drift cycles are plotted in Figure 9a. The cyclic behaviour is stable and ductile until failure, with a clear and well developed plastic phase.

The experimental response is asymmetrical due to tolerance problems at the base of this specimen. The bending moment at the bottom section increased until the end of the test. After attaining 5% drift, there was no failure. A further half-cycle up to 6% drift did not provoke any moment loss.

A full series of cycles at 6% drift could not be made, because of setup limitations. The foundation did not exhibit any visible cracking. Damage developed along the height of the column (Figure 9b), with plastic deformations developing at the back of the mechanical device.

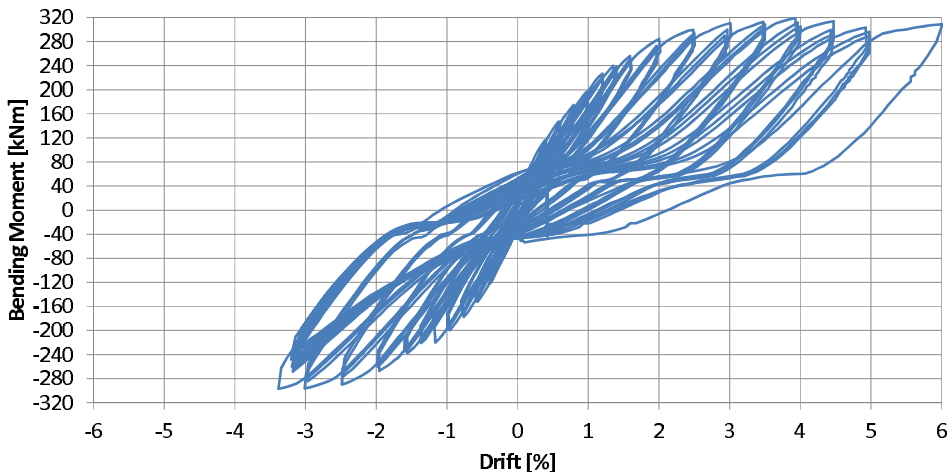


Figure 9a – Couplers: hysteretic cycles.

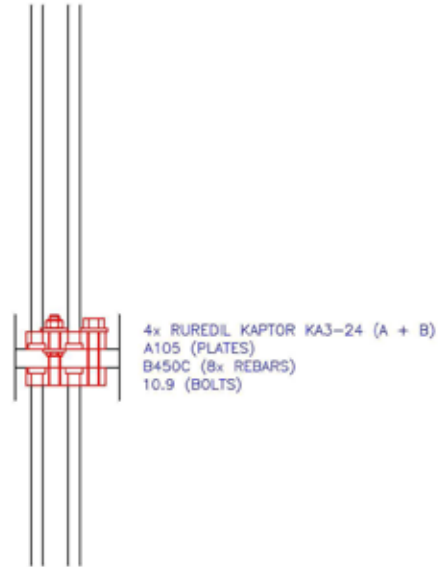


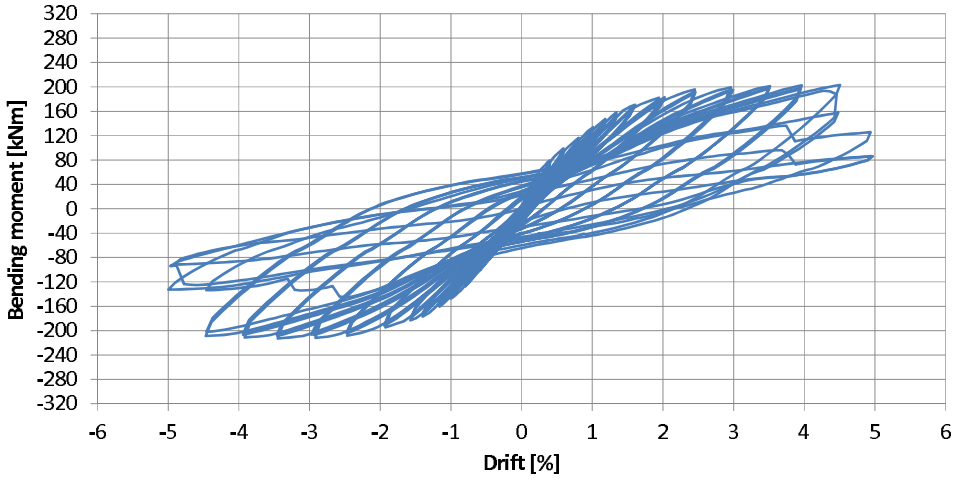
Figure 9b – Couplers: specimen at the end of the test and details of the anchoring device.

#### 4. PROTRUDING BARS

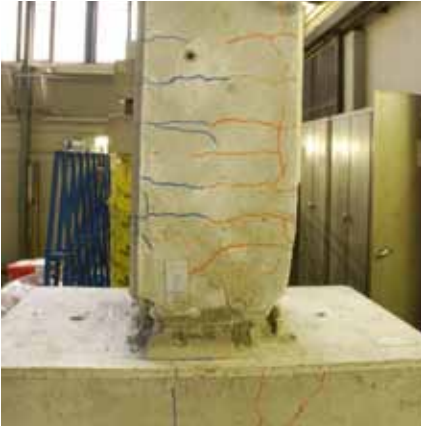
Protruding bars are a common *wet connection*, where the longitudinal bars of the column protrude from its bottom and are inserted in situ into large-diameter corrugated pipes embedded inside the foundation block. The column is provided with provisional props during the placement of the column and the pipes are filled with no-shrinkage high-strength mortar. In the connection tested in this project the extremity of each bar does not protrude directly from the bottom of the column, but is fitted up with an *end-cropped internally-threaded bush*; a short bar is screwed in situ inside the bush and protrudes from the bottom section of the column; in this way, possible distortions of the protruding bars are prevented during the handling of the precast columns. If the thread is applied without previous enlargements, this discontinuity creates a weak point in the longitudinal reinforcement. Special truncated-cone threaded couplings are used to avoid a strong reduction of the tensile resistance of the rebars.

The specimens tested in this project have a minimum reinforcement (steel ratio = 1%; 8Ø16 mm bars). The hysteretic curves are plotted in Figure 10a, in terms of moment-drift cycles. The cyclic behaviour is stable and ductile until failure.

The failure started at 4.5% drift because of the progressive rupture of the bars embedded in the foundation in correspondence of the threaded part (Figure 10b). The foundation exhibited some small cracks, but its contribution to the overall deformation was minimal. The bars embedded in the corrugated pipes and the corrugated pipes embedded in the foundation did not show any pull-out tendency.



(a)



(b)

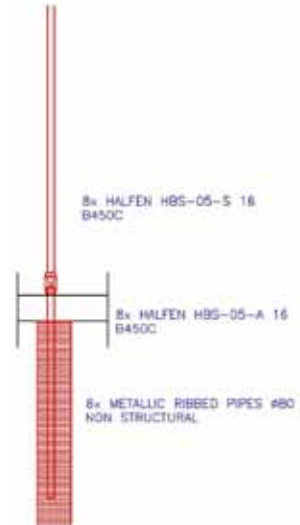


Figure 10 – Post-inserted protruding bars: (a) hysteretic cycles; and (b) lateral face parallel to the load direction at the end of the test and details of the anchoring device.

The over-dimensioned bush coupling of the bars avoided any negative effect on the ductile behaviour of the connection. Up to failure, the plastic hinge developed in the column base with a diffused cracking. At the end of the test, all the 6 rebars at both column sides perpendicular to the loading were broken and some exhibited early buckling.

## 5. DESIGN CONSIDERATIONS

The length of the plastic hinge and the shape of the hysteretic cycles were rather different in the various specimens. The length of the plastic hinge modifies the deformation profile at the base of the column (Figure 11) and brings in a concentration of the plastic strains, to the detriment of the *displacement ductility* of the column. As for the shape of the hysteretic curves, the pinching behaviour reported for some connections are an indication of reduced energy dissipation.

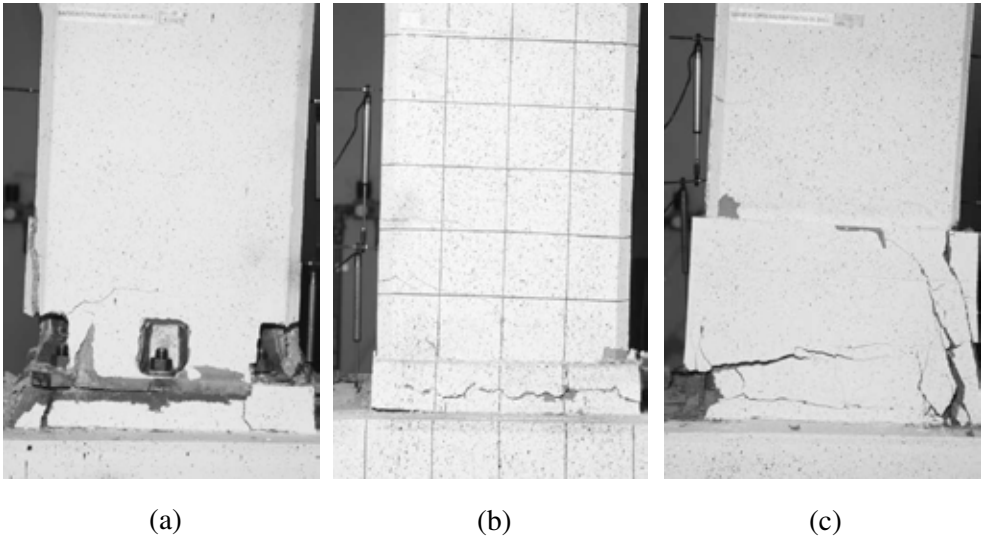


Figure 11 - Displacements at the column base immediately before failure: (a) column shoes at 4.5% drift; (b) post-inserted protruding bars at 4.0% drift; and (c) couplers at 6.0% drift (afterwards, no failure was achieved).

In Figure 12 the diagrams of the specific dissipated energy per cycle are reported. The dissipated energy is related to the area included in each force-displacement cycle, while the specific energy refers to the ratio between this area and the area of an equivalent perfect plastic cycle.

The standard bolted socket and the couplers are little efficient in dissipating specific energy, while the dissipation capability of protruding bars is similar to that of well-designed concrete members subjected to high drift levels, and the same holds – to a lesser extent - for inverted shoes. Hence, the force reduction factor  $q$  specified by the codes and referring to well-designed concrete frames should be reconsidered, if the mechanical connections investigated in this research project are used.

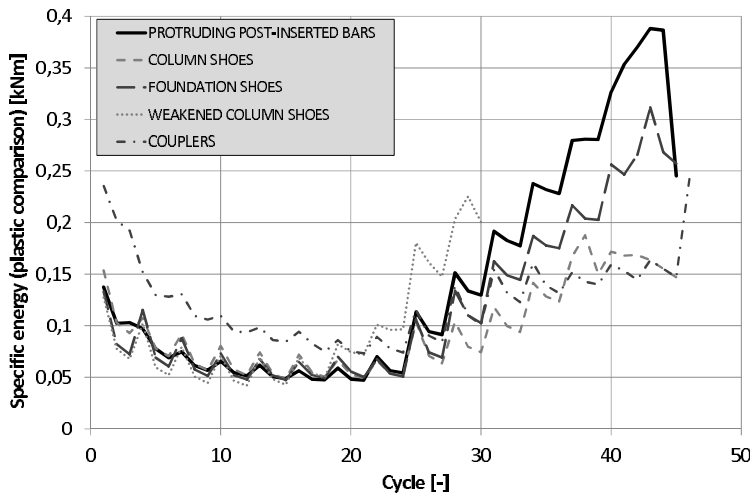


Figure 12 - Specific energy per cycle: comparison with equivalent perfect plastic systems.

## 6. MODELLING AND CALIBRATION

Several numerical analyses were carried out to describe the response of the connections, to fit the experimental results and to calibrate the models. The aim was to derive simple tools to be used in everyday practice.

After the failure mechanism was identified and confirmed by testing, the column-to-foundation sub-assemblies were analysed with the aid of a computer code (SAP2000), where a lumped-plasticity model was adopted, columns were discretized by means of in-series beam elements and a zero-length nonlinear link placed at the base of the column represented the characteristics of the plastic hinge. The nonlinear moment-curvature diagram was calculated for the critical section, considering the mean strength for both the concrete and the reinforcement.

The well-known Sargin model was adopted for the concrete, with some modifications after the stress peak to introduce the confinement provided by the stirrups (constant stress past the peak). A tri-linear stress-strain relationship was assumed for the steel (initial linear-elastic branch up to yielding, followed by linear hardening up to the stress peak and by linear softening until failure). In Figure 13a the moment-curvature curve of the current section reinforced with 8Ø16 mm bars) and subjected to axial compression (380 kN) is plotted. The steep decrease of the resistance is due to the breaking of the external bars, that reduces the lever arm of the two central bars. The end of the curve corresponds to the breaking of the central bars. In Figure 13b the geometry and the static scheme of the numerical model of the column are sketched (the cyclic displacement is applied to the top support). The zero-length link at the base of the column was modelled with a nonlinear moment-rotation curve, where the rotation is obtained

by multiplying the curvature by the length of the effective plastic hinge. The beam element representing the column were provided with an elastic behavior, where the reduced stiffness due to cracking is attributed to the cracked portion and the gross stiffness to the top un-cracked portion. To model the nonlinear hysteretic behaviour, a *pivot model* (Dowell *et al*, 1998) was used within the zero-length element, whose hysteretic parameters were calibrated on the basis of the experimental results.

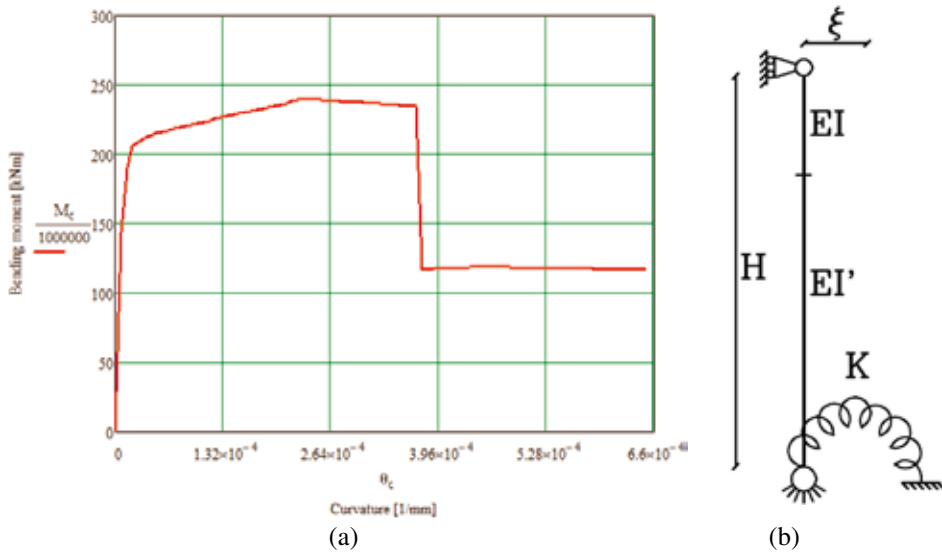


Figure 13 - Current section reinforced with 8Ø16 mm bars, subjected to a constant axial force (380 kN): moment-curvature diagram (a); and geometry and restraints (b).

The length of the plastic hinge was taken from the literature, with some adjustments suggested by the experimental observations. The threaded portions do affect the effective length of the plastic hinge. In particular, for a standard thread like those commonly used in the column shoes bar-anchors, the ultimate elongation of one single rebar in tension can be evaluated from:

$$\Delta_u = \epsilon_u L_{\text{thread}} + [f_u A_{\text{net}} / (A_0 E_s)] L_0^* \quad \text{if } (A_0 / A_{\text{net}}) \geq (f_u / f_y)$$

$$\Delta_u = \epsilon_u L_{\text{thread}} + [\epsilon_y + (f_u A_{\text{net}} / A_0 - f_y) (\epsilon_u - \epsilon_y) / (f_u - f_y)] L_0^* \quad \text{if } (A_0 / A_{\text{net}}) < (f_u / f_y)$$

where:  $L_0^* = L_0 (A_{\text{net}} / A_0)$  = length of the strain penetration including the reduction of the axial capacity according to a linear bar-concrete bond model for embedded rebars (see Figure 14, where the partially-threaded bar-anchor (a) and the elastic-plastic law adopted for the steel (b) are sketched).

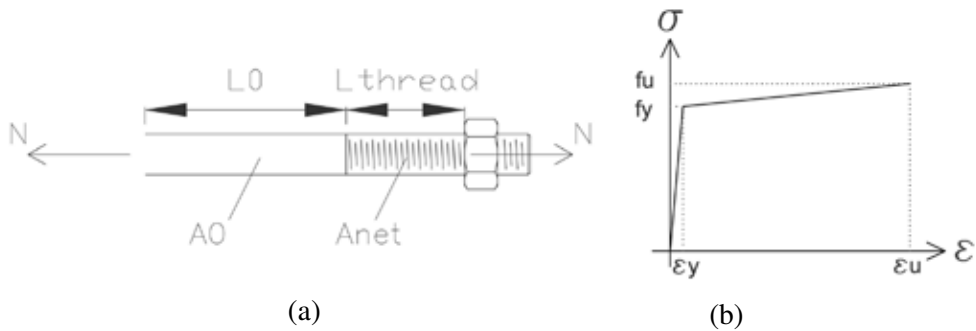


Figure 14 - Threaded bar-anchor in tension: (a) lateral view; and (b) elastic-hardening bi-linear stress-strain law adopted for the steel.

For non-standard threading processes, such as the truncated cone used in the connections with post-inserted protruding bars, a direct evaluation by testing of the modifications to be attributed to the ultimate elongation induced by the thread is suggested. The results from a tensile test performed on a normal non-threaded rebar (Bar 2) and on a truncated-cone threaded bar pulled by the nut (Bar 1) are reported in Table 1 (note that the roughly similar stresses are accompanied by very different elongations, as threaded Bar 1 undergoes a plastic elongation much smaller than that of unthreaded Bar 2 ( $= 6/14 = 43\%$ )).

Table 1. Experimental results from tensile tests

Bar	Nom. Diameter	Length	Mass	Section	Tolerance	Yielding		Failure		Elongation Ag		Elongation Agt	
						Fy kN	fy MPa	Ft kN	fu MPa	mm	%	mm	%
1	16	555	857	196,71	-2,12	515	515	119,8	596	106	6	6,3	
2	16	555	857	196,71	-2,12	522	522	124	617	114	14	14,3	

The following assumptions were introduced in the calculations:

- Standard shoes  $L_p = \chi d$
- Inverted shoes  $L_p = kL_c \geq L_{sp}$
- Weakened shoes  $L_p = kL_c \geq L_{sp}$
- Couplers  $L_p = kL_c + L_{sp} \geq 2L_{sp}$
- Protruding bars  $L_p = kL_c + L_{sp} \geq 2L_{sp}$
- Protruding bars (not weakened by the thread)  $L_p = kL_c + L_{sp} \geq 2L_{sp}$
- Protruding bars (weakened by the thread)  $L_p = \chi d$

where  $L_p$  is the effective length of the plastic hinge;  $L_c$  is the shear span from the base to the counter-flexure point;  $L_{sp}$  is the length of the strain penetration;  $d$  is the free (from the upper nut) threaded length of the rebars going into the foundation;  $\chi$  is a length coefficient given by the relationship between the ultimate elongation of the rebar and the ultimate elongation of the threaded portion  $\Delta u^*/\Delta u_{thread}$  (always  $\geq 1$  and involving the elongation due to the plain section portion of the rebar). If the



thread continues into the foundation, the embedment should be considered with a length not larger than the length of the strain penetration  $L_{sp}$ .

The length of the strain penetration and the coefficient  $k$  were taken from Priestley *et al* (2007), as:

$$L_{sp} = 0.022 f_y \varnothing \quad \text{and} \quad k = 0.2(f_u/f_y - 1) \leq 0.08$$

where  $f_y$  and  $f_u$  are the strength at yielding and the ultimate strength of the steel.

In particular, with reference to the bar-anchor M20 made of B450C steel, designed according to the standard bolted-socket technology with a free thread length  $L_{thread}$  of 80 mm, the final elongation is:

$$\Delta u^* = 0.075 \times 80 + [0.002 + (540 \times 245 / 314 - 450) (0.075 - 0.002) / (540 + 450)] \times 154.4 = 6.32 \text{ mm}$$

$$\text{with } L_0^* = 0.022 \times 450 \times 20 \times (245 / 314) = 154.4 \text{ mm}$$

Hence the *length coefficient* is

$$\chi = \Delta u^* / \Delta u_{thread} = 5.57 / (0.075 \times 80) = 1.05.$$

In Figure 15 the experimental and the analytical cycles are compared for the different connections.

For post-inserted protruding bars, the experimental resistance was used to calibrate the model ( $f_y = 510$  MPa and  $f_u = 610$  MPa). For the other specimens the mean strength was calculated by multiplying the characteristic values ( $f_y = 450$  MPa and  $f_u = 540$  MPa) by 1.08. these values were used in the analysis of standard and inverted bolted sockets.

On the whole, the numerical results are in satisfactory agreement with the test results, with some differences.

In the case of protruding bars, the extension of the plastic hinge would lead to a large displacement ductility (7-9% expected for the ultimate drift), while in the test with post-inserted protruding bars the collapse did occur at 4.5% drift, because of the early breaking of the bars in threaded zone.

Taking into consideration the experimental yield drift of 1.5%, it is worth noting that, considering the reduction of the plastic branch observed in the tensile test, the plastic branch would have become  $(8 - 1.5) \times 0.43 + 1.5 = 4.3\%$ , in good agreement with the experimental results. In the case of standard shoes, the behaviour is well predicted by the analysis.

In the case of the connection with inverted shoes, the maximum force is satisfactorily predicted, but the same cannot be said of the ductility, which is affected by an earlier and unexpected failure in the bush coupling.

In the case of the connection with couplers, both the maximum forces and the displacements are satisfactorily predicted. (Note that the asymmetry of the hysteretic cycles is due to the actual loading sequence).

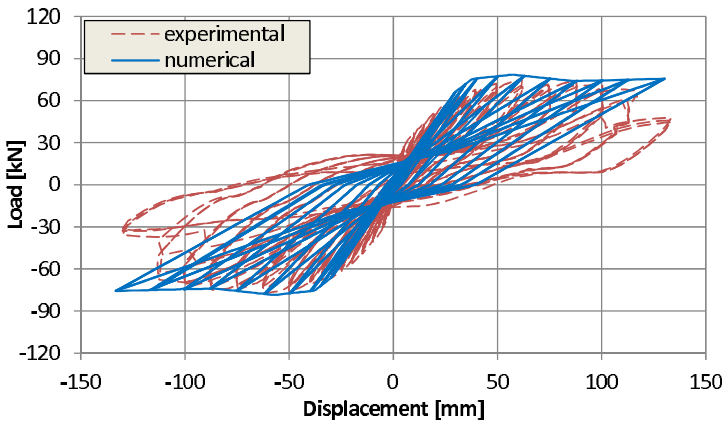
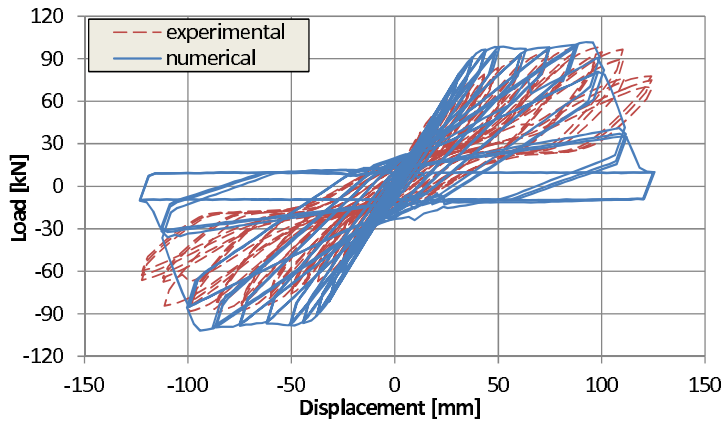
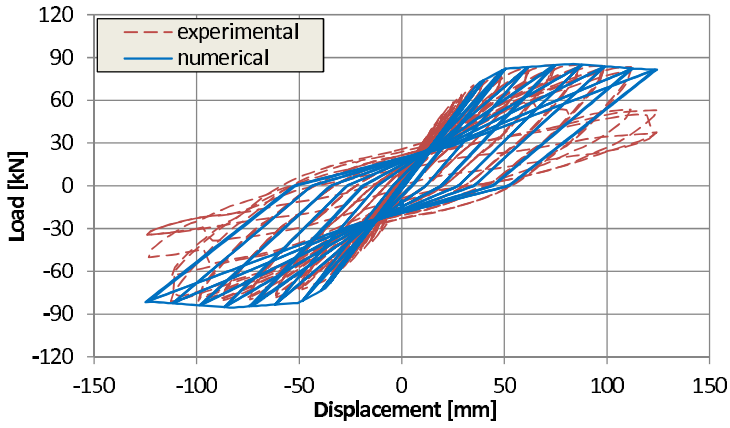


Figure 15a,b,c – Fitting of the experimental results: (a, top) protruding separated bars; (b, middle) standard bolted sockets; and (c, bottom) inverted bolted sockets.

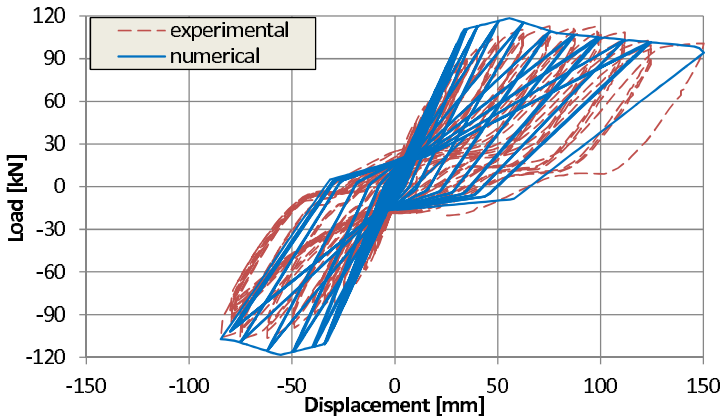


Figure 15d – Fitting of the experimental results: couplers.

## 7. CONCLUSIONS

Five types of column-to-foundation connections were tested under cyclic loading, to investigate their mechanical performance, in terms of failure mode, position of the plastic hinge, shape of the hysteretic cycles and energy dissipation.

In all the tested connections similar envelope curves were found from the cycles. Sizeable differences were observed concerning displacement ductility, (because of the different length of the plastic hinge), and energy dissipation (due to the different hysteretic shape). In particular, the technology based on column shoes bolted sockets concentrates the plastic hinge into a well-defined short-length region and the technology based on post-inserted protruding bars concentrates the plastic hinge close to the weakened discontinuity.

The connections based on column shoes bolted sockets and on couplers show sizeable pinching effects, with rather *narrow* hysteretic cycles.

The tests brought to the front line the unsatisfactory behavior of the welds in critical area, especially in the connections based on weakened column shoes bolted sockets and in few other cases.

A numerical investigation allowed to validate the proposed formulations for the definition of the plastic hinge length for each technology, and to calibrate the hysteretic parameters. What appears from the tests performed so far is that a new definition of the behaviour factor  $q$  is mandatory when using such structural systems in seismic design.

A correction of the  $q$  factor in the case of cantilever-type frames can be formulated taking advantage of the displacement ductility evaluated by means of the proposed formulations. Further limitations to the value of the  $q$  factor are suggested whenever the area enveloped by the hysteretic cycles is significantly smaller than in the case of well detailed reinforced-concrete sections.

## ACKNOWLEDGEMENTS

This project was developed within the framework of the Research Project “SAFECAST” financially supported by the European Communities within the Programme FP7-SME-2007-2 , Grant Agreement No. 218417 (2009).

## REFERENCES

- CEN-EN 1998-1:2004 (2004). *Eurocode 8: Design of Structures for Earthquake Resistance – Part 1 General Rules, Seismic Actions and Rules for Buildings*, European Committee for Standardization, Brussels, Belgium.
- Dal Lago A. (2012). “The Kaptor System for the Design of Earthquake-Resistant Connections” (in Italian). *Proc. Proc. Workshop on “Connections in Precast Structures”*, Bergamo (Italy), October 5, 10 pp.
- Dal Lago B. and Dal Lago A. (2012). “Precast Structures with Adaptable Restraints”. *Proc. 15<sup>th</sup> WCEE Congress*, Lisbon (Portugal), Sept. 24-28, Ref. Code 2305, 10 pp.
- Dal Lago B., Lamperti T.M. and Toniolo G. (2012). “Experimental Investigation on Column-Foundation Connections for Pre-Fabricated Structures” (in Italian). *Proc. 19<sup>th</sup> CTE Congress*, Bologna (Italy), November 8-10, pp. 121-129.
- Dowell R. K., Seible F. and Wilson E. L. (1998). “Pivot Hysteresis Model for Reinforced Concrete Members”. *ACI Structural Journal*, Vol.95, No.5, pp. 607-617.
- Fagà E., Bianco L., Bellotti D., Bolognini D. and Nascimbene R. (2010). “Cyclic Behaviour of Pre-Fabricated Column-to-Foundation Connections Based on Metallic Plates and Embedded Bars” (in Italian). *Proc. 18<sup>th</sup> CTE Congress*, Brescia (Italy), November 11-13, pp. 21-30.
- Halfen HCC Column Shoe Connections – Technical Product Information. *Tech. Catalogue*.
- Halfen HBS-05 Screw Connections – Technical Product Information. *Technical Catalogue*.
- Metelli G., Beschi C. and Riva P. (2011). “Cyclic Behaviour of a Column-to-Foundation Joint for Precast Structures”. *EJECE*, Vol. 15, No. 9, pp. 1297-1318.
- Nakaki S. D., Stanton J. F. and Sritharan S. (1999). “An Overview of the PRESSS Five-Story Precast Test Building”, *PCI J.*, Vol. 44, No. 2, March-April, pp. 26-39.
- Priestley M.J.N., Calvi G.M. and Kowalsky M.J. (2007). *Displacement-Based Seismic Design of Structures*. IUSS Press, Pavia (Italy), 721 pp.
- SAP 2000 Integrated Finite Element Analysis and Design of Structures. *Analysis Reference Manual*.
- Toniolo G. D. (2012). “SAFECAST Project - European Research on Seismic Behaviour of the Connections of Precast Structures”. *Proc. 15<sup>th</sup> WCEE World Conference*, Lisbon (Portugal), Sept. 24-28, Reference Code 1389, 10 pp..

## **SIMPLIFIED APPROACH FOR PUNCHING SHEAR IN FIRE CONDITIONS**

Emmanuel Annerel<sup>1</sup>, Limin Lu<sup>2</sup>, Luc Taerwe<sup>3</sup>

### **ABSTRACT**

Concrete structures often consist in flat slabs supported by a grid of columns. For this kind of structures, the flat slab-column connection is sensitive to punching shear. Design codes, such as the EN 1992-1-1, provide equations to take care of this failure type. During a fire, however, the actual punching load may increase due to the effects of restrained thermal dilation, such an increase being not yet covered in the design codes. In this paper, the Eurocode punching model is used as a basis for a simplified approach to assess the punching shear resistance of flat R/C slabs in fire conditions. The model is adapted by introducing the deterioration of fire-related material properties according to EN 1992-1-2, as well as the loss of concrete cover due to explosive spalling. The accuracy of the proposed model is tested by two independent test programmes consisting of real-scale fire tests on flat concrete slabs, the first carried out by Kordina in 1993 and the second by the authors of this paper in 2010. Adequate agreement is found for both test programmes.

**KEYWORDS:** concrete, fire, flat slabs, punching shear, Eurocodes

---

<sup>1</sup> Postdoctoral Researcher, <sup>2</sup> Researcher, <sup>3</sup> Professor  
Laboratory Magnel for Concrete Research, Department of Structural Engineering,  
University of Ghent, Ghent, Belgium

## 1. INTRODUCTION

Underground structures such as car parks are often designed and built as flat slabs supported by a grid of columns. This type of structure is sensitive to punching failure, since the slabs have a large span-to-depth ratio (25 to 30 in R/C slabs; 35 to 40 in P/C slabs, see Bamonte et al., 2009), and both the bending moments and shear forces are locally rather large due to the point-like support offered by the columns. Therefore, equations are given in the design codes, such as the Eurocodes, to design the structure at ambient temperature with respect to possible punching failure. On the other hand, during fire, additional actions can be introduced into the structure because of the restrained thermal displacements. Meanwhile, materials properties (namely strength and stiffness) decrease due to the heating process. The restrained thermal displacements can increase the punching load and make punching more probable (Bamonte et al., 2009; Annerel et al., 2012b). For the actions ensuing from the restrained thermal displacements, as well as for the loss of punching-shear capacity in fire, no design guidelines are yet available. In this paper, both effects are considered and discussed.

In the literature, the collapse of the roof of an underground car park in Gretzenbach (Switzerland) during a fire on 11 November 2004 is reported as being caused by punching. During the intervention of the firemen, seven persons were killed. The subsequent fire investigation revealed design and construction mistakes resulting in an overload caused by the soil on top of the roof and a reduced punching-shear capacity due to a smaller effective depth than that specified in the design (Muttoni et al., 2005). In the framework of this accident, a comprehensive project was set up in Belgium in 2009, with the objective of performing fire tests on concrete flat slabs (columns without drop panels). In this paper, the test results are used to propose a simplified calculation method that can provide indications on the punching resistance of a fire-exposed slab-column connection. The calculation procedure is tested with reference to the experimental data of Kordina (1993).

As a basis for the simplified calculation method, the punching model described in EN 1992-1-1 (CEN, 2004a) is used, in combination with the decay of the fire-related materials properties according to EN 1992-1-2 (CEN, 2004b). Though designers are familiar with this model, the background of its coefficients is not completely understood, especially with reference to the application in fire conditions, so that the model can only be used as an indication of the punching resistance at high temperature, but cannot be used for a-priori modeling.

## 2. LARGE- SCALE FIRE TESTS ON PUNCHING

The punching resistance of flat concrete slabs exposed to fire has been so far the subject of a limited number of tests documented in the technical-scientific literature. Hereafter, the test results by Kordina (1993) and those by the authors (Annerel et al., 2011/2012a) are summarized.

## 2.1 Kordina (1993)

Kordina reported 14 real-scale experiments on flat concrete slabs to study the punching resistance in fire conditions (fire-exposed intrados, ISO 834 fire curve, see Table 1 for details and test results).

In the test setup, the specimen (= flat slab) was connected to a column stub. A rod contained in a central hole along the axis of the stub and passing through the slab was anchored to the bottom face of the stub and pulled upwards by means of a hydraulic jack, that was fixed to a reaction frame on top of the slab. In this way, the column stub pushed against the slab. The upward load applied to the column stub was resisted by 8 downward concentrated forces exerted by as many ball joints. These ball joints were distributed on top of the slab along a circle with a diameter of 2.20 m (see the sketch of the setup in Bamonte et al., 2012) and were connected to the reaction frame. Among the 14 square slabs (side = 2.5 m), 10 slabs (designated 1 to 10) had a thickness of 0.20 m and 4 (designated A to D) had a thickness of 0.15 m. The column stub measured 0.25 x 0.25 x 0.4 m.

Table 1 – Details of the slabs tested by Kordina (1993) and test results.

Test number	1	2	3	4	5	6	7	8	9	10
$f_c$ [N/mm <sup>2</sup> ]	45	45	51	51	33	33	53	53	43	43
Long. Reinf. [%]	0.56	0.56	1.54	1.54	1.54	1.54	0.56	1.54	0.56	0.56
Shear reinf. [mm <sup>2</sup> ]	-	452	-	678	-	-	-	-	-	452
Effective depth [mm]	167	167	167	167	167	167	167	167	167	167
Test duration [min]	120	120	27	17	90	90	29	70	90	22
Service load [kN]	229	372	330	520	232	238	404	334	227	359
Failure load $V_T$ [kN]	492	475	550	810	386	380	500	568	410	460
$V_T$ /service load [-]	2.15	1.28	1.67	1.56	1.66	1.60	1.24	1.70	1.81	1.28
Load increased during fire (> service load)	NO	NO	YES	YES	YES	YES	YES	YES	YES	YES
Spalling	NO	NO	YES	YES	NO	NO	YES	YES	YES	YES

Test number	A	B	C	D
$f_c$ [N/mm <sup>2</sup> ]	39	39	37	37
Long. Reinf. [%]	1.75	1.75	1.75	1.75
Shear reinf. [mm <sup>2</sup> ]	-	-	-	-
Effective depth [mm]	120	120	120	120
Test duration [min]	14	8	180	92
Service load [kN]	287	287	260	160
Failure load $V_T$ [kN]	345	360	>260	>260
$V_T$ /service load [-]	1.20	1.25	>1	>1
Load increased during fire (> service load)	YES	YES	NO	NO
Spalling	NO	NO	NO	NO

The steel ratio of the longitudinal reinforcement was 0.56% and 1.54% in the 0.2m thick slabs (No.1-10), but only three slabs (No. 2 , 4 and 10) had shear reinforcement ( $452 \text{ mm}^2 = 0.196\%/m^2$  or  $678 \text{ mm}^2 = 0.160\%/m^2$ ,  $\varnothing 6\text{mm}$ - bars, positioned at 240 and 325 mm from the centre of the slab, respectively). The steel ratio of the 0.15m-thick slabs (A-D) was 1.75% and no shear reinforcement was provided.

According to Table 2.9 of EN 1992-1-2 about the fire resistance of flat slabs, the slabs with thickness of 0.2 m have a REI 180 (minimum slab thickness larger than 200 mm, bar axis-to-surface distance smaller than 50 mm) and the slabs with thickness of 0.15 m have a REI 30 (minimum slab thickness larger than 150 mm, bar axis-to-surface distance larger than 10 mm; REI 180/30 = fire resistance in terms of bearing capacity, integrity and insulation above 180 or 30 minutes; ISO 834 standard fire curve).

The compressive strength on cylinders ( $\varnothing 150 \text{ mm}$ ; height 300 mm) at the time of testing was comprised between 33 to 51 N/mm<sup>2</sup>.

The slabs were loaded prior to heating by a service load calculated as 0.7 times the punching resistance at the ultimate limit state, according to EN 1992-1-1. For Slabs 1, 2, C and D, this load was maintained during the fire test for respectively 120, 120, 180 and 92 minutes; subsequently, the load was increased until punching failure. Comparing the values  $V_T$  obtained in the punching-shear tests with the service load, a safety factor between 1.28 and 2.15 was found.

For the other slabs, the service load was increased during the first 30 minutes of the fire in order to simulate the increase of the load caused by restrained thermal displacements. In a first group of slabs (Slabs 3, 4, 7, 10, A and B) the failure occurred 8 – 29 minutes after the onset of the fire, under increasing loads. In particular, in Slabs 3, 4, 7 and 10 the failure was accompanied by severe spalling with the detachment of the concrete cover along the bottom reinforcement (mean spalling depth = 50 mm). The moisture content in the concrete at the moment of testing was close to 4%. The failure load was 1.24-1.67 times the service load.

In a second group of slabs (Slabs 5, 6, 8 and 9) the failure did not occur during the increase of the load, but later. At a 30 minutes fire duration, the load level ranged from 1.26 to 1.46 times the service load. At a 90 minutes fire duration, the load was further increased until failure and the resulting safety margin was comprised between 1.60 and 1.80.

All 14 experiments tests were characterized by the formation of a punching cone. In the 0.2m thick slabs the top diameter of the cone varied between 1.28 and 1.86 m and the average cone angle was 32°.

Furthermore, the deflections of the 0.2 m thick slabs were found to be opposite to the punching load throughout the test, this being demonstration that the thermally induced deformation (directed towards the fire) was larger than the deflection due to the load as such. The 0.15 m thick slabs exhibited the same behaviour during the first 30 minutes, but later the deflection reversed and followed the direction of the load.



## 2.2 Annerel et al. (2011) and Annerel et al. (2012a)

In 2010, the authors tested six real-scale slab specimens in punching. Four specimens were subjected to ISO 834 fire along their intrados for 120 minutes (designation: S0, S1, S2 and S5) and two specimens were tested at ambient temperature (designation: S0b and S5b, same geometry and reinforcement as S0 and S5). The size of the specimens was 3.2 x 3.5 x 0.25 m and the size of the column stub was 0.3 x 0.3 x 0.65 m. During each fire test, two specimens were tested simultaneously.

Similarities with the test programme by Kordina can be found in the test setup, in the compressive strength on cylinders ( $\varnothing$  150 mm, height 300 mm) close to 33 N/mm<sup>2</sup> and in the longitudinal reinforcement ratio (0.6%). The slabs were loaded according to the service loads specified in EN 1992-1-1 for a grid of 6 x 6 m, and this load was kept constant for 120 minutes; after which, the load was increased up to failure.

With respect to Kordina's tests there are differences in the larger size of the slabs (but the concrete cover is smaller = 26 mm) and in the amount of shear reinforcement (stirrups  $\varnothing$  6mm), namely 226 mm<sup>2</sup>, 452 mm<sup>2</sup> and 1130 mm<sup>2</sup> (details of the position of the reinforcement can be found in Annerel et al. (2012a)). Table 2 summarizes the details of the specimens and the test results regarding the punching failure of the six slabs tested.

Table 2 – Details of the specimens tested by Annerel et al. (2012a) and test results.

Test number	S0	S1	S2	S5
$f_c$ [N/mm <sup>2</sup> ]	32.9	32.9	31.3	31.3
Long. Reinf. [%]	0.6	0.6	0.6	0.6
Shear reinf. [mm <sup>2</sup> ]	0	226	452	1130
Effective depth [mm]	212	212	212	212
Duration of the test [min]	120	120	20	120
Service load [kN]	270	336	402	420
Failure load $V_{20^\circ C}$ [kN]	988	-	-	1050
Failure load $V_T$ [kN]	588	627	-	-
$V_T$ /service load [-]	2.17	1.87	-	-
Load increased during fire (> service load)	NO	NO	NO	NO
Spalling	YES	YES	YES	YES

In the second fire test (on Slabs S2 and S5), a technical error consisting in a wrong connection of the hydraulic lines prevented the measurement of the loads. However, based on the deflections measured during the loading period prior to heating (until the service load was attained), the load applied to Slab S2 was 1.5-2 times the service load, whereas the load applied to Slab S5 was only a fraction of

the service load (50-150 kN, close to 10-30%). Being overloaded, Slab S2 failed in punching after 20 minutes of fire duration.

The net concrete cover was 26 mm for the flexural reinforcement (distance from bar axis to concrete surface = 32 mm; bar diameter = 12 mm) and 20 mm for the stirrups ( $\varnothing$  6mm). According to Table 5.9 of EN 1992-1-2 for flat slabs, the specimen without stirrups S0 has a fire resistance of REI 90. However, since the required bar axis-to-surface distance for REI 120 is 35 mm, the actual fire resistance of the slabs will be close to REI 120 as the distance is already 32 mm.

### **3. SIMPLIFIED APPROACH FOR PUNCHING SHEAR IN FIRE CONDITIONS, BASED ON TEST DATA FROM ANNEREL (2012a)**

As mentioned in the introduction, a punching model is given in EN 1992-1-1 to design concrete structures at ambient temperature. This model is taken as the basis of a refined zone model, that - for the specific cases studied in this paper - allows to calculate the punching shear resistance of the slabs tested by the authors.

The calculation consists of two steps: (1) thermal analysis; and (2) mechanical analysis. Firstly, the cross section of the slab is divided into thin layers. The temperature of each layer is computed at each time step

Secondly, the concrete properties are adjusted to the average temperature of each layer and the punching shear resistance at each time step is evaluated. It should be observed that this approach can only be used to have a rough indication on the punching resistance at high temperature and not to model the phenomenon.

More testing and fundamental research is necessary to formulate a complete model. Furthermore, the model takes into account spalling, whereas in the design of concrete structures exposed to fire, spalling is generally ignored.

#### **3.1 Thermal field**

The slabs are assumed to be heated only from the bottom. The ISO 834 fire curve is adopted in both the fire tests and the finite element simulation. The heating of the slab including the column stub at the bottom is calculated as a 2D sectional problem with the package DIANA.

The reinforcement is neglected in the evaluation of the thermal field, something that is generally taken from granted and that is justified by the low steel amount and by the high thermal diffusivity of the steel. As a matter of fact, these factors prevent the reinforcement from affecting significantly the thermal field of the cross section. The concrete section is divided into small square elements with a side length of 10 mm. The average temperature of these elements is calculated at each time step. The emissivity related to the concrete surface is taken as 0.7, whereas a convection factor of 25 W/m<sup>2</sup>K is adopted at the heated surface. The thermal conduction coefficient and the specific heat of concrete are taken from EN 1992-1-2.

### 3.2 Mechanical analysis

Flat slab-column connections fail due to punching shear when a punching cone is developed. In the model of EN 1992-1-1, the angle of the punching cone with respect to the slab bottom is taken as  $26.6^\circ$ . The EN 1992-1-1 method is based on the assumption that the slab fails when inclined cracking starts near the column face and reach the extrados of the slab.

The perimeter of the intersection of this punching cone with the horizontal plane containing the axes of the top reinforcement is called *basic control perimeter* ( $u_1$ ). Based on this failure mechanism, a semi-empirical *critical section method* is used to calculate the punching shear resistance of a flat slab.

At ambient temperature, the design value of the punching shear capacity of a flat slab is given by Equations 1 and 2, respectively for a slab without and with shear reinforcement. In these equations, the punching resistance is a function of concrete shear strength, which is given as a function of the compressive strength.

$$V_{Rd,c} = [(0.18/\gamma_c) k (100 \rho_1 f_{ck})^{1/3} + k_1 \sigma_{cp}] u_1 d \quad (1)$$

$$V_{Rd,cs} = 0.75 \times V_{Rd,c} + 1.5 \times (d / S_r) A_{sw} (f_{yk,ef} / \gamma_s) \sin \alpha \quad (2)$$

where:  $k = 1 + (200/d)^{1/2} \leq 2$  with d in mm

with

$\rho_1$  tensile reinforcement ratio of the slab [-]

$f_{ck}$  characteristic compressive strength of the concrete [N/mm<sup>2</sup>]

$u_1$  basic control perimeter [mm]

d effective depth of the slab [mm]

$S_r$  radial spacing of perimeters of shear reinforcement [mm]

$A_{sw}$  area of one perimeter of shear reinforcement around the column [mm<sup>2</sup>]

$f_{yk,ef}$  effective characteristic yield strength of the punching shear reinf. [N/mm<sup>2</sup>]

$\alpha$  angle between the shear reinforcement and the plane of the slab [°]

$\gamma_c$  partial safety factor for concrete [-]

$\gamma_s$  partial safety factor for steel [-]

At high temperature, authors' proposal is to calculate the punching-shear resistance by using Equation 3, which can be derived from Equations 1 and 2, with  $\sigma_{cp} = 0$  (no compression stresses from the lateral directions of the slab,  $\sigma_{cp} = 0$ ). The partial safety factors are taken as 1 according to EN 1992-1-2 and the factor 0.75 of  $V_{Rd,cs}$  is dropped (in agreement with NBN B15-002).

$$V_T = \eta_a 0.18 k (100 \rho_l f_{ck})^{1/3} u_l d + 1.5 (d / S_r) A_{sw} f_{yk,ef}(T_{h,ef}) \sin \alpha \quad (3)$$

where:

$\eta_a$  average reduction factor of the punching shear strength of the slab; it is calculated by the reduction factor of each layer  $\eta(T_i)$ :

$$\eta_a = \frac{1}{n} \sum_{i=1}^n \eta(T_i)$$

where :

$T_i$  is the temperature [ $^{\circ}\text{C}$ ] of layer  $i$  ( $i = 1 \dots n$ )

$T_{h,ef}$  is the effective temperature of the stirrups [ $^{\circ}\text{C}$ ]

To introduce the influence of fire on punching-shear resistance, a global reduction factor  $\eta_a$  is introduced in  $V_{Rd,c}$ . It is proposed not to reduce the compressive strength as such, because it is doubtful whether the shear strength at high temperature is a function of the compressive strength similarly to what happens at room temperature. For the decrease of  $V_{Rd,c}$  as a function of the temperature by means of  $\eta_a$ , the two curves specified in EN 1992-1-2 are adopted, for the decrease of the compressive strength and for the decrease of the tensile strength, respectively.

A better agreement with the fire tests was found when using the tensile-strength loss curve.

The decrease of the yield strength of the stirrups with the temperature is implemented according to EN 1992-1-2 based on the *effective tension area*. The *effective tension area* is that part of the cross section which is in tension just before the development of the first crack.

In EN 1992-1-1, equations are given to calculate the depth of the effective area, resulting in  $h_{ef} = 80$  mm. In Equation 3, the yield strength of the stirrups is taken as function of the temperature corresponding to this effective depth, namely  $f_{yk,ef}(T_{h,ef})$ .

### 3.3 Calculation results

The loss of punching resistance upon heating is calculated with Equation 3 for the 4 slabs, namely S0, S1, S2 and S5. The compressive strength of the concrete, its Young's modulus and the strength at yielding of the flexural and shear reinforcement are:

- $f_c = 33 \text{ N/mm}^2$ ;
- $E_c = 31000 \text{ N/mm}^2$ ;
- $f_y = 500 \text{ N/mm}^2$ .

Figures 1-4 show the heat-induced loss of punching resistance, given as the ratio between the punching strength at high temperature  $V_T$  and that at ambient temperature  $V_{20^\circ\text{C}}$ .

Figures 1 and 2 show the calculation results when no spalling is considered. In Figure 1, the calculations are based on the loss of the compressive strength, whereas in Figure 2 the calculations are based on the loss of the tensile strength. After 120 minutes of ISO 834 fire, the results based on the compressive strength exhibit a loss in terms of punching resistance close to 15%, while the results based on the tensile strength the loss is more severe, being close to 25%.

These losses are smaller than those found experimentally (close to 40% in Slabs S0 and S1), and the difference may be due to the loss of concrete cover (spalling), as observed during the fire tests.

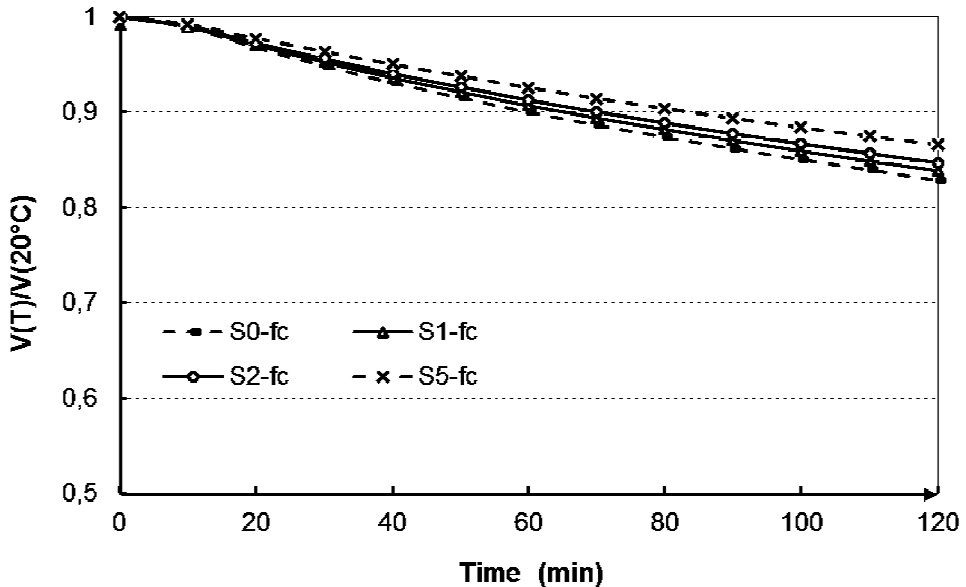


Figure 1 – Plot of the punching-shear resistance as a function of time in a ISO 834 fire, when using the  $f_c^T/f_c$ -curve and neglecting the spalling.

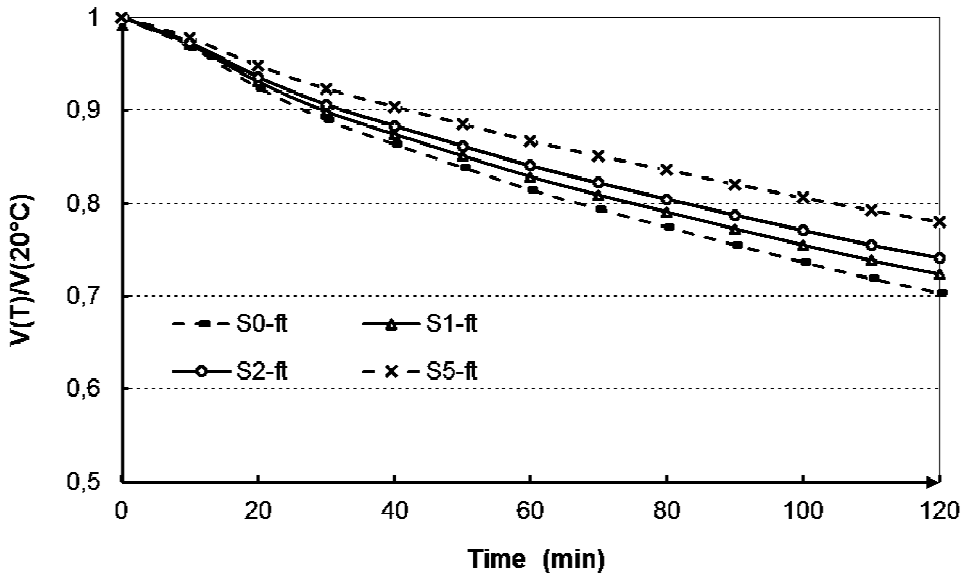


Figure 2 – Plot of the punching-shear resistance as a function of time in a ISO 834 fire, when using the  $f_t^T/f_t$ -curve and neglecting the spalling.

Therefore, concrete spalling of the cover of the bottom reinforcement was introduced in the calculations as a gradual loss of the outer layers. When a temperature of 350°C is reached in one layer, this layer is removed from the thermal and mechanical calculations. This spalling criterion was proposed by Kodur and Dwaikat (2008) on the basis of a number of tests. This process goes on until the concrete cover of 26 mm is totally removed. The results are given in Figures 3 and 4, where reference is made to the strength loss in compression and in tension, respectively.

Figures 3 and 4 clearly show that the spalling of the bottom cover has a sizeable influence on the punching-shear resistance, as the additional losses due to spalling are close to 10-15%.

The experimental values of the punching-strength loss after 120 minutes are close to 25-30% of the initial values, something that is justified by the calculations when spalling is neglected and the decay in tension is introduced (Figure 2).

Furthermore, Figure 4 (where the decay in tension and cover spalling are introduced), shows that an additional punching shear loss due to spalling of about 10-15% occurs. At 120 minutes, the punching strength loss is close to 40% for slabs S0, S1 and S2, which is in good agreement with the fire tests.

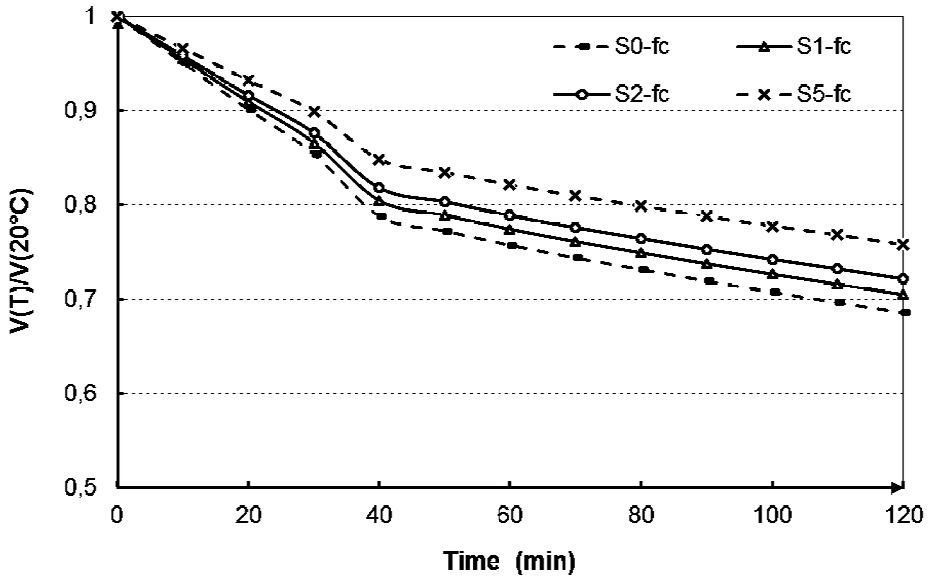


Figure 3 – Plot of the punching-shear resistance as a function of time in a ISO 834 fire, when using the  $f_c^T/f_c$ -curve and introducing spalling.

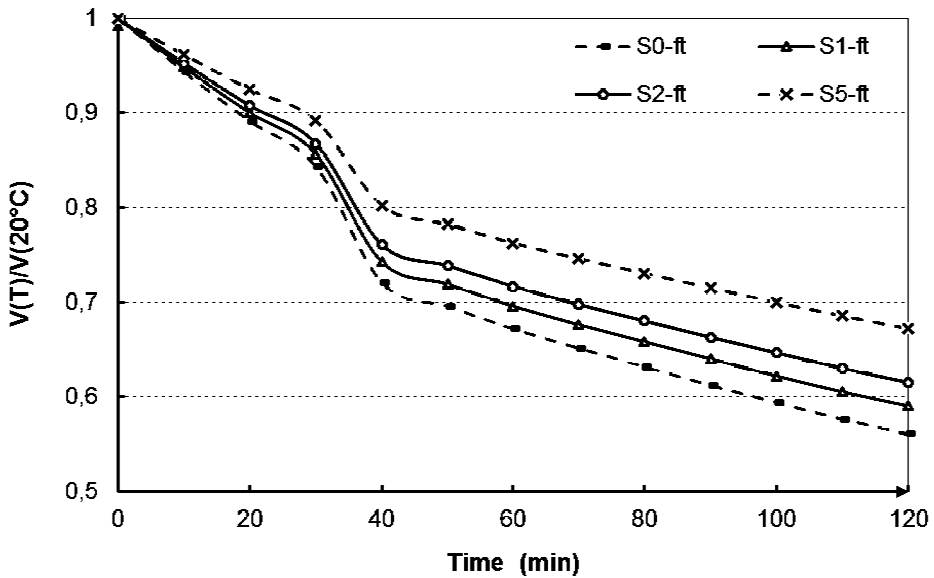


Figure 4 – Plot of the punching-shear resistance as a function of time in a ISO 834 fire, when using the  $f_t^T/f_t$ -curve and introducing spalling.

To summarize the numerical results obtained by reducing the tensile strength and including the spalling, the resistances to punching of the four slabs tested in fire are reported in Table 3, at the beginning of the fire ( $t = 0$ ;  $V_{20^\circ\text{C}}$ ) and after 120 minutes ( $V_T$ ).

Table 3 – Calculated punching-shear resistances.

Slab	Punching resistance $V_{20^\circ\text{C}}$ [kN]	Punching resistance $V_T$ after 120 min heating [kN]	$V_T/V_{20^\circ\text{C}}$ [-]
S0 (*)	747	419	0.56
S1 (**)	816	487	0.60
S2 (***)	885	556	0.63
S5 (****)	1090	761	0.70

(\*) No stirrups; (\*\*, \*\*\*, \*\*\*\*) with stirrups: steel ratio = 0.080, 0.086, 0.129%/m<sup>2</sup>, respectively.

The calculations show a significant improvement of the punching shear resistance when the steel ratio of the stirrups is increased. A satisfactory agreement is found with the experimental value for Slab S5 for the test at ambient temperature (1050 kN, Table 2). On the other hand, for Slab S0 (no stirrups) the experimental value of the punching resistance (988 kN, Table 2) is rather close to the numerical value obtained for Slab S5 (1090 kN, Table 3). The calculated punching strength of Slab S0 (747 kN, Table 3) is then about 250 kN lower than the experimental value. After 120 minutes of ISO 834 fire, the residual punching resistance is comprised between 56% and 70% of the resistance before the fire, which is a sizeable reduction.

#### 4. COMPARISON WITH TESTS REPORTED BY KORDINA

To have a further verification of the calculation approach, the punching-shear tests reported by Kordina are examined.

In Figures 5 and 6 the calculated punching resistance according to Eq. 3 (0.2 m-thick slabs) is plotted as function of fire duration, for given values of the compressive strength, longitudinal steel ratio and amount of stirrups. The resistances  $R(T)$  are indicated by means of a continuous line with a marker (reference is made to the tensile-strength reduction curve provided by EN 1992-1-2). The punching resistance decreases more steeply in Figure 6 than in Figure 5 in the first 30 minutes, since in Figure 6 a progressive spalling is introduced (final depth = 50 mm, as mentioned in the report by Kordina).

Figures 5 and 6 illustrate the loading paths up to failure  $E(T)$  adopted in the fire tests by Kordina (dashed lines). Only the failure moment is marked by using the same marker adopted for the same slab in the curves of the resistance versus time (slabs are designated as in the original report by Kordina).



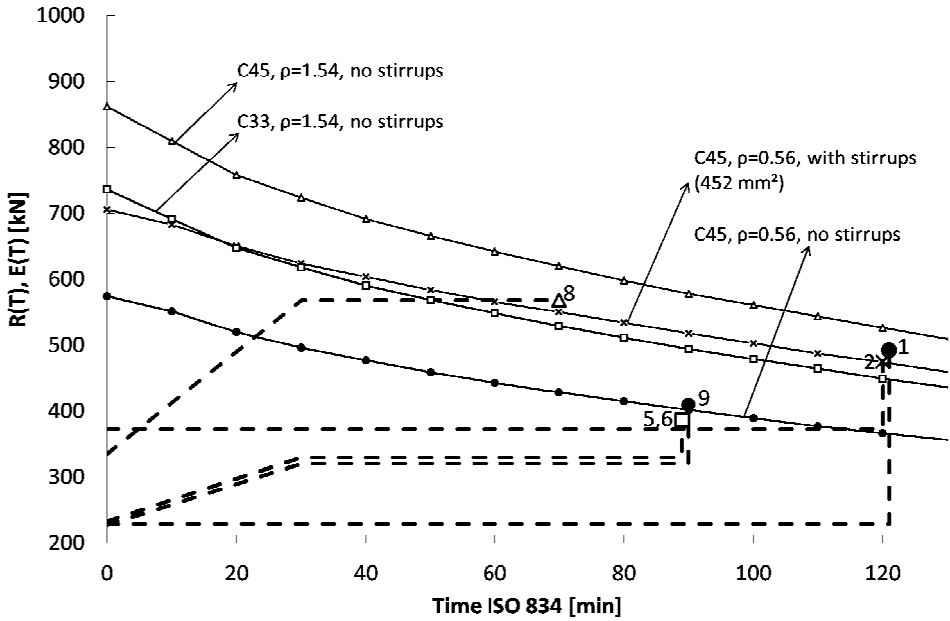


Figure 5 – Slabs without cover spalling: simplified model proposed by the authors versus the test results by Kordina (1993).

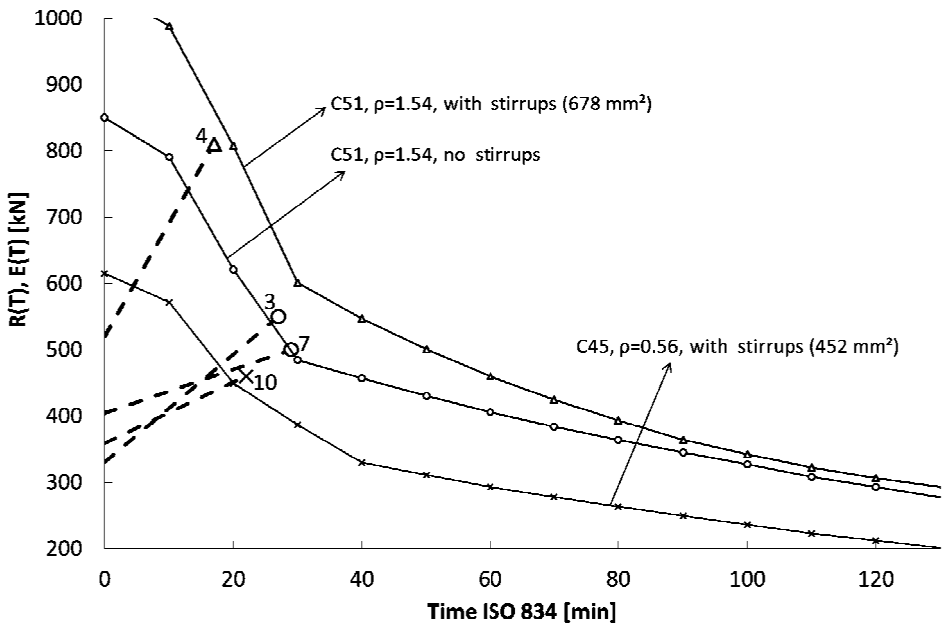


Figure 6 – Slabs subjected to cover spalling: simplified calculation model proposed by the authors versus the test results by Kordina (1993).

The model proposed by the authors fits well the test results of Slabs 2-4 and 7-10, but over/under-estimates the test results of Slab 1, and of Slabs 5 and 6, respectively.

## 5. CONCLUSIONS

- The calculations based on the EN1992-1-2 model for punching resistance of flat slabs provide reasonable results when spalling is included in the analysis, by removing the bottom cover (as observed in the tests) and if the thermally-induced strength loss is according to the steeper degradation curve given in EN 1992-1-2 for the tensile strength; the model fits reasonably well the experimental results by Kordina.
- The loss of the concrete cover due to spalling contributes to an additional loss (up to 10-15%) of the punching resistance; to avoid structural problems, the spalling risk should be reduced as much as possible.
- The proposed calculation procedure should only be used to have an indication about the punching resistance at high temperature, and not to model such a complex phenomenon as punching.

## ACKNOWLEDGEMENTS

This research project was financially supported by IWT Flanders through the SBO Project 080010: “Fundamental design approaches for the improvement of fire safety in car parks”.

## REFERENCES

- Annerel E., Lu L. and Taerwe L. (2011). “Punching Shear Tests on Flat Concrete Slabs at High Temperatures”. *2nd Int. RILEM Workshop on Concrete Spalling due to Fire Exposure*, E. Koenders and F. Dehn eds., October 5-7, Delft (The Netherlands), RILEM Publications S.A.R.L., pp. 125-131.
- Annerel E., LU L. and Taerwe L. (2012a). “Punching Shear Tests on Flat Concrete Slabs exposed to Fire”. *Fire Safety Journal*, <http://dx.doi.org/10.1016/j.firesaf.2012.10.013>.
- Annerel E., Taerwe L., Merci B., Jansen D., Bamonte P. and Felicetti R. (2012b). “Thermo-Mechanical Analysis of an Underground Car Park Structure Exposed to Fire”. *Fire Safety Journal*, <http://dx.doi.org/10.1016/j.firesaf.2012.07.006>.
- Bamonte P., Felicetti R and Gambarova P.G. (2009). “Punching Shear in Fire-Damaged Reinforced Concrete Slabs”. American Concrete Institute, *ACI Special Publication SP 265*, pp. 345-366.

- Bamonte P., Fernández Ruiz M. and Muttoni A. (2012). “Punching Shear Strength of R/C Slabs Subjected to Fire”. *7<sup>th</sup> Int. Conf. on Structures in Fire – SIF 2012*, M. Fontana, Frangi A. and Knobloch M. eds., June 6-8, Zurich (Switzerland), ETH Zurich pub., pp. 689-698.
- CEN (2004a). *EN 1992-1-1, Eurocode 2: Design of concrete structures – Part 1-1: General rules and rules for buildings*. Pub. by CEN, Brussels (Belgium).
- CEN (2004b). *EN 1992-1-2, Eurocode 2: Design of Concrete Structures – Part 1-2: General Rules – Structural Fire Design*. Pub. by CEN, Brussels (Belgium).
- Kodur V.K.R. and Dwaikat M.B. (2008). “Flexural Response of Reinforced Concrete Beams Exposed to Fire”. *Structural Concrete*, Vol. 1, No. 9, 45-54.
- Kordina K. (1993). *Flat Slabs under Fire – Redistribution of the Internal Forces and Punching Tests*. Institut für Baustoffe, Massivbau und Brandschutz, Technische Universität Braunschweig, CEN/TC 250/SC 2/PT 1-2 Doc N35, 1993, 20 pp.
- Muttoni A., Fürst A. and Hunkeler F. (2005). *Collapse of the Roof of the Underground Car Park in Staldenacker – Gretzenbach* (in German: *Deckeneinsturz der Tiefgarage am Staldenacker in Gretzenbach*). Medieninformation vom 15.11.2005, Solothurn, Switzerland, November, 14 pp.



## **PRE-STRESS LOSS AND CAMBER EVOLUTION IN SELF-COMPACTING WING-SHAPED STRUCTURAL MEMBERS**

Marco Breccolotti<sup>1</sup>, A. Luigi Materazzi<sup>2</sup>

### **ABSTRACT**

Pre-stressed wing-shaped members are today frequently used in the construction of the long-span roofs often required in precast buildings. As a matter of fact, roofs spanning over 30 meters are built by assembling a number of these thin-walled members. In order to optimize their design and to take advantage of their potential in terms of load-bearing capacity, the transfer of huge forces from the pre-tensioned strands to the concrete is a critical issue. Hence, having information on the in-time evolution of these forces and of the ensuing deformations is necessary, not only in the long run but also in the time period immediately after concrete casting and during concrete hardening (a few weeks).

Within this context, the Department of Civil and Environmental Engineering of the University of Perugia (Perugia, Italy) and a major prefabrication firm of Central Italy have recently completed an experimental campaign on pre-tensioned wing-shaped members, to investigate the in-time evolution of the pre-stressing stresses and of the camber during the different stages of concrete hardening.

Numerical comparisons based on EC2 are also performed, with two objectives: to check the reliability of the numerical procedure adopted by the authors and to ascertain whether using self-compacting concrete (as in the manufacture of the specimens tested in this project) brings in any sizeable difference with respect to the predictions based on EC2, which refers basically to ordinary concrete.

**KEYWORDS:** pre-stressed prismatic shells, wing-shaped members, pre-stress loss, camber evolution.

---

<sup>1</sup> Assistant Professor, <sup>2</sup> Professor,  
DICA - Department of Civil and Environmental Engineering, University of Perugia,  
Perugia, Italy

## 1. INTRODUCTION

Pre-stressed wing-shaped members are today frequently used in the construction of the long-span roofs often required in precast buildings. As a matter of fact, roofs spanning over 30 meters are built by assembling a number of these thin-walled members, that may be placed side-by-side or with a certain transverse spacing, often rather huge.

In order to optimize the design of these thin-walled members and to take advantage of their potential in terms of load-bearing capacity, pre-stressing is extensively used, via steel strands that apply to members in question huge forces.

The exploitation of the mechanical properties of the materials, the entity of the pre-stressing forces (necessary to ensure an appropriate bearing capacity) and the requirement that the in-service camber be upward (for aesthetic and functional reasons), makes it mandatory to check and monitor the actual state of pre-stress and camber. Checking and monitoring are currently limited to the control of P/C bridge girders (see – for instance – Roller et al., 2011; Roller et al., 2003; Barr et al., 2005; Al-Omaishi et al., 2009). In this specific case, predictive tools for both deflection and camber, based on test results (Martin, 1977; Stallings et al., 2003; Barr and Angomas, 2010; Tadros et al., 2011), are increasingly used, in combination with structural monitoring techniques (Dwairi et al., 2010).

In order to assess all the possible causes of pre-stress losses and to monitor the evolution of the camber in wing-shaped members during and after concrete casting and hardening, the firm Manini Prefabbricati S.p.A. and the Department of Civil and Environmental Engineering of the University of Perugia have recently completed an experimental campaign on full-scale pre-tensioned specimens, to investigate their behaviour during various stages of their early life. Strain gauges, load cells and displacement transducers were used to measure the actual pre-stress losses and the evolution of the camber in the first 3 weeks after concreting and curing. The results of the tests are presented and discussed in this paper, and – whenever possible – the experimental measurements are critically compared with the theoretical predictions, in order to improve the design provisions and the construction process.

## 2. PRESTRESSED WING-SHAPED MEMBERS

The wing-shaped members studied in this research project have a nominal width of 250 cm, a depth of 71 cm and a length of 16.9-19.80 m. Their V-shaped section at the same time facilitates the removal of the rainwater and the installation, and guarantee the overall stability (Figures 1 and 2).

The materials used in the manufacture of the wing-shaped members have the following properties:

- Self-compacting concrete C45/55 (compressive strength  $f_{cj}$  at the application of pre-stressing = 29-33 MPa);

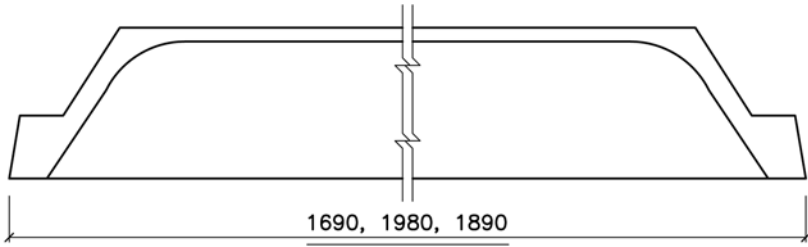


Figure 1 – Longitudinal view of the P/C wing-shaped members tested in this project (measurement unit: cm).

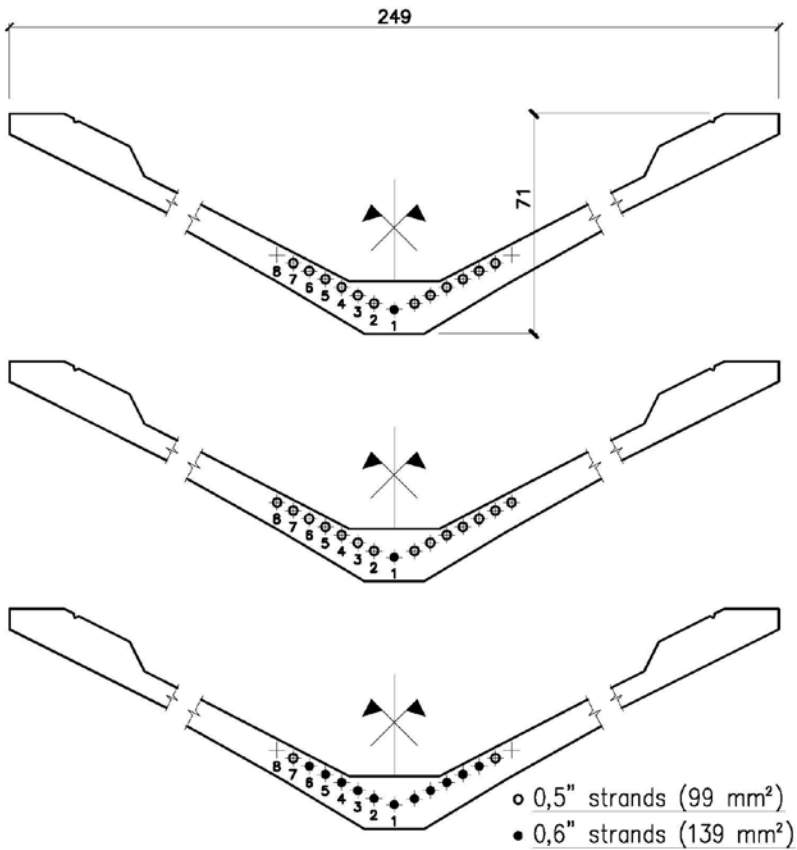


Figure 2 – Cross-sections and pre-stressing strands of the wing-shaped members tested in this project; from top to bottom: Tests 1, 2 and 3 (measurement unit: cm).

- Low-relaxation strands ( $f_{ptk} = 1860$  MPa; initial pre-stressing tension  $\sigma_{pi} = 1400$ - $1500$  MPa);
- B450C steel bars;
- Steel welded-wire mesh B450A.

### 3. EXPERIMENTAL SETUP

The experiments involved three different pre-tensioned specimens cast in different seasons, using a jig which is composed of a movable abutment, a casting bed and a fixed abutment. The anchor heads are blocked in the abutments by means of conical keys. At midspan the steel formwork (which provides the reaction forces required by the abutments to counterbalance the pre-tensioning of the strands) hosts a special device to release the strands and let the prestressing force to be transferred to the concrete member. The specimens differ in their overall length, pre-stressing reinforcement and initial pre-stressing tension (Table 1). A longitudinal view is shown in Figure 1, while Figure 2 shows the cross sections with different pre-stressing strand arrangements.

The members were instrumented with various sensors in order to monitor the pre-stress forces and the evolution of the camber after the release of the strands and the application of the pre-stressing forces.

In particular, the following sensors were used (see Figure 5 for their positions):

- No. 12 strain gauges for measuring the deformation in the strands, appropriately protected from the fresh concrete by means of a water-proof coating in the concreting phase (Figure 3);
- No. 3 strain gauges for measuring the deformation of the concrete surface (the installation was performed after the removal of the upper formwork);
- No. 2 strain gauges embedded in the fresh concrete for the measurement of the deformation of the concrete inside the bulb;
- No. 2 displacement transducers for measuring the vertical displacement, placed in the mean longitudinal plane, at one-fourth and three-fourth of the span;
- No. 2 load cells for measuring the pre-stressing force in as many strands, placed between each anchoring head and the abutment holding all the anchoring heads (Figure 4);
- No. 3 thermocouples, 2 embedded in the fresh concrete for measuring its temperature, and the third one for measuring the ambient temperature.

### 4. RESULTS OF THE EXPERIMENTAL TESTS

The most relevant test results are presented and commented here with reference to:

- Tension in the strands;
- Deformation of the concrete;
- Evolution of the camber;
- Temperature.



#### 4.1 Pre-stressing stress

The tension in the strands was measured by means of (a) electrical strain gauges (SG) glued to the wires of the strands, and (b) load cells placed between the anchoring heads of two strands and the abutment holding all the anchoring heads.

The values of the tensile stress measured on 4 strands during the tensioning in Test 2 are shown in the Figure 6. In this figure the loss of pre-stressing caused by

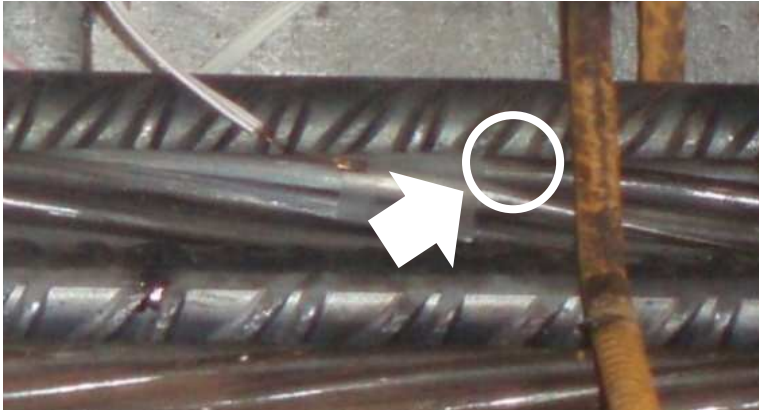


Figure 3 – Strain gauge glued to a pre-stressing strand before the application of the water-proof coating.



Figure 4 – Load cells mounted on two pre-stressing strands.

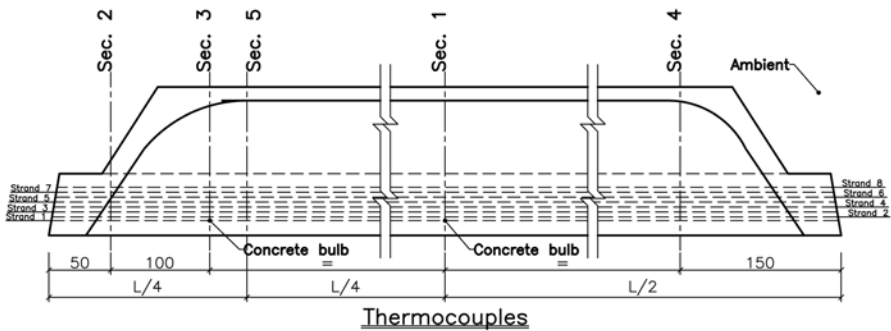
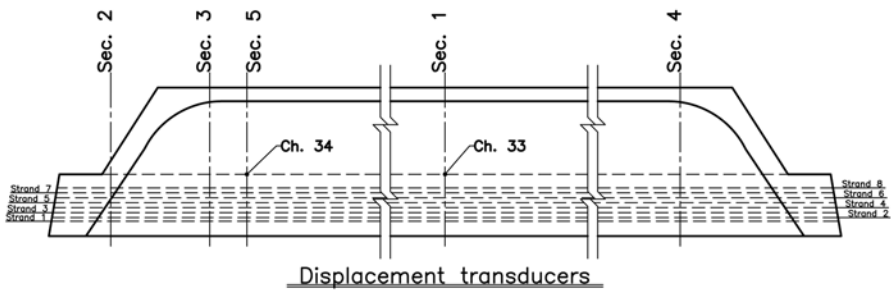
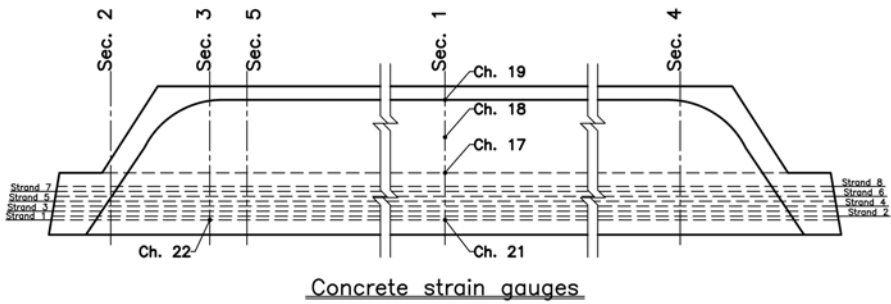
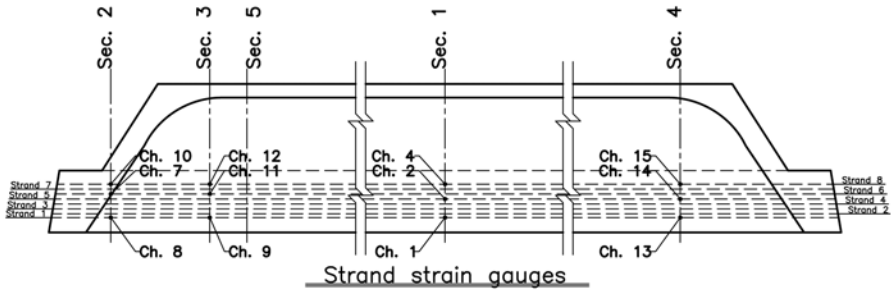


Figure 5 – Positions of the sensors (measurement unit: cm).

Table 1: Length, pre-stressing strands and initial pre-stressing of the specimens.

Test No.	Length (m)	Strands (mm <sup>2</sup> )	$\sigma_{pi}$ (MPa)
1	16,9	1 x 139 + 12 x 99	1400
2	19,8	1 x 139 + 14 x 99	1500
3	18,9	11 x 139 + 2 x 99	1450

Table 2: Sensors of the monitoring system.

Channel	Sensor	Object	Position
1	SG	Strand 1	Sec. 1
2	SG	Strand 5	Sec. 1
4	SG	Strand 8	Sec. 1
7	SG	Strand 6	Sec. 2
8	SG	Strand 1	Sec. 2
9	SG	Strand 1	Sec. 3
10	SG	Strand 8	Sec. 2
11	SG	Strand 6	Sec. 3
12	SG	Strand 8	Sec. 3
13	SG	Strand 1	Sec. 4
14	SG	Strand 5	Sec. 4
15	SG	Strand 8	Sec. 4
17	SG	Concrete	Sec. 1
18	SG	Concrete	Sec. 1
19	SG	Concrete	Sec. 1
21	SG	Concrete	Sec. 1
22	SG	Concrete	Sec. 3
33	LVDT	--	Sec. 1
34	LVDT	--	Sec. 5

the wedge draw-in and by the elastic deformation of the steel formwork produced by the stretching of the successive strands is plotted as a function of time.

Similar results hold for Test 3 (Figure 7). In this case the perfect correspondence between the measurements made with strain gauges (SG) and with the load cells (LC) is remarkable indeed.

In the same figure, it is also possible to observe the reduction of the pre-stress losses depending on the order in which tendons are tensioned, and the effect of a second tensioning.

For example, in Strand 1 the pre-stress increased by 40 MPa (from 1325 MPa at the end of the 1<sup>st</sup> tensioning phase to about 1365 MPa at the end of 2<sup>nd</sup> tensioning phase).

The time history of the tensile stress measured during the hardening phase up to pre-stress transfer of Test 3 is shown in Figure 8.

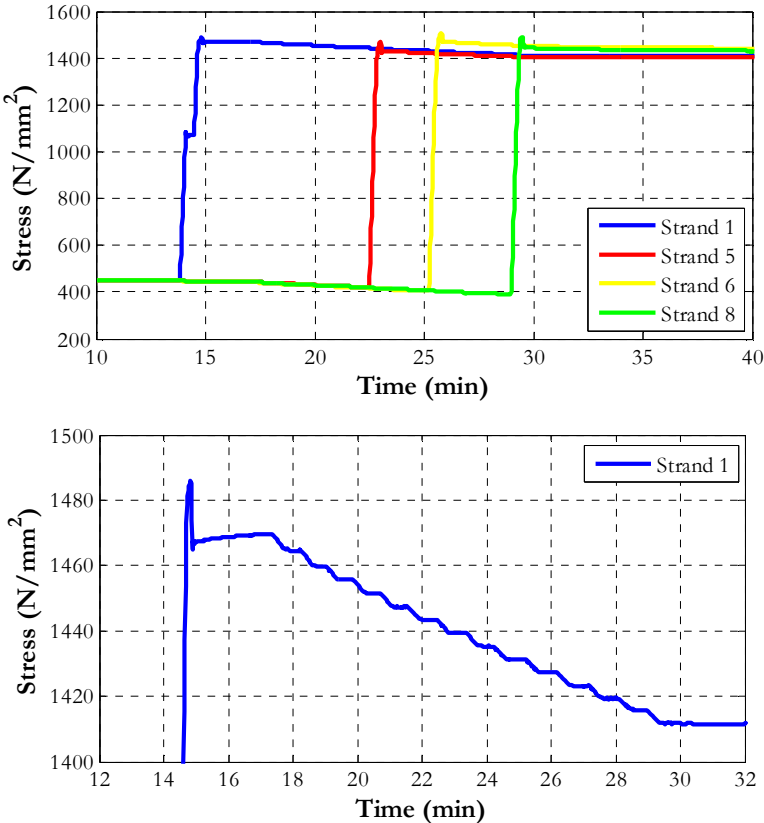


Figure 6 – Test 2: tensile stresses in the strands at stretching (top); tension losses of Strand 1 due to wedge slip and subsequent tensioning of the strands (bottom).

## 4.2 Concrete deformation

Two strain gauges embedded in the concrete close to Strand 1 made it possible to monitor the evolution of deformation in the concrete at Sections 1 and 3.

The results of these measurements are shown in Figure 9.

During the first phase (about 2 hours) a rather limited shortening occurs, followed by a longer phase of elongation, resulting from shrinkage and thermal effect, up to the instant when the strands are released and cut. Releasing and cutting the strand produce an abrupt shortening due to the elastic deformation of the concrete affected by the transfer of pre-stressing.

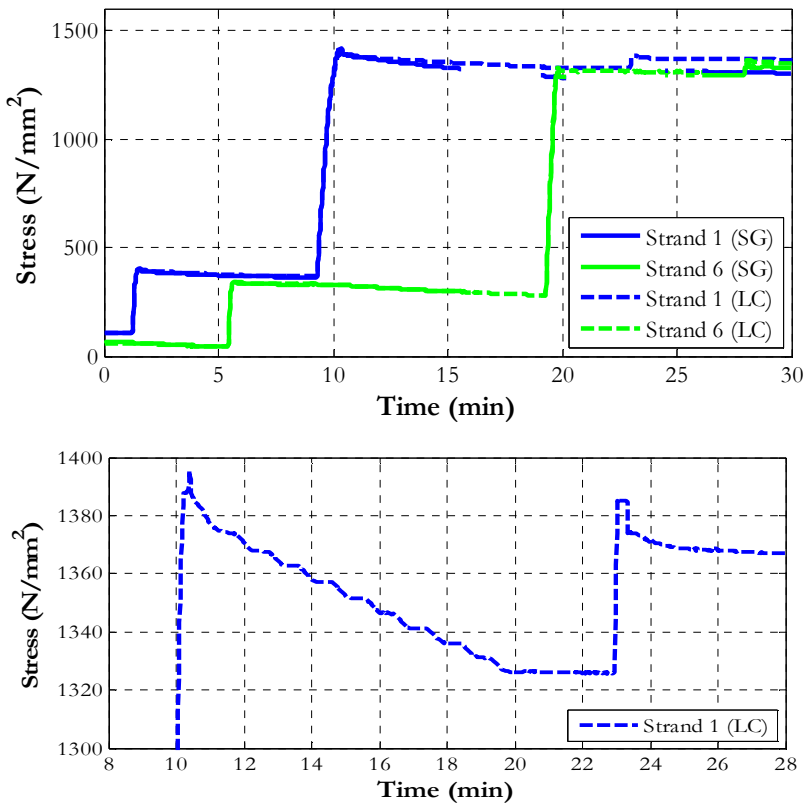


Figure 7 – Test 3: tensile stresses in the strands after tensioning (top); tension losses in Strand 1 due to wedge slip and subsequent tensioning of the strands (bottom).

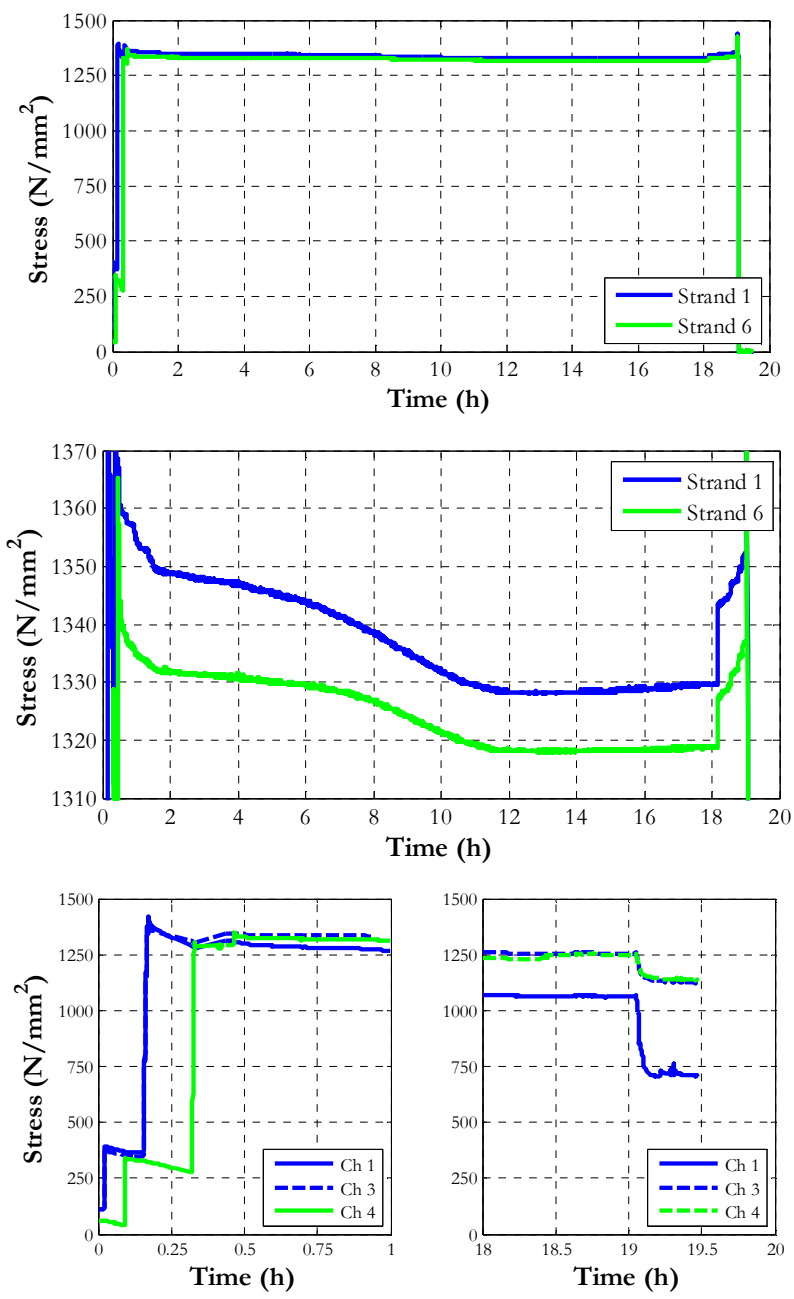


Figure 8 – Test 3: tensile stress in the strands as measured in the first 20 hours by the load cells (top and intermediate figures); and zoom of the stress-time curves as measured in the first hour by the electrical strain gauges (bottom figures).

For longer time periods, the effect on concrete deformation of the daily variation of the temperature is superimposed to the effect of creep and shrinkage; the combined effect produces a gradual but continuous increase of the deformation.

### 4.3 Camber monitoring

A certain camber is always desirable at the serviceability limit state (SLS) in slender members like the wing-shaped members in question. The camber can be easily measured in the factory, and can also be used to check the actual state of pre-stressing.

The evolution of the camber was monitored at mid-span (Section 1) and in the sections at L/4 (Section 3), for 21 days after the release of the strands.

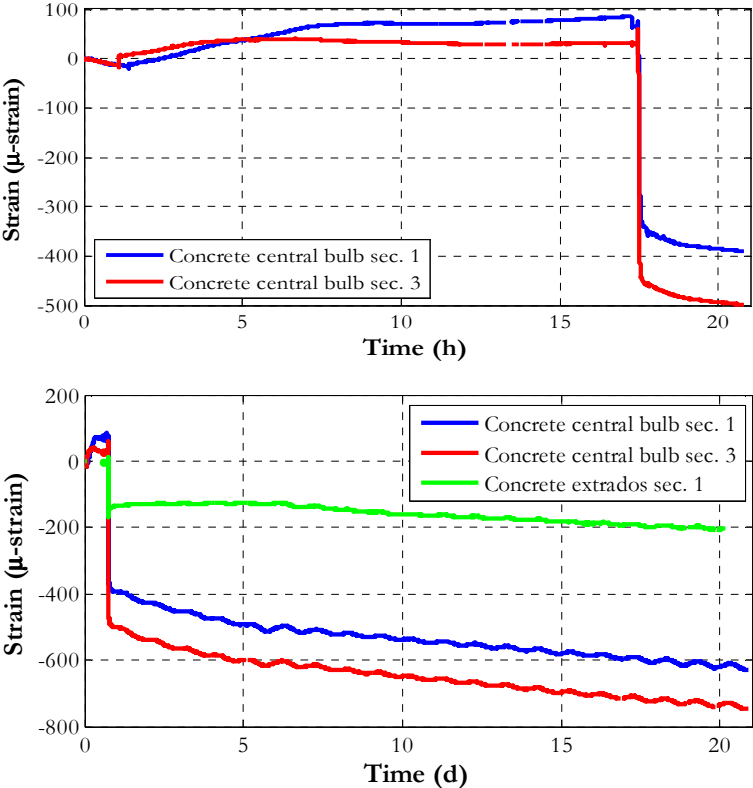


Figure 9 – Test 2: short-term (top) and long-term (bottom) concrete deformation, as a function of time (hours and days, respectively).

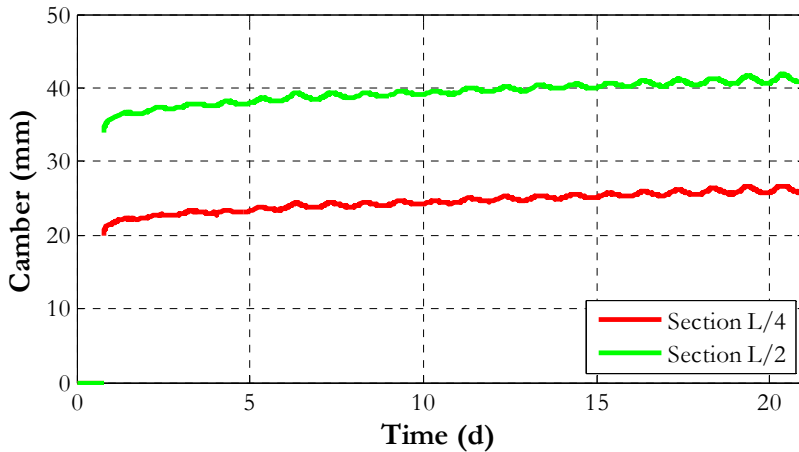


Figure 10 – Test 2: camber time history.

The results of the measurements are shown in Figure 10. For Sections 1 and 5 starting from the elastic deformation at strand release equal to 34 and 20 mm, the camber increased in 21 days to approximately 42 and 27 mm, respectively.

In this case, even the rather small effect of the temperature variation during the nights and the days can be observed (of course, it is superimposed to the much higher creep and shrinkage deformations).

#### 4.4 Temperature

The variation of the concrete temperature in correspondence to Strand 1 was detected both at mid-span (Section 1) and at the end of the pre-stressing transfer zone (Section 3). Figure 11 illustrates the time histories of the temperatures, together with the environmental temperature measured during Test 3. In both sections the chemical reactions of cement hydration is responsible for a temperature rise of about 22 °C, which - added to the ambient temperature of 15 °C - leads to a maximum temperature of 37 °C.

Furthermore, it can be noted that after about 12 hours from the instant when the temperature of concrete reaches its maximum value and the concrete starts cooling, the tensile stress of the strands measured by the load cells begins to slowly increase (Figure 8).

In fact, in the interval between the 12<sup>th</sup> and 18<sup>th</sup> hour, a decrease of 5°C and an increase of 2 MPa were recorded in the concrete and in the pre-tensioned reinforcement, respectively. The stress increase would have been much higher in case of no relaxation in the pre-tensioned reinforcement. Hence, it is evident that, even in the phase of concrete self-heating, the temperature increase is responsible for a significant pre-stress loss.



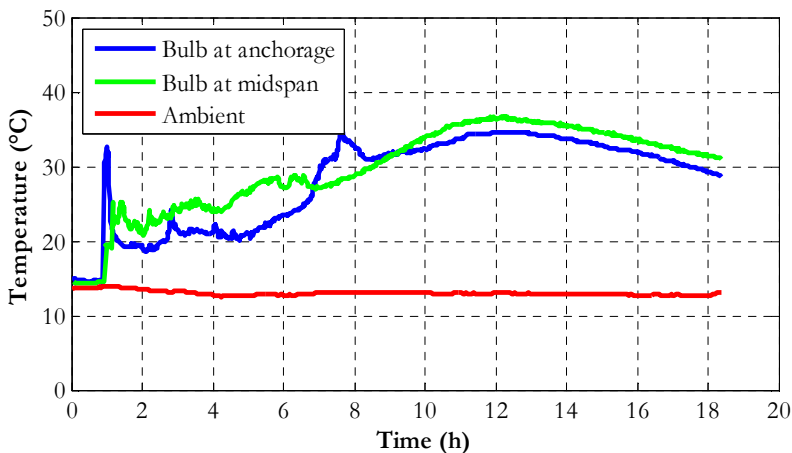


Figure 11 – Test 3:temperature time history.

## 5. CALIBRATION OF THE DESIGN PARAMETERS

The adjustment of some nominal parameters assumed in the design phase, such as the factors that influence the evaluation of the pre-stress loss in the short- and long-term and those involved in the assessment of camber evolution, was carried out, taking into account the experimental results. These parameters are treated separately in the following sections.

### 5.1 Pre-stress loss

#### 5.1.1 Immediate losses

In the case of pre-stressing strands tensioned individually between the abutments interconnected by the casting bed (i.e. the pre-tensioning system), the elastic deformations of the casting bed produce a pre-stress loss that can be summarily evaluated. During the tests, the pre-stress loss of the first strand put in tension (due to the elastic deformation of the casting bed because of the tensioning of the remaining strands) was measured by load cells and strain gauges. The values of these losses are reported in the Table 3.

After the tensioning of  $n$  strands, each having area  $A_i$ , with initial tension  $\sigma_0$ , the final tension of the first-tensioned strand (assuming no load eccentricity) can be estimated via Eq.1:

$$\sigma_{1,fin} = \sigma_0 \left( 1 - \sum_{i=2}^n \frac{A_i}{A_{1w}} \right) \quad (1)$$

where  $A_{fw}$  is the cross section of the steel structure of the casting bed.

The average pre-stress loss due to the elastic deformation of the interconnection between the trestles during the tensioning of  $n$  strands is:

$$\Delta\sigma_{m,fin} = \frac{1}{2n} \sigma_0 \sum_{i=2}^n \frac{A_i}{A_{fw}} \quad (2)$$

The experimental findings made it possible to evaluate the summation in the right-hand side member of Eq.2 and to assess the pre-stress loss due to the elastic deformation of the casting bed.

In the Tests 1, 2 and 3 the average pre-stress loss was close to 2% of the initial pre-stresses (= 29.5, 31.1 and 25.3 MPa, respectively). This loss can be introduced directly in the calculations or can be significantly reduced by further tensioning the strands as done - for example in Test 3 - where about 40 MPa were recovered in the case of Strand 1 (Figure 7).

Reading the force variations measured by means of the load cells allowed to quantify the pre-stress loss due to wedge draw-in at the fixed anchorage and by means of the electrical strain gauges glued to the strands.

The two measurements turned out to be in perfect agreement. Table 4 shows the measured values of these losses. In particular, although new wedges and new cylinders were used during the tests, the following different losses were observed for the 0.5" (99 mm<sup>2</sup>) and 0.6" (139 mm<sup>2</sup>) strands:

$$\Delta N_{cun,99} = 40.3 \text{ MPa} \quad (3)$$

$$\Delta N_{cun,139} = 24.5 \text{ MPa} \quad (4)$$

The pre-stress losses for the relaxation of the strands were quantified following the indications of EC2 (CEN, 2004) for low-relaxation strands (Class 2):

$$\frac{\Delta\sigma_{pr}}{\sigma_{pi}} = 0.66 \rho_{1000} e^{9.1\mu} \left( \frac{t}{1000} \right)^{0.75(1-\mu)} 10^{-5} \quad (5)$$

$$\text{where } \rho_{1000} = 2.5\% \text{ and } \mu = \frac{\sigma_{pi}}{f_{pk}} .$$

This equation refers to the losses that would occur at the temperature of 20 ° C. To take into account the actual test conditions, where the hydration reaction of the cement produced a temperature increase in the strands, an equivalent time was calculated on the basis of the following equation (EC2):

$$t_{eq} = \frac{1.14 T_{max} - 20}{T_{max} - 20} \sum_{i=1}^n (T_{(\Delta t_i)} - 20) \Delta t_i \quad (6)$$

Table 3. Experimental pre-stress loss due to the elastic deformation of the casting bed and of the abutments used for pre-tensioning the strands.

Test n.	Initial stress (MPa)	Strand n.	Strand area (mm <sup>2</sup> )	Pre-tens. strand n (A <sub>i</sub> )	Pre-stress loss (MPa)
1	1400	1	139	12 (99)	64.4
2	1500	1	139	14 (99)	66.9
3	1450	1	139	10 (139)	56.2

Table 4. Experimental pre-stress loss due to wedge draw-in.

Test n.	Strand n.	Strand area (mm <sup>2</sup> )	Pre-tens. strand (MPa)
1	1	139	29.4
2	1	139	21.8
2	5	99	40.3
2	6	99	37.5
2	8	99	43.5
3	1	139	25.1
3	6	139	21.9

Table 5. Computed pre-stress loss due to strand relaxation (in 18 hours).

Test n.	T <sub>max</sub> °C	T <sub>med</sub> °C	t <sub>eq</sub> hours	Pre-stress loss (MPa)
2	56	43	1286	38.9
3	37	26	59	18.5

Table 6. Computed pre-stress loss due to thermal variations.

Test	$T_{\max}-T_0$	Pre-stress loss
n.	°C	(MPa)
2	26	26.5
3	22	22.4

The theoretical values of the pre-stress losses due to steel relaxation are shown in the Table 5.

Pre-stress losses can take place as well, as a result of the thermal variations in the concrete during the hardening process. EC2 provides the following simplified formula for steam curing (§ 10.5.2):

$$\Delta N_{temp} = 0.5 A_p E_p \alpha_c (T_{max} - T_0) \quad (7)$$

Although in this case no steam curing was used, significant temperature variations were detected during concrete hardening (Figure 11).

Consequently, the pre-stress loss due to the heating of both concrete and prestressing steel turned out to be sizeable. The values of these losses are summarized in the Table 6 for the 2<sup>nd</sup> test carried out in August and the 3<sup>rd</sup> test carried out in December.

At the release of the strands, the pre-stressing force is transmitted to hardened concrete, which shortens elastically, depending on concrete modulus of elasticity at that time.

The pre-stress losses measured experimentally in correspondence to Strand 1 are shown in the Table 7. The numerically-evaluated losses were 91 and 106 MPa in Tests 2 and 3, respectively; hence, the agreement with the experimental results is very good. The value of concrete elastic modulus at strands release was evaluated on cubic samples according to the UNI 6556 standard. Its value, equal to 32.8 GPa, is in good agreement with the value derived from testing cubic specimens (= 33.3 GPa).

The total immediate loss can be evaluated by assuming – at least in the short term – the absence of any interdependence among the individual pre-stress losses, taking care of the following losses due to: (a) elastic deformation of the pre-tensioning jig (= 28.6 MPa); (b) wedge draw-in (that depends on strand diameter); (c) steel relaxation (that depends on initial pre-tensioning); (d) temperature of the concrete; and (e) elastic concrete shortening.

The theoretical values of the total immediate pre-stress loss vary in the range 213.2 - 244.5 MPa, as summarized in the Table 8. These values appear to be in good agreement with the experimentally-measured values for the specimens tested in this project (Table 9).

Table 7. Experimental pre-stress loss due to concrete elastic deformation.

Test	Strand	Strand area	Pre-stress loss
n.	n.	(mm <sup>2</sup> )	(MPa)
1	1	139	82.7
2	1	139	90.0
3	1	139	113.0

Table 8. Theoretical total immediate pre-stress loss (MPa).

Season	Strand 0.5"	Strand 0.6"
Summer	244.5	228.7
Winter	229.0	213.2

Table 9. Experimental total immediate pre-stress loss (MPa).

Test	Strand	Initial stress	Stress at transfer	$\Delta\sigma$
n.	n.	(MPa)	(MPa)	(MPa)
2	1	1500	1260	240
3	1	1450	1216	234
3	6	1450	1206	244

### 5.1.2 Time-dependent losses

In the following, the long-term pre-stress losses due to strands relaxation, as well as to concrete shrinkage and creep are analysed.

At the end of Test 2, after 21 days the pre-stressing loss due to relaxation (see Section 5.1.1 for the numerical evaluation) was 53.6 MPa. The average temperature from the 2<sup>nd</sup> day to the 21<sup>st</sup> day was assumed to be 27°C.

The shrinkage-induced loss at 21 days was evaluated according to EC2 provisions for normal concrete, as the sum of the losses due to drying shrinkage and autogenous shrinkage, since no specific indications are provided for self-compacting concrete:

$$\varepsilon_{cs} = \varepsilon_{cd} + \varepsilon_{ca} \quad (8)$$

with

$$\varepsilon_{cd}(t) = \beta_{ds}(t, t_s) \cdot k_h \cdot \varepsilon_{cd,0} \quad (9)$$

$$\varepsilon_{ca}(t) = \beta_{as}(t) \cdot \varepsilon_{ca}(\infty) \quad (10)$$

Assuming  $f_{ck} = 45.7$  MPa,  $k_h = 1.0$ ,  $h_0 = 70$  mm,  $t = 21$  days, the pre-stress loss due to shrinkage is  $\Delta\sigma_s = 38.0$  MPa.

Similarly, the loss due to concrete creep at 21 days was evaluated as follows:

$$\Delta\sigma_c = \frac{E_p}{E_{ci}} \sigma_c(t_0) \varphi(t, t_0) \quad (11)$$

Assuming  $f_{cm} = 54.6$  MPa,  $h_0 = 70$  mm,  $t_0 = 0.75$  days and taking into account the effect of temperature time history (as required for steel relaxation), the pre-stress loss due to creep is  $\Delta\sigma_c = 31.8$  MPa.

To take into account the mutual interaction between individual pre-stress losses, the following equation (EC 2) was used to evaluate the total pre-stress loss:

$$\Delta\sigma_{p,c+s+r} = \frac{\frac{E_p}{E_{cm}} \varphi(t, t_0) \cdot \sigma_{c,Qp} + \varepsilon_{cs} E_p + 0,8 \Delta\sigma_{pr}}{1 + \frac{E_p}{E_{cm}} \frac{A_p}{A_c} \left( 1 + \frac{A_c}{I_c} z_{cp}^2 \right) [1 + 0,8 \varphi(t, t_0)]} \quad (12)$$

It is now simple to evaluate the variation of the strain in the centroid of the pre-stressing steel:

$$\Delta\varepsilon_{p,c+s+r} = \frac{\Delta\sigma_{p,c+s+r}}{E_p} \quad (13)$$

Assuming perfect bond between the steel and the concrete, the strain variation in the pre-stressing steel is equal to that in the concrete at the same level.

An indication of the soundness of the evaluation of the pre-stressing losses following the pre-stress transfer at strands release can be obtained by observing Figure 9.

Face to the experimentally-measured strain variation – from the instant of cutting the strands up to the 21<sup>st</sup> day – close to 2.3 ‰ (230 microstrains corresponding to a pre-stress variation of 46.9 MPa), the theoretical value of the pre-stress variation is 46.5 MPa (the effects of relaxation, shrinkage and creep were calculated with Eq. 13).

There is no practical difference between the pre-stress loss derived by the experimental findings and the calculated pre-stress loss! The total long term theoretical losses amount to 106.7 MPa.

## **5.2 Camber evolution**

In Test 2 the elastic camber induced by the combined action of the pre-stressing force and the self-weight was 35 and 41 mm at mid-span, after the release of the strands (= at the pre-stress transfer) and at 21 days, respectively, see Section 4.3 (Figure 10). Numerical analysis overestimated a bit both displacements (38.8 mm and 45.6, respectively, which means +11% in both cases). The agreement between the predicted and the experimental values, however, should be considered very satisfactory, even more since there is a number of uncertainties concerning – for instance – the relative humidity, the 3D distribution of the temperature, the effective surface area in contact with the environment and the manufacturing tolerances (mainly referring to the actual geometry of the sections).

## **6. CONCLUDING REMARKS**

In this research project, an experimental investigation and a number of theoretical analyses were carried out to have first-hand information on the actual pre-stress losses and camber evolution in the first weeks past concrete casting, curing and hardening, concerning pre-stressed pre-tensioned wing-shaped members.

The results of the analysis give information on:

- pre-stress losses due to the elastic deformation of the steel trestle holding the anchored heads of the strands;
- actual pre-stress losses due to wedge draw-in at the anchored extremities;
- influence of temperature time history on the development of pre-stress losses for steel relaxation and concrete creep;
- accuracy of the predictive formulas about pre-stress losses provided by EC 2 in the case of special structural members such as pre-stressed pre-tensioned wing-shaped members made of self-compacting concrete.

Appropriate corrective actions are proposed as well to reduce – as much as possible – the pre-stress loss during concrete casting, curing and hardening, and suitable values for the design parameters are calibrated to correctly predict pre-stress losses and camber evolution.

## **ACKNOWLEDGEMENTS**

The Authors are grateful to Dr. Paolo Manni and Dr. Graziano Baldograni of Manini Prefabbricati S.p.A. (S. Maria degli Angeli, Perugia, Italy) for their valuable support in organizing the experimental campaign.

The cooperation and expertise of Prof. Cinzia Buratti and Dr. Michele Goretti of CIRIAF, Inter-University Centre for Pollution and Environmental Issues - University of Perugia were instrumental in guaranteeing the reliability of the measurement of the thermal field.

## REFERENCES

- Al-Omaishi N., Tadros M. K. and Seguirant S. J. (2009). "Estimating prestress loss in pretensioned, high-strength concrete members". *PCI Journal*, Fall, pp. 132-159.
- Barr P. J. and Angomas F. (2010). "Differences between Calculated and Measured Long-Term Deflections in a Prestressed Concrete Girder Bridge". *Journal of Performance of Constructed Facilities*, Vol.24, No.6, pp. 603-609.
- Barr P. J., Stanton J. F. and Eberhard, M. O. (2005). "Effects of Temperature Variations on Precast, Prestressed Concrete Bridge Girders". *Journal of Bridge Engineering*, Vol.10, No.2, pp. 186-194.
- CEN - European Committee for Standardization. EN 1992-1-1 (2004). *Eurocode 2: Design of concrete structures – Part 1-1: General rules – General rules and rules for buildings*. Brussels, Belgium.
- Dwairi H. M., Wagner M. C., Kowalsky M. J. and Zia P. (2010). "Behavior of Instrumented Prestressed High Performance Concrete Bridge Girders". *Construction and Building Materials*, Vol.24, pp. 2294-2311.
- Martin L. D. (1977). "A Rational Method for Estimating Camber and Deflection of Precast Prestressed Members". *PCI Journal*, January-February, pp. 100-108.
- Roller J. J., Russell H. G., Bruce R. N. and Alaywan W. R. (2011). "Evaluation of Prestress Losses in High-Strength Concrete Bulb-Tee Girders for the Rigolets Pass Bridge". *PCI Journal*, Vol.10, pp. 110-134.
- Roller J. J., Russell H. G., Bruce R. N. and Hassett, B. (2003). "Effects of Curing Temperatures on High Strength Concrete Bridge Girders". *PCI Journal*, Vol.5, pp. 72-79.
- Stallings J. M., Barnes R. W. and Eskildsen S. (2003). "Camber and Prestress Losses in Alabama HPC Bridge Girders". *PCI Journal*, September-October, pp. 2-16.
- Tadros M. K., Fawzy F. and Hanna K. E. (2011). "Precast, Prestressed Girder Camber Variability". *PCI Journal*, Winter, pp. 135-154.
- UNI – Italian Standardization Institute. UNI 6556 (1976). *Tests on Concrete to Determine the Secant Modulus of Elasticity in Compression* (in Italian).



## **STRUCTURAL BEHAVIOUR OF HISTORICAL STONE ARCHES AND VAULTS: EXPERIMENTAL TESTS AND NUMERICAL INTERPRETATION**

Marco Bovo<sup>1</sup>, Claudio Mazzotti<sup>2</sup> and Marco Savoia<sup>3</sup>

### **ABSTRACT**

A thorough assessment of the actual structural behavior and load-carrying capacity is strongly required in order to properly design strengthening interventions on both historical and existing buildings. This is even more necessary when dealing with constructions made of heterogeneous materials like masonry or stonework, where conventional assessment techniques may not give satisfactory results. This paper presents the findings of an extensive experimental investigation and of a number of numerical simulations concerning two large buildings of the 19<sup>th</sup> century.

In-situ tests were carried out on different types of stone arches, with the purpose of investigating their mechanical response and the structural behavior of stonework under different combinations of in-plane loads. Arches were tested with symmetric and asymmetric combinations of static and dynamic loads, in order to investigate the key parameters controlling the structural system. A number of cores extracted from stone elements and reconstructed stonework walls were also tested under compression in the laboratory, in order to evaluate the compressive strength of the masonry. The experimental data were compared with the numerical results obtained by means of a refined finite-element model describing a portion of the building, consisting of walls, arches and vaults.

Finally, the numerical model was used to perform nonlinear analyses in order to assess the ductility of the arches under horizontal forces, including the stiffening effect of the vaults.

**KEYWORDS:** arch, historic stonework, nonlinear analysis, experimental tests, cross vaults.

---

<sup>1</sup>Research Assistant, <sup>2</sup>Associate Professor, <sup>3</sup>Professor,  
DICAM - Department of Civil, Chemical, Environmental and Materials Engineering,  
University of Bologna, Bologna, Italy.

## 1. INTRODUCTION

Masonry is an extensively-used building material in Italy, as demonstrated by most of the Italian residential buildings of the past, that are made of masonry, with a large percentage built more than one century ago. The fundamental characteristic of this system mainly lies in its handmade construction process, which allows extreme versatility and rather high building rates.

As proved by historical buildings, masonry-related technologies are very flexible and adaptable, as masonry buildings exhibit a rigid skeleton consisting in natural or artificial blocks connected by a deformable link, the mortar. This aspect is crucial, especially with reference to the ductility required by the resistance to seismic events (Mallardo et al., 2008).

Therefore, it is imperative to assess the actual building capacity, in terms of resistance and ductility, in order to optimize the design and to adopt the techniques best suited to structural repairing and strengthening. The behavior of historic stonework in particular depends on a number of different factors, the most important being the geometry of the structure, the shape and strength of the stone, the constraints, the thickness of the mortar layers and the properties of the interface between the mortar and the stone (Hayen et al., 2009). In this perspective, experimental activities should – in general – accompany any complex mathematical model, especially to work out the dynamic parameters (Conte et al. 2011).

The present paper is focused on the study of the structural behaviour of two large masonry buildings, located in Trieste (Italy) and known as “ex-Silos Storehouses”. Each two-storey structure, built in the 19<sup>th</sup> Century with natural stones and mortar, to store wheat coming from the port of Trieste consists of thick longitudinal walls connected by a series of transverse stone arches separated by brickwork vaults. At present, the two huge buildings are in an advanced state of deterioration. A series of experimental in-situ load tests (Bovo et al., 2012) were carried out in order to assess the actual state of the buildings and their safety level, the objective being the tuning of the strengthening and rehabilitation techniques.

Stone cores and portions of stonework (specimens) were collected in-situ and tested in the laboratory in order to evaluate the mechanical strength of the masonry and of its constituents.

Linear finite elements models were developed with two objectives, first to better interpret and reproduce the experimental tests, and second to investigate the interaction between the arches, the cross vaults and the tunnel vaults, in order to define equivalent membrane elements to be introduced into the analysis, as a means to describe in a simpler way the actual (curved) geometry.

Finally, nonlinear analyses were carried out under vertical and horizontal loads with the objective of assessing the structural reliability against seismic forces and – more generally - to check the behavior of this type of vaulted structures under horizontal forces.

## 2. THE BUILDINGS AND THEIR HISTORY

The history of the “ex-Silos Storehouses” (called “Silos” in the following) is strictly related to the opening of the so-called “Southern Railway” of the Hapsburg Empire. The Railway Station and the newly designed port of Trieste were built at the northern edge of the city, between St. Theresa’s Lazaretto and the butchery, that is the area alongside Nuovo Lazaretto Street.

The upper floor of each two-storey building was built at the level of the railway platform (roughly 10 metres above the sea level) and the large area between the two buildings had room for five tracks for as many freight trains.

Each of the two parallel buildings (290 m long, 26 m wide and 10 m high) is made of Istria’s sandstone masonry and exhibits arched windows along the four façades.

The bottom storey of each building was used as bonded warehouse (to store goods until the custom duties were paid). A set of hydraulic lifts allowed moving the goods between the storeys.

On 27 July 1857, the emperor Francesco Giuseppe attended the opening ceremony of the last section of the Southern Railway, linking Ljubljana in Slovenia to Trieste, and the Southern Railway was completed, between Vienna and the Adriatic Sea. After few years, the Railway Station turned out to be insufficient and unsuitable to catch up with the development of Trieste’s commercial activity. So, eight years past the opening ceremony, the railway platform was lowered from 10 metres to 3 metres above the sea level (= seashore level).

As an extension of the original project, the engineer Gustav Lahn designed a passenger railway station, and - in place of the existing administrative offices at the end of the storehouses - a new three-storey transverse building was constructed in 1865. This building, about 50 m long and known as “Silos”, differed from the storehouses buildings for its rectangular windows (instead of the arched windows) and its big pediment on the façade with a central rose window.

Wilhelm Flattich’s project replaced Lahn’s project and the passenger station changed its look, as it was lengthened on both long sides and broadened towards the sea. The station was opened on 19 June 1878. In 1891 the tax-free port - established in 1719 by permission of the emperor Charles VI - was abolished, and in the following years the construction the new Trieste’s port (1906) led to the progressive abandonment of the buildings of the “Silos” complex.

After the first World War, the “Silos” were used as storehouses for any kind of goods, while during the second World War they became a resting place for the troops at the front. In 1968 the “Silos” came under the protection of the Historical Preservation Office.

Unfortunately, two fires damaged the front building in 1970 and 1971, respectively. In 1975, the buildings were included in a requalification project of the whole area, and their transformation into an auditorium was envisaged.

### 3. GEOMETRY OF BUILDINGS

A survey of the entire storehouses shows that the complex consists of two main buildings with similar structural and geometric characteristics, completed at the front by another smaller building (not considered in the present investigation).

Their plan dimensions are 250 x 27-28 metres, arranged as shown in Figure 1, with a courtyard about 27 metres wide (Savoia and Carli, 2010). The buildings have two floors, with a 21 metres total height (Figure 2).

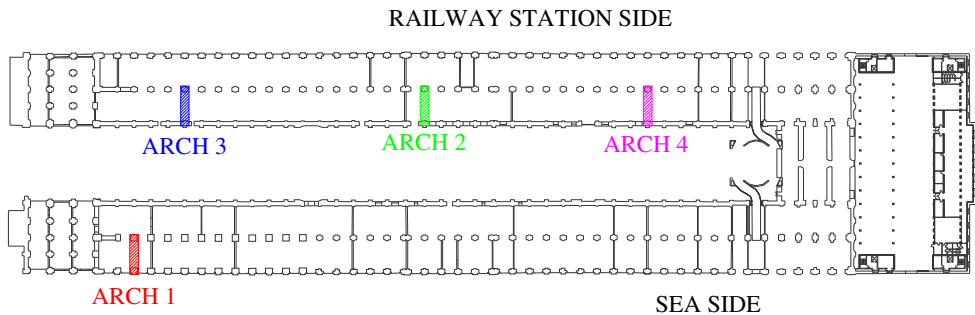


Figure 1 – Plant of the ground floor of the storehouses with indication of the arches subject to testing.

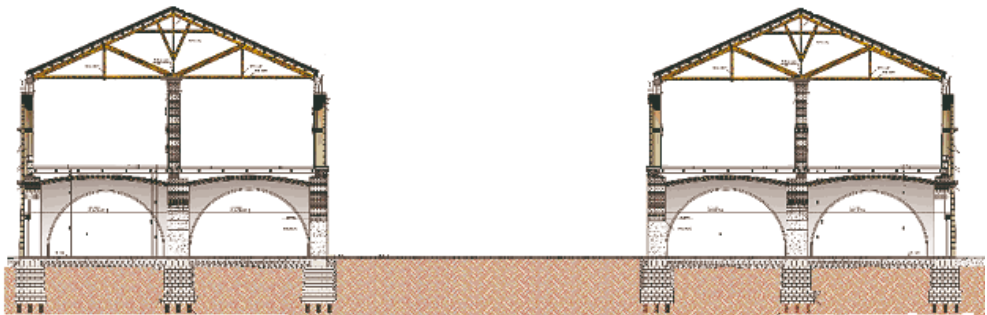


Figure 2 – Typical transverse section of the two buildings.

The structure bearing the floor of the second storey was supported by peripheral walls along the long sides of the building and by inner regularly-spaced columns (spacing = 6.5 m) longitudinally connected by arches. The load-bearing walls are made of squared limestone blocks with joints of poor hydrated-lime mortar. Moreover, on the façade there are stone columns both externally and internally, the latter facing the courtyard. The thickness of the peripheral walls at the ground level is approximately 1.60 metres.

In both buildings, the floor of the second storey is supported by vaults, whose key is at about 8 metres from ground level. Each vault in turn is supported by the transverse arches, by the central longitudinal arch and by the side walls of the longitudinal façades. The longitudinal central arches have a free span of about 5 metres, and are about 2 metres wide, as the bearing columns. On the contrary, the transverse arches of the buildings have a spacing of 6.5 metres, a free span of about 10-11 metres, a height at the key of 6-6.5 metres, and a height along the walls and the central columns of 2-2.5 metres from the ground.

The arches provide considerable stiffness and load-carrying capacity to the structure. In particular, the transverse arches connect the central columns with the peripheral walls and bear both the vaults and the upper floor. The brickwork vaults have constant thickness (40-45 cm) and are plastered both along the intrados and the extrados.

The vaults are tunnel-shaped, except the last three bays per building, where cross vaults are present. The bricks used in the construction of the vaults have very high mechanical properties, and the lime-mortar joints exhibit a high-quality texture. The vaults bear the timber floor of the second storey, whose structure consists of 1m-spaced beams supporting timber planks and - in some areas - a concrete overlay similar to a slab (of more recent construction).

#### **4. EXPERIMENTAL TESTS AND NUMERICAL INTERPRETATION**

Four arches of the buildings have been selected as representative of the different types. Figure 1 shows the plan view of the two buildings with the indication of the arches in question. In order to determine the mechanical characteristics of the peripheral walls, a series of compression tests on prismatic portions of the stonework (size = width x length x thickness = 60 x 130 x 60 cm), were performed in the Structural Engineering and Geotechnics Laboratory of the University of Bologna.

One specimen was tested on site, while three specimens were extracted from the existing peripheral walls and two were reconstructed using stone blocks collected in-situ (Uday et al, 2010; Hayen et al., 2009) and tested in the laboratory.

Then, further five tests in compression on small-diameter cores extracted from stone blocks were carried out ( $\varnothing = H =$  roughly 54 mm).

These tests (Tables 1 and 2) allowed to evaluate the mechanical properties of the stonework and of the stone blocks.

The relatively small values of the compressive strength of the stonework (especially if compared with the very high compressive strength of the bricks) are mainly due to the large and highly irregular thickness of the mortar layers, as well as to their rather low mechanical strength. (Both factors give the masonry a very high deformability and induce very inhomogeneous stresses in the bricks, see Figure 3).

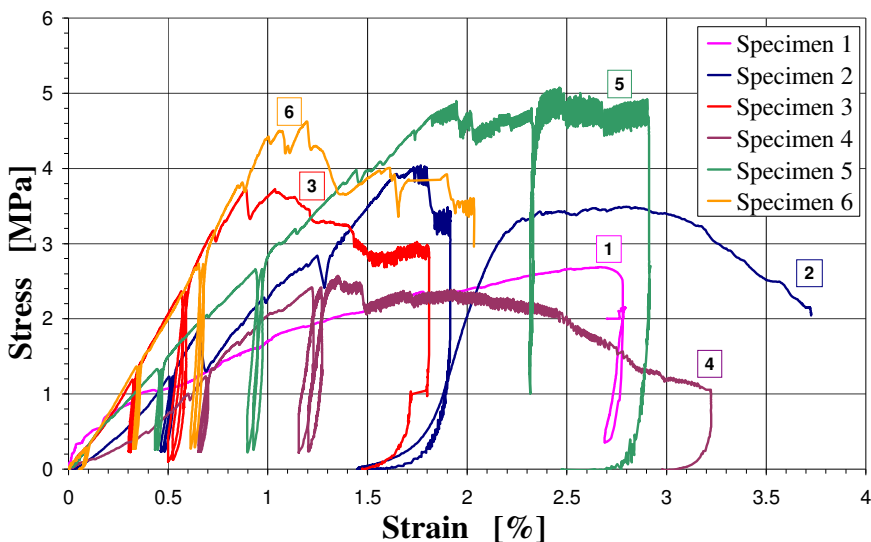


Figure 3 - Experimental stress – strain curves obtained from the six prismatic specimens extracted from the stonework (size 60 x 130 x 60 cm).

Table 1 - Identification code, type, size, density, ultimate strength, compression strength and elastic modulus of the 6 prismatic specimens (called *panels*).

Panel ID	Type of specimen	L [mm]	B [mm]	H [mm]	$\rho$ [kg/m <sup>3</sup> ]	$P_u$ [kN]	$f_{cb}$ [MPa]	E [MPa]
1	Tested on site	400	460	820	-	494	2.68	273
2	Extracted	623	641	1105	2465	1613	4.04	320
3	Extracted	657	634	1330	2459	1554	3.73	488
4	Extracted	655	620	1225	2582	1044	2.57	255
5	Reconstructed	629	588	1165	2700	1875	5.08	262
6	Reconstructed	595	604	1209	2590	1662	4.63	449

Three different types of tests, on four representative on-site transverse arches, were performed: static tests with symmetric vertical load, static tests with asymmetric vertical load and dynamic tests.

Table 2 - Identification code, diameter, height, density, compression strength of the brick cores extracted from stone blocks ( $\varnothing = H =$  roughly 54 mm).

Core ID	$\varnothing$ [mm]	H [mm]	$\rho$ [kg/m <sup>3</sup> ]	$f_{cp}$ [MPa]	$f_{cp,mean}$ [MPa]
1 - 1	54.16	54.27	2636	161.4	158.1
1 - 2	54.06	54.30	2651	154.6	
1 - 3	54.40	54.18	2618	158.3	
2 - 1	54.46	54.10	2603	156.2	160.2
2 - 2	54.34	53.81	2625	166.2	
2 - 3	54.19	54.19	2617	158.2	
3 - 1	54.32	54.25	2529	102.0	94.4
3 - 2	54.13	54.10	2524	91.6	
3 - 3	54.12	53.88	2522	89.5	
4 - 1	54.22	54.27	2614	134.2	137.2
4 - 2	54.19	53.25	2619	130.1	
4 - 3	54.24	53.63	2595	147.3	
5 - 1	54.51	54.55	2560	133.6	152.8
5 - 2	54.28	54.44	2606	172.0	

The symmetric static tests consist in applying two increasing forces at the quarters of the arch, while in asymmetric tests the load was applied only to one quarter of the arch. A properly-designed steel reaction system allowed to perform the static load tests by pulling the arches from below (see Arch No. 1 in Figure 4).

During the static load tests, both vertical and horizontal displacements in representative points were recorded. The position of the instruments during the static tests is shown in Figures 5 and 6. A Wild optical level with sensitivity of 0.01 millimetres was used in order to measure the arch vertical deflection in the positions indicated by L1 – L5. A wire displacement transducer was used in order to confirm the optical measurements of the mid-span deflection. Other six displacement inductive transducers - LVDTs (Linear Variable Differential Transformers) with a sensitivity of 0.001 millimetres were used to measure the horizontal displacements of the wall-arch connection (LVDT7 and LVDT8) and to evaluate the mean strains in the key brick (LVDT3 and LVDT4).



Figure 4 – Static test of Arch No.1 (Fig.1): application of the pull-down loads.

In Figs. 5 and 6, the positions of the 6 LVDTs (LVDT 3 - 8), of the 5 graduated rods used with the optical level, and the wire transducer (T1) are indicated. The dynamic tests were carried out to evaluate the natural frequencies of the arches. In these tests, a mass was hung to the arch intrados by means of a high-strength steel wire, in a lateral position. Then, the mass was instantaneously released and the acceleration in a number of selected points of the intrados was recorded using three piezoelectric accelerometers. Processing the accelerograms allowed to determine the power spectral density of the signal, and to evaluate the natural frequencies. In Figure 7, the accelerometers are indicated with A6, A7 and A8.

For each of the four arches tested either statically or dynamically, the identification number, the maximum static load applied in the symmetric/asymmetric static test, the mass released in the dynamic test and the first two natural frequencies are reported in Table 3.



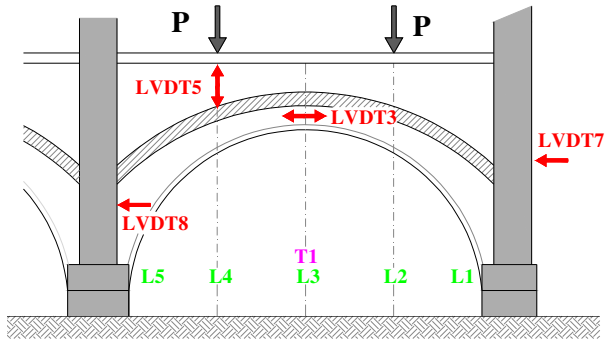


Figure 5 – Instrumentation used in the symmetric static tests.

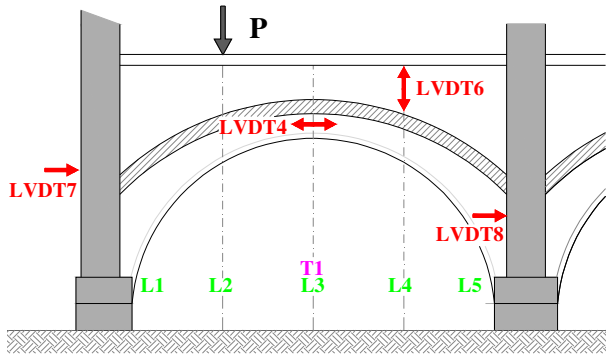


Figure 6 – Instrumentation used in the asymmetric static tests.

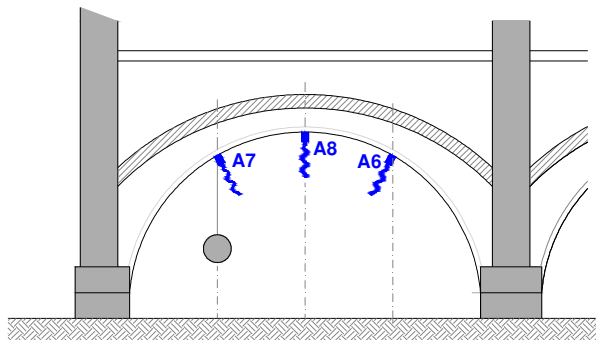


Figure 7 – Positions of the mass and of the accelerometers used during the dynamic tests.

Table 3 - Summary of the dynamic tests carried out on four arches.

Arch ID	Maximum static load in the symmetric test [kN]	Max. static load in the asymmetric test [kN]	Mass released in the dynamic test [kg]	$f_1$ [Hz]	$f_2$ [Hz]
1	250	-	250	9.0	15.8
2	250	250	250	15.6	19.5
3	350	350	250	12.1	17.9
4	350	350	250	15.0	18.6

The results obtained from the tests on Arch No. 4 are extensively discussed in the following. (The tests on the other three arches gave very similar results).

In order to validate the numerical procedure and to investigate the interactions among the contiguous structural members (longitudinal and transverse arches, and connecting cross vaults), numerical simulations were performed by means of a 3D finite element model reproducing the portion of the structure astride Arch No.4, closest to the Railway Station (Figure 8). This portion is comprised between the section containing the two arches preceding Arch No. 4 (and its companion in the same cross-section) and the plane containing the arches following Arch No.4.

Following a classical approach commonly found in the literature, brickwork and stonework are modelled in different ways, at different approximation levels, by means of micro-elements, smeared elements and macro-elements, each approach having its own advantages and drawbacks.

In Gambarotta et al. (1997a), a mortar-joint damage model is proposed for the application to micro elements, while in a companion paper (Gambarotta et al., 1997b) a homogenization procedure is proposed to formulate a smeared element. In the two papers, some applications of both models are reported. In Mistler et al. (2006) other applications of the smeared model are presented, the focus being on the advantages of this approach. In Galasco et al. (2004) a macro-element is adopted, that proves to be very reliable. In Szołomicki (2009) a homogenised approach based on limit analysis is described, and the issues concerning the calibration and sensitivity of the model are addressed. Furthermore, in Stablon et al. (2012) a new approach is described, which is based on a homogenized damage model, that automatically takes care of the strain localization.

In the present work, the constitutive model adopted to represent the complex interaction between the mortar and the blocks is a homogenised model, where the properties of the finite element take care of the global behaviour of both the brickwork and the stonework.

The numerical model is based on about 310000 "brick" finite elements with 6 or 8 nodes. Since in the experimental tests the loads did not exceed the service loads, in the numerical analyses carried out to reproduce the experimental results

linear elasticity was assumed for the materials, with  $E = 1800 \text{ MPa}$  and  $\nu = 0.20$  for all structural members. The value adopted for the elastic modulus is typical of masonry structures and was obtained by means of a simple optimization technique, by comparing numerical and experimental results. Of course, the previous value of  $E$  is larger than in the case of walls, because in arches the mortar layers are usually more regular and smaller than in walls.

For both symmetric and asymmetric loads, the fitting of the test results is in general very satisfactory and in some cases excellent (Figures 9-13 and Figures 15-20).

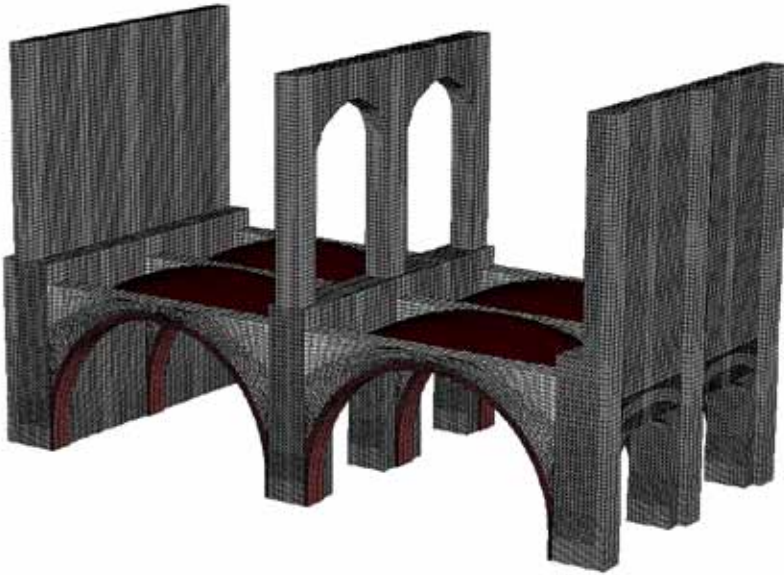


Figure 8 – Finite-element model aimed at investigating the behaviour of the transverse arches and vaults under static loads, and their modal characteristics under impulsive loads.

Figure 9 shows the vertical displacement of Arch No.4 for three symmetric load levels (150, 250 and 350 kN). As expected, the vertical displacement regularly increases towards the key.

The evolution of the horizontal mean strain in the key brick (calculated from the measurements yielded by LVDT3 and LVDT4) is shown in Figure 10 under symmetric loads. As for the asymmetric static loads, Figure 11 shows that the maximum value of the vertical displacement occurs under the applied point load, at the quarter of the span.

Last but not least, the vertical displacement evaluated by means of the optical instrument is in good agreement with that yielded by the wire transducer (Fig. 12).

The evolution of the horizontal mean strain in the key brick (calculated from the measurements yielded by LVDT3 and LVDT4) is shown in Figure 13 under asymmetric loads.

Finally, the horizontal displacements measured at the arch-column connection and at the arch-lateral wall connection under asymmetric loads are plotted in Figure 14.

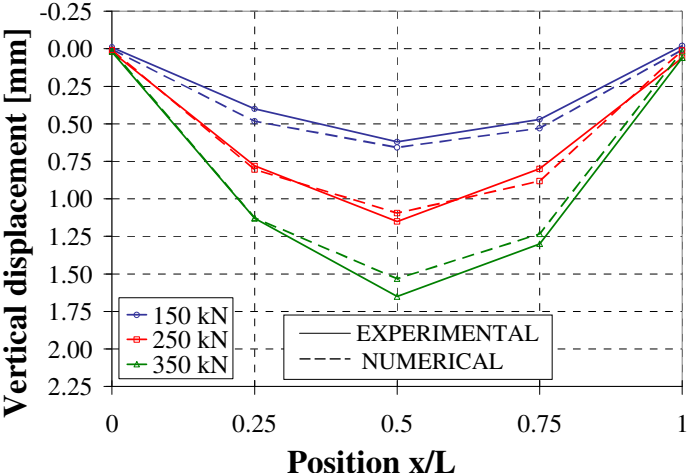


Figure 9 – Arch No. 4 – Vertical displacement: fitting of the test results under static symmetric loads (see Fig.5).

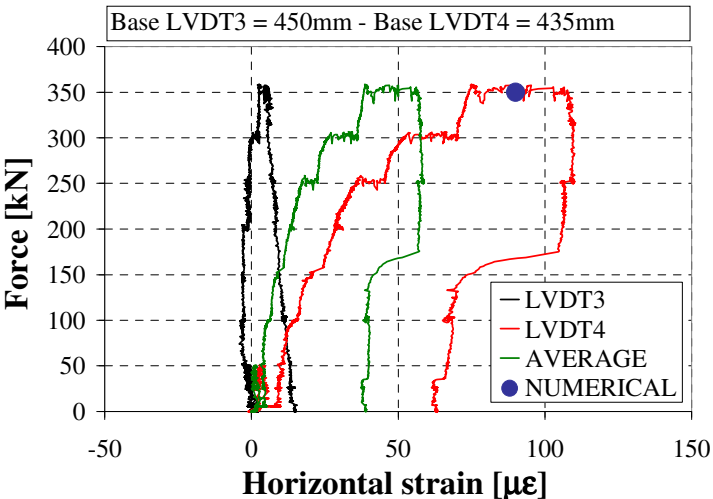


Figure 10 – Arch No. 4 - Horizontal strain in the key brick: fitting of the test results under static symmetric loads (see Fig.5).

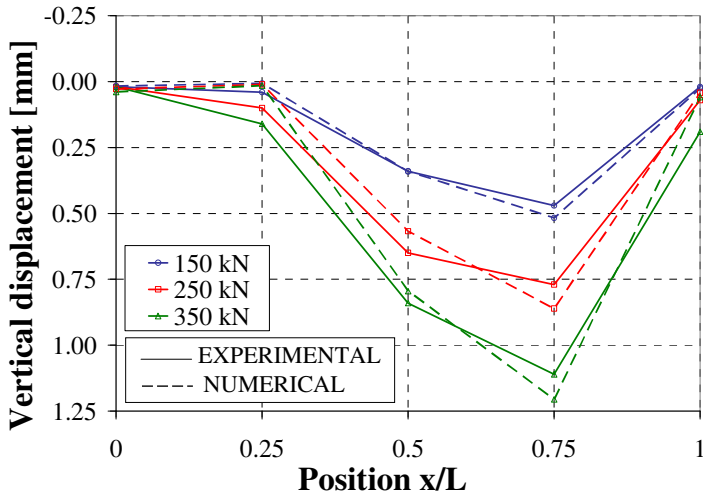


Figure 11 – Arch No. 4 - Vertical displacement: fitting of the test results under the static asymmetric load (see Fig.6).

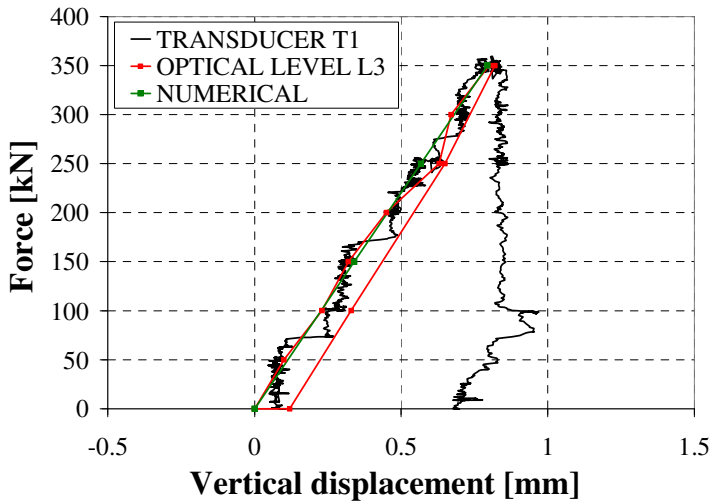


Figure 12 – Arch No. 4 - Vertical displacement at mid-span: fitting of the test results under the static asymmetric load (see Fig.6).

Both LVDT7 and LVDT8 recorded negative displacements under asymmetric loads (Fig.14), which means that the arch toes moved towards the central line of the building for about 0.1 mm; on the contrary, under symmetric loads, the arch toes moved outwards, as expected.

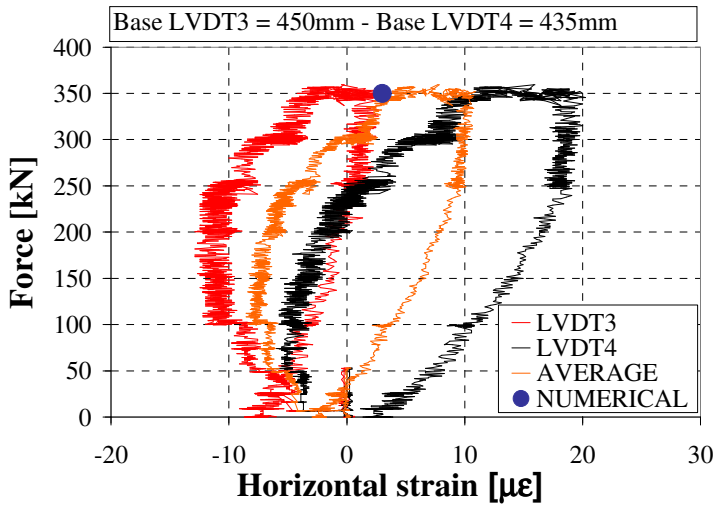


Figure 13 – Arch No. 4 - Horizontal strains in the key brick under the static asymmetric load applied at the quarter of the span (see Fig.6).

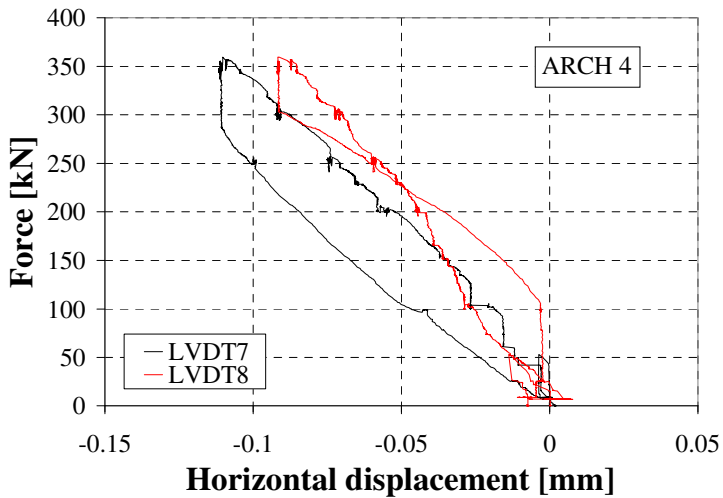


Figure 14 – Arch No. 4 - Horizontal displacements of the peripheral wall (LVDT7) and of the intermediate column (LVDT8) under static asymmetric loads.

In order to compare the results obtained in the on-site tests on all arches, the vertical displacements measured under symmetric and asymmetric static loads are plotted in Figures 15-17 and 18-20, respectively.

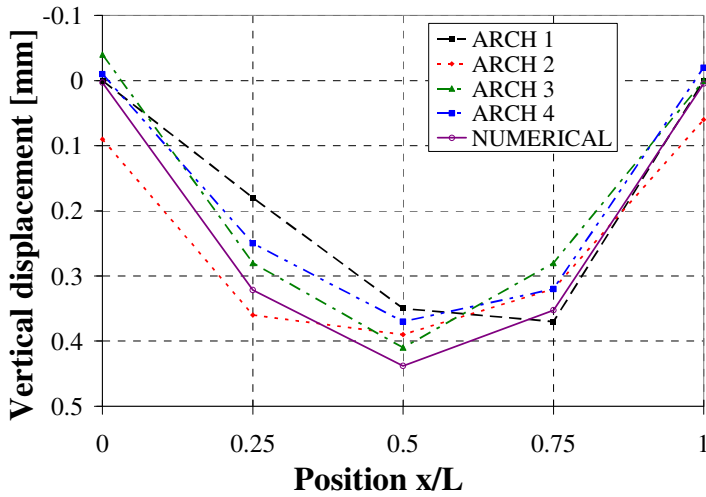


Figure 15 – Arches No. 1-4 - Vertical displacements under static symmetric loads applied at the quarters of the span ( $P = 100$  kN, see Fig.5).

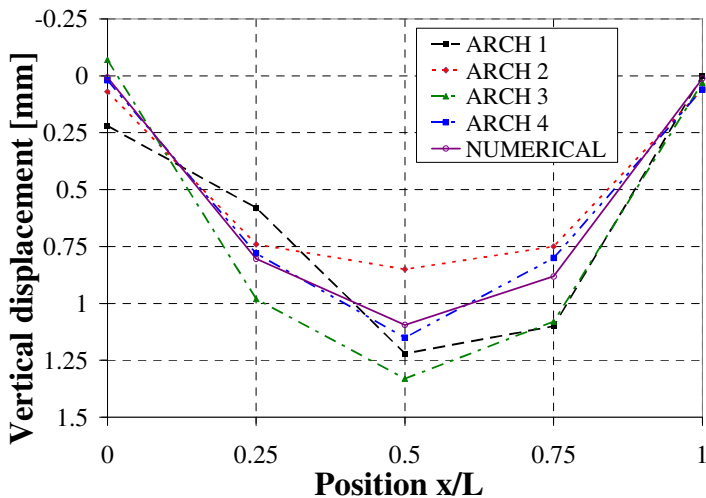


Figure 16 – Arches No. 1-4 - Vertical displacements under static symmetric loads applied at the quarters of the span ( $P = 250$  kN, see Fig.5).

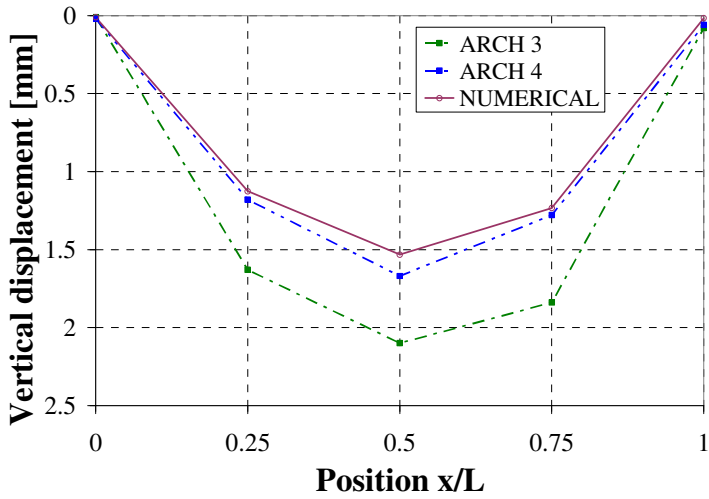


Figure 17 – Arches No. 3, 4 - Vertical displacements under static symmetric loads applied at the quarters of the span ( $P = 350$  kN, see Fig.5).

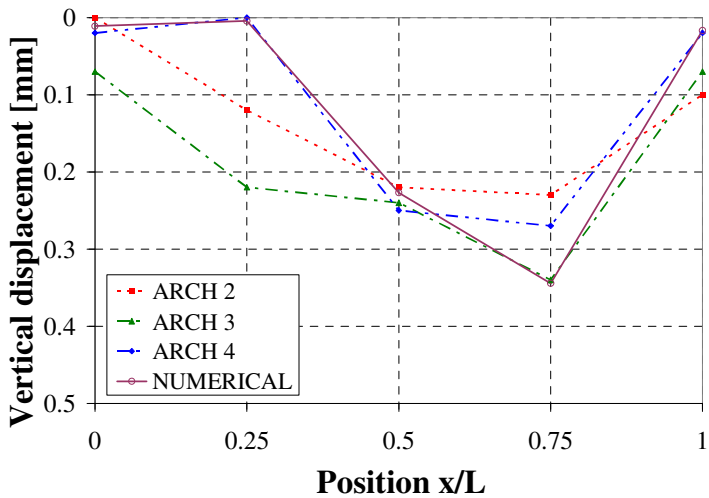


Figure 18 – Arches No. 2, 3, 4 - Vertical displacements under the static asymmetric load applied at the quarter of the span ( $P = 100$  kN, see Fig.6).



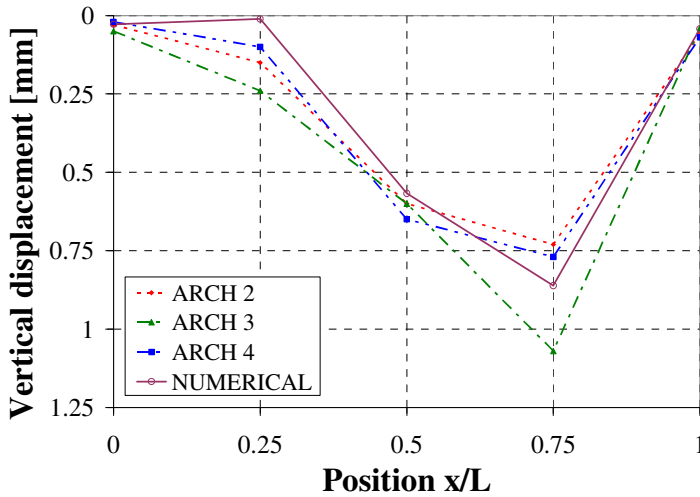


Figure 19 – Arches No. 2, 3, 4 - Vertical displacements under the asymmetric load applied at the quarter of the span ( $P = 250$  kN, see Fig.6).

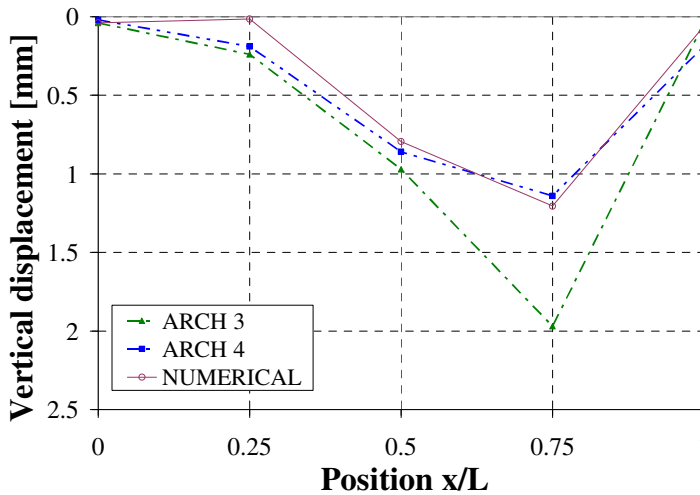


Figure 20 – Arches 3, 4 - Vertical displacements under the asymmetric load applied at the quarter of the span ( $P = 350$  kN, see Fig.6).

The arches show similar results under symmetric loading; as their deflections are comparable and very similar. A slightly nonlinear behaviour can be observed, as the displacements yielded by the tests are larger than those predicted by the

linear FE model, when the maximum value of the applied loads is attained ( $P = 350 \text{ kN}$ ).

Under the asymmetric loads, the results have similar trends but with significantly different values, as was expected, since each of the four tested arches exhibited rather different deterioration levels and different “boundary” situations especially in terms of type of the upper floor, peripheral walls and internal partitions, all these factors having an influence on the overall mechanical-structural behaviour.

The numerical results satisfactorily fit the experimental findings with respect to both displacements and strains, this being a demonstration that FE modelling can capture realistically the structural behaviour of the actual building, including the interaction between the arches and the vaults, with a sizeable reduction of the deflections. In particular, the vertical displacements obtained numerically properly describe the experimental behaviour, while the local strains are matched with a less satisfactory approximation, as showed in Figures 10 and 13.

As for dynamic-test interpretation, the three diagrams of the Power Spectral Density - PSD of the signals (obtained by post-processing the three recorded accelerograms) are reported in Figures 21a - c. The first two natural frequencies of Arch No. 4 can be identified as 15.0 and 18.6 Hz, respectively.

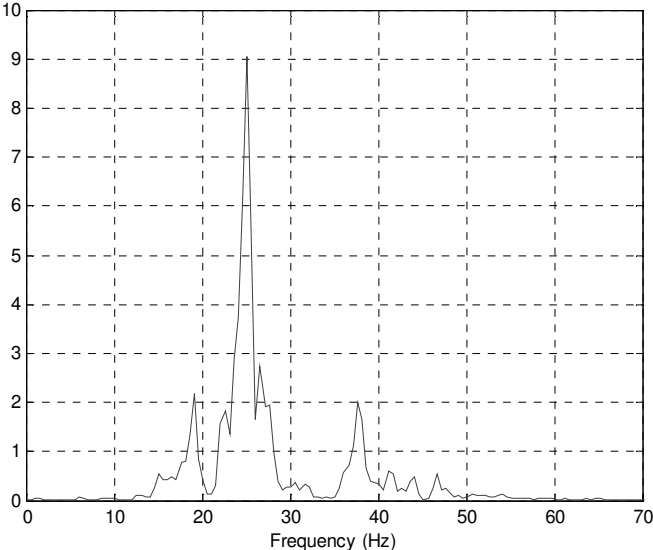


Figure 21a – Arch No. 4: plot of the Power Spectral Density - PSD of the accelerations measured by the accelerometers A6 during the dynamic tests.

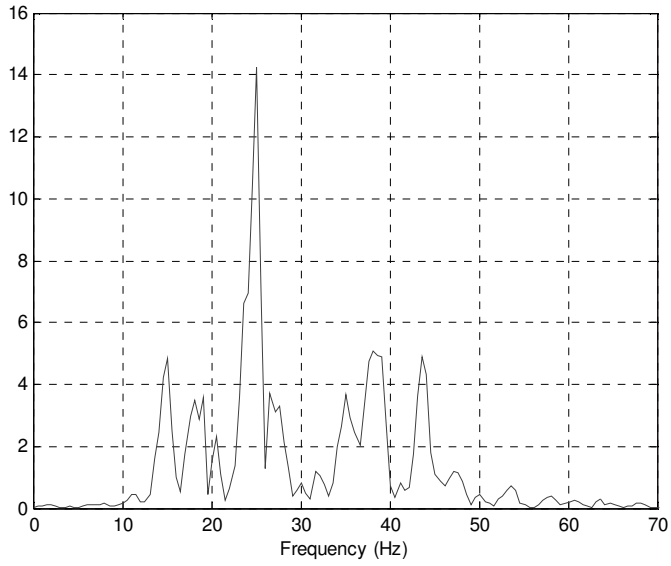


Figure 21b – Arch No. 4: plot of the PSD of the accelerations measured by the accelerometers A7 during the dynamic tests.

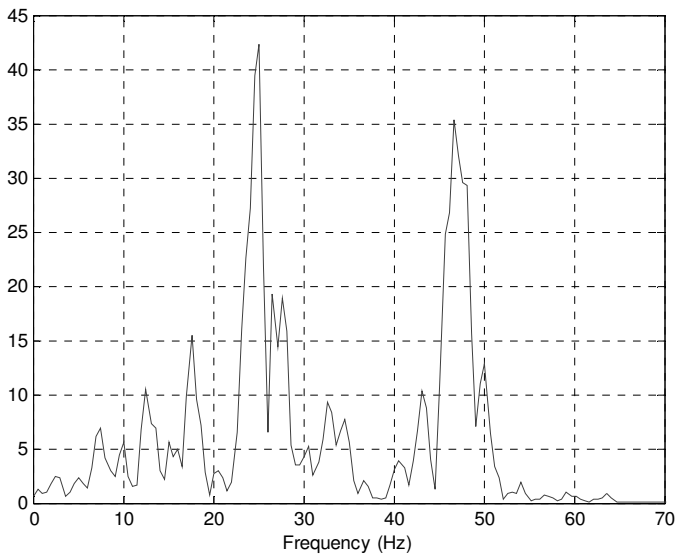


Figure 21c – Arch No. 4: plot of the PSD of the accelerations measured by the accelerometers A8 during the dynamic tests.

A dynamic modal analysis was carried out as well by means of the previously-described FE elastic model, in order to identify numerically the natural frequencies (Figure 22). In spite of the limited extension of the transverse portion of the building considered in the modelling, the first calculated frequency (exciting a considerable mass percentage in the vertical direction)  $f_{1,\text{numerical}} = 12.7$  Hz turned out to be quite close to  $f_{1,\text{experimental}} = 15$  Hz for Arch No. 4. A possible explanation for that discrepancy may be found in the connection between the portion of the building subjected to investigation and the rest of the building. This connection (neglected in the numerical model) increases the structural stiffness of the actual structure and, consequently, brings in higher values for the natural frequencies. One can conclude that the application of FE modelling - according to the proposed procedure and for the type of structure in question - can properly describe the dynamic behaviour of the structure under service conditions.

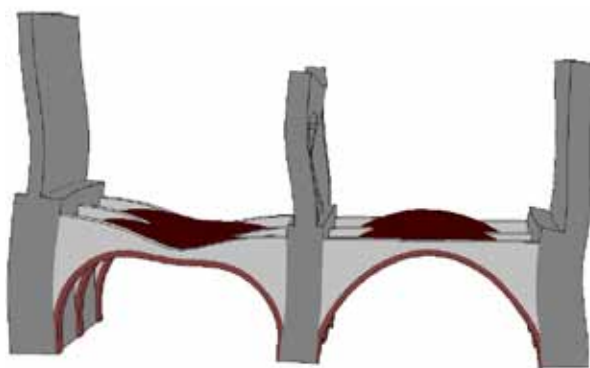


Figure 22 - Modal shape of the first eigenmode of the structure.

## 5. NUMERICAL MODELLING OF THE STRUCTURAL BEHAVIOR UNDER HORIZONTAL LOADS

An appropriate assessment of the membrane and flexural stiffness of the horizontal (or sub-horizontal) diaphragms is fundamental in order to reliably predict the seismic response of a structure. As discussed in Cattari et al. (2008), the role of the floor diaphragms is sizeable with reference to both structural stiffness and the transfer of the seismic loads to the vertical members. In fact, should the floors be prone to in-plane deformations, the vertical members would move independently from each other, and transferring the horizontal action from any members exhibiting a strong nonlinear behaviour (*diaphragms*) to still operative members (*columns*) would be hardly possible. Conversely, assuming stiff diaphragms may

lead to a dangerous overestimation of the redistribution of the horizontal actions among the vertical members.

In order to assess, albeit approximately, the transverse stiffness of the vaulted floor under horizontal loads, a linear-static analysis was performed by applying a transverse horizontal force of 1000 kN to the central arches and by constraining the transverse displacements of the model in the sections containing the lateral arches. The analysis was carried out without (Figure 23) and with (Figure 24) the cross vaults, with the objective of defining the role of the vaulted floors in redistributing the seismic forces aligned with the shorter axis of the building (*transverse seismic forces*). This study allowed to evaluate the elastic mechanical parameters to be attributed to the equivalent horizontal 3D diaphragm, as defined in Cattari et al. (2008). In this way, the diaphragms replaced the vaults in the numerical analysis.

The values of the displacement in the control point A (Fig. 23) are summarized in Table 4, where reference is made to the FE models shown in Figures 23 and 24.

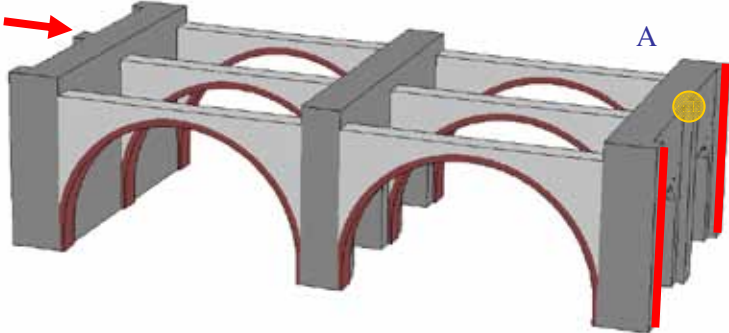


Figure 23 – Finite element model devoid of vaults used in the study of the transverse translational stiffness of the building.

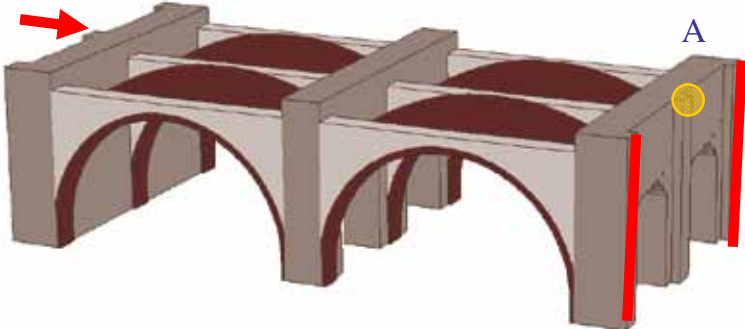


Figure 24 - Finite element model including the vaults used in the study of the transverse translational stiffness of the building.

Table 4 - Contribution of the vaults to the transverse stiffness of the building (values obtained for an horizontal load of 1000 kN).

Point	FE model with vaults $\delta_A'$ [mm]	FE model without vaults $\delta_A''$ [mm]	Contribution of the vaults $(\delta_A'' - \delta_A') / \delta_A''$
A	0.12	0.56	78.5 %

The results show that the transverse stiffness of the brickwork vaults is about 79% of the transverse stiffness of the whole structure. Therefore, the vaults play a fundamental role in redistributing the horizontal forces among the arches.

In order to assess the ductility of the arch-vault system, nonlinear static incremental analyses were carried out by using the FE model reported in Figure 25. In this analysis, the nonlinear behaviour of the materials was modelled by homogenized properties for stonework and brickwork (Mistler et al., 2006).

This model is not very cumbersome from a computational viewpoint and allows to analyse large structures. The yielding criterion is the classical Mohr-Coulomb criterion (0.1 MPa for cohesion and 21° for the friction angle). The failure criterion is based on the maximum compressive stress, i.e. on the attainment of the strength in compression (4 MPa).

As remarked in Galasco et al. (2006), the use of pushover analysis for buildings with membrane deformable diaphragms presents more critical aspects than the simpler case of the structures with stiff floors. For example, the choice of the control node is one of the crucial aspects of the pushover approach with in-plane deformable diaphragms. In fact, remarkably different response curves can be obtained by changing the control node, even if it belongs to the same floor. Another important issue is the selection of the vertical and horizontal force distributions, since in deformable-storey structures, the effects of higher order modes may be sizeable.

In this study, the need of simplifying the numerical analysis suggested to prescribe an incremental horizontal displacement in point B (located at the floor level, Fig. 25) and the resulting horizontal force was monitored at the base level.

The alternative procedure, based on increasing a predefined distribution of forces (e.g. proportional to the initial stiffness), does not seem to be realistic because of the continuous evolution of the stiffness due to local damage in the materials; hence, this procedure was not adopted.

The numerically-obtained base shear-horizontal displacement curve at point B is plotted in Figure 26, where the ideal equivalent bilinear curve is plotted as well. The elastic-perfectly plastic diagram is determined in such a way that the areas under the two curves, actual and ideal, be the same. From the equivalent bilinear curve it is possible to assess the ductility of the arch-vault system ( $\mu = 32 / 17.8 = 1.80$ ). This value, representative of the entire structure, indicates a satisfactory

ductility and is within the expected range for brickwork systems. At collapse, masonry crushing is localized at the bottom of the central arch; hence – at least from a theoretical viewpoint - the vaulted system may undergo higher horizontal displacements (see for instance Van Mele et al., 2012).

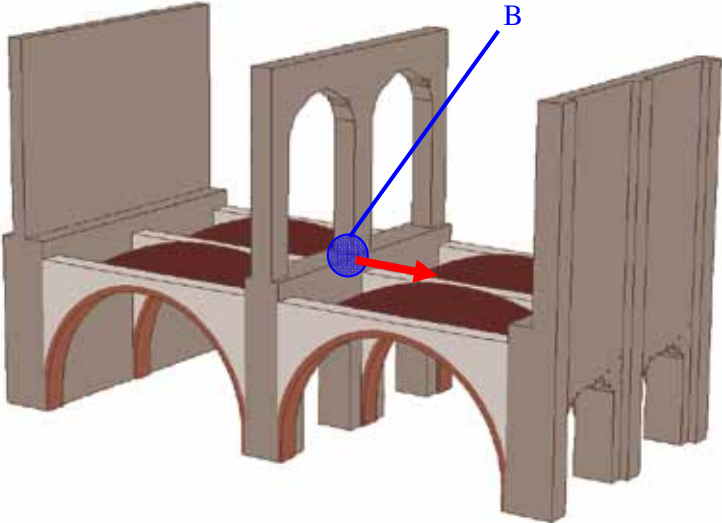


Figure 25 – Nonlinear FE model used in the study of the ductility of the arch-vault system.

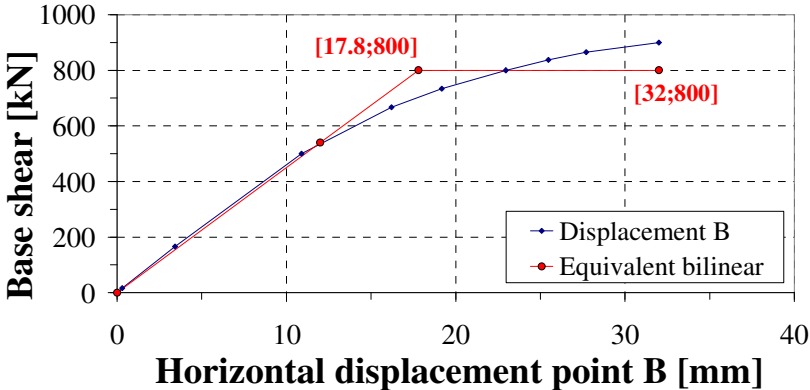


Figure 26 - Capacity curve obtained from the static incremental analysis performed by means of the FE model shown in Figure 25, under horizontal loads, and elastic-perfectly plastic equivalent curve.

## 6. CONCLUSIONS

The interpretation of the experimental tests, carried out on four stone arches, allowed to estimate the mechanical and structural properties of the building, with reference to the bearing system consisting of arches and vaults. Taking advantage of the static and dynamic tests, a finite element model was calibrated in order to describe the experimental tests.

The satisfactory fitting of the experimental results confirms the reliability of the numerical model, that may be used in further more complicated analyses. In this perspective, linear and nonlinear analyses were carried out with reference to horizontal loads, showing that vaults play a leading role in redistributing the forces among parallel arches, to the advantage of structural robustness.

Finally, the pushover analysis showed that the structural system bearing the horizontal loads has a sizeable ductility. These two characteristics (force-redistribution capability and ductility ) are instrumental in effectively withstanding seismic forces. To this purpose, the analyses carried out in this project clarify the role of the vaults, that should be appropriately protected from early failures during a seismic event.

Any possible retrofitting should respect the actual structural behaviour, which is characterized by the sizeable contribution given by the vaults to the total stiffness of the structure.

## ACKNOWLEDGEMENTS

The financial support by the Italian Department of Civil Protection (RELUIS 2010 Grant – Task 2.3.1. and Task 1.1.2) is gratefully acknowledged.

## REFERENCES

- Bovo M., Mazzotti C. and Savoia M. (2012). “Analysis of Structural Behaviour of Historical Stone Arches and Vaults: Experimental Tests and Numerical Analyses”. *8<sup>th</sup> Int. Conf. on Structural Analysis of Historical Constructions - AHC2012*, Wroclaw (Poland), October 15-17, V.1, pp. 635-643.
- Cattari S., Resemini S. and Lagomarsino S. (2008). “Modelling of Vaults as Equivalent Diaphragms in 3D Seismic Analysis of Masonry Buildings”. *6<sup>th</sup> Int. Conf. on Structural Analysis of Historical Construction - SAHC2008*, Bath (United Kingdom), July 2-4, V.1, pp. 517-524.
- Conte C., Rainieri C., Aiello M. A. and Fabbrocino G. (2011). “On-site Assessment of Masonry Vaults: Dynamic Tests and Numerical Analysis”. *Geofizika*, Vol. 28, pp. 127-143.



- Galasco A., Lagomarsino S., Penna A. and Resemini S. (2004). "Nonlinear Seismic Analysis of Masonry Structures". *13<sup>th</sup> World Conf. on Earthquake Eng. - WCEE*. Vancouver (Canada), August 1-6, Paper no. 843, pp. 1-15.
- Galasco A., Lagomarsino S. and Penna A. (2006). "On the Use of Pushover Analysis for Existing Masonry Buildings". *1<sup>st</sup> European Conf. on Earthquake Eng. and Seismology*, Geneva (CH), Sept. 3-8, Paper no. 1080 (CD-ROM).
- Gambarotta L. and Lagomarsino S. (1997a). "Damage Models for the Seismic Response of Brick Masonry Shear Walls. Part I: The Mortar Joint Model and its Applications". *Earthquake Eng. and Struct. Dynamics*, V.26, pp.423-439.
- Gambarotta L. and Lagomarsino S. (1997b). "Damage Models for the Seismic Response of Brick Masonry Shear Walls. Part II: The Continuum Model and its Applications". *Earthquake Eng. and Struct. Dynamics*, V.26, pp. 441-462.
- Hayen R., Van Balen K. and Van Gemert D. (2009). "Triaxial Interaction of Natural Stone, Brick and Mortar in Masonry Constructions. *1<sup>st</sup> WTA International PhD Symposium*, Leuven (Belgium), Oct. 8-9, Paper no. 18 (CD-ROM).
- Mallardo V., Malvezzi R., Milani E. and Milani G. (2008). "Seismic Vulnerability of Historical Masonry Buildings: A Case Study in Ferrara". *Engineering Structures*, V. 30, pp. 2223-2241.
- Mistler M., Butenweg C. and Meskouris K. (2006). "Modelling Methods of Historic Masonry Buildings under Seismic Excitation". *Journal of Seismology*, V.10, pp. 497-510.
- Savoia M. and Carli R. (2010). "The Use of Sonic Techniques to Assess the Efficacy in Rehabilitating Historical Masonry" (in Italian). *18<sup>th</sup> Congress of Italian Building Experts - C.T.E.*, Nov. 11-13, Brescia (Italy), Vol. 2, pp. 1163-1172.
- Stablon T., Sellier A., Domede N., Plu B. and Dieleman L. (2012). "Influence of Building Process on Stiffness: Numerical Analysis of a Masonry Vault Including Mortar Joint Shrinkage and Crack Re-closure Effect. *Materials and Structures*, V. 45, pp. 881-898.
- Szólomicki J. P. (2009). "Structural Behaviour of Masonry Vaults". *18<sup>th</sup> Int. Conf. on the Application of Computer Science and Mathematics in Architecture and Civil Engineering*. Weimar (Germany), July 7-9, (CD-ROM).
- Uday Vyvas C. V. and Venkatarama Reddy B. V. (2010). "Prediction of Solid Block Masonry Prism Compressive Strength Using FE Model". *Materials and Structures*, V. 43, pp. 719-735.
- Van Mele T., McInerney J., DeJong M. J. and Block P. (2012). "Physical and Computational Discrete Modelling of Masonry Vault Collapse". *8<sup>th</sup> Int. Conf. on Structural Analysis of Historical Constructions - SAHC2012*, Wroclaw (Poland), October 15-17, Vol. 3, pp. 2552-2560.



## ACKNOWLEDGEMENTS

The Editorial Board is grateful to Patrick Bamonte (MI), Luca Bertolini (MI), Stefano Gangiano (IC), Luigi Cedolin (MI), Matteo Colombo (MI), Dario Coronelli (MI), Frank Dehn (DL), Giovanni Di Luzio (MI), Roberto Felicetti (MI), Liberato Ferrara (MI), PierGiorgio Malerba (MI), Franco Mola (MI), Aurelio Muttoni (CH), Radu Pascu (RO), Marco Pisani (MI), Paolo Riva (BG), Gaetano Russo (UD) and Ralejs Tefpers (GT), who reviewed the papers in the years 2010-2012.

BG = University of Bergamo, Bergamo – Italy

CH = Ecole Polytechnique Fédérale de Lausanne – EPFL, Lausanne - Switzerland

DL = Technical University of Leipzig , Leipzig - Germany

GT = Chalmers University of Technology, Göteborg - Sweden

IC = Italcementi Group, Bergamo - Italy

MI = Politecnico di Milano, Milan - Italy

RO = Technical University of Bucarest, Bucarest - Romania

UD = University of Udine, Udine - Italy



## PREPARATION OF MANUSCRIPTS

### General

- Size of the volume: 165 x 240 mm.
- Area in which the text must be typed: 129 x 195.
- Upper, lower, left and right margins: 20, 25, 18 and 18 mm.
- Abstract, text, references, captions, titles of the tables: single spaced, left- and right-justified, 11 Times New Roman.
- Figures, tables and captions: skip two lines between the text and each figure or table, skip one line between each figure (table) and its caption (title), skip two lines between each caption (title of the table) and the text.
- Tables: put the title over the table.
- Maximum suggested number of pages: 30.

### First page

- Top left corner: identification of the volume (3 lines, 11 Times New Roman) as in the papers published in V.31; then skip at least three lines.
- Title: centered, upper-case letters, bold characters, 13 Times New Roman; then skip at least two lines.
- Authors' names: centered, upper and lower case, 11 Times New Roman; then skip at least three lines.
- Abstract: preceded by the heading **ABSTRACT**, left- and right-justified, any length with the only limit of being contained in the 1<sup>st</sup> page (together with the keywords and the affiliation), 11 Times New Roman.
- Keywords: preceded – on the same line - by **KEYWORDS**: up to 5 keywords should be indicated (left- and right-justified, 11 Times New Roman; skip two lines between the last line of the abstract and the keywords).
- Indentation: 5 spaces at the beginning of each paragraph, except the first paragraph.
- Affiliation (10 Times New Roman): at least two lines below the abstract, preceded by a full straight line, at the foot of the page, with academic or professional position, department or division, employer (university, research center, company, firm ...), city, state.

### Following pages

- Indentation: 5 spaces at the beginning of each paragraph, except the first paragraph following the heading or sub-heading of each chapter or sub-chapter.

- Headings:

<b>1. INTRODUCTION</b>	(1 <sup>st</sup> level, chapters)
<b>1.1 Materials</b>	(2 <sup>nd</sup> level, subchapters)
1.1.1 <u>Concrete</u>	(3 <sup>rd</sup> level, subchapters)
- Skip two lines between the end of a chapter and the heading of the following chapter.
- Skip one line between the end of a sub-chapter and the heading of the following sub-chapter.
- Skip one line between each heading or sub-heading and the following text.
- Fill each page with text/figures/tables/references in order to avoid half-filled pages. If the last page is not full, place the references in two partial columns of similar length.
- Fill each page in such a way that its last line be aligned with the last lines of the other pages, in accordance with the page format.

### Captions, quotations, references and appendixes

- Captions (to be placed under the figure) and titles of the tables (to be placed over the table): short captions or titles (less than one line) should be centered; long captions or titles (two or more lines) should be left- and right-justified.

Examples:

Figure 1 – Fracture energy vs. temperature.

Table 1 – Geometry of the specimens: L = span; b = section width;  $\Delta L$  = distance between the point loads; and d , t = depth and thickness of the mid-span notch.

- Quotations within the text: ..... Chopra (1995) or ..... Black and White (1998) or .... Black *et al.* (2000) or ... (White, 1995; Black, 2002; Gray, 2003a) [add a letter like “a”, “b”, “c”, ..... if two or more papers published in the same year by the same author(s) are cited in the references].
- References: should be in alphabetic order (numbered references, like [5], are accepted whenever the references are very numerous and/or cumbersome):

Black K. and White E. (1998). “Experimental Studies on Concrete”. *Journal of Concrete Constructions*, Vol.00, No.00, 000-000.

Black K., Gray C. and White E. (2000). “Concrete Modeling”. *Proc. 4<sup>th</sup> Int. Conf. on Advances in Concrete Mechanics*, ed. by B. Green and W. Brown, City, State, Date, Vol.1, 000-000.

Chopra A.K. (1995). *Dynamics of the Structures*. Pub. by Prentice-Hall, Upper Saddle River, New Jersey (USA), 000 pp.

- Skip 6pt between two successive references.
- Appendixes: the sections “References” and “Notation” should not be indicated as appendixes; any appendix should be placed past the sections “References” and “Notation”, and should be indicated with Roman numbers.
- For the quotation of a paper published in Studies and Researches, adhere to the following example:

Regan P.R. and Kennedy Reid I.L. (2009). "Assessment of Concrete Structures Affected by Cover Delamination – Part 1: Effect of Bond Loss". *Studies and Researches – Annual Review of Structural Concrete*, Ed. by Politecnico di Milano and Italcementi, V. 29, pub. by Starrylink (Brescia, Italy)\*, 245-275.

### **Format of the keywords**

**KEYWORDS** : bond, chlorides, corrosion, reinforced concrete, shear capacity

### **Paper submission**

The papers should be submitted (as a Word file) to any member of the Editorial Board by January 15 of the year of publication. Each paper will be reviewed by at least two independent reviewers, and the reviews will be sent back to the author(s) by February 15. The final texts should be sent back to the Editorial Committee by mid March. The volume is published in late April.

Research-oriented papers about rather general topics treated theoretically, experimentally or numerically are published in the Section “Technical Papers”, while design-oriented papers, presentation of built structures, short contributions on specific technical or professional topics, and test reports will be published in the Section “Technical Notes”.

(\*) From Vol. 32 included, the publisher is: IMREADY srl (Galazzano, Republic of San Marino).







**POLITECNICO  
DI MILANO**

Dipartimento  
di Ingegneria Strutturale



**Italcementi**  
Italcementi Group

A world class local business

# La Scuola F.lli Pesenti-Politecnico di Milano

## Anno accademico 2011-2012

### e avvio

## Anno accademico 2012-2013

### **1 LA DIREZIONE DELLA SCUOLA: RIFLESSIONI E AUSPICI**

### **2 CONTINUITÀ E AGGIORNAMENTO DELLE ATTIVITÀ DI DIDATTICA POST-LAUREA**

- 2.1 *Innovazione per i Corsi di Master Universitari 2011-2012*
- 2.2 *Avvio della V edizione del Corso di Master in “Progettazione Sismica delle Strutture per Costruzioni Sostenibili “*
- 2.3 *Attività seminariale*
- 2.4 *Nuove Attività di “atelier progettuale” con gruppi di allievi Master 2011-2012*
- 2.5 *Attivazione dei Corsi di Master 2012-2013*
- 2.6 *Convenzioni di collaborazione tra la Scuola F.lli Pesenti e enti pubblici e privati*

### **3 INIZIATIVE IN CORSO – SINERGIE TRA RICERCA E DIDATTICA DEI MASTER**

- 3.1 *I temi di ricerca caratterizzanti le attività della Scuola, con particolare riferimento a quelli del restauro e adeguamento in aree sismiche dell’Edilizia Storica e del Moderno*
- 3.2 *Contatti internazionali*
  - 3.2.1 *Iniziative a conclusione del progetto IRSES (VII Programma Quadro)*

- 3.2.2 Partecipazione comitato organizzativo del 30° Convegno Internazionale IAHS-International Association for Housing Science –Politecnico di Milano – Milano 17/20 sett. 2013 .-150° Politecnico di Milano*
- 3.2.3 Iniziative di presentazione della Scuola F.lli Pesenti presso università straniere*
- 3.2.4 Tirocini collaborativi multidisciplinari ed internazionali*

## 1 La direzione della Scuola: riflessioni e auspici

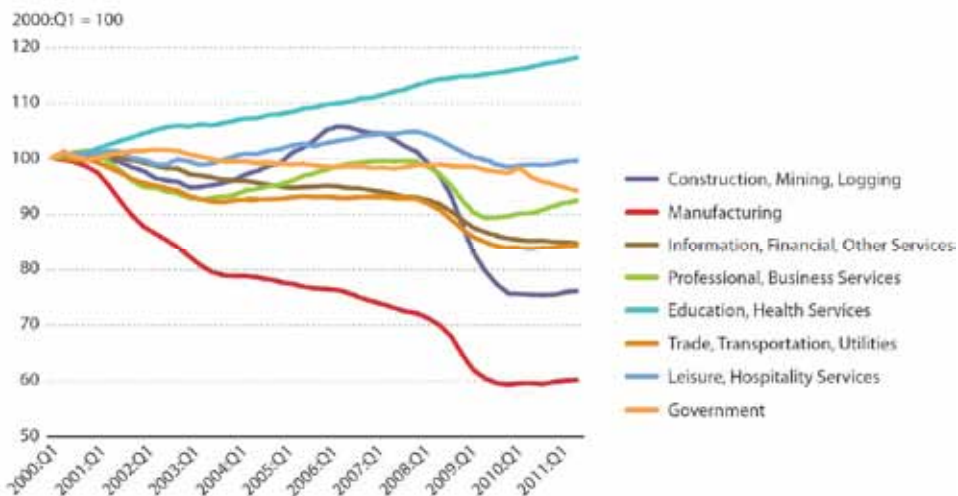
In queste prime pagine del rapporto è opportuno riproporre, come accennato lo scorso anno accademico, due punti focali del rinnovamento che l'*high education* deve prepararsi ad affrontare, con particolare riferimento alle professioni dell'ingegnere e dell'architetto:

- a) un tecnicoingegnere con più ampie competenze e capacità decisionali
- b) una offerta di formazione più diffusamente fruibile

Entrambi i punti, a) e b), fortemente dibattuti a livello internazionale, hanno come fondamento la consapevolezza che l'*education*, nella sua più vasta accezione, è, e sempre più può rappresentare, leva di sviluppo e civilizzazione a livello globale.

Il grafico sotto riportato, sicuramente sottolinea tale consapevolezza, anche se, come verrà brevemente accennato più avanti, le sfide per adempiere a tali missioni richiedono forti capacità di innovazione in un sistema, quale quello della formazione, fondamentalmente ancora riproponentesi in forme tradizionali e statiche.

Evolution of Sectoral Employment, 2000:Q1–2011:Q3



SOURCE: Bureau of Labor Statistics/Haver Analytics.

In particolare, facendo riferimento alla figura dell'ingegnere civile (comprendente anche la figura dell'ingegnere edile, non prevista differenziata come figura professionale del nord America) sono esplicitivi i sottotitoli del rapporto dell'ASCE (American Society of Civil Engineering) 2009 "VISION for Civil Engineering in 2025-a roadmap for the profession", qui di seguito riportati:

*"Entrusted by society to create a sustainable world and  
Enhance the global quality of life,*

*Civil engineers*

*Serve competently, collaboratively, and ethically as master:*

- *planners, designers, constructors, and operators of society's economic and social engine of the built environment;*
- *stewards of the natural environment and its resources;*
- *innovators and integrators of ideas and technology across the public, private, and academic sectors;*
- *managers of risk and uncertainty caused by natural events, accidents, and other threats; and*
- *leaders in discussion and decisions shaping public environmental and infrastructure policy. "*

Cioè, in poco più di 10 anni, lo sviluppo sostenibile rivolto al miglioramento globale della qualità della vita richiede profondi cambiamenti nelle figure professionali, in particolare dell'ingegnere, coinvolgendo l'offerta di formazione, intesa necessariamente nella sua accezione più vasta di life-long education ; offerta che deve evolversi nei contenuti, sfida più difficile, nelle forme, al fine di consentire una fruizione più ampia possibile e continuativa, sempre più e meglio utilizzando la tecnologia informatica. Di seguito ancora un grafico previsionale, in cui si inserisce l'E-Learning fra le attività in espansione negli anni a venire.

Le più rinomate Università del Nord America stanno consorziandosi per affrontare sinergicamente l'impegno tecnologico/economico per l'utilizzo e/o il perfezionamento di loro piattaforme informatiche specifiche per l' Online Education

Nella presentazione di Rafael Reif, Presidente del MIT, "OUR MISSION IS TO TRANSFORM LEARNING" in cui viene presentato il consorzio "EdX" tra MIT, HARVARD e Berkeley , si legge:

*"EdX represents a unique opportunity to improve education on our campuses through online learning, while simultaneously creating a bold new educational path for millions of learners worldwide".*

Nella stessa presentazione Drew Faust, Harvard President :

*"EdX gives Harvard and MIT an unprecedented opportunity to dramatically extend our collective reach by conducting groundbreaking research into*

*effective education and by extending online access to quality higher education.* “

EdX è solo una delle numerose recenti piattaforme universitarie online (altre startup : Coursera, Udacity) che attualmente offrono i cosiddetti MOOCs “massive open online courses”, cioè corsi gratuiti, ovviamente offerti dalle più rinomate Università americane.

La nostra realtà nazionale è chiaramente molto diversa, ma simili principi e previsioni di sviluppo attengono anche alla nostra realtà formativa, sicuramente per la formazione post-laurea, cioè quella rivolta alle classi dei lavoratori che possono , attraverso i corsi online, non solo aggiornare le loro conoscenze tecnico-professionali, ma anche migliorare le loro credenziali lavorative ai fini di upgrading di carriera .



Queste sono le prospettive su cui si focalizzano le scelte della Scuola Master F.lli Pesenti e gli investimenti, con spirito pionieristico, per una offerta sempre più completa e tecnicamente valida di e-learning, anche per corsi con crediti.

## 2 Continuità e aggiornamento delle attività di didattica post-laurea

### 2.1 Innovazione per i Corsi di Master Universitari 2011-2012

Come sinteticamente riportato nella citazione di “VISION for Civil Engineering in 2025-a roadmap for the profession”, alle future figure dell'ingegnere civile, e sicuramente anche dell'architetto, si richiede l'apertura a competenze in nuovi campi tecnico-gestionali.

La consapevolezza e l'assunzione di tale responsabilità è alla base del nuovo programma di contenuti nei corsi di Master che la Scuola F.lli Pesenti ha sottoposto e richiesto di approvare al Senato Accademico del Politecnico di Milano per l'anno 2011-2012.

Tali innovazioni sono in parte individuabili anche dai titoli dei 5 corsi di Master proposti, attivati e in conclusione, mentre si sta scrivendo questo rapporto.

Brevemente, i nuovi contenuti didattici hanno interessato maggiormente i Master :

Edifici e Infrastrutture Sostenibili  
Project Management delle Opere Strutturali e Infrastrutturali  
Progettazione Sismica delle Strutture per Costruzioni Sostenibili

con nuove opportunità e argomenti , sia svolti in aula sia applicativi, così riassumibili e offerti anche per gli allievi degli altri Master della Scuola:

- Certificazione CENED per certificatore energetico su albo regionale
- Nuova Unità Didattica sugli aspetti procedurali e legali richiesti nelle Gare per Appalti Internazionali
- Tutoraggio pomeridiano, soprattutto rivolto agli allievi stranieri
- Scuola estiva all'Aquila, in collaborazione con l'Università dell'Aquila .
- Incremento delle attività di “atelier progettuali”.

Qui di seguito la tradizionale locandina illustrativa.

L'opportunità di iscrizione all'albo professionale per “Certificatori Energetici”, offerta anche online, ha riscosso particolare consenso : il corso con le lezioni specifiche si è ripetuto con 4 edizioni , con partecipazione anche di esterni ai corsi di Master; l'attestato, conseguibile con il superamento di un esame con commissione esterna, è stato conseguito dal 98% degli iscritti totali, comprensivi degli allievi che hanno seguito

onsite e quelli che hanno seguito online. Per la modalità online si è richiesta la messa a punto di controlli in remoto per le verifiche di effettiva frequenza dell'iscritto e la possibilità di ammissione all'esame finale; la tecnologia messa a punto è stata approvata dall'Ente Regionale CENED, e attualmente i nostri corsi online sono accreditati presso la Regione Lombardia, e visti con molto interesse anche dalle altre regioni: abbiamo avuto parecchi iscritti anche di professionisti non residenti in Lombardia.

**QUOTA DI PARTECIPAZIONE:**  
4.5.500,00 + 500,00 per contributi di Ateneo.

**QUOTA BASE DI PARTECIPAZIONE PER SINGOLE UNITÀ DIDATTICHE:** 4.400,00 (con addebito di partecipazione)

**STAGE E BORSE DI STUDIO OFFERTE DA:**



**Master School F.lli Pesenti**

Politecnico di Milano

Finanziamento:

italcimenti  
italcimenti group

Collaborazione di gestione:

CONSIGLIO PER LE COSTRUZIONI DELL'INGEGNERIA STRUTTURALE IN EUROPA

Collaborazione scientifica:

Dipartimento di Ingegneria Strutturale

DIPARTIMENTO BEST

MIP

Accreditamento: sistema qualità:



CENED  
Certificazione Europea degli Edifici

SCUOLA MASTER F.LLI PESENTI  
POLITECNICO DI MILANO  
DIPARTIMENTO DI INGEGNERIA STRUTTURALE  
P.ZZA LEONARDO DA VINCI, 32  
20133 MILANO - ITALY

Info: Dott.ssa Sara Giussani  
Tel: +39 02-2399.4305/4396 - Fax: +39 02-2399.4220  
Email: scuolamaster@stru.polimi.it  
Site web: <http://masterpesenti.stru.polimi.it>

**Master School F.lli Pesenti**

Politecnico di Milano  
Anno Accademico 2011-2012

Verengono attivati presso il Politecnico di Milano i seguenti Master:

- “Programmazione delle Strutture in Calcestruzzo Betonati”
- “Structural Concrete - Structural Design”
- “Project Management delle Opere Strutturali e Infrastrutturali”
- “Project Management of Civil Structures and Infrastructure”
- “Edifici e Infrastrutture Sostenibili”
- “Sustainable Building and Infrastructures”
- “Programmazione Scientifica delle Strutture per Costruzioni Sostenibili”
- “Design of Sustainable Buildings Structures”
- “Design and Management of Structural Technologies in Construction Works” (English in English)

Presidente Prof. Ing. Antonio Miglacci  
Direttore Prof.ssa Arch. Ing. Paola Ronca

Come consuetudine, si sono organizzate visite tecniche presso i maggiori cantieri di sviluppo immobiliare, nell'area metropolitana di Milano, con seminari illustrativi in loco.

Di seguito alcuni momenti delle visite.



Alcune immagini delle visite degli allievi Master nei due più importanti e attivi poli di sviluppo immobiliare di Milano :Garibaldi-Repubblica e City-life/Tre torri.



*L'edificio "il bosco verticale"*





*Il gruppo in city life*

## *2.2 Avvio della V edizione del Corso di Master in “Progettazione Sismica delle Strutture per Costruzioni Sostenibili “*

L'attività continuativa di collaborazione con l'Università dell'Aquila, in particolare rivolta alla analisi quantitativa del danno in seguito al sisma per gli edifici del centro storico e allo studio e preparazione/sperimentazione di malte innovative e di migliori prestazioni da proporre nei progetti preliminari per il loro consolidamento e adeguamento, è stata la chiave di volta per lo svolgimento della V edizione del Master, dove la quasi totalità degli iscritti ha potuto svolgere stage o esperienza diretta su edifici ubicati all'Aquila, grazie anche all'attivazione della Scuola estiva a fine luglio 2012.

Il Master è stato inaugurato con il Seminario del prof. Dante Galeotta della Facoltà di Ingegneria dell'Università dell'Aquila, a cui hanno partecipato dottorandi e ricercatori del Politecnico.

Viene di seguito riportata la locandina illustrativa e alcune slides di danni in edifici universitari :



**POLITECNICO  
DI MILANO**

Dipartimento  
di Ingegneria Strutturale



**Italcementi**  
Italcementi Group

A world class local business

## **Scuola Master F.II Pesenti**

Lunedì 20 febbraio, ore 9

Aula Scuola Master F.II Pesenti – piazza Leonardo da Vinci 32

**Lezione inaugurale della IV edizione del Master di II livello in**

**“Progettazione Sismica delle Strutture per Costruzioni Sostenibili”**

**La lezione sarà tenuta dal prof. Dante Galeota  
Facoltà di Ingegneria, Università dell’Aquila**

***“Il Contributo dell’Ateneo dell’Aquila  
nella Ricostruzione Post-Sisma”***



**D.I.S.A.T.**

Dipartimento di Ingegneria delle Strutture delle  
Acque e del Terreno



## **MASTER IN INGEGNERIA SISMICA**

*Politecnico di Milano 20 Febbraio 2012*

**L'Aquila**

**Recupero e conservazione di edifici colpiti dal sisma**

*Prof. DANTE GALEOTA*

*D.I.S.A.T. Dipartimento di Ingegneria delle Strutture, delle Acque e del Terreno, Università degli Studi dell'Aquila*

Milano 20/02/2012



Palazzo Carli, Rettorato – Polo Centro



Facoltà di Ingegneria  
AMPLIAMENTO



La nuova iniziativa, della “**Summer School**”, offerta agli allievi Master e in collaborazione con le Università dell’Aquila, Perugia e Venezia, è stata concordata , come docenza, e organizzata come accoglienza grazie alla collaborazione di alcuni giovani docenti della Scuola Pesenti e dell’Aquila.

Le “Summer School” sono corsi intensivi di alta formazione caratterizzati da:

- **organizzazione didattica non convenzionale** (tour, esperienze laboratoriali, attività esercitative, incontri culturali, testimonianze aziendali, lezioni di cucina...);
- **durata limitata** (indicativamente da 1 a 6 settimane);
- **approccio multidisciplinare**;
- **respiro internazionale** (esperienze all'estero, incontro con studenti e docenti stranieri di altri atenei, didattica erogata preferibilmente, ma non esclusivamente, in lingua inglese);
- riconoscimento di crediti ECTS (dove possibile).

Di seguito alcuni momenti della Summer School di fine luglio 2012, dove le lezioni si sono svolte in luoghi diversi del territorio aquilano, e la locandina.



## 2.3 Attività seminariale

Di seguito vengono riportati alcuni momenti di attività seminariali svoltesi con l'illustrazione dei temi di ricerca attualmente attivi presso la Scuola Pesenti. In ordine temporale :

MARZO 2012



POLITECNICO  
DI MILANO

Dipartimento  
di Ingegneria Strutturale



**Italcementi**  
Italcementi Group

**Scuola Master F.lli Pesenti**

Workshop didattico

*“Isolamento sismico.*

*Richiami di base, risposta strutturale, principi di progettazione e applicazioni”*

*Prof. Mauro Dolce*

*Direttore dell'Ufficio Rischio Sismico e Vulcanico  
Dipartimento della Protezione Civile  
Roma*

26 marzo 2012 – ore 9.15/12.15

presso

Scuola Master F.lli Pesenti  
Politecnico di Milano

*“Seismic isolation was first applied more than twenty years ago using natural rubber isolation systems, but now there are many types of isolations and, however the field is undergoing rapid changes. Seismic isolation is now playing an increasing role in the design of earthquake resistant structures, but there is still a reluctance by structural engineers to venture into what is perceived to be a new and perhaps complicated design procedure.”*

*By James Marshall Kelly (Professor Emeritus – University of California at Berkeley)*

GIUGNO 2012

Incontro-Seminario tenuto il 4 giugno 2012 dal prof. Alberto Franchi presso la nuova sede dell' I-lab di Italcementi, ad una delegazione di docenti universitari e professionisti egiziani , membri del

## Housing & Building National Research Center Cairo-Egypt



Il tema guida dell'incontro si è focalizzato sulle prime prove effettuate presso il Politecnico di Milano sul comportamento del cemento fotocatalitico TX, sottoposto a situazioni di invecchiamento accelerato in camera climatica.

Tale studio è stato inquadrato nella più ampia sperimentazione in atto, in vista di applicazione estensiva per il restauro delle facciate di "Torre Velasca" in Milano .

GIUGNO 2012



CONSORZIO PER LE  
COSTRUZIONI DELL'INGEGNERIA STRUTTURALE in EUROPA

Scuola Master Fratelli Pesenti

Politecnico di Milano

## PER IL BUON SERVIZIO DEGLI ALTI EDIFICI: DALLA TEORIA ALLA PRATICA

### A – Il progetto di alti edifici soggetti a vento e sisma

lunedì 18 giugno 2012, ore 10.00- 13.00

introducono:	prof. ing. Antonio Migliacci	(Consorzio CIS-E- Politecnico di Milano)
	ing. Michele Masnaghetti	(Construction Director Hines Italia)
	prof. ing. Alberto Franchi	(Consorzio CIS-E- Politecnico di Milano)
intervengono:	prof. Ing. Alberto Zasso	(Politecnico di Milano)
	ing. Danilo Campagna/Alessandro Aronica	(MSC Associati s.r.l.)
	ing. Aldo Castoldi	(P&P Consulting Engineers s.r.l.)
	ing. Pietro Crespi	(Politecnico di Milano)

### B – Un tema originale di sicurezza: la presenza di alberi sui balconi di alti edifici

martedì 19 giugno 2012, ore 17.00- 19.30

introducono:	prof. ing. Antonio Migliacci	(Consorzio CIS-E- Politecnico di Milano)
	ing. Michele Masnaghetti	(Director Manager Hines Italia)
intervengono:	prof. ing. Alberto Franchi	(Consorzio CIS-E- Politecnico di Milano)
	ing. Luca Buzzoni	(Arup Italia)
	ing. Pietro Crespi	(Politecnico di Milano)
	ing. Nicola Longarini	(Consorzio CIS-E- Politecnico di Milano)

### C - Il collaudo di grandi complessi strutturali

mercoledì 20 giugno 2012, ore 17.00- 19.30

introducono:	prof. ing. Antonio Migliacci	(Consorzio CIS-E - Politecnico di Milano)
	ing. Eugenio Montessori	(Construction Manager- Galotti, Hines Italia)
intervengono:	ing. Nicola Longarini	(Consorzio CIS-E- Politecnico di Milano)
	ing. Sergio Sgambati	(BMS Progetti s.r.l.)
	ing. Bruno Finzi	(Ce.A.S. s.r.l.)
	ing. Gabriele Cozzaglio/Luca Strata	(Studio Cozzaglio Milano - Studio Strata Parma)

Con il patrocinio di:

Politecnico di Milano

Collegio Ingegneri ed Architetti della Provincia di Milano – il presidente: ing. Bruno Finzi

Ordine degli Ingegneri della Provincia di Milano – il presidente: ing. Stefano Calzolari

AULA BELTRAMI - Dip. Ingegneria Strutturale del Politecnico di Milano  
p.zza Leonardo da Vinci 32 - 20133 Milano  
LA PARTECIPAZIONE È GRATUITA



OTTOBRE 2012

MADEexpo Giovedì 18 ottobre 2012 - Ore 10,30

**“Caratteristiche prestazionali delle Armature per il Calcestruzzo Armato”.**

Una tavola rotonda per discutere di normativa, affidabilità e innovazione

Padiglione 10 - Area Forum

Organizzato da INGENIO

Programma

Calcestruzzo armato: approfondiamo l'argomento

Ing. Andrea Dari

Il problema della corrosione

Prof. Ing. Luca Bertolini

La progettazione della duttilità delle armature in zona sismica

Prof. Ing. **Alberto Franchi**

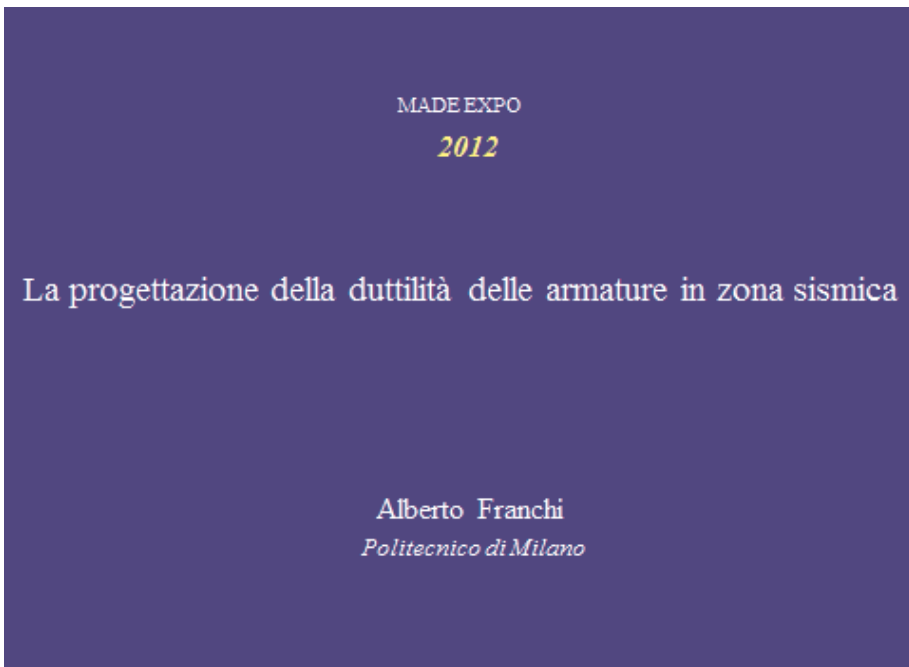


Tavola rotonda

Sono invitati: ANSFER – ASSOBTETON - ASSOTRAFILRETI  
ATECAP - CENTRO INOX - SISMIC

**MADEexpo Venerdì 19 ottobre 2012 - Ore 13,30**

**FORUMdella TECNICA delle COSTRUZIONI**

**“Edifici storici: Innovazione nella tradizione per il rinforzo dei sistemi costruttivi in muratura in zona sismica”**

**Padiglione 10–Sala Gamma – 2° Piano**

**Paola Ronca** (Politecnico di Milano-Scuola F.Ili Pesenti)

**Pietro Crespi** (Politecnico di Milano- DIS)

Modera: Mauro Nalin (Ordine degli Ingegneri di Genova)



**EDIFICI STORICI: INNOVAZIONE NELLA TRADIZIONE  
PER IL RINFORZO STRUTTURALE DEI SISTEMI COSTRUTTIVI  
IN MURATURA IN ZONA SISMICA**

*MILANO, 19 ottobre 2012*

**prof. arch. ing. Paola Ronca**  
*Docente ordinario di «Tecnica delle Costruzioni»  
e  
«Restauro e Riabilitazione Strutturale»  
Direttrice della Master School «F.Ili Pesenti»  
Facoltà di Ingegneria Civile-Politecnico di Milano*

**2.4 Nuove Attività di “atelier progettuale” con gruppi di allievi Master 2011-2012**

In questo ultimo paragrafo di illustrazione dei momenti e attività significative e più gratificanti di collaborazione docenti-allievi, ci piace riportare la seguente testimonianza scritta da una allieva brasiliana a conclusione della sua esperienza di Master :

“Gent. ma Dott.ssa Ronca,

voglio ringraziarla per avermi dato questa opportunità, perché senza la borsa di studio non mi sarebbe stato possibile seguire il Corso di Master a Milano.

Ne approfitto per sottolineare che lei è stata una eccellente didatta, sia nelle lezioni da lei tenute, sia per aver letto riga per riga la presentazione da me preparata per l'esame finale, migliorandola e permettendomi di imparare a scrivere un lavoro, il che mi sarà utile anche in futuro.

A conti fatti mi spiace di non essere potuta venire a Milano prima, per avvantaggiarmi al meglio della vostra didattica. E' vero che l'apprendimento a distanza è utile per chi lavora – come è il mio caso – ma il contatto diretto con gli esperti è una esperienza irrinunciabile.

La ringrazio ancora e resto a sua disposizione per ulteriori sviluppi della tematica che ho trattato nella mia tesi.

Cordiali saluti

--

**Silvana Leticia Testoni**

Arquiteta- Architetto

Setor de Arquitetura - Settore di architettura e ingegneria

AMAC – Associação dos Municípios do Acre - Brasile

Novo número:(68) 21063800 - Nuovo recapito

telefonico +0055(68)2163800

[www.amac-acre.org.br](http://www.amac-acre.org.br)

Di seguito alcuni esempi dei lavori svolti durante l'attività di “ATELIER” da gruppi di allievi Master.

### I° esempio

#### **Edifici Funzionali per l'EXPO 2015**

**Concorso per idee a procedura aperta** Ente banditore: EXPO 2015  
Milano

Gruppo di lavoro del Politecnico di Milano e Consorzio CIS-E

Coordinatore Prof. Ing. Edmondo Vitiello, collaboratori :Ing. Alessandro Zichi, Ing. Mario Maistrello

Gruppo di allievi della Scuola Master F.Ili Pesenti 2011-2012.

Nel master plan per l'area EXPO 2015, a Milano, sono previsti edifici dei servizi di due tipologie: a stecca ed isolati. La modularità e l'assemblaggio a secco dei moduli funzionali, consentono da un lato di realizzare l'intervento in un tempo di tre mesi, e di poter essere smontati al termine della manifestazione e poter essere riutilizzati in altri contesti. Tutte le scelte, a questo punto, sono state focalizzate pensando al suo ciclo di vita esteso, sia per quanto riguarda i costi, sia per quanto riguarda gli aspetti strutturali e l'impatto ambientale delle soluzioni costruttive. Per quanto riguarda l'aspetto energetico, si è pensato di realizzare degli spazi funzionali e spazi esterni, cercando di mitigare il microclima locale, con la riduzione il più possibile degli impianti per il raffrescamento, sia con l'utilizzo di soluzioni che riducessero l'effetto isola di calore. Studiati in tale contesto, sia le parti prettamente costruttive, che gli aspetti funzionali tecnologici. L'intervento è stato verificato con la certificazione LEED, e per l'edificio funzionale si ottiene una certificazione minima Gold.



Il lavoro progettuale svolto è stato illustrato a tutti gli allievi della Scuola, con un workshop didattico.

Lo scopo del workshop e' quello di illustrare ad allievi e docenti, tutti gli aspetti sviluppati, dall'organizzazione a gruppi sincroni, alla tempistica, alla consegna degli elaborati, per il lavoro elaborato e consegnato, aderendo al call di EXPO2015 per concorso di idee.

## Scuola Master F.Ili Pesenti

Workshop didattico

*“On like-for-likebasis: didattica e innovazione ai Master  
F.Ili Pesenti-DIS  
Le Architetture di Servizio del Sito di EXPO-Milano-2015”*

Organizzato da : proff. E. Vitiello , P. Ronca

7 marzo 2012 -- ore 14,30

Presso

Sala Biblioteca “A. Dei Poli” della Scuola F.Ili Pesenti-DIS

Il progetto e' stato redatto necessariamente da gruppi di progettazione talvolta separati con compiti specializzati.

Il workshop e' quindi articolato nella sequenza dei temi :

- a. Significato di questa esperienza all'interno dei Corsi di Master*
- b. Concetti generali e tecnologici del progetto*
- c. Architettura del progetto*
- d. Concetti di architettura sostenibile introdotti nel progetto*

**Il secondo esempio di seguito riportato si inserisce nelle iniziative promosse per le celebrazioni del**

150° anno di fondazione del Politecnico di Milano

### 2° esempio

#### **Una proposta sostenibile per il parcheggio del Campus Leonardo e l'Urban –Center**

Gruppo di lavoro del Politecnico di Milano e Consorzio CIS-E

Coordinatore Prof. Ing. Edmondo Vitiello,

Gruppo di progettazione

Prof. Arch. Luisa Ferro; Prof. Arch. Sara Protasoni; Ing. Alessandro Zichi; Ing. Mario Maistrello; Ing. Mario Fagioli; Arch. Viola Bertini; Arch. Elena Ciapparelli; Arch. Luisa Montanari

Collaboratori Studenti Scuola Master F.Ili Pesenti:

Ing. Carlo Mulas; Ing. Nicola Baglivi; Arch. Luana Gugliotta;

Il campus Leonardo da Vinci, Politecnico di Milano, diventa il Landmark per l'ateneo a Milano. Un tale edificio, necessita di una nuova immagine, da un lato e di una nuova apertura verso la città.

Il parcheggio, e il nuovo infopoint-urban center, diventano elementi strategici, consentendo di creare nuovi servizi all'ateneo e di rimuovere dalla superfici la circolazione e il parcheggio delle autovetture.

La piazza viene ridisegnata, riprendendo la antica connotazione di luogo del relax e incontro della popolazione e degli studenti.

Vi trova posto anche la galleria fotovoltaica sulla piazza, nuovo luogo di studio all'aperto, e di esposizione delle attività sviluppate all'interno dell'ateneo.

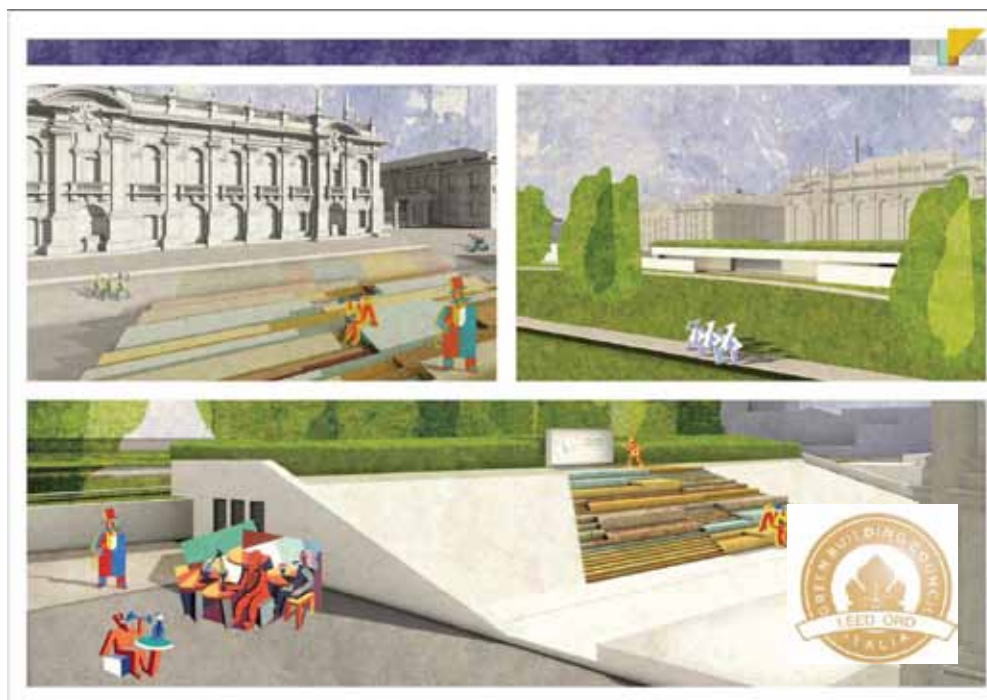
L'intervento viene seguito anche per quanto riguarda l'impatto ambientale sia degli edifici nuovi, che gli esistenti.

Il tema è stato affrontato secondo tre macrotemi:

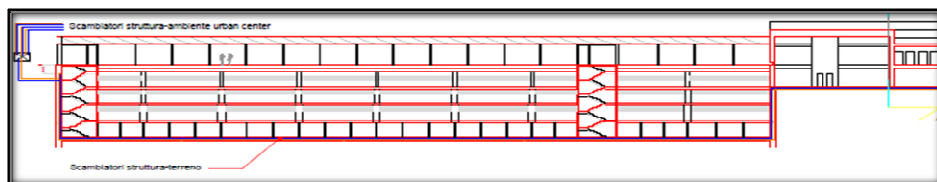
- Il landmark, Il LEED Gold per l'Urban Center e l'infopoint per il 150° anniversario del Politecnico di Milano, comprensivo di spazio espositivo (destinabile anche in auditorium) e servizi al verde e alla piazza (bar, mediateca), che sarà gestito dal Politecnico, tramite uffici previsti con funzione anche di Infopoint.

- Una piazza pubblica, attrezzata non solo per la viabilità ma anche per la permanenza, il relax, e occasionalmente gli eventi all'aperto in una zona con tribune-palco. Questo spazio urbano si estende lungo tutto il fronte del Politecnico e lo collega al verde della restante parte di piazza Leonardo, la pensilina fotovoltaica, da un lato costituisce una galleria sulla piazza dove svolgere attività di esposizione aperte alla città, dall'altro, luogo di permanenza per gli studenti.

- Parcheggi interrati e strutture attive come "accumulatori di energia"; su più piani, il parcheggio, da un lato contribuisce a liberare la Piazza Leonardo dalle macchine che ora occupano la piazza, dall'altra le sue strutture, costituiscono degli "accumulatori di energia" geotermica. Il parcheggio, dispone di aree di parcheggio coperte e presidabili per la ricarica di auto elettriche (con energia proveniente dai pannelli solari della copertura della nuova piazza), aree dedicate per parcheggio coperto di moto, bici, e per racks del bike sharing. Aree di parcheggio interrato ampiamente finestrate, e quindi adatte anche alle auto a gas (metano e GPL).



L'urbanpoint viene sviluppato con l'implementazione della certificazione LEED, che consente di confrontare l'impatto ambientale e di inserire i molteplici aspetti legati alla sostenibilità nell'edificio



### Lo scambiatore nell'Urban Center-infopoint

L'Urban center, diventa un campo di sperimentazione di un sistema "Attivo" in cui le strutture, diventano un serbatoio di energia. Da un lato sono stati studiati dei pacchetti performanti, e a basso impatto ambientale, dall'altro, l'edificio, viene dotato di un sistema tipo geotermico, che riduce il carico termico annuale.

Il principio è elementare:

L'aumento dell'inerzia termica delle parti strutturali di un edificio portano ad ampliare lo sfasamento termico, durante i cicli diurni e stagionali; D'altra parte, è risaputo che, il terreno, vedasi nel caso della geotermia, è un serbatoio di "energia".

Come si possono integrare questi aspetti:

I manufatti in cemento armato, che costituiscono il parcheggio, le fondazioni, le strutture interrato, le strutture in elevazione e gli impalcati dell'Urban Center-Infopoint, realizzati per ragioni strutturali, sia in opera che prefabbricati, possono diventare, con costi aggiuntivi trascurabili, elementi di scambio termico; le tubazioni che trasportano un fluido vengono fissate alle armature convenzionali così da costituire il circuito primario di un sistema che utilizza l'energia geotermica come sorgente calda o fredda di un ciclo termodinamico inverso che può funzionare come pompa di calore o come frigorifero. Il circuito così realizzato, anche se non collegato ad una macchina frigorifera, costituisce un sistema "free-cooling" e conferisce maggior inerzia all'edificio così da ridurre i consumi energetici annuali.

Seguono gli schemi descrittivi

La proposta progettuale, è stata affrontata in maniera integrata, onde poter affrontare tutti gli aspetti legati dalla sostenibilità.

Non si parla più solo di energia, ma di impatto a livello urbano da un lato, materiali da costruzione, gestione delle acque, dall'altra, insomma di qualità della vita.

Il progetto pensato, intende essere tassello di quello che deve essere la nuova immagine del Politecnico di Milano a 150 anni dalla sua fondazione: una immagine di vitalità e intraprendenza, ma soprattutto un progetto sostenibile confrontabile con le migliori realtà dei campus internazionale

Qui di seguito alcuni momenti di presentazione del progetto al Rettore, nell'ambito della più ampia iniziativa del "Campus Sostenibile"



*Il rettore, il prorettore e il direttore amministrativo, incuriositi dal Progetto*



E' degna di menzione , a conclusione di questo paragrafo, la lettera ricevuta dalla nostra allieva, proveniente da Tirana,

Antonella Salijai

In cui viene selezionata per partecipare all'International Workshop - BANDO EXPO

**From:** Comunicazione <Comunicazione@polimi.it>

**To:** Comunicazione <Comunicazione@polimi.it>

**Sent:** Friday, September 7, 2012 4:16 PM

**Subject:** Bando Expo - richiesta conferma partecipazione

Dear student,

You have been selected to participate in the "Cluster International Workshop".

We kindly ask you to confirm your participation by e-mail to [comunicazione@polimi.it](mailto:comunicazione@polimi.it) within Monday 10 September 2012, as required by the call.

Greetings , Simona Olgiati

### *2.5 Attivazione dei Corsi di Master 2012-2013*

Come espresso nell'introduzione al presente rapporto, la Scuola Master F.lli Pesenti ha voluto, con l'attivazione dei Corsi 2012-2013, perfezionare la propria offerta sia nei contenuti sia nella forma, rendendo sempre più fruibile la modalità *e-learning*, come brevemente illustrato dall'immagine sottostante.

Inoltre, seguendo quanto suggerito dalla richiesta degli anni precedenti, e come anche descritto nel paragrafo 2.4, l'attività pomeridiana negli "atelier" progettuali di gruppo , all'interno della Scuola, grazie alle opportunità, anche economiche, e sinergie offerte dal Consorzio CIS-E, con la guida costante di tutor particolarmente dediti agli allievi stranieri, è stata prevista anche per i Corsi di Master 2012-2013, appena iniziati.

Nei 5 Corsi di Master approvati dal Senato Accademico del Politecnico di Milano, mantenendo le ore di *didattica frontale* in aula, comunque con possibilità di partecipazione sincrona degli iscritti online, verranno offerte possibilità di sviluppo di temi progettuali reali.



Dall' A.A. 2012/2013:



Blackboard è la PRIMA piattaforma al mondo utilizzata nel settore dell'istruzione.

- Insegnamento Online (Blackboard LEARN)
- Insegnamento SINCRONO (Blackboard COLLABORATE)

Questo è il significato della grafica della locandina illustrativa 2012 2013, dove vengono riportati alcuni dei lavori elaborati e/o seguiti da gruppi di allievi Master.



Dipartimento di  
Ingegneria Strutturale



Italcementi  
Italcementi Group

## Master School F.III Pesenti Politecnico di Milano Anno accademico 2012-2013

### "Edifici ed Infrastrutture Sostenibili"

#### UK "Sustainable Buildings and Infrastructures"

L'accordo viene posto sui requisiti di sostenibilità che ogni progettista, alle varie scale, deve, e sempre più dovrà, garantire nelle varie fasi del progetto, fino all'opera compiuta.

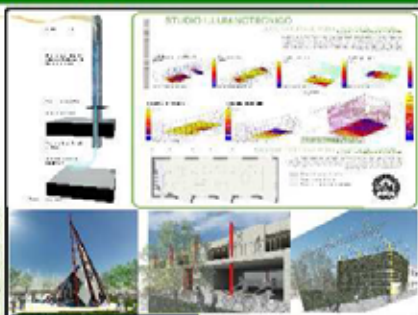
Ogni progetto e realizzazione, che si tratti di un singolo edificio o di interventi su scala urbana, deve rispettare primariamente sia la protezione dell'ambiente, sia lo sviluppo sostenibile del territorio. Il Master fornisce gli standard e gli strumenti progettuali, riconosciuti a livello internazionale dal Green Building Council, attraverso la procedura LEED.



Consorzio Housing Contest

Contestualizzando la progettazione a basso impatto ambientale nella realtà normativa nazionale, gli iscritti al Master delle Scuole F.III Pesenti possono

ottenere, senza oneri finanziari aggiuntivi, l'abilitazione professionale alla certificazione energetica



Giardino Expo 2015



### "Progettazione sismica delle strutture per costruzioni sostenibili"

#### UK "Design of Seismic Sustainable Structures"



Prove in sito ed in laboratorio

Il Master universitario in "Progettazione sismica delle strutture per costruzioni sostenibili" ha lo scopo di fornire conoscenze specialistiche per la progettazione e l'adeguamento sismico di edifici, ponti e strutture speciali. In calcestruzzo armato e in strutture miste, con riferimento agli Eurocodici ed alle più importanti normative internazionali, anche nell'ottica della sostenibilità.

L'attenzione è posta sulla progettazione critica e consapevole secondo le ultime normative internazionali e le raccomandazioni degli Enti preposti allo Sviluppo Sostenibile, alla sicurezza delle strutture e delle infrastrutture, riferendosi particolarmente al Dipartimento della Protezione Civile. Gli sbocchi occupazionali previsti sono presso studi professionali di ingegneria ed architettura, uffici tecnici di Enti pubblici e imprese di costruzioni, Laboratori di Ricerca e Laboratori per la sperimentazione su strutture e materiali ed Uffici della Protezione Civile.

### Consorzio CIS-E

#### Attività di formazione post-laurea

Il Consorzio mette a disposizione le sue strutture di direzione e tecnico-amministrative per la promozione, gestione e sviluppo della Scuola Master F.III Pesenti del Politecnico di Milano.



#### Attività di consulenza

Il Consorzio CIS-E mette a disposizione, attraverso una attenta e responsabile selezione, le competenze tecnico-scientifiche e professionali dei docenti, nonché le infrastrutture di Laboratorio delle Università e degli Enti di Prova consorziali per fornire soluzioni di qualità ai problemi evidenziati dal Settore delle Costruzioni nel suo complesso.

Molte innovazioni nei contenuti didattici delle lezioni sono state apportate ai due Master ad **indirizzo gestionale** :

### Project Management delle Opere Strutturali e Infrastrutturali

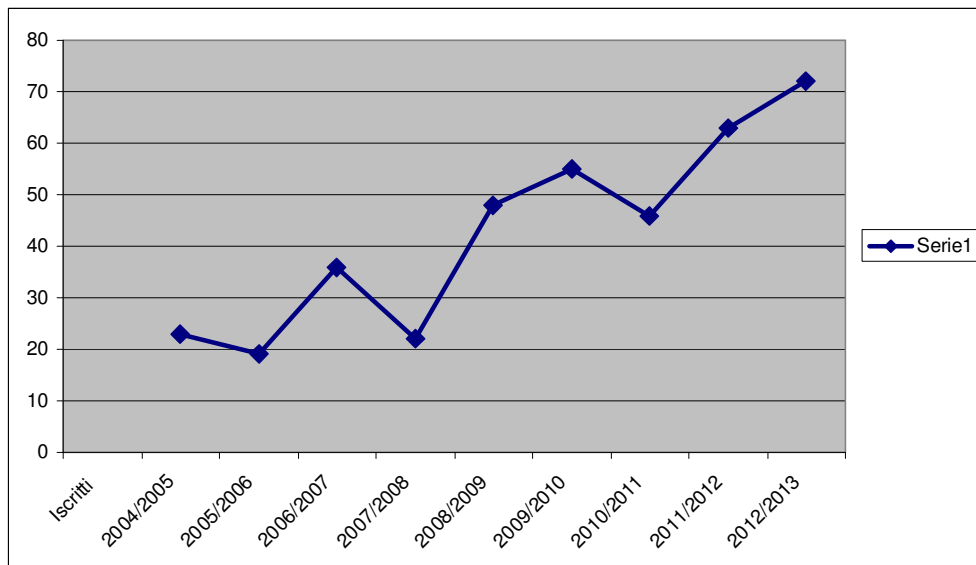
#### Design and Management of Structural Technologies in Construction Works

Dove si sono concordate nei contenuti e formalizzate specifiche Unità Didattiche che verranno tenute da nuove figure di docenti , provenienti da enti diversi, quali la Università Bocconi, la Società Horocapital, la Società Salini-Grandi Progetti, La Società di Sviluppo Immobiliare HINES-Italia e il gruppo IDeAFimit.

Per il Master in “Design and Management”, le cui lezioni sono tenute prevalentemente in inglese, si è organizzata una nuova attività di tutoraggio continuo (tutti i pomeriggi del primo semestre), con la doppia finalità di fornire spiegazioni aggiuntive per i contenuti svolti a lezione e contemporaneamente introdurre gli allievi stranieri a familiarizzarsi con la lingua italiana, per poter poi essere introdotti nell’esperienza dello stage.

Come di consueto, l’andamento delle iscrizioni nei Corsi di Master CFU della Scuola Pesenti :

*(AA 2010-2011 i locali della Scuola non erano disponibili)*



L'assoluta novità, singolarità e attualità dei contenuti didattici organizzati e offerti in tali Master, di cui riportiamo di seguito il dettaglio di alcuni argomenti, è stata immediatamente colta e ha prodotto un incremento notevole di iscrizioni per il Corso di Master in “ *Project Management delle Opere Strutturali e infrastrutturali*” (+ 60%, rispetto all'edizione precedente)

Di seguito la descrizione particolareggiata delle Unità Didattiche in cui si articola il Master;

i contenuti nuovi che verranno introdotti riguardano principalmente le seguenti Unità :

Unità 16 - AN INTRODUCTION TO VALUE INVESTING

Unità 18 - ASSESSING AND MANAGING RISK IN REAL ESTATE INVESTING

Unità 19 - PA - NORME E PROCEDURE

Unità 20 - GESTIONE DELLE GARE A LIVELLO NAZIONALE E INTERNAZIONALE

Unità 21 - AN INTRODUCTION TO MACROECONOMIC TRENDS



## Project management delle opere strutturali ed infrastrutturali

<b>Unità 1</b>		Materiali da costruzione			
Argomenti trattati		In questa unità vengono illustrati i materiali e le relative applicazioni più comunemente utilizzate nel mondo delle costruzioni. Gli approfondimenti riguardano la natura dei materiali, le loro caratteristiche meccaniche, fisiche e chimiche, la lavorazione industriale, l'applicazione e la durabilità. Particolare attenzione verrà data all'analisi dell'impatto ambientale nel suo ciclo di vita (Life Cycle Assessment).			
<b>ore</b>	24	<b>Periodo</b>	novembre 2012	<b>Referente</b>	Prof. A. Franchi

<b>Unità 2</b>		Fondamenti d'ingegneria gestionale			
Argomenti trattati		L'unità ha come scopo quello di avvicinare lo studente ai fondamenti dell'ingegneria gestionale. In particolare i focus saranno sulla contabilità esterna - bilancio con documenti correlati, operazioni elementari di contabilità, lettura del bilancio e degli indici -, su quella interna - controllo di gestione e principali tecniche, equilibrio di breve e l'analisi di break even -, sulla valutazione degli investimenti - metodi di valutazione DCF e non DCF, flussi di cassa - sulla pianificazione della supply chain - logistica in uscita, produzione, valutazione dei fornitori e ciclo di pianificazione e controllo - e infine sulla gestione dei progetti - organizzazione per progetti, tecniche di controllo reticolari, pianificazione e ri-pianificazione. L'unità prende in esame la gestione di un progetto di immobiliare dal punto di vista del committente privato partendo dalla definizione del team di progetto con la individuazione e selezione dei singoli partecipanti e la predisposizione dei progetti preliminari, definitivi ed esecutivi, l'impostazione della gara d'appalto con la definizione dei documenti di gara, la selezione dei partecipanti, l'assegnazione dei lavori e successiva gestione dell'appalto fino al completamento dei lavori.			
<b>ore</b>	104	<b>Periodo</b>	novembre 2012 - febbraio 2013	<b>Referente</b>	Prof. Cigolini

<b>Unità 3</b>		Energia ed impianti			
Argomenti trattati		Partendo da una panoramica generale riguardante le politiche energetiche in atto e future, si approfondiranno i temi di risparmio energetico nelle costruzioni dell'involucro, passando in rassegna i principali sistemi di generazione e concludendo con l'utilizzo di software di modellazione e di analisi energetica finalizzati all'ottimizzazione del sistema Edificio Impianto. In aggiunta si affronteranno in questa unità temi importanti quali la progettazione e i case history sulle costruzioni a basso consumo, la bioclimatica, l'involucro e la sua performance, la progettazione delle schermature, del verde ed infine la scelta consapevole dei materiali da costruzione.			
<b>ore</b>	28	<b>Periodo</b>	novembre 2012	<b>Referente</b>	Prof. G. Chiesa

<b><u>Unità 7</u></b>	Il conceptual design				
Argomenti trattati	Il Conceptual Design rappresenta una delle primissime fasi del processo progettuale, in cui si analizzano tutte quelle variabili che andranno ad incidere su fattori quali costi, prestazioni, affidabilità, sicurezza. Questo pone il team di progettazione a prendere quelle decisioni strategiche che andranno ad incidere sul futuro della progettazione e sulla costruzione del manufatto. Per questo motivo si ritiene opportuno dedicare un'intera unità a questa fase progettuale, ad oggi sottovalutata, ma che può determinare la sostenibilità economica dell'intero progetto.				
<b><u>ore</u></b>	15	<b><u>Periodo</u></b>	novembre 2012 - gennaio 2013	<b><u>Referente</u></b>	Arch. V Grassi

<b><u>Unità 10</u></b>	Protocollo LEED				
Argomenti trattati	L'unità ha come scopo quello di avvicinare lo studente al mondo dell'edilizia sostenibile, con particolare attenzione ai requisiti, all'evoluzione e alla gestione dello standard LEED Italia Nuove Costruzioni e Ristrutturazioni. Si analizzeranno nel dettaglio sia la fase di Design che di Construction del protocollo LEED entrando nel merito di progetti concreti al fine di focalizzare l'attenzione sull'applicazione dei crediti legati alla certificazione.				
<b><u>ore</u></b>	17	<b><u>Periodo</u></b>	novembre 2012	<b><u>Referente</u></b>	Ing. A. Zichi

<b><u>Unità 12</u></b>	La progettazione del cantiere e della sicurezza				
Argomenti trattati	L'unità ha come scopo quello di orientare lo studente sullo studio di progetti al fine di analizzare le problematiche esecutive e gestionali sin dalla fase di design trattando le problematiche riguardanti la progettazione e la cantierizzazione dello stesso, rispettando i requisiti di qualità e sicurezza. Gli aspetti che verranno analizzati saranno incentrati in primis, sul quadro legislativo in essere approfondendo gli aspetti giuridico normativi come base per la progettazione e programmazione.				
<b><u>ore</u></b>	21	<b><u>Periodo</u></b>	gennaio 2013	<b><u>Referente</u></b>	Prof. M. Trani

<b><u>Unità 13</u></b>	La gestione del cantiere, della costruzione e del costruito				
Argomenti trattati	L'obiettivo dell'unità è di calare le nozioni fondamentali del project management, sia di natura tecnica che economica, sulle attività necessarie per gestire un cantiere, le varie fasi della costruzione, e il ciclo di vita o di servizio del costruito. Il software 4D BIM-Based Modeling, operativo nella fase di progettazione canonica, nella fase di progettazione costruttiva, nella fase di costruzione, e nella fase di manutenzione, verrà ampiamente illustrato.				
<b><u>ore</u></b>	20	<b><u>Periodo</u></b>	gennaio 2013 - febbraio 2013	<b><u>Referente</u></b>	Prof. A. Ciribini

<b><u>Unità 16</u></b>		An Introduction to Value Investing			
Argomenti trattati		Familiarizzare gli allievi del master in "Project management delle opere strutturali e infrastrutturali" con le idee del Value Investing. Prima di valutare e, quindi, di gestire investimenti immobiliari e/o in infrastrutture (e questo vale anche per investimenti di ogni altro genere), occorre sapere che cosa cercare e dove cercare. Le idee del Value Investing costituiscono chiare e semplici, ma anche affidabili, linee guida per farlo. Una società di sviluppo immobiliare, prima di valutare quantitativamente un investimento, farebbe bene a valutarlo qualitativamente, secondo le idee del Value Investing. Altrettanto potrebbe essere suggerito ad un'Impresa, che stesse valutando un intervento in project financing.			
<b><u>ore</u></b>	18	<b><u>Periodo</u></b>	gennaio 2013 - febbraio 2013	<b><u>Referente</u></b>	ing. G. Franchi

<b><u>Unità 17</u></b>		Progettazione urbana			
Argomenti trattati		Il corso mira a fornire una panoramica sulle problematiche che caratterizzano il progetto urbano. Lo scopo è quello di enfatizzare l'attenzione ad una cultura del "progetto urbano" tesa alla individuazione e al perseguimento di obiettivi di conservazione, riordino e sviluppo, capace di assicurare al territorio e ai suoi abitanti, la dotazione di servizi e attrezzature necessaria al raggiungimento di un soddisfacente livello di qualità di vita.			
<b><u>ore</u></b>	27	<b><u>Periodo</u></b>	gennaio 2013 - febbraio 2013	<b><u>Referente</u></b>	prof. A. Del Bo

<b><u>Unità 18</u></b>		Assessing and Managing Risk in Real Estate Investing			
Argomenti trattati		Il ritorno che può fornire un investimento immobiliare è sufficiente da giustificare il rischio? Prima di tutto occorre definire che cosa davvero sia il rischio, quali siano gli strumenti per quantizzarlo e che informazioni essi effettivamente conferiscano. Dopodiché, è possibile studiare modi per controllarlo e minimizzarlo. L'obiettivo del corso in oggetto è di definire, quantizzare, e controllare il rischio legato ad ogni investimento immobiliare.			
<b><u>ore</u></b>	10	<b><u>Periodo</u></b>	febbraio 2013	<b><u>Referente</u></b>	Prof. F. Reggiani



<b>Unità 19</b>	P.A. Norme e procedure				
Argomenti trattati	L'unità ha l'obiettivo di far conoscere allo studente quali sono gli iter burocratici, le tempistiche, le procedure da seguire e gli oneri, progettuali e finanziari, richiesti dalla Pubblica Amministrazione per la realizzazione di interventi immobiliari di diversa complessità. Nello specifico verrà definito come scegliere i titoli abilitativi (Permessi di Costruire, D.I.A., S.C.I.A., C.I.L.A., etc.) e realizzare interventi edili secondo la normativa; come avviare e gestire le pratiche edilizie, i nulla osta, i pareri dei diversi Enti pubblici e le convenzioni tra pubblico e privato per la realizzazione di Piani Attuativi e Piani Integrati. I temi ed i casi pratici proposti saranno inquadrati nel corpus legislativo vigente a livello nazionale, aggiornato con i recenti provvedimenti normativi.				
<b>ore</b>	6	<b>Periodo</b>	febbraio 2013	<b>Referente</b>	Ing. E. Salvetti

<b>Unità 20</b>	Gestione delle gare a livello nazionale e internazionale				
Argomenti trattati	L'unità è divisa in due parti: la prima di natura tecnica, mentre la seconda di natura giuridica/legale. In particolare, nella prima parte saranno affrontati i seguenti argomenti: la partecipazione ad una gara, dalla fase di prequalifica all'offerta; l'esecuzione del progetto, dalla firma del contratto alla redazione del certificato finale; casi pratici. Nella seconda parte, invece, saranno affrontati i seguenti argomenti: le nozioni di base, dalla contrattualistica internazionale ai finanziatori dei progetti; i contratti FIDIC, i subappalti e i contratti di fornitura, aspetti giuridici rilevanti alla gestione del progetto, la disciplina in materia di lotta alla frode e alla corruzione, casi pratici e simulazioni.				
<b>ore</b>	36	<b>Periodo</b>	febbraio 2013 - marzo 2013	<b>Referente</b>	Ing. A. Zaffaroni - Avv. M. Padovan

<b>Unità 21</b>	An Introduction to Macroeconomics Trends				
Argomenti trattati	Familiarizzare gli allievi del master in "Project management delle opere strutturali e infrastrutturali" con gli indicatori che tracciano i macro trends a livello economico. Un'economia sempre più globalizzata, richiede una maggiore comprensione di quelli che possono essere gli impatti a livello paese dei principali trends economici in atto. La capacità di valutare un possibile investimento immobiliare, anche sotto questa luce permette di pesare maggiormente determinati "rischi" e/o opportunità.				
<b>ore</b>	12	<b>Periodo</b>	febbraio 2013 - marzo 2013	<b>Referente</b>	Dott. R. Carraro

### [VI edizione del Master in " Progettazione Sismica delle Strutture per Costruzioni Sostenibili"](#)

Nella seduta di nov 2012 del Senato Accademico è stata approvata l'attivazione della VI edizione del Master.

Come accennato per gli altri Master, anche quest'ultimo , e ancor più , sarà caratterizzato da contenuti e modalità di svolgimento nuovi , rispetto alle edizioni precedenti.

.Grazie alla collaborazione del Prof. Federico Bucci, prorettore per il polo di Mantova del Politecnico, è in fase di attivazione una convenzione con la Camera di Commercio di Mantova per definire l'offerta del contributo

economico per possibili allievi Master della comunità locale che, con assistenza e tutoraggio di docenti del Politecnico, affrontino temi di diagnostica e sviluppo di proposte di adeguamento per edifici, ubicati nell'area di Mantova, che hanno sperimentato effetti del recente sisma. Di seguito la locandina del Master.



POLITECNICO  
DI MILANO



## Master Universitario di secondo livello in:

### PROGETTAZIONE **SISMICA** DELLE STRUTTURE PER COSTRUZIONI **SOSTENIBILI**

Direttore: prof. Ing. Alberto Franchi



Politecnico di Milano  
Scuola Master Fratelli Pesenti



Italcementi  
Italcementi Group

&



Blackboard

Dal 1927 l'eccellenza nella formazione post-lauream, sinonimo di leadership nelle conoscenze tecnico-ingegneristiche

Tra le piattaforme informatiche nel settore dell'istruzione online, più utilizzate al mondo

## LA FORMAZIONE POST-LAUREAM IN AULA O SUL VOSTRO PC

**DURATA:** Marzo 2013 - Febbraio 2014

**TERMINE ISCRIZIONI:** 21 Gennaio 2013

**LINGUA:** Italiano

**CREDITI:** 60 Crediti Formativi Universitari (CFU)

**COSTO:** MODALITÀ FRONTALE: 6.000 €  
MODALITÀ ONLINE: 3.500 €

**CONTATTI:** per informazioni ed invio domande d'ammissione:  
MODALITÀ FRONTALE:  
prof. Ing. Alberto Franchi (tel. +39 02 2399 4245, [alberto.franchi@polimi.it](mailto:alberto.franchi@polimi.it))  
dott.ssa Sara Giussani (tel. +39 02 2399 4305, [scuolamaster@stru.polimi.it](mailto:scuolamaster@stru.polimi.it))  
MODALITÀ ONLINE:  
dott. Ing. Mario Tropea (tel. +39 02 2399 4341, [tropea@stru.polimi.it](mailto:tropea@stru.polimi.it))

**BANDO:** [http://www.polimi.it/Index.php?id=3367&cod\\_master=775](http://www.polimi.it/Index.php?id=3367&cod_master=775)

## PROGETTAZIONE SISMICA DELLE STRUTTURE PER COSTRUZIONI SOSTENIBILI

### OBBIETTIVO

#### FORMATIVO:

- Formazione di professionisti specializzati nella progettazione e nell'adeguamento sismico di edifici, ponti e strutture speciali in calcestruzzo armato e miste con riferimento alle più importanti normative nazionali e internazionali, anche nell'ottica di progettare costruzioni sostenibili per l'intero ciclo di vita delle stesse.

La nuova edizione 2013-2014 si arricchisce di un'Unità sulle "Costruzioni Storiche", che si svolgerà presso il Polo di Mantova del Politecnico di Milano. Tale istituzione mette a disposizione una serie di borse di studio, le Infrastrutture di supporto alla didattica, i corsi studio su cui approfondire le conoscenze nonché un supporto all'accoglienza degli allievi.

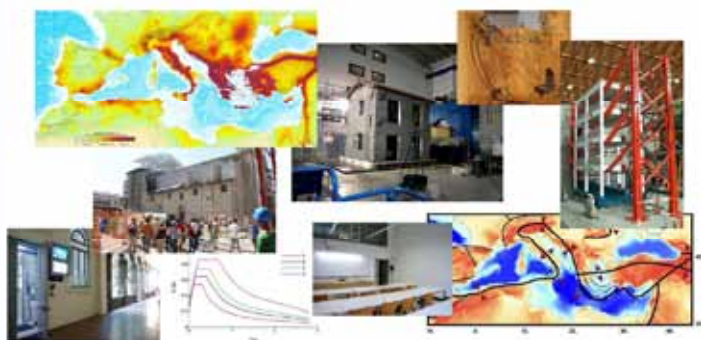
### UNITÀ

#### DIDATTICHE:

- Sismologia applicata all'ingegneria - Strutture prefabbricate - Costruzioni esistenti recenti  
- Fondazioni e opere di sostegno - Isolamento sismico - Costruzioni esistenti storiche  
- Progettazione antisismica degli edifici - Esercitazione finale e/o stage  
- Analisi strutturale

### REQUISITI:

- Laurea V.O., Laurea Specialistica o Magistrale N.O. in Ingegneria, Architettura, discipline affini, o titoli equivalenti riconosciuti dal Sistema Universitario Italiano (obbligatorio)  
- Invio domanda di ammissione completa entro il 21.01.2013 (obbligatorio)  
- Invio lettera motivazionale (preferenziale)



## Perché un Master ONLINE della Scuola Master F.III Pesenti



- > Possibilità di frequentare un Master di II livello del Politecnico di Milano da qualsiasi luogo e senza interrompere la propria attività lavorativa
- > Possibilità di conoscenza e interrelazione con docenti universitari ed esperti del settore pubblico e privato
- > Possibilità di seguire le lezioni e le esercitazioni in modalità SINCRONA (partecipazione attiva alle lezioni e interazione con studenti e docenti in remoto) o ASINCRONA (ascolto e visione delle Sessioni di lezioni registrate)
- > Possibilità di sfruttare la prestigiosa offerta didattica della Scuola Master F.III Pesenti completamente ONLINE, supportati da una piattaforma all'avanguardia e da un tutor sempre a disposizione di ciascuno studente
- > Garanzia di serietà e qualità a costi contenuti

## 2.6 Convenzioni di collaborazione tra la Scuola F.III Pesenti e enti pubblici e privati

L'attività di stage e sviluppo tesi di Master è sempre più incentrata nella ricerca di temi reali di progettazione, nelle diversificate fasi, su cui responsabilizzare gli allievi, inseriti durante la seconda fase del Master

in veri ambienti lavorativi, anche dal punto di vista delle tempistiche nelle risposte corrette e precise da fornire al committente.

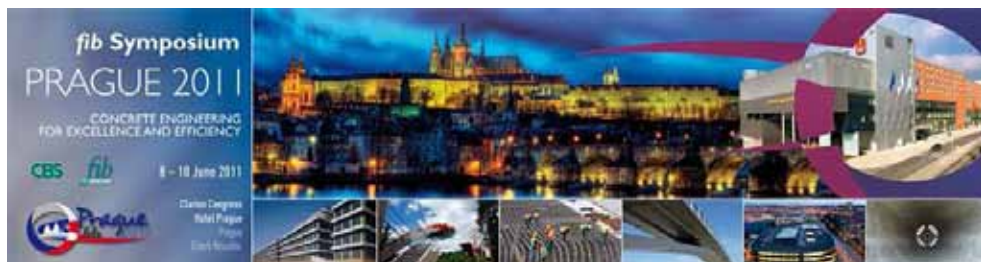
Con questo intento si sono ricercate e predisposte le Convenzioni di Collaborazione con alcuni enti sotto elencati, che vedono nella Scuola Master F.lli Pesenti possibilità di proficue e continue collaborazioni :

- Ordine degli Ingegneri della Provincia di Milano
- Fondazione Brambilla
- Comune di Trezzo sull'Adda
- Camera di Commercio di Mantova

### 3 Iniziative in corso – sinergie tra ricerca e didattica dei Master

#### 3.1 *I temi di ricerca caratterizzanti le attività della Scuola, con particolare riferimento a quelli del restauro e adeguamento in aree sismiche dell'Edilizia Storica e del Moderno*

I principali temi di ricerca diretti da alcuni docenti della Scuola con il coinvolgimento di allievi ed ex allievi della Scuola, possono essere sinteticamente espressi dai titoli di alcuni degli articoli scientifici presentati e inviati per la pubblicazione a convegni internazionali :



#### **EXPERIMENTAL TESTS OF A NEW DURABLE AND SUSTAINABLE PHOTO-CATALYTIC PLASTER FOR THE FACADES OF “TORRE VELASCA” Building IN MILANO**

**Authors:** Paola Ronca, Pietro Crespi, Alberto Franchi, Giovanni Franchi

Torre Velasca building (briefly Torre Velasca) is one of the outstanding reinforced concrete tall building Italian architecture, testimony of the so called “Modern Heritage”, see among others (Fiori and Prizzon, 1982). Not only the bearing structure, but even the finishing architectural elements of the facades are made in reinforced concrete.

An extensive experimental monitoring program has been undertaken for the assessment of the actual mechanical and electro-chemical conditions of the facade structural and non structural elements, supporting design proposals and renovation construction procedures.

The paper recalls, at first, some aspects of the monitoring phase, already extensively illustrated and commented in different previous papers (Ronca, Franchi and Migliacci, 2009; Ronca et al., 2009).

Then, the focus of present paper is on the presentation of some experimental results on the mechanical and physical properties of a new cementitious plaster to be adopted for the renovation works.

Major features to be evaluated are durability and photocatalytic performance in time of the new plaster.

**Authors:** Alberto Franchi, Pietro Crespi , Flavio Pizzamiglio, Paola Ronca, Giuseppe Silvestro

**Title:** “An in situ diagonal compression test for brick walls”

**Abstract:** The paper illustrates some tests on brick walls of an historic building in L’Aquila (Palazzo Paone), damaged by the recent earthquake and consolidated-reconstructed-renovated during 2012. The brick walls of the building, like most of the buildings down town L’Aquila, are made of bricks connected with a very poor lime mortar. Moreover, the central part of the walls are made of even poor materials. As a conclusion the walls can be considered as made of two external layers (15-20 cm) with the intermediate layer made of bricks very poorly connected. Almost any consolidation process which aims to increase the mechanical properties include the injection of mortar inside the thickness of the wall. Present work aims to evaluate the actual benefits of the injections by comparing two tests, one before and one after injection. The emphasis is on the experimental technique which allows an in situ experimental control of the shear resistance of the wall after the pick, during the unstable softening branch. This technique aims to control better the ductility factor of the walls, and therefore answering to a crucial question of the designer.

**Authors:** Pietro Crespi, Aly Moussad, Alberto Franchi, Nicola Longarini

**Title:** “An experimental investigation of the wind forces on trees ”

**Abstract:** The paper illustrates the experimental techniques and the experimental results obtained at the Wall of Wind (WoW) of Florida International University (FIU). The motivation of the scientific work comes from unresolved questions that the designer of high rise buildings in Milano had to deal with in the design of the flower box containing trees up to 6-7 m high. The question was: can the tree fall down the terrace by turning inside the box or by breaking the trunk of the tree? How can we evaluate the forces due to wind? Thanks to the Real Estate Investment promoter, HINES Italia, an experimental program has been organized and implemented at a wind tunnel facility (WoW at FIU) which could allow for testing trees.

**Authors:** Ronca Paola, Crespi Pietro, Alberto Franchi, Nicola Longarini

**Title:** “Investigation on the cause of damages in a historical masonry industrial plant”

**Abstract:** The paper illustrates a set of experimental-numerical

investigations with the aim of explaining the cause of progressive crack opening in a industrial plant which was built at the beginning of 1900. The plant was built at the end of a drainage canal at Sermide, Province of Mantova -Italy. The two buildings, which constitute the plant, have both, architectural and engineering important value at the same time. Damages have been reported since the opening of the plant: cracks have developed in several places, closed and reopened during more then 100 year of life. Recent earthquake in Italy has damaged severely structures in that area, but only minor damages have been reported on the two chimneys which remember the time when energy was produced by burning coal. A seismic assessment of the chimneys is presented as well.

**Authors:** Pietro Crespi, Alberto Franchi, Giuseppe Silvestro

**Title:** “ [Seismic vulnerability of a dry dock in Messina, Italy](#)”

**Abstract:** The paper presents the results of numerical investigations, based on a set of experimental tests, for the analysis of seismic vulnerability of a dry dock plant in Messina, property of the Italian Navy. The dry dock is one the oldest plant in Europe, built around the mid of 1800 and it experienced the devastating earthquake of 1908. The aims of the investigations:

1. Explain the presence of cracking, on the concrete slab which represent the bottom of the basin, which opens and closes during the operations of emptying-filling the basin.
2. Asses the seismic vulnerability of the plant.

L'importanza dei temi connessi alla [vulnerabilità sismica delle costruzioni](#), nuove ed esistenti, è sempre più la [Linea Guida che la Scuola F.lli Pesenti, in sinergia con altri gruppi di ricercatori del Politecnico e di altre Università](#), segue per fornire propri contributi innovativi nella ricerca delle migliori soluzioni, in termini di [sicurezza](#), [sostenibilità](#) e [durabilità](#) (senza nulla voler togliere alla triade vitruviana).

Molto significativi in questa ottica sono i primi risultati ottenuti attraverso la campagna di prove sperimentale [su muretti ricostruiti con muratura tipica \(“apparato aquilano”\) degli edifici del centro storico dell'Aquila e rinforzati con malta appositamente studiata presso il CTG di Italcementi, con proprietà meccaniche e di aderenza particolarmente compatibili con il tessuto murario originale](#).

Al Direttore del CTG-Italcementi Group e al suo personale tecnico sono rivolti i ringraziamenti per il supporto economico e tecnico. Non essendo ancora stati pubblicati i risultati, che, se confermati da ulteriori

test di laboratorio, potrebbero garantire capacità di rinforzo delle strutture murarie storiche, veramente nel rispetto sia della sicurezza strutturale sia della conservazione storica, vengono qui di seguito riportate solo alcune immagini delle diverse fasi in cui si è sviluppata la ricerca, e cioè:

- Studio morfologico caratterizzante le tipologie della muratura storica dell'Aquila
- Scelta e raccolta di materiale originario per la ricostruzione e stoccaggio di provini/walletes
- Studio della messa a punto della tecnica di rinforzo, a base di malta performante e compatibile
- Studio della modalità di esecuzione strumentale della “prova di resistenza a taglio”
- Messa a punto della strumentazione per la riapertura del laboratorio della Facoltà di Ingegneria dell'Aquila, per la realizzazione delle prove sperimentali sui muretti.
- Realizzazione dei getti per il “rinforzo” strutturale di alcuni dei muretti
- Studio delle modalità di carico dei muretti/provini e di lettura dei risultati
- Confronto e interpretazione dei risultati delle prove



*Nella foto alcuni dei provini ricostruiti riproducendo, in composizione morfologica e materica, la tipica muratura storica aquilana*





*La cassaforma e preparazione dei muretti da rinforzare con intonaco di malta strutturale messa a punto in collaborazione con i tecnici del CTG*



*Uno dei provini “rinforzati” in fase di maturazione*



*Prova su muretto rinforzato con sole "iniezioni" con malte additivate*



*Il provino con intonaco strutturale, strumentato per la prova di "taglio" nel laboratorio dell'Università dell'Aquila*

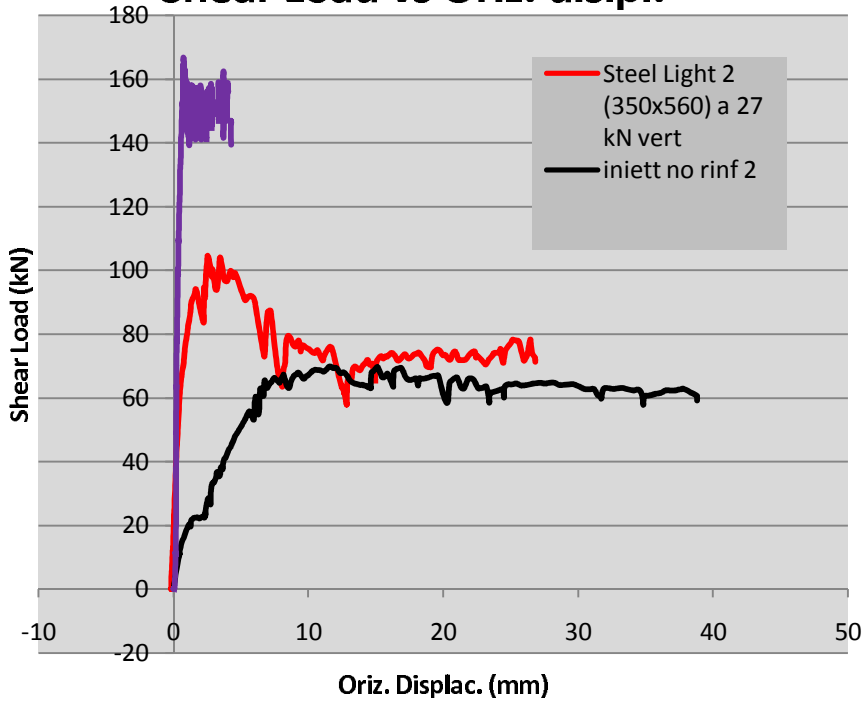


*Rottura del muretto per “taglio”*

I risultati della prima campagna di sperimentazione sono stati molto positivi, avendo evidenziato per i muretti rinforzati con la tecnica dell’intonaco strutturale con malta CTG (italcsteelfibres 1) sia capacità di resistenza e duttilità molto superiori non solo a quelle, ovviamente, dei muri solo iniettati/non rinforzati, ma anche a quelle di muretti rinforzati con tecniche diverse e già in uso commercialmente (grafico in rosso), come sinteticamente illustrato nel grafico sottostante, sia ottime caratteristiche di aderenza alla muratura originaria (proprietà fisica fondamentale per una tecnica rivolta al miglioramento strutturale dell’esistente), come illustrato nella fotografia successiva al grafico, dove “frantumi” del provino evidenziano ancora aderenza della due parti:

Tali risultati molto incoraggianti, sono già stati in parte raggruppati, commentati e preparati per la necessaria diffusione, anche se necessitano di ulteriori prove, sia nei riguardi di alcuni parametri fisico-meccanici dei materiali, sia per l’approntamento della strumentazione della prova stessa.

## Shear Load vs Oriz. displ.



Di seguito alcune slides presentate al Convegno presso il MADEexpo 2012

### Esempio di prova in laboratorio

#### Provino soggetto ad azione combinata di Carico assiale e taglio

*Consorzio CIS-E/Politecnico Mi  
Università di L'Aquila*  
Prof. Alberto Franchi  
Prof. Paola Ronca  
Prof. Dante Galeota  
Ing. Pietro Crespi  
Ing. Amedeo Gregori  
Ing. Giuseppe Silvestro



### Esempio di prova in laboratorio

#### Risultati

*Consorzio CIS-E-Politecnico di Milano e  
Università di L'Aquila*  
Prof. Alberto Franchi  
Prof. Paola Ronca  
Prof. Dante Galeota  
Ing. Pietro Crespi  
Ing. Amedeo Gregori  
Ing. Giuseppe Silvestro



Sempre rimanendo nell'ambito della sperimentazione di nuove malte e tecniche per il rinforzo delle murature storiche in zona sismica, l'attività del gruppo Scuola Master Pesenti/Univ Dell'Aquila/Consorzio CIS-E, incoraggianti risultati si sono ottenuti attraverso “*prova diagonale in situ*”, messa a punto e realizzata a “controllo di spostamento” ( una prova svolta in controllo di spostamento permette di cogliere anche il comportamento post-picco del carico, cioè la fase di softening fino al raggiungimento della resistenza residua) attualmente frontiera della ricerca per le strutture in muratura, su un muro di edificio storico dell'Aquila, per verificare in situ (non solo su provini di laboratorio) la reale efficacia e miglioramento sismico di muratura rinforzata con iniezione di malta additivata.

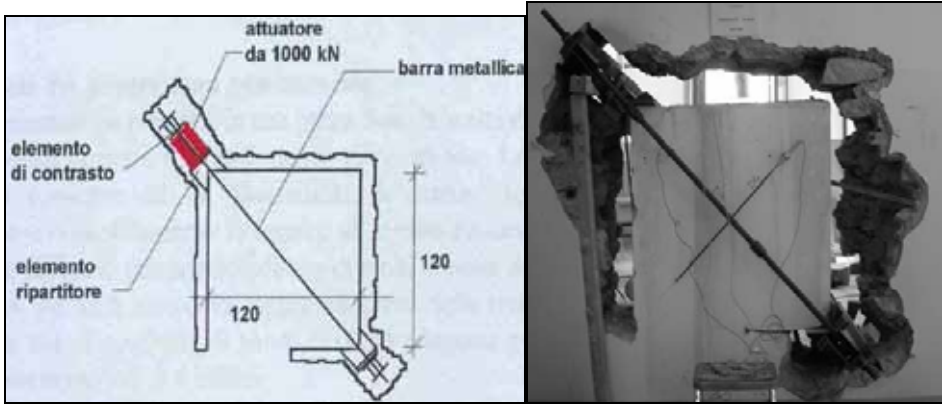
Di seguito il frontespizio del rapporto di tale attività ( il rapporto completo è disponibile presso il consorzio CIS-E) , e a seguito alcune foto , commenti esplicativi e risultati

Si ringrazia l'Impresa Paterlini (Socia del Consorzio CIS-E) per la fiducia e disponibilità logistica e di personale garantita durante tutte le fasi della prova.

<b>Relazione di prova in situ del 04 ottobre 2012</b>	
<b>Committenza:</b>	<i>Consorzio CIRA – Impresa Paterlini</i>
<b>Tipologia di prova:</b>	<i>Prova di compressione diagonale su n°2 pannelli in muratura</i>
<b>Localizzazione:</b>	<i>Palazzo Paone Tatozzi – Via Vittorio Emanuele, L'Aquila</i>
<b>Laboratorio incaricato:</b>	<i>Laboratorio Prove Materiali – Politecnico di Milano</i>
<b>Tecnici esecutori:</b>	<i>ing. M. Lamperti – sig. A. Cocco</i>
<b>Emissione report:</b>	<i>30 novembre 2012</i>

INTRODUZIONE	2
DESCRIZIONE DELLA PROVA	3
FASI DI ESECUZIONE DELLA PROVA	5
CAMPIONI DI PROVA	5
STRUMENTAZIONE E MODALITÀ DI ESECUZIONE	6
RISULTATI DI PROVA	8

Il Direttore del Consorzio CIS-E  
*prof. ing. Alberto Franchi*



*Schema teorico e immagine modello di una prova di compressione diagonale.*

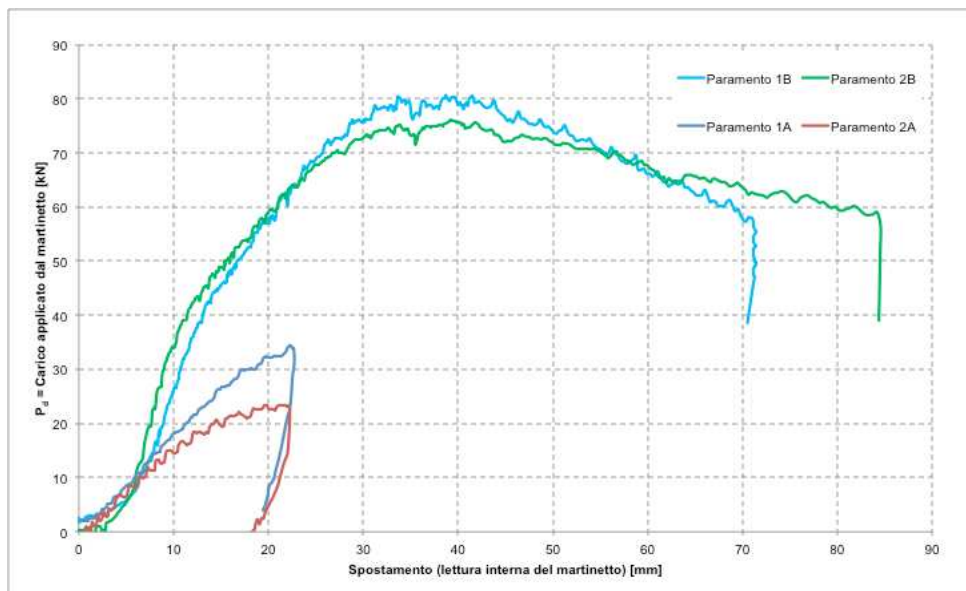


*Fase di allestimento della prova*

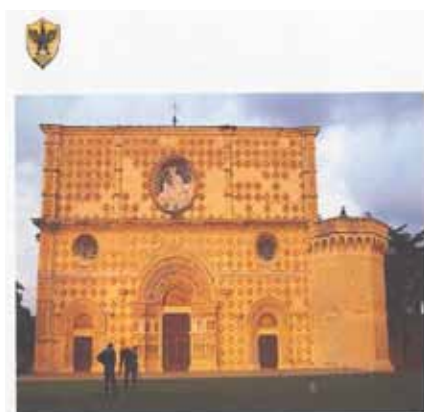


*Rottura del muro con particolare della fessurazione diagonale*

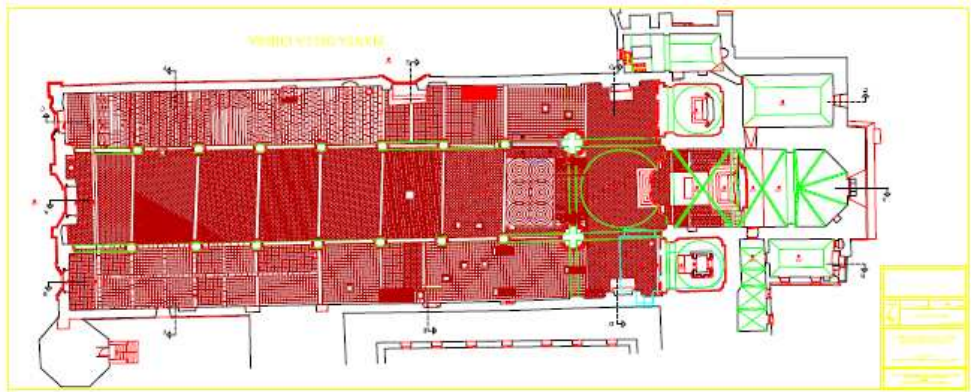
Il grafico successivo sintetizza i risultati delle due prove : Paramento A (sulle due facce del muro) non iniettato con malta, e Paramento B, iniettato con malta. Gli ottimi risultati, sia rispetto al parametro "capacità portante" e, soprattutto, rispetto al parametro "duttilità" si commentano da soli.



L'attività svolta, e sopra brevemente illustrata, dai docenti, ricercatori e ingegneri direttamente coinvolti con la Scuola Master e con il CIS-E e colleghi dell'Università dell'Aquila, presso anche alcuni cantieri aperti per la ricostruzione del centro storico della città, si sta ulteriormente rafforzando nel "[Progetto di Restauro e Ricostruzione della Basilica di S. Maria di Collemaggio](#)", di cui di seguito l'immagine della facciata, la parte crollata e il rilievo della pianta







*Pianta della Basilica di Collemaggio (in verde la porzione barocca crollata o gravemente danneggiata dal sisma 2009)*

### 3.2 Contatti internazionali

#### 3.2.1 Iniziative a conclusione del progetto IRSES (VII Programma Quadro)

Con i primi mesi del 2013 si chiuderà il Progetto PIRSES (**Building with Environmentally Sustainable Structural Timber**), durato tre anni per lo scambio di ricercatori tra i Dipartimenti del Politecnico di Milano , Università di Stoccarda , Università di Sassari e Università di Christchurch (N.Z.), riguardante gli ambiti di sviluppo di edifici in legno e misti, con il coordinamento della prof.ssa Paola Ronca.

Nell'ambito delle iniziative per l'attuazione di tale progetto (molto comunque limitato, per una sua proficua ricaduta, da regole troppo restrittive ed economicamente insostenibili), l'attività più rilevante della coordinatrice è individuabile attraverso i seguenti prodotti :

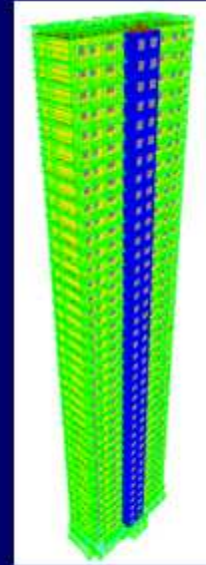
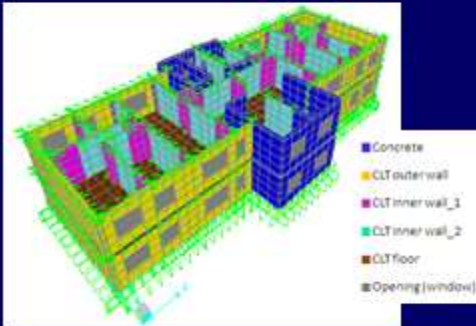
--**A**) Organizzazione del Seminario ad invito presso il MADEexpo – ottobre 2012:

Edifici XLAM  
Multipiano , ecosostenibile e antisismico

Prof. Jan-Willem van de Kuilen

Dove la insostituibile presenza di un “CORE” e solai di piano in **calcestruzzo armato** è condizione necessaria per la funzionalità statica e antisismica di edifici alti con uso diffuso di XLAM.

## Edifici XLAM multipiano, ecosostenibile e antisismico



Prof. Jan-Willem van de Kuilen

January 7, 2013



--B) Collaborazione nell'assistenza per tesisti di Laurea Magistrale e dottorandi con il gruppo di ricercatori dell'Università di Christchurch su strutture per edifici in legno e miste, con particolare riferimento a capacità antisismiche, e la successiva divulgazione per pubblicazione internazionale, di cui le due seguenti, attualmente in fase di scrittura :

*Design investigation technique for HIGH LEVEL PERFORMANCE building subjected to seismic action*

Ronca, Crespi, Bonardi, Palermo Pampanin

*High performance wooden buildings subjected to seismic action*

Ronca, Crespi, Bonardi, Palermo Pampanin

Nella foto il folto gruppo di "Woodenresearches" dell'Università di Canterbury/Christchurch, con cui la collaborazione non terminerà certo alla conclusione del PIRSES.



3.2.2 *Partecipazione comitato organizzativo del 30° Convegno Internazionale IAHS-International Association for Housing Science –Politecnico di Milano – Milano 17/20 sett. 2013 .-150° Politecnico di Milano*

	<p><b>IAHS (International Association for Housing Science)</b> since 1972</p>	
<p><b>Dal 17 al 20 settembre 2013</b> Politecnico di Milano</p> <p><b>XXXIX IAHS World Congress</b> on Housing - Changing Need, Adaptive Buildings, Smart Cities</p>		
<p><b>Contacts</b></p> <p><b>Prof. Emilio PIZZI</b> IAHS 2013 Congress Chair Dean, School of Architectural Engineering Politecnico di Milano</p> <p>E-mail: <a href="mailto:iahs2013@polimi.it">iahs2013@polimi.it</a> IAHS 2013 website: <a href="http://www.iahshousing2013.polimi.it">www.iahshousing2013.polimi.it</a></p>		
<p>HOSTED BY</p> <p><b>POLITECNICO DI MILANO</b> since 1863</p>	<p>With the 150<sup>th</sup> celebration program anniversary since its foundation</p> <p><b>POLITECNICO DI MILANO</b></p> <p><b>150<sup>o</sup></b></p> <p>Share the success of</p> <p><b>BEST DEPARTMENT</b> Building Environment Science and Technology</p>	<p>And with the organizing contribution of</p> <p><b>CIS-E Consortium</b> Consortium per le Costruzioni dell'ingegneria Strutturale in Europa - Consortium for Structural Engineering Construction in Europe Conference administrative, scientific and logistic partner</p>

### 3.2.3 *Iniziative di presentazione della Scuola F.lli Pesenti presso università straniere*

Si è ultimamente avviata la rivisitazione e rifacimento di alcuni “Manifesti” di presentazione della Scuola F.lli Pesenti del sito web , per concretizzare a livello istituzionale la collaborazione con Centri di Ricerca/ Formazione e con Università straniere.

In particolare sono stati presi contatti per possibili scambi di docenti e allievi tra le seguenti Università :

- Pechino
- Abu Dabi
- AAST- Arab Academy for Science and Technology – Cairo, Egypt

Di seguito alcune slides di illustrazione presso tali Università della Scuola Master F.lli Pesenti :

la presentazione completa è sul sito web della Scuola Pesenti :

<http://masterpesenti.stru.polimi.it>



Politecnico di Milano  
Scuola Master Fratelli Pesenti



Italcementi  
Italcementi Group

## PRESENTATION FOCUS ON THE MAIN ACTIVITIES

**Fratelli Pesenti Master School**  
Polytechnic of Milan



## Aims and Mission of the Master School

“From the Spring of Tech-Scientific and Cultural Tradition towards Innovation”

Traditions

### 1. Cultural Background

Italy is a country with excellences in Architecture, either Historic and Modern, as well as in the field of Structural Mechanics and Engineering design. The education in Engineering and Architecture in Polytechnic of Milan University is deeply characterized by these heritages. The Master School F.lli Pesenti was founded at the Polytechnic in 1927 to spread and develop this heritage, as source of innovation.

### 2. Economical Background

Milan is the second-largest city in Italy and the capital of Lombardy. Its urban area is the 5th largest in the Europe. Milan is the main industrial, commercial and financial centre of Italy and a leading global city.

### 3. Geographical Background

Italy's central location in the Mediterranean area, its shape, with large variety of climate and seismic activity, gives actual challenges to Engineers and Architects.



## School Historical facts

### 1927 - Historical date for the University of Engineering

#### (R. Politecnico) Milano



New building at  
Piazza Leonardo da Vinci



Dr. Antonio Fantoli



Dr. Uff. Ing. Cesare Fantoli



Institute of the Foundation **FRATELLI PESENTI** for the insert of the :  
“Specialized School for the Reinforced Concrete Constructions”  
Near the “Institute of Bridges and Great Special Structures”

The Foundation of *F.lli Pesenti* was signed in the presence of the Director of the Polytechnic: **prof. Fantoli**, and in the presence of the family representatives **Gr. Uff. Ing. Cesare Pesenti** and **POn. Antonio Pesenti**.

### In February of 1928 started the first Academic Year.

During the opening ceremony, **prof. ing. Jorini**, (first Director) presented the main program of this Institution:

“(…) Beside aiming at the creation of high-levels scientific culture, necessary for future engineers, we must provide them with proper technical, artistic, economic conditions, so that they can become capable of immediate practical use of this techniques”



prof. ing. F. A. Jorini



Sen. prof. ing. Gaetano Fantoli  
Director of the Polytechnic



## POSTGRADUATE COURSES

Offered Courses A.A. 2012/2013:

DESIGN OF REINFORCED CONCRETE STRUCTURES

➤ ON-SITE + ONLINE SUPPORT

SUSTAINABLE BUILDINGS AND INFRASTRUCTURES

➤ ON-SITE + ONLINE

PROJECT MANAGEMENT OF CIVIL STRUCTURES  
AND INFRASTRUCTURES

➤ ON-SITE + ONLINE

DESIGN AND MANAGEMENT OF STRUCTURAL  
TECHNOLOGIES IN CONSTRUCTION WORKS (I LEVEL)

➤ ON-SITE + ONLINE SUPPORT

DESIGN OF SEISMIC SUSTAINABLE STRUCTURES IN  
CONSTRUCTION WORKS

➤ ON-SITE + ONLINE SUPPORT



## International Master Courses

“New engineering education paradigm”

Practical intelligence  
Analytical intelligence  
Creative intelligence

*“A four/five years engineering curriculum can no longer do the job of training future engineers at the time when new knowledge in science and engineering is exploding...*

*other professions have moved ahead : it now takes nine years to train a doctor, seven years to educate a lawyer, etc”.*

*Deion Hampton, ASCE'S President*

**What about engineers and architects?!**

### 3.2.4 Tirocini collaborativi multidisciplinari ed internazionali

La ricerca di innovazione e sviluppo internazionale nei programmi dei Corsi di Master della Scuola F.lli Pesenti è testimoniata anche dall'evoluzione delle proposte e svolgimento per le attività di internship ricercate e svolte all'estero.

.....

Alcuni esempi di seguito elencati:

#### **Master Scuola Pesenti – a.a. 2010/2011 Stage all'estero**

1. Studente: Jorge Alberto Diaz  
Azienda: Politecnico di Milano – DIS  
Progetto: sviluppo consapevole delle aree metropolitane nella foresta amazzonica - **Brasile**

2. Studente: Silvana Leticia Testoni  
Azienda: Politecnico di Milano – DIS  
Progetto: sviluppo consapevole delle aree metropolitane nella foresta amazzonica – **Brasile**

3. Studente: Anedda Stefano  
Azienda: Impregilo  
Progetto: Ingula Pump Storage Scheme – Ladysmith– **Sudafrica**

4. Studente: Kul Onder  
Azienda: Varyap Varlibaslar Yapi Sanayi ve Turizmyat. Tic. As.  
Progetto: construction site engineer – **Istanbul**

#### **Master Scuola Pesenti – a.a. 2011/2012 Stage all'estero**

1. Studente: Akram Ahmed Daw Balluz (master project management)  
Azienda: Politecnico di Milano – DIS  
Progetto: Rehabilitation and renewal of 2 fevrie Hotel – **Togo**

2. Studente: Fabrizio Bassan (master project management)  
Azienda: Politecnico di Milano – DIS

Progetto: Assistenza direzione lavori – analisi e verifica contabilità di cantiere – verifica avanzamento lavori riguardo a copertura palazzo di giustizia – **Tblisi (Georgia)**

3. Studente: Cappelletti Alessandro (master edifici e infrastrutture)  
Azienda: Urbanism Planning Architecture Italia  
Progetto: la sostenibilità nei paesi mediorientali – **Emirati Arabi Uniti** (trasferta)

4. Studente: Corluhan Seher Ayse (master design and management)  
Azienda: Hakan Kiran Mimarlik ve Yapi Hizmetleri A.S.  
Progetto: sviluppo nuove soluzioni e tecniche – **Turchia**

5. Studente: Costa Enrico (master project management)  
Azienda: Ferretti International  
Progetto: coordinatore ufficio tecnico di cantiere – **Misurata – Libia**

6. Studente: Do Luca (master project management)  
Azienda: Salini  
Progetto: construction of Tokwe – **Mukorsi Dam – Zimbabwe**

7. Passaghe Maria Giovanna (master edifici e infrastrutture sostenibili)  
Azienda: Buro Happold Engineers Limited  
Progetto: partecipazione alla ricerca ed applicazione di soluzioni caratterizzate da elevata sostenibilità energetica ed ambientale per progetti e ricerche del team sostenibilità con approfondimento sistemi di certificazione ambientale (es. LEED) – **Londra**

8. Studente: Pau Stefania (master edifici e infrastrutture sostenibili)  
Azienda: Evolve  
Progetto: progetto relativo alla sostenibilità – **Bellinzona**

9. Studente: Sulis Silvia (master progettazione delle strutture in c.a.)  
Azienda: S.P.S. Srl Studio Progetti Strutturali  
Progetto: assistenza alla progettazione strutturale – **Vienna** (trasferta)

10. Studente: Tunaboylu Erbil (master design and management)  
Azienda: Ozcem Construction Company  
Progetto: progetto relativo al settore architettura/design – **Istanbul**

11. Studente: Karagulle Sinem (master design and management)  
Azienda: DBArchitects  
Progetto: progetto relativo al settore architettura/design – **Istanbul**





ISBN 978-88-904292-6-2



9 788890 429262

**Euro 40,00**